ON THE SYNTHESIS, MEASUREMENT AND APPLICATIONS OF SOLAR ENERGY MATERIALS AND DEVICES

A thesis submitted to The University of Manchester for the degree of

Doctor of Philosophy

in the Faculty of Engineering and Physical Sciences

Punarja Kevin

School of Chemistry

2016

TABLE OF CONTENTS

Word count: 59,769 **Page count**: 280

LIST OF FIGURES

LIST OF SCHEMES

LIST OF TABLES

ABSTRACT

Punarja Kevin

January 2016

"**On the Synthesis, measurement and applications of solar energy materials and devices**": A thesis submitted to **The University of Manchester** for the degree of **Doctor of Philosophy** in the **Faculty of Engineering and Physical Sciences**.

Second generation solar cells based on thin film semiconductors emerged as a result of the past ten years of intense research in the thin film preparation technology. Thin film solar cell technology can be cost effective as it uses comparatively cheap materials suitable for solar building integration. Chemical Vapour Deposition (CVD) is a well-known method for the deposition of high quality thin films.

This thesis describes the synthesis of novel tin(II)dithiocarbamate [$Sn(S_2CNEt_2)_2$] and bis(diphenylphosphinediselenoato) tin(II) [$Sn(Ph_2PSe_2)_2$] and these complexes as single source precursor for the deposition of SnS and SnSe and by using the combination of [$Sn(Ph_2PSe_2)_2$] with [$Cu(acac)_2$], Cu_2SnSe_3 thin films were deposited by AACVD. By using suitable combinations of metal complexes ([$^nBu_2Sn(S_2CNEt_2)_2$], [$Cu(S_2CNEt_2)_2$] [$Zn(S_2CNEt_2)_2$] [$Zn(Se_2CNEt_2)_2$] [$Zn(acac)_2$], [$Sn(OAc)_4$], [$Cu(PPh_3)\{Ph_2P(Se)NP(Se)Ph_2\}$] thin films and nanocomposites of CZTS, CFTS, CZTSe, CFTSe, CZFTS, , CZFTSe, CZTSSE, CFTSSe and CZFTSSe were prepared. The effect of precursor concentration and deposition temperature on the structure, morphology and composition of the thin films were studied in detail using by powder X-ray diffraction (p-XRD), scanning electron microscopy (SEM), energy dispersive X-ray spectroscopy (EDX), transmission electron microscopy (TEM), selected area electron diffraction (SAED) and elemental mapping. This thesis addressing the structural inhomogeneity, control of growth and material characterization is expected to yield closer performance parity between CZTS–Se and CIGS solar cells. A series of systematic experiments were carried out. Through AACVD and simple solvothermal methods CZFTS nanoparticles and thin films were prepared. The simple, potentially, low-cost nature of the CZTS nanoparticles and the enhancement of charge carrier mobility achieved suggest that these nanoparticles have potential in the improvement of OFETs and perhaps other organic electronic devices.

DECLARATION

No portion of the work credited to the author in this thesis has been submitted in support of an application for another degree or qualification of this or any other university or institute of learning.

Punarja Kevin

COPYRIGHT STATEMENT

ACKNOWLEDGMENTS

Firstly I would like to thank Professor Paul O'Brien for encouraging me to pursue a PhD and in particular for his recommendation that I consider working in the Solar Energy Material Group here in Manchester.

A great number of people have helped contribute to my work and I am indebted to them without which my synthesis would be redundant. I thank Dr. Azad M. Malik and Dr. David. J. Lewis for their support in parts of my project and also to Professor Bruce Hamilton who kindly gave support for physical measurements of the developed films. All technical staff in School of Chemistry and Materials in the University of Manchester who gave training and support in characterization techniques especially Dr. Jim Raftery, Dr. Chris Muryn, Matthew Smith, Gary Harrison, Dr. Christopher Wilkins, Michael Faulkner and Xiang Li Hong. I am very pleased to give thanks to Prof. Peter Skabara and his group of West CHEM, Department of Pure and Applied Chemistry, University of Strathclyde for their great support in making devices and testing there. Pretty much all group members past and present have helped in some way and to them I am grateful.

Finally thanks to my husband Mr. Kevin D. Miranda and my parents for their never failing support and encouragement. Above all my humble gratitude to Almighty God for thy blessings, grace and support throughout my life

LIST OF ABBREIVATIONS

AACVD	aerosol-assisted chemical vapour deposition
acac	aceylacetonate
ALD	atomic layer deposition
bcc	body-centered cubic
ca	circa
CBD	chemical bath deposition
CBM	conduction band minimum
CVD	chemical vapour deposition
DCM	dichloromethane
DDT	dichlorodiphenyltrichloroethane
dedtc	diethyldithiocarbamate
eg	exempli gratia
EDX	energy dispersive x-ray spectroscopy
Eg	bandgap
EPR	electron paramagnetic resonance
Et	ethyl
et al	et alia
etc	et cetra
eV	electron volt
FC	field cooling
fcc	face-centered cubic
FEG	field emission gun
FFT	fast fourier transform
GC	gas chromatography
HWCVD	hot wire chemical vapour deposition
ICDD	international center for diffraction data
*i*Pr	isopropyl
K	Kelvin
KeV	kilo electron volt
KS	kesterite
LED	light-emitting diode
LPCVD	low-pressure chemical vapour deposition

MBE	molecular beam epitaxy
Me	methyl
mL	milli liter
mmol	milli mole
MOCVD	metal organic chemical vapour deposition
mpt	melting point
MS	mass spectroscopy
*n*Bu	normal butyl
NC	nanocrystals
nm	nanometers
NMR	nuclear magnetic resonance
*n*Pr	normal propyl
OAc	acetate
Oam	oleylamine
OFETs	organic field- effect transistors
P3HT	poly(3-hexylthiophene)
PC	powder crystal
Ph	phenyl
PVD	physical vapour deposition
p-XRD	powder X-ray diffraction
QD	quantum dots
RTCVD	rapid thermal chemical vapour deposition
SAED	selected area electron diffraction
SC	single crystal
SEM	scanning electron microscopy
SQUID	super-conducting quantum interference device
SSP	single source precursors
ST	stannite
TEM	transmission electron microscopy
TF	thin film
TGA	thermogravimetry analysis
THF	tetrahydrofuran
TTF	tetrathiafulvalene
TMS	tetramethylsilane

TOP	trioctylphosphine
UV/Vis	ultra violet/ visible
VBM	valence band maximum
XANES	x-ray absorption near edge structure
ZFC	zero field cooling

LIST OF SYMBOLS AND CONSTANTS

θ	angle of incidece
Å	Angstrom
I	angular momentum quantum number
Eg	band gap
μB	Bohr magneton
k	Boltmann constant
Z	charge
μ	chemical potential
δ	chemical shift
d	distance
eV	electron volt
ε	energy
FT	Fourier transform
J	isotropic exchange parameter
B	magnetic field
H	magnetic field
m	magnetic quantum number (orbital angular momentum)
χ	magnetic susceptibility
M	magnetisation
m	mass
A	molar absorption coefficient
X	mole fraction
S	net spin (resultant spin existing on a defined moiety)
I	nuclear angular momentum
M	nuclear magnetic moment

h	Planck's constant
n	population
$f(\varepsilon)$	probability of a state
K	pseudocontact shift parameter
R	residual factor
Ω	resistance
Rwp	Rietveld parameter
m_s	spin projection quantum number
s	spin quantum number (single ion spin)
∑	sum of
T	temperature
λ	wavelength
wR2	weighted residual factor
D	zero-field splitting parameter

For the purpose of the thesis, many compounds have been given an abbreviated notation. The notation obeys the following rules: They are contained within braces { }, to differentiate them from actual chemical formulae which are generally contained within square brackets [ ] in the order of the metal followed by the ligands. The oxidation states are shown as in Roman numerals, so tin in the oxidation state plus two is written: Sn(II) or as superscript Sn^{2+}.

CHAPTER - I

Introduction

1.1. Rationale for submitting the thesis in an alternative format

The thesis author has been fortunate in being able to publish her results in peer reviewed journals as communications and articles as results have been gained. Timely publication of results is especially critical in the field for several reasons. Firstly the work is largely interdisciplinary, the research is directed through discussions with other chemists, theorists and physicists and so getting up-to-date research into the public domain is of importance. Secondly the research is equipment expensive. Access to expensive and sought after national facilities is dependent on quality research, invariably demonstrated by publications in high level journals. The same is true in the pursuit of new funding sources from bodies such as the EPSRC. It has therefore been necessary, and preferable, to publish during the course of the author's PhD studies. The published papers cover all of the aspects of the author's work and so are deemed suitable for submission as a part of this thesis.

1.2. Organisation of the thesis

Chapter I provides preface to the thesis, and describes the contribution the author has made to the published material. Chapter II describes the context of the research. Chapter III reviews the work done in the field to-date. Chapters IV to XIV contain peer-reviewed publications and manuscripts of preparation. Chapter XV consists of a summary of the work undertaken and provides an outlook for future study. Chapter XVI contains references which are cited outside of chapters five to ifteen. Appended I details the methodology employed during the research. Appended II Review paper, entitled "Routes to tin chalcogenide materials as thin films or nanoparticles: a potentially important class of semiconductor for sustainable solar energy conversion"

1.3.Contributing authors

Chapter IV, Paper 1, entitled "Thin films of tin(II) sulfide (SnS) by aerosol-assisted chemical vapour deposition (AACVD) using tin(II) dithiocarbamates as single-source precursors" is a full paper written by the thesis author with contributions from Mohammad Azad Malik. Synthesis was performed principally by the thesis author. X-ray crystallography was performed principally by the thesis author with contributions from

James Raftery. P-XRD, SEM, EDX analysis was carried out by the author and PL measurements were carried out principally by the author with the help of David J. Lewis.

Chapter V, Paper 2 entitled "The aerosol assisted chemical vapour deposition of SnSe and Cu_2SnSe_3 thin films from molecular precursors" is a communication written by the thesis author. The precursor synthesis was principally carried out by the author with contributions from Sajid. N. Malik.

Chapter VI, Paper 3 entitled "Composition Focusing in the Deposition of Copper Zinc Tin Sulfide (CZTS) by AACVD" is a draft paper written by the thesis author. The cell fabrication was carried out principally by the author with the contribution from Saif Haque of Imperial College. The resistance measurements were carried out by Ian Hashworth and Bruce Hamilton. The PV measurements were carried out principally by the author with help of Eric Whittaker and Bruce Hamilton from the School of Electrical and Electonic Engineering.

Chapter VII, Paper 4 entitled "Growth of $Cu_2ZnSnSe_4$ and $Cu_2FeSnSe_4$ thin films by AACVD from molecular precursors" is a full paper written by the thesis author. The precursor synthesis was carried out principally by the author with contributions from Sajid N.Malik and M. A. Malik.

Chapter VIII, Paper 5 entitled "The AACVD of $Cu_2FeSn(S_xSe_{1-x})_4$: potential environmentally benign solar cell materials" principally written by the thesis author with contribution from M. A. Malik on the selenium precursor synthesis.

Chapter IX, Paper 6 entitled "The controlled deposition of $Cu_2(Zn_yFe_{1-y})SnS_4$, $Cu_2(Zn_yFe_{1-y})SnSe_4$ and $Cu_2(Zn_yFe_{1-y})Sn(S_xSe_{1-x})_4$ thin films by AACVD: potential solar cell materials based on earth abundant elements" is a full article written by the thesis author. The p-XRD calculations were principally carried out by the author with the help of Paul O'Brien. TEM elemental map was carried out principally by the author with the help of Matthew Smith.

Chapter X, Paper 7 entitled "Morphology and band gap controlled AACVD of CdSe and CdS_xSe_{1-x} thin films using novel single source precursors: *Bis*(diethyldithio /diselenocarbamato) cadmium(II)" is a full paper principally written by the author. The precursor synthesis was principally carried out by thesis author with minor contribution from M. A. Malik. The PL measurements were taken by the author with contribution from D. J. Lewis.

Chapter XI, Paper 8 entitled "The deposition of $Cu_2ZnSnS_{(1-x)}Se_x$ thin films with tunable band gaps" is a full article written by the author with contributions from Paul O'Brien. The precursor complexes principally synthesised by the author with contribution from M. A. Malik. Rietveld refinement carried out principally by the author with contributions from Gary Harrison.

Chapter XII, Paper 9 entitled "Synthesis of Nanoparticulate Alloys of the Composition $Cu_2Zn_{1-x}Fe_xSnS_4$: Structural, Optical, and Magnetic Properties" is a communication written by the thesis author. SQUID measurements were carried out by Simon Mcadams. The crystal phase analysis was carried out by the author with contributions from Paul O'Brien.

Chapter XIII, Paper 10 entitled "Stannite Cu_2FeSnS_4 nanoparticles for solar energy applications" is a full draft written by the thesis author. Magnetic measurements were taken by Simon Mcadams and TEM characterisation was principally carried out by the author with contribution from Xiang Li Hong.

Chapter XIV, Paper 11 entitled "Nanoparticles of Cu_2ZnSnS_4 Performance Enhancing Additives in Organic Field-Effect Transistors" is a full article with the parts concerning quantum dots written by the thesis author with device fabrication and characteristics part contributed by Joseph Cameron, Rupert G. D. Taylor, Neil J. Findlay, Anto R. Inigo and Peter J. Skabara of the University of Strathclyde.

CHAPTER - II

Introduction to the Field of Study

The main focus of this chapter is to give a brief introduction to semiconducting materials, band energy diagrams, band gap tuning and kesterite and stannite materials. A comparison of reported solar cell efficiencies of kesterite and stannite materials is recorded in the form of a table. This chapter includes an overview of solar cells developed during past few years using semiconducting materials with their function, advantages and disadvantages. The types of precursors used for the deposition of thin films and nanoparticles with techniques used for the deposition of thin films and nanoparticles are presented in detail.

2.1 Semiconductors and Semiconducting materials

Semiconductors are generally categorised as small band gap insulators. The term "semiconductor for this class of materials arise from the fact that the conductivity values of these materials lies in between that of conductors (10^{4}-10^{-8} Ω cm^{-1}) and insulators (less than 10^{-8} Ω cm^{-1}) eg. Ge and Si. Semiconductors are widely used in most electronic and technologically important devices.

2.1.1. Band structure

Atomic orbitals combine to form molecular orbitals. When two atomic orbitals combine, two molecular orbitals result. One molecular orbital is formed with the sum of energies lower than the relative energies of the individual atomic orbitals; they are referred to as the 'bonding' orbital. The other molecular orbital is formed with the sum of energies higher than the relative energies of the individual atomic orbitals and is termed the 'anti-bonding' orbital. If 'N' valence electron atomic orbitals with the same energy combine, 'N' possible molecular orbitals will result; 'N/2' will be lowered in energy and 'N/2' with higher energy with respect to the sum of the energies of the combined atomic orbitals. The 'bonding' band is called the **valence band (VB)** and the 'anti-bonding' band is called the **conduction band (CB)** and the gap between them is called the band gap. The electrons of a single free-standing atom occupy atomic orbitals, which form a discrete set of energy levels. When a large number of atoms (about 1020 or more) are combined together to form a solid, the number of orbitals becomes exceedingly large, and the difference in energy between them becomes very small, so the levels may be considered to form continuous bands of energy rather than discrete energy levels. However, some intervals of energy contain no orbitals, no matter how many atoms are aggregated, forming a 'band gap'. Like atomic orbitals, each

molecular orbital can contain at most two electrons of opposite spin. Metals contain a band that is partly filled and partly empty regardless of temperature; therefore they are highly conductive. In case of insulators and semiconductors the valence band is fully occupied and the conduction band is almost unoccupied. Only when electrons are excited to the conduction band from the valence band, can current flow in these materials. The main difference between

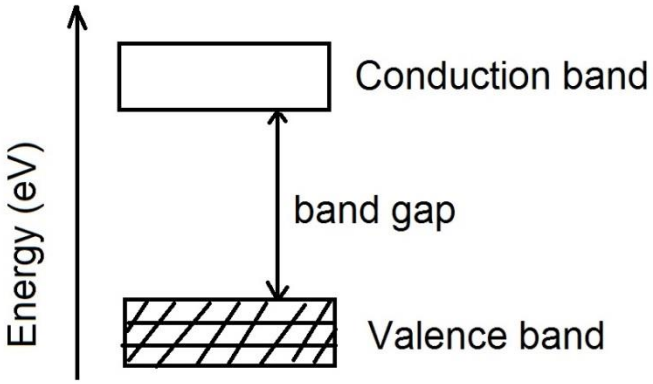

Figure 1: Schematic representation of energy bands in an insulator or semiconductor.

Insulators and semiconductors is that the bandgap between the valence band and conduction band is larger in an insulator (band gap of semiconductors eg: Si-1.09 eV, Ge-0.67 eV and 1.43 eV for GaAs band gap for insulators eg: diamond is 5.5 eV and SiO_2 is 9 eV). The band gap of the insulator and undoped semiconducting materials are depicted schematically in Figure 1.

The energy of electrons cannot lie outside these bands. Electrons can be promoted from one band to another by the absorption of photons with sufficient energy. Generally, materials with a band gap above 3 eV are considered as insulators and those with a band gap below 3 eV are considered as semiconductors, because the thermal energy at 300 K is not sufficient enough to allow the movement of electrons from the valence band to conduction band. As a result, such materials have fully filled valence band and an empty conduction band.

According to the Fermi-Dirac distribution, electrons and protons are considered as fermions which have charge, mass and additionally have half–integer spin. The Pauli exclusion principle states that no two fermions or electrons can have the same set of quantum

numbers. Hence, for two electrons within same orbital have one electron spin up and the other spin down.

Statistically, the distribution of fermions/electrons in the available energy levels is according to the Fermi-Dirac distribution:

$$f(\varepsilon) = 1/\exp\{(E-\mu)/KT)\} + 1 \quad \text{..... Eq. 1}$$

Where, $f(\varepsilon)$ is the occupation probability of a state of energy ε, K is Boltzmann's constant, μ is the chemical potential, and T is the temperature in Kelvin.

The distribution describes the probability for a quantum state of energy E being occupied at a particular temperature T. Thermodynamic properties can be calculated by knowing the energies of the available electron states and the degeneracy of the states. At absolute zero the value of the chemical potential, μ, is defined as the **Fermi energy**. At room temperature, the chemical potential for metals is virtually the same as the Fermi energy. For a pure undoped semiconductor at finite temperature, the chemical potential always lies halfway between the valence band and the conduction band.

On increasing temperature, or by absorbing photons of sufficient energy, electrons can be excited to the conduction band from the valence band, creating an electron-hole pair. By the application of an applied electric field, the electron in the conduction band can gain momentum therefore an overall movement of charge which creates an imbalance in positive and negative momentum and results in an electric current. The principle behind semiconductor optical devices such as light-emitting diodes (LEDs) is the creation of an electron-hole pair which recombines when the electron drops into the valence band, leading to emission of energy as a photon.

2.1.2. Intrinsic and extrinsic semiconductors

Structurally atoms in semiconductors share all the four valence electrons tetrahedrally with each other by simple covalent bonds. Therefore, at room temperature a few electrons gain enough energy to break the attractive force and jump from the valence shell by creating a vacancy, called ‘hole’ which is considered as a positive charge. These electrons and holes move in an electric field contribute to electrical conduction, known as intrinsic semiconductors.

The conductivity of a semiconductor material can be improved by the addition of elements with either three (trivalent) or five (pentavalent) valence electrons by a process called doping and the semiconductors obtained upon doping are called extrinsic semiconductors. Depending on the type of impurity added extrinsic semiconductors are classified into n-type when the added impurity is a pentavalent element and p-type if the impurity is a trivalent element.

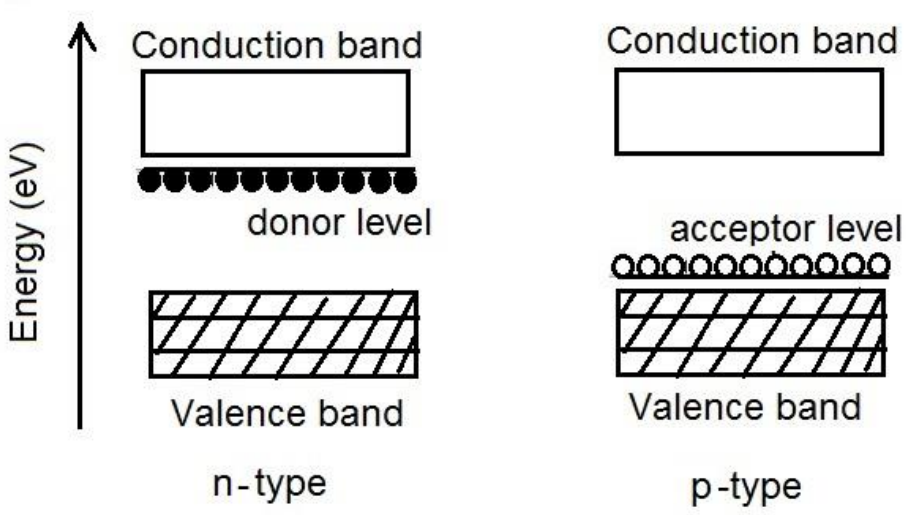

Figure 2: Schematic representation of n-type (left) and p-type (right) semiconductors.

Semiconductors formed by the addition of pentavalent donor atoms such as P and As in place of the tetravalent element in the lattice bring an extra free electron to the valence shell which in turn increases the conductivity. These electrons are called 'majority current carriers'. These extra electrons make an additional donor level ~0.01 eV just below the bottom of the conduction band hence increase the conduction (Figure 2). Whereas, the addition of trivalent donor atoms such as B and Al to replace the tetravalent element in the lattice results in the formation of an extra hole in the crystal lattice. The conductivity of these materials is improved due to the presence of these holes in the lattice, which are called predominant or majority current carriers. These holes create an acceptor level of ~0.01 eV just above the valence band and hence increase the conduction (Figure 2).

2.1.3. Direct and indirect band gap semiconductors

In a **Direct band gap semiconductor** the valence band maximum (VBM) and the conduction band minimum (CBM) occurs with the same value of electron momentum. Whereas, in an **Indirect band gap semiconductor** on the other hand, VBM and CBM

occur at a different value of momentum. It is easy to produce an electron-hole pair in a direct band gap semiconductor, where the band gap energy, E_g equal to the photon energy as there is no need to give extra momentum for the electron excitation. Whereas, in an indirect band gap semiconductor, to produce an electron-hole pair, the electron needs to give an extra momentum for its excitation along with the photon energy.

2.1.4. Nanosized Semiconductor

Semiconductor materials can be classified into three types,

(i) Bulk inorganic semiconductors
(ii) Inorganic semiconductor nanocrystal and
(iii)Molecular semiconductors

Semiconductor nanocrystals (NCs) are tiny light-emitting particles on the nanometer scale. When the diameter of the nanocrystal material is smaller than the exciton Bohr radius (typically; 1 to 10 nm) such NCs are termed quantum dots (QDs). The properties of QDs are mainly determined by size effects; hence the size-controlled synthesis of colloidal QDs has become one of the main focuses of research over past two decades. Semiconducting materials are characterised by their direct or indirect band structures or band gap energy (E_g). Materials with band gap energy in the range of 0 to 4 eV are of more interest, as they require a minimum amount of energy to excite electrons from the VBM to CBM. [1-3]

The band structures can be further modified and shifted to blue or can tune the light emission from these particles throughout the ultraviolet, visible, near-infrared, and mid-infrared spectral ranges by the quantum confinement effect which leads to spatial enclosure of the electronic charge carriers within the nanocrystal, which can be achieved [1-5] via making one dimension of the semiconducting material less than its Bohr exciton radius. In the semiconducting NCs, the quantized levels can be seen as discrete levels, whereas as a continuous band in case of bulk materials (Figure 3). Hence, tuning the size of the NCs leads to the fine-tuning of the band gap and is useful in controlling the optical and electrical properties of such materials. Apart from size-effects, the physical and chemical properties highly depend on composition, structure, shape and surface chemistry, which make them very attractive for uses in many applications. [6–9]

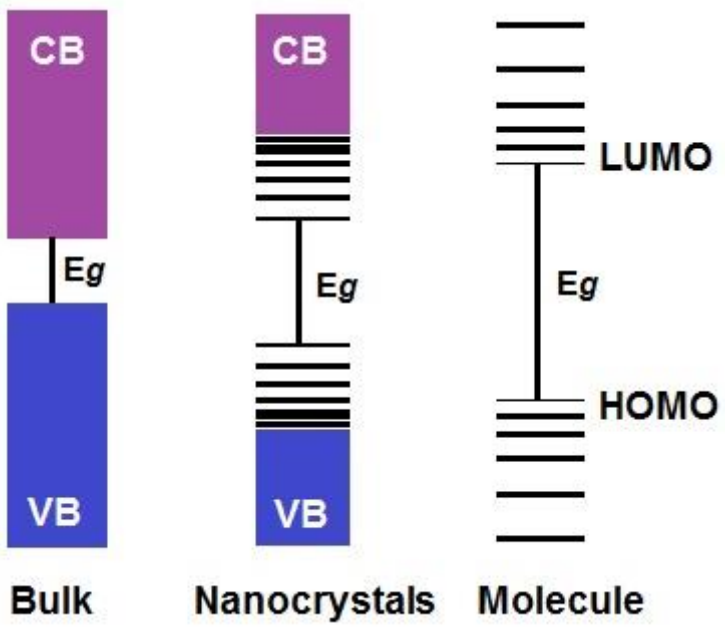

Figure 3: Schematic representation of the electronic energy states of bulk, nanocrystals and molecular semiconducting materials.

2.1.5. Compound semiconductors

In addition to Group IV elements, compounds of Group III and Group V elements and compounds of Group II and Group VI elements are often used as semiconductors. All of these materials have an average of 4 valence electrons. In a semiconductor such as GaAs, doping can be accomplished by slightly varying the stoichiometry. A slight increase in the proportion of As produces *n*-type doping, and a slight increase in the proportion of Ga produces *p*-type doping.

Starting from the II-VI parent several binary, ternary and multinary semiconducting materials can be derived. Figure 4 shows a number of semiconducting materials derived from parent II-VI semiconductor by cation mutation; one of the Group II cations can be replaced by one Group III (I-III-VI) or by replacing two Group III atoms by one Group II and one Group IV atom (I_2–II–IV–VI_4) compound, or by replacing two Group II atoms by one Group I atom and one Group III (–III–II_2–VI_4); or by replacing half of the Group II atom by another Group II atoms (I_2–II–II-III-VI_4). By controlling the atomic ratios, through the mutation process one can perform band engineering to tailor the material properties for a specific application. There are many possible compositions allowed in each category hence proper screening and studies are required to find the suitable composition. [11] This family of materials can be tuned to obtain suitable band gaps optimal for solar cells, [12] spintronics, [13] thermoelectrics [14] and new classes of topological insulators. [15]

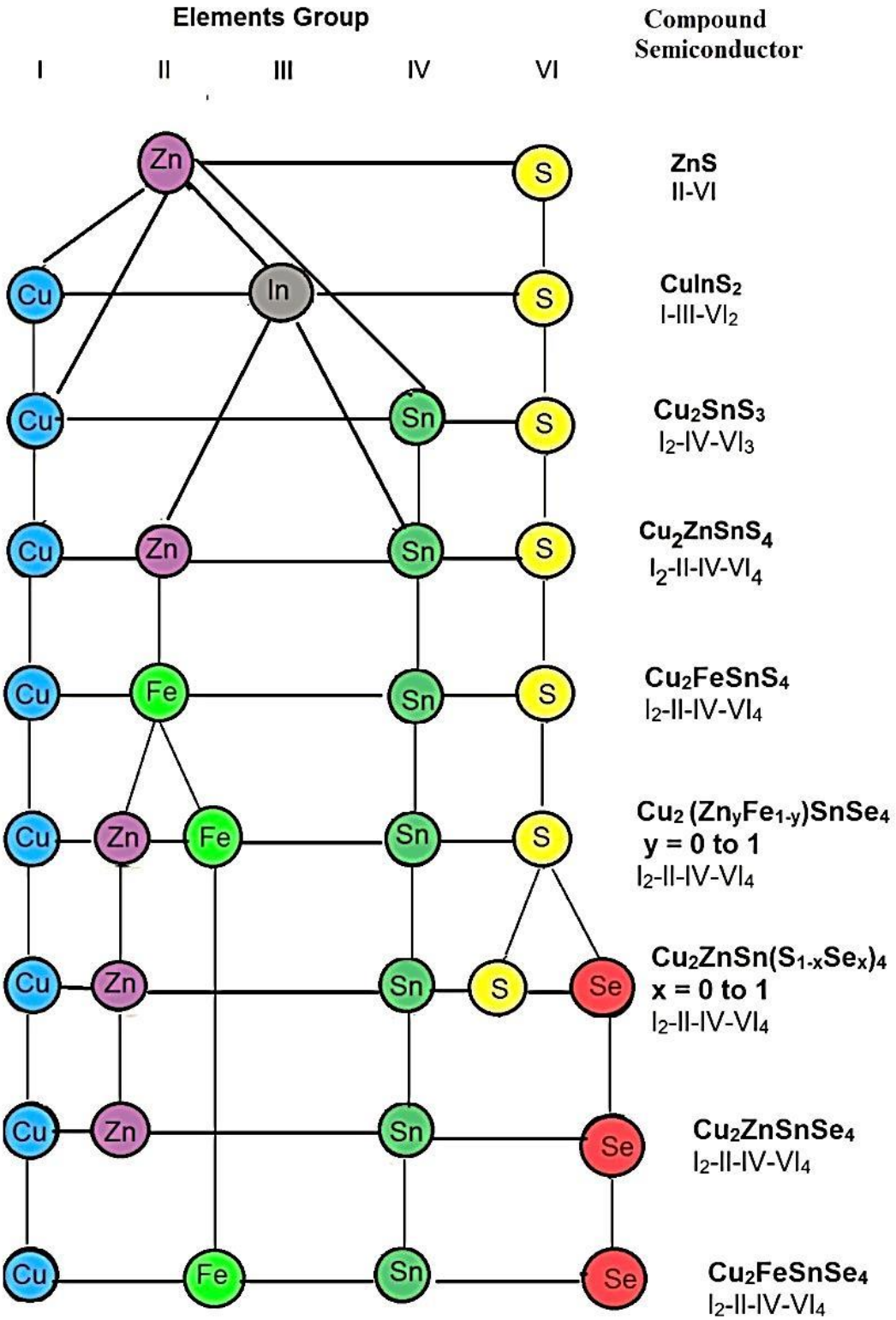

Figure 4: Schematic representation of the structure development tree for the formation of binary, ternary and multinary semiconductors starting from II–VI parent compound.

2.2. Band structures of semiconductor NCs

2.2.1. Tin(II) Sulfide and Tin(IV) Sulfide

SnS shows lowest binding energies and ionisation potentials among metal chalcogenides, because of its co-ordination environment and the level of repulsion between orbitals. [16] The binding energy of Sn $5s^2$ orbitals is considerably lower compared to other metal orbitals. The structure of SnS is

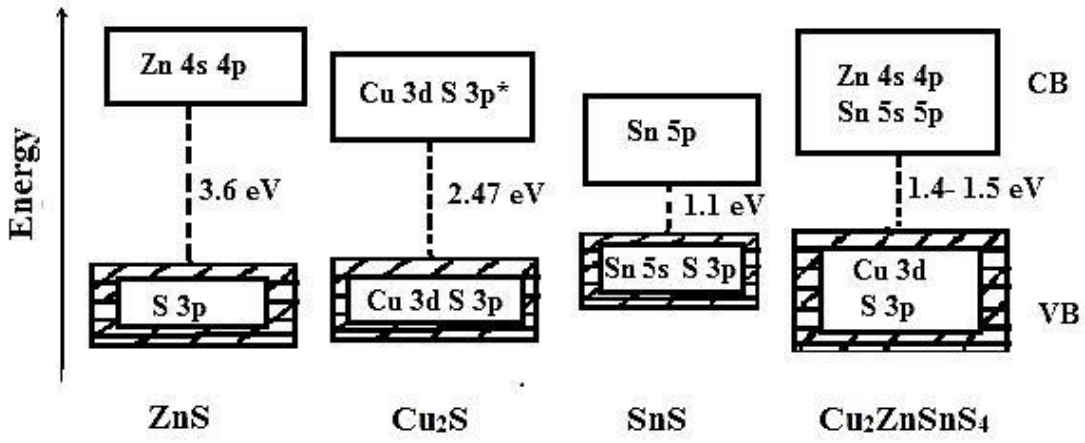

Figure 5: Band gap energies of ZnS, Cu_2S, SnS and Cu_2ZnSnS_4. [19-33]

similar to that of rocksalt with a distorted octahedral structure and different types of bond lengths due to the sterochemically active lone pair in its valence shell. [17] There are three short (ca. 2.6Å) and three long (ca. 3.2 Å) Sn-S bonds due to different cation environments. [17] SnS materials show an indirect band gap of 1.1 eV. [20, 21] In SnS the VB is formed by the interaction of antibonding Sn 5s and S 3p orbitals and conduction band is formed by the 5s orbitals (Figure 5). [18-21] The band gap values are also close to those found for quaternary Cu_2ZnSnS_4 and related selenide materials. [18, 22-25] In contrast, the ionisation potential of Sn related of $CuInSe_2$ has been reported as 5.7 eV. [22, 24]

In this lower oxidation state of Sn (i.e., II), the $5s^2$ orbitals are formally occupied, with the CB formed from the empty 5p band as shown in Figure 5. The interaction of Sn 5s and S 3p results in antibonding states at the top of the VB. [16] The ionisation potential of SnS is lower than other metal-chalcogenide semiconductors [16] due to the coordination environment, level of repulsion and low binding energy of Sn $5s^2$ orbitals. [27] In case of Sn (IV) sulfides, according to the first approximation, the lowest level of the CB is formed of Sn 5s states and the rest of the CB formed of Sn 5p states with a significant contribution

from S p_x, p_y orbitals but no contribution from p_z orbitals. The VBM is formed from symmetric p orbital contribution from S. [19] Optical absorption measurements SnS_2 showed an indirect gap of ~ 2.2 eV. [19, 26]

2.2.2. Band structure of Zinc Sulfide (ZnS)

The VB mainly formed from the 3p orbitals of S atom and the 4s and 4p orbitals of Zn atoms mainly contribute to CB in ZnS. The energy gap between the VB and CBM in ZnS is 3.6 eV. [28] The hybridization of the Zn d states with the S p states as well as with the S d states is quite strong. The overlap of S 3p and Zn 4s orbitals in the VB and CB indicates a mixed ionic–covalent bonding character (Figure 5). [29] ZnS materials show a direct band gap of 3.5 eV, close to the experimental band gap reported in literature (3.6 eV). [30]

2.2.3. Band structure of CuS and Cu_2S

The VB is composed of Cu 3d and S 3p hybridised orbitals and the CB is formed by the Cu 3d (e_g) orbitals. On top of the CB the hybridised orbitals of S 3p and Cu 3d (t_{2g}) orbital. The band gap of Cu_2S materials is found to be around 2.47 eV (Figure 5) and the CuS is about 1.26 eV but the band gap values vary because of the different stoichiometric composition of Cu_xS. [31] It can be seen that the Cu_2S nanostructures shows the p-type conduction and the CuS nanostructures shows n-type conduction. [31, 32]

2.2.4. Band structure of Cu_2ZnSnS_4 (CZTS), $Cu_2ZnSnSe_4$ (CZTSe) and $Cu_2ZnSn(S_{1-x}Se_x)_4$ (CZTSSe) alloys

The CZTS structure is similar to ZnS but its band gap (~1.5 eV) is closer to that of Cu_2S. [33-35] In Cu based chalcogenides the VBM is formed by the antibonding p orbitals of the anion (S/Se) and the Cu 3d orbitals. In CZTS, the CBM is mainly formed of Sn 5s and S 3p* states and no contribution from Zn 4s orbitals, as the atomic energy of Zn 4s is higher than that of Sn 5s. The VBM is formed by the overlap of Cu 3d and S 3p orbitals (above 2 eV). The experimental and gap of CZTS is between 0.1 to 2 eV (Figure 6). [36] Studies showed that the band gap of Cu_2ZnGeS_4 and Cu_2ZnSiS_4 is larger than that of CZTS as the Sn in CZTS is replaced with Ge or Si. [37, 38] The lowering of band gap from CZTS to CZTSe was studied using computational methods. [11, 39, 40] The valence band is higher

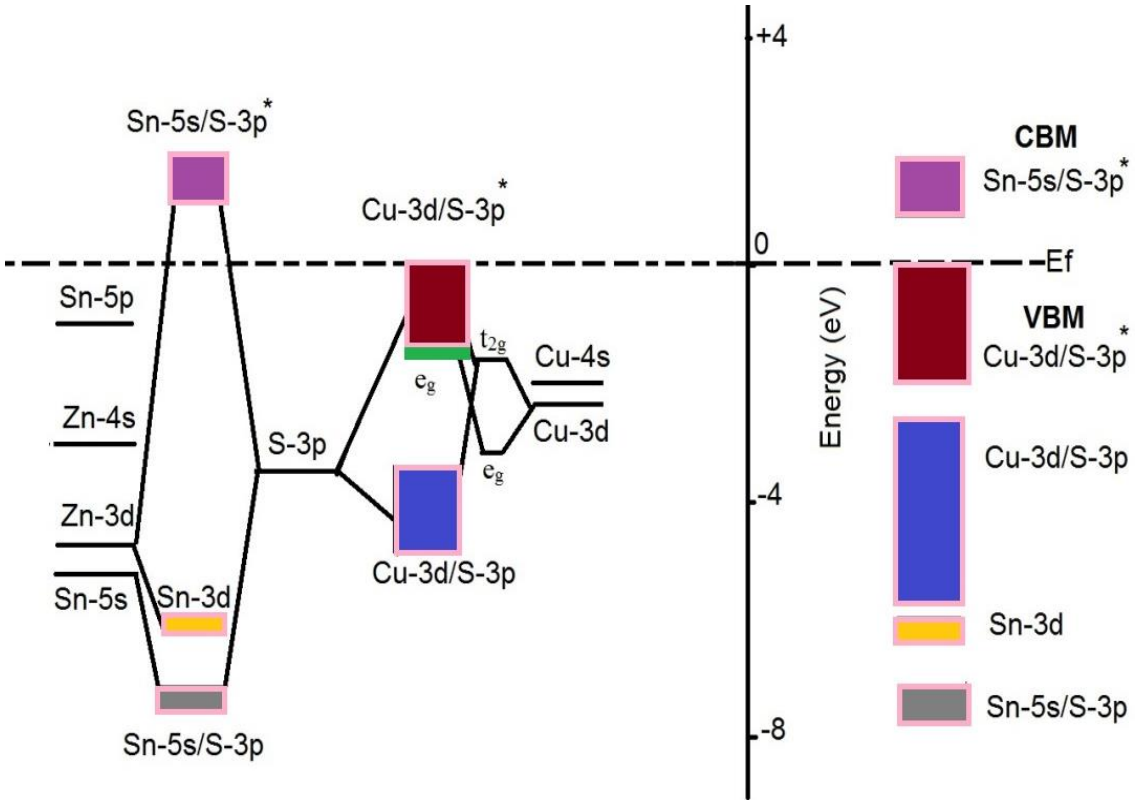

Figure 6: MO diagram and band gap of Cu_2ZnSnS_4 quaternary system. [36]

and the conduction band is lower in CZTSe compared to CZTS, which shows both the electron and hole states mainly localized on CZTSe rather than CZTS when an interface is made between them. The band gap of these alloys depends on the CBM and VBM. The S p level is lower than Se p, thus the VBM of the sulfides is lower than that of the selenides; as an example the VBM of ZnS is 0.52 eV lower than that of ZnSe. [41]. A contradictory phenomenon is found in Cu based chalcogenides; there is no large difference in the band gap as expected due to p-d hybridization. The hybridization is stronger in shorter bonds. The Cu-S bond is shorter than the Cu-Se bond hence it pushes the antibonding VBM level up compared to that of the Cu-Se bond. Because of these factors, the band gap between CZTS and CZTSe is reduced to 0.15 eV only (Figure 7).

A similar reduction in band gap is seen in other Cu based chalcogenide pairs such as $CuGaS_2$, $CuGaSe_2$, $CuInS_2$ and $CuInSe_2$ (Figure 7). In addition to that, the CBM of CZTS and CZTSe is formed by the antibonding state of the anion s orbital and Sn 5s orbitals. The energy of the s orbital of S is lower than that of Se (~0.2 eV), but because of the shorter bond length of Sn-S makes the level of repulsion between Sn and S stronger in CZTS compared to CZTSe. Therefore, CBM moves up in CZTSe compared to that of CZTS. As a result, in $Cu_2ZnSn(S_{1-x}Se_x)_4$ alloy the conduction band offset (~0.35 eV) is larger than the

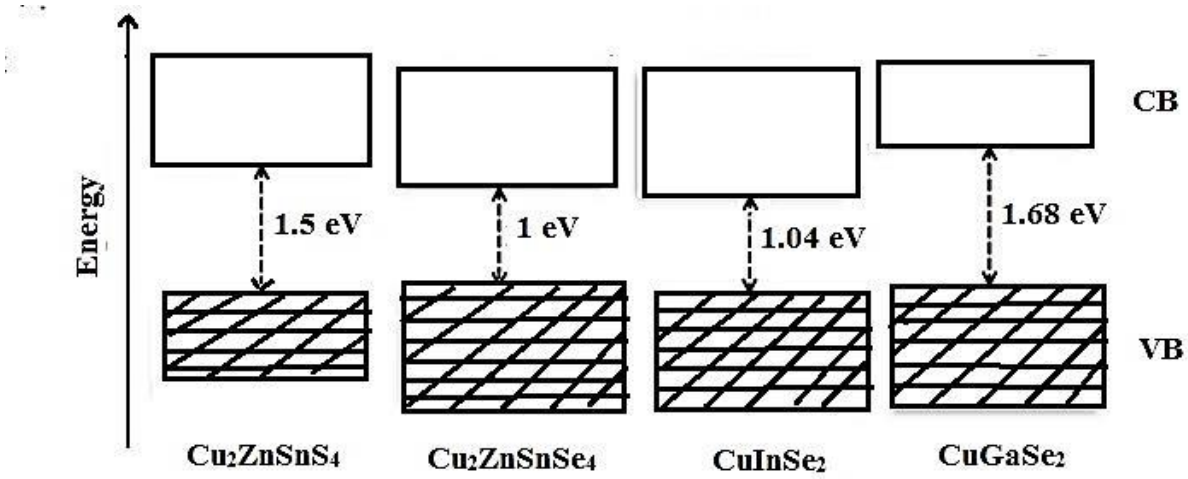

Figure 7: The band alignment between Cu_2ZnSnS_4, $Cu_2ZnSnSe_4$, $CuInSe_2$, and $CuGaSe_2$ (including the effects of spin-orbit coupling). [37-42]

valence band offset (0.15 eV) therefore, as the Se content increases, the CBM downshift plays a more important role than the VBM upshift which in turn leads to a reduction in the band gap. Thus varying the composition of x (Se) the CBM downshift and VBM uplift plays the role in band gap tuning. Calculations of the absorption spectrum agree well with this energy shift. [42] The optical absorption spectra of $Cu_2ZnSn(S_{1-x}Se_x)_4$ alloys show a linear shift of the band edge states as a function of the composition x, the absorption the spectra shift to the lower energy side as the band gap decreases.

2.2.5. Band structure of Cu_2FeSnS_4 (CFTS) and $Cu_2Zn_{1-x}Fe_xSnS_4$ (CZFTS) alloys

The Cu-Fe alloys (eg: CFTS) show a lower band gap compared to Cu-Zn alloys (eg. CZTS). Li *et al*. [41] demonstrated the lowering of band gap, by comparing the MO energies of the 3d orbitals of Fe^{3+} and Cu^{+}. The 3d orbitals of Fe^{3+} are half filled hence the S 3p and 3s orbitals prefer mixing with Fe 3d orbitals compared to the Cu^{+} 3d orbitals. The XANES spectra (S K and L edge) indicate that the Cu^{+} 3d band lies 1.2 eV above the Fe^{3+} 3d band and these values are in good agreement with the MO energy band by the first principles calculations. [43, 44]

Based on the first principles calculations in CZTS quaternary semiconductor, VBM formed by the hybridization of Cu 3d and S 3p orbitals and CBM is mainly formed by antibonding combination of Sn 5s and S 3p orbitals, whereas, the Zn 3d orbital has a weaker influence on the band gap. [17, 45-47] In addition to this, in CFTS the partially filled Fe^{3+} 3d orbitals interact more actively than the fully filled Zn 3d orbitals during the formation of conduction

band and minimize the s-p repulsion between Sn and the chalcogens resulting in a lowering of the CBM and which in turn leads to a decrease in the band gap (Figure.8).

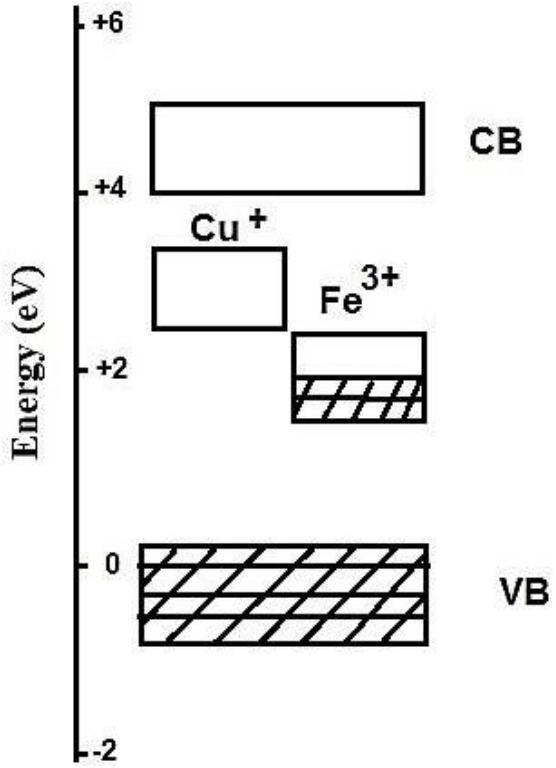

Figure 8: MO/ band structure of Cu^{+}-Fe^{3+}-Sn^{4+}-S^{2-} system with tetrahedral structure. [43-48]

In $Cu_2Zn_{1-x}Fe_xSnS_4$ (CZFTS) alloys as the Zn (1-x) content increases, there are more chances of Sn-5s and S-3p repulsion. Therefore, the CBM state rises up with the decrease in concentration of x, which results in an increase in the band gap with decrease in concentration of Fe or increase in concentration of Zn. These results showed good agreement with the reported literature band gap of these alloys. [48]

2.3. Kesterites and Stannites

Kesterite and stannite are the two main structural modifications which became the focus of my research. The kesterite structure is known for Cu_2ZnSnS_4 and the stannite structure for Cu_2FeSnS_4. [49] Computational studies showed that the difference in energy between the kesterite and stannite phases is less than *ca.* 3.2 kJ mol^{-1} $(formula\ unit)^{-1}$, hence stannite is comparatively less stable than kesterite. [50-52] This may be due to the ordered Cu/Zn sub lattice compared to the Cu/Fe sub lattice. These two polymorphs always coexist in samples because of the very small energy difference between them [50, 52] and have different space groups because of the difference in the distribution of cations Cu^{+}, Zn^{2+} and Fe^{2+}.

According to Hall *et al*. [49] in the stannite structure with *I*42*m* space group, Fe is located at the 2a positions (0,0,0) and Cu at 4d positions (0,½,¼). Whereas, in the kesterite structure, one of the Cu atoms occupies the 2a position (0,0,0) and the remaining Zn and Cu atoms occupy the 2d (0,¼,¾) and 2c positions (0,½,¼) respectively; leading to a new space group *I*4. The Sn in both the structures is at the 2b positions (0, 0, ½). [49-51] In stannite the sulfur anion lies on the (110) mirror plane at 8i (x, x, z) and in the kesterite structure at 8g (x, y, z) respectively. Structurally, all cations and anions are located in a tetrahedral bonding environment as in the zinc blende structures of ZnS or ZnO but with a different order of the cation sub lattices. Kesterite is characterized by the alternating layers of CuSn, CuZn, CuSn, and CuZn cations at z = 0, ½, ½, and ¾ positions.[36,52,53] The structure of CZTS and CFTS after Hall *et al*. [49] is shown in Figure 9. Schorr *et al.* [54] by neutron diffraction studies refined the stannite and kesterite structures. [54] Detailed studies on the $Cu_2(Zn,Fe)SnS_4$(CZFTS) alloys showed that: there is a structural transition from kesterite to stannite, with a decrease in Zn:Fe ratio. [53, 54] Recently Bonazzi *et al*. [53] confirmed the presence of dominant pseudo-cubic structures in zinc rich compositions of CZFTS alloys. The main reasons for structural similarities of the kesterite and stannite structures are similar cross-sections of Cu and Zn, very small difference in the ionic radius of Zn^{2+} (0.64 Å) and Fe^{2+} (0.66 Å) and the high solubility of Fe in the CZTS alloys. [49-52]

The kesterite and stannite CZTS are derived from zinc blende structure, by replacing the Zn cations. In these structures, each anion (Se or S) is coordinated by one Zn, two Cu and one Sn atoms. The existence of these three different cations results in three different cation-anion bond lengths, which leads to anion displacement from the ideal zinc blende site. [55] Khadka and Kim *et al*. [56] reviewed the kesteritic and stannitic phases. Shibuya *et al.* [57] through first principles calculations confirmed the high solubility of Fe in Cu_2ZnSnS_4 and also showed that in the $Cu_2Zn_{1-x}Fe_xSnS_4$ system a phase transition from kesterite to stannite is found to be at Zn/Fe ratio around 0.4.

Evstigneeva *et al.* [58] demonstrated the existence of the stannite structure in $Cu_{2-x}Fe_{1-x}SnS_4$ by the Rietveld method. In these structures, the metal atoms are filled in the tetrahedral cavities of the sulfur close packing. In general, the Sn and Fe atoms occupy the tetrahedral 1*a* positions (0 0 0) located at the vertices of a cubic unit cell and tetrahedral 3*c* positions (0,½, ½) located at the centres. The Cu and (Fe+ Sn) atoms are distributed in an ordered fashion throughout the structure. The Cu atoms occupied at the centres of lateral

faces of the cube with the coordinates (½,0,½) and (0,½, ½) whereas, the (Fe + Sn) atoms occupied at the centres of the cube bases with coordinates (½, ½,0).

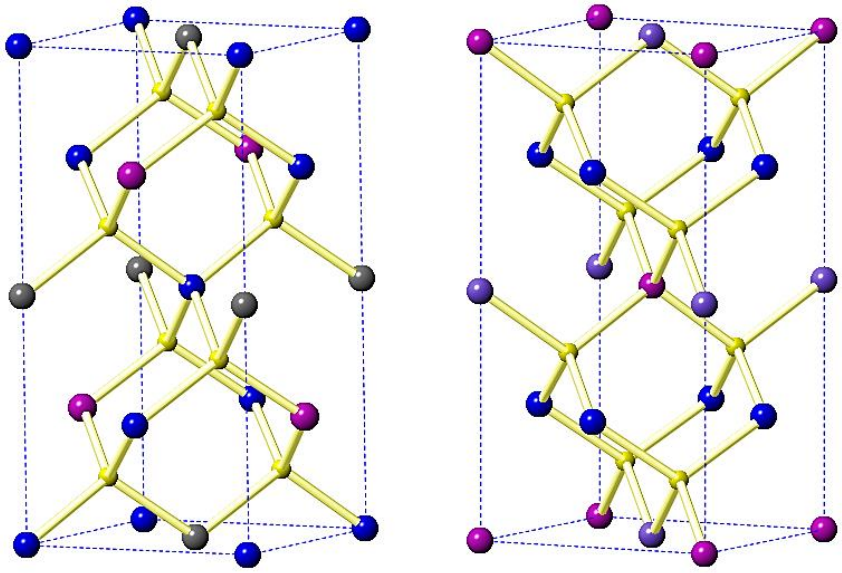

Figure 9: Structural models of the kesteritic (left) and stanitic (right) structures after Hall [49], copper blue, sulfur yellow, tin grey and iron/zinc purple.

Huang *et al.* [59] demonstrated that kesterite type CZTS crystal structures are derived from the zinc blende crystal structure; by substituting elements from the lattice sites of two adjoining unit cells. In one of the types, the Zn^{2+} ions in the zinc blende structures are replaced by Cu^{+} and Fe^{3+} in a 1:1 ratio as an eg: in CIGS, the In^{3+} and Ga^{3+} are incorporated instead of Fe^{3+}. In the formation of the kesterite structure, the Fe^{3+} are replaced by Fe^{2+} and Sn^{4+} and in case of CZTS, Zn^{2+} ions take the position of Fe^{2+}. The crystal structures of CZTS and CIGS only differ in the identity of the atoms present at the Fe^{3+} site of the chalcopyrite structure. This structure also showed similarities in the optical and electronic properties of these two polymorphs. [59] The lattice constants, band gap energies and crystal samples of available kesterite and stannite structures from literature studies are shown in Table 1.

In kesterite and stannite structures the (110), (112), and (102) surfaces have lower cleavage energies than those of the (100) and (001). The powder X-ray diffraction (p-XRD) spectrum of CZTS [74, 75] showed that the peaks corresponding to interplanar distances of (110), (112), and (102) are more distinct than the (100)/(001) planes. From Figure 10 it is clear that

Table 1: The lattice constants, band gap energy and crystal sample of available kesterite (KS) and stannite (ST) structures obtained by experimental and theoretical studies. Thin films (TF), powder crystals (PC), Nano crystals (NC) and Theory/Experiment (T/E).

Chalcogenide	structure	a (Å)	c(Å)	η=c/2a	band gap (eV)	Sample Type	T/E	Ref
CZTS	KS	5.454	10.885	0.9979	1.54	-	T	57
	KS	5.428	10.864	1.001	-	PC	E	54
	KS	5.434	10.856	0.9989	-	PC	E	53
	KS	5.452	10.834	0.9936	1.65	-	T	58
	KS	5.435	10.822	0.9956	-	PC	E	59
	KS	5.432	10.84	0.9978	-	TF	E	60
	KS	5.426	10.81	0.9961	1.45	TF	E	61
	ST	5.417	10.932	1.009	1.4	-	T	58
	ST	5.431	10.956	1.009	1.36	-	T	57
	KS	5.441	10.821	0.9944	1.508	TF	E	56
	KS	5.419	10.854	1.0015	1.5	PC	E	63
CFTS	KS	5.426	11.038	1.017	1.74	-	T	54
	ST	5.45	10.74	0.9853	1.28	PC	E	62
	ST	5.444	10.729	0.9854	-	PC	E	54
	ST	5.489	10.76	0.9801	1.85	-	T	57
	ST	5.45	10.76	0.9872		PC	E	49
	ST	-	-	-	1.33	NC	E	64
	ST	-	-	-	1.35	NC	E	65
	ST	-	-	-	1.32	NC	E	66
	ST	5.449	10.726	0.9842	-	PC	E	53
	ST	5.46	10.725	0.9821	-	PC	E	67
	ST	5.46	10.92	1	1.33	NC	E	68
	ST	10.43	10.79	0.9935	1.22	TF	E	69
	ST	5.443	10.76	0.9885	1.36	TF	E	56
	ST	5.442	10.756	0.9881	1.37	TF	E	70
CFTSe	ST	5.664	11.33	1.0017	-	PC	E	67
	ST	5.694	11.286	0.991	-	SC	E	71
	ST	-	-	-	1.19-1.25	NC	E	72
	ST	5.689	11.284	0.9917	1.1	TF	E	73

	ST	5.685	11.293	0.9932	1.11	TF	E	70
CZFTS	ST	5.432	10.823	0.9962	-	PC	E	53
	ST	5.427	10.837	0.9984	-	PC	E	54
	ST	5.441	10.796	0.9921	1.427	TF	E	56
CZTSe	KS	5.695	11.345	0.996	1	PC	E	15

preferential growth occurs along the (110), (112) and (102) directions. [76] Yu *et al*. [77] demonstrated that the most preferred growth direction in CZTS films on glass or Mo substrate is the (112) direction and there was not much difference in the stability between the kesterite and stannite phases. Experimental studies also hinted that, in order to make and stabilize a kesterite CZTS, it is important to make use of the (001) and (100) surfaces, as this favours kesterite over stannite and disfavours the formation of wurtzite structures. Investigation on the effects of Se additions on the cleavage energies of kesterite and stannite CZTS showed that the addition of Se can stabilize kesterite. The Se alloying stabilizes all surfaces of both phases, mostly for the (001) and (100) surfaces. The presence of about 50 % of Se in the composite, the surface energies of (001) and (100) planes were lowered by ~0.2−0.3 J/m^2, whereas for the other three directions, a decrease of only ~0.1 J/m^2 was seen: which is favourable for the kesterite formation. [76-77]

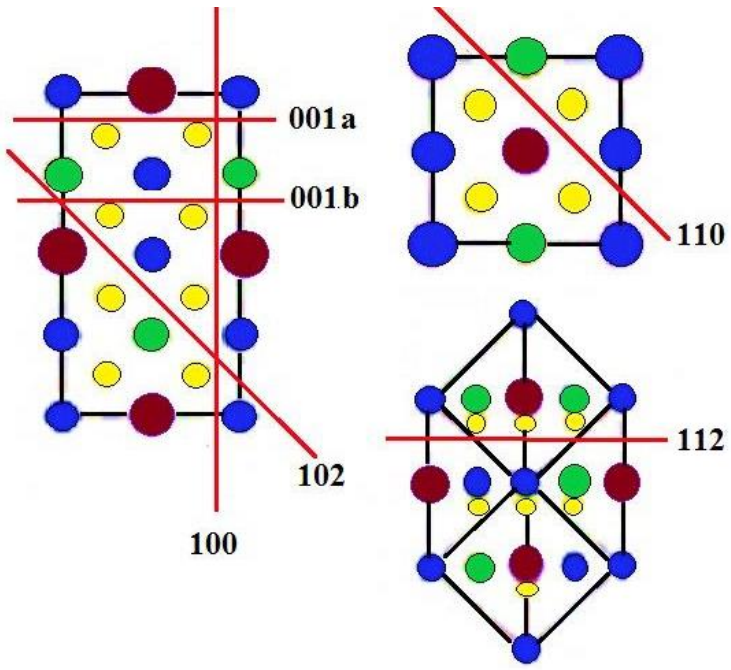

Figure 10: The structure of kesterite and stannite phases. Red lines indicate the cleavage planes identified with Miller indices. [76]

2.4. Solar cells

Photovoltaic (PV) solar cells are attractive and promising alternatives to fossil fuels as they are renewable in terms of the use of earth abundant materials. [78-80] It has been assumed that the present energy needs of the world can be met by covering 0.16% of the Earth's land surface with PV solar cells with an efficiency of about 10%. [78] The direct band gaps of semiconductors have large absorption coefficients; therefore, much smaller thicknesses of these materials could be used. Because of this the TF solar cells need only mm thickness of active layers for efficient performance. [81] Most thin-film photovoltaic (PV) devices are made using direct band gap semiconductors with their absorption coefficients exceeding that of crystalline Si. PV solar cells are mainly classified into four classes they are,

(i) Organic solar cell
(ii) Dye- sensistized solar cells
(iii) Kesterite solar cells
(iv) Perovskite solar cells

2.4.1. Organic solar cells

These cells are made by using organic layers as the name implies. Organic based cells are broadly classified into two types. They are

(i) Donor/acceptor heterojunction cells and
(ii) Dye sensitized solar cells (DSSC's).

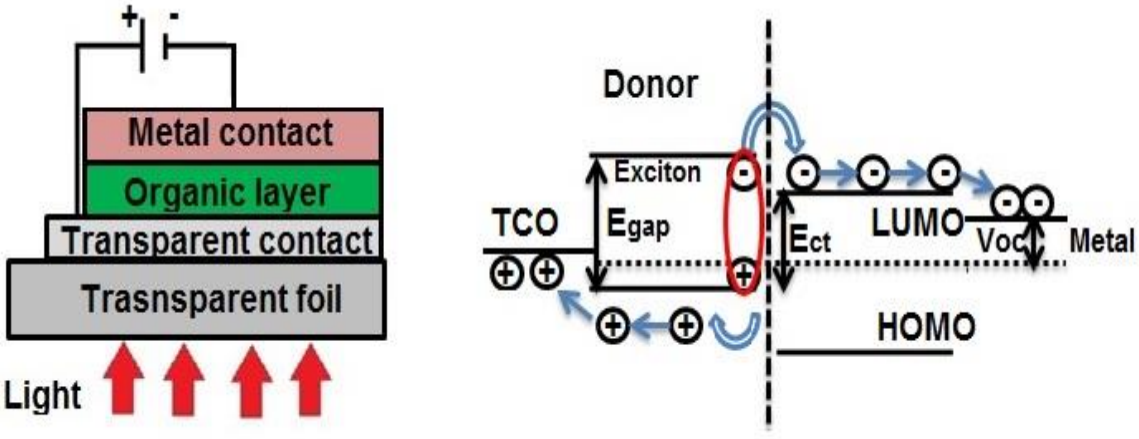

Figure 11: Schematic representation of an organic layer cell (left) and the possible electron transfer (right). [82]

Donor/acceptor heterojunction cells: In these solar cells, a mixed donor (n-type) and acceptor (p-type) conducting layers are deposited. Figure 11 shows the schematic

representation of a donor/acceptor solar cell and the possible electron transfer. These layers are selected based on their energy level split or the energy band. Preferably the donor should be strong light absorbing materials.

The base materials of these hetero junction solar cells are made of solutions or vapour deposited conjugated polymers or small molecules. The main polymers used are poly- 3-hexyl-thiophene (P3HT), fullerene derivative of phenyl-C61-butyric acid methyl ester (PCBM), perylenetetracarboxylic bisbenzimidazole (PTCBI) and copper phthalocyanine (CuPc). Studies showed that improved efficiency of the P3HT/PCBM cell was achieved by thermal annealing, because efficient phase segregation occurred during annealing. [82] After many years CuPc/PTCBI bilayer solar cells were converted into bulk-heterojunction solar cells. [83] Later on, fullerenes were used as acceptor materials in polymer solar cells because of its excellent charge transport properties. [84]

2.4.2. Dye sensitized solar cells (DSSC)

Dye-sensitized solar cells (DSSCs) are one of the most promising cost effective alternatives to conventional solar cells. [85-88] In the DSSCs a thin molecular layer or a mesoporous film of a sensitizer dye is adsorbed on a wide band gap n-type semiconductor such as TiO_2, ZnO or SnO_2. Then the large inner surface of the sponge like open-pore n-type films is covered by the dye, which shows a high optical density at very thin films thicknesses (2-10 mm). [82]

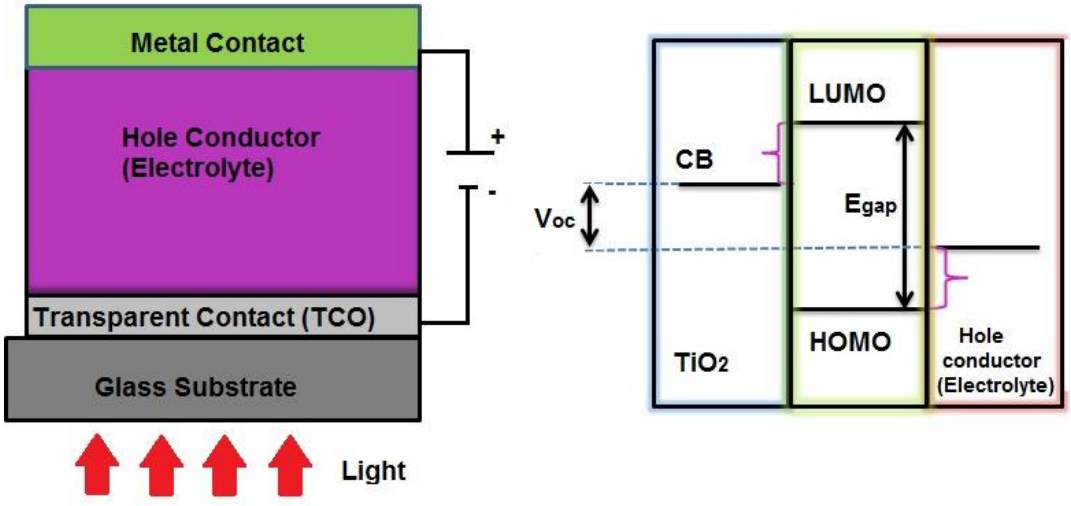

Figure 12: p-type DSSC with spiro-MeOTAD, basic model (left) and level diagram (right). [89]

The main dyes used in DSSC are N719, Y123, ID504, and the hole conductor spiro-MeOTAD. To date some p-conductors DSSC have been developed. The standard dye used today is the spiro-MeOTAD which is a triarylamine with very high solubility which in turn helps to make very good contact in case of p-type DSSCs. Figure 12 shows the schematic representation of a p-type DSSC with spiro-MeOTAD.

In recent years CZTS has become the focus of attention in the field of photovoltaics. [90] Traditionally DSSCs are single junction solar cells, fabricated with a dye sensitised n-type (n-DSSC) or a dye sensitised p-type (p-DSSC) and a counter electrode (CE). Recently, p-DSSCs and n-DSSCs have been combined and fabricated into double junction solar cells (pn-DSSC) which show better theoretical efficiency than that of the single junction DSSCs. [91, 92]. One of the key components in DSSCs is the counter electrode, which collects electrons from the external circuit to reduce I_3^- to I^-. [93] Pt was used as the counter electrode for the regeneration of iodine/iodide electrolyte system as it possesses a high electro catalytic activity. But Pt is very expensive and scarce. [94] The synthetic technique used for the development of the Pt-based

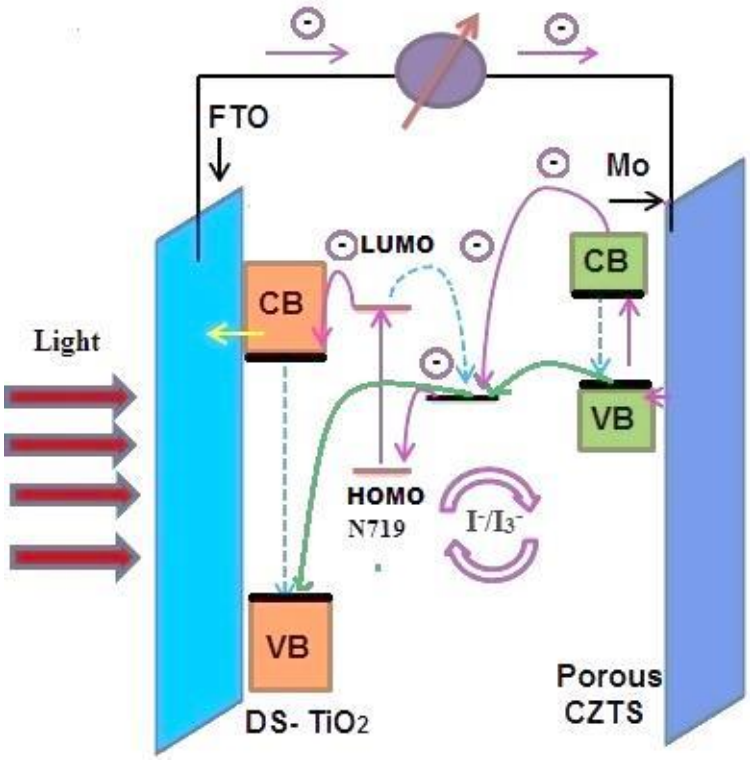

Figure 13: Scheme for the DS-TiO2/CZTS solar cell. Schematic diagram of possible electron transfer and recombination is also shown. The green arrows indicate the possible electron transfer and the dashed blue arrows show the possible electron recombination. The pink arrows are the most possible electron transfer route of a double junction solar cell. [99]

solar cells cell involves the use of toxic organic solvents including some ligand exchange treatment. [95] Therefore, thin films with earth-abundant elements made by low-cost, industrially scalable and non-toxic approaches would be essential for the development of Pt-free counter electrodes in DSSCs. Many promising compounds such as iron sulfide, cobalt sulfide, nickel sulfide, CFTS nanoparticles and CZTS have been investigated as a counter electrode in DSSCs. [95-97]

A significant enhancement in the fill factor (FF) (defined as the ratio of the maximum power from the solar cell to the product of V_{oc} and I_{sc}) for the DSSCs with CZTS thin film CE is attributed due to the porous morphology and decrease in the internal resistance of elements. [98] The electrodeposited CZTS DSSCs achieved 7.3% efficiency. The CZTS cell was made by the sequential deposition of the metals followed by annealing. The schematic diagram of a DS-TiO2/CZTS solar cell with possible electron transfer is shown in Figure 13. [99] DSSCs fabricated with CFTS as a counter electrode showed excellent power conversion efficiency of 8.03%, which is relatively better than that of the Pt counter electrode. The improved performance is due to the superior catalytic activity of the CFTS in iodine/iodide electrolyte. [100]

2.4.3. Kesterite and Stannite solar cells

Single junction solar cells made with GaAs [101], CdTe [102] and $Cu(In,Ga)Se_2$ (CIGS) [102] have proved high efficiencies. However, the toxicity of As and Cd limits the wide use of CdTe and GaAs. [103-105] The use of CIGS, solar cells is also limited because indium is scarce. [106] Several materials with band gap between 1 to 2 eV have been tested to make efficient solar cells. Materials such as SnS, FeS_2, Bi_2S_3, Cu_2S and $Cu_2ZnSn(S,Se)_4$ (CZTS) were tested and Cu_2S and $Cu_2ZnSn(S,Se)_4$ (CZTS) showed efficiencies up to 10%. [107, 108] However Cu_2S is unstable due to the diffusion of copper and hence CZTS was found to be the most promising candidate as a future absorber material. In the CZTS type cells, the CZTS layer acts as a p-type material with a layer of CdS, ZnS, ZnO or $Zn(OH)_2$ as n-type layer. Figure 14 shows a schematic representation of the CZTS solar cell. The electron-hole pairs are generated in the CZTS layer by the absorption of photons. These electron-hole pairs can be separated by the application of an electric field at the interface between p-type and the n-type membrane on top when the exciton binding energies are below kT and the charge carriers can be collected at the electrodes. [78]

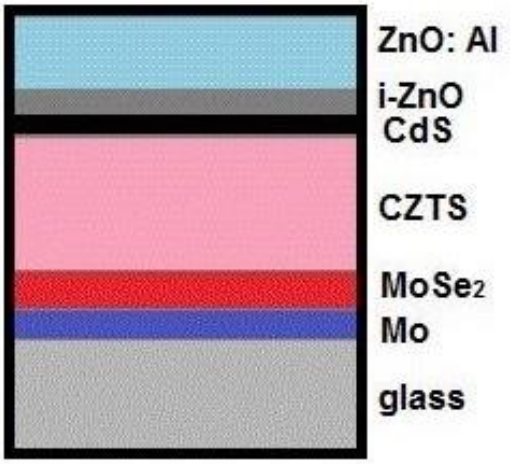

Figure 14: Schematic diagram of a CZTS solar cell.

2.4.4. Perovskite solar cells

In very recent years, hybrid solar cells based on organic and inorganic halide perovskites as absorbers have emerged as a promising class for cost-efficient photovoltaics devises. The first perovskite solar cells were developed by replacing the organic dye in the dye-sensitized

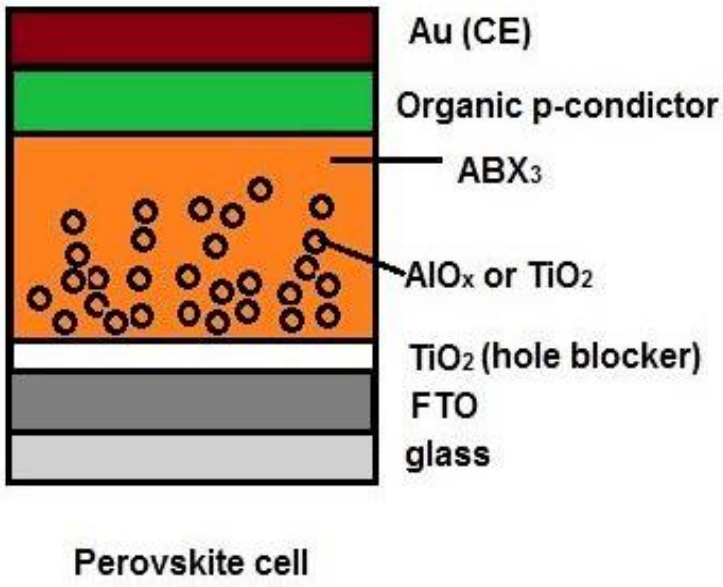

Figure 15: Schematic representation of a hybrid perovskite solar cell.

solar cell by $CH_3NH_3PbI_3$ (ABX_3). [109] The perovskite DSSC's showed efficiencies over 9%. [110] Snaith et al. developed a device set up for a thin-film inorganic solar cell without a mesoporous n-type material [111] The perovskite solar cell is also called a hybrid

solar cell since the material is built of an organic cation and an inorganic poly-anion as shown in Figure 15. [78]

2.5. Synthesis of Nanosized Semiconductor

Great efforts have been made to develop synthetic approaches for the production of high quality, crystalline, semiconductor NCs and thin films. According to the state of the reaction medium, the synthetic routes can be divided into main four classes;

(i) Vapour-phase approach,
(ii) Solid-phase approach,
(iii) Liquid-phase approach, and
(iv) Two-phase approach.

Some of the main techniques for the synthesis of semiconductor NCs are ball milling, [186] chemical vapour deposition (CVD), [112, 113] metal-organic vapour chemical deposition (MOCVD), [187] molecular beam epitaxy (MBE), [113-117] magnetron sputtering [118] and laser ablation. [119]

2.5.1. Synthesis of Nanoparticles

The liquid-phase approach has proven more efficient in the synthesis of well-defined semiconductor NCs than the vapour and solid-phase approaches due to instrumental, precursor limitations and inefficient in terms of control over synthesis and quality of the NCs. The NCs synthesised by the liquid-phase approach are also referred to as colloidal semiconductor nanocrystals (CS-NCs) and are dispersed in suitable solvents, forming stable suspensions with the use of capping ligands/surfactants. [120] Tuneable energy structures, high optical absorption coefficients, large dipole moments, and the potential multiple exciton generation properties are the main attractions of this method. [121] For large scale device manufacturing, solution based techniques such as spin-coating, inkjet printing, and roll-to-roll casting using stable colloidal suspensions are more preferred because of low fabrication cost and ultrahigh throughput. [122, 123]

Based on the types of reaction media, the liquid-phase approach can be further divided into three types:

(i) Aqueous-based approaches: This involves chemical precipitation methods [124,125] and hydrothermal methods [124-127] which use environmentally friendly, biocompatible solvents and works at mild reaction temperatures. [128] The main disadvantage of these methods are lack of control on the morphology of NCs.

(ii) Organic-based approaches: In this method, high boiling organic solvents are used and the NCs synthesised have fine controlled morphology with the use of the organic ligands. [129-132] This involves the hot-injection method, [133] non-injection method [134-137] and the solvothermal method using autoclaves. [138-140]

(iii) Aqueous-organic approaches: These methods are generally known as the interface-mediated method or liquid-solid-solution (LSS) method [141-145] as the reactants involved are in different phases and the nanocrystals formed at the interface of aqueous and organic media. This method was originally introduced by Li [143] and An *et al*. [144] and was successfully applied in the synthesis of variety of nanocrystals including polymer nanoparticles. [143] Nanocrystals prepared by these methods, are often spherical or have common shapes favoured by their crystal structures. Mild reaction conditions and control over stoichiometry are the advantages of this method. [145]

According to the LaMer model NCs formation mainly consists of two stages; a nucleation stage and crystal growth stage. [146] Initially, the precursors are dispersed in suitable solvents; monomers are generated by chemical reaction between precursors. As the concentration of monomers reach a super-saturation level, nuclei will be formed by the self-nucleation and aggregation of monomers. The aggregation of monomers continues on these pre-existing nuclei, when the concentration of monomers drops below a critical level the nanocrystal growth occurs. New nuclei are also formed during the nanocrystals growth, which results in a size widening of the nanocrystals, size control of NCs mainly aims at narrowing the size distribution.[147] For controlling the size and size-distribution of NCs, the reaction parameters such as;

(i) reaction temperature and time,
(ii) injection temperature of the reactant in the case of hot-injection methods,
(iii) reactivity and the concentration of precursors,
(iv) solvent, surfactant and pH.

The first strategy to adopt is to separate nucleation from the growth process. The nucleation process can be triggered by injecting the precursors into solvents at a higher temperature, followed by a reduction of the reaction temperature which then separates nucleation from growth. This method was introduced by Murray *et al*. through the successful synthesis of monodisperse cadmium chalcogenide nanocrystals with high-quality. [135] In this method, dimethyl cadmium ($Cd(CH_3)_2$) was used as a Cd source; and bis(tri/dimethylsilyl) sulfide/selenide/telluride were used as the chalcogenide source. Solvents used were tri-n-

octylphosphine (TOP) and tri-n-octylphosphine oxide (TOPO). The precursors were injected at 300 °C and the average sized CdX (X = S, Se, Te) NCs obtained within the temperature range of 112-115 °C. This kind of rapid injection of precursors into a hot solvent is called the hot-injection method. To improve the quality of NCs by this method, rapid quenching of the reaction mixture or size-selective precipitation can be added with the procedure. These additional techniques were applied in the above mentioned synthesis of CdSe NCs; by dispersing the NCs in 1-butanol followed by the addition of methanol until the opalescence persisted followed by centrifugation. [133]

Non-injection methods were used in the synthesis of ternary and quaternary chalcogenides such as CIS and CZTS NCs. In this method the precursor mixture was dissolved in a suitable solvent followed by the addition of a capping agent like oleylamine (OA) and then heating to a desired temperature under inert conditions. Figure 16 shows the schematic representation of the apparatus for the non-injection method. The particle size can be controlled by varying the reaction times and concentration of the precursor mixture. As an example in the synthesis of $CuInS_2$ NCs, CuI, $In(OAc)_3$ and DDT were mixed in the octadecene (ODE) solvent, followed by the addition of OA heated up to 200°C under Ar. [136] The particle size was controlled (3.5 to 7.3 nm) by varying reaction times (20 - 120 min).

A similar thermolysis route has been adopted in the synthesise of wurtzite CZTS NCs, which involved the thermolysis of a mixture of metal dithiocarbamates: copper(II) diethyldithiocarbamate [$Cu(dedtc)_2$], zinc(II) diethyldithiocarbamate [$Zn(dedtc)_2$], tintetra-(diethyldithiocarbamate) [$Sn(dedtc)_4$], in the presence of hexadecanethiol and trioctylamine at 100 °C, followed by heating to 250 °C for variable time span, depending on the desired particle sizes. [135]

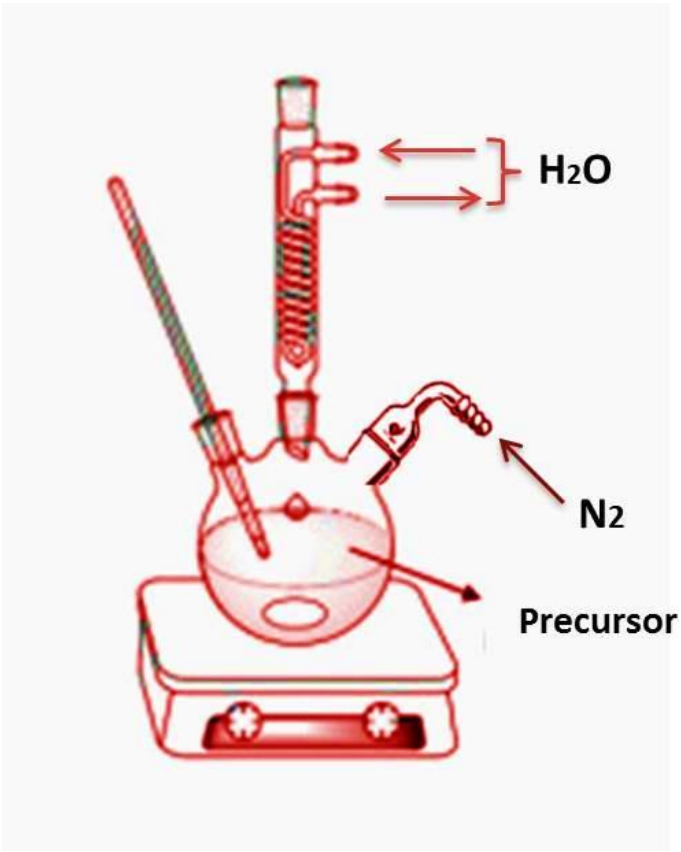

Figure 16: Schematic representation of the apparatus setting for the non-injection method.

2.5.2. Synthesis of Thin Films

For the synthesis of thin films several methods were adopted. Among them chemical vapour deposition which produces high purity and high performance thin film materials.[148] In a typical CVD process the substrate is exposed to one or more volatile precursors which react and/or decompose on the substrate to produce the desired deposit. CVD processes are extremely complex and involve a series of gas phase and surface reactions. [148-150]

The main steps involved are;

(i) Evaporation and transport precursors in the bulk gas flow region into the reactor

(ii) Gas phase reactions of precursors in the reaction zone to produce intermediates

(iii) Mass transport of reactants to the substrate surface

(iv) Nucleation and surface chemical reactions leading to film formation

(v) Mass transport of remaining fragments of the decomposition away from the reaction zone.

There are different types of chemical vapour deposition available they differ by means of how chemical reactions are initiated (activation process) and the process condition used. The types of CVD include:

(i) Atmospheric pressure CVD (APCVD): CVD process under atmospheric pressure

(ii) Low-pressure CVD (LPCVD): CVD at a reduced pressure tends to reduce unwanted gas-phase reactions hence can improve the film uniformity quality.

(iii) Direct liquid injection CVD (DLICVD): Precursor solutions are injected in a vaporization chamber towards reactors. This technique is suitable for use on liquid or solid precursors.

(iv) Plasma-Enhanced CVD (PECVD): Allows deposition at lower temperatures by the help of plasma.

(v) Remote plasma-enhanced CVD (RPECVD): CVD process similar to PECVD except the wafer been removed from the plasma region allows processing temperatures down to room temperature.

(vi) Atomic layer CVD (ALCVD): used to deposit successive layers of different substances to produce layered films with crystalline structures.

(vii) Hot wire CVD (HWCVD)/Catalytic CVD or hot filament CVD (HWCVD): The source gases decomposed chemically by a hot filament.

(viii) Metalorganic chemical vapour deposition (MOCVD): CVD by the use of metalorganic compounds as precursors.

(ix) Hybrid physical chemical vapour deposition (HPCVD): Involves chemical decomposition of precursor gas and the vaporisation of solid source.

(x) Rapid thermal CVD (RTCVD): It uses heating lamps or other methods to rapidly heat the wafer substrate only which helps in reducing unwanted gas phase reactions that can lead to particle formation.

(xi) Aerosol assisted CVD (AACVD): CVD process in which the precursors are transported to the substrate by means of a liquid/gas aerosol, which can be generated ultrasonically.

2.5.3. Aerosol assisted CVD (AACVD)

This technique is suitable for use with non-volatile precursors. AACVD is a simple technique which can operate at an ambient-pressure using the nebulization of precursor molecules, followed by transport of the aerosol by an inert carrier gas such as argon or

nitrogen to a substrate surface heated in a furnace where thermal decomposition of the precursor occurs. The apparatus set up is shown in Figure 17. AACVD has been widely applied in the deposition of complex systems and has enabled the use of less volatile precursors than more conventional CVD methods. These have included high temperature superconductors and other oxides. [148] Ranges of stoichiometry controlled thin films of CdS, ZnS, and $Cd_{1-x}Zn_xS$ were deposited from $Cd(SOCCH_3)_2$-TMEDA and $Zn(SOCCH_3)_2$-TMEDA (TMEDA = N,N,N,N-tetramethylethylenediamine). [148, 149] Marks *et al*. reported the deposition of metallic silver thin films using tris(phosphino)boratosilver(I) complexes [150] and Parkin *et al*. [151, 152] reported a single step route to the deposition of super hydrophobic surfaces through AACVD and deposition of ZnO thin films by AACVD. Wijayantha *et al*. [153] synthesised polycrystalline α-Fe_2O_3 electrodes by aerosol-assisted chemical vapour deposition from a ferrocene precursor. Mazhar *et al*. [154] demonstrated, the deposition of high quality $NiTiO_3$ thin films from a single-source hetero bimetallic complex $[Ni_2Ti_2(OEt)_2(\mu\text{-}OEt)_6(acac)_4]$ precursor. [154]

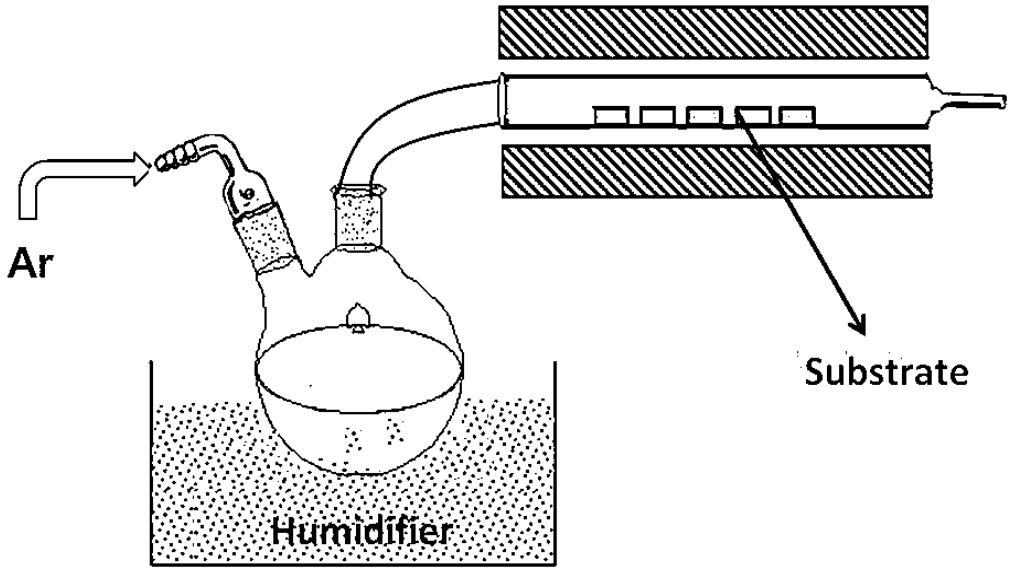

Figure 17: The experimental set up for the AACVD deposition of thin films.

This method successfully applied for α-Fe_2O_3 using $[Fe_6(PhCOO)_{10}(acac)_2(O)_2(OH)_2C_7H_8)]$. [154] AACVD has recently been used for the deposition of various semiconductor materials including SnS, [155] CZTS, [156] $CuInSe_2$, [157] $CuGaSe_2$, [158] $CuIn_{0.7}Ga_{0.3}Se$, [158] MoS_2, [159] inorganic-organic perovskite $(CH_3NH_3)PbBr_3$. [160] Hussain *et al*. [161] reported different morphologies of hexagonal FeSe from 1-benzoyl-3-(4-ferrocenylphenyl)selenourea under the influence of surfactants (span and triton) and temperature. [162] Very recently bismuth vanadate ($BiVO_4$) thin film

photo electrodes prepared by AACVD on fluorine doped tin oxide (FTO) glass substrates were produced. $BiVO_4$ photo electrodes are promising for use in PEC water-splitting cells. [161,162]

2.6. Precursors for the Synthesis of Nanoparticles and Thin films

The main consideration in the synthesis of semiconductor nanocrystals is the selection of a suitable precursor. The main attractions of metalchalcogenide precursors are it should be stable, have a direct metal-chalcogen bond, easily

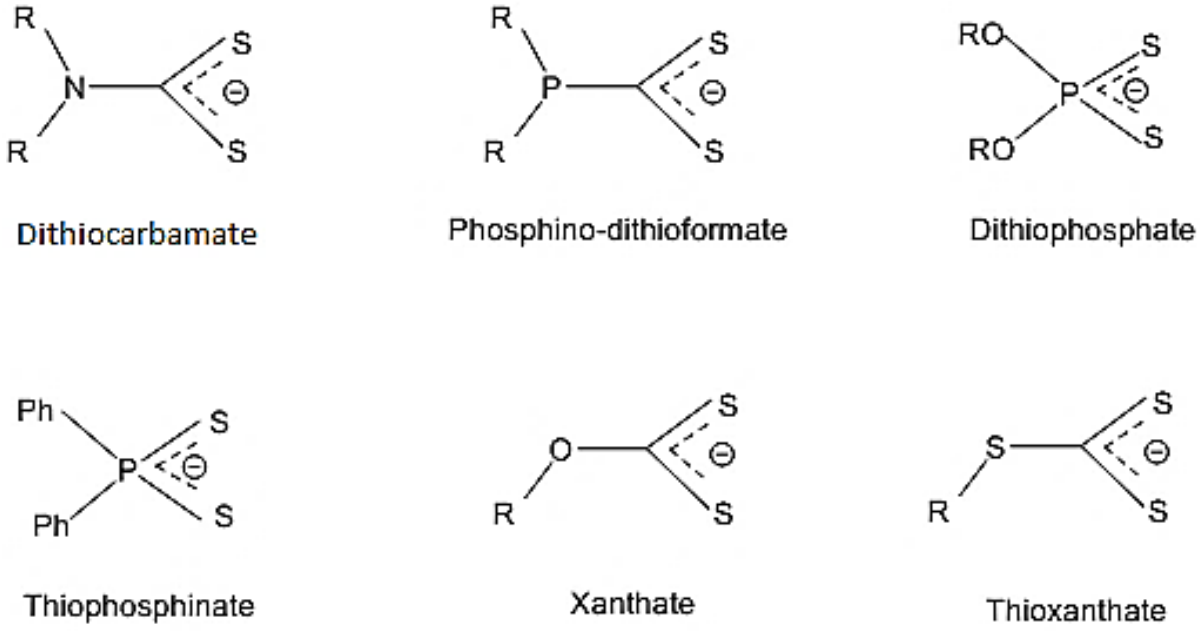

Figure 18: The main ligands used as precursors for the synthesis of semiconducting NCs.

volatile and should decompose at a comparatively low temperature. Figure 18 shows the main precursors used by researchers for the synthesis of metal-chalcogenide semiconductors:

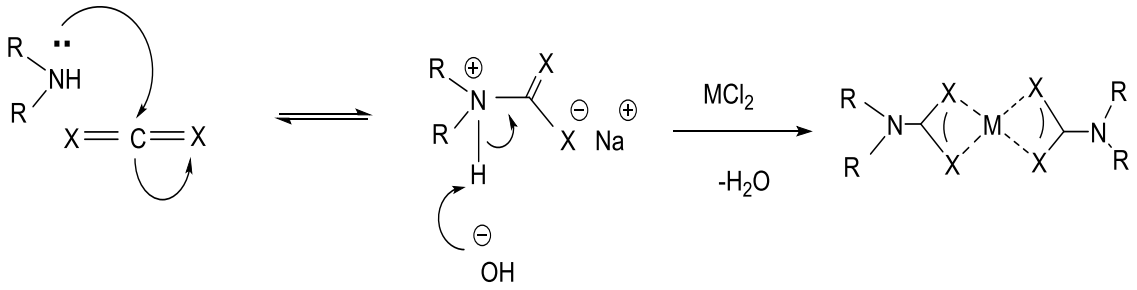

where, X = S or Se, M= Zn, Cu,Sn,Fe,Cd, Ni, Sb

Scheme 1: The formation of metal dithio/selenocarbamato complexes.

the metal-dithio/selenocarbmates, metal-xanthates, metal-dithio/selenophosphates, metal dithio/selenophosphinates, dithio/selenophosphinatoformates, metal-thioxanthates etc. Dithiocarbamate complexes have some advantages over other precursors. They can stablisise a wide range of oxidation states and hence can bind with all metals including Cu, Zn, Fe, Sn, Cd, Ni, Sb, Bi, Ni etc. The compounds formed are stabilised by resonance. Dithiocarbamate C-S bonds are easier to break than P-S bonds because, compared to oxygen, sulfur atoms possess lower electronegativity hence can stabilise the metal complexes more easily.

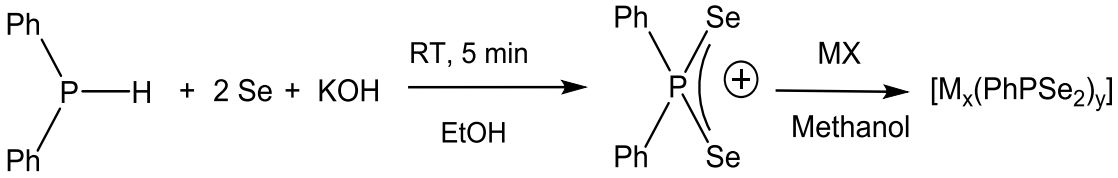

In MX M= Cu, Zn, Sn, Fe and X = S, Se

Scheme 2: The formation of metal selenophosphinato complexes

Dithiocarbamates with symmetrical and unsymmetrical R groups can be made, depending on the substituent. The general formulae for symmetrical metal dithiocarbamates are $[M(E_2CNR_2)_2]$ and for unsymmetrical are $[M(E_2CNR_1R_2)_2]$ where R_1 = Me, Et, or *i*Pr and R_2 = Et, *n*Pr, *i*Pr, or *n*Bu. The formation of metal dithio/selenocarbamato complexes are shown in Scheme 1 and thiophosphinato complexes in Scheme 2.

2.7. Summary

Based on the above discussion, the aims of this project fall into four broad categories. Firstly to synthesise metal organic complexes. This will be achieved by using a range of synthesis of ligands and then reacting with metal salts to make metal-chalcogenide bonds, such that they may bind to the labile coordination position on the central metal, hence on decomposition will give metal chalcogenide compounds. The metal organic complexes will be structurally characterised by methods including NMR, IR, MS, elemental analysis and single crystal X-ray diffraction. The decomposition of the as-synthesised metal-organic complexes will be analysed by the thermal gravimetric analysis.

The second broad theme is to use these complexes and mixtures of them for the deposition of thin films including SnS, SnSe, Cu_2SnSe_3, Cu_2ZnSnS_4, $Cu_2ZnSnSe_4$, Cu_2FeSnS_4, $Cu_2FeSnSe_4$ $Cu_2FeSn(S_xSe_{1-x})_4$, $Cu_2ZnSn(S_xSe_{1-x})_4$ $Cu_2(Zn_yFe_{1-y})SnS_4$,

$Cu_2(Zn_yFe_{1-y})SnSe_4$, $Cu_2(Zn_yFe_{1-y})Sn(S_xSe_{1-x})_4$,CdSe and CdS_xSe_{1-x} by Aerosol Assisted Chemical Vapour deposition (AACVD) technique. The effect of alkyl groups, coordinating atoms, deposition temperatures and composition of precursor on phases and morphologies of the films will be studied. The structure, morphology and composition of the deposited films will be characterised by using powder X-ray diffraction (p-XRD), scanning electron microscopy (SEM), energy dispersive X-ray spectroscopy (EDX), transmission electron microscopy (TEM), selected area electron diffraction (SAED) and atomic force microscopy (AFM). The optical and electrical properties of the films will be studied by UV-Vis and room temperature resistance measurements. Detailed parametric studies will be carried out to optimise the deposition parameters for Cu_2ZnSnS_4, thin films for the fabrication of a simple Dye Sensitized Solar Cell (DSSC) and its performance under one sun radiation.

The third aim of this project is the development of a novel synthetic technique for the synthesis of $Cu_2Zn_{1-x}Fe_xSnS_4$ nanoparticles (x = 0 to 1) with detailed compositional studies based on the p-XRD patterns and EDX. The optical and magnetic properties of these materials will be analysed by UV-Vis spectroscopy and SQUID magnetometry. A final aim of this project is to develop electronic devices such as organic field-effect transistors (OFETs), LED's etc.

CHAPTER - III

Literature review of $Cu_2Zn_zFe_{1-z}Sn(S_{1-x}Se_x)_4$ semiconductors and solar cells.

3.1. Photovoltaic performance of copper based chalcogenides and development of improved efficiency materials

The efficiency and stability of copper chalcogenide structures can be improved by the addition of metals like Al, Ga and In to them. The photovoltaic performances of copper based ternary composites with formulae $CuXS_2/Se_2$ (X - Al, Ga, In) were studied in detail, amongst these $CuInS_2/Se_2$ have shown high efficiencies (~ 20%). However, the very low annual production of In makes it less economic. [163] The crystal structure of these ternary materials $CuXS_2/Se_2$ resembles the zinc-blende structure, in which each of the two cations Cu^+ and X^{3+} is tetrahedrally coordinated by four anions of S/Se, but the S/Se anion is coordinated by $2Cu^+$ and $2X^{3+}$. The conduction band of $CuXS_2/Se_2$ is mainly composed of Cu 3s orbitals hybridized with the p orbitals of element X, and the valence band is dominated by Cu 3d orbitals hybridized with S-3p or Se-4p. [164,165]

The direct band gap of $CuXS_2$ can be adjusted by doping with different elements, X or replacing S with Se. The DA (donor-acceptor) pair in the band structure can be introduced by the incorporation of X. Usually; the donor is mainly the copper vacancy while the acceptor is mainly the Cu–X antisite defect (X^{2-}_{Cu+}). [166] It has been demonstrated that the donor–acceptor transition directly affects the photoluminescence rather than the band gap transition. [167, 168] Further studies later showed that the addition of Zn^{2+} and Sn^{4+} into Cu_2S/Cu_2Se can modify their properties in the solid solution just like In^{3+} does in $CuInS_2$. [165,169] In the crystal structure, anions of S/Se act as a backbone and the Cu^+ and X^{3+} distributed in the crystal structure, which then leads to the formation of different defects as the Cu–X antisite defects by the misdistribution of Cu^+ and X^{3+}. [166] In the crystal structure of CZTS, the S^{2-} anions work as a backbone, while the Zn^{2+}, $Cu^{+,}$ and Sn^{4+} are distributed as mobile ions and free holes are introduced in the structure; which cause the p-type conduction as shown in Figure 19. [166]

Cu_2ZnSnS_4 (CZTS) is a strong absorber material; as it consists of earth abundant and non-toxic elements, hence easy to scale up to meet the present demand. [62,170-172]

Consequently, CZTS related materials such as $Cu_2ZnSnSe_4$ (CZTSe) and $Cu_2ZnSn(S,Se)_4$ (CZTSSe), Cu_2FeSnS_4 have also attracted considerable attention as an absorber for single junction thin film solar cells in recent years. Some of the main properties of CZTS based material which is making it more attractive: mainly it is a kesterite type material and its crystal structure is similar to that of CIGS but differs only in the identity of the atoms present

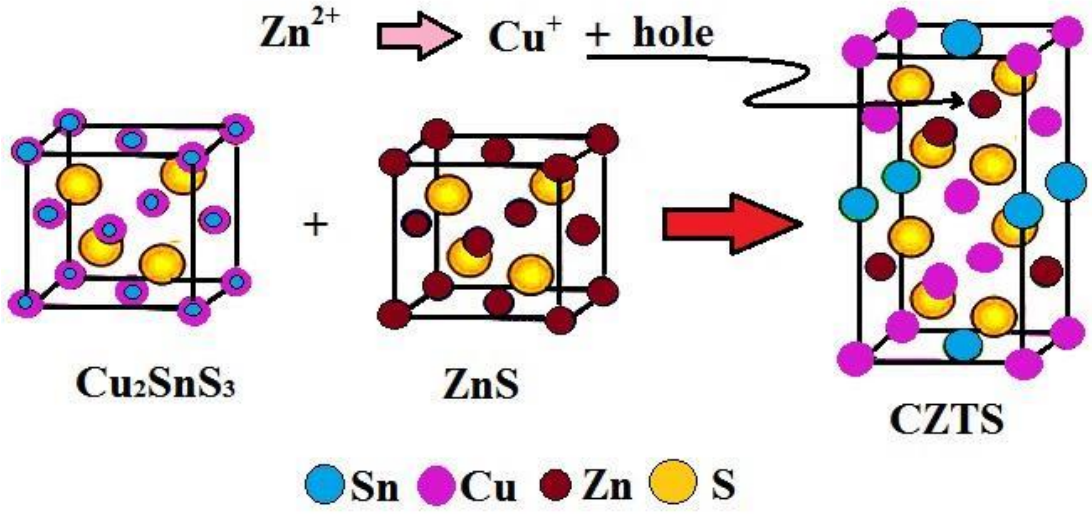

Figure 19: CZTS formation from Cu_2SnS_3 and ZnS replacing Zn^{2+} by Cu^+ and hence producing hole/ acceptor site.

at the Fe^{3+} site of the chalcopyrite structure from where it is derived. This structural similarity helps to account for the similar optical and electronic properties of the two materials. [173]

The absorption coefficient and effect of composition on the band gap of the fabricated films were studied by using UV-Vis spectroscopy. The absorption coefficient (α) is calculated using the relation [59,174,175]

$$\alpha(\lambda) = (1/t)\ln\{[1 - R(\lambda)]/T(\lambda)\} \quad \text{..... Eq. 2}$$

Where, t is the thickness of the film, T(λ) is transmittance, and R(λ) is reflectance of the sample.

The optical band gap of the sample is determined from the relation

$$\alpha h\nu = C(h\nu - Eg)^n, \text{ [59,175]} \quad \text{..... Eq. 3}$$

Where, Eg is band gap energy, h is Planck's constant, ν is the frequency of the photon, and C is a constant. The value of exponent "n" in the above relation depends on upon the nature

of the optical transition. Since quaternary semiconductor is the material of direct band gap nature [174-176] the value of "n" is taken as ½.

The CZTS-based solar cells possess a high theoretical efficiency as the Shockley–Queisser limit (SQL) of CZTS-based materials is about 30.9% (for a band gap of 1.0 eV), [176, 177] which is closer to the SQL maximum for a single junction solar cell (33.7%) with a band gap of 1.34 eV. [177] Another reason for the high efficiency of CZTS-based materials is: they are direct band gap semiconductors with high absorption coefficients of 10^4-10^5 cm^{-1}. [111] Therefore, a 2.5 μm thick CZTS film with an $\alpha = 10^4$ cm^{-1} can absorb more than 90% of the incident light, which makes them highly cost effective. [178] CZTS-based materials are p-type semiconductors with a hole density of around 10^{16} cm^{-3}, which is found to be the main cause for the high efficiency of CIGS solar cells. [177]

Several experimental studies, on the phase formation of CZTS-based films, were conducted and concluded that the kesterite structures are more useful in solar cell applications of CZTS than the stannite structure, as the kesterite contain a very high concentration of non-stoichiometric intrinsic defects. [178-181] Studies also revealed that it is very difficult to avoid the secondary phases in CZTS because the Cu and Sn-rich phase accumulated near the top and are Zn-rich at the bottom of the kesterite films. [182,183] In stoichiometric CZTS and CZTSe materials, the density of [$2Cu_{Zn}^{+}+Sn_{Zn}^{2+}$] can be as high as 10^{18} cm^{-3} which induce a downward shift in the conduction band edge by 0.4 eV in CZTS and 0.1 eV in CZTSe. [184] CZTS with an off-stoichiometric composition showed comparatively high efficiency: a Cu-poor and Zn-rich composition, with [Cu]/[Zn + Sn] ratio of around 0.8 and a [Zn]/[Sn] ratio of around 1.2. [185] Based on theoretical reports, it has been argued that an off-stoichiometry is favourable for attaining higher efficiencies as it avoids the deep-level donor defects such as Sn_{Zn}^{2+} and its related recombination clusters such as [$2Cu_{Zn}$ + Sn_{Zn}^{2+}]. The formation of Cu_{Zn} and copper vacancy (V_{Cu}) are seen in CZTS and CZTSe, the deeper acceptors are Cu_{Zn} hence it is more effective as a trap and recombination centre which in turn leads to high-efficiency solar cells [184, 186] Under Cu-poor and Zn-rich conditions, the density of Cu_{Zn} is higher than V_{Cu}, hence shows a higher efficiency. [185] These results were supported by the low-temperature PL of CZTS, where two shallow acceptors with energies; 10 ± 5 and 30 ± 5 meV were found above the valence band edge. [124]

Solar cell performances using CZTSSe absorbers with different stoichiometric ratios also demonstrated high efficiency for Zn-rich phases. This might be due to the avoidance of

unwanted Zn-poor secondary phases and the formation of less detrimental ZnS secondary phase. A Cu-poor composition was favourable, due to the avoidance of Cu_2S which can introduce shunting pathways because of its low resistivity. Shunting pathways usually lower the fill factor (FF) of the solar cells. High Sn concentration leads to the SnS_2 which is less detrimental to device performance. [187] Additionally, Cu-poor solar cells with lower Zn concentration have shown high efficiency, as it can avoid the formation of ZnS or ZnSe phases. [188] It has been noticed that the region adjacent to the CZTSe/ZnSe interface; was found to be Cu and Sn poor which introduce trap states which slow down the flow of charge carriers. [189] There are chances of formation of n-type ZnSe in this situation; which reduce the transport of the minority charge carriers towards the p–n junction and narrows the conduction pathways for charge carriers, which in turn increase the shunt resistance (Rs) and lowers the FF of the solar cell. The formation of nanometer-sized ZnSe network can be avoided by using the Cu-rich and Zn-rich films. The stability and composition of CZTS currently hold a challenge as theoretical studies revealed, only for a small range of chemical potentials, the CZTS phases are stable, and precipitates like CuS or Cu_2S are easily formed during its synthesis. [190]

The performance of CZTS materials can be further improved; by controlling of the stoichiometry of the materials and by the incorporation of extrinsic impurities, such as Fe (to replace Zn from CFTS) or Se (to replace S and form CZTSe). [169, 191, 192] Substituting the S with Se in CZTS-based solar cells improves solar cell performance. [40,193] Theoretical studies suggested that the higher efficiencies of CZTSe compared to CZTS is due to the formation Sn_{Zn}^{2+} and selenium voids (V_{Se}), which are considered as the deep level donor defects. CZTS and CZTSe has a smaller downward conduction band edge shift caused by [$2Cu_{Zn}$+ Sn_{Zn}^{2+}] leads to lesser electron trapping effect. [194] These improvements in the efficiency of the solar cell when S are replaced by Se had been experimentally investigated. [194-196] When CZTS-based solar cells with a different [S]/[S + Se] ratio (0.35, 0.8, and 1) were compared; it was found that solar cells with a lower [S]/[S + Se] ratio had a higher efficiency (7.4%, 5.3%, and 3.5%). This is because the current density (Jsc) increased due to the improved carrier concentration and the defect depth also found to be increasing with increasing [S]/[S + Se] ratio.[194-196] Deeper defects are comparatively less desirable as they act as effective recombination centres. Although high efficiency CZTS-based solar cells with Se, the use of Se is less favourable in terms of material abundance as the abundance of Se is almost similar to In. [111, 195]

The band gap of CZTS material decreases with increase in Fe ratio, because of the contributions from delocalised Zn s orbitals by the more localised Fe d orbitals, which results in the spatial confinement of the electronic wave function and a decrease in bandwidth. [197] The ease of incorporation of Fe in CZTS allows for the selective tuning of the band gap and the lattice parameters. For Si, which has an indirect band gap of 1.12 eV at 300 K, the optimal band gap for a top layer is between 1.70 and 1.76 eV. [198,199] The Fe/Zn ratio of the alloy enters the optimal band gap region at around x = 0:8 and at this composition stannite is thermodynamically stable, the mismatch in the lattice at this composition was found to be is less than 1%, which enhances the formation of the heterostructure. For larger Fe concentrations, the band gap increases and the slight decrease in the lattice volume makes the CZFTS alloy a future solar cell candidate. [194] The post sulfurized CZFTS ($0 \leq z \leq 1$) films deposited by spray pyrolysis showed absorption coefficient values above 1×10^4 cm^{-1} in the visible range, which is a benchmark for the absorber layer in thin-film solar cells. [197] In order to determine the bandgap energy Eg (Z) of an alloy $A_{(1-Z)}B_Z$, according to the band gap bowing model for alloys, the Vegard type analysis can be used. The compositional dependence of the band gap can be described by the following equation. [194, 200, 201]

$$Eg(Z) = (1 - Z)Eg(A) + ZEg(B) - b\,(Z(1 - Z)) \qquad \text{..... Eq. 4}$$

which represents a linear approximation between the band gaps of the pure constituents A[Eg(A)] and B [Eg(B)] corrected by the alloy specific "optical bowing constant" b.
In order to apply Eq. (4) to $CZTS_{(1-x)}Se_x$ alloy and CZ(z)F(1-z)TS

$$Eg\ CZTSSe(x) = xEg\ CZTSe + (1 - x)Eg\ CZTS - bx(1 - x) \qquad \text{... Eq. 5}$$

$$Eg\ CZFTS(z) = zEg\ CZTS + (1 - z)Eg\ CFTS - bz(1 - z) \qquad \text{..... Eq. 6}$$

Where, b is the specific "optical bowing constant" which describes the degree of nonlinearity.
This variation can be demonstrated by the combination of effects, including

(i) electron exchange and redistribution as a consequence of the difference between the electronegativities of atoms,
(ii) the impact of crystal lattice variation on band structure, and
(iii) differently positioned constituents resulting from the internal structural relaxation of the anion-cation bond lengths and angles. [192,151]

The bowing constant b can be obtained by fitting. Some of the experimental data were found to be best fitted with parabolic function and bowing constant b = 0.1 ± 0.05 eV. [56] The relatively small bowing constant suggests good miscibility of CZFTS alloy. [56, 141, 152] Similarly, the zinc alloyed iron pyrite $(Fe,Zn)S_2$ has been reported to have parabolic band gap tuning with increasing Zn content. [73] Therefore, the parabolic trend of the band gap with increasing Zn content is probably influenced by the following factors:

(i) The difference between electronegativities of Zn (1.65) and Fe (1.83) atoms contributes to exchange and redistribution of electrons and
(ii) The change in the crystal lattice with variation in (Zn, Fe) stoichiometry in CZFTS crystal greatly impacts band structure. [141, 202]

Shibuya et al. by the first principle studies reported the band gap variations of CZFTS alloys. Their band gap with varying Zn:Fe composition in CZFTS alloy varied slightly from parabolic if the structural transition from stannite to kesterite is considered but showed more bowing in the experimental studies. [56, 57, 202-207] This is because the reported band gap was a quasiparticle gap, which excluded on-site excitations associated with the iron d- band. [192, 207] The structural transition needs further studies and needs to consider various factors and parameters to get improved efficiency.

In 1966, Katagiri et al. reported first CZTS vacuum-deposited solar cell with 0.66% power conversion efficiency. [62] Very recently, 5.2% efficiency was reported from the p-n junction. [208] In 2008, by the optimization of the metallic precursor concentration, deposition parameters and growth techniques the PCE of 6.7% from a vacuum-based CZTS solar cell was achieved. [209] In 2010, PCE to 9.7% was reported from the solution processed hydrazine-based CZTSSe material, [61] whereas the solar cell developed by the colloidal nanocrystal-based CZTSSe showed a PCE 7.2% [193] mean time the CZTS based solar cells fabricated by thermal evaporation method showed a PCE of 6.8 %. [210] A 10.1% PCE was achieved for the kesterite absorbers, such as $Cu_2ZnSn(Se,S)_4$ thin-film solar cell made by hydrazine-based solution processing. In 2011, a PCE of 10.1% was obtained from kesterite type $Cu_2ZnSn(Se,S)_4$ thin-film solar cell made by hydrazine-based solution processing. [211] By 2012, vacuum based methods provide a lower efficiency of 9.15% using the CZTSe absorber layer by the co-evaporation method. [212] CZTSSe-based TFSCs indicate the best efficiency of 11.1% is achieved using a solution based hybrid slurry process.[213] In 2014, the highest efficiency 12.6% was reported for CZTS-Se solar cell. [214-217]

Chalcogenides of the Cu_2-II-III-IV-VI_4 (II = Zn, Cd; IV = Ge, Sn; VI = S, Se) family including Cu_2ZnSnS_4 (CZTS), $Cu_2ZnSnSe_4$ (CZTSe), $Cu_2ZnSn(S_{1-x}Se_x)_4$ (CZTSSe), Cu_2FeSnS_4(CFTS), $Cu_2FeSnSe_4$(CFTSe), $Cu_2ZnzFe_{1-z}SnS_4$ (CZFTS) have been extensively studied as alternative photon absorber due to their high absorption coefficient (~104 cm^{-1}) in the visible spectrum range and optimal bandgap 1 to 1.5 eV. All these materials were formed from earth-abundant and relatively cheap and environmentally benign elements. The structural, morphological, optical and electrical properties of these materials can be tailored by controlling the synthetic parameters such as compositions, temperature, and time. The fabrication and the efficiencies of the solar cells made from these materials are reviewed. The main solar energy efficiency of quarternary and multnary copper based chalcogenide materials; synthetic techniques, band gap, the configuration of a solar cell or DSSC's and the efficiency of the as synthesised devices are shown in Table 2.

Table 2: Synthetic techniques, band gap, the configuration of devices made and efficiencies of some of the main copper based quarternary and multinary solar energy materials. Thin films (TF), Nanocrystals (NC) and efficiency (PCE).

TF/NC	Method of synthesis	Compounds used	Band gap (eV)	Configuration of cell/device	PCE (%), V_{OC} (mV), J_{SC} (mA cm^{-2}) and FF (%)	ref
3.2. Cu_2ZnSnS_4 (CZTS)						
TF	spray pyrolysis	CuCl, $ZnCl_2$, $SnCl_4$, $SC(NH_2)_2$	1.46	--	--	171
TF	electron-beam (EB) evaporation	Metallic Cu, Zn, Sn and S powder	1.45	SLG/Mo/CZTS/CdS/ZnO/Al	PCE = 0.66, V_{OC} = 400, J_{SC} = 6.0 and FF = 20	172
TF	argon beam sputtering	Metallic Cu, Zn, Sn and S powder	--	SLG/Mo/CZTS/CdS/ZnO/Al	J_{SC} = 0.1 and V_{OC} = 265 mV	170, 236
TF	electroplating	Metallic Cu, Zn, Sn and S powder	--	SLGITO/i-ZnO/CdS/CZTS	PCE = 7.3, V_{OC} = 567, J_{SC} = 22 and FF = 20	229

TF	EB evaporation	Metallic Cu, Zn, Sn and S powder	1.46-1.6	Mo/SLG/CZTS/CdS/Al:ZnO/Al	PCE = 2.62, V_{OC} = 522.4, J_{SC} =14.11 and FF = 35.54.	237
TF	radio frequency (RF) magnetron sputtering	Cu_2S, ZnS and SnS	1.51	--	--	238
TF	sputtering	Metallic Cu, Zn and Sn	1.5	--	--	239
TF	EB evaporation/sulfurization	Metallic Cu, ZnS, Sn, N_2/H_2S		Mo/SLG/CZTS/CdS/Al:ZnO/Al	PCE = 4.53, V_{OC} = 629, J_{SC} = 12.53 and FF = 58	240
TF	ion beam sputtering	Metallic Cu, Zn and Sn	1.51	--	--	241
TF	pulsed laser deposition (PLD)	Cu_2S, ZnS and SnS_2	1.5	--	--	242
TF	spraying	CuCl, $ZnCl_2$, $SnCl_4$, $SC(NH_2)_2$	1.5	--	--	243
TF	Electrodeposition/ annealing	$CuCl_2$, $ZnCl_2$, $SnCl_2$/ S powder	1.49	glass/Mo/ CZTS/CdS/ZnO/ITO/Ni-Al	PCE = 0.8, V_{OC} = 295, J_{SC} = 8.7 and FF = 32	195

TF	Electroplating/ sulfurization	$CuSO_4$,$ZnSO_4$, Sn SO_4, H_2SO_4 and $PdCl_2$	--	glass/Mo/ CZTS/CdS/ZnO:Al/Al	PCE = 0.98 , V_{OC} = 262 and J_{SC} = 9.85	244
TF	Electrodeposition/ annealing	$CuSO_4$, $Sn(SO_3CH_3)_2$, CH_3SO_3H, $ZnSO_4.7H_2O$	--	glass/Mo/ CZTS/CdS/i-ZnO/ZnO:Al	PCE = 3.2, V_{OC} = 480, J_{SC} = 15.3 and FF = 45	245
TF	Non-vacuum electrodeposition	Cu(II), Zn(II) and Sn(IV) metal salts	1.54	glass/Mo/ CZTS/CdS/i-ZnO/ZnO:Al/Ni-Al	PCE = 3.6 , V_{OC} = 511, J_{SC} = 16.2 and FF = 43	246
TF	electrodeposition /sulfurization	$CuSO_4$, $ZnSO_4$, $SnCl_2$ and $Na_3C_6H_5O_7$		glass/Mo/CZTS/CdS/ZnO/Ni–Al	PCE = 3. 16 and V_{OC} = 540	247
TF	spin coating	$Cu(CH_3COO)_2$, $Zn(CH_3COO)_2$, $SnCl_2$, $CH_3OCH_2CH_2OH$ and $HOCH_2CH_2NH_2$		SLG/Mo/CZTS/CdS/Al:ZnO/Al	PCE = 1.01, VOC = 390, JSC = 7. 8 and FF = 33, PCE = 1.61, VOC = 554 and FF = 33	248-250
TF	spin coating	$Cu(CH_3COO)_2$, $Zn(CH_3COO)_2$, $SnCl_2$, $CH_3OCH_2CH_2OH$ and $HOCH_2CH_2NH_2$		Al/ Al:ZnO/CdS/CZTS/Mo/SLG	PCE = 2.03, V_{OC} = 575, J_{SC} = 9.69 and FF = 36	251
TF	sol-gel spin coating	$CuCl_2$, $ZnCl_2$, $SnCl_2$ and $SC(NH_2)_2$	1.5	--	--	252
TF	pulsed laser deposition (PLD)	Cu, Zn, Sn pellets and S powder	1.5	SLG/Mo/ CZTS/CdS/Al:ZnO	PCE = 1.74, V_{OC} = 546, J_{SC} = 6.78 and FF = 48	253

TF	sputtering	Cu metal, ZnS, SnS, H_2S	1.45	SLG/Mo/ CZTS/CdS/Al:ZnO	PCE = 5.74 ,V_{OC} = 662, J_{SC} = 15.7 and FF = 55	254
TF	co-sputtering	Cu, SnS, ZnS, and S		SLG/Mo/ CZTS/CdS/Al:ZnO	PCE = 6.77, V_{OC} = 610, J_{SC} = 17.9 and FF = 62	172
TF	EB evaporation/sulfurization	Cu, SnS, and ZnS		glass/Mo/CZTS/CdS/ZnO:Al/Al	PCE = 1.79, V_{OC} = 478, J_{SC} = 9.78 and FF = 38	255
TF	RF co-sputtering	Cu, SnS, and ZnS		SLG/Mo/ CZTS/CdS/Al:ZnO	PCE = 6:77, V_{OC} = 610, J_{SC} = 17. 9 and FF= 62	209
TF	RF co-sputtering/sulfurization	Cu, SnS, and ZnS /H_2S		SLG/Mo/ CZTS/CdS/Al:ZnO	PCE = 4.1, V_{OC} = 612, J_{SC} = 10.6 and FF = 62.3 (5% of H_2S) PCE = 8, V_{OC} = 634, J_{SC} = 9.5 and FF = 62.7 (20% H_2S).	256
TF	DC magnetron sputtering followed by sulfurization	metallic Cu, Zn Sn and S vapor	1.43	--	--	257, 258
TF	spraying on hot substrate	CuCl, $Zn(O_2CCH_3)_2$ $SnCl_4$ and $SC(NH_2)_2$	1.40 - 1.45	--	--	259

TF	PLD/annealing	Cu_2S, ZnS, SnS_2 and H_2S	1.48	--	--	260
TF	magnetron co-sputtering	Metallic Cu, Zn, Sn and S	1.52± 0.01	--	--	261
TF	evaporation	Metallic Cu, Zn, Sn and S	--	SLG/Mo/CZTS/CdS/i-ZnO/Al:ZnO(or ITO)/MgF_2(or Ni–Al)	PCE = 6.8, V_{OC} = 587, J_{SC} = 17.8 and FF = 65	210
TF	RF magnetron sputtering/ sulfurized	Metallic Zn, Sn, Cu and S	1.47	In_2O_3/CdS/CZTS/Mo/SLG	PCE = 3.7, V_{OC} = 425, J_{SC} = 16.5 and FF= 53	262
TF	DC magentron sputtering / sulfurization	Metallic Cu, Zn, Sn and S	--	Al/ Al:ZnO/i-ZnO/CdS/CZTS/Mo/glass	PCE = 4.59, V_{OC} = 545, J_{SC} = 15.44 and FF = 54.6	263
TF	thermal evaporation/ annealing	Cu, SnS, ZnS and H_2S	1.51± 0.01	SLG/Mo/CZTS/CdS/Al:ZnO/Ni/Al	PCE = 4.1, V_{OC} = 541, J_{SC} = 13.0 and FF = 59.8	264
TF	thermal evaporation	Metallic Cu, Zn,Sn and S	--	SLG/Mo/CZTS/CdS/i-ZnO/Al:ZnO/Ni/Al/MgF_2	PCE = 8.4, V_{OC} = 661, J_{SC} = 19.5 and FF = 65.8	265
TF	PLD	Cu_2S, ZnS and SnS_2	1.53-1.98	--	--	266

TF	PLD technique	Cu_2S, ZnS andSnS_2	1.54, 1.52	glass/Mo/CZTS/CdS/Al:ZnO/Al	PCE = 3.14, V_{OC} = 651, J_{SC} = 8.76 and FF = 55; PCE = 2.02, VOC = 585 mV, JSC = 6.74, FF = 51	267, 268
TF	spray pyrolysis	$SnCl_2$, $SnCl_4$, CuCl, $Zn(O_2CCH_3)_2$ and $SC(NH_2)_2$	1.5	Al/ZnO:Al/In_2S_3/CZTS/Mo/glass	V_{OC} = 380 and J_{SC} = 2.4	269
TF	ultrasonic spray pyrolysis	$SnCl_4$, CuC_2 , $ZnCl_2$ and $SC(NH_2)_2$	1.5	--	--	270
TF	Ball milling/ Screen printing	Metallic Cu, Zn,Sn and S	1.49	PI/Mo/CZTS/CdS/ZnO:Al/Al- grid	PCE = 0.49, V_{OC} = 386, J_{SC} = 4.76 and FF = 27	271
TF	CBD	Cu(II) salt, SnS and ZnS	--	SLG/Mo/CZTS/CdS/Al:ZnO/Al	PCE = 0.16, V_{OC} = 210 and J_{SC} = 2.4	272
NC	hot injection	$Zn(C_5H_7O_2)_2$, $[CH_3COCH=C(OH_3]_2SnBr_2$, OA and S powder		FTO/ CZTS/ N719 –Ru dye/ TiO_2/ (ES-004).	PCE = 7.37, V_{OC} = 800, J_{SC} = 17.7 and FF = 52. 2	273
TF	successive ionic layer adsorption and reaction (SILAR)	CuCl, $ZnSO_4$, $SnCl_4$, C_2H_5NS	1.55	SLG/Mo/CZTS/CdS/Al:ZnO/Al	PCE = 0.12, V_{OC} = 128.8, J_{SC} = 0.96 and FF = 24	274

TF	successive ionic layer adsorption and reaction (SILAR)	CuCl, $ZnSO_4$, $SnCl_4$ and S or Na_2S	--	SLG/Mo/CZTS/CdS/Al:ZnO/Al	PCE = 0.396, V_{OC} = 280.5, J_{SC} = 0.563 and FF = 62	275
TF	flash evaporation	ZnS, CuS and SnS		--	--	276
TF	successive ionic adsorption and reaction (SILAR)	$CuSO_4$, $SnSO_4$, $ZnSO_4$, Na_2S.	1.25 - 1.47	CZTS (working electrodes) ITO (counter electrode) [Eu (III)$(NO_3)_3$], (electron scavenger)	PCE = 1.06 and Jsc = 8.27	278
TF	thermal evaporation/annealing	ZnS, metallic Sn, Cu and S	1.44, 1.56	--	PCE = 3.52, V_{OC} = 484, J_{SC} = 14.56 and FF = 50.1	279, 280
TF	DC magnetron sputtering/sulfurization	Cu–Sn alloy, Zn metal, S powder	--	DSSC : TiO_2/FTO/ N719 (photoanode) CE: TO/CZTS	PCE = 7.94, V_{OC} = 740.5, Jsc = 17.2 and FF = 62	281
TF	open atmosphere chemical vapour deposition (OACVD)	$Cu(C_5H_7O_2)_2$, $Zn(C_5H_7O_2)_2$ and $Sn(C_5H_7O_2)_2$	--	Al/Al-doped-ZnO/CdS/CZT(S,O)/Mo/soda-lime glass substrate	PCE = 6.03, V_{OC} = 658, J_{SC} = 16.5 and FF = 55	282
TF	sputtering/sulfurization	Zn, Sn, Cu, S and H_2S	--	SLG/Mo/CZTS/CdS/Al:ZnO/Al	PCE = 5.1, Voc = 573, Jsc = 18.38 and FF = 48	230, 234

TF	Spin coating/sulfurization	$Cu(CO_2CH_3)_2 \cdot H_2O$, $Zn(CH_3COO)_2$, $SnCl_4$, L-cysteine and ethanol	1.45	DSSC: TiO_2 (photoanode as the working electrode) CZTS/FTO (CE)	PCE = 3.14, Voc = 724 and Jsc = 6.71	235
TF	PLD	Cu_2S, ZnS and SnS_2	1.54	Glass/Mo/CZTS/CdS/ZnO:Al/Al	PCE = 4.13, Voc = 700, Jsc = 10.01 and FF = 59	231
TF	slurry sulfurization	$Cu(CO_2CH_3)_2 \cdot H_2O$, $Zn(CH_3COO)_2$, $SnCl_4$, and L-cysteine	1.45, 1.48	TiO_2 /FTO (photoanode) CZTS/FTO or Pt/FTO (CE)	PCE = 3.141,V_{OC} = 0.724, Jsc = 6.71 and FF = 64.61	207
NC	the hot injection method	$Cu(C_5H_7O_2)_2$, $Zn(CH_3COO)_2$, $Sn(CH_3COO)_4$, S powder, OLA and triphenyl phosphate (TPP)	1.48	SLG/ Mo/CZTS/CdS/i-ZnO/ ITO/ Ni/Al	PCE = 3.6, Voc = 431, Jsc = 23.28 and FF= 35.78	283
NC	the hot injection method	$Cu(C_5H_7O_2)_2$, $Zn(CH_3COO)_2$, $(CH_3CO_2)_4Sn$, S and OLA	1.5	--	--	284
NC	high-temperature arrested precipitation	$Cu(C_5H_7O_2)_2$, $[Zn(O_2CCH_3)_2]$, [SnCl2 ·2H2O], S in OLA	1.3	Au/CZTS/CdS/ ZnO/ITO	PCE = 0.23, V_{OC} = 321, J_{SC} = 1.95 and FF = 37	285
NC	solvothermal approach	$CuCl_2$, $Zn(CH_3COO)_2$, $SnCl_4$ and S in ethylene diamine	1.5	--	--	286

NC	hot-injection	$CuCl_2$. $2H_2O$, $ZnCl_2$, $SnCl_4.H_2O$, dodecanethiol (DDT) and OLA	1.4	--	--	287
NC	non-injection	$[Cu(dedtc)_2]$, $[Zn(dedtc)_2]$, $[Sn(dedtc)_4]$, hexadecanethiol and trioctylamine	1.55	--	--	138
NC	one-pot heating process	$Cu(acac)_2$, $Zn(OAc)_2$, $SnCl_2$, n-dodecanethiol and oleylamine	--	--	--	288
NC	one-pot heating process	CuI, $SnCl_4.5H_2O$ and $Zn(EtXn)_2$, oleylamine and dodecanethiol solution	1.45–1.55	--	--	289
NC	colloidal one pot synthesis	$Cu(C_5H_7O_2)_2$, $Zn(O_2CCH_3)_2$, $SnC_{l4}\cdot(H_2O)_5$, OLA and ODE , bis(trimethylsilyl) sulfide $((TMS)_2S)$	1.5	--	--	290
NC	colloidal one pot synthesis	$CuCl_2$, $Zn(dedc)_2$, $Sn(dedc)_4$, DT and OA	--	--	--	291
NC	thermal decomposition	$Cu(CH_3COO)_2$, $Fe(NO_3)_3$, $SnCl_2$ and $SC(NH_2)_2$	--	--	--	292

NC	controlled injection	$Zn(CH_3COO)_2 \cdot 2H_2O$, $CuCl_2$, $SnCl_2$, and OLA	--	--	--	293
NC	hydrothermal process	$CuCl_2$, $ZnCl_2$, $SnCl_4$, Na_2S and ethylene diamine	1.55 eV	--	--	294
NC	hot injection	Cu(OAc), $Zn(OAc)_2$, SnI_4 and OLA	--	--	--	295

3.3. $Cu_2ZnSnSe_4$ (CZTSe)

TF	Thermal decomposition	$Cu(NO_3)_2$.$5H_2O$, $Zn(NO_3)_2 \cdot 6H_2O$, $SnCl_4$. $5H_2O$, ethanol, and 1,2-propanediol	--	CdS/ ZnO/ZnO:Al/C layer/CZTSe	PCE = 4.2 , V_{OC} = 362, J_{SC} = 22.2 and FF = 49.6	296
TF	thermal co-evaporation	Metallic Cu, Zn, Sn and S	--	SLG/Mo/NaF/CZTSe/CdS/ZnO/Ni/Al/ MgF_2	PCE = 9.15, Voc = 377, Jsc = 37.4 and FF = 64.9	212, 233
TF	spray pyrolysis/annealing	$CuCl_2$, $ZnCl_2$, $SnCl_4 \cdot 5H_2O$ and $SC(NH_2)_2$	--	ITO/i-ZnO/ In_2S_3/CZTSe/Mo/glass	PCE = 2.39, Voc = 0.36 V and Jsc = 16.91	223
TF	Electrodeposition/ selenization	Metallic Cu, Zn, and Cu10Sn90 (alloy), Se	--	Al:ZnO/i-ZnO /CdS /$Cu_2ZnSnSe_4$ /$MoSe_2$, TiN/ Mo/glass	PCE = 7.0, V_{OC} = 369, J_{SC} = 32.4 and FF = 58.5	297

TF	DC sputtering and selenization	Metallic Cu, Zn, Sn and H_2Se	--	SLG/Mo/NaF/CZTSe/CdS/ZnO/Ni-Al	PCE = 6.3, J_{SC} = 31.3, V_{OC} = 390 and FF = 52	298
TF	DC sputtering and selenizing	Metallic Cu, Zn, Sn, H_2Se or Se	--	SLG/Mo/NaF/CZTSe/CdS/ZnO/Ni-Al/ MgF_2	PCE = 9.7, V_{OC} =408 mV, Jsc = 38.9 and FF = 61.4	227
TF	Vacuum deposition	Cu, Zn, and Sn and Se	--	SLG/Mo/$MoSe_2$/CZTSe/CdS/TCO/ MgF_2	PCE = 8.9, Voc 331, Jsc = 36.7 and FF= 58.8	228
TF	annealing	(Cu_2SnSe_3) /ZnSe	--	Glass/Mo/CZTSe/CdS/i-ZnO/ZnO:Al/ Al-grid	PCE = 7.14, Voc 385, Jsc = 42.6 and FF= 54.2	299
TF	DC-sputtering/selenizing	Cu10Sn90, metallic Zn and Cu and Se	--	glass/Mo/CZTSe/CdS/i-ZnO/ZnO:Al/ /Ni-Al	PCE = 10.4, Jsc = 39.7, Voc = 394 and FF = 66.4	300
NC	hot-injection	($Cu(OAc)_2$, $ZnCl_2$,$SnCl_2 \cdot 2H_2O$	--	--	--	301

3.4. $Cu_2ZnSn(S_{1-x}Se_x)$ (CZTSSe)

TF	Electrodeposition	$CuSO_4$, $ZnSO_4$, $SnSO_4$, $Na_2S_2O_3$, $Na_3C_6H_5O_7$ and $C_4H_4K_2O_6$	--	--	--	302
TF	hydrazine-based liquid process	Cu_2S, Zn, Sn, SnSe, Se, hydrazine	--	Glass/ Mo/CZTSSe/CdS/ZnO/ITO	PCE = 10.1, V_{OC} = 517, J_{SC} = 30.8 and FF = 63.7	211
NC	hydrazine-based liquid process	Cu_2S,ZnSnSe, Se, hydrazine	--	Glass/ Mo /CZTSSEe/CdS/In_2S_3/ZnO/ITO	PCE =12.7, V_{OC} = 466, J_{SC} = 38.9 and FF = 69.8	214, 217
TF	Spray coating	NaHS, CH_3CN, $SnCl_4$, $ZnCl_2$, CuCl, H_2O and ethanol	1.1-1.13	Glass/ Mo/CZTSSe/CdS/ZnO/ITO	PCE = 8.6, V_{OC} = 460, J_{SC} = 30.9 and FF = 60	219
TF	Spin coating/annealing	$Cu(OAc)_2 \cdot H_2O$, $SnCl_2.2H_2O$, ZnCl, $SC(NH_2)_2$, DMSO and Se	1.1	glass/Mo/$MoSe_2$/CZTSSe/CdS/ZnO/ITO	PCE = 8.32, V_{OC} = 443, J_{SC} = 31.2 and FF = 60.2	220
TF	Electrodeposition/ annealing	$CuSO_4 \cdot 5H_2O$, $ZnSO_4 \cdot 7H_2O$, $SnCl_2$, trisodium citrate, S and Se	--	glass/Mo/$MoSe_2$/CZTSSe/CdS/ZnO/AlZnO/ Ni-Al.	PCE = 8.0, V_{OC} = 390, J_{SC} = 35.3 and FF = 58	221

TF	Spin coating/hydrazine	Cu_2S, S, SnSe, Zn,Se and hydrazine	1.2	glass/Mo/ CZTSSe/In_2S_3/ CdS/ZnO/ITO/ Ni-Al.	PCE = 7.19, V_{OC} = 435 and J_{SC} = 29.2	222
TF	Spin coating/annealing	$Cu(CH_3COO)_2 \cdot H_2O$, $ZnCl_2$, $SnCl_2.2H_2O$, $SC(NH_2)_2$, DMSO and Se	--	Ni-Al/ITO/ZnO/CdS/CZTSSe/Mo/SLG	PCE = 4.1, V_{OC} = 400, J_{SC} = 24.9 and FF = 41.2	224
TF	sputtering	Cu, SnS_2, ZnS, H_2S and Se	1.05-1.32	--	--	303
TF	Co-sputtering	Cux(S,Se)y, Znx(S,Se)y, Snx(S,Se)y, SnS and S	--	glass/Mo/CZTSSe/CdS/i-ZnO/AlZnO	PCE = 9.3, V_{OC} = 520 and J_{SC} = 28.3	225
TF	spin coating/hydrazine	Cu, ZnS, SnS_2, S and Se	1.08-1.12	glass/Mo/CZTSSe/CdS/ZnO/ITO/Ni-Al.	PCE = 11.1, V_{OC} = 460, J_{SC} = 34.5 and FF = 69.8	213
TF	Solution based method/annealing	$CuCl_2$, CTS, ZnS, SnS, CuS, and Cu7S4, OLA, Se and trioctylphosphine	1.1	SLG/Mo/CZTSSe/CdS/i-ZnO/ITO	PCE = 8.5, V_{OC} = 451, J_{SC} = -29 and FF = 64.9	232
TF TF	spin coating/hydrazine	Metallic Cu, Zn, Sn, S and Se	--	glass/Mo/CZTSSe/CdS/ZnO/ITO/Ni-Al/MgF_2	PCE = 12.6, V_{OC} = 513.4, J_{SC} = 35.2 and FF = 69.8	108
TF	screen printing and high-pressure sintering (PHS) process	Metallic Cu, Zn, Sn, S, and Se	1.2	Ag/ITO/i-ZnO/CdS/CZTSSe/Mo/soda-lime glass	PCE = 2.63, V_{OC} = 372, J J_{SC} = 18.7 and FF= 37.8	304

TF	annealing	CTS (Cu_2SnS_3), ZnS, SnS, THF and Se vapour	1.07	Ag/ITO/i-ZnO/CdS/CZTSSe/Mo/soda glass	PCE = 9.02, V_{OC} = 445, J_{SC} = 32.01 and FF = 63.3	305
TF	electrodeposition/selenization	$CuSO_4.5H_2O$, $ZnSO_4$. $6H_2O$ $SnSO_4$. H_2O, $Na_3C_6H_5O_7$.$2H_2O$ and tartaric acid	1.40-1.08	--	--	306
NC	colloidal	CuI, $Zn(CH_3COO)_2.2H_2O$, $SnCl_2.2H_2O$, OLA and 1-dodecanethiol	1.0 to 1.2	--	--	307
TF	Sintering	$Cu_2S(Se)$, ZnS(Se), SnS_2, Sn, S, and Se powders	1.13-1.52	--	--	308
TF	PLD	$Cu_2S(Se)$, ZnS(Se), SnS_2, Sn, S, and Se powders	0.96-1.5	--	--	309
TF	solution-based approach and a post-annealing	Cu(OAc), $Zn(OAc)_2$, $SnCl_2$, thioacetamide and Se pellets	1.46-1.14	--	--	310
NC	Hot injection/annealing	$Cu(C_5H_7O_2)_2$, $Zn(C_5H_7O_2)_2$, $[CH_3COCH=C(O-)CH_3]_2SnBr_2$] and OLA	1.05	SLG/Mo/ CZTSSe/CdS /ZnO /ITO	PCE = 6.7, V_{OC} = 0.42 V, J_{SC} = 30.4, FF = 52.7	193

NC	Solution based method/ annealed	CuI, ZnI_2, SnI_2, Na_2S and Na_2Se		Al /B-doped ZnO/i-ZnO/CdS/ CZTSSe/Mo/SLG	PCE = 5.4, V_{OC} = 415, J_{SC} = 29. 6 and FF = 44	311
NC	Simple spraying of colloidal solution/Se annealing	$CuCl_2$, $ZnCl_2$, $SnCl_4$, NaHS, NaHSe and acetonitrile	1.13	SLG/Mo/ CZTSSe/CdS /ZnO /ITO	PCE = 8.6, V_{OC} = 460, J_{SC} = 30.9 and FF = 60	312
NC	Hot injection/ selenisation	$Cu(C_5H_7O_2)_2$, $Zn(C_5H_7O_2)_2 \cdot xH_2O$, $[CH_3COCH=C(O-)CH_3]_2$, $SnCl_2$ OLA and S powder	1.1	SLG/Mo/ CZTSSe CdS/i-ZnO /ITO / Ni/Al/MgF_2	PCE = 9.0, V_{OC} = 404, J_{SC} = 35.1 and FF = 63.7	218, 313

3. 5. Cu_2FeSnS_4 (CFTS)

NC	hydrothermal	$CuCl_2.2H_2O$, $FeCl_3.3H_2O$, $SnCl_4.5H_2O$ and NH_2CSNH_2 (Tu)	--	--	--	314
NC	thermolysis in oleylamine/dip coating /annealing	S powder, $Cu(CO_2CH_3)_2 \cdot H_2O$, $FeCl_2$, $SnCl_2$ and oleylamine	--	--	--	315
NC	hot-injection	$Cu(acac)_2$, $Fe(acac)_2$ $SnCl_2$, S and OLA	1.28± 0.02	--	--	316

NC	hot injection	$Cu(acac)_2$, $Fe(acac)_3$, $SnCl_4.5H_2O$, OLA, (1-DDT) and tert-dodecanethiol (t-DDT)	1.54, 1.46	--	--	64
NC	solvothermal method	$CuCl_2.2H_2O$, $FeCl_3.3H_2O$, $SnCl_2.2H_2O$, (CH_4N_2S) and N,N-dimethylformamide (DMF)	1.28	--	--	63
NC	ultrasound-assisted microwave irradiation	$Cu(NO_3)_2.3H_2O$, $FeCl_2.4H_2O$, $SnCl_2.2H_2O$ and CH_3CSNH_2	1.35	--	--	65
NC	thermal decomposition	$Cu(CH_3COO)_2$, $Fe(NO_3)_3$, $SnCl_2$, and $SC(NH_2)_2$	1.40	--	--	317
NC	microwave irradiation	$Cu(NO_3)_2 \cdot 3H_2O$, $Fe(NO_3)_3 \cdot 9H_2O$, $SnCl_2 \cdot 2H_2O$, H_2NCSNH_2, and ethylene glycol	1.52	--	--	318
NC	solvothermal	Ethylene glycol (EG), $CuCl_2.2H_2O$, $SnCl_4.5H_2O$, $FeCl_2$ and $SC(NH_2)_2$	1.33	--	--	68
NC	reflux method	$CuCl_2.2H_2O$, $FeCl_3.2H_2O$, $SnCl_4.5H_2O$, CH_4N_2S, ethylene glycol (EG) andtriethylenetetramine (TETA)	1.32	--	--	66

TF	spray pyrolysis	$CuCl_2 \cdot 2H_2O$, $FeCl_3 \cdot 6H_2O$, $SnCl_2 \cdot 2H_2O$, and H_2NCSNH_2	1.46-1.65	CFTS film (photocathode) and iodine/iodide electrolyte, TiO_2/ITO or FTO (CE)	PCE = 8.03, J_{SC} = 14.57, V_{OC} = 750 and FF = 73	100
NC	electrospinning technique	$CuCl_2$, $FeCl_3$, $SnCl_2$ and DMF	--	--	--	319
TF	spray pyrolysis	$Cu(CH_3COO)_2$, $FeCl_3$. $6H_2O$, $SnCl_2.2H_2O$, $SC(NH_2)_2$ and S	1.37	--	--	70

3.6. $Cu_2FeSnSe_4$ (CFTSe)

NC	one-pot solvothermal method	$CuCl_2.2H_2O$, $FeCl_2$, $SnCl_4$. $4H_2O$ and Se powder	1.12	--	--	166, 320
TF	RF magnetron sputtering/selenization	Metallic Cu, Fe Sn, Se powder	1.10	--	--	73
NC	solvothermal method	$CuCl_2$. $2H_2O$, $SnCl_4.5H_2O$, $FeCl_2$ and Se powder	1.19-1.25	--	--	72, 226
TF	spray pyrolysis	$Cu(CH_3COO)_2$, $FeCl_3$. $6H_2O$, $SnCl_2.2H_2O$, $SC(NH_2)_2$ and Se	1.37-1.11	--	--	70

TF	RF magnetron sputtering/ selenization	Metallic Zn, Fe and Cu, Se powder	1.19	glass/Mo/CFTSe(CIAS)/CdS/i-ZnO/AZO	J_{SC} = 0.79, V_{OC} = 94 and FF = 27	321
NC	hot-injection	$Cu(acac)_2$, $Fe(acac)_2$, $SnCl_2$, OLA and alkyl ammonium selenide	--	--	--	322

3. 7. $Cu_2(Zn_zFe_{1-z})SnS_4$ (CZFTS)

TF	Thermal method	Metallic Cu, Zn, Sn, Fe and S powder	--	--	--	323
TF	spray pyrolysis/ sulfurization	$CuCl_2$, $ZnCl_2$, $SnCl_4{\cdot}5H_2O$, $SC(NH_2)_2$ and S powder	1.36 - 1.97	--	--	56
TF	pulsed laser deposition	Cu_2S, ZnS, FeS and SnS_2	1.33- 1.74	--	--	324
NC	hot injection	$Cu(acac)_2$, $Zn(acac)_2$, $Fe(acac)_2$, $SnCl_2$, OLA and S	1.25 - 1.52	--	--	325

3.8. Summary

In summary, the potential applications of these materials are reviewed in detail: the synthetic pathways starting from simple to complex techniques and less efficient to more efficient device fabrications were analysed. The urge for cost effective highly efficient devices and synthetic methods to avoid draw backs of the current devices and techniques are well explored. Some of these techniques are simple and useful which needs further research in order to get high-efficiency low-cost devices. Many synthetic routes need further studies and the fabrication techniques are not meeting the current demand of devices. Moreover, stability of the devices and techniques are more challenging. Excellent techniques with minimum short comings for developing highly efficient, economic and very stable solar cells and devices is an area for potential research in the near and far future.

CHAPTER - IV: PAPER -1

"Thin films of tin(II) sulfide (SnS) by aerosol-assisted chemical vapour deposition (AACVD) using tin(II) dithiocarbamates as single-source precursors"

Punarja Kevin, David. J. Lewis, M. A. Malik, J. Raftery, Paul O'Brien, *J. Cryst. Growth,* 2015, **415**, 93-99.

Journal of Crystal Growth 415 (2015) 93–99

Contents lists available at ScienceDirect

Journal of Crystal Growth

journal homepage: www.elsevier.com/locate/jcrysgro

Thin films of tin(II) sulphide (SnS) by aerosol-assisted chemical vapour deposition (AACVD) using tin(II) dithiocarbamates as single-source precursors

Punarja Kevin [a], David J. Lewis [a,b], James Raftery [a], M. Azad Malik [a], Paul O'Brien [a,b,*]

[a] School of Chemistry, University of Manchester, Oxford Road, Manchester M13 9PL, United Kingdom
[b] School of Materials, University of Manchester, Oxford Road, Manchester M13 9PL, United Kingdom

ARTICLE INFO

Article history:
Received 26 March 2014
Received in revised form
3 July 2014
Accepted 10 July 2014
Communicated by Dr. M. Tischler
Available online 17 July 2014

Keywords:
B1. Sulphides
B3. Solar cells
Chemical vapour deposition processes

ABSTRACT

The synthesis of the asymmetric dithiocarbamates of tin(II) with the formula $[Sn(S_2CNRR')_2]$ (where R=Et, R'=*n*-Bu (**1**); R=Me, R'=*n*-Bu (**2**); R=R'=Et (**3**)) and their use for the deposition of SnS thin films by aerosol-assisted chemical vapour deposition (AACVD) is described. The effects of temperature and the concentration of the precursors on deposition were investigated. The stoichiometry of SnS was best at higher concentrations of precursors (250 mM) and at 450 °C. The direct electronic band gap of the SnS produced by this method was estimated from optical absorbance measurements as 1.2 eV. The composition of films was confirmed by powder X-ray diffraction (p-XRD) and energy dispersive analysis of X-rays (EDAX) spectroscopy.

1. Introduction

Tin monosulphide (SnS) [1] is a promising candidate amongst the IV–VI semiconductors for sustainable photovoltaic and optoelectronic applications [2]. SnS has intense absorbance ($\alpha \sim 10^4\ cm^{-1}$) across the electromagnetic (EM) spectrum, and a direct band gap of 1.4 eV [3], similar to that of silicon, and can harvest solar radiation from the near-infrared region of the EM spectrum and upwards in energy. The constituent elements, tin and sulphur, are abundant, inexpensive, less toxic and generally less environmentally harmful as compared with materials such as lead sulphide (PbS) and cadmium sulphide (CdS). The SnS binary system is simpler compared to multicomponent materials with potential for photovoltaic applications such as copper zinc tin sulfides (CZTS) [4,5] and the copper indium gallium sulphides and selenides (CIGS, CIGSe) [6]. Theoretical solar conversion efficiency values of SnS are ca. 24% [7]. So far, solar cells using SnS absorbers with efficiencies of only ca. 2% have been developed [8], and thus the potential for improvement is great.

Processes used for deposition of SnS thin films include chemical bath deposition (CBD) [9], successive ionic layer adsorption and reaction (SILAR) [10,11] and electrochemical deposition [12–14]. Other methods such as thermal evaporation [15], chemical vapour transport (CVT) [16], atomic layer deposition (ALD) [17,18], spray pyrolysis [19,20], dip deposition [21], and pyrolysis [22] have also been reported.

Chemical vapour deposition (CVD) using single-source precursors is a facile route to SnS thin films. Variations of CVD processes such as aerosol-assisted chemical vapour deposition (AACVD) [23,24] and atmospheric pressure chemical vapour deposition (APCVD) [25,26] have attracted attention for the deposition of SnS due to their ease of use and potential for scale up. AACVD in particular offers the advantage that less-volatile precursors can be used, thus widening the types of molecules that can be used to deposit thin films. Single-source precursors in particular offer an advantageous route in CVD especially, as complicating factors such as pre-reaction in the vapour can be avoided [27]. SnS thin films have been deposited by CVD from thiocarbamate precursors such as $Sn(S_2CNEt_2)_4$ [28,29]. ($Sn(S_2CNEt_2)_4$, tin thiolates and dithiolates [25,28,30], as well as from tribenzyl tin(IV) chloride-thiosemicarbazone compounds [23]. We have previously reported the deposition of SnS thin films by AACVD using heteroleptic di-organo tin(IV) *bis*-dialykyldithiocarbamate complexes of formula $[Sn(C_4H_9)_2(S_2CN(RR')_2)_2]$ (R, R'=ethyl; R=methyl, R'=butyl; R, R'=butyl; R=methyl, R'=hexyl) and $[Sn(C_6H_5)_2(S_2CN(RR')_2)_2]$ (R, R'=Et; *R*=Me, R'=*n*-Bu; R, R'=n-Bu; R=R'=Et) [31]. We report

* Corresponding author at: School of Materials, University of Manchester, Oxford Road, Manchester M13 9PL, United Kingdom. Tel.: +44 161 275 4653.
E-mail address: Paul.O'Brien@manchester.ac.uk (P. O'Brien).

http://dx.doi.org/10.1016/j.jcrysgro.2014.07.019

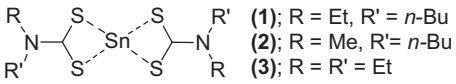

Fig. 1. The *bis*-(dialkyldithiocarbamato)tin(II) complexes studied as precursors for producing SnS thin films by AACVD.

here the growth of SnS thin films using tin(II) complexes of general formula $[Sn(S_2CNRR')_2]$ (Fig. 1). These pre-cursors contain tin in the correct oxidation state for SnS, and may thus give a straightforward route towards this interesting material.

2. Experimental

2.1. General

Reagents and solvents were purchased from Sigma Aldrich or Fisher and used without further purification. All reactions were performed under inert atmosphere. The compounds produced were dried in vacuo at ambient temperature in a vacuum desiccator over calcium chloride.

2.2. Instrumentation

NMR spectra were recorded using a Bruker NMR instrument. Mass spectra were recorded using a Kratos Concept 1S instrument or a Micromass Platform II instrument. Melting points were recorded using a Stuart SMP-10. Microanalysis was performed using a Thermo Scientific Flash 2000 Organic Elemental Analyser by the University of Manchester analytical service. Thermogravimetric analyses were performed using MT TGA/DSC 1. FTIR spectra of compounds were measured using a using Specac ATR. Single crystal X-ray diffraction was run using a Bruker Prospector diffractometer and copper K_α radiation ($\lambda = 1.54178$ Å). The structure was solved by direct methods and refined by full-matrix least-squares fit on F^2. All non-H atoms were refined anisotropically. All calculations were carried out using SHELXTL [32]. p-XRD patterns of thin films deposited on glass substrate were measured using a Bruker AXS D8 Discover diffractometer, using copper K_α radiation ($\lambda = 1.54178$ Å). Films were scanned repetitively over a range of diffraction angles (2θ) using a step size of 0.05° with a dwell time of 0.5 s. SEM analysis was performed using a Philips XL-30 scanning electron microscope in secondary electron mode, and EDAX carried out using a DX4 instrument. Films were coated with elemental carbon using an Edwards model E306A thermal evaporator prior to SEM and EDAX analyses. EDAX analysis using Espirit software included an automatic correction for carbon coating. Band gaps were measured using a Varian Cary 5000 UV–vis absorption spectrometer.

2.3. Synthesis of $[Sn(S_2CN((C_2H_5)(C_4H_9))_2]$ **(1)**

N,*N*-ethylbutyl amine (5.0 g, 49 mmol, 1.0 eq.) and NaOH (2.0 g, 49.4 mmol) in methanol (100 mL) were mixed and cooled to 0–5 °C, followed by the dropwise addition of carbon disulphide (3.8 g, 49 mmol, 1.0 eq.) The resulting mixture was then stirred for a further 30 min, followed by the dropwise addition of tin(II) chloride (4.7 g, 24.5 mmol, 0.5 eq.) in methanol (25 mL). The reaction mixture was stirred for a further hour, after which time a creamy or pale yellow powder formed which was filtered and washed with hexane and dried and kept under vacuum to give the title product as a cream powder. Yield = 3.1 g (27%). M.pt.: 121–125 °C: Elemental analysis: Calc. for $C_{14}H_{28}N_2S_4Sn$: C 35.7 H 6.0 N 5.9 S 27.2 Sn 25.2%. Found C 35.8 H 5.8 N 5.8 S 26.8 Sn 24.4%. FTIR (ν_{max}/cm^{-1}) 2953(w), 2926(w), 2865(w) 1489(s) 1441(m) 1299 (m), 1253(m), 1204(m), 1189(m) 1121(m). ^1H NMR (400 MHz, $CDCl_3$) δ ppm: 0.96 (6H, *t*, Bu CH_3), 1.38 (8H, *q*, CH_2), 1.77 (6H, *t*, CH_3), 3.72 (4H, *q*, Et NCH_2), 3.82 (4H, *t*, $J = 8$ Hz, Bu NCH_2). ^{119}Sn NMR (149 MHz, $CDCl_3$) δ ppm: −522 (s). Crystals of **(1)** suitable for single crystal X-ray diffraction were grown from diffusion of hexane into a chloroform solution of the tin(II) complex.

2.4. Synthesis of $[Sn(S_2CN((CH_3)(C_4H_9))_2]$ **(2)**

(2) was synthesised by the method presented for complex **(1)**, but using *N*,*N*-methylbutyl amine (4.3 g, 49 mmol, 1.0 eq.) and tin(II) chloride (4.7 g, 24.5 mmol, 0.5 eq.) to give a pale yellow powder. Yield = 4.1 g (35%). Elemental analysis: Calc. for $C_{14}H_{24}N_2S_4Sn$: C 32.4 H 5.5 N 6.3 S 28.9 Sn 26.8%. Found C 32.2 H 5.4 N 6.1 S 23.0 Sn 25.6%. M.pt. 125–128 °C. FTIR (ν_{max}/cm^{-1}): 2924.9 (s), 2854(w), 1489 (s),1385 (s), 1236 (m), 1188 (s), 1142 (m), 1075 (m) 966 (s). ^1H NMR (400 MHz, $CDCl_3$) δ ppm: 0.9 (6 H, *t*, $J = 8$ Hz, But CH_3),1.3(4H, *q*, Bu CH_2),1.75 (4H, *m*, But CH_2) 3.18 (6H, *s*, $J = 8$ Hz, NCH_3, 3.58 (4 H, *t*, $J = 7.35$ Hz, NCH_2). ^{119}Sn NMR (149 MHz, $CDCl_3$) δ ppm: −538 (s).

2.5. Synthesis of $[Sn(S_2CN(C_2H_5))_2]$ **(3)**

(3) was synthesised by the addition of tin(II) chloride (4.1 g, 22 mmol, 1.0 eq.) in methanol (50 mL) to the trihydrated monosodium salt of diethyl dithiocarbamate (10 g, 44 mmol, 2.0 eq.) in methanol (100 mL). The product precipitated as a fine yellow powder which was isolated by filtration, washed with hexane (2 × 20 mL) and dried under vacuum to furnish the title product. Yield = 5.4 g (59%). M.pt. 120–128 °C. Elemental analysis: Calc. for $C_{16}H_{32}N_2S_4Sn$: C 28.9 H 4.9 N 6.7 Sn 28.6%. Found C 28.3 H 4.8 N 6.5 Sn 27.0%. M.pt. 123–125 °C. FTIR (ν_{max}/cm^{-1}): 2965 (w), 2941 (w), 1509 (s), 1483 (s), 1350 (m), 1260 (m), 1142 (m), 1199 (m) 1131 (m). ^1H NMR (400 MHz, $CDCl_3$) δ ppm: 0.90 (6H, *t*, $J = 8$ Hz, Hex CH_3), 1.35 (12H, *t*, Hex Et, CH_3), 3.08 (8H, *q*, $J = 16$ Hz, NCH_2). ^{119}Sn NMR (149 MHz, $CDCl_3$) δ ppm: −523 (s).

2.6. Deposition of tin sulphide thin films by aerosol assisted chemical vapour deposition (AACVD) using tin(II) dithiocarbamate precursors.

In a typical deposition, 0.4–2.5 mmol of precursor **(1)**, **(2)** or **(3)** was dissolved in 10 mL of THF in a two-necked round-bottom flask. The AACVD apparatus used for deposition has been described elsewhere [31]. Briefly, A quartz tube reactor containing borosilicate glass substrates (~1 cm × 2 cm and 1 mm thick laid short end-to short end) were placed in a pre-warmed Carbolite furnace. The reactor tube was connected to the flask with a piece of reinforced rubber tubing. The precursor solution was then set up over an ultrasonic humidifier which formed the aerosol. The aerosol droplets were carried to the reactor tube by a constant flow of argon (160–180 $cm^3\ min^{-1}$) into the round-bottom flask for thermal decomposition to deposit products onto the substrate.

3. Results and discussion

3.1. Synthesis of precursors

Tin(II) dithiocarbamates **(1)** and **(2)** were prepared in good yield from the reaction of carbon disulphide with a secondary amine in the presence of a base, followed by metathesis of tin(II) chloride to yield the homoleptic tin(II) complexes. Compound **(3)** was accessed directly from metathesis of $SnCl_2$ with the commercially available sodium salt of diethyl dithiocarbamate. ^{119}Sn NMR spectra of **(1)**–**(3)** showed single peaks in the range −520 to −540 ppm, indicative of a single tin(II) environment.

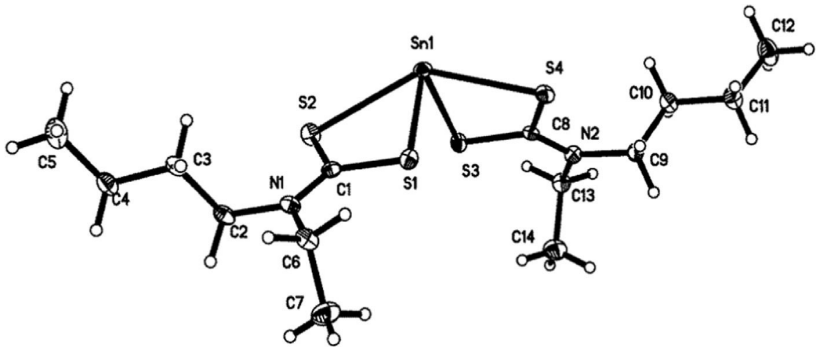

Fig. 2. Crystal structure of **(1)** from X-ray diffraction data. Selected bond lengths (Å) and bond angles (°): Sn1–S1,2.570(7); Sn1–S2-2.835(8); Sn1–S4, 2.73(7); S(1)–Sn(1)–S(2), 66.40(2); S(3)–Sn(1)–S(4), 67.84(2); S(4)–Sn(1)–S(2), 140.36(2); S(1)–Sn(1)–S(3)-95.89(2); S(1)–Sn(1)–S(4),85.65(2); S(3)–Sn(1)–S(2), 86.89(2).

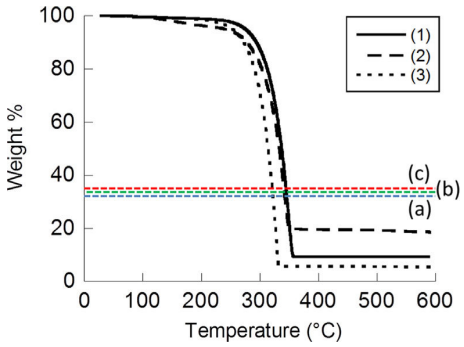

Fig. 3. TGA traces of compounds **(1)**–**(3)**. Horizontal lines (a), (b) and (c) represent the theoretical % weight loss required to produce SnS from compounds **(1)**, **(2)** and **(3)**: 32% (blue), 34% (green) and 36% (red) respectively. (For interpretation of the references to colour in this figure legend, the reader is referred to the web version of this article.)

3.2. Single crystal X-ray diffraction studies of a precursor.

Crystals of complex **(1)**, grown by diffusion of hexane into a chloroform solution of **(1)**, were studied by single crystal X-ray diffraction. The tin(II) ion is coordinated to four sulphur atoms via two bidentate dithiocarbamate ligands (Fig. 2). Each ligand forms a four-membered SnS_2C ring with a short (2.5650(7), 2.5762(7) Å) and a long (2.8356(8), 2.7379(7) Å) Sn–S distances. The sulphur atoms with long Sn–S bonds are pushed further apart (S(4)–Sn(1)–S(2) angle 140.36°) while those with short Sn–S bonds are closer together (S(3)–Sn(1)–S(1) angle is 95.89°). The coordination environment of the tin centre is best described as a distorted square pyramid with the formal lone pair of electrons on Sn(II) occupying the apex of the pyramid. Data for the crystal structure is given in the Supporting Information.

3.3. Thermogravimetric analysis.

The decomposition of the complexes was studied using thermogravimetric analysis (TGA) in the range 25–600 °C at a heating rate of 10 °C min^{-1} under a nitrogen atmosphere (Fig. 3). Complexes **(1)**–**(3)** showed a single-step decomposition, with the majority of the mass loss occurring in the temperature range 300–400 °C. Solid residues which remain after for **(1)** and **(2)** are ca. 10% of the original weight for both complexes. Similarly, **(3)** decomposes in a single step to leave ca. 17% of residue. For precursors **(1)** and **(2)** the theoretical final mass should be 32% and 34% of the original mass for decomposition to SnS respectively, whilst for **(3)** this figure is 36%. More weight is lost than the theoretical amount required for the production of SnS in all cases. The experimental weight losses do not equate to the oxides of tin (SnO or SnO_2) nor to elemental sulphur. We therefore presume that during the TGA analysis that some sublimation occurs in the major weight loss step before stable products are produced.

3.4. Deposition of thin films by AACVD.

Thin films of tin(II) sulphide were deposited on glass substrates by AACVD using THF solutions of precursors **(1)**, **(2)** and **(3)** at 4 mM concentration, using deposition temperatures of 450 °C and 500 °C. Grey adherent films were observed in all cases. The deposited films were analysed by powder X-ray diffraction (p-XRD). The p-XRD patterns of thin films deposited from complexes **(1)**–**(3)** at 450 °C and 500 °C can be partly indexed to orthorhombic SnS (PDF Card No. 00-033-1375, herzenbergite) (Fig. 4),with the relatively highest intensity peak observed at $2\theta = 31.50°$, corresponding to the (111) plane. Peaks could be indexed as SnS: 25.98° (120), 27.44° (021), 30.44 ° (101), 39.01° (131), 45.48° (002), 48.51° (211) and 51.04° (122). Diffraction patterns show an additional peak at 33.50 ° which has been attributed to a SnO_2 cassiterite phase [31].

Scanning electron microscopy (SEM) was used to investigate the morphology of SnS thin films produced from AACVD. Bundles of sheets consisting of small crystallites were deposited with precursor **(1)**. Precursor **(2)** gave uniformly distributed cross linked bundles of sheets at 450 °C and 500 °C. Bundles of sheets were also produced from precursor **(3)** at both temperatures (Fig. 5). A summary of the morphologies of films is presented in Table 1. Analysis of the SnS films by EDAX spectroscopy revealed that the Sn:S stoichiometry was quite variable (Table 1). Films produced at 450 °C and 500 °C from precursor **(1)** generally gave near-to-stoichiometric (percentage basis) SnS (55:45 and 49:51 respectively), whereas precursors **(2)** and **(3)** gave non-stoichiometric, tin-rich films in the ratio ca. 60:40, at both deposition temperatures.

3.5. Investigating the effect of precursor concentration

An investigation into the effect of the precursor concentration in the THF solution used for AACVD was conducted. Intensities of p-XRD diffraction peaks obtained from films deposited at 450 °C using four different concentrations of complexes **(1)**–**(3)** (80 mM, 170 mM and 250 mM) are shown in Fig. 6. The diffraction peaks from films deposited were again indexed to orthorhombic SnS (herzenbergite, PDF Card No. 00-033-1375). The intensity of the SnO_2 peak decreased with increasing concentrations of precursor. At a concentration of 250 mM the peak corresponding to SnO_2 was

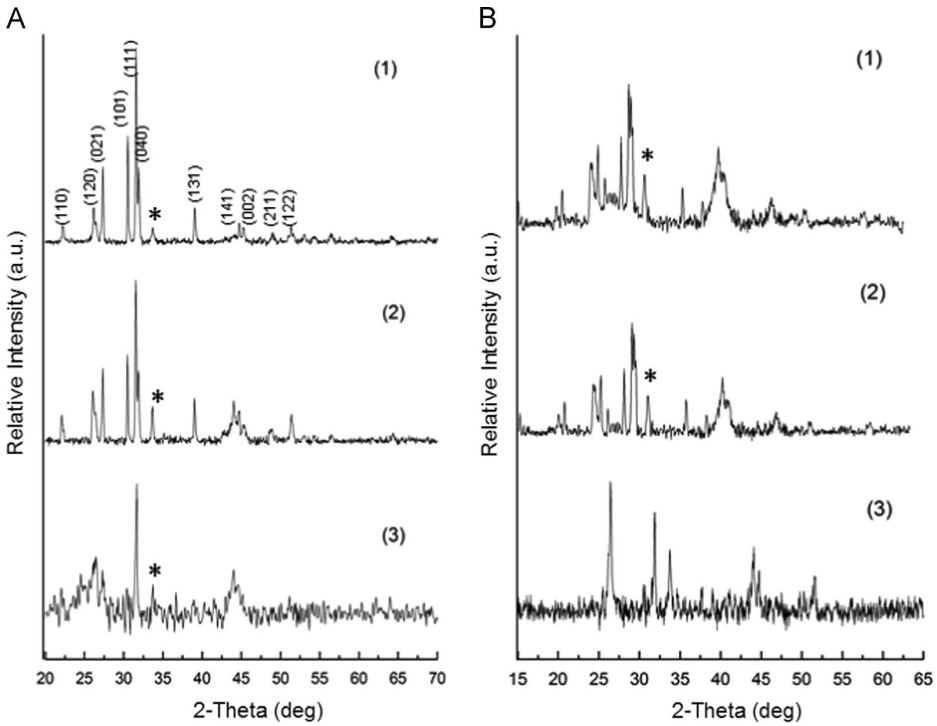

Fig. 4. p-XRD patterns of tin sulphide thin films deposited on glass substrates by AACVD using 40 mM of precursors **(1)**–**(3)** at A) 450 °C and B) 500 °C. Films were deposited over 45 min in all cases. The (*hkl*) reflections corresponding to crystallographic planes in SnS (herzenbergite, PDF Card No. 00-033-1375) are labelled for **(1)** at 450 °C only for clarity purposes. *=reflections attributed to SnO_2.

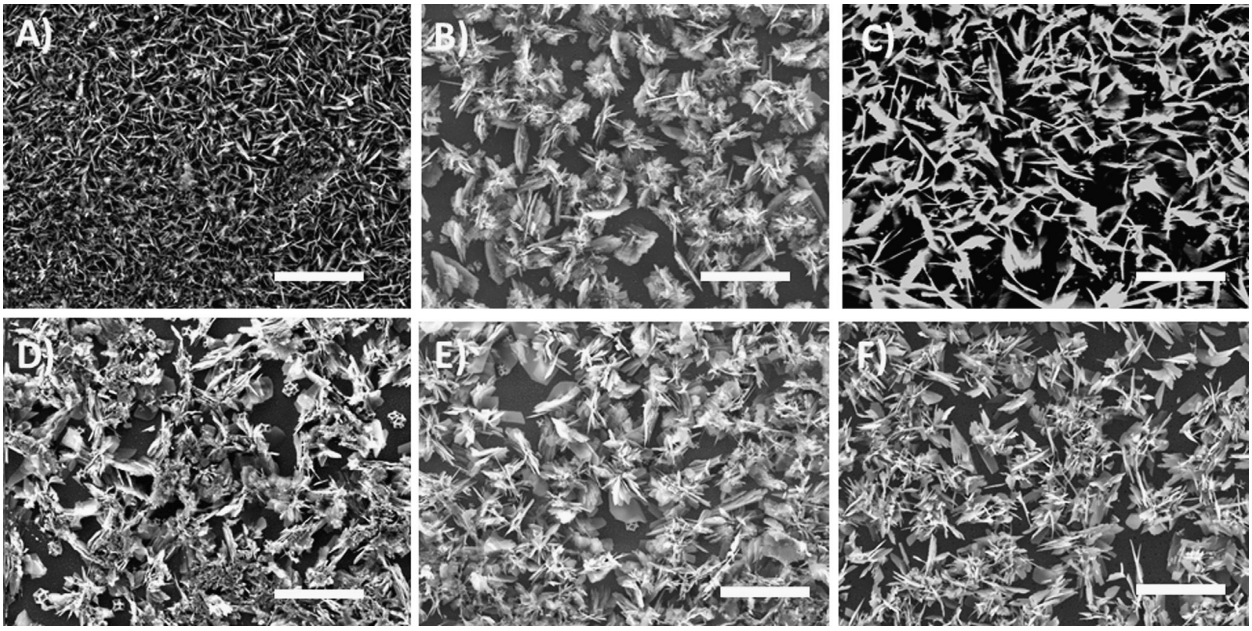

Fig. 5. Secondary electron SEM images of thin films deposited at different temperatures on glass substrates using precursors **(1)**–**(3)** at a concentration of 40 mM. (A) **(1)** at 450 °C, (B) **(2)** at 450 °C, (C) **(3)** at 450 °C. All films were deposited over 45 min. Scale bars 10 μm. (D) **(1)** at 500 °C, (E) **(2)** at 500 °C, (F) **(3)** at 500 °C. Scale bars 20 μm.

diminished to a vanishingly low intensity. Thus it was possible to produce pure films of SnS, eliminating contamination by oxides of tin.

Higher concentrations of precursors **(1)**–**(3)** at 450 °C led to films of a generally similar crystallite morphology by SEM (Fig. 7). The morphologies of the films at every temperature and concentration investigated in this study are summarised in Table 1.

The elemental composition of thin films deposited from using higher concentrations of all precursors was investigated. EDAX spectroscopy revealed the tin: sulphur stoichiometry of films

(Table 1). At higher concentrations the Sn:S ratio approaches 1:1 for both precursors **(2)** and **(3)** at 450 °C. The same trend was also observed for SnS films deposited using **(1)** as the single-source precursor, but for this precursor the stoichiometry by EDAX spectroscopy was 1:1 using a 250 mM solution. In general then, the use of higher concentrations of precursors is crucial for the formation of stoichiometric or near-to-stoichiometric films of SnS for all precursors studied. The results are summarised in Fig. 8 and the EDAX data used to plot the graph is presented in Table 1.

3.6. Determination of band gap for a stoichiometric SnS film.

UV–vis absorption spectroscopy was used to estimate the optical band gap of the best film of SnS, grown using 250 mM precursor **(1)** and a deposition temperature of 450 °C. Extrapolation of the linear region of the plot of $(\alpha h\nu)^2$ as a function of photon energy ($h\nu$), where α is the wavelength-dependant absorption coefficient of SnS (for these films, $\alpha(\lambda) > 10^4$ cm^{-1} in the linear region), estimates a direct band gap of 1.2 eV (Fig. 9). Measured direct band gaps of thin films of SnS have previously been quoted in the range 1.0–1.7 eV depending on the deposition method used. For instance, SnS films produced by Ray et al. using dip deposition with tin(II) chloride and thiourea precursors gave SnS with a direct band gap of 1.4 eV by photo-conductivity measurements [21]. O'Brien and co-workers used optical spectroscopy to evaluate direct band gaps of SnS deposited from similar organo-tin(IV) dithiocarbamate complexes, with values for the films of SnS deposited from the equivalent precursor to **(2)** estimated as 1.2 eV, 1.2 eV, 1.6 eV and 1.7 eV for deposition temperatures of 400 °C, 450 °C, 500 °C and 530 °C respectively

Table 1
Summary of SnS films produced by AACVD: elemental composition from EDAX spectroscopy, morphology of films from SEM and optical band gaps obtained from precursors **(1)-(3)** at different temperatures and precursor concentrations.

Deposition temperature (°C)	Precursor concentration (mM)	EDAX (%)		Morphology	Band gap (eV)
		Sn	S		
[Sn($S_2CN(C_2H_4)(C_4H_9)$)$_2$] (1)					
450	40	55	45	Bundles of sheets	–
450	80	55	45	Bundles of sheets	–
450	170	51	49	Bundles of sheets	–
450	250	50	50	Bundles of sheets	1.2 eV, direct
500	40	49	51	Bundles of sheets	–
[Sn($S_2CN(CH_3)(C_4H_9)$)$_2$] (2)					
450	40	58	42	Bundles of sheets	–
450	80	58	42	Bundles of sheets	–
450	170	52	48	Bundles of sheets	–
450	250	53	47	Bundles of sheets	–
500	40	64	36	Bundles of sheets	–
[Sn($S_2CN(C_2H_4)_2$)$_2$] (3)					
450	40	59	41	Bundles of sheets	–
450	80	58	42	Bundles of sheets	–
450	170	54	46	Bundles of sheets	–
450	250	53	47	Bundles of sheets	–
500	40	61	39	Bundles of sheets	–

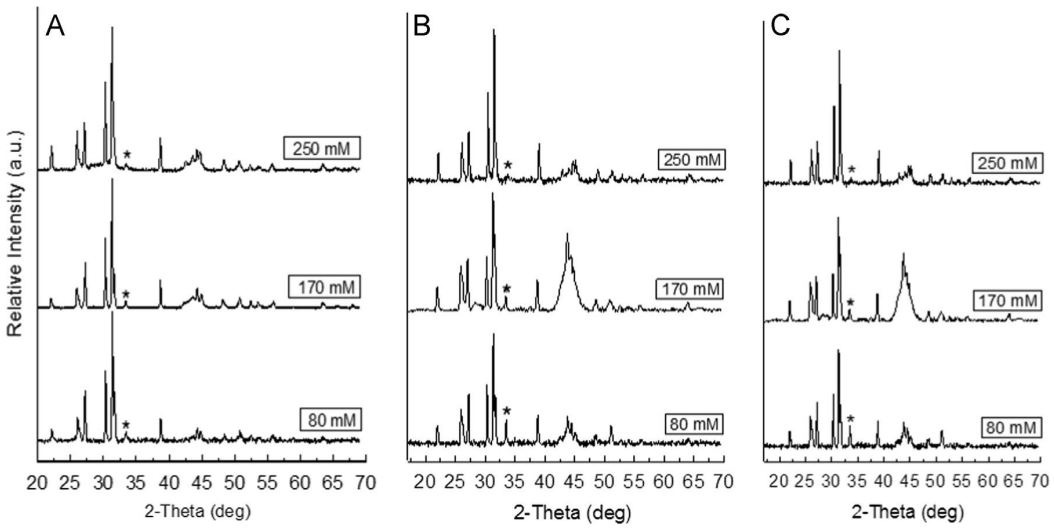

Fig. 6. p-XRD patterns of SnS thin films deposited on glass substrates by AACVD using (A) 80 mM, 170 mM and 250 mM of **(1)** at 450 °C, (B) 80 mM, 170 mM and 250 mM of **(2)** at 450 °C and (C) 80 mM, 170 mM and 250 mM of **(3)** at 450 °C. All films were deposited over 45 min. *=reflection attributed to SnO_2.

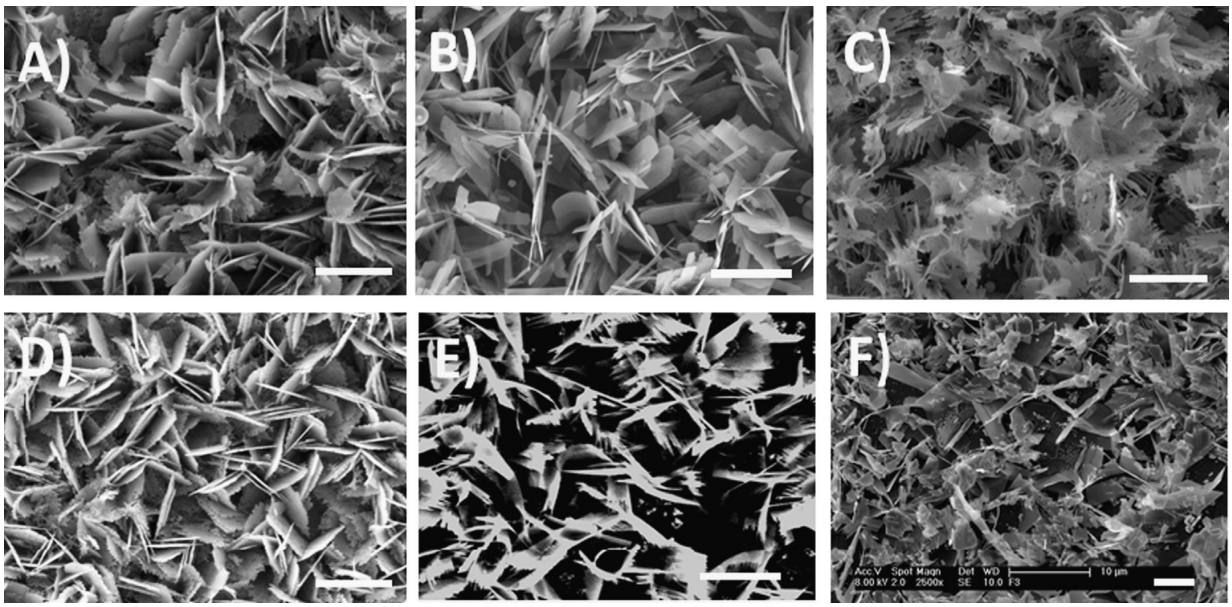

Fig. 7. Secondary electron SEM images of thin films deposited by differing concentrations of precursors **(1)**, **(2)** or **(3)** at 450 °C, precursor/amount: (A) **(1)**/170 mM (B) **(1)**/250 mM, (C) **(2)**/170 mM, (D) **(2)**/250 mM, E) **(3)** /170 mM, (F) **(3)**/250 mM. All films were deposited over 45 min. Scale bars: 5 μm.

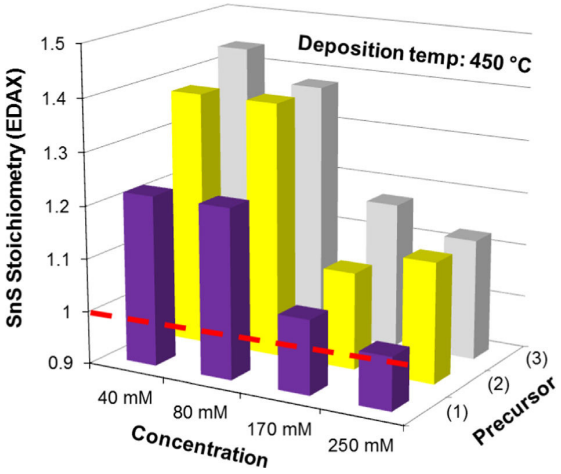

Fig. 8. The effect of concentration of precursors **(1)**–**(3)** on the stoichiometry (%Sn divided by %S found experimentally by EDAX) of SnS films deposited at 450 °C by AACVD. The dashed line indicates an ideal 1:1 Sn:S stoichiometry i.e. SnS.

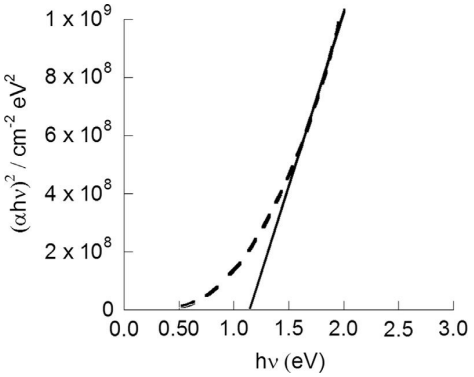

Fig. 9. Determination of the optical band gap for SnS produced by AACVD using precursor **(1)** (250 mM, 450 °C deposition temperature, 45 min deposition time) by extrapolation of the linear region in $(\alpha h\nu)^2$ as a function of photon energy.

[31]. The increasing band gap energy was attributed to a combination of strain, defects, charged impurities, disorder at grain boundaries and particle size confinement. Contributions from SnO_2 and carbon impurities in the films were not ruled out. Gao et al. prepared SnS films using chemical bath deposition from a mixture of tin(II) chloride, ammonium citrate and sodium thiosulfate at 60 °C and pH 6 which were found to have direct band gaps in the range 1.0–1.3 eV [9]. Bulk SnS is known to have a direct band gap of 1.4 eV [3]. Thus, the orthorhombic SnS film produced by this method from **(1)** has a direct band gap (1.2 eV) that corresponds well to previously reported films from various deposition routes, including dip deposition (1.4 eV) [21], AACVD (1.2–1.7 eV [31] and 1.2 eV [30]), atmospheric pressure CVD (1.2–1.3 eV) [29], chemical bath deposition (1.0–1.3 eV) [9] and thermal evaporation (1.3 eV) [15] all of which give the same phase of SnS (orthorhombic) and have similar surface morphology, and from their optical band gap are expected to be similar in composition and texture to bulk orthorhombic SnS (1.4 eV).

4. Conclusions

In summary, we report the synthesis unsymmetrical dithiocarbamates of tin(II) of the formula $[Sn(S_2CNRR')_2]$ (where R=ethyl, R'=n-butyl, **(1)**; R=methyl, R'=n-butyl, **(2)**; and R=R' ethyl, **(3)**) for the deposition of SnS thin films by AACVD. Decomposition of the complexes has been studied using TGA measurements. Tin sulphide (SnS) thin films have been deposited at a range of temperatures by AACVD without an external sulphur source or

co-reagents. SnS was deposited by AACVD using complexes (**1**)–(**3**) at 450 or 500 °C with some contamination from SnO_2. AACVD deposition of SnS thin films at 450 °C using precursors (**1**)–(**3**) at varying concentrations was studied. The films produced at lower concentrations were moderately contaminated with SnO_2 which at high concentrations reduced to negligible levels as evidenced by p-XRD measurements. SEM combined with EDAX spectroscopy of the SnS films have been used to characterise the structure, morphology and elemental composition of SnS thin films. A direct band gap of ca. 1.2 eV was estimated from optical absorbance measurements of an SnS film of good morphology and composition.

Acknowledgements

PK is funded by the University of Manchester. This work was funded by the Engineering and Physical Sciences Research Council (grant number EP/K039547/1).

Appendix A. Supporting information

Supplementary data associated with this article can be found in the online version at http://dx.doi.org/10.1016/j.jcrysgro.2014.07.019.

References

[1] T. Jiang, G.A. Ozin, J. Mater. Chem. 8 (1998) 1099–1108.
[2] (a) K. Ramasamy, M.A. Malik, N. Revaprasadu, P. O'Brien, Chem. Mater. 25 (2013) 3551–3569;
(b) D.J. Lewis, P. Kevin, O. Bakr, C.A. Muryn, M.A. Malik, P. O'Brien, Inorg. Chem. Front. 1 (2014) 577–598.
[3] O. Madelung, Semiconductors – Basic Data, 2nd edition, Springer-Verlag, Berlin, 1996.
[4] K. Ramasamy, M.A. Malik, P. O'Brien, Chem. Sci. 2 (2011) 1170–1172.
[5] K. Ramasamy, M.A. Malik, P. O'Brien, Chem. Commun. 48 (2012) 5703–5714.
[6] L.M. Peter, Philos. Trans. R. Soc. A – Math. Phys. Eng. Sci 369 (2011) 1840–1856.
[7] J.J. Loferski, J. Appl. Phys. 27 (1956) 777–784.
[8] (a) P. Sinsermsuksakul, K. Hartman, S.B. Kim, J. Heo, L. Sun, H.H. Park, R. Chakraborty, T. Buonassisi, R.G. Gordon, Appl. Phys. Lett. 102 (2013) 053901–053905;
(b) We note that in the time between online publication and final proofs that SnS devices with efficiencies of 4.4% have been reported see;
(c) P. Sinsermsuksakul, L. Sun, S.W. Lee, H.H. Park, S.B. Kim, C. Yang, R. G. Gordon, Adv. Energy Mater. 4 (2014) 1400496.
[9] C. Gao, H.L. Shen, Thin Solid Films 520 (2012) 3523–3527.
[10] C. Gao, H. Shen, L. Sun, H. Huang, L. Lu, H. Cai, Mater. Lett. 64 (2010) 2177–2179.
[11] B. Ghosh, M. Das, P. Banerjee, S. Das, Semicond. Sci. Technol. 23 (2008).
[12] J.R.S. Brownson, C. Georges, G. Larramona, A. Jacob, B. Delatouche, C. Levy-Clement, J. Electrochem. Soc. 155 (2008) D40–D46.
[13] S.Y. Cheng, G.A. Chen, Y.Q. Chen, C.C. Huang, Opt. Mater. 29 (2006) 439–444.
[14] M. Ichimura, K. Takeuchi, Y. Ono, E. Arai, Thin Solid Films 361 (2000) 98–101.
[15] S.S. Hegde, A.G. Kunjomana, M. Prashantha, C. Kumar, K. Ramesh, Thin Solid Films 545 (2013) 543–547.
[16] S.K. Arora, D.H. Patel, M.K. Agarwal, J. Cryst. Growth 131 (1993) 268–270.
[17] J.Y. Kim, S.M. George, J. Phys. Chem. C 114 (2010) 17597–17603.
[18] P. Sinsermsuksakul, J. Heo, W. Noh, A.S. Hock, R.G. Gordon, Adv. Energy Mater. 1 (2011) 1116–1125.
[19] M. Calixto-Rodriguez, H. Martinez, A. Sanchez-Juarez, J. Campos-Alvarez, A. Tiburcio-Silver, M.E. Calixto, Thin Solid Films 517 (2009) 2497–2499.
[20] R.D. Pike, H. Cui, R. Kershaw, K. Dwight, A. Wold, T.N. Blanton, A.A. Wernberg, H.J. Gysling, Thin Solid Films 224 (1993) 221–226.
[21] S.C. Ray, M.K. Karanjai, D. DasGupta, Thin Solid Films 350 (1999) 72–78.
[22] P. Boudjouk, D.J. Seidler, D. Grier, G.J. McCarthy, Chem. Mater. 8 (1996) 1189–1196.
[23] B.P. Bade, S.S. Garje, Y.S. Niwate, M. Afzaal, P. O'Brien, Chem. Vapor Depos. 14 (2008) 292–295.
[24] P. Marchand, I.A. Hassan, I.P. Parkin, C.J. Carmalt, Dalton Trans. 42 (2013) 9406–9422.
[25] T.G. Hibbert, M.F. Mahon, K.C. Molloy, L.S. Price, I.P. Parkin, J. Mater. Chem. 11 (2001) 469–473.
[26] L.S. Price, I.P. Parkin, T.G. Hibbert, K.C. Molloy, Chem. Vap. Depos. 4 (1998) 222–225.
[27] M.A. Malik, M. Afzaal, P. O'Brien, Chem. Rev. 110 (2010) 4417–4446.
[28] G. Barone, T.G. Hibbert, M.F. Mahon, K.C. Molloy, L.S. Price, I.P. Parkin, A.M. E. Hardy, M.N. Field, J. Mater. Chem. 11 (2001) 464–468.
[29] A.T. Kana, T.G. Hibbert, M.F. Mahon, K.C. Molloy, I.P. Parkin, L.S. Price, Polyhedron 20 (2001) 2989–2995.
[30] I.P. Parkin, L.S. Price, T.G. Hibbert, K.C. Molloy, J. Mater. Chem. 11 (2001) 1486–1490.
[31] K. Ramasamy, V.L. Kuznetsov, K. Gopal, M.A. Malik, J. Raftery, P.P. Edwards, P. O'Brien, Chem. Mater. 25 (2013) 266–276.
[32] G.M. Sheldrick, Acta Crystallogr. Sec. A 64 (2008) 112–122.

Supporting Information

Thin Films of SnS by Aerosol-Assisted Chemical Vapour Deposition (AACVD) Using Tin(II) Dithiocarbamates as Single-Source Precursors

Punarja Kevin,[1] David J. Lewis,[1,2] James Raftery[1] M. Azad Malik[1] and Paul O'Brien.[1,2,*]

[1]*School of Chemistry, University of Manchester, Oxford Road, M13 9PL, United Kingdom.*

[2]*School of Materials, University of Manchester, Oxford Road, M13 9PL, United Kingdom.*

*Corresponding Author: Professor Paul O'Brien FRS

Email: Paul.O'Brien@manchester.ac.uk.

Tel: +44 (0) 161 275 4653

Table S1: Data from crystal structure of **(1)**.

Parameter	Result
Formula	$C_{14}H_{28}N_2S_4Sn$
Formula weight, M	471.31
Structure and Space group	Monoclinic, $P(2)_1/n$
unit-cell dimensions	
a	13.5900(9) Å
b	8.6283(5) Å
c	17.749(11) Å
α	90 °
β	103.956(2)°
γ	90 °
V	2019.8 Å ^{3}

Z	4
density, D	1.55 Mg m^{-3}
temperature, T	100(2) K
reflections collected/unique	
reflections	14032/3897
R_{int}	0.0461
for [I>2σ(I)]	
R_1	0.0363
wR_2	0.0936
for all data	
R_1	0.037
wR_2	0.0944
goodness of fit, GOF	1.081

CHAPTER – V: PAPER - 2

"The aerosol assisted chemical vapour deposition of SnSe and Cu_2SnSe_3 thin films from molecular precursors"

Punarja Kevin, Sajid N. Malik, Mohammad A. Malik, Paul O'Brien, *Chem. Commun.,* 2014, **50**, 14328-14330

ChemComm

COMMUNICATION

View Article Online
View Journal | View Issue

The aerosol assisted chemical vapour deposition of SnSe and Cu_2SnSe_3 thin films from molecular precursors†

Cite this: *Chem. Commun.*, 2014, 50, 14328

Received 28th August 2014,
Accepted 29th September 2014

DOI: 10.1039/c4cc06792d

www.rsc.org/chemcomm

Punarja Kevin,[a] Sajid N. Malik,[ab] Mohammad A. Malik[a] and Paul O'Brien*[a]

Tin selenide (SnSe) and copper tin selenide (Cu_2SnSe_3) thin films have been deposited onto glass substrates by AACVD using $[Sn(Ph_2PSe_2)_2]$ or a mixture of $[Sn(Ph_2PSe_2)_2]$ and $[Cu(acac)_2]$ respectively.

Tin selenide (SnSe) is a p-type semiconductor with a direct band gap of 0.9 eV and an indirect band gap of 1.3 eV. The material finds application in optoelectronic devices,[1] as a thermoelectric material and in lithium ion batteries.[2] Various methods have been used for the deposition of SnSe thin films which include atmospheric pressure chemical vapour deposition (APCVD),[3] pyrolysis,[4] thermal evaporation[5] and chemical bath deposition (CBD).[6] Cu_2SnSe_3 is also a p-type semiconductor. In both cubic and wurtzitic forms, Cu_2SnSe_3 has a band gap close to 1.5 eV whereas the rhombohedral form has a direct band gap of 0.84 eV.[7] Cu_2SnSe_3 has a high optical absorption co-efficient $>10^4$.[8] Its Hole transport is chiefly controlled by the Cu–Se electro-conductive frame work.[9] Cu_2SnSe_3 is based on earth abundant elements, has a simple crystal structure and phase diagram as compared to other quaternary chalcogenides. These features make Cu_2SnSe_3 an attractive candidate for variety of optoelectronic and solar energy applications.[10] The uses of Cu_2SnSe_3 are being explored in: acousto-optic applications,[11] thermo-electronics,[12] and biomedical applications.

Cu_2SnSe_3 nanocrystals have been synthesized by employing a variety of techniques including: a microwave assisted polyol method,[13] colloidal synthesis[14] and flash evaporation methods.[15] However, there are very few reports on the deposition of thin films. Kim *et al.* have recently reported the growth of Cu_2SnSe_3 crystals on soda lime glass substrate by the co-evaporation method.[16] They studied the effect of substrate temperature on phase transformations between cubic and monoclinic phases and determined optical properties. The precise control of both the morphology and stoichiometry of Cu_2SnSe_3 films remains a challenge. Chemical Vapour Deposition (CVD) is a promising technique for deposition of such films and can provide control over phase, morphology and microstructure. The utility of conventional CVD is limited by its dependence on volatile precursors. AACVD is a variant of CVD in which less or non-volatile precursors are flash evaporated. Sharma *et al.* have deposited SnSe thin films by AACVD at 490 °C and 530 °C using a diorganotin(IV)-2-pyridyl selenoate complex as single source precursor.[17]

Previously, we have reported the synthesis and use of selenophosphinate complexes for deposition of binary, ternary and quaternary metal chalcogenide thin films by AACVD.[18,19] Krauss *et al.* reported the structure and the use of bis(diphenyldiselenophosphinato)lead(II) complex as a precursor for PbSe nanoparticles.[20] The deposition of CZTS thin films from diethyldithiocarbamato-complexes of Cu, Zn and Sn by AA-CVD has also been reported.[21] Suitable mixtures of precursor materials with comparable thermal decomposition rate facilitate deposition and provide effective stoichiometric control especially in the deposition of more complex semiconductor materials.[21] We have now synthesized a new complex bis(diphenylphosphinediselenoato)tin(II) $[Sn(Ph_2PSe_2)_2]$ and used it as a single source precursor for the deposition of tin selenide (SnSe) thin films by AACVD. We have also used it in combination with bis(2,4-pentanedionato)copper(II) $[Cu(acac)_2]$ for the deposition of Cu_2SnSe_3 thin films.‡

The preparation of $[Sn(Ph_2PSe_2)_2]$ complex was carried out in two steps. Potassium diphenylphosphinodiselenoate was prepared by the reaction of diphenylphosphine, elemental selenium and potassium hydroxide as reported by Gusarova *et al.*[22] The ligand was then reacted with $SnCl_2$ to give corresponding $[Sn(Ph_2PSe_2)_2]$ complex. The product was characterized by FTIR, NMR, mass spectrometry and elemental analysis. Thermogravimetric analysis of the complex showed decomposition between 350 °C and 400 °C to give a ~21% residue corresponding to SnSe (Fig. S1, ESI†).

The deposition of SnSe by AACVD was carried out by using a 0.19 mmol solution of $[Sn(Ph_2PSe_2)_2]$ in THF (15 mL).

[a] *The School of Chemistry and The School of Materials, The University of Manchester, Oxford Road, M13 9PL Manchester, UK. E-mail: paul.obrien@manchester.ac.uk; Fax: +44-(0)161-2751411; Tel: +44-(0)161-2751411*

[b] *School of Chemical and Materials Engineering (SCME), National University of Sciences and Technology (NUST), Islamabad 44000, Pakistan*

† Electronic supplementary information (ESI) available. See DOI: 10.1039/c4cc06792d

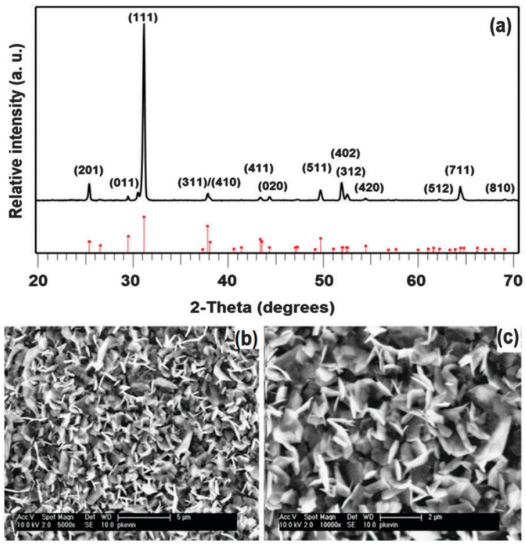

Fig. 1 (a) p-XRD pattern of SnSe thin film deposited from $[Sn(Ph_2PSe_2)_2]$ precursor at 400 °C. Vertical lines below show standard ICDD pattern 00-048-1224 for orthorhombic SnSe (b) and (c) SEM images of as deposited thin film at 400 °C.

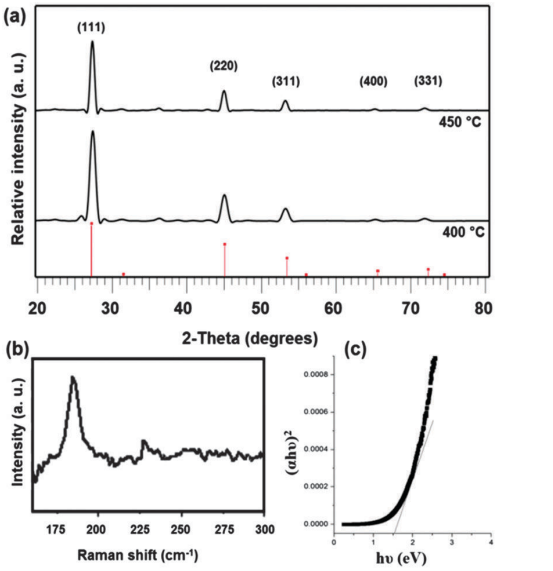

Fig. 2 (a) p-XRD pattern of Cu_2SnSe_3 thin film deposited from $[Sn(Ph_2PSe_2)_2]$ and $[Cu(acac)_2]$ precursors at 400 and 450 °C indexed with standard ICDD pattern 03-065-4145 for cubic Cu_2SnSe_3 (b) Raman spectrum and (c) band gap plot for Cu_2SnSe_3 thin film deposited at 400 °C.

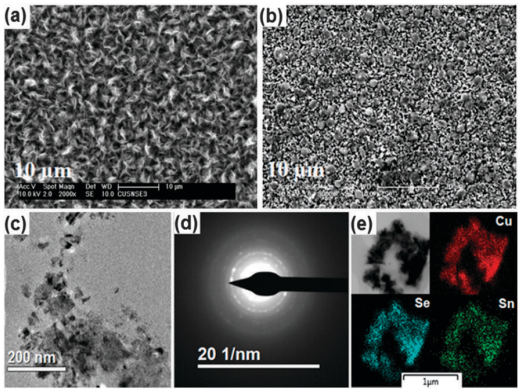

Fig. 3 SEM images of Cu_2SnSe_3 thin films deposited at (a) 400 °C and (b) 450 °C. (c) TEM image (d) SAED pattern and (e) EDX elemental of a single Cu_2SnSe_3 particle.

Deposition was carried out at 350 and 400 °C with an Ar flow rate of 180 sccm for 45 min. No deposition occurred at 350 °C whereas dark brown, well adhered films were obtained on glass substrates at 400 °C. Fig. 1a shows p-XRD pattern of SnSe thin films deposited at 400 °C. The pattern is indexed to the standard ICDD pattern 00-048-1224 of orthorhombic SnSe with preferred orientation along (111) plane. SEM images (Fig. 1b and c) show the uniform morphology of microcrystalline SnSe thin films. The morphology of the films is based on irregular sheets with an average size of *ca.* 1.5 μm. Relative atomic percentage of Sn and Se atoms determined by EDX measurements was found to be 48 : 52 which is fairly close to the expected value of individual grains. The band gap of SnSe was found to be 1.1 eV (Fig. S2, ESI†) which is close to that reported previously for this material.[1]

The deposition of Cu_2SnSe_3 was carried out by using a mixture of $[Cu(acac)_2]$ (0.38 mmol) and $[Sn(Ph_2PSe_2)_2]$ (0.19 mmol) in 15 mL THF at three different temperatures (350, 400 and 450 °C) for 1 hour. Deposition at 350 °C produced no thin films whereas those at 400 and 450 °C produced uniform, shiny dark brown films. The p-XRD patterns (Fig. 2a) of the thin films deposited at 400 °C and 450 °C correspond to the standard ICDD pattern 03-065-4145 for cubic Cu_2SnSe_3 phase with space group $F\bar{4}3m$.

Films deposited at 400 °C had a uniform morphology (Fig. 3a) whereas two distinct types of crystallites were seen in those deposited at 450 °C. The films deposited at 400 °C consist of clusters of nanocrystalline flakes whilst the images of those deposited at 450 °C show larger semispherical crystallites thinly scattered in a background of irregularly shaped nanocrystallites. EDX analysis showed the chemical composition as Cu : Sn : Se 2.1 : 1.0 : 2.9 for thin films deposited at 400 °C and Cu : Sn : Se 1.9 : 1.0 : 2.6 for the films deposited at 450 °C. These results clearly show that the films deposited at 400 °C are of better quality being uniform in morphology and having better stoichiometry. The Raman spectrum of the thin films deposited at 400 °C is given in Fig. 2b which shows a strong peak at ~180.6 cm^{-1} with a minor peak at 232 cm^{-1}. These peaks correspond with the reported values (179.9 and 231.6 cm^{-1}) for A_1 and A_2 symmetry modes of Cu_2SnSe_3.[15] The absence of peaks at 150 and 260 cm^{-1} for CuSe and SnSe shows the deposition of pure Cu_2SnSe_3. Fig. 2c shows the band gap of the films deposited at 400 °C as ~1.5 eV. This value is in agreement with that reported previously for Cu_2SnSe_3.[23–25]

The deposited material was scratched from the films deposited at 400 °C and was further investigated by using transmission

electron microscopy (TEM). TEM image (Fig. 3c) show similar flake like crystals as observed in SEM. Selected area electron diffraction (SAED) pattern showed distinct rings suggesting the polycrystalline nature of the material (Fig. 3d). Elemental mapping of a single particle as shown in Fig. 3e exhibited even distribution of Cu, Sn and Se in the crystal.

A new complex, $[Sn(Ph_2PSe_2)_2]$ has been synthesised and used as single source precursor in combination with $[Cu(acac)_2]$ for the deposition of monophasic tin selenide (SnSe) and copper tin selenide (Cu_2SnSe_3) thin films onto glass substrates by AACVD at 400 °C and 450 °C. This is the first deposition of thin films of this material by AACVD which has potential applications in photovoltaics and optoelectronics.

We thank EPSRC for funding the instruments under grant number (EP/K039547/1) for characterization of compounds. PK thanks The School of Chemistry, The University of Manchester for funding.

Notes and references

‡ Synthesis of $[Sn(Ph_2PSe_2)_2]$: Ethanolic solution of KOH (1.5 mmol in 5 mL) and metallic Se powder ~100 mesh (0.158 g, 2.0 mmol) were added to ethanolic solution of diphenylphosphine (1.05 mmol in 6 mL EtOH) at room temperature under nitrogen. Vigorous stirring of the suspension was carried out at room temperature for ~5 minutes until all the Se dissolved. Colourless solution thus obtained was filtered and concentrated in rotary evaporator. The residue upon grinding in Et_2O (10 mL) gave potassium diphenylphosphinodiselenoate as white powder upon decanting the solvent and washing with Et_2O. Methanolic solution of $SnCl_2$ was added drop wise to a solution of 1.911 g (5 mmol) of potassium diphenylphosphinodiselenoate in 100 mL methanol. The precipitate formed was filtered, washed with hot methanol and dried. Yield (91%). Elemental analysis calc. (%) for $C_{24}H_{20}P_2Se_4$: C 35.81, H 2.50, P 7.70, Sn 14.75; found: C 34.94, H 2.65, P 7.30, Sn 15.01; FTIR 3049 cm^{-1} (Ar–C–H), 685 cm^{-1} (P–C) and 539 cm^{-1} (P═Se); ^1H NMR (400 MHz, $CDCL_3$, Me_4Si) δ = 7.81 ppm (dd, 8H, J 3.9, 7.1, 8.9, 4 × o-Ph), 7.44 ppm (m, 12H, 4 × p-Ph and 4 × m-Ph); ^{13}C NMR δ = 127 ppm & 132 ppm (–Ph); APCI-MS: $[Ph_2PSe_2]^+ = m/z$ 344.8.

1 C. L. Zhang, H. H. Yin, M. Han, Z. H. Dai, H. Pang, Y. L. Zheng, Y. Q. Lan, J. C. Bao and J. M. Zhu, *ACS Nano*, 2014, **8**, 3761–3770; P. Kevin, D. J. Lewis, J. Raftery, M. A. Malik and P. O'Brien, *J. Cryst. Growth*, DOI: 10.1016/j.jcrysgro.2014.07.019; D. J. Lewis, P. Kevin, O. Bakr, C. A. Muryn, M. A. Malik and P. O'Brien, *Inorg. Chem. Front.*, 2014, **1**, 577.
2 E. Schonherr and W. Stetter, *J. Cryst. Growth*, 1975, **30**, 96–98; L.-D. Zhao, *et al.*, *Nature*, 2014, **508**, 373–377.
3 N. D. Boscher, C. J. Carmalt, R. G. Palgrave and I. P. Parkin, *Thin Solid Films*, 2008, **516**, 4750–4757.
4 P. Boudjouk, D. J. Seidler, S. R. Bahr and G. J. McCarthy, *Chem. Mater.*, 1994, **6**, 2108–2112.
5 C. A. R. M. Sahayaraj, A. Mohan, V. Arivazhagan and S. Rajesh, *Chalcogenide Lett.*, 2014, **11**, 47–52; N. Sabli, Z. A. Talib, W. M. M. Yunus, Z. Zainal, H. S. Hilal and M. Fujii, *Electrochemistry*, 2014, **82**, 25–30.
6 B. Pejova and I. Grozdanov, *Thin Solid Films*, 2007, **515**, 5203–5211.
7 J. Fan, W. Carrillo-Cabrera, L. Akselrud, I. Antonyshyn, L. D. Chen and Y. Grin, *Inorg. Chem.*, 2013, **52**, 11067–11074.
8 Y. T. Zhai, S. Y. Chen, J. H. Yang, H. J. Xiang, X. G. Gong, A. Walsh, J. Kang and S. H. Wei, *Phys. Rev. B*, 2011, **84**, 075213; G. H. Chandra, O. L. Kumar, R. P. Rao and S. Uthanna, *J. Mater. Sci.*, 2011, **46**, 6952–6959.
9 G. Marcano, C. Rincon, L. M. de Chalbaud, D. B. Bracho and G. S. Perez, *J. Appl. Phys.*, 2001, **90**, 1847–1853.
10 L. Zhu, Y. H. Qiang, Y. L. Zhao, X. Q. Gu, D. M. Song and C. B. Song, *Acta Phys.-Chim. Sin.*, 2013, **29**, 2339–2344; C. B. Song, Y. L. Zhao, D. M. Song, L. Zhu, X. Q. Gu and Y. H. Qiang, *Int. J. Electrochem. Sci.*, 2014, **9**, 3158–3165.
11 G. Marcano, L. M. de Chalbaud, C. Rincon and G. S. Perez, *Mater. Lett.*, 2002, **53**, 151–154.
12 M. Ibanez, D. Cadavid, U. Anselmi-Tamburini, R. Zamani, S. Gorsse, W. H. Li, A. M. Lopez, J. R. Morante, J. Arbiol and A. Cabot, *J. Mater. Chem. A*, 2013, **1**, 1421–1426.
13 H. Grisaru, V. G. Pol, A. Gedanken and I. Nowik, *Eur. J. Inorg. Chem.*, 2004, 1859–1864.
14 J. J. Wang, A. Singh, P. Liu, S. Singh, C. Coughlan, Y. N. Guo and K. M. Ryan, *J. Am. Chem. Soc.*, 2013, **135**, 7835–7838.
15 G. H. Chandra, O. L. Kumar, R. P. Rao and S. Uthanna, *J. Mater. Sci.*, 2011, **46**, 6952–6959.
16 K. M. Kim, H. Tampo, H. Shibata and S. Niki, *Mater. Lett.*, 2014, **116**, 61–63; K. M. Kim, H. Tampo, H. Shibata and S. Niki, *Thin Solid Films*, 2013, **536**, 111–114.
17 R. K. Sharma, G. Kedarnath, A. Wadawale, C. A. Betty, B. Vishwanadh and V. K. Jain, *Dalton Trans.*, 2012, **41**, 12129.
18 C. Q. Nguyen, A. Adeogun, M. Afzaal, M. A. Malik and P. O'Brien, *Chem. Commun.*, 2006, 2179; C. Q. Nguyen, A. Adeogun, M. Afzaal, M. A. Malik and P. O'Brien, *Chem. Commun.*, 2006, 2182; C. Q. Nguyen, M. Afzaal, M. A. Malik, M. Helliwell, J. Raftery and P. O'Brien, *J. Organomet. Chem.*, 2007, **692**, 2669.
19 S. Mahboob, S. N. Malik, N. Haider, C. Q. Nguyen, M. A. Malik and P. O'Brien, *J. Cryst. Growth*, 2014, **394**, 39–48.
20 C. M. Evans, M. E. Evans and T. D. Krauss, *J. Am. Chem. Soc.*, 2010, **132**, 10973–10975.
21 K. Ramasamy, M. A. Malik and P. O'Brien, *Chem. Sci.*, 2011, **2**, 1170; K. Ramasamy, V. Kuznetsov, K. Gopal, M. A. Malik, J. Raftery, P. P. Edwards and P. O'Brien, *Chem. Mater.*, 2013, **25**(3), 266–276; K. Ramasamy, M. A. Malik and P. O'Brien, *Chem. Commun.*, 2012, **48**, 5703–5714; D. J. Lewis and P. O'Brien, *Chem. Commun.*, 2014, **50**, 6319.
22 A. V. Artem'ev, S. F. Malysheva, N. K. Gusarova and B. A. Trofimov, *Synthesis*, 2010, 2463–2467.
23 J. J. Wang, A. Singh, P. Liu, S. Singh, C. Coughlan, Y. N. Guo and K. M. Ryan, *J. Am. Chem. Soc.*, 2013, **135**, 7835–7838.
24 S. J. Li and D. C. Pan, *J. Cryst. Growth*, 2012, **358**, 38–42.
25 M. E. Norako, M. J. Greaney and R. L. Brutchey, *J. Am. Chem. Soc.*, 2011, **134**, 23–26.

Supplementary Material

The aerosol assisted chemical vapour deposition of SnSe and Cu_2SnSe_3 thin films by molecular precursor approach

Punarja Kevin, Sajid N. Malik, Mohammad A. Malik, and Paul O'Brien*

Experimental

Chemicals and instruments

Diphenylphosphine, Se powder ~ 100 mesh, zinc (II) chloride, copper (II) chloride, copper (I) chloride, tin (II) chloride, toluene and dichloromethane were purchased from Sigma-Aldrich and used as received. Ethanol and methanol used as solvents in the reactions were also used without further purification. All synthetic manipulations were carried out under nitrogen using standard Schlenk line techniques. 1H NMR spectra were recorded on Bruker AC400 FT-NMR spectrometer and a Kratos Concept 1S instrument was used to record mass spectra. FTIR spectra were recorded on Perkin Elmer FTIR instrument. Elemental analyses were performed by the University of Manchester microanalysis facility. Melting points were recorded using a Stuart melting point apparatus and are uncorrected

Deposition of thin films

Glass slides (1 x 3 cm) were used as substrates for the deposition of thin films. Substrates were thorough cleaned and sonicated in acetone for 30 minutes to remove any possible contamination. Deposition of thin films was carried out by using a home built AACVD kit.[26] In a typical deposition experiment, precursor complex (or a suitable combination of precursors) was dissolved in 15 mL THF taken in a two-necked 100 mL round-bottom flask. The flask was then connected with an argon gas inlet which passed through the solution and carried the aerosols generated by a PIFCO ultrasonic humidifier to the reactor tube connected to other neck of the flask and placed in a Carbolite furnace. Argon flow rate was controlled at 180 Sccm through a Platon flow gauge. Carrier gas transferred aerosols generated in the flask to the hot zone of the reactor. Thermolysis of both the solvent and the precursor at the hot substrate surface due to thermally induced reactions lead to deposition onto substrates. p-XRD patterns were recorded on a Bruker D8 AXE diffractometer (Cu-Kα) from 20 to 80 degrees with a step size of 0.05. Raman spectra were recorded on Horiba T64000 triple 0.64m Raman spectrometer system. Uv-Vis-NIR absorption spectra were recorded using Perkin Elmer λ-1050 spectrophotometer. Morphology and microstructure of thin films were investigated by using a Philips XL 30 FEGSEM and film composition was studied by EDX analysis using a DX4 instrument. TEM images were recorded on a Tecnai F30 microscope operated at an accelerating voltage of 300 kV.

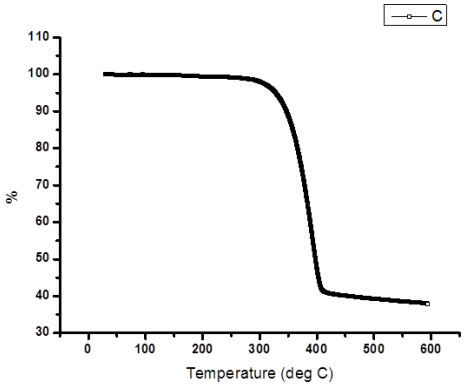

Figure S1. Thermal decomposition (TGA) for the decomposition of [Sn ($PhPSe_2$)$_2$]

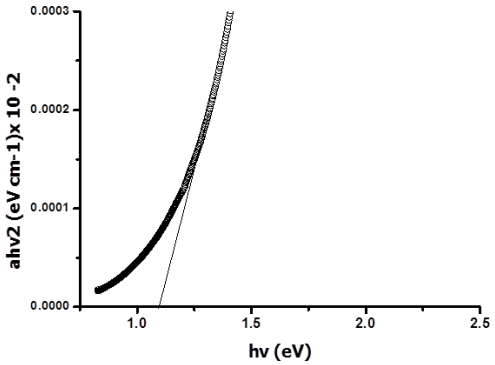

Figure S2. Band gap of SnSe thin films deposited at 400 °C. .

CHAPTER – VI : PAPER - 3

"Composition Focusing in the Deposition of Copper Zinc Tin Sulfide (CZTS) by AACVD"

Punarja Kevin, Bruce Hamilton, Eric Whittaker, Ian Hawkins, Paul O'Brien,

, *Thin solid films*, page: C1-C19 - Manuscript ready for submission

Composition Focusing in the Deposition of Copper Zinc Tin Sulfide (CZTS) by AACVD

Punarja Kevin,[a] Ian Hawkins,[c] Eric Whittaker,[c] Bruce Hamilton,[c] Paul O'Brien, [a,b*]

[a] School of Chemistry, University of Manchester, Oxford Road M13 9PL

[b] School of Materials, University of Manchester, Oxford Road M13 9PL.

[c]School of Electrical and Electronic Engineering, University of Manchester, Oxford Road M13 9PL

Abstract: The influences of deposition temperature and the stoichiometric ratios of the precursors on the composition of CZTS thin film deposited by Aerosol Assisted Chemical Vapour Deposition (AACVD) have been investigated. The tin content of the films and its effect on band gaps was studied. The valence states and binding energies of the film's constituent elements were investigated by high resolution X-ray photo electron spectroscopy (XPS). Electrical resistance of the selected films showed above room temperature hysteresis in conductivity.

Keywords

Chemical vapour deposition process, thin films, solar cells, sulfides, band gap.

Introduction

Copper zinc tin sulfide (CZTS) is one of the newer absorber materials for solar cells and is made from relatively nontoxic, low cost and earth abundant elements. Solar cells based on kesterite CZTS thin films have shown a maximum efficiencies of up to 11.1 % under laboratory conditions[1] (theoretical efficiency ~32.2%) making this material benign material a

potentially a leading candidate for thin films solar cells.[1-3] CZTS has good properties for PV with a high absorption coefficient $>10^4$ and a direct band gap of ~ 1.45 eV.[4-13] Many techniques including spray pyrolysis,[14] sputtering,[15] hybrid sputtering,[16] sulfurization,[17] photo chemical deposition,[18] pulsed laser deposition,[19,20] sol-gel sulferisation,[19] thermal evaporation,[21] co evaporation,[21] sol-gel spin coating[22] and spray pyrolysis [23] have been used to deposit CZTS thin films. We have previously reported the deposition of CZTS thin films with good morphology and a composition close to 2:1:1:4 by Aerosol Assisted Chemical Vapour Deposition (AACVD). [24] This method has the potential to produce good quality large area semiconductor thin films. The technique also offers the possibility of good control over the stoichiometry, morphology and crystallinity. The advantages of such methods was reported and reviewed in detail.[24-28]

CZTS can be formed in two phases: kesterite (KS) (space group I_4)[25] and stannite (ST) (space group I_42 m) and the binding energy difference between these phases is calculated as ~3-4 meV.[25] KS is more stable than ST as the KS structure possesses lower strain[29] and Madelung energy[29] and CZTS usually crystallizes in the KS structure, but may contain a very high concentration of intrinsic defects related to non-stoichiometry in the cation sublattice.[30] The growth method and grain boundaries of kesterite materials were explored recently.[31]

Many researchers discussed the marked dependence of the properties of CZTS on stoichiometry.[32] The [Cu]/[Zn]+[Cu] and [Zn]/[Sn] ratios in a film strongly influences the: morphology, phase purity and optical properties.[33] The deposition of CZTS thin films with controlled stoichiometric composition, structure and morphology is still a challenge. The efficiencies reported for the pure sulfide CZTS solar cells are ~ 6.8% by thermal co-evaporation of elemental sources[34] or co-sputtering method.[35,36] Using a vacuum process,

Shin *et al*. used Cu-poor and Zn-rich CZTS to fabricated a solar cell with an efficiency of 8.4% similar in other reports.[1,33,37,38] Inks of CZTS/CZTSe nanoparticles have been used for the large-scale printing of solar cells on glass or polymer substrates with reported efficiencies up to 13%.[39] Solution processes often rely on environmentally harmful metal-hydrazine complexes which are rather difficult to handle.[1,38-41] Long-chained alkyl stabilizers were found to be efficient in controlling the size and shape of CZTS/CZTSe nanoparticles which were later proved to reduce the efficiencies of solar cells due to carbon contamination which was hard to remove.[24,42] In 2012 Moholkar and co- workers[43] reported CZTS thin film solar cells with an improved PCE of 4.13 % (with V_{OC} = 700 mV, J_{SC} = 10.1 mA cm^{-2} and FF = 0.59). The improvement in efficiency was achieved by varying the chemical composition ratio, a = [Cu]/[Zn]+[Cu] of the target material from 0.8 to 1.2 in step of 0.1 by keeping Zn/Sn constant. Pure kesterite CZTS with direct band gap energy of the CZTS thin films were found to be decreasing from 1.72–1.53 eV with increase of [Cu]/ [Zn]+[Cu]

Dye sensitised solar cells (DSSCs), with nanoporous TiO_2 as the photoanode, showed conversion efficiency of 12 % potentially a cost effective alternatives to more conventional CZTS solar cells.[44] Zhan *et al*. reported a double junction solar cells (pn-DSSCs) fabricated by the dye-sensitized n-type TiO_2 (DS-TiO_2) as the photo anode and porous CZTS film as the photocathode with an efficiency of 1.23 %. The external quantum efficiencies (EQEs) of the solar cells prove that the porous CZTS acts as a light absorber as well as a CE.[45] However, there is no substantial development in p-type CEs. Narrow band gap p-type semiconductors composed of earth abundant elements such as CZTS has recently opened route to hybrid DSSC's. Very recently, the dye sensitised solar cells with the CZTS counter electrode (CE) layer deposited by slurry sulfurisation process showed a comparable photovoltaic conversion efficiency (3.141%) to that with a Pt CE (2.761%). This showed that the CZTS films have

the potential for developing a low cost and highly efficient CE.[46] Aydil et al. demonstrated the factors that control the excess Sn composition in CZTS films prepared using Sn rich precursors by ex. Situ sulfidisation (by sulfadization the excess Sn was evaporated as SnS) process by varying temperatures and consolidated results using triangular phase diagrams.[47]

Herein we report the deposition of CZTS using a combination of copper (II), zinc(II) and tin(IV) complexes in different ratios to study the composition and morphology of the deposited material. We observe stoichiometry focussing in contrast to the results of physical deposition.

Experimental

Sodium diethyldithiocarbamate dihydrate, zinc chloride, dibutyltin dichloride, methanol, chloroform and tetrahydrofuran were purchased from Sigma Aldrich and used without further purification. The glass microscopic slides were obtained from Delta technologies Ltd.

Synthesis of precursors

The synthesis of the complexes $[Cu(S_2CNEt_2)_2]$ (**1**), $[Zn(S_2CNEt_2)_2]$ (**2**) and $[Sn(Bu)_2(S_2CNEt_2)_2]$ (**3**) was carried out in accordance with the previously reported procedures.[24] In a typical reaction, sodium diethyldithiocarbamate was reacted with the corresponding metal salt in a 2:1molar ratio in methanol at room temperature. The precipitate thus obtained was filtered, washed with 100 mL of hot methanol, dried in vacuum and recrystallized from chloroform. The complexes were characterised by elemental analysis, IR, NMR, mass spectra and melting point measurements.

Deposition of thin films

In a typical deposition experiment, a precursor mixture of $[Cu(S_2CNEt_2)_2]$ (**1**) (1.55 mM), $[Zn(S_2CNEt_2)_2]$ (**2**) (0.77 mM) and $[Sn(Bu)_2(S_2CNEt_2)_2]$ (**3**) (0.77 mM) (molar ratio of 2:1:1)

was dissolved in 15 mL THF. This solution was then loaded in to a two necked 100 mL flask connected with an argon gas inlet. Flow rate of argon was controlled using a Platon flow gauge. 14-15 borosilicate glass substrates of 1 cm^2 were placed horizontally inside the reactor as previously described.[14] Argon flow rate was maintained at 160-180 *sccm* for 45 min. Deposition experiments were carried out at 350 °C, 380 °C, 400 °C and 450 °C. To study the effect of concentration at a particular temperature, ratio of molar concentration of two precursors either **(1)** and **(2)** or **(2)** and **(3)** or **(1)** and **(3)** was kept constant with an appropriate molar ratio and the other precursor concentration was varied to control the stoichiometry.

Methods

The p-XRD patterns were recorded on a Bruker D8 AXE diffractometer using Cu-Kα radiations. The samples were mounted flat and scanned between 10 and 120° in a step size of 0.02 with a varying count rate depending upon the sample quality. Rietveld refinements were carried out in Topaz p-XRD software. The morphology and microstructure of thin films were investigated by using a Philips XL 30 FEGSEM and film composition was studied by EDX analysis using a DX4 instrument at 20 KV with WD 10 mm. Raman spectra measurements taken using a Renishaw 1000 Micro Raman system with an excitation wavelength of 520 nm, the measurement range set from 100 to 700 cm^{-1}. UV-VIS measurement carried with a Perkin Elmer Lambda 1050 spectrophotometer (PSI) and scanned across the range from 250–1000 nm. Electrical resistance measured were carried out using a Jandel four probe conductivity meters at room temperature using 1 μA current. XPS analysis was carried out by using a Kratos Axis Ultra in the School of Materials in The University of Manchester.

Results and discussion

The combination of precursor mixture was selected based on the TGA analysis.[24] The precursors $[Cu(S_2CNEt_2)_2]$, $[Zn(S_2CNEt_2)_2]$ and $[Sn(Bu)_2(S_2CNEt_2)_2]$ gave DTG peaks at 284 °C, 303 °C and 300 °C respectively and gave the metal chalcogenide residues. The strategy for the deposition experiments was to optimise the deposition temperature first at a fixed molar ratio of precursors and then vary the molar ratio of precursors at the optimised temperature. Deposition experiments were carried out between 350 and 450 °C using the 2:1:1 molar ratio of precursors. Precursor ratios were subsequently varied systematically to obtain the optimum precursor concentrations and ratios. The deposited films were then characterised by p-XRD, SEM, EDX, Raman and UV/Vis spectroscopy and electrical resistance measurements. Finally a photovoltaic cell was fabricated by depositing CZTS layer on top of ITO-coated glass substrate with a thin layer of TiO_2 under the optimized AACVD conditions.

Effect of temperature

Initial CZTS depositions were carried out using a 2:1:1 ratio of Cu, Zn and Sn precursors respectively at 350, 380, 400 and 450 °C (Table S1 in supporting information) SEM images shows that films deposited at 350 °C, were polycrystalline with uniform morphology. The supporting information Table S1 shows that the films were Sn rich and Zn deficient at 350 and 380 °C. On increasing the deposition temperature the percentage of Sn decreased and that of Zn increased gradually and being close to stoichiometric percentage of CZTS at 400 °C. These films were still slightly Zn rich which may have an advantageous effect on solar cell efficiencies.[33]

The p-XRD patterns of the deposited films at all these temperatures are shown in Figure 1(a) show major peaks at 2θ (112) and other peaks at 2θ for : (200), (211), (220) and (312) which correspond to kesterite (ICDD: 26-0575) of CZTS. The SEM images showed two different morphologies as shown in Figure (1a) but EDX point scan on each type of morphology gave no considerable differences in atomic percentage but showed minor difference in copper and Sn compositions ~0.1 to 0 (Supporting information Table S1).

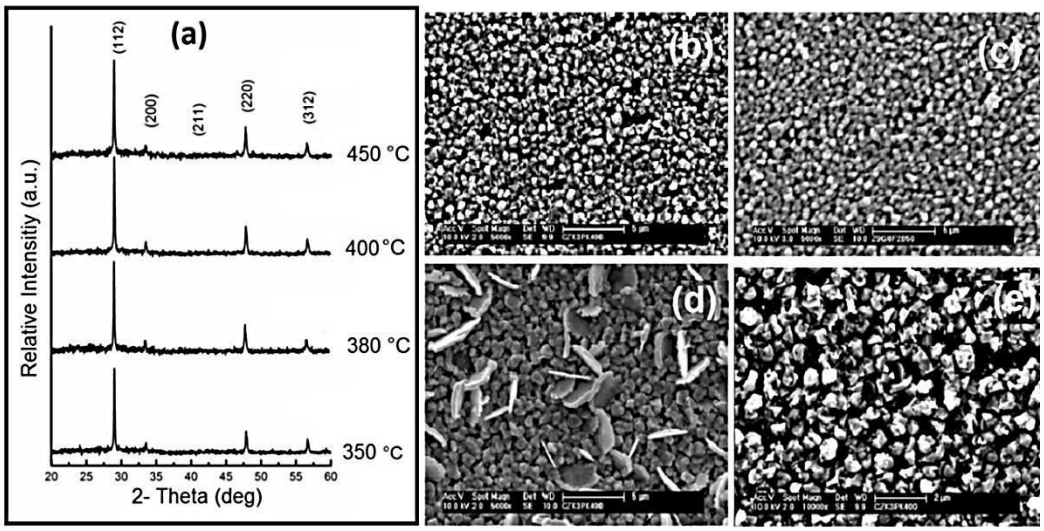

Figure 1: (a) p-XRD patterns are indexed to kesterite (ICDD: 26-0575) of CZTS and SEM images b to (e) are for the CZTS thin films deposited at 350, 380, 400 and 450 °C respectively, at [Zn] = 0.77mM.

Effect of molar molar ratio of precurosrs on the stoichiometry of CZTS thin films

The effect of varying the [Zn]/[Cu] ratio on the composition of CZTS thin films grown at 400 °C was investigated by using different [Cu] concentrations whilst keeping that of [Zn] constant, these results are summarised in Figure S1 (supporting information Table S2).concentration of [Zn] = [Sn] = 0.77 mM were kept constant whilst the [Cu]/[Zn] ratio was varied from 1.88 to 2.20 as shown in Figure S1.

The effect of increasing the ratio of [Cu]/[Zn] was most obvious in change observed in the composition of tin and sulfur in the deposited films. On increasing the [Cu]/[Zn] ratio from 1.88 to 2.20 the percentage of sulfur throughout increases from 45.04% to 47.95 % until [Cu]/[Zn] ratio of 1.90 then starts dropping to *ca* .41.49 % at the [Cu]/[Zn] ratio of 2.20. Tin composition initially decreases from 15.67 % to 12.04 % and then increases to 19.59 % at a [Cu]/[Zn] ratio of ~ 2.20. The stoichiometries of Cu and Zn change only slightly across the range and that of copper stayed between 27.83 %-29. 31 %.; similarly Zn remained around an average of 12.00%. From these results it is clear that the best stoichiometric composition of CZTS obtained at [Zn]/[Cu] ~ 1.00:1.91.

The p-XRD patterns of all the films deposited at 400 °C with differing [Cu]/[Zn] ratio are of kesterite CZTS (ICDD: 26-0575). The intensity of peaks varied with the size of crystallites size (Figure 3(a)). There are clear differences in the p-XRD patterns of the films deposited with the higher [Cu]/[Zn] of ~2.20 which showed a broad peak at 2θ value of 44 deg (labelled (*) in supporting information Figure S2(a). This peak with a comparatively low intensity was present in all patterns except the films deposited at [Cu]/[Zn] of ~1.91. The SEM images of the films deposited at this precursor ratio (~1.91) showed uniform morphology with irregularly shaped crystallite of 500-600 nm size supporting information Figure S2(b)whereas those deposited at lower or higher ratios were showing a morphology based on hexagonally shaped large crystallites (4-5 μm) on a background of irregularly shaped nanocrystallites (500-600 nm size).

The Band gaps of all the films were measured by absorbance spectroscopy and the results plotted as $(\alpha h\nu)^2$ vs $h\nu$ (where α = absorption coefficient, h = Planks constant, ν = frequency which is equal to c/λ where c = velocity of light and λ = wavelength of light) are given in supporting information Figure S3(a). The thickness of the films was found to be ~1 μm. The

band gap of the films significantly changed with the change in Sn composition. As the Sn stoichiometric percentage increases the band gap increases; which is consistent with the previous reports.[48,49] The band gap of the films with lowest Sn composition (12 %) was observed as 1.5 eV whereas those with highest Sn composition (18 %) had a band gap of 2.7 eV. The Raman spectra of all the films showed main CZTS peaks at shifts of 338 and 287 and 351 cm^{-1} except the films with highest Sn composition which showed an additional Raman peak at 220 cm^{-1} corresponding to SnS[50-54] (supporting information Figure S3).

The experiments at 400 °C were repeated using different [Cu]/[Zn] from 1.88 to 2.2 and different [Sn]/[Zn] from 0.90 to 1.30 whilst keeping the other composition constant. The results obtained for the compositions of S, Sn, Zn and Cu are shown in supporting information Table S2. On increasing the [Cu]/[Zn] from 1.88 to 2.20 the percentage of sulfur throughout increases until a [Cu]/[Zn] of 1.90 and then starts dropping at the [Cu]/[Zn] of 2.20 at 400°C . The tin composition initially decreased and then increases with varying [Sn]/[Zn] from 0.90 to 1.30 to *ca* 20 % at a [Cu]/[Zn] of ~ 2.20. The stoichiometries of Cu and Zn change only slightly across the range of [Sn]/[Zn] from 0.90 to 1.30 and that of copper stayed between 27.83%-29. 31%.; similarly Zn remained around an average of 12.00%. It can be seen that, the stoihiometric atomic percentage of Sn on the films increases from 11.01% (0.79) to 20.83% (2.10) as the [Sn]/[Zn] precursor ratio increased from 0.90 to 1.30. On the other hand, stoichiometric percentage composition of S on the films first increased from 49.96% (3.37) to 47.40% (4.11) when [Sn]/[Zn] ratio increased from 0.90 to 1.10 then it fall to 42.82% (3.47) at [Sn]/[Zn] reached ~1.30. Stoichiometric percentage composition of Cu on films also show same trend as S composition change in contrary to that Zn composition decreased till [Sn]/[Zn] ratio from 0.90 to 1.20 and only at 1.30 it slightly went up to 12.33(1.00).The SEM images, Raman and UV-Vis spectra images are shown in supporting information Figure S4.

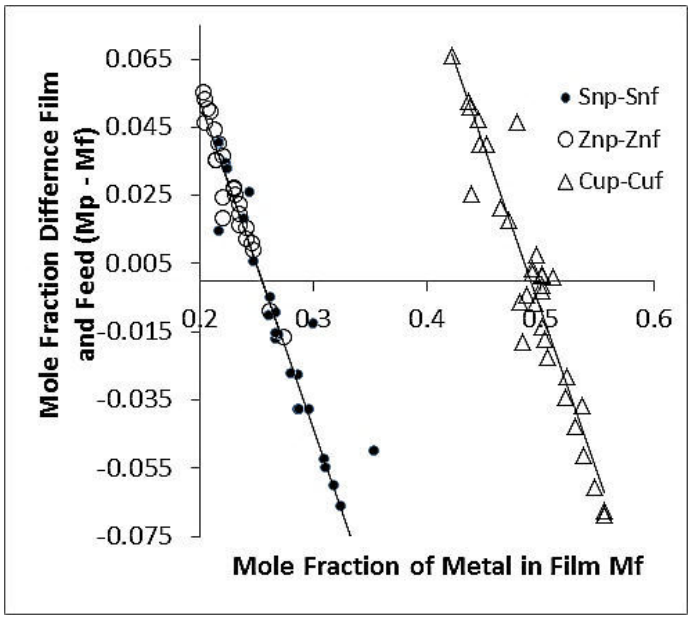

Figure 2: Difference plot showing the relation between mole fraction of metal in films vs the mole fraction difference of metal in film and feed.

The stoichiometric composition of the films with [Sn]/[Zn] precursor ratio. This observation confirmed that the best composition of thin films is obtained at [Cu]/[Zn] ratio of ~ 1:1.91. EDX results for composition of thin films are consolidated in Figure 2. A standard 'three component phase diagram is used to correlate the molar concentration of precursor and the stoichiometric composition of films Figure 3. The triangular phase diagram shows that the films deposited are concentrated in around the stoichiomentric region for CZTS. Moreover the difference plot or delta plots (Figure 2) show more consistent straight lines of metal concentration in precursor and that in CZTS. Both these graphical analysis showing good control over stoichiometry can be achieved and systematised for reproducible AACVD deposition.

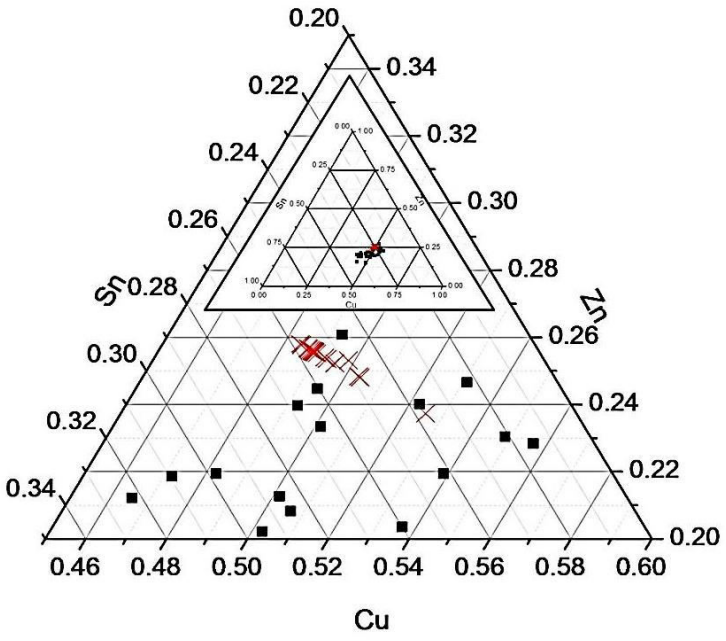

Figure 3: Compositional analysis in a 'triangular phase diagram' correlating the molar concentration of precursors and the stoichiometry of CZTS Thin films deposited at 400 °C, 45 min. Black squares and line shows the molar composition of precursors and the red crosses represent the stoichiometric composition of films.

Supporting information Table S2 and Figure S5 show the EDX results obtained for the composition of films deposited at 400 °C and at molar ratios of [Cu]/[Zn]/[Sn] at ~1.91:1:1; the composition of films remained almost the same as expected for CZTS (Supporting information Figure S2).

The p-XRD patterns of all these films, at these precursor ratios, matched with kesterite CZTS and showed no other phases Figure 4. SEM images showed uniform morphology for all the films with an average crystallite size of 500 nm (Figure 4)**.** The thickness of the films, at [Zn] = 0.77mM, was found to between 1- 2 µm (Figure 4). Band gaps for all these films were found to be between 1.4-1.5 eV (Figure 5) consistent with those reported previously.[53-55]

Phase purity of the films was also confirmed by Raman spectra which showed peaks at 287, 338 and 351 cm^{-1} corresponding to CZTS (Figure 5).[55]

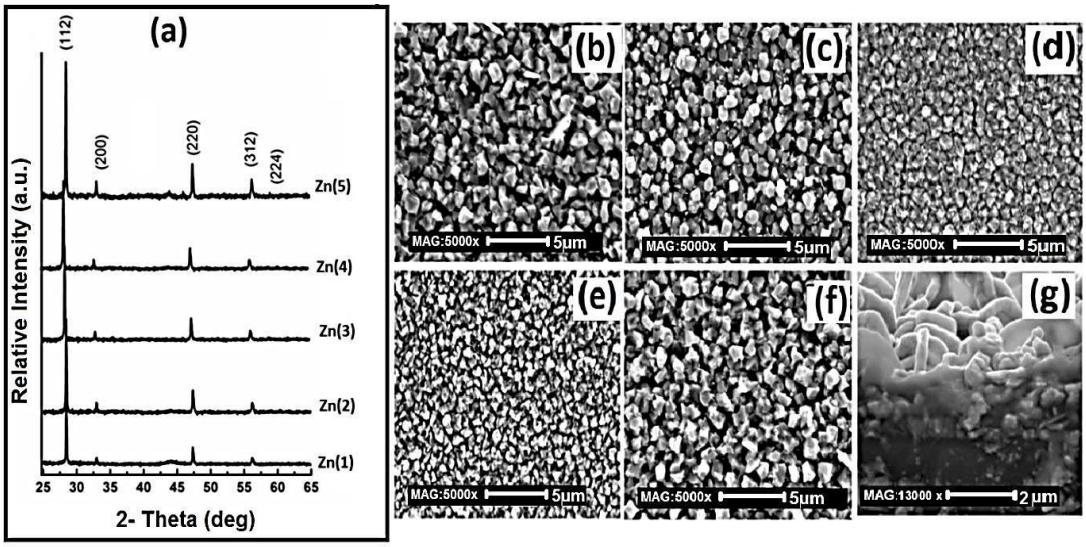

Figure 4: (a) p-XRD patterns for CZTS films deposited at 400°C, 45min at Cu: Zn ratio 1:1.91 at different Zn ratio, labeled from Zn(1)–Zn(5), Peaks are matched with kesterite CZTS (ICDD: 26-0575), **(b)-(f)** are SEM images labeled of CZTS films deposited under the same condition and (**g**) shows thickness of film deposited at 400 °C when [Zn] = 0.77mM.

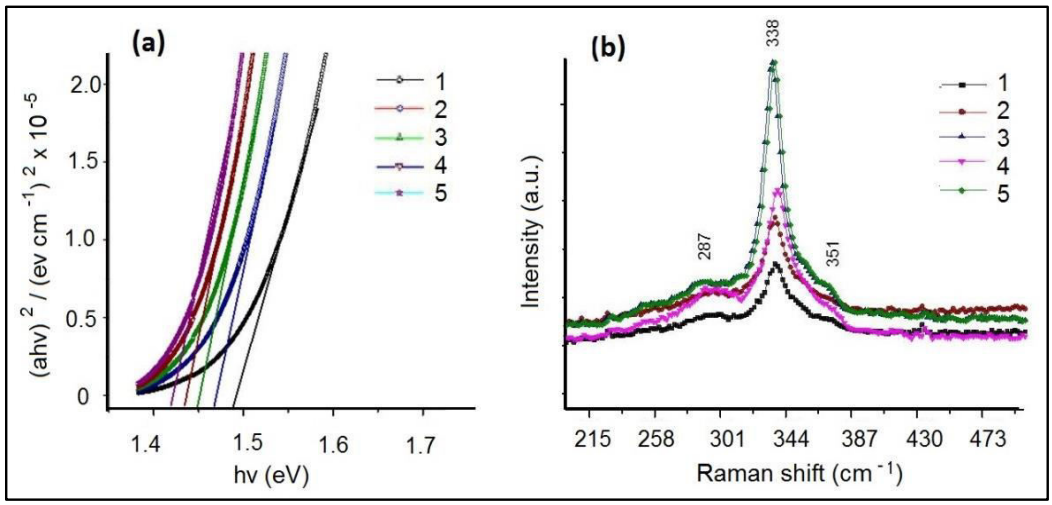

Figure 5: (**a**) UV-Vis spectrum of CZTS films deposited at 400°C temperature, 45min individually at Cu: Zn ratio 1:1.91 labeled from (K1)-(K5) with increase in Zn precursor

concentration and **(b)** Raman spectra labled from (L1)-(L5) of CZTS films deposited at the same condition.

XPS Spectra of CZTS thin films deposited at optimum conditions

The valence states of the elements in the CZTS thin films deposited under the optimal conditions ([Zn] = 0.77 mM) at 400 °C with precrusror ratio [Cu]/[Zn]/[Sn] equivalent to 1:1:1.91were examined using XPS (Figure 6).

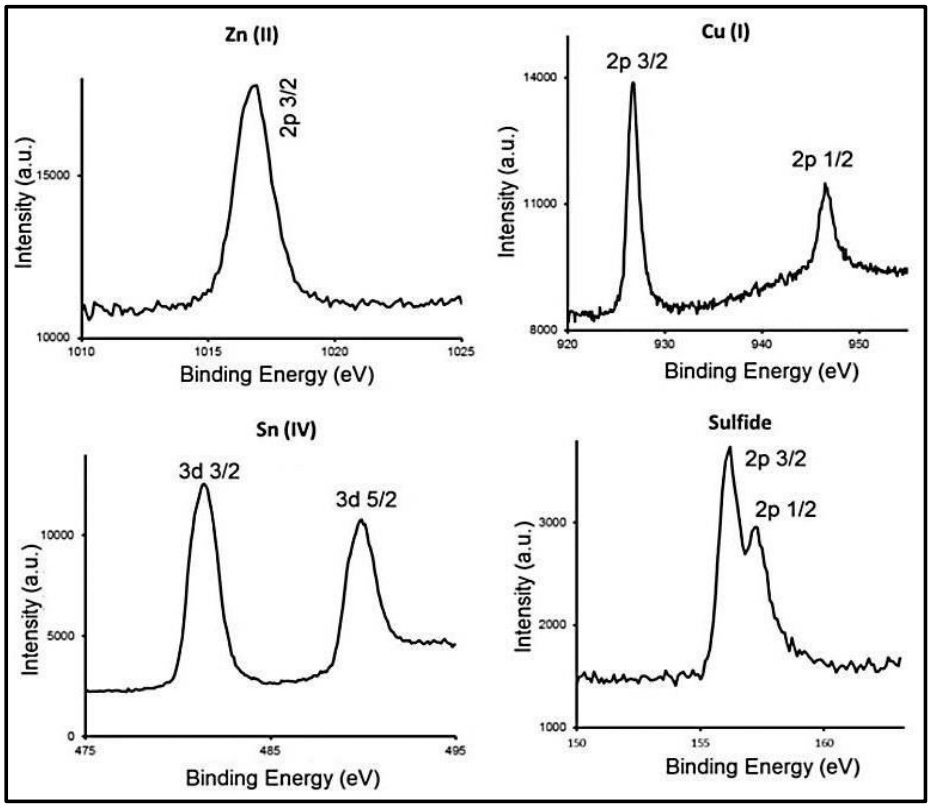

Figure 6: High resolution XPS analysis for CZTS thin films deposited at 400 °C, 45 min at 45 min of [Cu]/[Zn]/[Sn] precursor ratio 1:1:1.91 (at [Zn] = 0.77 mM).

The valence state of Cu and Sn aren Cu(I) and Sn (IV). Sulfur is as ntsulfide (S^{2-}) and the zinc is divalent . High resolution XPS had been used for calculating binding energies

(BE). The corresponding BE's for Zn $2p_{3/2}$, Cu $2p_{3/2}$, Cu 2p ½, Sn $3d_{5/2}$, Sn $3d_{3/2}$, S $2p_{3/2}$ and S 2p ½ are located at 1017 eV, 929 eV, 949 eV, 483eV, 494 eV, 158eV and 160 eV respectively.[56-58]

Elemental maps of CZTS thin films deposited under optimum conditions

Selected area elemental maps of CZTS thin films deposited at 400 °C for 45 min from a Cu/Zn/Sn ratio 1:1:1.91 of precursor mixture (at [Zn]= 0.77 mM) are shown in Figure 7. The images showed uniform distribution of constituent elements throughout the selected area of the film.

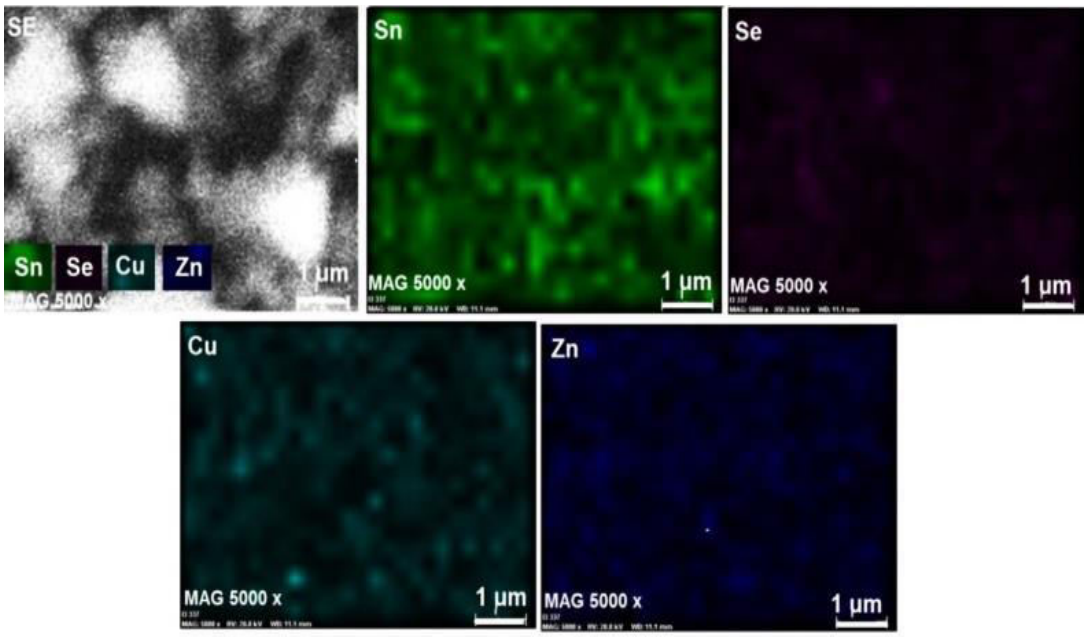

Figure 7: Elemental maps of CZTS thin films deposited at 400 °C, 45 min of [Cu]/[Zn]/[Sn] precursor ratio 1:1:1.91 (at [Zn] = 0.77 mM). SE is the scattered image of the film.

Electrical properties of optimised CZTS films

The room temperature electrical sheet resistance measured for films ~1µm thick deposited using the optimal conditions (400 °C, 45 min Ar flow 180 sccm) The films are

semiconducting with sheet resistance 1.10, 1.25, 1.3, 1.3 and 1.4 KΩ/cm^2 respectively for zinc feed concentrations of 0.75, 0.77. 0.78, 0.79 and 0.81 mM. These results compare well to others e.g at 400 °C by AACVD.[24] Yu *et al.* reported that layer by layer CZTS films deposited by by sol-gel method without sulfurization (thickness ~0.9 and 1.2 μm) gave sheet resistance of 5.25 x 10^3 KΩ/ cm^2 and 4.08 KΩ/ cm^2 respectively.[58] Mkawi *et al.* reported that the films deposited by an electrochemical method exhibited a p-type conductivity and the measured resistance decreased from 9.82×10^3 to 9.67×10^2 Ω /cm^2 (9.82 to 0.967 KΩ/ cm^2) with increasing Cu content in the films[59] which agrees well with the reports indicating that main Cu-rich and Sn-rich powders have the lowest grain resistance.[60]

The temperature dependence of electrical transport properties gives useful insight into the nature of the microscopic material properties which control carrier scattering, confinement and localisation. In this work electrical conduction was measured over the temperature range 40K-400K. The data shown in Figure 8 was obtained for sample deposited at 400 °C for 45 min from a Cu/Zn/Sn ratio 1:1:1.91 of precursor mixture (at [Zn]= 0.77 mM) and is representative of the AACVD structurers described here.

Kesterite materials grown by a variety of methods tend to show complex transport behaviour[61,62] in which hopping or thermalisation over internal barriers controls carrier movement. A generalised form of transport equation which invokes three dominant hopping or thermalisation regimes has been shown to describe transport in Kesterite materials (61, 62) and is also true for the data shown in Fig (X). Three distinct thermalisation modes were used to fit our data, each mode dominating transport in particular temperature regions. At low temperatures (<60K) Mott variable range hopping dominates but nearest neighbour hopping limits transport between at intermediate temperatures (60K-185K). For higher temperatures (185K - 400K), thermionic emission over grain boundary potential barriers dominates σ.

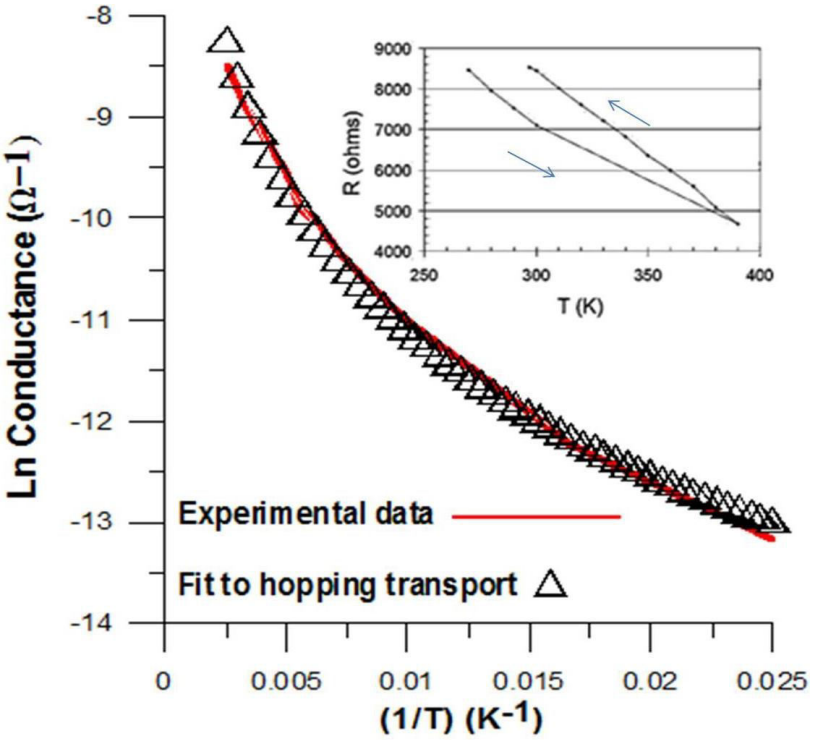

Figure 8: Temperature dependent conductance. Main plot shows conductance against 1/T and compares data with a fit to a model which included three hopping type mechanisms. The inset shows the hysteresis in R for the T.

Each mechanism yields a distinct exponent in an expression for overall conductivity and any temperature T:

$$\sigma(T) = \sigma_1 e^{-\left(\frac{T_0}{T}\right)^{1/4}} + \sigma_2 e^{-\left(\frac{E_{nn}}{kT}\right)} + \sigma_3 T^{-\frac{1}{2}} e^{-\left(\frac{E_{gb}}{kT}\right)}$$

where, σ_1, σ_2 and σ_3 represent respectively the $T \rightarrow \infty$ conductivity limit for Mott variable range hopping, nearest neighbour hopping and thermionic emission over grain boundaries. The energy term associated with T_0 in the Mott variable range hopping conductivity expression is given by (Mott N F and Davis E A 1971 Electronic Processes in Non-Crystalline Materials (Oxford: Clarendon):

$$kT_0 = \frac{\xi^{-1}}{n_0} = E_{MVRH}$$

where ζ is the particle localisation length at the hopping site and n_0 is the electron density at the Fermi energy. The energy exponent terms for the two other thermal processes are, straightforwardly average values for the nearest neighbour hopping energy (E_{nn}) and the grain boundary barrier energy (E_{gb}). We determine from the fitting exercise that following values for the energy terms which characterise the complex hopping transport behaviour of our material:

Hopping mechanism	**T range in which dominant**	**Extracted activation energy**
Mott-variable range hoping	T <60K	5 meV (T_0/T ≈900 at 50K)
Nearest neighbour hopping	60<T<185K	37 meV
Grain boundary hopping	T>185K	19 meV

We note however that, near to and above room temperature, i.e. for carrier transport dominated by grain boundary effects, we obtained clear evidence of hysteresis in slowly scanned current-voltage measurement used to obtain conductance data. This is shown in the form of a resistance plot in the inset to Fig (X). The intuitive explanation for such behaviour is that some net charge trapping occurs during the non-equilibrium current flow process. Such charge accumulation for materials with a dominant (majority) carrier type, holes in our p material, will naturally add to the repulsive charge and hence barrier height at grain boundaries. Each hole trapping event at a grain boundary, for example, will add a repulsive term for subsequent incoming holes. The observation of hysteresis suggests that the hopping

energy at grain boundaries is likely to be depend critically on doping level and temperature and grain boundaries may show dynamically varying properties in these low conductivity materials.

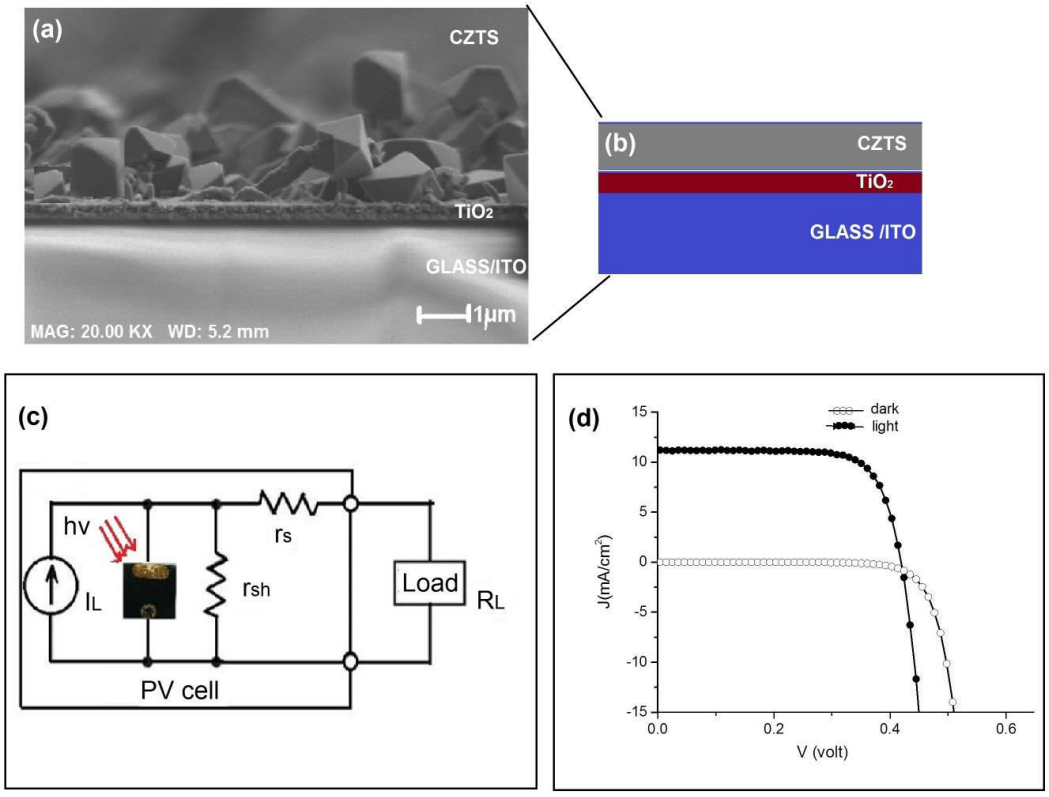

Figure 9: (a) The SEM cross sectional image of the device (b) model diagram of the device, (c) is the an idealised equivalent circuit for the solar cell used for the measurement of cell properties and (d) J-V curve for obtained for the device.

We have confirmed the suitability of the method for fabrication a PV-cell by depositing CZTS (1:1:1.91 molar ratio of precursors at 400 °C, 45 min and 180 sccm Ar flow) onto a preformed backplane consisting of glass/ITO substrate with a thin layer of TiO_2 layer (n-type). The corss sectional image and a model diagram shown in Figure 9 (a) and 9 (b). The instrument set up for the measurement of cell properties are as shown in fFgure 9 (c). Figure 9 (d) shows the J-V curve for the fabricated p-n junction. The cell showed good photoresponse in light condition than in dark. The cell properties of the solar cell; open

circuit volatage 428 mV, short circuit current denisty 12.5 mA/cm^2, fill factor of 0.72 and the conversion efficiency was 2.39%, which is solar cells fabricated by this method is very close to the efficiency of dye sensitised solar cells with the CZTS counter-electrode (CE) (Eff = 3.141%) but very close to that with a Pt CE (Eff = 2.761%).[47] The efficiency of the cells showed good improvement compared to the double junction solar cell was also constructed with dye-sensitized porous TiO_2 films as the photoanode and porous CZTS films as the photocathode (1.15% to 1.23%).[45]

Conclusion

We have used a relatively simple precursor system to demonstrate stoichiomentric control in CZTS. The results are compared to recent 'combinatorial' approaches to such materials.[22,41,43] Close to optimal deposition temperature was seen at 400 °C. This temeperature for controlled deposition by CVD can be contrasted with the 600 °C for 8 h needed to sulfide metal alloy films. At the later elevated temperatures evaporation of sulfides, especially from copper precursor one is more volatile, from the film can be an important or limiting factor controlling stoichiometry and dependent properties. We have recently demonstrated the successful use of MOCVD for a range of materials in the k

esterite family.[24]. This study demonstrates the potential of this method in the parent system, with a greater empahsis on the details of stoichiometry and properties. It also serves to demonstrate that our relatively simple techniques can lead to films with tolerable electrical and optical properties. A simple demonstration cell has been prepared we intend to contine this work by developing further the family of precursors and materials of improved functionality.

The mole ratio of [Cu]/[Zn] precursors and deposition temperature both play a crucial roles in determining the stoichiometry, band gap and morphology of deposited films. All the

deposited films have been characterised by p-XRD, SEM, EDX, Raman, XPS and UV/Vis spectroscopy. The electrical measuements display hysteresis in the conductivity especially near and above room temperature. These films are stable with suitable band gap and conductivity hence is a best candidate for fabrication of solar cells and devices. Under one sun (100 $mWcm^{-2}$) illumination, the dye sensitised sandwich type solar cells comprised of a sensitised TiO_2 photoanode as the working electrode, as prepared CZTS/FTO thin films or Pt/FTO as a CE showed a comparable photovoltaic conversion efficiency (Eff = 3.141 %) to that with a Pt CE (Eff = 2.761%). It indicates that the as prepared CZTS films had potential for developing low cost and high efficient CE. The efficiency of the device made by the deposition of a thin layer of CZTS 2.39 % suggests the promise of the system. It that the as prepared CZTS films have potential especially for an environment-friendly and earth-abundant elemental composition and a narrow band gap.

Acknowledgement

PK thanks the University of Manchester for partial funding. This work was also funded by the Engineering and Physical Sciences Research Council (grant number EP/K039547/1).

Appendix

Supporting information: Supplementary data associated with this article can be found in the online version at http://dx.doi.org

References

1. T. K. Todorov, J. Tang, S. Bag, O. Gunawan, T. Gokmen, Y. Zhu, and D. B. Mitzi, *Adv. Energy Mater.* 3 (2013) 34;
2. (a) A. R. Barkhouse, O. Gunawan, T. Gokmen, T. K. Todorov, and D. B. Mitzi, *Prog. Photovolt. Res. Appl.* 20 (2012) 6. (b) X. Liu1, Y. Feng, H. Cui, F. Liu, X. Hao , G.

Conibeer, D. B. Mitzi, M. Green, *Prog. Photovolt: Res. Appl.* (2016) DOI: 10.1002/pip. (c) M. A. Green, K. Emery, Y. Hishikawa, W. Warta, E. D. Dunlop, *Prog. Photovolt: Res. Appl.* 23 (2015) 805–812.

3. T. Shibuya, Y. Goto, Y. Kamihara, M. Matoba, K. Yasuoka,L. A. Burton, A. Walsh, *Appl. Phys. Lett*., 104 (2014) 021912-914;
4. J. J. Scragg , P. J. Dale , L. M. Peter , G. Zoppi , I. Forbes , *Phys. Stat.Solidi B,* 245 (2008) 1772-1776.
5. (a) C. Steinhagen , M. G. Panthani , V. Akhavan , B. Goodfellow , B. Koo , B. A. Korgel , *J. Am. Chem. Soc.* 131 (2009) 12554-12559. (b) S. Schorr, H.-J. Hoebler , M. Tovar , *Eur. J. Mineral.* 19 (2007) 65.
6. T. K. Todorov, K. B. Reuter, D. B. Mitzi, *Adv. Mater.* 22 (2010) E156.
7. R. Haight , A. Barkhouse , O. Gunawan , B. Shin , M. Copel , M. Hopstaken , D. B. Mitzi , *Appl. Phys. Lett.* 98 (2011) 253502-25308.
8. Y.B. K. Kumar, G. S. Babu, P. U. Bhaskar, V. S. Raja, *Sol. Energy Mater. Sol. Cells* 93 (2009) 1230–1237.
9. J. S. Seol , S. Y. Lee , J. C. Lee , H. D. Nam , K. H. Kim , *Sol. Energy Mater. Sol. Cells* 75 (2003) 155-159.
10. H. Katagiri, K. Saitoh, T. Washio , H. Shinohara , T. Kurumadani , S. Miyajima , *Sol. Energy Mater. Sol. Cells* 65 (2001) 141-145.
11. M. Kurihara , D. Berg , J. Fischer , S. Siebentritt , P. J. Dale , *Phys. Stat. Solidi,* 6 (2009) 1241-1247 .
12. (a) A. Redinger , S. Siebentritt , *Appl. Phys. Lett.* 97 (2010) 092111-17.(b) A. Redinger , D. M. Berg , P. J. Dale , S. Siebentritt , *J. Am. Chem. Soc.* 133 (2011) 3320-3325.
13. N. Nakayama and K. Ito, *Appl. Surf. Sci.* 92 (1996) 171-174.

14. J. Seol, S. Lee, J. Lee, H. Nam, and K. Kim, *Sol. Energy Mater. Sol. Cells*, 75 (2003) 155-159.
15. T. Tanaka, T. Nagatomo, D. Kawasaki, M. Nishio, Q. Guo, A. Wakahara, A. Yoshida, and H. Ogawa, *J. Phys.Chem. Solids,* 66 (2005) 1978–1981.
16. M. Kurihara, D. Berg, J. Fischer, S. Siebentritt and P. J. Dale, *Phys. Status Solidi C,* 6 (2009) 1241-1244.
17. K. Moriya, J. Watabe, K. Tanaka and H. Uchiki, *Phys. Status Solidi*, 3 (2006) 2848-2852.
18. K. Tanaka, N. Moritake and H. Uchiki, *Sol Energ Mat Sol C*, 91 (2007) 1199-1201.
19. K. Moriya, K. Tanaka and H. Uchiki, *Jpn. J. Appl. Phys. 1*, 46 (2007) 5780-5781.
20. T. Tanaka, D. Kawasaki, M. Nishio, Q. X. Gu and H. Ogawal, *Phys. Status Solidi C,* 3 (2006) 2844-2847.
21. M. Y. Yeh, C. C. Lee and D. S. Wuu, *J Sol-Gel Sci Techn*, 52 (2009) 65-68.
22. Q. Guo, G. M. Ford, W-C. Yang, B. C. Walker, E. A. Stach, H.W. Hillhouse, R. Agrawal, J. *Am. Chem. Soc.* 132 (2010) 17384–17386.
23. R.J. Deokate,A. D. Adsool, N. S. Shinde, S. M. Pawar,C. D. Lokhande, *Energy Procedia*, 54 (2014) 627 – 633.
24. K. Ramasamy, M. A. Malik and P. O'Brien, Chem. Sci. 2 (2011) 1170-1172; K. Ramasamy, M. A. Malik, P. O'Brien, *Chem. Commun*, 48 (2012) 5703-5714.
25. P. Marchand, I. A. Hassan, I. P. Parkin, C. J. Carmalt, *Dalton Trans*., 42 (2013) 9406–9422
26. M. N. McCain, S. Schneider, M. R. Salata, T. J. Marks, *Inorg. Chem.* 47 (2008) 2534-2542.

27. (a)C. R. Crick,I. P. Parkin, J. Mater. Chem., 19 (2009) 1074–1076. (b) D. S. Bhachu, D. O. Scanlon, E. J. Saban, H. Bronstein, I. P. Parkin, C. J. Carmalt, R. G. Palgrave, *J. Mater. Chem. A*. 3 (2015) 9071-9073
28. M. R. Waugh, G. Hyett, I. P. Parkin, *Chem. Vap. Deposition* 14 (2008) 366–372
29. (a) J. E. Bernard, L. G. Ferreira, S. H. Wei, A. Zunger, *Phys. Rev. B*, 38 (1988) 6338-6342. (b) R. Magri, S. H. Wei, A. Zunger, *Phys. Rev. B* 42 (1990) 11388-11391 (c) A. Walsh, S. Chen, S-H. Wei, X-G. Gong, *Adv Energy Mater,* 2 (2012) 400-404.
30. S. Schorr, H-J. Hoebler, M. Tovar, *Eur. J. Mineral*, 19 (2007) 65-69.
31. X. Liu, H. Cui, C. Kong, X. Hao, Y. Huang, F. Liu, N. Song, G. Conibeer, M. Green, Applied Physics Letters 106 (2015) 131110-131116.
32. (a) H. Katagiri . *Jpn J Appl phys*. 40 (2001) 500-506. (b) T. Kobayashi, *Jpn J Appl phys.*, 44 (2005) 783-786.
33. K. Tanaka, Y. Fukui, N. Moritake and H. Uchiki, *Sol Energy. Mat. Sol C*, 95 (2011) 838-842.
34. K. Wang. O. Gunawan, T. Todorov, *Appl.Phys. Lett.* 97 (2010) 143508, 1–3.
35. H. Katagiri, K. Jimbo, S. Yamada, *Appl. Phys. Express*. 1 (2008) 041201-2.
36. D. B. Mitzi, O. Gunawan, T.K. Todorov, K. Wang, S. Guha, Sol. Energy Mater. Sol. Cells, 95 (2011) 1421-1424.
37. B.Shin, O. Gunawan, Y. Zhu, N. A. Bojarczuk, S. J. Chey , S. Guha, *Prog. Photovolt: Res. Appl.* 21 (2013) 72–76,
38. D. J. Lewis, P. Kevin, O. Bakr, C. A. Muryn, M. A. Malik, P. O'Brien, *Inorg. Chem. Front.* 1 (2014) 577-598.
39. S. Bag, O. Gunawan, T. Gokmen, Y. Zhu, T.K. Todorov, D.B. Mitzi, *Energy Environ. Sci.,* 5 (2012) 7060-7065.

40. W. Yang, H.S. Duan, B. Bob, H. Zhou, B. Lei, C.H. Chung, S.H. Li, W.W. Hou, Y. Yang, *Adv. Mater.* 64 (2012) 6323-6329.

41. D.J. Milliron, D.B. Mitzi, M. Copel, C.E. Murray, *Chem. Mater.* 2006, **18**, 587; P.K. Sarswat, M.L. Free, *J. Cryst. Growth*, 372 (2013) 87-90.

42. Y. Cao, M. S. Denny , J. Jonathan, V. Caspar , E. William, Farneth , Q. Guo , A. S. Ionkin , L. K. Johnson , M. Lu , I. Malajovich , D. Radu , H. D. Rosenfeld, K. R. Choudhury , Wei Wu. *J. Am. Chem. Soc.* 134 (2012) 15644–15647.

43. A. V. Moholkar, S. S. Shinde, G. L. Agawane, S. H. Jo, K. Y. Rajpure, P. S. Patil, C. H. Bhosale, J. H. Kim, *J. Alloys Compounds*, 544 (2012) 145–151.

44. T. V. Arjunan and T. S. Senthil, *Mater. Technol*. 28 (2013) 9–14.

45. P. Dai, G. Zhang, Y. Chen, H. Jiang, Z. Feng, Z. Lin and J. Zhan, *Chem. Commun*., 48 (2012) 3006–3008.

46. S. Chen, J. Tao, H. Tao, Y. Shen, L. Zhu, J. Jiang, X. Zeng and T. Wang *Materials Technology: Adv. Perform.Mater.* 30 (2015) 306-312: Ennaoui, M. Lux-Steiner, A. Weber, D. Abou-Ras, I. Kotschau, H. W. Schock, R. Schurr, A. Holzing, S. Jost, R. Hock, T. Voss, J. Schulze and A. Kirbs, *Thin Solid Films*, 517 (2009) 2511-2514.

47. M. C. Johnson, C. Wrasman, X. Zhang, M. Manno, C. Leighton, E. S. Aydil, Chem. Mater. 27 (2015) 2507-2514.

48. E. Zillner, A. Paul, J. Jutimoosik, S. Chandarak, T. Monnor, S. Rujirawat, R. Yimnirun, X.Z. Lin, A. Ennaoui, T. Dittrich, M Lux-Steiner, *Appl. Phys. Lett.* 102 (2013) 221908-912.

49. M. Altosaar, J. Raudoja, K. Timmo, M. Danilson, M. Grossberg, J. Krustok and E. Mellikov***,*** *Phys. status solidi (a),* 205 (2008) 167-170.

50. D. H. Fan, R. Zhang, H. R. Peng, *Adv. Mater. Research* 534 (2012) 156-159.

51. P. A. Fernandes, P. M. P. Salome and A. F. da Cunha, *Thin Solid Films*, 517 (2009) 2519-2523.

52. M. Altosaar, J. Raudoja, K. Timmo, M. Danilson, M. Grossberg, J. Krustok and E. Mellikov*, Phys. status solidi (a),* 205 (2008) 167-170.

53. C. L. Wang and A. Manthiram, *Acs Sustain. Chem. Eng*. 2 (2014) 561-568.

54. Q. J. Guo, H. W. Hillhouse and R. Agrawal, *J. Am. Chem Soc*, 131 (2009) 11672-11679.

55. F. Jiang, H. Shen, and W. Wang, *J. Electron. Mater.* 41 (2012) 2204–2209.

56. C. Gonzalez, G. M. Ribeiro, E. R. Viana, P. A. Fernandes, P. M. P. Salome, K Gutierrez, A. Abelenda, F. M. Matinaga,J. P. Leitao, A. F. da Cunha, *J. Phys. D. Appl. Phys.,* 46 (2013) 155107-155114.

57. H. Katagiri, K. Jimbo, W. S. Maw, K. Oishi, M. Yamazaki, H. Araki, A. Takeuchi, *Thin Solid Films,*517 (2009) 2455–2460.

58. X. Yu, A. Ren, F. Wang, C. Wa, ng, J. Zhang, W. Wang, L. Wu, W. Li, G.Zeng, L. Feng, *Inter.J. Photo ener.* ID 861249 (2014) 1-6

59. E.M. Mkawi, K. Ibrahim, M. K. M. Ali, A. S. Mohamed, *Int. J. Electrochem. Sci*. 8 (2013) 359 -368.

60. T. Tanaka, A. Yoshida, D. Saiki, K. Saito,Q. Guo, M. Nishio , T. Yamaguchi, *Thin Solid Films* 518 (2010) S29-S33.

61. V. Kosyak, M. A. Karmarkar, M. A. Scarpulla, *Appl. Phys. Lett.* 100 (2012) 263903:1-5,

62. M. Z. Ansari, N. Khare, *J. Appl. Phys.* 117 (2015) 025706: 1-7.

Composition Focusing in the Deposition of Copper Zinc Tin Sulfide (CZTS) by AACVD

Punarja Kevin,[a] Bruce Hamilton,[c] Eric Whittaker,[c] Ian Hawkins,[c] Paul O'Brien, [a,b*]

Table S1: EDX results of films deposited at temperatures 350, 380, 400 and 450 °C, precursor concentration 2:1:1 at [Zn]= 0.77 mM, 45 min. Stoichiometric composition of Zn set to unity

Molar ratio of precursors (1):(2): (3)	**Deposition temp (°C)**	**EDX Analysis (At. % of element/ At. % Zn)**			
		Zn	Cu	Sn	S
2: 1: 1	350	10.80 (**1.00**)	26.00 (**2.40**)	22.42 (**2.10**)	40.80 (**3.80**)
2: 1: 1	380	10.30 (**1.00**)	27.50 (**2.70**)	19.31 (**1.90**)	42.90 (**4.22**)
2: 1: 1	400	14.20 (**1.00**)	26.00 (**1.80**)	15.20 (**1.10**)	44.60 (**3.14**)
2: 1: 1	450	22.80(**1.00**)	24.90 (**1.10**)	10.71 (**1.10**)	41.80 (**2.03**)

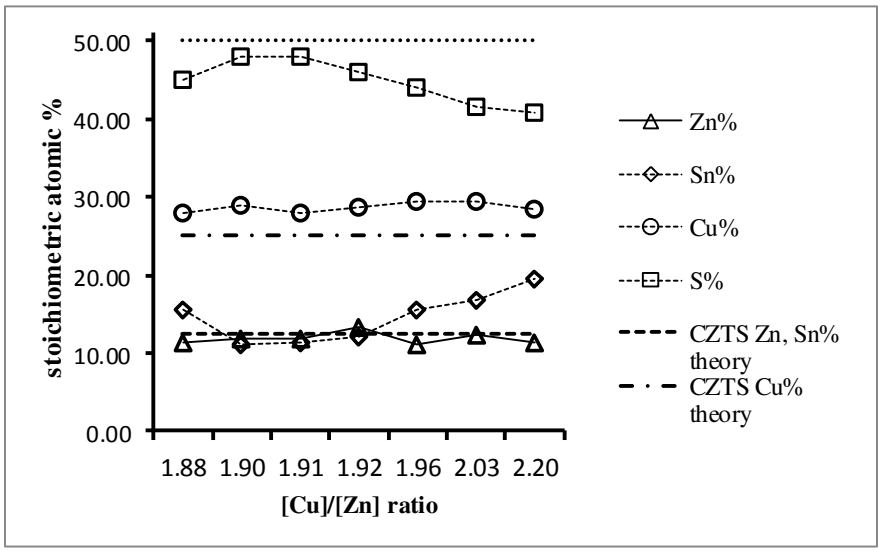

Figure S1: Molar ratio of [Cu]: [Zn] (precursors) vs stoichiometric ratio for films deposited at 400 °C for 45 min at precursor concentration of Zn = Sn = 0.77. Theoretical stoichiometric compositions of CZTS are shown as dotted line.

Table S2: Consolidated precursor composition and EDX results of CZTS films deposited using different molar ratios of precursors at 400 °C, 45 min.

[Zn]	[Sn]	[Cu]	Zn%	Sn%	Cu%	S%
5.15	5.15	9.68	10.89	15.91	27.08	46.41
5.15	5.15	63.96	12.42	20.97	26.92	39.68
5.15	5.15	9.80	10.77	17.71	29.00	42.50
5.15	5.15	9.82	11.89	11.20	28.96	47.95
5.15	5.15	9.83	12.98	13.81	26.26	46.95
5.15	5.15	68.80	13.36	21.54	27.17	37.93
5.15	5.15	9.85	11.87	23.04	27.02	38.07
5.15	5.15	9.88	12.94	18.32	27.94	40.80
5.15	5.15	9.98	9.09	22.90	25.62	42.93
5.15	5.15	10.01	10.81	20.49	25.92	42.77
5.15	5.15	10.11	14.99	14.15	28.34	42.53
5.15	5.15	10.46	9.05	21.35	29.93	39.68
5.33	5.33	10.00	11.44	15.67	27.83	45.04
5.33	5.33	10.20	11.88	11.19	28.95	47.95
5.330	5.330	10.16	11.76	11.28	27.99	47.85
5.330	5.330	10.18	13.35	12.04	28.75	45.94
5.33	5.33	10.47	11.04	15.63	29.31	44.02
5.33	5.33	10.80	12.44	16.71	29.34	41.49
5.33	5.33	11.80	11.25	19.59	28.35	40.79
5.4	10.29	5.40	11.89	11.20	28.96	47.95
5.5	10.83	5.50	12.25	13.92	26.32	47.52
4.98	4.98	9.36	12.36	20.23	31.15	36.25
4.98	4.98	9.45	12.53	19.04	27.48	40.94
4.98	4.98	9.47	11.05	20.49	22.98	45.46
4.98	4.98	9.49	12.25	13.92	26.32	47.52
4.98	4.98	9.51	13.31	13.16	28.97	43.26
4.98	4.98	9.80	13.88	15.50	28.52	44.08
4.98	4.98	9.96	12.44	15.89	32.79	38.88
4.98	4.98	10.10	12.44	16.72	29.35	41.49
4.98	9.96	4.482	13.92	11.01	26.11	49.96
4.98	9.96	4.98	12.25	13.92	26.32	47.52
4.98	9.96	5.48	11.54	12.72	28.34	47.4
4.98	9.96	5.98	11.42	15.51	25.11	44.96
4.98	9.96	6.47	12.33	20.83	26.01	42.82

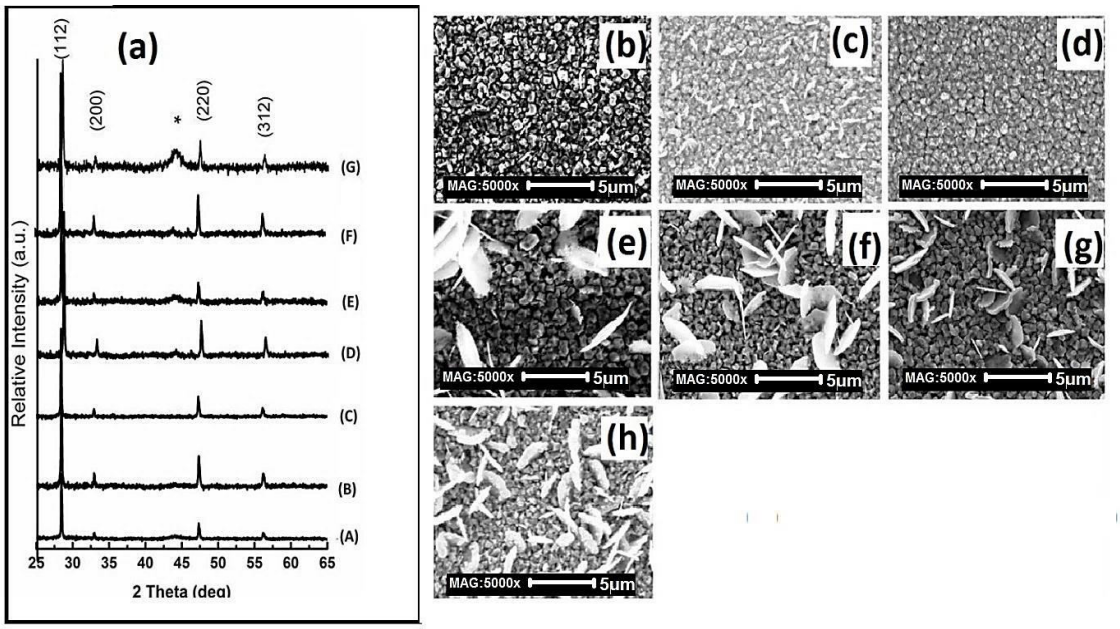

Figure S2: (a) p-XRD patterns labelled from A to G. Peaks are indexed to kesterite CZTS (ICDD: 26-0575) (**b**) to (**h**) SEM images for films with [Cu]:[Zn] ratio at [Zn] = [Sn] = 0.77 mM at 400 °C, 45 min deposition.

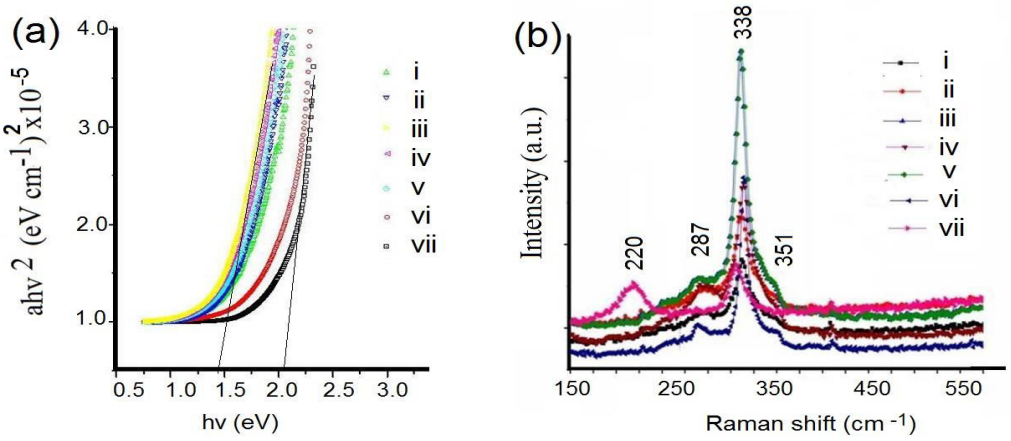

Figure S3: (**a**) band gap measurement i- vii (**b**): Raman spectra numbered as i - vii of films deposited with different [Cu]:[Zn] ratio [Zn] = [Sn] = 0.77mM, with decrease in [Cu]:[Zn] ratio at 400 °C, 45 min deposition.

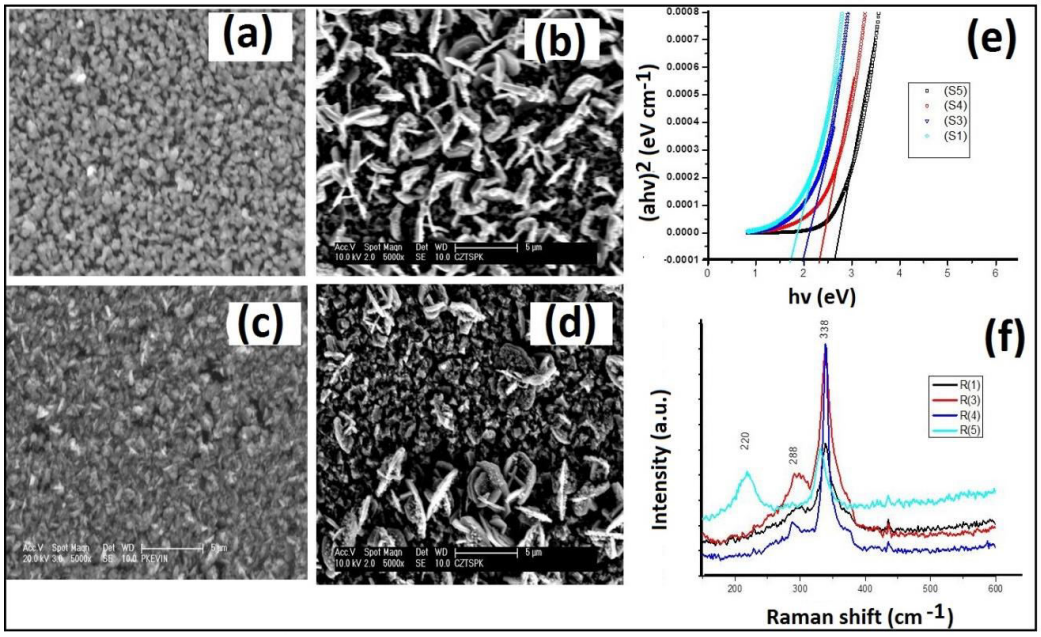

Figure S4: **(a)-(d)** are SEM images of films deposited at 400 C at [Sn]:[Zn] ratios from 0.9 to 1.3 where [Zn]:[Cu] = 1.00 :1.91; **(e)** shows the band gap of films labeled S1, S3, S4 and S5 for [Sn]:[Zn] ratios from 0.9 to 1.3 and **(f)** Raman spectra labeled as R1, R3, R4 and R5 of films at [Sn]:[Zn] ratios from 0.9 to 1.3 deposited at 400 °C at different [Sn]:[Zn] ratios where [Zn]:[Cu] is 1.00 :1.91. (excluded [Zn]:[Sn] = 1.00, [Zn] = 0.77mM).

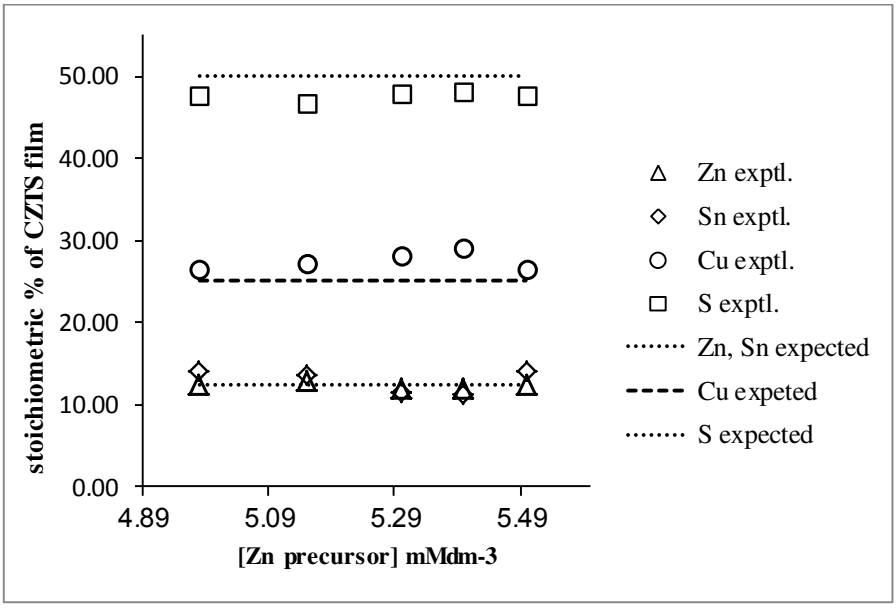

Figure S5: [Zn] precursor *vs* stoichiometric % for films deposited at 400 °C for 45 min at fixed molar ratio of [Cu]:[Zn]:[Sn] at ~1.91:1:1.

CHAPTER - VII : PAPER - 4

"Growth of $Cu_2ZnSnSe_4$ and $Cu_2FeSnSe_4$ thin films by AACVD from molecular precursors"

Punarja Kevin, Sajid N. Malik, Mohammd A. Malik, Paul O'Brien, *Mater. Lett.* 2015, **152,** 60-64.

Materials Letters 152 (2015) 60–64

Contents lists available at ScienceDirect

Materials Letters

journal homepage: www.elsevier.com/locate/matlet

Growth of $Cu_2ZnSnSe_4$ and $Cu_2FeSnSe_4$ thin films by AACVD from molecular precursors

Punarja Kevin [a], Sajid N. Malik [a,c], Mohammad Azad Malik [b,*], Paul O'Brien [a,b,**]

[a] School of Chemistry, The University of Manchester, Oxford Road, M13 9PL, UK
[b] School of Materials, The University of Manchester, Oxford Road, M13 9PL, UK
[c] School of Chemical and Materials Engineering, National University of Sciences and Technology, Islamabad 44000, Pakistan

ARTICLE INFO

Article history:
Received 23 December 2014
Accepted 18 March 2015
Available online 26 March 2015

Keywords:
Chemical vapour deposition
$Cu_2ZnSnSe_4$
$Cu_2FeSnSe_4$
Thin films
Molecular precursors

ABSTRACT

Phase pure $Cu_2ZnSnSe_4$ (CZTSe) and $Cu_2FeSnSe_4$ (CFTSe) thin films have been deposited onto glass substrates by Aerosol Assisted Chemical Vapour Deposition (AACVD) using mixtures of (triphenylphosphine)(tetraphenyldiselenoimidodiphosphinato)copper(I) [$Cu(PPh_3)[Ph_2P(Se)N(Se)PPh_2]$], *tris*(2,4-pentanedionato)iron(III) [$Fe(acac)_3$], tin(IV) acetate [$Sn(OAc)_4$] and *bis*(2,4-pentanedionato)zinc(II) [$Zn(acac)_2$]. Structure, morphology and optical properties of the deposited films were studied. The band gaps of CZTSe and CFTSe films were found to be between 1.0 and 1.2 eV.

1. Introduction

Kesterite type compounds such as Cu_2ZnSnS_4 (CZTS), $Cu_2ZnSnSe_4$ (CZTSe), Cu_2FeSnS_4 (CFTS) and $Cu_2FeSnSe_4$ (CFTSe) are considered to be amongst the better solar cell materials; they contain earth abundant elements with high absorption coefficient and have good stabilities [1–4]. CZTSe films have been prepared by various methods including: co-evaporation [5], sputtering techniques [6] and selenization [7]. CFTS and CFTSe nano-sheets have been synthesised by solvothermal [8] and hot injection methods [9]. Recently Cao et al. reported the morphological evolution in CFTSe nanoparticles obtained *via* a solvothermal method [10]. Meng et al. reported the synthesis of CFTSe thin films by magnetron sputtering followed by an annealing process [11].

There are no reports in the literature for the deposition of these materials by Chemical Vapour Deposition (CVD) from molecular precursors. CVD has the potential to deposit high quality semiconductor thin films [12]. We have reported the CVD of the parent CZTS kesterite phase, $CuInSe_2$, $CuGaSe_2$ and $CuIn_{0.7}Ga_{0.3}Se_2$ and many binary and ternary materials [13]. We now report the deposition of CZTSe and CFTSe by Aerosol Assisted (AA) CVD using a novel combination of metal–organic precursors.

2. Experimental

Methanol, tetrahydrofuran (THF), $Cu(NO_3)_2$, iron(III) acetylacetonate, zinc(II) acetylacetonate, tin(II) acetate and dichloromethane were purchased from Sigma-Aldrich and used as received. Solvents (ethanol and methanol) were used without any further purification or drying. Synthetic work was carried out under inert atmosphere of nitrogen using standard Schlenk line techniques. NMR spectra were recorded on a Bruker AC400 FT-NMR spectrometer whereas the APCI-MS spectra were recorded using a Kratos Concept 1S instrument. Perkin-Elmer FTIR instrument was used to record FTIR spectra. Elemental analyses and TGA were performed by the University of Manchester microanalysis facility. Melting points were recorded using a Stuart melting point apparatus and are uncorrected.

Synthesis of precursors: Synthesis of [Cu(PPh3){Ph2P(Se)NP(Se)Ph2}]. Complex [$Cu(PPh_3)[Ph_2P(Se)NP(Se)Ph_2]$] was synthesised by using the procedure reported by Woolins et al. [14]. A 150 mL methanol solution of 1.2 g (2.6 mmol) $K[Ph_2P(Se)NP(Se)Ph_2]$ was mixed with a solution of $Cu(PPh_3)_2NO_3$ (1.4 g, 2.1 mmol) in 100 mL methanol. The mixture was stirred for 30 min and the precipitate thus formed was filtered off. The filtrate on rotary evaporation gave a pinkish powder. The product was recrystallised from CH_2Cl_2. Yield: 64% [$Cu(PPh_3){Ph_2P(Se)NP(Se)Ph_2}$]; m. p; 221–223 °C. Elemental Analysis: Calc. for $C_{42}H_{35}CuNP_3Se_2$: C, 58.1; H, 4.1; N, 1.6; Cu, 7.32; P, 10.70% and Found; C, 57.87; H, 3.92; N; 1.48 Cu, 7.27; P, 10.64%. ^{31}P NMR (400 MHz, $CDCl_3$, rel. to 85% H_3PO_4): $\delta = 26.14$ ppm with two P–Se satellites, $J1_{P-Se} = 576$ Hz. FTIR: 3050 cm^{-1} (υC-H), 1165 cm^{-1} (υ_{as}-P_2N), 1100, 755 cm^{-1} (υ_s-P_2N), 690, 545 (υ-P–Se). Mass spec: *m*/*z*-869, 670, 460, 341. TGA showed single step decomposition between 250 and 320 °C with residue ~15% which is closer to the expected CuSe (16%).

* Corresponding author. Tel.: +44 161 2754652.
** Corresponding author at: School of Chemistry, The University of Manchester, Oxford Road, M13 9P, UK. Tel.: +44 161 2751411.
E-mail addresses: azad.malik@manchester.ac.uk (M.A. Malik), paul.obrien@manchester.ac.uk (P. O'Brien).

http://dx.doi.org/10.1016/j.matlet.2015.03.087
0167-577X/

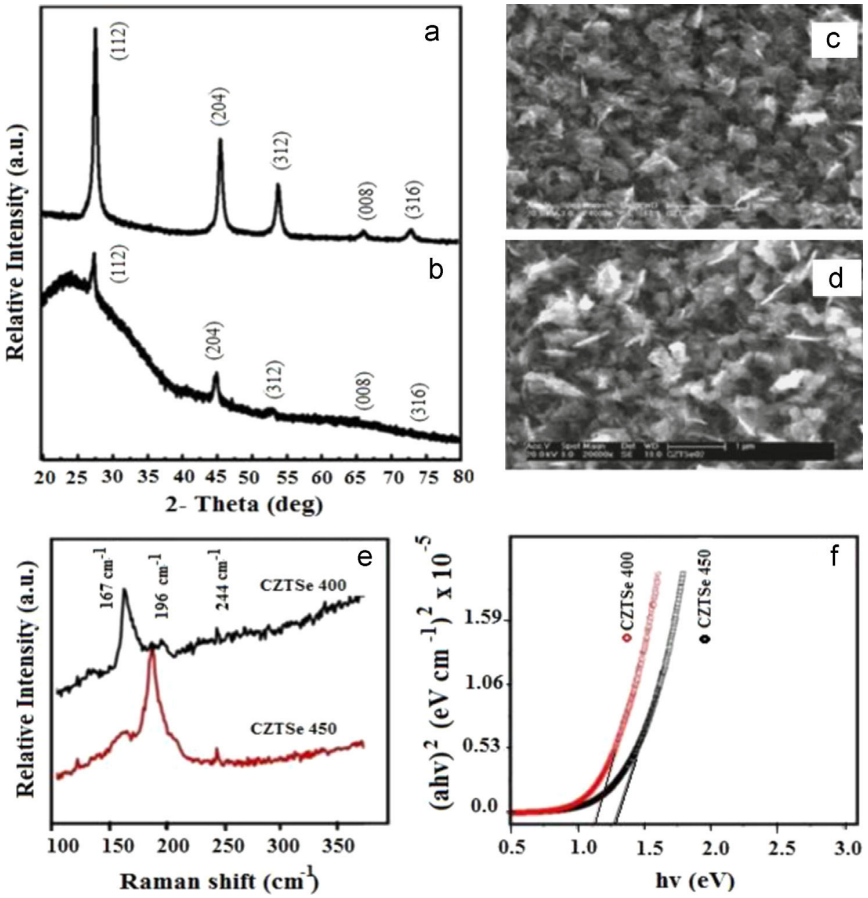

Fig. 1. (a, b) p-XRD pattern of CZTSe thin film deposited at 450 °C and 400 °C respectively, peaks are indexed with standard JCPDS 52-0868 for CZTSe (c) and (d) SEM images of thin films deposited at 450 and 400 °C, respectively.

Deposition of thin films: The deposition of CZTSe thin films by AACVD was carried out by using a solution of [$Cu(PPh_3)\{Ph_2P(Se)NP(Se)Ph_2\}$] (0.38 mmol), [$Zn(acac)_2$] (0.19 mmol) and [$Sn(OAc)_4$] (0.19 mmol) in 20 mL THF. Depositions were carried out at 350 °C, 400 °C and 450 °C for 50 min under argon flow rate of 180 sccm. The deposition of CFTSe was carried out by using a mixture of [$Cu(PPh_3)[Ph_2P(Se)NP(Se)Ph_2]$], (0.38 mmol), [$Sn(OAc)_4$] (0.19 mmol) and [$Fe(acac)_3$] (0.19 mmol) in 20 mL THF at 300, 350 and 400 °C for 50 min. Substrates used for the deposition of thin films were glass slides (1×3 cm^2) which were thoroughly cleaned by sonication in acetone for 30 min. A self-designed AACVD kit was used to carry out deposition of thin films. Typical deposition experiment involved dissolving a mixture of precursors in 20 mL THF. This solution is then loaded in a two-necked 100 mL round-bottom flask connected with an argon gas inlet on one side and reactor tube containing substrates on the another side. Argon carrier gas passing through the solution transported the aerosols generated by ultrasonic humidifier to the reactor tube placed in a Carbolite furnace at desired deposition temperature. A Platon flow gauge was used to maintain argon flow rate at 180 sccm. Thermally induced decomposition of both the solvent and the precursor at the hot substrate surface resulted in deposition onto substrates.

Characterisation of Thin Films: The Bruker D8 AXE diffractometer (Cu-Kα) was used to record p-XRD patterns. Thin films were scanned from 20° to 80° with a step size of 0.05. Raman spectra were recorded on Horiba T64000 triple 0.64m Raman spectrometer system. UV–vis–NIR absorption spectra were recorded using a Perkin-Elmer λ-1050 spectrophotometer. The morphology of the thin films was studied by SEM imaging using a Philips XL 30 FEGSEM. EDX analyses were performed using a DX4 instrument. TEM images were recorded using Philips CM200 FEG-TEM operated at an accelerating voltage of 200 kV.

3. Results and discussion

AACVD at 350 °C using 2:1:1 molar ratio of [$Cu(PPh_3)\{Ph_2P(Se)NP(Se)Ph_2\}$]:[$Zn(acac)_2$]:[$Sn(OAc)_4$] gave no deposition, whereas uniform and well adhered dark brown films were deposited onto glass substrates at 400 °C and 450 °C. Fig. 1(a) and (b) shows the p-XRD pattern of CZTSe thin films deposited at 450 °C and 400 °C, respectively. The p-XRD patterns matched with the standard JCPDS: 52-0868 for tetragonal $Cu_2ZnSnSe_4$ with I-42m space group. p-XRD patterns for films deposited at 450 °C show comparatively sharper peaks than those deposited at 400 °C. p-XRD patterns show slight amorphous nature for the films deposited at 400 °C. No additional peaks for binary materials such as ZnSe, SnSe or ternary material (Cu_2SnSe_3) were observed which suggests that the films are phase pure.

The SEM images (Fig. 1(c) and (d)) show uniform morphology based on randomly oriented plate-like crystallites with an average size of *ca* 0.8 μm for the films deposited at 450 °C and *ca* 1 μm for those deposited at 400 °C which were less flaky and found to be a mixture of dark and white crystallites. The thickness of the films as

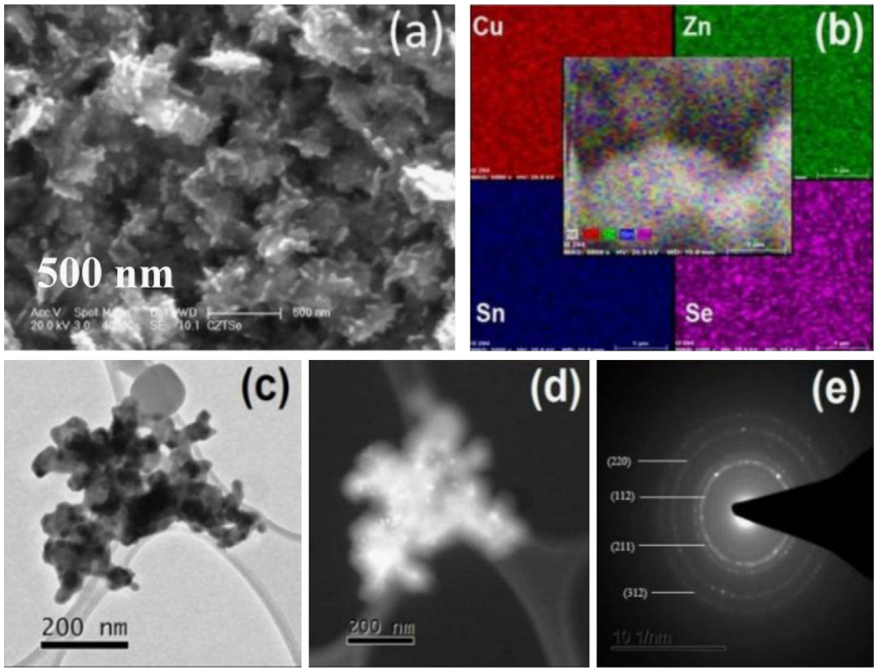

Fig. 2. (a) SEM image (b) elemental map (c, e) TEM bright, dark and SAED pattern of CZTSe deposited at 450 °C (e) Raman spectra and (f) band gap of CZTSe films deposited at 400 and 450 °C.

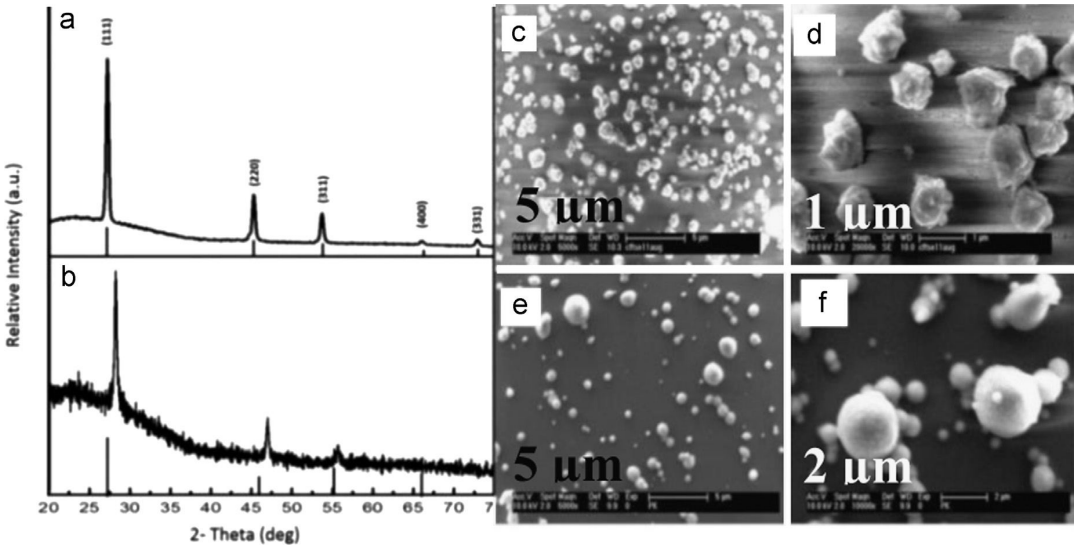

Fig. 3. (a, b) p-XRD patterns for films deposited at 350 and 400 °C respectively. Peaks are indexed with the standard JCPDS: 27-0167 for Stannite CFTSe. (c, d) and (e, f) SEM images of thin films deposited at 350 and 400 °C, respectively.

measured by SEM was found to be *ca* 0.8 μm and 1.0 μm for the films deposited at 400 and 450 °C respectively. Relative atomic percentage of Cu, Zn, Sn and Se atoms as measured by EDX analyses of the films deposited at 400 °C gave the values for Cu (23.72%), Zn (11.77%), Sn (6.8%) and Se (57.74%) which suggested a stoichiometric composition as $Cu_{2.0}Zn_{1.0}Sn_{0.6}Se_{4.9}$. The EDX analyses for films deposited at 450 °C were Cu (22.4%), Zn (14.4%), Sn (10.7%) and Se (52.4%) which gives a stoichiometric composition of $Cu_{1.9}Zn_{1.2}Sn_{0.9}Se_{4.3}$.

The Raman spectrum of the films (Fig. 1(e)) deposited at 400 °C showed a strong peak at 167 cm^{-1} and weaker peaks at 200 cm^{-1} and 245 cm^{-1} whereas thin films deposited at 450 °C showed stronger peak at 196 cm^{-1} and weaker peaks at 166.4 cm^{-1} and 245 cm^{-1}. These peaks were closer to those reported previously (167, 196, 244 cm^{-1}) for $Cu_2ZnSnSe_4$ [15]. It has been reported that the peak at 196 cm^{-1} is the characteristic A_1 Raman mode for CZTSe corresponding to the vibration of Se atoms surrounded by motionless neighbouring atoms [15,16]. Raman spectra of CZTSe for films deposited at 450 °C showed no sign of the binary phases. The direct band gaps of the thin films as measured from Tauc plots (Fig. 1(f)) deposited at 400 and 450 °C were found to be *ca* 1.12 eV and 1.25 eV respectively which are slightly higher than those

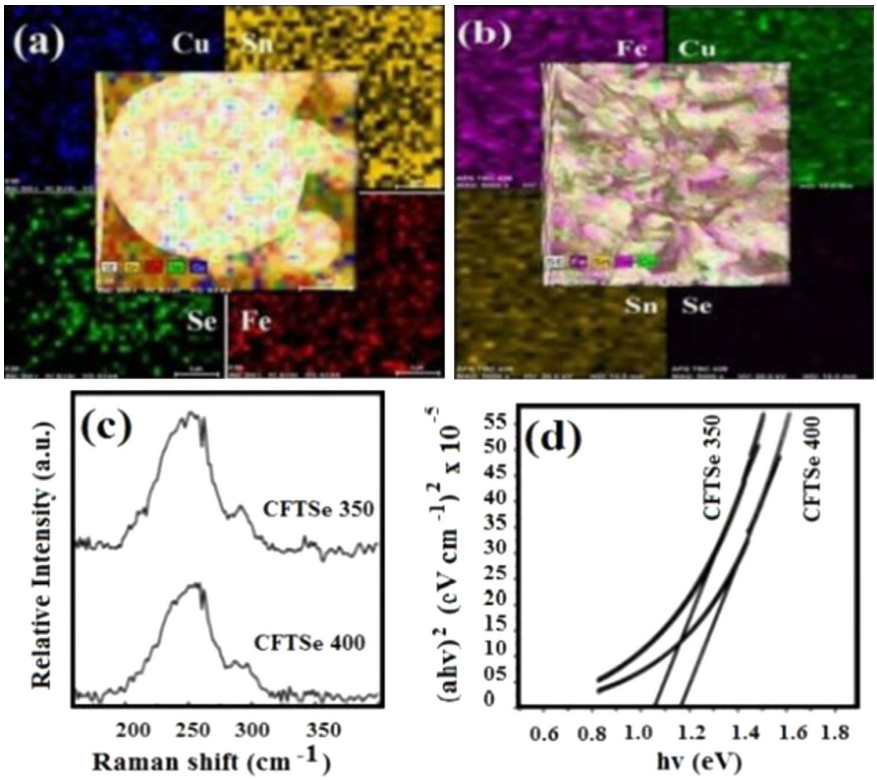

Fig. 4. (a, b) Selected area elemental maps for CFTSe thin films deposited at 350 and 400 °C respectively. (c, d) Raman spectra and band gap for CFTSe films deposited at 350 °C and 400 °C (labelled individually).

reported for CZTSe materials (1.06 eV) [15,16]. Tauc plots for band gap measurement were obtained by plotting $(ah\upsilon)^2$ vs $h\upsilon$ (a=absorption coefficient, h=Plank's constant, $\upsilon=c/\lambda$ where c=velocity of light and λ=wavelength). The graph is then extrapolated to the Energy axis giving the band gap (E_g). Thin film deposited at 400 °C showed a lower band gap than the one at 450 °C because of the Se rich and Sn deficient stoichiometry as shown by the EDX analyses.

EDX elemental mapping of films obtained at 450 °C for $Cu_2ZnSnSe_4$ showed uniform composition throughout the selected area of the films (Fig. 2(b)). The bright field and dark field transmission electron microscopy images (TEM) of the material scratched from the films deposited at 450 °C showed clusters comprising of nanoparticles in dark and bright field (Fig. 2(c) and (d)). Selected area electron diffraction (SAED) pattern of these films given in Fig. 2(e) showed distinct rings corresponding to major lattice planes (112, 204, 312, 400 and 316) of CZTSe.

The deposition of CFTSe was carried out by using a mixture containing 2:1:1 molar ratio of $[Cu(PPh_3)\{Ph_2P(Se)NP(Se)Ph_2\}]$:$[Sn(OAc)_4]$:$[Fe(acac)_3]$ precursors in 20 mL THF for 50 min. No significant deposition occurred at 300 °C whereas uniform brownish and dark brown films were obtained at 350 °C and 400 °C, respectively.

p-XRD patterns for films deposited at 350 and 400 °C are shown in Fig. 3(a) and (b) respectively. Peaks are matched with standard patterns for Stannite type CFTSe materials with space group 1-42m (JCPDS: 27-0167). Films deposited at 350 °C showed peaks at 2-theta values (27.17 (112), 45.07 (204), 53.41 (116), 65.65 (400) and 72.41 (316)) which correspond to the standard $Cu_2FeSnSe_4$ patterns (JCPDS: 27-0167), whereas the films deposited at 400 °C showed slight shift from the standard p-XRD patterns for CFTSe.

SEM images for films obtained at 350 °C showed flower like irregular crystallites of less than 1 μm in size (Fig. 3(c) and (d)) and the films deposited at 400 °C with larger and smaller irregular and regular spherical morphologies (Fig. 3(e) and (f)). EDX results of films deposited at 350 °C showed atomic percentage of Cu (25.11%), Fe (11.57%), Sn (9.17%) and Se (54.13%) which gave stoichiometry of $Cu_{2.17}Fe_{1.0}Sn_{0.8}Se_{4.6}$. Films deposited at 400 °C showed elemental analysis results for large spherical particles as Cu (13.33%), Fe (15.66%), Sn (26.2%) and Se (45.22%) and for small particles as Cu (27.05%), Fe (16.62%), Sn (12.59%) and Se (42.62%) giving an average of Cu (20.19%), Fe (17.2%), Sn (19.4%) and Se (43.91%) which gives a stoichiometric composition of $Cu_{1.4}Fe_{1.1}Sn_{1.3}Se_{3.0}$ showing higher percentage of Sn and lower percentage of Cu and Se. Selected area elemental maps for films deposited at 400 and 350 °C showed uniform distribution of elements throughout the film as shown in Fig. 4(a) and (b), respectively.

Raman spectra of films obtained at 400 °C showed a broad strong peak at ~209 cm^{-1} and a less intense peak at ~270 cm^{-1} (Fig. 4(c)) which is in agreement with the reported value of CFTSe (209, 270 cm^{-1}) [8–10]. The thickness of the films deposited at both temperatures was found to be *ca* 1 μm. Band gap measurement of films deposited at 400 °C using Tauc plots showed value ~1.18 eV whereas films deposited at 350 °C showed band gaps of ~1.05 eV (Fig. 4(d)) which closely matches with the reported value (1.12 eV) [17].

The deposited CZTSe thin films showed Kesterite phase whereas CFTSe thin films were in Stannite phase. The optical band gaps of the CZTSe films are slightly higher (1.12 and 1.25 eV) than those of CFTSe (1.05 and 1.18 eV) which is expected due to the presence of iron which reduces the optical band gap [18]. The morphology of the CZTSe films are predominantly based on

densely distributed flake like crystallites whereas the SEM images of CFTSe films show semi-spherical clusters of smaller crystallites with varying size thinly distributed on the surface of substrate.

4. Conclusions

CZTSe and CFTSe thin films have been deposited by AACVD at temperatures between 350 and 450 °C. Films were characterised by p-XRD, SEM, EDX, and Raman spectroscopy. Deposited materials showed different phases, CZTSe as Kesterite and CFTSe as Stannite. Band gap measurements showed that CZTSe films have higher band gaps at both deposition temperatures than those of CFTSe as expected. Selenium rich films were found to have lower band gap values as compared to those with selenium deficient. The films deposited at higher temperatures were found to have less Se content and hence gave higher optical band gaps than those deposited at the lower temperatures.

Acknowledgement

We thank Gary Harrison for XRD, Mathew Smith for TEM, PK thank the University of Manchester for funding. We thank Engineering and Physical Sciences Research Council (EPSRC) for funding of instruments under Grant number (EP/K039547/1) for characterisation of the compounds.

References

[1] Katagiri H, Jimbo K, Yamada S, Kamimura T, Maw. WS, Fukano T, et al. Appl Phys Express 2008;1:141201–2.
[2] Mitzi DB, Gunawan O, Todorov TK, Wang K, Guha S. Sol Energy Mater Sol Cells 2011;95:1421.
[3] Barkhouse DAR, Gunawan O, Gokmen T, Todorov TK, Mitzi DB. Prog Photovol 2012;20:6.
[4] Yan C, Huang C, Yang J, Liu F, Liu J, Lai Y, et al. Chem Commun 2012;48:2603.
[5] Gwak J, Jung S, Park SH, Ahn S, Cho A, Shin K, et al. Electron Mater Lett 2012;8:187;
Repins I, Beall C, Vora N, DeHart C, Kuciauskas D, Dippo P, et al. Sol Energy Mater Sol Cells 2012;101:154.
[6] Wibowo RA, Kim WS, Lee ES, Munir B, Kim KH. J Phys Chem Solids 2007;68:1908.
[7] Volobujeva O, Raudoja J, Mellikov E, Grossberg M, Bereznev S, Traksmaa R. J Phys Chem Solids 2009;70:567.
[8] Zhang XY, Ramasamy NZB,K, Wang YF, Lin BP, Gupta A. Chem Commun 2012;48:4956.
[9] Liu Y, Hao M, Yang J, Jiang L, Yan C, Huang C, et al. Mater Lett 2014;136:306.
[10] Cao M, Zhang BL, Huang J, Sun Y, Wang LJ, Shen Y. Chem Phys Lett 2014;604:15.
[11] Meng X, Deng H, He J, Zhu L, Sun L, Yang P, et al. Mater Lett 2014;117:1.
[12] Ramasamy K, Malik MA, O'Brien P. Chem Sci 2011;2:1170.
[13] Mahboob S, Malik SN, Haider N, Malik MA, O'Brien P. J Cryts Growth 2014;394:39.
[14] Novosad J, Necas M, Marek J, Veltsistas P, Papadimitriou C, Watanabe M, et al. Inorg Chim Acta 1999;290:256.
[15] Grossberg M, Krustok J, Raudoja J, Timmo K, Altosaar M, Raadik T. Thin Solid Films 2011;519:7403.
[16] Ahn S, Jung S, Gwak J, Cho A, Shin K, Yoon K, et al. Appl Phy Lett 2010;97:021905.
[17] Zhang M, Cao L, Sun Y, Shen Y, Wang L. Mater Lett 2013;93:111.
[18] Shibuya T, Goto Y, Kamihara Y, Matoba M, Yasuoka K, Burton LA, et al. Appl Phys Lett 2014;104:021912.

CHAPTER – VIII : PAPER - 5

"The AACVD of $Cu_2FeSn(S_xSe_{1-x})_4$: potential environmentally benign solar cell materials"

Punarja Kevin, Mohammad A. Malik, Paul O'Brien, *New J. chem.* 2015, **39**, 7046- 7053

NJC

PAPER

View Article Online
View Journal | View Issue

Cite this: *New J. Chem.*, 2015, **39**, 7046

The AACVD of $Cu_2FeSn(S_xSe_{1-x})_4$: potential environmentally benign solar cell materials†

Punarja Kevin,[a] M. Azad Malik*[b] and Paul O'Brien*[ab]

Received (in Montpellier, France) 11th May 2015,
Accepted 29th June 2015

DOI: 10.1039/c5nj01198a

www.rsc.org/njc

Films of $Cu_2FeSn(S_xSe_{1-x})_4$ (CFTSSe) have been deposited by aerosol assisted chemical vapour deposition (AACVD) using mixtures of $[Fe(S_2CNEt_2)_3]$, $[Bu_2Sn(S_2CNEt_2)_2]$ and $[Cu(S_2CNEt_2)_2]$ as precursors for the end member CFTS and of $[Cu(PPh_3)(Ph_2P(Se)NP(Se)Ph_2)]$, $[Sn(OAc)_4]$ and $[Fe(acac)_3]$ for CFTSe. CFTSSe thin films were deposited from $[Fe(S_2CNEt_2)_3]$, $[Bu_2Sn(S_2CNEt_2)_2]$ and $[Cu(PPh_3)(Ph_2P(Se)NP(Se)Ph_2)]$. The structures, morphologies, compositions, electrical and optical properties of these materials were studied by SEM, XRD, EDX, Raman spectroscopy, electron spectroscopy, UV-Vis measurement and using a four probe conductivity meter.

Introduction

Kesterites are the direct band gap semiconductor materials with an optical absorption coefficient larger than 10^4 cm^{-1}. Their band gaps can be tuned by controlling the ratio of S to Se in the composition to cover the visible and infrared regions of the solar spectrum (E_g: 1.0–1.5 eV).[1,2] Narrow band gap *p*-type semiconductors are of interest in hybrid dye sensitized solar cell (DSSC) technology.[3] CdTe and Cu_2InGaS_4 (CIGS) are the common *p*-type semiconductors, however due to the scarcity and cost of Te, In and Ga they are not suitable for mass commercial applications.[4] Cu_2FeSnS_4 (CFTS) and Cu_2ZnSnS_4 (CZTS) have been investigated as counter electrodes in DSSCs.[5–7] Dye-sensitized solar cells fabricated with the CFTS thin film as a photocathode in an iodine/iodide electrolyte showed a power conversion efficiency of 8.03%; CFTS could be a cheaper alternative to Pt in DSSCs and can also be used in conventional solar cells.[8]

The presence of Fe in place of Zn also improves the efficiency as Fe is more soluble in the lattice and hence increases the conductivity.[9,10] Copper–iron–tin sulfide/selenide (CFTS and CFTSe) materials are also based on earth abundant, environmentally-benign elements. They provide potentially cheaper and more cost-effective alternatives to the CIGS family. Their band gaps lie between 0.9 and 1.5 eV, making them suitable as absorbers in PV-cells.[11,12] The magnetic properties and phase characteristics of CFTS semiconductors have been studied in detail.[13]

There are various reports of the preparation and deposition of these materials. A solution based synthesis of CFTS was reported recently using metal salts and sulfur in hot oleylamine. The stannite phase of CFTS nanocrystals was obtained with particles of diameter between 15 and 25 nm.[14] Jiang *et al.* reported a non-aqueous strategy for the synthesis of hierarchical porous quaternary chalcogenide Cu_2FeSnS_4 as a hollow chain microsphere by a microwave method using $CuCl_2$, $FeCl_3$, $SnCl_4$ and thiourea in benzyl alcohol and octadecylamine.[15] Recently Guan *et al.* synthesized flower like CFTS nanoparticles by a microwave method using $Fe(NO_3)_3$, $SnCl_2$, $Cu(NO_3)_2$ and thiourea in ethylene glycol.[16] The structure of Cu_{2-x} Fe_{1-x} SnS_4 was investigated by the Rietveld method by Evastigneeva *et al.*[17] Zhang *et al.* have reported the phase controlled synthesis of wurtzitic CFTS nanoparticles with a band gap of 1.50 eV.[13] The performance of photovoltaic cells can be further improved by controlling the composition of the material and by the incorporation of extrinsic impurities such as Fe or Se in place of Zn and S, respectively, *e.g.* as in CZTS or CFTS.[18,19] Varying the Fe : Zn ratio in CFTS and the S : Se ratio in CZTS can tune both the band gap and the lattice parameter.[13,20,21]

AACVD is a simple technique which can operate at an ambient pressure by the nebulization of precursor molecules, followed by transport of the aerosol by an inert carrier gas such as argon or nitrogen, to a substrate surface heated in a furnace, where thermal decomposition of the precursor occurs. The method has been widely applied in the deposition of complex systems and has enabled the use of less volatile precursors than those used in more conventional CVD methods. AACVD has been successfully used in the deposition of a wide range of materials including metallic Ag,[22] ZnO,[23] Fe_2O_3,[24] $NiTiO_3$,[25] SnS,[26,27] CZTS,[28] $CuInSe_2$,[29] $CuGaSe_2$,[29] $CuIn_{0.7}Ga_{0.3}Se$,[29] MoS_2,[30] $(CH_3NH_3)PbBr_3$,[31] SnSe,[32] Cu_2SnSe_3,[32] and $BiVO_4$.[33] In this paper we report the deposition of CFTS, CFTSe and CFTSSe as thin films by AACVD.

[a] *School of Chemistry, The University of Manchester, Oxford Road, Manchester, M13 9PL, UK*
[b] *School of Materials, The University of Manchester, Oxford Road, Manchester, M13 9PL, UK. E-mail: azad.malik@manchester.ac.uk, paul.obrien@manchester.ac.uk*

† Electronic supplementary information (ESI) available: TGA, rietveld analysis and band gap measurement. See DOI: 10.1039/c5nj01198a

Experimental

Precursor synthesis and characterization

Preparation of the complexes was performed under an inert atmosphere of dry nitrogen using standard Schlenk techniques. All reagents were purchased from the Sigma-Aldrich chemical company and used as received. Solvents were distilled prior to use. Elemental analysis was performed at the micro-analytical laboratory of the University of Manchester. TGA measurements were carried out using a Seiko SSC/S200 model from 10 to 600 °C with a heating rate of 10 °C min^{-1} in nitrogen. Melting points were recorded on a Stuart melting point apparatus and uncorrected. Compounds $[Cu(S_2CNEt_2)_2]$ (**1**), $[Fe(S_2CNEt_2)_3]$ (**2**), $[^nBu_2Sn(S_2CNEt_2)_2]$ (**3**), and $[Cu(PPh_3)(Ph_2P(Se)NP(Se)Ph_2)]$ (**4**) were synthesized and recrystallized as reported in the literature.[34–36] Complexes $[Sn(OAc)_4]$ and $[Fe(acac)_3]$ were used as purchased.

Deposition of thin films

The thin films were deposited using AACVD. Glass slides (1 × 2 cm) were used as substrates for the deposition of thin films. The substrates were thoroughly cleaned and sonicated in acetone for 30 minutes to remove contamination. In a typical deposition experiment, a precursor complex (or a suitable combination of precursors) was dissolved in 20 mL THF in a two-neck 100 mL round-bottom flask. The round-bottom flask was kept in a water bath above the piezoelectric modulator (PIFCO ultrasonic humidifier model 1077). The aerosol droplets of the precursor thus generated were transferred into the hot wall zone of the reactor by a carrier gas (argon). The argon flow rate was controlled to be 180 sccm using a Platon flow gauge. Both the solvent and the precursor were evaporated, and the precursor vapor reached the heated substrate surface where thin films were deposited between 300 and 400 °C.

Deposition of CFTS thin films

In a typical deposition of CFTS $[Cu(S_2CNEt_2)_2]$ (2.80 mmol), $[Fe(S_2CNEt_2)_3]$ (1.40 mmol), and $[Bu_2Sn(S_2CNEt_2)_2]$ (1.40 mmol) were mixed in 20 mL of THF in a two-neck flask in argon (200 sccm). Depositions were carried out at 300, 350 and 400 °C on glass substrates for 50 minutes.

Deposition of CFTSSe thin films

Thin films of $Cu_2FeSn(S_xSe_{1-x})_4$ (CFTSSe) were deposited by using a mixture of $[Cu(PPh_3)(Ph_2PSe)_2N_2]$ (2.80 mmol), $[Fe(S_2CNEt_2)_3]$ (1.40 mmol), and $[(Bu)_2Sn(S_2CNEt_2)_2]$ (1.40 mmol) (2 : 1 : 1) dissolved in 20 mL THF at 300 and 350 °C for 50 minutes.

Deposition of CFTSe thin Films

The deposition of CFTSe was carried out by using a mixture containing a 2 : 1 : 1 molar ratio of $[Cu(PPh_3)(Ph_2P(Se)NP(Se)Ph_2)]$ (2.80 mmol) and $[Sn(OAc)_4]$ (1.40 mmol) $[Fe(acac)_3]$ (1.40 mmol) precursors in 20 mL THF at 300 to 400 °C for 50 min.

Characterisation of thin films

The *p*-XRD patterns were recorded on a Bruker D8 AXE diffractometer using Cu-Kα radiation. The samples were mounted flat and scanned between 10° and 120° in a step size of 0.05 with a varying count rate depending upon the sample. Rietveld analysis of the *p*-XRD patterns was carried out using the TOPAZ software. The morphology and the microstructure of thin films were investigated by using a Philips XL 30 FEGSEM and the film composition was studied by EDX analysis using a DX4 instrument at 20 KV with WD 10 mm. Raman spectra measurements were performed in a Renishaw 1000 Micro Raman system with an excitation wavelength of 520 nm and the measurement range was set from 100 to 700 cm^{-1}. UV-Vis measurement was carried out in a Perkin Elmer Lambda 1050 spectrophotometer (PSI), scanned across the range from 250 to 1000 nm. The electrical resistance was measured using a Jandel four probe conductivity meter at room temperature using 1 μA current.

Results and discussion

The molecular precursors used in this study are crystalline solids, soluble in most organic solvents and are stable at room temperature for periods of months. The stoichiometries of the deposited films were controlled by varying the molar ratio of the precursors. The properties of the deposited materials were investigated by structural and optical techniques.

Thermal decomposition of precursors

Thermal decomposition studies were carried from 10 to 600 °C, at a heating rate of 10 °C min^{-1} in nitrogen. All compounds except **3** show rapid single step decompositions between 250 and 350 °C (ESI,† Fig. S1). The residual mass of the $[Fe(S_2CNEt_2)_3]$ complex was found to be about 18% which is close to the calculated percentage of FeS (17.5%). The $[Bu_2Sn(S_2CNEt_2)_2]$ complex decomposed slightly faster than the other complexes and the residual mass was found to be ∼34% which agrees with the calculated residual mass of SnS_2. $[Cu(S_2CNEt_2)_2]$ gave ∼9–10% residue which is found to be half or less than half of the mass of the expected metal chalcogenides; Cu_2S (27%). TGA of $[Cu(PPh_3)(Ph_2P(Se)NP(Se)Ph_2)]$ showed single step decomposition between 250 and 320 °C with a final residue of ∼10% which was less than the expected value for Cu_2Se (16%).

The TGA studies help us to understand the decomposition patterns of complexes and also give us the idea of possible deposition temperatures to be used. Compound $[Cu(S_2CNEt_2)_2]$ (**1**) has a midpoint for decomposition at *ca.* 350 °C, which is similar to that for $[Fe(S_2CNEt_2)_3]$ (**2**) and $[^nBu_2Sn(S_2CNEt_2)_2]$ (**3**) has a midpoint for decomposition at 310 °C. The selenium precursor $[Cu(PPh_3)(Ph_2P(Se)NP(Se)Ph_2)]$ (**4**) has a lower midpoint for decomposition at 300 °C. The first two thiocarbamato compounds are hence reasonably well-matched in terms of thermal stability. The selenium precursor (**4**) has a lower decomposition temperature, but also decomposes in clear two stages, the first presumably being the loss of the adduct ligand, however complete decomposition is achieved at 325 °C; the other copper precursor fully decomposed only at *ca.* 350 °C. The best stoichiometries are obtained, in all cases, at 350 °C, which is probably a reflection of the varying thermal stabilities of the precursors.

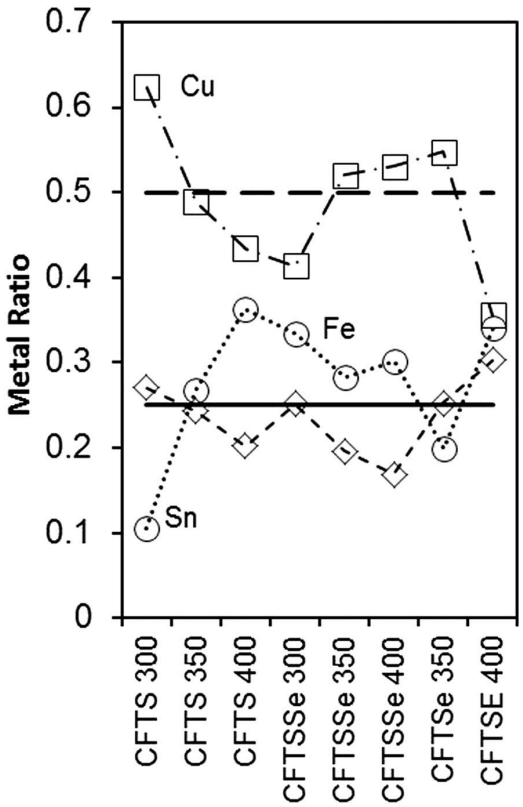

Fig. 1 Correlation of the feed rate (horizontal lines are at Cu (0.5) and Fe or Sn (0.25)) with measured metal mole fractions by EDX plotted for each element on the *y*-axis.

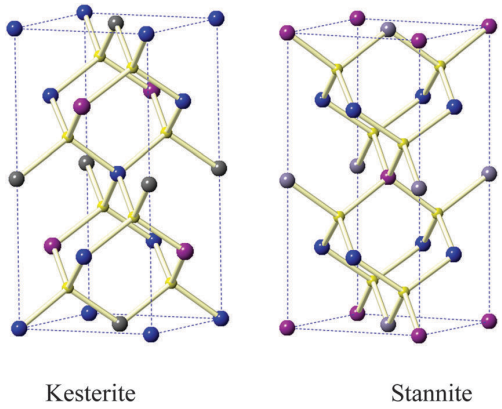

Fig. 2 Structural models of the kesteritic and stannitic forms of $Cu_2(Fe_{1-x}Zn_x)SnS$ (after Hall[36]); copper, blue; sulfur, yellow; tin, grey and iron/zinc, purple.

Structural studies of thin films

These films were deposited from various mixtures of precursors at temperatures between 300 and 400 °C. In all cases the metal precursor ratios were set to stoichiometric ratios for the phases *i.e.* 2 : 1 : 1 [Cu] : [Fe] : [Sn], with the precursors being varied in nature to control the selenium content. The compositions of the films obtained from EDX measurements using an electron microscope are summarized in Fig. 1 and Table 1. Iron incorporation is consistently close to the stoichiometric ratio calculated from the feed rate. There have been many structural studies of the various materials formed when iron is substituted into kesterite (CZTS). The parent structures are shown in Fig. 2. Hall *et al.*[36] carried out a single crystal X-ray study of the changes in the structure as the ratio of zinc to iron was varied and found that kesterite is pseudo-cubic with 2a ≅ c, and that the stannites are more pronounced in their tetragonal nature. Compositions of $Cu_{1.98}Fe_{0.29}Zn_{0.72}Cd_{0.01}Sn_{0.99}S_4$ kesteritic form and $Cu_2Fe_{0.81}Zn_{0.18}Cd_{0.08}SnS_4$ stannitic form, from naturally occurring samples, were studied.

More recently Bonazzi *et al.*[37] have studied variation in the system in more detail finding that the pseudo-cubic form dominates in zinc rich compositions $x > 0.5$. The samples we have studied are ferroan with varying compositions of sulfur or selenium (*i.e.* $x = 0$). However, the powder patterns we have obtained (Fig. 1) are dominated by the cubic reflections, providing the potential for a simplified analysis of the data for comparative purposes *vide infra*. All Rietveld fits were consistent with the older pseudo cubic reports. There have been other studies of such systems[38] and the structure of $Cu_2FeZnSnSe$ has been reported to be kesteritic.[39]

The deposition of CFTS films at 300, 350 and 400 °C produced thin black, adherent specular films (Scheme 1). The *p*-XRD patterns

Table 1 Consolidated *p*-XRD and EDX analysis of CFTS, CFTSe and CFTSSe thin films deposited at different temperatures

Film	Temp. (°C)	Stoichiometry	Rietveld[a] a	Cubic[b] a	Literature a	Literature c	(ICCD)[ref.]
CFTS	300	$Cu_{2.1}Fe_{0.92}Sn_1S_{3.3}$	5.4328(2)	5.46(2)	5.4495(6)[c]	10.726(2)[c]	Ref. 19
CFTS	350	$Cu_{1.8}Fe_{0.90}Sn_1S_{2.80}$	5.4261(6)	5.45(1)	5.4495(6)[c]	10.726(2)[c]	Ref. 19
CFTS	400	$Cu_{1.2}Fe_{0.55}Sn_1S_{1.8}$	5.414(4)	5.402(1)	5.4495(6)[c]	10.726(2)[c]	Ref. 19
CFTSSe	300	$Cu_{1.2}Fe_{0.75}Sn1S_{0.14}Se_{3.4}$	—	5.487(7)	—	—	—
CFTSSe	350	$Cu_{1.8}Fe_{0.69}Sn_1S_{1.8}Se_{1.5}$	—	5.506(1)	—	—	—
CFTSSe	400	$Cu_{1.7}Fe_{0.56}Sn_1S_{1.8}Se_{1.02}$	—	5.510(5)	—	—	—
CFTSe	350	$Cu_{2.74}Fe_{1.26}Sn_1Se_{5.9}$	5.714(0)	5.663(3)	5.7200[d]	11.286[d]	00-052-0098[21]
CFTSe	400	$Cu_{1.0}Fe_{0.88}Sn_{1.0}Se_{2.26}$	—	5.64(6)	5.7200[d]	11.286[d]	00-052-0098[21]

[a] For details see sup publication. [b] From peak position and $a^2 = d^2(h^2 + k^2 + l^2)$. [c] For cubic ICDD 00-53-0575 gives $a = 5.4233$ Å. [d] For cubic analysis ICDD 00-027-0167 gives $a = 5.685$ Å.

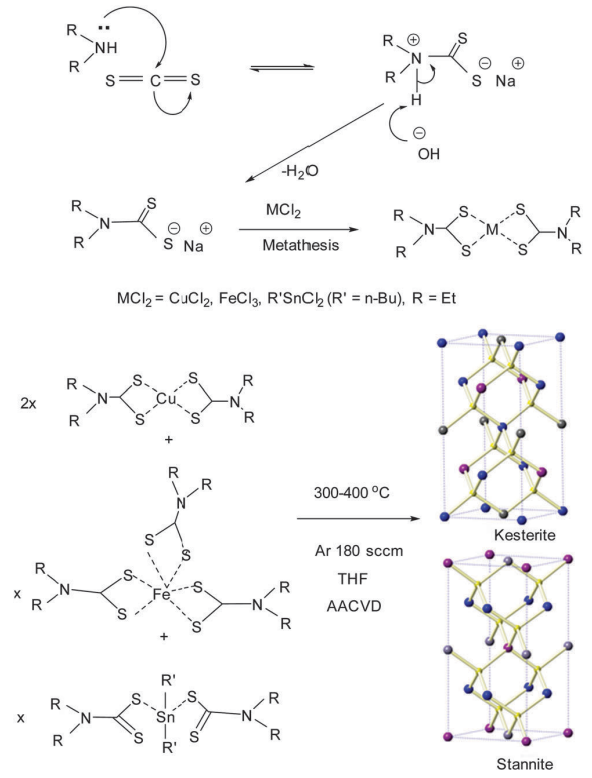

Scheme 1 Synthesis and deposition of thin films by AACVD.

of all these films correspond to pseudo-cubic CFTS (ICDD 00-053-0575 a = 5.4233). The main peaks appeared at 28.49° (111), 33.0° (002), 47.4° (022), 56.2° (113), and 69.2° (400) (Fig. 3). Some additional reflections were seen most notably in the pattern of films deposited at 400 °C, which may be due to Mawsonite (ICDD: 01-086-2274). Rietveld analysis of the films deposited at 350 and 400 °C (R_{wp} = 3.11 and 4.61) is detailed in the ESI† (Fig. S2(a) and (b), Tables S1 and S2). Rietveld refinement gave cubic fits with a = 5.4261(6) Å and 5.414(4) Å for the CFTS films deposited at 350 and 400 °C (Table 1).

In order to provide a consistent comparison of the films d spacings for each sample were also calculated from the principal peaks with the cubic indices. These are in good agreement for the known phases and the results of Rietveld refinements are all summarized in Table 1. The CFTSSe thin films deposited using an equimolar ratio of selenium and sulfur precursors at 300 and 350 °C again gave thin black, adherent films. The p-XRD patterns of CFTSSe showed clear shifts from that of CFTS (Fig. 3). There seems to be a trace of an impurity in the film deposited at 300 °C and Rietveld analysis gave no matching with any of the known parent CFTS and CFTSe phases.

No significant deposition of CFTSe occurred at 300 °C whereas uniform brownish and dark brown films were obtained at 350 and 400 °C. The p-XRD patterns of films deposited at 350 °C (Fig. 3) matched with standard cubic patterns (ICDD: 00-027-0167, a = 5.6850 Å). The peaks are at values 27.16 (111), 45.07 (220), 53.41 (311), 65.65 (400) and 72.41 (316). Rietveld analysis is given in the ESI† (Fig. S2(c) and Table S3) with a = 5.713(0) Å and Rwp = 2.56. The p-XRD patterns of the films deposited at 400 °C showed only cubic CFTSe peaks however, a slight shift in peak positions was observed.

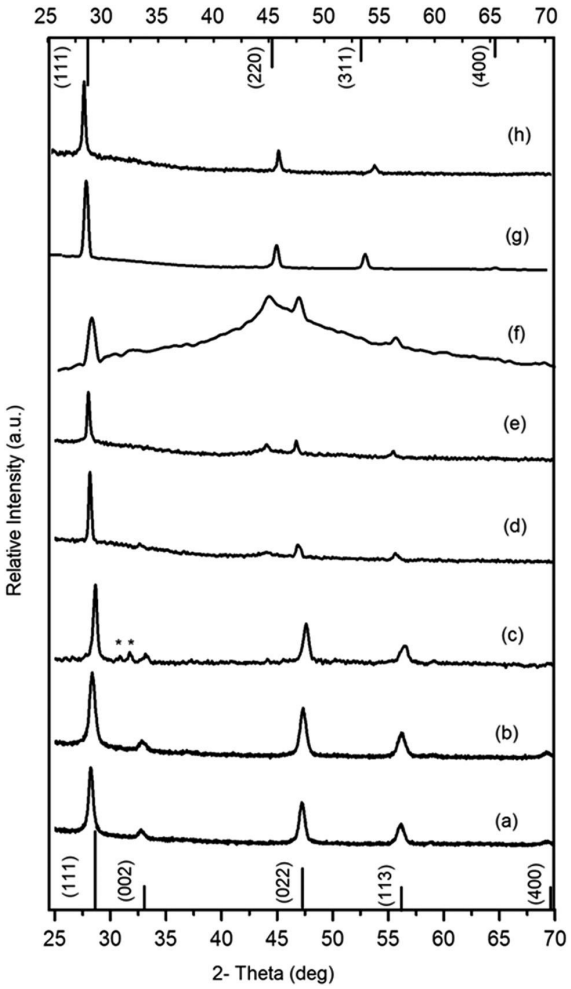

Fig. 3 p-XRD patterns of CFTS and CFTSe films deposited at 300, 350 and 400 °C (a)–(c) and (f)–(h), respectively, and $Cu_2FeSn(S_xSe_{1-x})_4$ (CFTSSe) films at 350 and 400 °C (d) and (e); the standard patterns for CFTS (bottom), CFTSe (top). (*) mark shows peaks from the Mawsonite phase of CFTS.

Morphology and compositional studies of thin films

The morphology of the CFTS thin films deposited at the three different temperatures is shown in Fig. 4(a)–(c).

The SEM images of the films deposited at 300 °C consist of irregular flakes of 1–2 μm which change to thicker hexagonal plates of about the same size at 350 °C, and further change to irregularly shaped smaller crystallites *ca.* 0.5–1 μm at 400 °C. The thickness of the films was ~1 μm. Elemental mapping of films deposited at 300 and 400 °C confirmed uniform composition throughout the selected area (Fig. 5(a) and (b)). The morphology of

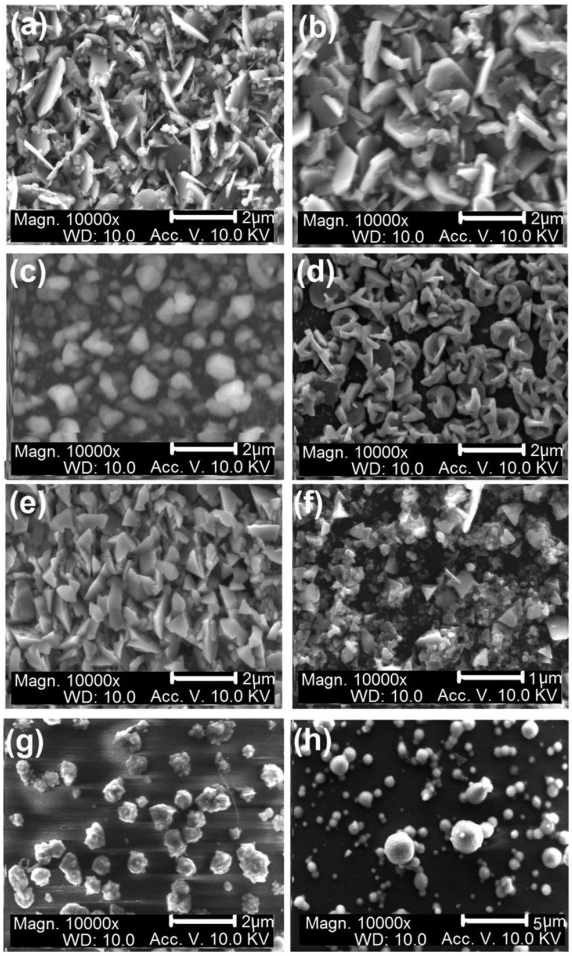

Fig. 4 (a)–(c) SEM images of CFTS thin films deposited at 300, 350 and 400 °C, respectively. (d)–(f) The SEM images of $Cu_2FeSn(S_xSe_{1-x})_4$ (CFTSSe) thin films deposited at 300, 350 and 400 °C. (g) and (h) The SEM images of CFTSe thin films deposited at 350 °C and 400 °C.

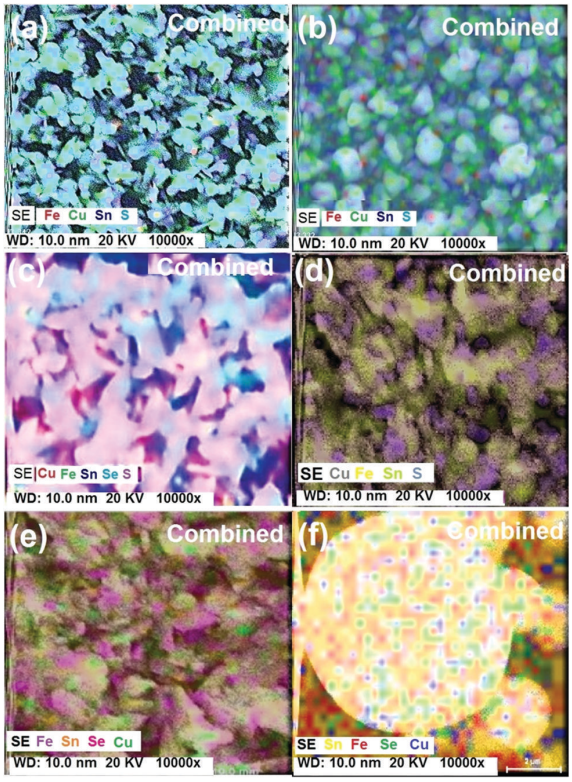

Fig. 5 Elemental mapping images of (a) and (b) the CFTS thin films deposited at 300 and 400 °C, (c) and (d) CFTSSe thin films deposited at 350 and 400 °C, and (e) and (f) CFTSe thin films deposited at 350 and 400 °C.

CFTSSe films deposited at 300 °C to 400 °C is shown in Fig. 4(d)–(f). The SEM images of particles of the films deposited at 300 °C consist of flower like clusters of irregular plates with an average size range of ~1.5 μm which changed to thicker irregular crystallites at 350 °C and then to large and small irregular flakes and clusters with size less than 1.0 μm. Selected area elemental map images of the films deposited at 350 and 400 °C showed uniform distribution of constituents over the entire area of the films (Fig. 5(c) and (d)).

SEM images of CFTSe films obtained at 350 °C showed flower like irregular crystallites of less than 1 μm in size (Fig. 4(g) and (h)). The CFTSe films deposited at 400 °C showed larger and smaller irregular and regular spherical morphologies. Selected area elemental map images are shown in Fig. 6.

The CFTS thin films deposited at 350 °C were scratched and the residue ground in hexane and used for TEM studies. The TEM image, elemental mapping and selected area electron diffraction (SAED) pattern are shown in Fig. 6. The TEM image shows irregular plate like crystallites of different sizes.

The SAED pattern showed three diffraction rings corresponding to (111), (002) and (004) planes of the cubic CFTS. The TEM-EDX and elemental mapping of the CFTS thin films over a 50 nm area of the material showed uniform composition of elements over the entire area. The weight percentage of the elements was found to be 22.9% Cu, 17.4% Sn, 12.1% Fe and 47.2% S which gave a stoichiometry as $Cu_{1.9}Fe_{1.0}Sn_{1.4}S_{3.9}$ which is close to that observed by SEM-EDX.

Raman spectra of CFTS films deposited at 300, 350 and 400 °C showed weak peaks at 218 and 285 cm^{-1} and a strong peak at 321 cm^{-1} which agree with the reported values for CFTS.[9] No peaks were observed at 282 cm^{-1} (FeS), or 190 or 314 cm^{-1} (SnS) confirming the absence of these impurities (Fig. 7).[12,21,25,26]

The Raman spectra of the CFTSSe thin films deposited at 300 °C gave a broad intense peak at about 210 cm^{-1} and a minor peak at around 290 cm^{-1}. The peak at 209 cm^{-1} was attributed to the A_1 modes of CFTSe and the peak at around 295 cm^{-1} was attributed to that of CFTS materials. The Raman spectra of the CFTSSe films deposited at 350 °C showed a peak at around 209 cm^{-1} and a less intensity peak at around 320 cm^{-1} which correspond to the A_1 Raman modes of CFTSe (209 cm^{-1})

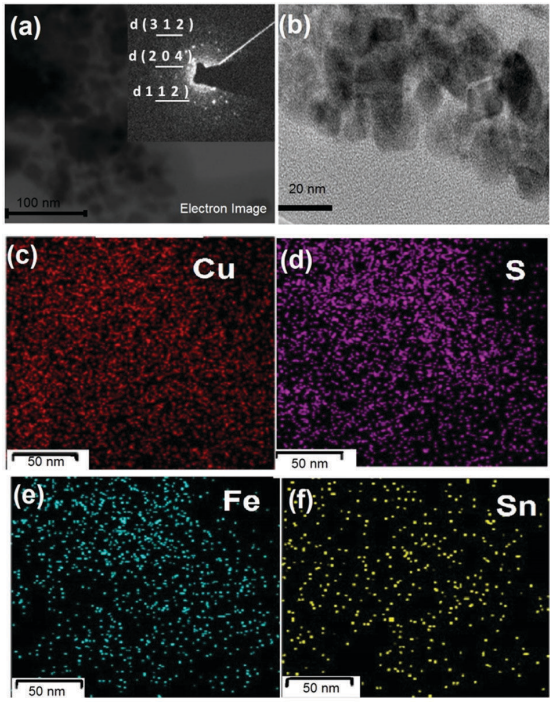

Fig. 6 (a) and (b) The HRTEM images of Cu_2FeSnS_4 thin films deposited at 350 °C, the inset in (a) shows the SAED pattern of CFTS. (c)–(f) Elemental mapping images.

and CFTS (325 cm^{-1}), and no peaks at 236 and 251 cm^{-1} were observed showing the absence of Cu_2SnSe_3 phases (Fig. 7).[32,40]

The Raman peaks for the CFTSSe films deposited at 400 °C showed an almost similar peak position for the sulfide and Se A_1 modes. The selenide peaks were less intense as compared to sulfide peaks for the films deposited at 350 °C. The Raman spectra results agree well with the EDX and *p*-XRD analysis in terms of the stoichiometric ratio of S to Se in the material at deposition temperatures of 300 and 350 °C. Raman spectra of the CFTSe films obtained at 350 °C showed a broad strong peak at ~209 cm^{-1} and a less intense peak at ~270 cm^{-1} (Fig. 3) which are in agreement with the reported peaks for CFTSe (209, 270 cm^{-1}).[40,41]

Optical and electrical properties of CFTS, CFTSe and CFTSSe thin films

The band gap of CFTS thin films deposited at 350 °C, from Tauc plots, was ~1.6 eV, close to those reported previously.[1–4,30–34] The CFTSe films deposited at 350 °C gave a value of 1.05 eV. The band gap value for the CFTSSe films deposited at 350 °C was found to be ~1.26 eV which lies between those of the CFTS (1.6 eV) and CFTSe (1.1 eV) films (ESI,† Fig. S3).[11–14,20,41–45] Band gaps values reported in the literature are 1.50 eV for stannite CFTS and 1.1 eV for CFTSe.[41–45] These measurements are in reasonable agreement with other estimates of composition.

The sheet resistance of the CFTS films deposited at 350 °C (at room temperature) was found to be 2.13 KΩ cm^{-2} which is higher than that reported previously for CZTS and CFTS.[40–46] The room temperature sheet resistance of CFTSe films was 1.48 KΩ cm^{-2} lower than that of CZTS materials.[44–46] The resistance of the CFTSSe films deposited at 350 °C and room temperature was 1.89 KΩ cm^{-2} which is significantly lower than that of CFTS films deposited at the same temperature.[40–44]

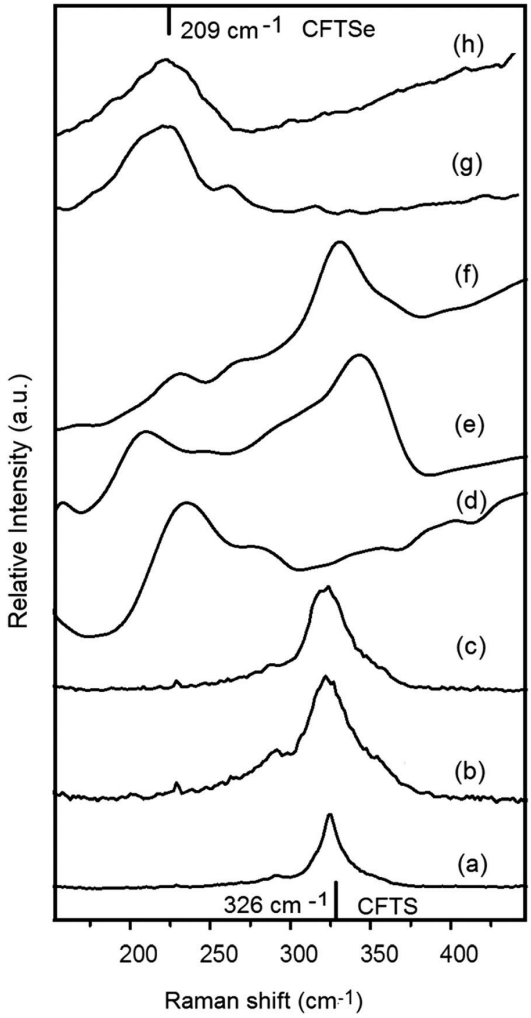

Fig. 7 (a)–(c) Raman spectra of CFTS thin films deposited at 300, 350, and 400 °C. (d)–(f), $Cu_2FeSn(S_xSe_{1-x})_4$ (CFTSSe) deposited at 350 to 400 °C. (g) and (h) CFTSe deposited at 300 and 350 °C.

Conclusion

Thin films of Cu_2FeSnS_4, $Cu_2FeSnSe_4$, and $Cu_2FeSn(S_xSe_{1-x})_4$ have been deposited by AACVD using mixtures of molecular precursors. The best films of each type, in terms of the stoichiometry structure and properties, were obtained, at 350 °C, for each composition. These results show that mixtures of these precursors provide a potentially useful route into this complex series of quaternary materials. The sheet resistance of

Cu_2FeSnS_4 (2.13 KΩ cm^{-2}), $Cu_2FeSnSe_4$ (1.48 KΩ cm^{-2}) and $Cu_2FeSn(S_xSe_{1-x})_4$ (1.89 KΩ cm^{-2}) and band gap values (1.1–1.6 eV) of all these materials are ideal for the solar cells. Further studies on thermal resistance, photovoltaic and magnetic properties of thin films are in progress.

Abbreviations

AACVD Aerosol assisted chemical vapour deposition
BG Band gap

Acknowledgements

PK is thankful to Gary Harrison for XRD and School of Chemistry and The University of Manchester for funding. We thank EPSRC for funding of instruments under grant number EP/K039547/1 for characterization of the compounds.

References

1 S. Chen, X. G. Gong, A. Walsh and S. H. Wei, *Appl. Phys. Lett.*, 2009, **94**, 041903.
2 H. Katagiri, K. Jimbo, W. S. Maw, K. Oishi, M. Yamazaki, H. Araki and A. Takeuchi, *Thin Solid Films*, 2009, **517**, 2455.
3 P. Dai, G. Zhang, Y. Chen, H. Jiang, Z. Feng, Z. Lin and J. Zhan, *Chem. Commun.*, 2012, **48**, 3006–3008.
4 S. S. Mali, P. S. Patil and C. K. Hong, *ACS Appl. Mater. Interfaces*, 2014, **6**, 1688–1696.
5 J.-Y. Park, J. H. Noh, T. N. Mandal, S. H. Im, Y. Jun and S. I. Seok, *RSC Adv.*, 2013, **3**, 24918–24921.
6 H. K. Mulmudi, S. K. Batabyal, M. Rao, R. R. Prabhakar, N. Mathews, Y. M. Lam and S. G Mhaisalkar, *Phys. Chem. Chem. Phys.*, 2011, **13**, 19307–19309.
7 Y.-C. Wang, D.-Y. Wang, Y.-T. Jiang, H.-A. Chen, C.-C. Chen, K.-C. Ho, H.-L. Chou and C.-W. Chen, *Angew. Chem., Int. Ed.*, 2013, **52**, 6694–6698.
8 R. R. Prabhakar, N. H. Loc, M. H. Kumar, P. P. Boix, S. Juan, R. A. John, S. K. Batabyal and L. H. Wong, *ACS Appl. Mater. Interfaces*, 2014, **6**, 17661–17667.
9 Q. Guo, G. M. Ford, W. C. Yang, B. C. Walker, E. A. Stach, H. W. Hillhouse and R. Agrawal, *J. Am. Chem. Soc.*, 2010, **132**, 17384–17386.
10 H. Katagiri, K. Jimbo, S. Yamada, T. Kamimura, W. S. Maw, T. Fukano, T. Ito and T. Motohiro, *Appl. Phys. Express*, 2008, **1**, 041201.
11 F.-J. Fan, Y.-X. Wang, X.-J. Liu, L. Wu and S.-H. Yu, *Adv. Mater.*, 2012, **24**, 6158.
12 X. Zhang, N. Bao, K. Ramasamy, Y.-H. A. Wang, Y. Wang, B. Lin and A. Gupta, *Chem. Commun.*, 2012, **48**, 4956; L. Chopra, P. D. Paulson and V. Dutta, *Prog. Photovolt.: Res. Appl.*, 2004, **12**, 69–92.
13 C. Rincón, M. Quintero, E. Moreno, C. Power, E. Quintero, A. Henao, M. A. J. Macías, G. E. Delgado, R. Tovar and M. Morocoima, *Solid State Commun.*, 2011, **151**, 947.
14 L. Li, X. Liu, J. Huang, M. Cao, S. Chen, Y. Shen and L. Wang, *Mater. Chem. Phys.*, 2012, **133**, 688.
15 L. Ai and J. Jiang, *J. Mater. Chem.*, 2012, **22**, 20586.
16 H. Guan, Y. F. Shi, B. X. Jiao, X. Wang and F. L. Yu, *Chalcogenide Lett.*, 2014, **11**, 9.
17 T. L. Evastigneeva and Y. K. Kabalov, *Crystallogr. Rep.*, 2001, **46**, 368.
18 S. Chen, A. Walsh, J.-H. Yang, X. G. Gong, L. Sun, P.-X. Yang, J.-H. Chu and S.-H. Wei, *Phys. Rev. B: Condens. Matter Mater. Phys.*, 2011, **83**, 125201.
19 R. Haight, A. Barkhouse, O. Gunawan, B. Shin, M. Copel, M. Hopstaken and D. B. Mitzi, *Appl. Phys. Lett.*, 2011, **98**, 253502.
20 G. Marcano, C. Rincón, S. A. López, G. Sánchez Pérez, J. L. Herrera-Pérez, J. G. Mendoza-Alvarez and P. Rodríguez, *Solid State Commun.*, 2011, **151**, 84–86.
21 D. B. Khadka and J. Kim, *J. Phys. Chem. C*, 2014, **118**, 14227.
22 M. N. McCain, S. Schneider, M. R. Salata and T. J. Marks, *Inorg. Chem.*, 2008, **47**, 2534–2542.
23 M. R. Waugh, G. Hyett and I. P. Parkin, *Chem. Vap. Deposition*, 2008, **14**, 366–372.
24 K. G. U. Wijayantha, S. Saremi-Yarahmadia and L. M. Peter, *Phys. Chem. Chem. Phys.*, 2011, **13**, 5264–5270.
25 A. A. Tahir, M. Mazhar, M. Hamid, K. G. U. Wijayantha and K. C. Molloy, *Dalton Trans.*, 2009, 3674–3680.
26 K. Ramasamy, V. L. Kuznetsov, K. Gopal, M. A. Malik, J. Raftery, P. Edwards and P. O'Brien, *Chem. Mater.*, 2013, **25**, 266–276.
27 P. Kevin, D. J. Lewis, J. Raftery, M. A. Malik and P. O'Brien, *J. Cryst. Growth*, 2015, **415**, 93–99.
28 K. Ramasamy, M. A. Malik and P. O'Brien, *Chem. Sci.*, 2011, **2**, 1170.
29 S. Mahboob, S. N. Malik, N. Haider, C. Q. Nguyen, M. A. Malik and P. O'Brien, *J. Cryst. Growth*, 2014, **394**, 39.
30 A. Adeogun, M. Afzaal and P. O'Brien, *Chem. Vap. Deposition*, 2006, **12**, 597–599.
31 D. J. Lewis and P. O'Brien, *Chem. Commun.*, 2014, **50**, 6319.
32 P. Kevin, S. N. Malik, M. A. Malik and P. O'Brien, *Chem. Commun.*, 2014, **50**, 14328–14330.
33 P. Brack, J. S. Sagu, T. A. N. Peiris, A. McInnes, M. Senili, K. G. U. Wijayantha, F. Marken and E. Selli, *Chem. Vap. Deposition*, 2015, **21**, 41–45.
34 M. Akhtar, J. Akhter, M. A. Malik, P. O'Brien, P. F. Tuna, J. Raftery and M. Helliwell, *J. Mater. Chem.*, 2011, **21**, 9737–9745.
35 M. B. Hursthouse, M. A. Malik, M. Motevalli and P. O'Brien, *J. Mater. Chem.*, 1992, **2**, 949.
36 S. R. Hall, J. T. Szymanski and J. M. Stewart, *Can. Mineral.*, 1978, **16**, 131–137.
37 P. Bonazzi, L. Bindi, G. P. Bernardini and S. Menchetti, *Can. Mineral.*, 2003, **41**, 639–647.
38 S. A. Kissin and D. R. Owens, *Can. Mineral.*, 1979, **17**, 125–135.
39 R. Infante Delga do and L. Rivera, *Mater. Lett.*, 1997, **33**, 67–70.

40 T. Shibuya, Y. Goto, Y. Kamihara, M. Matoba, K. Yasuoka, L. A. Burton and A. Walsh, *Appl. Phys. Lett.*, 2014, **104**, 02192.
41 M. Z. Cao, B. L. Zhang, J. Huang, Y. Sun, L. J. Wang and Y. Shen, *Chem. Phys. Lett.*, 2014, **604**, 15–21.
42 X. Meng, H. Deng, J. He, L. Zhu, L. Sun, P. Yang and J. Chu, *Mater. Lett.*, 2014, **117**, 1–3.
43 J.-Y. Park, J. H. Noh, T. N. Mandal, S. H. Iam, Y. Jun and S. I. Seok, *RSC Adv.*, 2013, **3**, 24918–24921.
44 X. Yu, A. Ren, F. Wang, C. Wang, J. Zhang, W. Wang, L. Wu, W. Li, G. Zeng and L. Feng, *Int. J. Photoenergy*, 2014, **6**, 846940.
45 E. M. Mkawi, K. Ibrahim, M. K. M. Ali and A. S. Mohamed, *Int. J. Electrochem. Sci.*, 2013, **8**, 359–368.
46 H. Katagiri, K. Saitoh, T. Washio, H. Shinohara, T. Kurumadani and S. Miyajima, *Sol. Energy Mater. Sol. Cells*, 2001, **65**, 141–148.

Supporting Information

The AACVD of $Cu_2FeSn(S_xSe_{1-x})_4$: A Family of Environmentally Benign Solar Cells Materials

Punarja Kevin,[a] Azad Malik,[b] Paul O'Brien*[a,b]

Punarja Kevin,[a] M. Azad Malik,[b] Paul O'Brien*[a,b]

[a]School of Chemistry, The University of Manchester, Oxford Road M13 9PL
[b]School of Materials, The University of Manchester, Oxford Road, M13 9PL

Synthesis of Precursors

Complexes $[Cu(S_2CNEt_2)_2]$,[1] (**1**) $[Fe(S_2CNEt_2)_3]$[2] (**2**) and $[Bu_2Sn(S_2CNEt_2)_2]$[3] (**3**) were synthesised using the methods reported previously. Thermal decomposition studies were done by thermogravimetric analysis (TGA) and the results were matching with the reported values (Figure S1).All complexes decompose at same range of temperature.

Synthesis of $[Cu(S_2CNEt_2)_2]$ (**1**) **:** Sodium salt of diethyldithiocarbamate (3 g, 1.3 mmol) was dissoloved in 50 mL of methanol in double neck 250 mL RB. Slow addition of methanolic solution of $Cu(NO_3)2$ (1.24 g, 0.65 mmol) gave black precipitate. Precipitate formed was isolated by filtration. Recrystallisation was performed using chloroform. Yield: 4.78g (73%), Mpt: 201 °C, IR (vmax/cm-1): 2979(w), 2868(w), 1501(s), 1434(m), 1270(s), 1205(m) and 1144(m), Elemental analysis: Calc. for $C_{10}H_{20}N_2S_4Cu$: C, 33.4; H, 5.5; N, 7.7; S, 35.6; Cu, 17.6 %. Found: C, 33.2; H, 5.3; N, 7.3; S, 35.2; Cu, 17.2 %.

Synthesis of $[Fe(S_2CNEt_2)_3]$ (**2**) : This complex was synthesised by method described for complex (1) using zinc acetate (1.46 g, 0.65 mmol), The crude product was obtained as white powder. Recrystallisation from chloroform, yielded colourless crystals. yield 4.81 g (79%), Mpt: 198-201 °C, IR (vmax/cm-1): 2967(w), 2938(w), 1478(s), 1429(m), 1352(w), 1296(w), 1296(m), 1270(s), 1050(s) and 950(s), Elemental analysis: Calc. for $C_{15}H_{30}N_3S_6Fe$: C, 35.98; H, 6.04 N, 8.39; S, 38.43; Fe, 11.15 %. Found: C, 35.7; H, 6.3; N, 8.4; S, 37.82; Fe, 11.0 %.

Synthesis of $[Bu_2Sn(S_2CNEt_2)_2]$ (**3**): Complex 3 was synthesised by method described for complex (1) using di-n-butyltin dichloride (2.02 g. 0.65 mmol). The methanol was removed by vacuum distillation. Recrystallization using ethanol-chloroform yielded colourless plates of crystals. White solid, yield 5.5 g, (67%), Mpt: 57 °C, IR (vmax/cm-1): 2953(w), 2924(w), 1483(s), 1456(m), 1417(s), 1353(m), 1298(m) 1253(s), 1205(s) and 1138(s), Elemental analysis: Calc. for $C_{18}H_{38}N_2S_4Sn$: C, 40.8; H, 7.2; N, 5.3; S, 24.2; Sn, 22.4 %. Found: C, 39.9; H, 7.5; N, 5.1; S, 22.8; Sn, 21.4 %.were synthesised using the method reported previously.

Synthesis of $Cu(PPh_3)[Ph_2P(Se)NP(Se)Ph_2]$(**4**): Step one involved the synthesis of potassium diphenylphosphinodiselenoate by reaction of diphenylphosphine, elemental selenium and potassium hydroxide as reported by Gusarova et al.[4] In step a 150 mL methanol solution of 1.2 g (2.6 mmol)

$K[Ph_2P(Se)P(Se)Ph_2]$ was mixed with a solution of $Cu(PPh_3)_2NO_3$ (1.4 g, 2,1 mmol) in 100 mL chloroform. Stirred for 30 min and the precipitate was filtered , filtrate on rotary evaporation gave a pinkish powder. The product was recrystallized from CH_2Cl_2. Yield: 64% $Cu(PPh_3)[Ph_2P(Se)NP(Se)Ph_2]$; m. p; 221-223 °C. Elemental Analysis : Calc. for $C_{42}H_{35}CuNP_3Se_2$: C, 58.1; H, 4.1; N, 1.6% and Found C, 57.87; H, 3.92; N, 1.48. 31P NMR (400 MHz, $CDCl_3$, rel. to 85% H_3PO_4): δ = 26.14 ppm with two P–Se satelites, 1JP–Se-576 Hz. FTIR: 3050 cm^{-1}(n C- H), 1165 cm^{-1} (n -P2N),1100, 755 cm^{-1} (ns-P2N), 690, 545 (n-PSe), 519, 505. Mass spec: m/z : 869 ,670, 460, 341. TGA showed single step decomposition between 250 to 320 °C with residue ~ 15% which is closer to the expected CuSe (16%) (Figure S1)

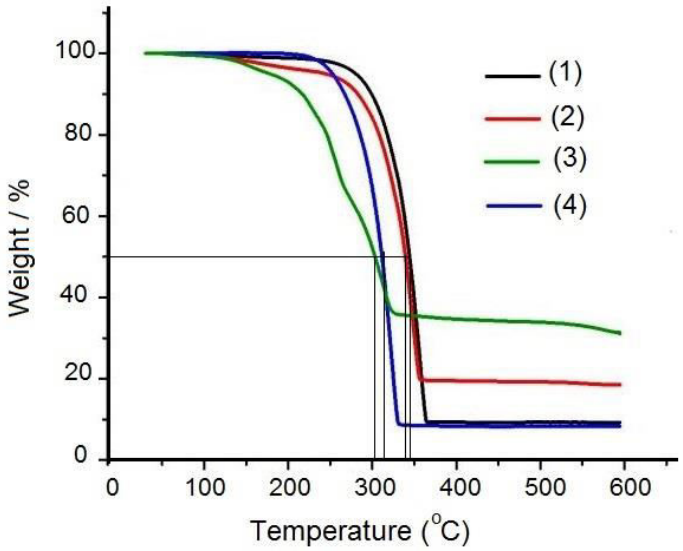

Figure S1: TGA analysis of precursors (**1-4**). Black vertical lines represent 50 % decomposition temperatures 349, 345,302 and 310 °C for precurosros (1) to (4) respectively. Thermal decomposition studies were carried from 10-600 °C, at a heating rate 10 °C min^{-1} under nitrogen.

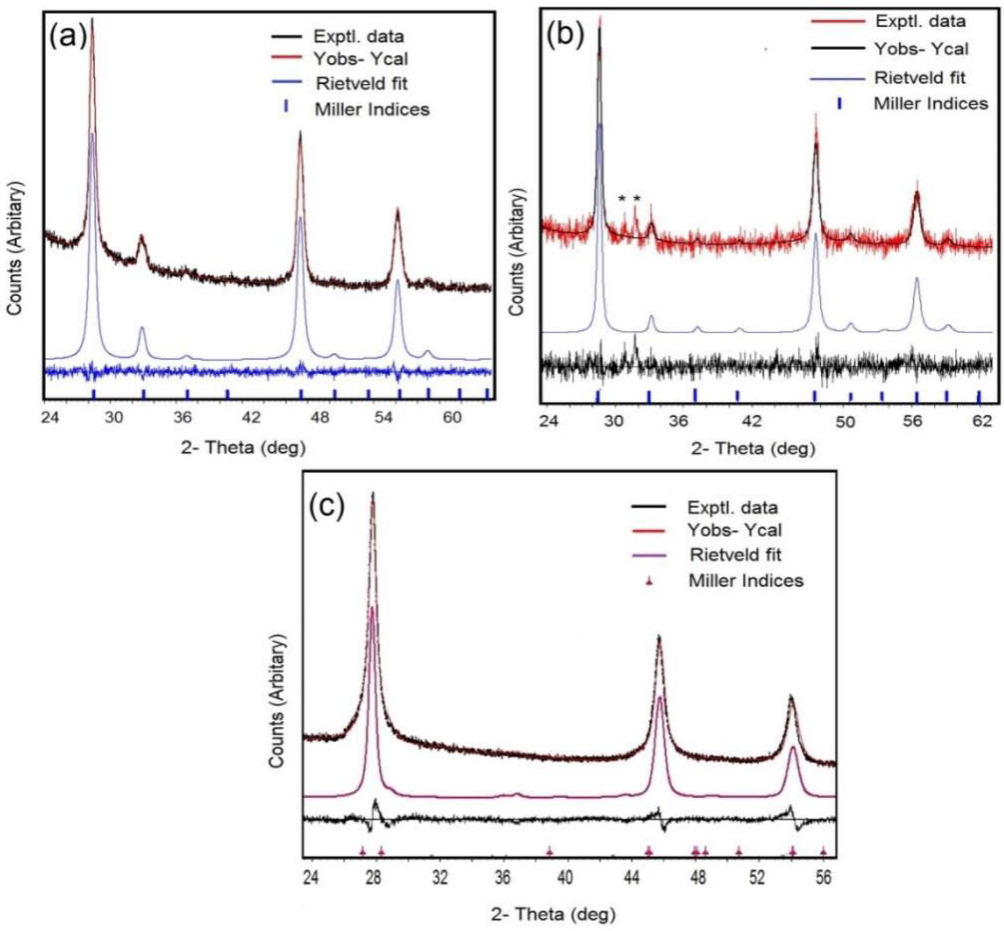

Figure S2: (a) and (b) are the Rietveld refinement of CFTS films deposited at 350 and 400 °C. (c) is the Rietveld refinement of CFTSe thin films deposited at 350 °C.

Table S1: Rietveld analysis of CFTS thin films deposited at 350 °C using CFTS (ICDD 00-053-0575 a = 5.4233). Rwp = 3.11, lattice constant a = 5.4261(6) Å.

h	k	l	d	2θ
1	1	0	3.82828	23.30030
0	1	1	3.82828	23.30030
1	1	1	3.12577	28.63786
0	2	0	2.70700	33.18699
0	0	2	2.70700	33.18699
1	2	0	2.42121	37.23970
0	2	1	2.42121	37.23970
0	1	2	2.42121	37.23970
2	1	0	2.42121	37.23970
1	2	1	2.21026	40.94553
1	1	2	2.21026	40.94553
2	1	1	2.21026	40.94553
2	2	0	1.91414	47.64074
0	2	2	1.91414	47.64074
2	2	1	1.80467	50.72824
0	3	0	1.80467	50.72824
0	0	3	1.80467	50.72824
1	2	2	1.80467	50.72824
2	1	2	1.80467	50.72824
3	1	0	1.71206	53.68519
0	1	3	1.71206	53.68519
0	3	1	1.71206	53.68519
1	3	0	1.71206	53.68519
1	1	3	1.63238	56.53389
3	1	1	1.63238	56.53389
1	3	1	1.63238	56.53389
2	2	2	1.56289	59.29181
0	2	3	1.50157	61.97298
2	3	0	1.50157	61.97298
3	2	0	1.50157	61.97298
0	3	2	1.50157	61.97298
2	3	1	1.44695	64.58891
3	1	2	1.44695	64.58891
1	3	2	1.44695	64.58891
2	1	3	1.44695	64.58891
1	2	3	1.44695	64.58891
3	2	1	1.44695	64.58891
0	0	4	1.35350	69.66219
0	4	0	1.35350	69.66219
1	4	0	1.31309	72.13493
0	1	4	1.31309	72.13493
4	1	0	1.31309	72.13493
0	4	1	1.31309	72.13493
2	3	2	1.31309	72.13493
3	2	2	1.31309	72.13493

Table S2: Rietveld analysis of CFTS thin films deposited at 400 °C using CFTS (ICDD 00-053-0575 a = 5.4233). Rwp = 4.61, lattice constant a = 5.414(4) Å.

h	k	l	d	2θ
0	0	2	5.41850	16.34580
0	1	1	4.85253	18.26770
1	1	0	3.83747	23.15939
1	1	2	3.13164	28.47864
0	1	3	3.00709	29.68472
0	2	0	2.71350	32.98337
0	0	4	2.70925	33.03659
0	2	2	2.42627	37.02153
2	1	1	2.36836	37.96088
1	1	4	2.21325	40.73491
2	1	3	2.01456	44.96065
0	1	5	2.01281	45.00167
2	2	0	1.91873	47.33916
0	2	4	1.91723	47.37857
2	2	2	1.80868	50.41383
0	0	6	1.80617	50.48904
0	3	1	1.78431	51.15177
3	1	0	1.71617	53.33955
3	1	2	1.63607	56.17541
1	1	6	1.63420	56.24519
0	3	3	1.61751	56.87819
2	1	5	1.61661	56.91280
2	2	4	1.56582	58.93703
0	2	6	1.50355	61.63710
3	2	1	1.49087	62.21933
0	1	7	1.48875	62.31760
3	1	4	1.44978	64.18962
3	2	3	1.38939	67.34077
0	3	5	1.38882	67.37218
0	4	0	1.35675	69.18728
0	0	8	1.35462	69.31130
0	4	2	1.31612	71.64552
2	2	6	1.31515	71.70660
4	1	1	1.30664	72.24684

Table S3: Rietveld analysis of CFTSe thin films deposited at 350 °C using CFTSe (ICDD: 00-027-0167, a = 5.6850 Å), Rwp = 2.56, lattice constant a = 5.713(0) Å.

h	k	l	d	2θ
1	1	0	4.02216	22.08222
1	1	1	3.28036	27.16219
0	2	0	2.84410	31.42860
0	0	4	2.83445	31.53838
0	2	2	2.54211	35.27763
2	1	1	2.48213	36.15913
1	1	4	2.31694	38.83680
2	1	3	2.11031	42.81715
0	1	5	2.10636	42.90144
2	2	0	2.01108	45.06256
0	2	4	2.00766	45.12353
2	2	2	1.89535	47.95965
0	0	6	1.88963	48.11386
0	3	1	1.87010	48.64885
3	1	0	1.79877	50.71142
3	1	1	1.71453	53.39470
2	1	5	1.69269	54.13931
2	2	4	1.64018	56.02222
0	2	6	1.57391	58.60447
3	2	1	1.56257	59.07185
0	1	7	1.55776	59.27216
3	1	4	1.51876	60.95367
3	2	3	1.45587	63.88925
0	3	5	1.45457	63.95308
0	4	0	1.42205	65.59634
0	0	8	1.41723	65.84792
0	4	2	1.37931	67.89933
2	2	6	1.37711	68.02304
4	1	1	1.36949	68.45367
2	1	7	1.36625	68.63848
3	3	0	1.34072	70.13483
1	1	8	1.33668	70.37849
3	3	2	1.30473	72.36931
3	1	6	1.30286	72.48959
4	1	3	1.29594	72.93848
3	2	5	1.29503	72.99844
4	2	0	1.27192	74.54668

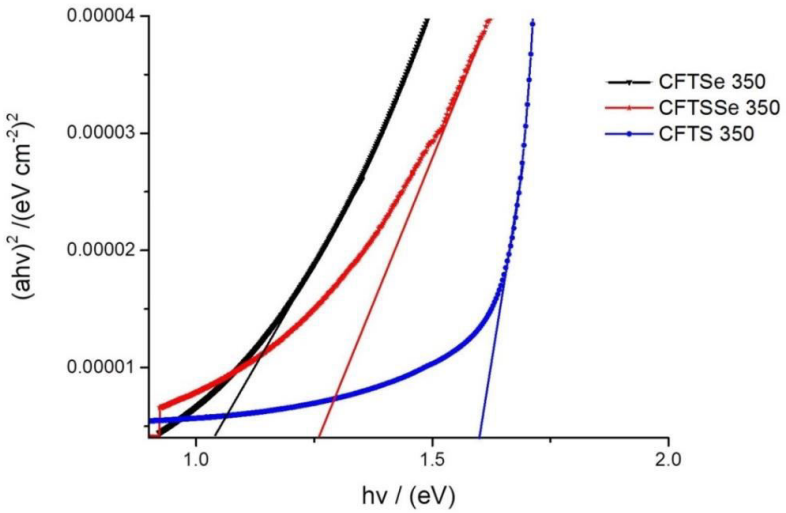

Figure S3: Tauc plot for the CFTS, CFTSSe and CFTSe thin films deposited at 350 °C.

Table S4: Calculation of band gap from Tauc plot

Material	Intercept (a)	Slope (b)	BG (eV)	R^2
CFTS 350	4.67 x10^{-4}	2.95 x10^{-4}	1.58	0.8972
CFTSSe 350	2.86 x10^{-4}	2.27 x 10^{-4}	1.25	0.9382
CFTSe 350	6.36 x 10^{-4}	5.78 x 10^{-4}	1.10	0.9561

References

1. Revaprasadu, N.; Malik, M. A.; O'Brien, *South African Journal of Chemistry* **2004**, 57, 40-43.
2. Akhtar, M.; Akhter, J.; Malik, M. A.; O'Brien, P.; Tuna, F.; Raftery, J.; Helliwell, M. *Journal of Materials Chemistry* **2011,** *21* (26), 9737-9745.
3. Ramasamy, K.; Kuznetsov, V. L.; Gopal, K.; Malik, M. A.; Raftery, J.; Edwards, P. P.; O'Brien, P.,. *Chemistry of Materials* **2013,** *25* (3), 266-276.
4. Trofimov,B. A; Artem'Ev, A. V.; Gusarova, N. K.; Malysheva, S. F.; Fedorov, S. V.; Kazheva, O. N.; Alexandrov G. G.; and. Dyachenko O. A.; *Synthesis*, 2009, 3332-3338.

CHAPTER - IX : PAPER - 6

"The controlled deposition of $Cu_2(Zn_yFe_{1-y})SnS_4$, $Cu_2(Zn_yFe_{1-y})SnSe_4$ and $Cu_2(Zn_yFe_{1-y})Sn(S_xSe_{1-x})_4$ thin films by AACVD: potential solar cell materials based on earth abundant elements"

Punarja Kevin, M. Azad Malik, Paul O'Brien, *J. Mater. Chem. C,* 2015, **3**, 5733-5741

Journal of Materials Chemistry C

PAPER

View Article Online
View Journal | View Issue

Cite this: J. Mater. Chem. C, 2015, 3, 5733

The controlled deposition of $Cu_2(Zn_yFe_{1-y})SnS_4$, $Cu_2(Zn_yFe_{1-y})SnSe_4$ and $Cu_2(Zn_yFe_{1-y})Sn(S_xSe_{1-x})_4$ thin films by AACVD: potential solar cell materials based on earth abundant elements†

Punarja Kevin,[a] Mohammad Azad Malik*[b] and Paul O'Brien*[ab]

Received 28th March 2015,
Accepted 4th May 2015

DOI: 10.1039/c5tc00867k

www.rsc.org/MaterialsC

Highly crystalline thin films of $Cu_2(Zn_yFe_{1-y})SnS_4$ (CZFTS), $Cu_2(Zn_yFe_{1-y})SnSe_4$ (CZFTSe) and $Cu_2(Zn_yFe_{1-y})Sn(S_xSe_{1-x})_4$ (CZFTSSe) have been deposited by aerosol assisted chemical vapour deposition (AACVD) from mixtures of dithio- or diseleno-carbamato, diselenophosphinato and acetylacetenato complexes. The structure, morphology, composition, optical and electrical properties of the deposited materials were investigated. The [Zn] : [Fe] and [S] : [Se] ratios are the important factors affecting the overall properties of these materials and can be controlled.

Introduction

Kesteric materials are considered to be amongst the better of the new absorbers for polycrystalline PV-solar cells.[1] The parent family encompasses Cu_2ZnSnS_4 (CZTS Kesterite), $Cu_2ZnSn(S_xSe_{1-x})_4$, (CZTSSe) and $Cu_2ZnSnSe_4$ (CZTSe).[1] The related iron containing phases $Cu_2(Zn_yFe_{1-y})SnS_4$ (CZFTS), $Cu_2(Zn_yFe_{1-y})SnSe_4$ (CZFTSe) and (CZFTSSe) have optical band gaps, large absorption coefficient and transport properties similar to those of CZTS.[2–4] There are few studies reported for materials that can form in both the kesteritic (space group $I\bar{4}8m$) and the stannitic (space group $I\bar{4}2m$) type dependent upon the [Zn]:[Fe] ratio.[4] The polymorphs have very small difference in thermodynamic stability. The addition of iron into CZTS thin films decreases the optical band gap which can improve the power conversion efficiency (PCE) of thin film solar cells (TFSCs). The solubility of iron in the CZTS derivatives plays a key role in controlling many parameters.[5]

The iron containing analogues are of particular interest for Si-based tandem solar cells as the lattice constant of Si (5.4311 Å) lies between two end members in the $Cu_2(Zn_yFe_{1-y})Sn(S_xSe_{1-x})_4$ series CFTS (5.414 Å) to CZTSe (5.435 Å). Variations in [Zn]:[Fe], or [S]:[Se] composition affect both the lattice spacing's and band gap.[2–6] The magnetic[5] and vibrational[7] properties of CZFTS alloys have also been investigated. Addition of Fe in CZTS thin films decreases the optical band gap energy which can improve the PCE of TFSCs.[2] Nanocrystals of the related $CuIn_xGa_{1-x}(S_ySe_{1-y})_2$ (CIGSSe) synthesized by colloidal methods, have band gaps tunable from 0.98–2.40 with changes in x and y from 0 to 1.[8]

AACVD is a simple technique which can operate at an ambient-pressure using the nebulization of the precursor molecules, followed by transport of the aerosol by an inert carrier gas such as argon or nitrogen to a substrate surface heated in a furnace where thermal decomposition of the precursor occurs.

AACVD has been widely applied in the deposition of complex systems and has enabled the used of less volatile precursors than more conventional CVD methods. These have included high temperature superconductors[9] and other oxides.[9] Stoichiometry controlled thin films of CdS, ZnS, and $Cd_{1-x}Zn_xS$ were deposited from $Cd(SOCCH_3)_2$–TMEDA and $Zn(SOCCH)_2$–TMEDA (TMEDA = *N*,*N*,*N*,*N*-tetramethylethylenediamine).[9] Marks *et al.* reported the deposition of metallic silver thin films using tris(phosphino)-boratosilver(I) complexes[10] and Parkin *et al.* reported a single step route to the deposition of super hydrophobic surfaces through AACVD and deposition of ZnO thin films by AACVD.[11] Wijayantha *et al.* reported the polycrystalline a-Fe_2O_3 electrodes by aerosol-assisted chemical vapour deposition from a ferrocene precursor.[12] Mazhar *et al.* reported the deposition of high quality $NiTiO_3$ thin films from a single-source heterobimetallic complex $[Ni_2Ti_2(OEt)_2(m\text{-}OEt)_6(acac)_4]$ precursor.[13] The method has also been successfully applied for α-Fe_2O_3 using $[Fe_6(PhCOO)_{10}(acac)_2(O)_2(OH)_2]_3C_7H_8$.[14] AACVD has recently been used for the deposition of various semiconductor materials including SnS,[15] CZTS,[16] $CuInSe_2$,[17] $CuGaSe_2$,[17] $CuIn_{0.7}Ga_{0.3}Se$,[17] MoS_2,[18] inorganic–organic perovskite $(CH_3NH_3)PbBr_3$,[19] SnSe and Cu_2SnSe_3.[19] Hussain *et al.* reported different morphologies of hexagonal FeSe from 1-benzoyl-3-(4-ferrocenylphenyl)selenourea under the influence of surfactants (span and triton) and temperature.[20] Very recently bismuth vanadate ($BiVO_4$) thin

[a] School of Chemistry, The University of Manchester, Oxford Road, M13 9PL, UK
[b] School of Materials, The University of Manchester, Oxford Road, M13 9PL, UK. E-mail: azad.malik@manchester.ac.uk

† Electronic supplementary information (ESI) available. See DOI: 10.1039/c5tc00867k

film photoelectrodes prepared by AACVD on fluorine doped tin oxide (FTO) glass substrates were produced, $BiVO_4$ photoelectrodes is promising for use in PEC water-splitting cells.[21] Recently the application of AACVD has been reviewed by Marchand *et al.*[9] β-In_2S_3 thin films deposited by AACVD, irrespective of different metal ligand design, generate comparable morphologies of thin films at different temperatures, the measured photoelectrochemical performance of these films were highly useful in fabricating electrodes for solar energy harvesting and optoelectronic application.[22]

Dhurba and reported the deposition of CZFTS thin films, by spray pyrolysis followed by sulfurization at ~500 °C.[7] Agawane *et al.* reported the effect of [Zn]:[Fe] ratio on the properties of CZFTS thin films deposited by a pulsed laser deposition technique but the formation of Cu-rich and Zn-poor large grains was found to affect these parameters.[2] We have used a series of molecular precursors for the deposition of binary and ternary materials.[22] Herein, we report the AACVD of CZFTS, CZFTSe and CZFTSSe thin films and detailed investigation on the effect of [Zn]:[Fe] and [S]:[Se] ratios on the structure, morphology, optical band gap and electrical resistance of these materials.

Experimental section

Preparations were performed under an inert atmosphere of dry nitrogen using standard Schlenk techniques. All reagents were purchased from Sigma-Aldrich chemical company and used as received. Solvents were distilled prior to use. Elemental analysis was performed by the University of Manchester micro-analytical laboratory. TGA measurements were carried out by a Seiko SSC/S200 model from 10 to 600 °C with a heating rate of 10 °C min^{-1} under nitrogen. Melting point was recorded on a Stuart melting point apparatus and uncorrected.

Synthesis of metal–organic complexes

The compounds $[Cu(S_2CNEt_2)_2]$, $[Fe(S_2CNEt_2)_3]$, $[^nBu_2Sn(S_2CNEt_2)_2]$, $[Zn(S_2CNEt_2)_2]$, $[Zn(Se_2CNEt_2)_2]$ and $[Cu(PPh_3)(Ph_2P(Se)NP(Se)Ph_2)]$ were synthesised and recrystallized as reported in literature, brief details follow.[14,23–25]

$[Cu(S_2CNEt_2)_2]$. Sodium diethyldithiocarbamate (13 mmol) was dissolved in methanol in a 500 mL double necked round-bottom flask. Slow addition of a methanolic solution of $Cu(NO_3)_2$ (6.5 mmol) gave a black precipitate, which was isolated by filtration. Recrystallization was performed using chloroform. Yield: 4.78 g (73%), Mpt: 201 °C, IR (ν_{max}/cm^{-1}): 2979(w), 2868(w), 1501(s), 1434(m), 1270(s), 1205(m) and 1144(m), elemental analysis: calc. for $C_{10}H_{20}N_2S_4Cu$: C, 33.4; H, 5.5; N, 7.7; S, 35.6; Cu, 17.6%. Found: C, 33.2; H, 5.3; N, 7.3; S, 35.2; Cu, 17.2%.

$[Fe(S_2CNEt_2)_3]$. Sodium diethyldithiocarbamate (13 mmol) with $Fe(NO_3)_3$ (4 mmol) gave a black powder which on recrystallization produced black shiny crystals. Yield 4.81 g (79%), Mpt: 198–201 °C, IR (ν_{max}/cm^{-1}): 2967(w), 2938(w), 1478(s), 1429(m), 1352(w), 1296(w), 1296(m), 1270(s), 1050(s) and 950(s), elemental analysis: calc. for $C_{15}H_{30}N_3S_6Fe$: C, 35.98; H, 6.04 N, 8.39; S, 38.43; Fe, 11.15%. Found: C, 35.7; H, 6.3; N, 8.4; S, 37.82; Fe, 11.0%.

$[Zn(S_2CNEt_2)_2]$. Produced by the reaction between zinc acetate (6.5 mmol) and sodium diethyldithiocarbamate (13 mmol) as described above. The crude product was obtained was a white powder which on recrystallization from chloroform gave colourless crystals. Yield 4.81 g (79%), Mpt: 181 °C, IR (ν_{max}/cm^{-1}): 2967(w), 2938(w), 1499(s), 1427(m), 1352(w), 1296(w), 1296(m), 1270(s), 1200(s) and 114 3(s), elemental analysis: calc. for $C_{10}H_{20}N_2S_4Zn$: C, 33.1; H, 5.5; N, 7.7; S, 35.4; Zn, 18.1%. Found: C, 32.7; H, 5.3; N, 7.4; S, 35.0; Zn, 18.0%.

$[Bu_2Sn(S_2CNEt_2)_2]$. The compound was synthesised as described before[11] using di-*n*-butyltindichloride (6.5 mmol) and sodium diethyldithiocarbamate (13 mmol). A white powdered product was isolated by vacuum filtration and recrystallized from a mixture of ethanol–chloroform, white shiny crystals obtained. Yield 5.5 g, (67%), Mpt: 57 °C, IR (ν_{max}/cm^{-1}): 2953(w), 2924(w), 1483(s), 1456(m), 1417(s), 1353(m), 1298(m) 1253(s), 1205(s) and 1138(s), elemental analysis: calc. for $C_{18}H_{38}N_2S_4Sn$: C, 40.8; H, 7.2; N, 5.3; S, 24.2; Sn, 22.4%. Found: C, 39.9; H, 7.5; N, 5.1; S, 22.8; Sn, 21.4%.

$[Zn(Se_2CNEt_2)_2]$. A solution of carbon diselenide (47.0 mmol) in methanol was added drop wise to a solution of diethylamine (47.0 mmol) and sodium hydroxide (47.0 mmol) in methanol at 5 °C while stirring. After 20 minutes the mixture was allowed to warm up to room temperature and a solution of zinc chloride (23.5 mmol) in dicholoromethane was added drop wise and stirred for 0.5 hour. A yellow precipitate thus obtained was filtered and dried in air and then in vacuum desiccator. Yield: 46%. For ^1H NMR ($CDCl_3$) peaks obtained at 1.89 $-(CH_3)_2CH$ group, 2.25 ($N(CH_3)_2$), 2.5 (NCH_2). Elemental analysis calc. for $C_{10}H_{24}N_2Se_2Zn$: C, 30.3; H, 6.1; N, 7.1% found: C, 30.1; H, 5.9; N, 6.8%.

$[Cu(PPh_3)][Ph_2P(Se)NP(Se)Ph_2]$. In a 150 mL methanolic solution of 1.2 g (2.6 mmol) $K[Ph_2P(Se)NP(Se)Ph_2]$ was mixed with a solution of $[Cu(PPh_3)_2NO_3]$ (1.4 g, 2.1 mmol) in 100 mL methanol. Then stirred for 30 minutes and the precipitate was filtered, the filtrate on rotary evaporation gave a pinkish powder. The product was recrystallized from dichloromethane resulted pinkish crystals were dried and purified under vacuum. Yield: 64% $[Cu(PPh_3)][Ph_2P(Se)NP(Se)Ph_2]$; m.p; 221–223 °C. ^{31}P NMR (400 MHz, $CDCl_3$, rel. to 85% H_3PO_4): δ = 26.14 ppm with two P–Se satelites, 1JP–Se-576 Hz. IR (ν_{max}/cm^{-1}): 3050 cm^{-1} (s) 1165 cm^{-1} (s) 1100, 755(m), 690(m) and 545(m). Mass spec.: *m*/*z*-869, 670, 460, 341. Elemental analysis: calc. for $C_{42}H_{35}CuNP_3Se_2$: C, 58.1; H, 4.1; N, 1.6% and found; C, 57.87; H, 3.92; N, 1.48%.

Deposition of thin films

The thin films were deposited using AACVD. Glass slides (1 × 2 cm) were used as substrates for the deposition of thin films. Substrates were thoroughly cleaned and sonicated in acetone for 30 minutes to remove any possible contamination. In a typical deposition experiment, precursor complex (or a suitable combination of precursors) was dissolved in 20 mL THF taken in a two-necked 100 mL round-bottom flask. The round-bottom flask was kept in a water bath above the piezoelectric modulator of a PIFCO ultrasonic humidifier (model 1077). The aerosol droplets of the precursor thus generated were transferred into the hot wall

zone of the reactor by a carrier gas (Argon). The Argon flow rate was controlled at 180 sccm by a Platon flow gauge. Both the solvent and precursor were evaporated, and the precursor vapor reached the heated substrate surface where thin film was deposited at 300–400 °C.

Deposition of CZFTS thin films

Thin films of $Cu_2(Zn_yFe_{1-y})SnS_4$ (CZFTS) were deposited using a mixture of $[Cu(S_2CNEt_2)_2]$ (2.78 mmol), $[Fe(S_2CNEt_2)_3]$ (0.7 mmol), $[Zn(S_2CNEt_2)_2]$ (0.7 mmol) and $[^nBu_2Sn(S_2CNEt_2)_2]$ (1.40 mmol) in the molar ratio 2 : 1 : 0.5 : 0.5 : 1 in 20 ml THF. The AACVD experiments were carried out as described above at 300 and 350 °C. The Fe-rich compositions of this material were deposited by increasing the ratio of the iron precursor as compared to that of zinc precursor. A mixture of $[Cu(S_2CNEt_2)_2]$ (2.78 mmol), $[Fe(S_2CNEt_2)_3]$ (1.0 mmol), $[Zn(S_2CNEt_2)_2]$ (0.4 mmol) and $[^nBu_2Sn(S_2CNEt_2)_2]$ (1.40 mmol) in 2 : 1 : 0.7 : 0.3 : 1 molar ratio in 20 ml THF was used to deposit films at 350 °C.

Deposition of CZFTSe thin films

The deposition of $Cu(ZnFe)SnSe_4$ was carried out by using a mixture of $[Cu(PPh_3)(Ph_2P(Se)NP(Se)Ph_2)]$, (2.78 mmol), $[Sn(CH_3CO_2)_4]$ (1.40 mmol) $[Zn(Se_2CNEt_2)_2]$ (0.7 mmol) and $[Fe(acac)_3]$ (0.7 mmol) in the molar ratio 2 : 1 : 0.5 : 0.5 : 1 in 20 mL of THF at 300 °C and 350 °C for 55 minutes. For the deposition of Fe-rich films a similar deposition was carried out at 350 °C with different ratio of $[Zn(S_2CNEt_2)_2]$ (0.4 mmol) (2.8 mmol) and $[Fe(acac)_3]$ (1.0 mmol) in 2 : 1 : 0.7 : 0.3 : 1 molar ratio in 20 mL THF and keeping other precursor concentrations same as in the previous experiment.

Deposition of CZFTSSe thin films

The $Cu_2(Zn_yFe_{1-y})Sn(S_xSe_{1-x})_4$ thin films were deposited by using $[Zn(Se_2CNEt_2)_2]$ (0.7 mmol) whilst keeping all the other precursors same as for Zn-rich CZFTS (1 : 0.5 : 0.5 : 1 in 20 mL of THF). The depositions were carried out at 300 °C and 350 °C. For the deposition of Fe-rich composition on the films, another deposition was carried out at 350 °C using $[Zn(Se_2CNEt_2)_2]$ (0.4 mmol) and $[Fe(S_2CNEt_2)_3]$ (1.0 mmol) in 2 : 1 : 0.7 : 0.3 : 1 molar ratio in 20 mL THF whilst keeping all the other concentrations same.

Characterisation of thin films

The p-XRD patterns were recorded on a Bruker D8 AXE diffractometer using Cu-Kα radiations. The samples were mounted flat and scanned between 10 and 120° in a step size of 0.05 with a varying count rate depending upon the sample. The morphology and microstructure of thin films were investigated by using a Philips XL 30 FEGSEM and film composition was studied by EDX analysis using a DX4 instrument at 20 kV with WD 10 mm. Raman spectra measurements taken in Renishaw 1000 Micro Raman system with an excitation wavelength of 520 nm, measurement range set from 100 to 700 cm^{-1}. UV-VIS measurement carried out in Perkin Elmer Lambda 1050 spectrophotometer (PSI), scanned across the range from 250–1000 nm. Electrical resistance measured using Jandel four probe conductivity meter under room temperature using 1 μA current. TEM samples were prepared by evaporating a drop of a dilute suspension of the sample in toluene or hexane on carbon coated copper grid. The excess solvent was allowed to dry completely at room temperature. TEM images and elemental maps were collected on Technai T20 microscope using accelerating voltage of 300 kV. TEM (nanoscale) elemental maps were measured using Aztec software.

Results and discussion

Thermal decomposition studies

Thermal decomposition studies were carried at 10–600 °C; heating rate 10 °C min^{-1} under nitrogen. All compounds show rapid single step decomposition between 250–350 °C (Fig. 1). The residual mass of $[Fe(S_2CNEt_2)_3]$ complex found to be about 18% which close to the calculated percentage of FeS (17.5%). The $[Bu_2Sn(S_2CNEt_2)_2]$ complex decomposed slightly faster than the other complexes and the residual mass found to be ~34% which agrees with the calculated residual mass of SnS_2. $[Zn(S_2CNEt_2)_2]$ and $[Zn(Se_2CNEt_2)_2]$ resulted with ~9–10% residue which found to be half or less than half of the mass of the expected metal chalcogenides; ZnS (27%) and ZnSe (20%). TGA of $[Cu(PPh_3)(Ph_2P(Se)NP(Se)Ph_2)]$ showed single step decomposition between 250 to 320 °C with residue ~10% which was lesser than the expected residual mass of CuSe (16%).

X-ray diffraction studies

The deposition of CZFTS materials at 300 °C gave very thin dark green films which did not diffract whereas black adherent films were deposited at 350 °C. The p-XRD pattern (Fig. 2) of these films was corresponding to the Zn-rich phase of $Cu_2Fe_{0.3}Zn_{0.7}Sn_1S_4$ (ICDD 04-015-0225) with the tetragonal space group $I\bar{4}2m$ with lattice parameters a = 5.42(2) Å and c = 10.86(4) Å. Rietveld refinement carried out on the p-XRD patterns of the deposited material using this Zn-rich standard space group showed very good fit with a Rietveld parameter R_{wp} = 2.85, space group $I\bar{4}2m$

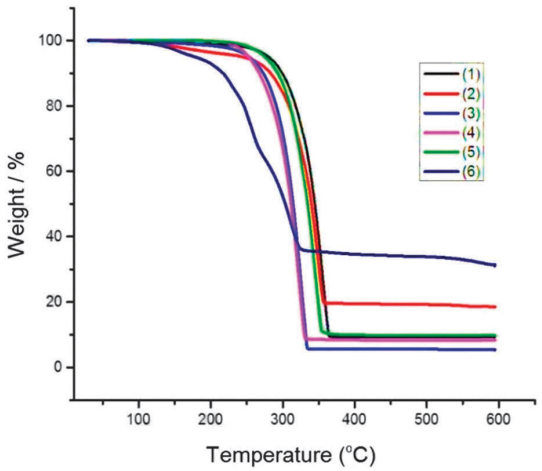

Fig. 1 TGA of $[Cu(S_2CNEt_2)_2]$ (**1**), $[Fe(S_2CNEt_2)_3]$ (**2**), $[Zn(S_2CNEt_2)_2]$ (**3**), $[^nBu_2Sn(S_2CNEt_2)_2]$ (**4**), $[Zn(Se_2CNEt_2)_2]$ (**5**) and $[Cu(PPh_3)(Ph_2P(Se)NP(Se)Ph_2)]$ (**6**) complexes.

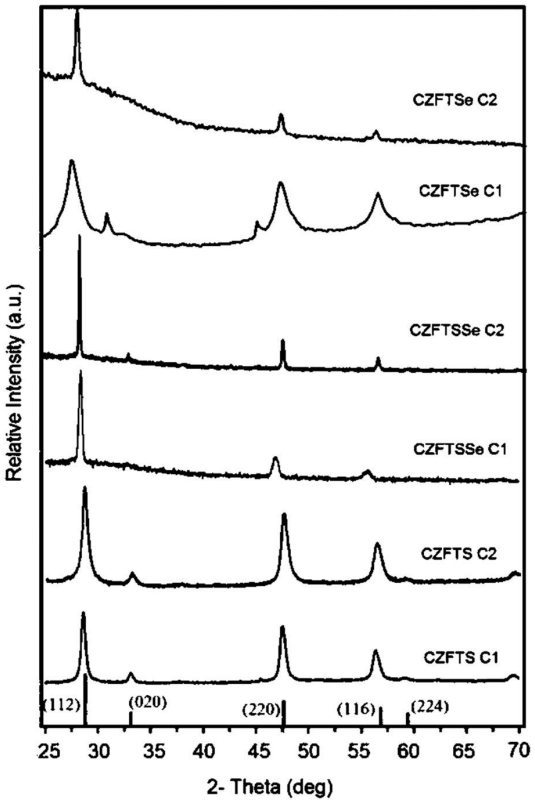

Fig. 2 p-XRD patterns of Zn-rich (C1) and Fe-rich (C2) phases of CZFTS, CZFTSe, CZFTSSe thin films deposited with different [Zn] at 350 °C.

with lattice parameters a = 5.411(4) Å and c = 10.862(3) Å (Fig. 3(a)). The main d-spacing for the planes were 3.13 Å (112), 1.91 Å (204), 1.91 Å (220), 1.63 Å (116) and 1.63 Å (312) respectively. The resultant d-spacing were well matched with the reported d-spacing for the corresponding planes at 3.13 Å (112), 1.91 Å (204), 1.91 Å (220), 1.63 Å (116) and 1.63 Å (312) respectively (ICDD: 04-015-0225) for $Cu_2Fe_{0.3}Zn_{0.7}Sn_1S_4$. The doublet planes were not well resolved possibly due to broadening of the peaks due to the small size of the particles compared to the bulk materials, but the material is very close to cubic. The details of calculated d-spacings and 2θ values are shown in Table S1 in the ESI.† The lattice parameters also estimated calculated from the principal peaks in the p-XRD patterns to a cubic cell giving a = 5.412(8) Å in good agreement with the values obtained from the Rietveld refinement (Table 1). This approach was also used for all films some of which did not give good fits in the Rietveld analysis.

CZFTS films deposited at 350 °C using a higher ratio of the Fe precursor (CZFTS C2 in Table 1) were very dark and uniform. The p-XRD pattern of as deposited films (Fig. 3(b)) corresponds to the Fe-rich phase of $Cu_2Fe_{0.7}Zn_{0.3}Sn_1S_4$ (ICDD: 01-015-0228). No additional phase or impurities were found in the p-XRD and showed good match to the stick patterns can be seen in Fig. 2. Rietveld refinement of the resultant p-XRD patterns analysed with the observed Fe-rich phase showed very good match with R_{wp} = 2.43 as shown in Fig. 3(b). The standard material possesses an $I\bar{4}2m$ space group with space group number 12 and a = 5.43(2) Å and c = 10.79(4) Å and the refined space group was found to be $I\bar{4}2m$ with lattice parameters a = 5.42 Å and c = 10.83 Å. The resultant d-spacing for the planes and planes were 3.13 Å (112),

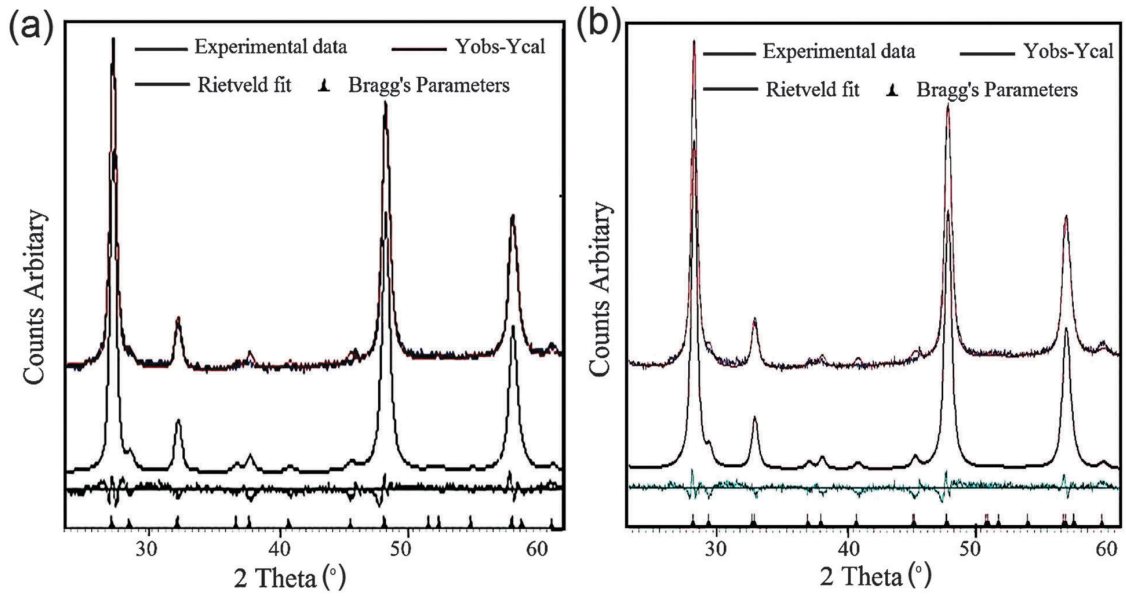

Fig. 3 (a) Rietveld analysis p-XRD patterns of CZFTS thin films deposited at 350 °C using 2 : 1 : 0.5 : 0.5 : 1 of $[Cu(S_2CNEt_2)_2]$: $[Fe(S_2CNEt_2)_3]$: $[Zn(S_2CNEt_2)_2]$: $[^nBu_2Sn(S_2CNEt_2)_2]$ precursors. The peaks fitted using $Cu_2Fe_{0.3}Zn_{0.7}Sn_1S_4$ (ICDD 04-015-0225) phase. (b) Rietveld analysis of p-XRD patterns of CZFTS thin films deposited at 350 °C using 2 : 1 : 0.7 : 0.3 : 1 of $[Cu(S_2CNEt_2)_2]$: $[Fe(S_2CNEt_2)_3]$: $[Zn(S_2CNEt_2)_2]$: $[^nBu_2Sn(S_2CNEt_2)_2]$ precursors. The peaks fitted using Fe-rich $Cu_2Fe_{0.7}Zn_{0.3}Sn_1S_4$ (ICDD: 01-015-0228) phase.

Table 1 Consolidated table showing measured parameters (band gaps, resistance, EDX, lattice constants) and the concentrations of individual components in the precursor mixtures for Zn-rich (**1**) and Fe-rich (**2**) phases of CZFTS, CZFTSe and CZFTSSe

Sample	T (°C)	[Cu] AACVD	[Cu] EDX	[Zn] AACVD	[Zn] EDX	[Sn] AACVD	[Sn] EDX	[Fe] AACVD	S EDX	Se EDX	a (Å) Riet	c (Å) Riet	a (Å) hkl	BG/eV	R/Ω
CZFTS (C1)	350	2.78	2.2	0.7	0.7	1.4	1.3	0.7	3.4	0	5.411(4)	10.862(3)	5.412(8)	1.72	2.48
CZFTS (C2)	350	2.78	1.9	0.4	0.3	1.4	1.3	1	3.2	0	5.418(7)	10.829(1)	5.415(2)	1.67	2.42
CZFTSSe (C1)	350	2.78	1.7	0.7	0.6	1.4	0.8	0.7	1.9	1.2	*x*	*x*	5.477(5)	1.64	2.31
CZFTSSe (C2)	350	2.78	2	0.7	0.4	1.4	0.8	1	2.1	1.7	*x*	*x*	5.429(8)	1.61	2.29
CZFTSe (C1)	350	2.78	2	0.7	0.7	1.4	1	0.7	0	3.1	*x*	*x*	5.429(7)	1.47	2.21
CZFTSe (C2)	350	2.78	1.8	0.4	0.3	1.4	0.9	1	0	3	*x*	*x*	5.492(7)	1.48	2.16

1.91 Å (220) and 1.63 Å (312) which found to be the same as the standard d-spacing for the planes *i.e.* 3.13 Å (112), 1.91 Å (220) and 1.63 Å (312) respectively (ICDD: 01-015-0228). The details of calculated d-spacing's and 2θ positions are given in Table S2 in the ESI.† The lattice parameters a calculated from the principal peaks in p-XRD patterns were 5.415 (2) (see Table S1, ESI†).

The deposition of $Cu(ZnFe)SnSe_4$ at 300 °C gave only amorphous material which did not show any diffraction by p-XRD whereas uniform dark brownish films were obtained at 350 °C. The p-XRD pattern of the thin films deposited at 350 °C are shown in Fig. 2, peaks show clear shifts from Zn-rich $Cu_2ZnFeSnS_4$ (ICDD: 00-83-0225) and Fe-rich $Cu_2ZnFeSnS_4$ (ICDD: 01-015-0228) phase as expected. The p-XRD pattern found to be broader because of the small particle size of individual crystallites and overlapping of peaks especially about 2θ: 47 to 48° and around 2θ: 55–56. The calculated lattice parameters from the p-XRD patterns was a = 5.429(7) Å (Table 1).

A similar deposition with more Fe precursor concentration at 350 °C gave thin brown films. The p-XRD patterns were analysed by comparing with the Zn-rich $Cu_2ZnFeSnS_4$ (ICDD: 00-83-0225) an Fe-rich $Cu_2ZnFeSnS_4$ (ICDD: 01-015-0228) phases (Fig. 2), it had been observed that the p-XRD patterns were shifted significantly from the reference patterns. The p-XRD patterns were further analysed using $Cu_2FeSnSe_4$ patterns (JCPDS: 00-027-0167) but none of the peaks no matching peaks were seen. The calculated lattice parameters from the p-XRD patterns was a = 5.492(7) Å (Table 1).

The deposition of $Cu_2(ZnFe)Sn(S_xSe_{1-x})_4$ using a mixture of precursors as described in the experimental part gave only a negligible amount of deposits at 300 °C whereas good quality black specular films were deposited at 350 °C. The p-XRD pattern of these films showed a clear shifts from those of the

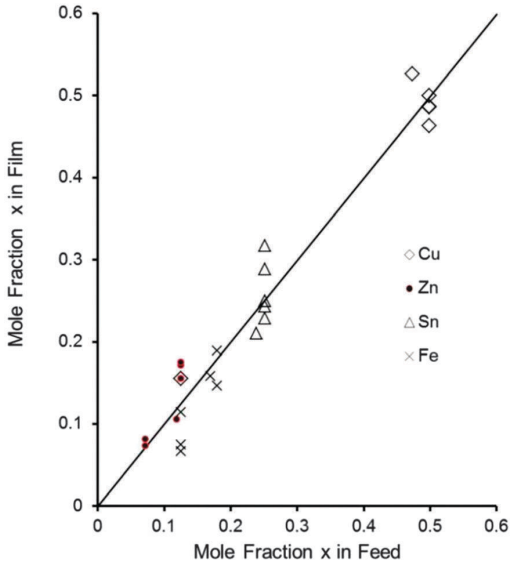

Fig. 4 Correlation between mole fraction of each metal (x) in the feed and observed amount in the film by EDX.

Fe-rich and Zn-rich phases of CZFTS indicating the formation of $Cu_2(Zn_yFe_{1-y})Sn(S_xSe_{1-x})_4$ as shown in Fig. 2. The calculated lattice parameter a = 5.477(5) Å (Table 1). Another deposition with more Fe precursors at 350 °C produced thin black films. The p-XRD pattern was compared with Fe-rich (ICDD: 01-015-0228) and Zn-rich (ICDD 04-015-0225) CZFTS patterns. The peaks showed larger shift from both reference patterns (Fig. 2). The lattice parameter a calculated from the p-XRD patterns was 5.429(8) Å (see Table 1).

SEM, EDX and TEM studies

Elemental analysis of the films confirmed that the metal content of all films correlated well with mole fraction of metal in the feed shown in Fig. 4. It is clear from the figure shows that a correlation between the mole fraction of Se in the precursor mixture and mole fraction of Se in the deposited thin films. From the graph it shows a linear correlation between the mole fraction of Se in the precursor and in the deposited thin films.

The SEM images of all deposited films showed different morphologies with ~1 μm thickness over the entire area of the substrate (Fig. 5). Zn-rich phase of CZFTS thin films deposited at 350 °C showed irregular flakes, less than 1 micron thickness. Elemental map confirmed of these films the uniform distribution of elements through the entire film (Fig. 6(a)). EDX confirmed the p-XRD results by showing the deposition of the Zn-rich films: Cu (28.42%), Zn (8.84%), Fe (3.97%), Sn (15.23%), S (43.54%) corresponding to $Cu_{2.2}Fe_{0.3}Zn_{0.7}Sn_{1.2}S_{3.4}$. SEM images of the CZFTS thin films deposited from higher concentration of iron precursor showed uniform flakes with an even distribution (Fig. 5(b)). EDX results revealed the composition as (Cu (25.92%) Zn (4.52%) Fe (9.5%) Sn (17.52%) S (45.54%)) giving an empirical formula of $Cu_{1.9}Fe_{0.7}Zn_{0.3}Sn_{1.3}S_{3.2}$ confirming the deposition of Fe-rich films. Elemental map of the films showed uniform composition of deposited material with constituent elements are shown in Fig. 6(b).

The SEM images of C(ZF)TSe thin films deposited at 350 °C showed irregular crystallites with size *ca.* 1 μm as shown in Fig. 5(c). EDX analysis results showed atomic percentage of Cu (28.55%), Zn (10.72%), Fe (3.55%), Sn (14.50%) and Se (42.65%)

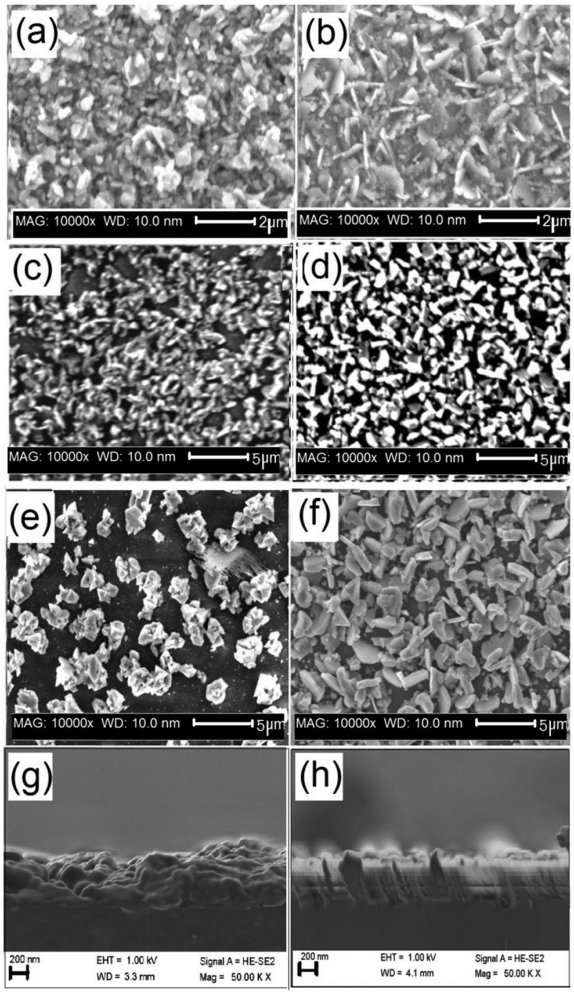

Fig. 5 (a) and (b) are the SEM images, Zn-rich (CZFTS C1) and Fe-rich (CZFTS C2) phases of CZFTS films (c) and (d) are the SEM images, Zn-rich (CZFTSe C1) and Fe-rich (CZFTSe C2) phases of CZFTSe. (e) and (f) are the SEM images, Zn-rich (CZFTSSe C1) and Fe-rich (CSFTSSe C2) phases of CZFTSSe films deposited at 350 °C. (g) and (h) are the cross sectional images of films (a) and (b).

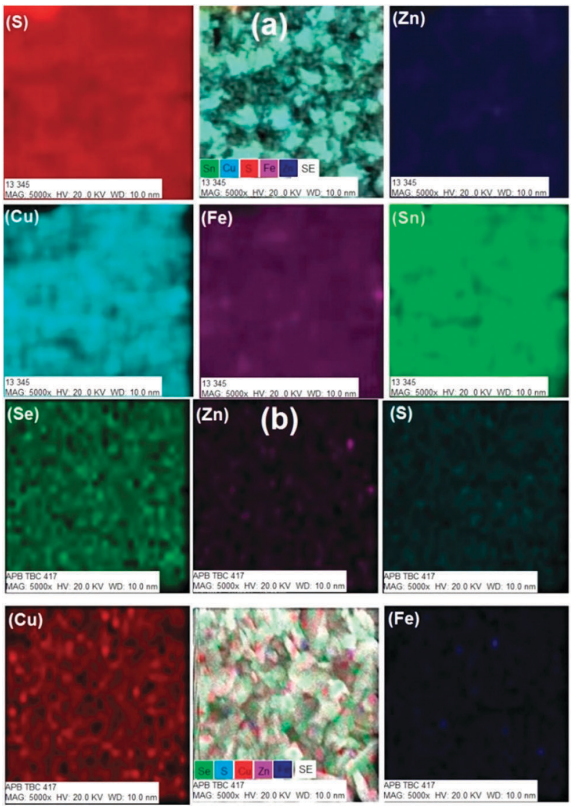

Fig. 6 Elemental map images for (a) (CZFTS C1) and (b) Zn-rich and Fe-rich (CZFTS C2) phases of CZFTS films deposited at 350 °C.

which gave a stoichiometric composition as $Cu_{2.0}Zn_{0.7}Fe_{0.3}Sn_{1.0}Se_{3.1}$; a Zn-rich phase.

SEM images with Fe-rich phases of C(ZF)TSe showed irregularly shaped crystallites (Fig. 5(d)). EDX analysis showed atomic percentage of Cu (26.13%), Zn (4.10%), Fe (11.21%), Sn (13.60%) and Se (44.13%) which gives a stoichiometric composition of $Cu_{1.8}Zn_{0.3}Fe_{0.7}Sn_{0.9}Se_{3.0}$ corresponding to Fe-rich phase.

The SEM images of $Cu_2(ZnFe)Sn(S_xSe_{1-x})_4$ thin films deposited at 350 °C showed morphology based on irregular plate like crystallites as shown in Fig. 5(e). The EDX analysis showed Cu (25.63%) Zn (8.74%) Fe (6.46%) Sn (12.46%) S(28.74%) and Se (17.94%) corresponding to $Cu_{1.7}Fe_{0.4}Zn_{0.6}Sn_{0.8}S_{1.9}Se_{1.2}$, the Zn-rich and S-rich stoichiometry.

The $(ZnFe)Sn(S_xSe_{1-x})_4$ films deposited with higher concentration of Fe at 350 °C on EDX analysis showed Cu (26.87%) Zn (5.13%) Fe (7.92%) Sn (11.15%) S (26.24%) and Se (22.85%) corresponding to $Cu_{2.1}Fe_{0.6}Zn_{0.4}Sn_{0.8}S_{2.1}Se_{1.7}$ which showed a Fe and S-rich stoichiometry. SEM images showed irregular plate like crystallites (Fig. 5(f)). The elemental map showed uniform composition throughout the material (ESI,† Fig. S1 and S2).

The Fe-rich CZFTS thin films (CZFTS C1) and Zn-rich (CZFTS C2) phases were further studied using TEM. The films were removed by scratching and ground, and dispersed in toluene for TEM analysis. The TEM images (Fig. 7) showed flaky irregular crystallites with size ranging from 10 to 30 nm. Selected area elemental map results further revealed the Zn-rich and Fe-rich phases in the nm scale. The *d*-spacing obtained from lattice fringes and diffraction patterns were in good agreement with the standard patterns for the Zn-rich and Fe-rich phases.

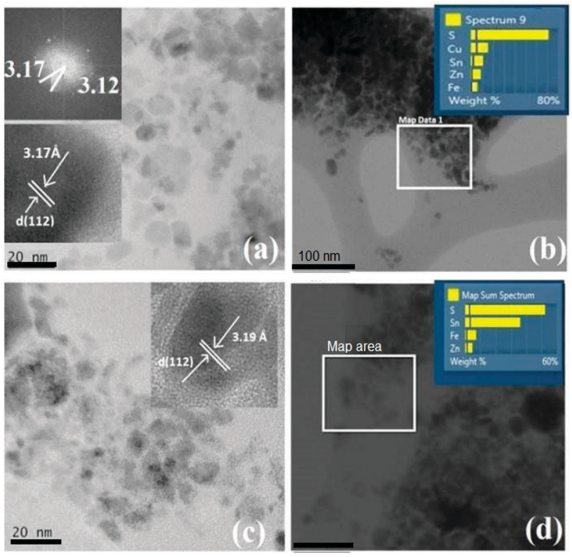

Fig. 7 (a) and (b) shows the TEM images and elemental map of CZFTS thin films deposited using 2 : 0.5 : 0.5 : 1 molar ratio of Cu, Fe, Fe and Sn precursors at 350 °C (CZFTS C1). (c) and (d) shows the TEM and elemental maps of CZFTS thin films deposited with 2 : 0.7 : 0.3 : 1 molar ratio of Cu, Fe, Zn and Sn precursor mixture at 350 °C (CZFTS C2). Inserts images in (a) and (c) shows the *d*-spacing of the particles.

Raman spectra and UV-visible spectra

The Raman spectra of films deposited with different [Fe] : [Zn] ratios of CZFTS, CZFTSe and CZFTSSe are shown in Fig. 8. Raman spectra showed peaks at ~340 cm^{-1} and 350 cm^{-1} for CZFTS Fe-rich and Zn-rich phases. The Zn-rich CZFTS showed a higher Raman mode than the Fe-rich material as reported previously.[2,7] Tauc plots drawn by plotting $(\alpha h\nu)^2$ against $h\nu$ of films deposited with different [Fe] : [Zn] ratios of CZFTS, CZFTSe and CZFTSSe are shown in ESI† Fig. S3 which clearly show the variation in bandgaps (ESI,† Table S3 and Table 1).

Raman spectra for the CZFTSSe films showed peaks at ~198, 228 and ~340 cm^{-1}. All these peaks are shifted from Raman peaks for CFTSe (209, 270 cm^{-1}) or CFTS (321, 284, 218 cm^{-1}) phases as expected.[7,8,26–28] Band gap measurements of CZFTS for Zn-rich composition showed 1.72 eV whereas those with Fe-rich composition gave a band gap of 1.67 eV, which are close to those reported previously.[2,7] Raman spectra obtained for the Fe-rich CZFTSe films showed a broad peak with low intensity at 230 cm^{-1}. The Zn-rich CZFTSe Raman shifts were observed at ~235 cm^{-1} which lies between the end materials CZTSe and CFTSe phases with their corresponding Raman modes at 209 cm^{-1} and 270 cm^{-1} respectively.[27]

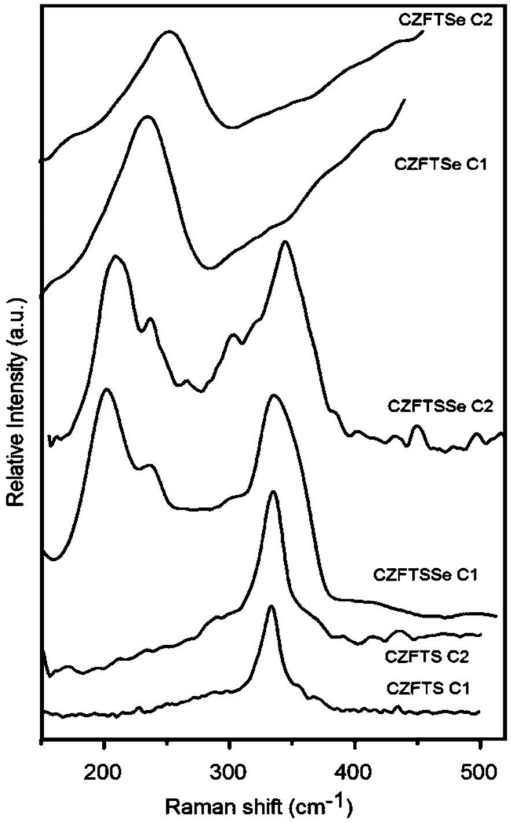

Fig. 8 Raman spectra of Zn-rich and Fe-rich (C2CZFTS (CZFTS C1 and CZFTS C2), CZFTSe (CZFTSe C1 and CZFTSe C2) and CZFTSSe (CZFTSSe C1 and CZFTSSe C2) thin films deposited at 350 °C using different precursor mixtures.

Here also the Zn-rich phases showed slightly higher Raman mode as observed in CZFTS.[2,7] The calculated band gaps were 1.48 and 1.47 eV for Zn-rich and Fe-rich CZFTSe thin films respectively which are in the range of CZTS, CZTSe, CZTSSe and CFTSe.[27–29] UV/Vis Tauc plots drawn by ploting $(\alpha h\nu)^2$ against $h\nu$ gave a band gap values of ~1.64 and 1.61 eV for Zn-rich and Fe-rich CZFTSSe thin films, which were closer to that of the Kesterite CZFTS phases.[2,6–8,14–20]

Electrical sheet resistance

Variation in the electrical sheet resistance with different Fe-compositions has been studied. The electrical resistance measured at room temperature were 2.48 KΩ sq^{-1} for Fe-rich thin films and 2.42 KΩ sq^{-1} for Zn-rich films of CZFTS values which lie between the electrical sheet resistance for parent materials CZTS (2.8 KΩ sq^{-1}) and CFTS (2.3 KΩ sq^{-1}).[9,28–31] The Fe-rich films showed comparatively lower resistance than the Zn-rich ones. The sheet resistance of the Zn-rich CZFTSe films and Fe-rich phases were observed as 2.10 KΩ sq^{-1} for and 2.07 KΩ sq^{-1} respectively, both values were lower than those for CZFTS (2.48 KΩ sq^{-1} and 2.42 KΩ sq^{-1}) as expected.

The resistance value for end materials were as CZTSe (2.12 KΩ sq^{-1}) and CFTSe (2.04 KΩ sq^{-1}). These resistance measurements for CZFTSSe materials were found to be 2.31 and 2.29 KΩ sq^{-1} for Zn-rich and Fe-rich films respectively. Both values are lower than those of CZFTS Fe-rich (2.48 KΩ sq^{-1}) and Zn-rich phases (2.42 KΩ sq^{-1}) but higher than the CZFTSe Zn-rich (2.10 KΩ sq^{-1}) and Fe-rich (2.07 KΩ sq^{-1}) phases[32,33] (ESI,† Fig. S4).

Vegard-type analysis were carried out using the measured band gap and sheet resistance values and is shown in Fig. 9. There is a reasonable linear correlation between the Se/S mole fraction in all samples and these properties for all the films.

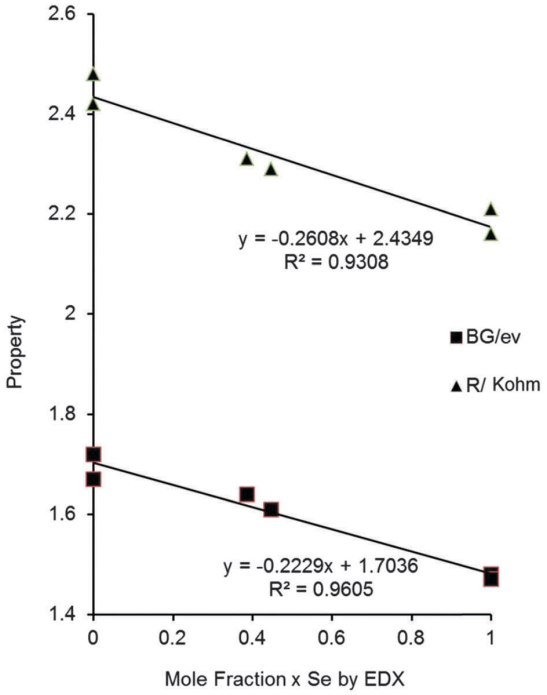

Fig. 9 Vegard-type plot for resistance and band gaps of all samples against the mole fraction of Se as measured by EDX (band gap eV, resistance KΩ sq^{-1}).

Conclusions

Thin films of CZFTS, CZFTSe and CZFTSSe have been deposited by AACVD. The ratios of the constituents: Zn, Fe, S and Se can be controlled by varying the concentrations of corresponding precursors and the deposition temperature. The band gaps of these materials lie between 1.0 eV and 1.7 eV on changing the [Zn]:[Fe] and [S]:[Se] ratios in the material. These band gaps are ideal for absorber material in thin film solar cells. The sheet resistance of the materials are good for polycrystalline CZTS PV-cells. The structural parameters for the films do not show any consistent variation with composition, and given the wide range of differing radii of the ions involved this observation is perhaps not surprising. There is a distinct irregular trend following the mole fraction of selenium (Table 1). The band gap and resistance of each film is overwhelmingly controlled by the selenium content as shown in Fig. 8. Dhurba and Kim have demonstrated the potential of such materials for solar cells.[7] We now present a viable CVD method for their deposition. The potential for the use of these materials in devices will be investigated in the future.

Acknowledgements

We thank EPSRC for funding instruments, under grant number EP/K039547/1), used for characterization of compounds. PK thanks the School of Chemistry, The University of Manchester for funding.

Notes and references

1 D. B. Mitzi, O. Gunawan, T. K. Todorov, K. Wang and S. Guha, *Sol. Energy Mater. Sol. Cells*, 2011, **95**, 1421–1436.
2 G. L. Agawane, S. W. Shin, S. A. Vanalakar, A. V. Moholkar and J. H. Kim, *Mater. Lett.*, 2014, **137**, 147–149.
3 X. Fontane, V. Izquierdo-Roca, E. Saucedo, S. Schorr, V. O. Yukhymchuk and M. Y. Valakh, *J. Alloys Compd.*, 2012, **539**, 190–194.
4 P. Bonazzi, L. Bindi, G. P. Bernardini and S. Menchetti, *Can. Mineral.*, 2003, **41**, 639.
5 T. Shibuya, Y. Goto, Y. Kamihara, M. Matoba, K. Yasuoka, L. A. Burton and A. Walsh, *Appl. Phys. Lett.*, 2014, **104**, 021912.
6 S. R. Hall, J. T. Szymanski and J. M. Stewart, *Can. Mineral.*, 1978, **16**, 131–137.
7 D. B. Khadka and J. J. Kim, *J. Phys. Chem. C*, 2014, **118**, 14227.
8 S. H. Chang, M. Y. Chiang, C. C. Chiang, F. W. Yuan, C. Y. Chen, B. C. Chiu, T. L. Kao, C. H. Lai and H. Y. Tuan, *Energy Environ. Sci.*, 2011, **4**, 4929–4932.

9 (*a*) P. Marchand, I. A. Hassan, I. P. Parkin and C. J. Carmalt, *Dalton Trans.*, 2013, **42**, 9406–9422; (*b*) M. Nyman, M. J. Hampden-Smith and E. A. Duesler, *Chem. Vap. Deposition*, 1996, **2**, 171–173.
10 M. N. McCain, S. Schneider, M. R. Salata and T. J. Marks, *Inorg. Chem.*, 2008, **47**, 2534–2542.
11 (*a*) C. R. Crick and I. P. Parkin, *J. Mater. Chem.*, 2009, **19**, 1074–1076; (*b*) M. R. Waugh, G. Hyett and I. P. Parkin, *Chem. Vap. Deposition*, 2008, **14**, 366–372.
12 K. G. U. Wijayantha, S. Saremi-Yarahmadia and L. M. Peter, *Phys. Chem. Chem. Phys.*, 2011, **13**, 5264–5270.
13 A. Tahir, M. Mazhar, M. Hamid, K. G. U. Wijayantha and K. C. Molloy, *Dalton Trans.*, 2009, 3674–3680.
14 A. Tahir, K. G. U. Wijayantha, S. Saremi-Yarahmadi, M. Mazhar and V. McKee, *Chem. Mater.*, 2009, **21**, 3763–3772.
15 (*a*) K. Ramasamy, V. L. Kuznetsov, K. Gopal, M. A. Malik, J. Raftery, P. Edwards and P. O'Brien, *Chem. Mater.*, 2013, **25**, 266K–276K; (*b*) P. Kevin, D. J. Lewis, J. Raftery, M. A. Malik and P. O'Brien, *J. Cryst. Growth*, 2015, **415**, 93–99.
16 K. Ramasamy, M. A. Malik and P. O'Brien, *Chem. Sci.*, 2011, **2**, 1170.
17 S. Mahboob, S. N. Malik, N. Haider, C. Q. Nguyen, M. A. Malik and P. O'Brien, *J. Cryst. Growth*, 2014, **394**, 39.
18 A. Adeogun, M. Afzaal and P. O'Brien, *Chem. Vap. Deposition*, 2006, **12**, 597–599.
19 (*a*) D. J. Lewis and P. O'Brien, *Chem. Commun.*, 2014, **50**, 6319; (*b*) P. Kevin, S. N. Malik, M. A. Malik and P. O'Brien, *Chem. Commun.*, 2014, **50**, 14328–14330.
20 R. A. Hussain, A. Badshah, M. Dilshad Khan, N. Haider, B. Lal, S. Ishtiaq Khan and A. Shah, *Mater. Chem. Phys.*, 2015, **159**, 152–158.
21 P. Brack, J. S. Sagu, T. A. N. Peiris, A. McInnes, M. Senili, K. G. U. Wijayantha, F. Marken and E. Selli, *Chem. Vap. Deposition*, 2015, **21**, 41–45.
22 M. A. Ehsan, T. A. Nirmal Peiris, K. G. Upul Wijayantha, M. M. Olmstead, Z. Arifin, M. Mazhar, K. M. Loa and V. McKeeb, *Dalton Trans.*, 2013, **42**, 10919–10928.
23 N. Revaprasadu, M. A. Malik and P. O'Brien, *J. Mater. Res.*, 1999, **14**, 3237; M. A. Malik, M. Motevalli and P. O'Brien, *Inorg. Chem.*, 1995, **34**, 6223; M. A. Malik, M. Motevalli, P. O'Brien and J. R. Walsh, *Organometallics*, 1992, **11**, 3136; A. A. M. Memon, M. Afzaal, M. A. Malik, C. Nguyen, P. O'Brien and J. Raftery, *Dalton Trans.*, 2006, 4499; D. J. Binks, S. P. Bants, D. P. West, M. A. Malik and P. O'Brien, *J. Mod. Opt.*, 2003, **50**, 299; C. Q. Nguyen, A. E. Adeogun, M. Afzaal, M. A. Malik and P. L. O'Brien, *Chem. Commun.*, 2006, 2182; M. A. Malik, M. Motevalli, T. Saeed and P. O'Brien, *Adv. Mater.*, 1993, **5**, 653; A. Panneerselvam, C. Q. Nguyen, M. A. Malik, P. O'Brien and J. Raftery, *J. Mater. Chem.*, 2009, **19**, 419–427; N. Revaprasadu, M. A. Malik and P. O'Brien, *S. Afr. J. Chem.*, 2004, **57**, 40–43.
24 M. Akhtar, J. Akhter, M. A. Malik, P. O'Brien, F. Tuna, J. Raftery and M. Helliwell, *J. Mater. Chem.*, 2011, **21**, 9737–9745.
25 M. B. Hursthouse, M. A. Malik, M. Motevalli and M. P. O'Brien, *J. Mater. Chem.*, 1992, **2**, 949.
26 E. S. Schorr, V. O. Yukhymchuk, M. Y. Valakh, A. Pérez-Rodríguez and J. R. Morante, *J. Alloys Compd.*, 2012, **539**, 190–194.
27 M. Cao, B. L. Zhang, J. Huang, Y. Sun, L. J. Wang and Y. Shen, *Chem. Phys. Lett.*, 2014, **604**, 15–21.
28 S. C. Riha, B. A. Parkinson and A. L. Prieto, *J. Am. Chem. Soc.*, 2011, **133**, 15272–15275.
29 C. Jiang, J. S. Lee and D. V. Talapin, *J. Am. Chem. Soc.*, 2012, **134**, 5010–5013.
30 X. Zhang, N. Bao, K. Ramasamy, Y. H. A. Wang, Y. Wang, B. Lin and A. Gupta, *Chem. Commun.*, 2012, **48**, 4956.
31 H. Katagiri, K. Saitoh, T. Washio, H. Shinohara, T. Kurumadani and S. Miyajima, *Sol. Energy Mater. Sol. Cells*, 2001, **65**, 141–148.
32 X. Yu, A. Ren, F. Wang, C. Wang, J. Zhang, W. Wang, L. Wu, W. Li, G. Zeng and L. Feng, *Int. J. Photoenergy*, 2014, **6**, 1–9.
33 E. M. Mkawi, K. Ibrahim, M. K. M. Ali and A. S. Mohamed, *Int. J. Electrochem. Sci.*, 2013, **8**, 359–368.

Supporting Information

The Deposition of $Cu_2(Zn_yFe_{1-y})SnS_4$, $Cu_2(Zn_yFe_{1-y})SnSe_4$ and $Cu_2(Zn_yFe_{1-y})Sn(S_xSe_{1-x})_4$ Thin Films by AACVD

Punarja Kevin,[a] Mohammad Azad Malik,*[b] Paul O'Brien*[ab]

X-ray Diffraction Studies

Rietveld refinements of p-XRD patterns

Table S1: Rietveld analysis results of CZFTS thin films deposited at 350 °C using the molar ratio 2:1:0.5:0.5:1 of $[Cu(S_2CNEt_2)_2]$: $[Fe(S_2CNEt_2)_3]$: $[Zn(S_2CNEt_2)_2]$: $[^nBu_2Sn(S_2CNEt_2)_2]$ precursors in 20 ml THF. Fitted against Zn-rich $Cu_2Fe_{0.3}Zn_{0.7}SnS_4$ phase (ICDD 04-015-0225) with resultant lattice parameters a = 5.41 (2) Å and c = 10.86 (4) Å. Rwp = 2.85.

	h	k	l	m	d	2 θ
1	1	1	0	4	3.82760	23.21996
2	1	1	2	8	3.12848	28.50799
3	0	1	3	8	3.00914	29.66405
4	0	0	4	2	2.71503	32.96427
5	0	2	0	4	2.70652	33.07088
6	0	2	2	8	2.42230	37.08435
7	2	1	1	16	2.36280	38.05370
8	1	1	4	8	2.21449	40.71109
9	0	1	5	8	2.01580	44.93145
10	2	1	3	16	2.01231	45.01365
11	2	0	4	8	1.91680	47.38986
12	2	2	0	4	1.91380	47.46874
13	0	0	6	2	1.81002	50.37407
14	2	2	2	8	1.80497	50.52475
15	0	3	1	8	1.77995	51.28628
16	3	1	0	8	1.71175	53.48805
17	1	1	6	8	1.63629	56.16724
18	3	1	2	16	1.63256	56.30699
19	2	1	5	16	1.61667	56.91050
20	0	3	3	8	1.61487	56.97981
21	2	2	4	8	1.56424	59.00238
22	0	2	6	8	1.50457	61.59058
23	0	1	7	8	1.49140	62.19477
24	3	2	1	16	1.48716	62.39162
25	3	1	4	16	1.44799	64.27829
26	0	3	5	8	1.38792	67.42177
27	3	2	3	16	1.38678	67.48466
28	0	0	8	2	1.35751	69.14278
29	0	4	0	4	1.35326	69.39124
30	2	2	6	8	1.31504	71.71373
31	0	4	2	8	1.31310	71.83605
32	2	1	7	16	1.30621	72.27411
33	4	1	1	16	1.30337	72.45698
34	1	1	8	8	1.27943	74.03570
35	3	3	0	4	1.27587	74.27724
36	3	1	6	16	1.24368	76.54020
37	3	3	2	8	1.24204	76.65964

38	3	2	5	16	1.23500	77.17695
39	4	1	3	16	1.23420	77.23652
40	0	2	8	8	1.21343	78.81156
41	0	4	4	8	1.21115	78.98916
42	4	2	0	8	1.21039	79.04833
43	4	2	2	16	1.18140	81.38853
44	0	1	9	8	1.17777	81.69240
45	0	3	7	8	1.17638	81.80980

Table S2: Rietveld analysis results of CZFTS thin films deposited at 350 °C using the molar ratio 2 : 1 : 0.7 : 0.3 : 1 of $[Cu(S_2CNEt_2)_2]$: $[Fe(S_2CNEt_2)_3]$: $[Zn(S_2CNEt_2)_2]$: $[^nBu_2Sn(S_2CNEt_2)_2]$ precursors in 20 ml THF. Fitted against Fe–rich phase of $Cu_2Fe_{0.7}Zn_{0.3}SnS_4$ (ICDD: 01-015-0228) with resultant lattice parameters a = 5.42Å, c = 10.83Å and Rwp = 2.43.

	h	k	l	m	d	2θ
1	1	1	2	8	3.12702	28.52165
2	0	1	3	8	3.00404	29.71556
3	0	2	0	4	2.70833	33.04818
4	0	0	4	2	2.70757	33.05762
5	0	2	2	8	2.42227	37.08490
6	2	1	1	16	2.36399	38.03374
7	1	1	4	8	2.21093	40.77952
8	2	1	3	16	2.01152	45.03220
9	0	1	5	8	2.01121	45.03948
10	2	2	0	4	1.91508	47.43512
11	0	2	4	8	1.91481	47.44212
12	2	2	2	8	1.80550	50.50914
13	0	0	6	2	1.80505	50.52248
14	0	3	1	8	1.78097	51.25464
15	3	1	0	8	1.71290	53.44952
16	3	1	2	16	1.63314	56.28506
17	1	1	6	8	1.63281	56.29744
18	0	3	3	8	1.61484	56.98070
19	2	1	5	16	1.61468	56.98684
20	2	2	4	8	1.56351	59.03282
21	0	2	6	8	1.50202	61.70654
22	3	2	1	16	1.48806	62.34978
23	0	1	7	8	1.48769	62.36722
24	3	1	4	16	1.44755	64.30038
25	3	2	3	16	1.38701	67.47207
26	0	3	5	8	1.38690	67.47764
27	0	4	0	4	1.35416	69.33832
28	0	0	8	2	1.35379	69.36033
29	0	4	2	8	1.31371	71.79729
30	2	2	6	8	1.31354	71.80814
31	4	1	1	16	1.30417	72.40511
32	2	1	7	16	1.30392	72.42131
33	3	3	0	4	1.27672	74.21935
34	1	1	8	8	1.27640	74.24075
35	3	3	2	8	1.24265	76.61543
36	3	1	6	16	1.24250	76.62601
37	4	1	3	16	1.23453	77.21189
38	3	2	5	16	1.23446	77.21717
39	4	2	0	8	1.21120	78.98526
40	0	4	4	8	1.21113	78.99051
41	0	2	8	8	1.21093	79.00624
42	4	2	2	16	1.18199	81.33876

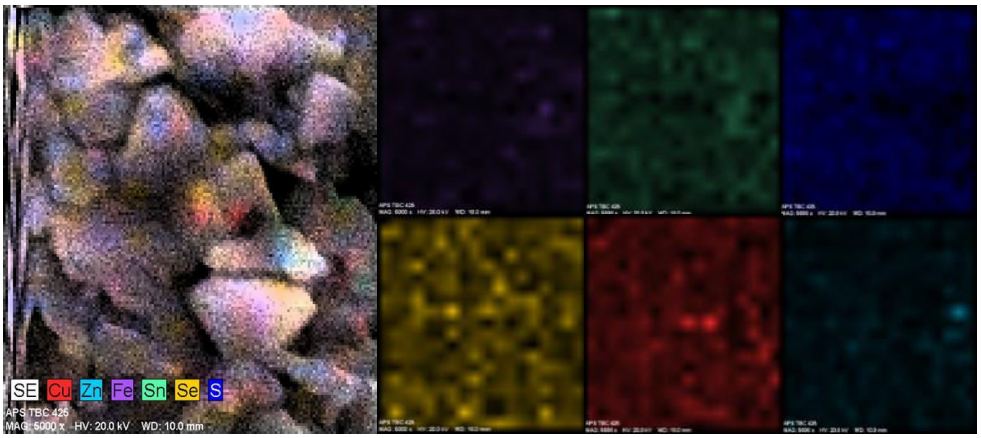

Figure S1: Elemental map of CZFTSSe thin film obtained at 350 °C.

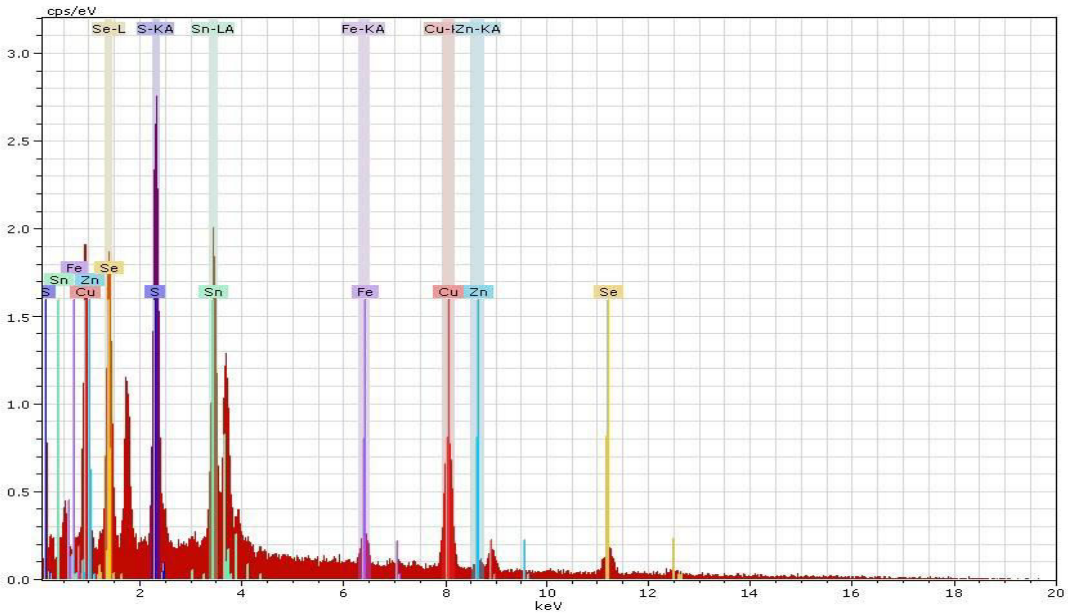

Figure S2: Elemental map/ EDX result of CZFTSSe thin film obtained at 350 °C.

Table S3: Band gap measurement from Tauc Plots.

Material	% Fe (y)	Intercept (a)	Slope (b)	BG (eV)	R^2
Cu2(ZnyFe1-y)SnSe4	3	2.66E-04	1.80E-04	1.48	8.994
Cu2(ZnyFe1-y)SnSe4	7	4.25E-05	2.89E-05	1.47	7.885
Cu2(ZnyFe1-y)Sn(SxSe1-x)4	4	4.79E-05	2.98E-05	1.61	9.192
Cu2(ZnyFe1-y)Sn(SxSe1-x)4	6	7.17E-05	4.37E-05	1.64	9.822
Cu2(ZnyFe1-y)SnS4,	3	2.49E-04	1.49E-04	1.67	8.792
Cu2(ZnyFe1-y)SnS4,	7	7.60E-04	4.42E-04	1.72	9.324

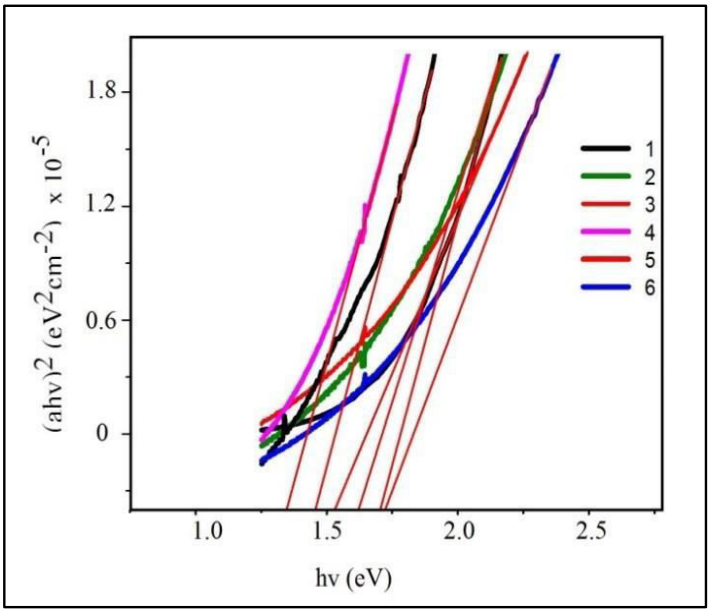

Figure S3: UV- Vis Tauc plots of CZFTSe (1,2), CZFTSSe (3, 4) and CZFTS (5, 6), thin films deposited at 350 °C using different Zn and Fe precursor composition, y represent mole fraction of Zn.

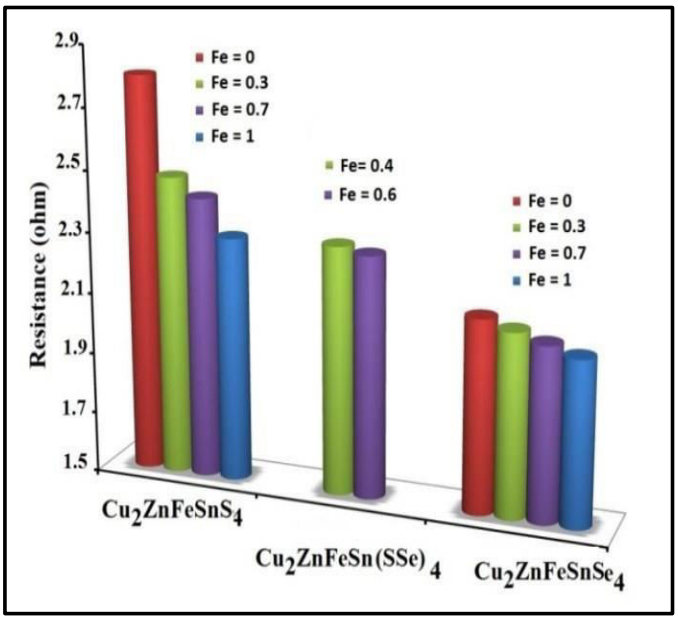

Figure S4 : Variation of electrical resistance with stoichiometric ratio of Fe for CZFTS, CZFTSe and CZFTSSe thin films deposited at 350 °C.

CHAPTER - X : PAPER - 7

"Morphology and band gap controlled AACVD of CdSe and CdS_xSe_{1-x} thin films using novel single source precursors: *Bis*(diethyldithio /diselenocarbamato) cadmium(II)"

Punarja Kevin, Yousef G. Alghamdi, David J. Lewis, Mohammad Azad Malik, *Materials Science in Semiconductor Processing*, 2015, **40**, 848–854

Materials Science in Semiconductor Processing 40 (2015) 848–854

Contents lists available at ScienceDirect

Materials Science in Semiconductor Processing

journal homepage: www.elsevier.com/locate/matsci

Morphology and band gap controlled AACVD of CdSe and CdS_xSe_{1-x} thin films using novel single source precursors: *Bis* (diethyldithio/diselenocarbamato)cadmium(II)

Punarja Kevin [a], Yousef G. Alghamdi [b], David J. Lewis [a], Mohammad Azad Malik [a,c,*]

[a] School of Materials, The University of Manchester, Oxford Road, Manchester M13 9PL, United Kingdom
[b] Department of Chemistry, Faculty of Science & Art-Rabigh, King Abdulaziz University, Jeddah, Saudi Arabia
[c] Department of Chemistry, University of Zululand, Private Bag X1001, Kwa-Dlangezwa 3886, South Africa

ARTICLE INFO

Article history:
Received 10 June 2015
Received in revised form
23 July 2015
Accepted 24 July 2015

Keywords:
Bis(diethyldiselenocarbamato)cadmium(II)
CdSe
CdSSe
AACVD
SEM

ABSTRACT

Cadmium selenide (CdSe) and cadmium sulfoselenide (CdS_xSe_{1-x}) are important semiconductor materials for photovoltaic and other optoelectronic applications. Highly crystalline thin films of CdSe and CdS_xSe_{1-x} have been deposited on glass substrates by Aerosol Assisted Chemical Vapour Deposition (AACVD) from *bis*(diethyldiselenocarbamato)cadmium(II) and a 1:1 and 2:1 mixtures of *bis*(diethyldiselenocarbamato)cadmium(II) and *bis*(diethyldithiocarbamato)cadmium(II). Films were characterised by p-XRD, SEM, EDX, Raman spectroscopy, photoluminescence (PL) and UV–vis absorbance spectroscopy. CdSe thin films showed a band gap of 1.73–1.75 eV whereas CdS_xSe_{1-x} films at 1.90–2.00 eV depending on the sulphur content in the films. PL emission and UV–vis absorbance spectra showed a clear blue shift for CdS_xSe_{1-x} films compared with CdSe. The band gap of CdSSe can be tuned by controlling the sulphur to selenium ratio in the alloy. The texture of the CdSe thin films changed considerably from randomly orientated to perfect rhombohedral crystallites by increasing the concentration of the precursors in the feed solution.

1. Introduction

CdSe is a semiconductor with a significant band gap of 1.7 eV [1,2] and finds applications in solid-state solar cells and photoconductors [3] photoanodes in photoelectrochemical (PEC) cells [4], field effect transistors and transducers [5]. Hexagonal phases of CdSe possess higher absorbance coefficients and good stability compared with other phases [6]. Ternary cadmium sulphoselenide (CdS_xSe_{1-x}) nanostructures and films are attractive as the band gap can be tuned from 1.72 to 2.42 eV which covers the entire visible spectra depending on the sulphur mole fraction in the alloy (x) [7,8]. CdS/CdSe and CdSSe materials have found applications in nano lasers [9], colour-tunable photoluminescence [10], and in tuneable magneto-optical emission [7,11].

A number of reports have appeared concerning single-source precursors for the deposition of II–VI materials [12]. Arnold and co-workers deposited a range of chalcogenides [13,14] from $M[ESi(SiMe)_3]_2$ (M=Zn, Cd, Hg; E=S, Se or Te) as precursors. A series of metal complexes with the general formula $[M(R_2PSe_2)_n]$ (M=Zn, Cd, Pb, In, Ga, Cu, Bi, Ni; R=^{i}Pr, Ph) have been synthesised and used for the growth of metal selenide thin films by CVD [15,16]. Other metal complexes with the general formula $[(M(E_2CNR_2)_2]$ (symmetrical) or $[M(E_2CNRR')_2]$ (unsymmetrical) (R, R′=alkyl, E=S, Se; M=Zn, Cd) are precursors that have been used for the deposition of II–VI thin films [17–27]. *Bis*(n-hexy(methyl)dithio/selenocarbamato)cadmium/zinc proved to be the best of the unsymmetrical derivatives for the growth of chalogenides [18–22]. Mixed alkyl/dithio- or diseleno-carbamato complexes $[M(E_2CNRR')_2]$ Where R=Me, Et, Bu^t or Me_3CCH_2, M=Zn or Cd; E=S or Se; R′=Me or Et have been used to deposit cadmium or zinc selenide thin films [23]. Imino-*bis*(dialkylphos-phineselenide) complexes $[M[(EP^iPr_2)_2N]_2]$ (M=Cd, Zn; E=S, Se) and $[M[(SePPh_2)_2N]_2]$ (M=Cd, Zn) complexes have been used as precursors for zinc/cadmium selenide films by LP-MOCVD [24,28] at temperatures between 400 and 500 °C. The mixed alkyl complex $[MeCd[(SeP^iPr_2)_2N]]_2$ was prepared from the comproportionation reaction of Me_2Cd and $[Cd[(SeP^iPr_2)_2N]_2]$ in anhydrous toluene [29]. The $[NH(SeP^iPr_2)_2]$ ligand is more thermally stable than bulky selenolate ligands, such as $[SeSi(SiMe_3)_3]^-$, and thermolysis of its complexes produces cleaner products with reduced contamination

* Corresponding author at: School of Materials, The University of Manchester, Oxford Road, Manchester M13 9PL, United Kingdom.
E-mail address: azad.malik@manchester.ac.uk (M. Azad Malik).

http://dx.doi.org/10.1016/j.mssp.2015.07.076
1369-8001/

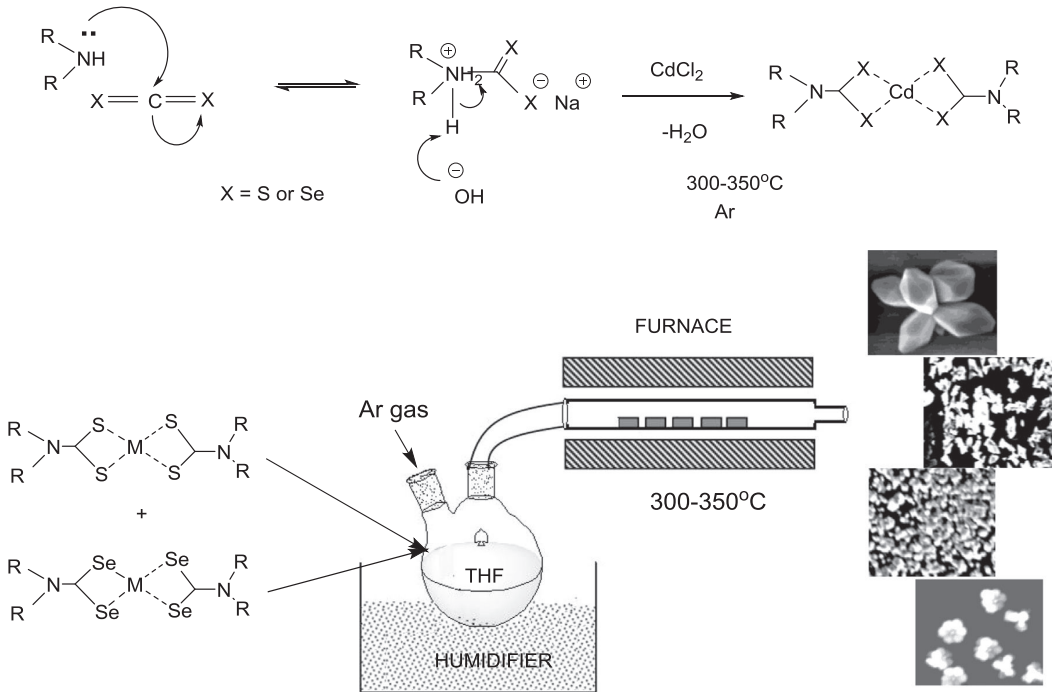

Scheme 1. Schematic diagram for synthesis of precursors and deposition of CdSe and CdS_xSe_{1-x} thin films.

caused by undesirable ligand degradation reactions. Other methods used to deposit CdSe thin films include vacuum evaporation and co-evoparation [30] molecular beam deposition [31], laser ablation [32], electrochemical deposition [33–35], spray pyrolysis [36–38], and chemical bath deposition [3,38–44]. A convenient and controllable hydrothermal synthetic method based on a reaction in an aqueous system to produce CdSe nanostructures of different sizes and shapes was reported [44]. Recently CdSe nanoparticles were prepared through a cetyltrimethyl ammonium bromide (CTAB) assisted hydrothermal using cadmium salt and $SeCl_4$ as precursors and hydrazine hydrate ($N_2H_4 \cdot H_2O$) as reductant. The varying the amount of cadmium salt, reaction time, temperature, surfactant and molar ratio of Cd:Se:CTAB, the nanoparticles with diameters less than 20 nm were synthesised [45].

Nano crystals and thin films of of CdSSe materials have been prepared by sintering [45] and physical vapour transport with varying S mole fractions using CdS or CdSe powder as source [7]. Mane et al. investigated hexagonal CdSe and CdSSe thin films deposited by chemical bath deposition (CBD) using a Cd salt, thiourea and sodium seleno phosphinates solution mixtures [46]. $CdS_{0.5}Se_{0.5}$ films obtained by electrochemical deposition on indium tin oxide (ITO) showed highest photoelectrochemical conversion efficiency [47]. Bhushan et al. reported the PC growth and decay, and PL emission spectral studies of chemically deposited films of CdSSe with the effect of variations in the composition, doping of flux and impurity and annealing on the films [48].

To the best of our knowledge CdSe or CdSSe thin films have never been deposited by AACVD method from diselenocarbamato complexes of cadmium. Herein we report the deposition of highly crystalline hexagonal CdSe thin films from *bis*(diethyldiselenocarbamato)cadmium(II) complex and CdSSe composite from a mixture of *bis*(diethyldiselenocarbamato)cadmium(II) and *bis* (diethyldithiocarbamato)cadmium(II) complexes and their detailed optical and structural characterisation.

2. Experimental

2.1. Synthesis of precursors

Bis(diethyldiselnocarbamato)cadmium(II) $[Cd(Se_2CNEt_2)_2]$ and *bis*(diethyldithiocarbamato)-cadmium(II) $[Cd(S_2CNEt_2)_2]$ complexes were synthesised as described in literature [17].

2.2. Deposition of thin films

For the deposition of CdSe thin films 7 and 14 mmol of $[Cd(Se_2CNEt_2)_2]$ precursor was dissolved in 15 ml tetrahydrofuran (THF). Depositions were carried out at temperatures of 250 and 300 °C. For the deposition of CdSSe thin films, $[Cd(Se_2CNEt_2)_2]$ and $[Cd(S_2CNEt_2)_2]$ precursors were mixed in 1:1 (7 mmol:7 mmol) and 2:1 (14 mmol:7 mmol) molar ratios and dissolved in 15 ml THF. Depositions were carried out 300 °C.

Glass slides (1 cm × 3 cm) were used as substrates for the deposition of thin films. Substrates were thoroughly cleaned and sonicated in acetone for 30 min to remove any possible contamination. Deposition of thin films was carried out by using a homemade AACVD kit. In a typical deposition experiment, precursor complex (or a suitable combination of precursors) was dissolved in 15 ml THF taken in a two-necked 100 mL round-bottom flask. The flask was then connected with an argon gas inlet which passed through the solution and carried the aerosols generated by a PIFCO ultrasonic humidifier to the reactor tube connected to other neck of the flask and placed in a Carbolite furnace. Argon flow rate was controlled at 160 sccm through a Platon flow gauge. Carrier gas transferred the aerosol generated in the flask to the hot zone of the reactor. Thermolysis of the precursor at the hot substrate surface leads to deposition onto substrates. Synthesis of complexes and deposition of thin films are schematically represented in Scheme 1.

2.3. Characterisatiion of thin films

The p-XRD patterns were recorded on a Bruker D8 AXE diffractometer (Cu-Kα) and scanned from 2θ=20 to 80° with a step size of 0.05°. Morphology and microstructure of thin films were investigated by using a Philips XL 30 FEG scanning electron microscope and film composition was studied by energy dispersive X-ray (EDX) spectroscopy using a DX4 instrument. Raman spectra were recorded using a Renishaw 1000 Micro Raman system. UV–vis absorbance spectroscopy was carried out using a Perkin Elmer Lambda 1050 spectrophotometer. PL emission spectra were measured using HORIBA Fluorolog FL3 iHR with an excitation wavelength of 400 nm.

3. Results and discussion

Bis(diethyldithio/diselenocarbamato)cadmium(II) complexes can easily be synthesised by a single step reaction and are stable at room temperature. Both complexes are soluble in most organic solvents. Both precursors decompose in the same temperature range (*vide infra*) making them suitable to be used as a mixture in different ratios to control the sulphur or selenium concentration in the composite material. The effect of precursor concentration and deposition temperature on the stoichiometric composition and morphology of the CdSe and CdSSe thin films were studied.

3.1. Thermogravimetric analysis

Thermogravimetric analysis (TGA) of $[Cd(Se_2CNEt_2)_2]$ and $[Cd(S_2CNEt_2)_2]$ precursors were studied in the temperature range 10–600 °C under nitrogen. The weight loss curves showed major single step decompositions between 250 and 350 °C with major weight loss of 68.26% and 64.50% respectively. The final residual value of $[Cd(Se_2CNEt_2)_2]$ found to be 31.74% which is closer to the calculated weight percentage of CdSe in the precursor (32%) and the final residual mass of $[Cd(S_2CNEt_2)_2]$ found to be 35.5% close to that of CdS weight percentage (35%). Hence these materials were deemed to be highly suitable for depositing CdSe, CdS, and CdSSe thin films by AACVD within a temperature range of 250–350 °C (Fig. 1).

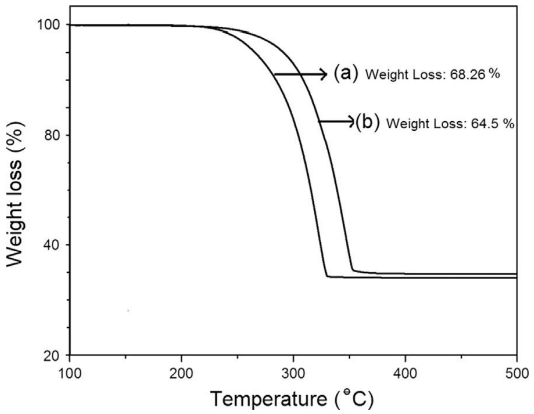

Fig. 1. (a) and (b) Thermogravimetric analysis of complexes $[Cd(Se_2CNEt_2)_2]$ and $[Cd(S_2CNEt_2)_2]$ under N_2.

3.2. Powder X-ray diffraction of CdSe thin films

CdSe thin film depositions were carried out at 250 and 300 °C using 7 and 14 mmol of $[Cd(Se_2CNEt_2)_2]$ in 15 ml THF. Negligible deposition occurred at 250 °C using both concentrations. Thin black adherent films were obtained at 300 °C at both concentrations. Fig. 2(a) shows the powder X-ray diffraction (p-XRD) diffraction patterns of CdSe films obtained at 300 °C using 7 mmol concentration of the precursor. Reflections corresponding to the (*hkl*) planes were observed at 2θ: 23.90° (100), 25.35° (002), 27.08° (101), 35.10° (102), 41.96° (110), 45.79° (103), 48.84° (200), 49.67° (112), 50.67° (201), 55.84° (202) and 79.41° (213) were matched with the hexagonal CdSe ICDD: 00-008-0459 (space group P63mc). Fig. 2(b) shows the p-XRD pattern of the films deposited at 300 °C using an increased concentration (14 mmol) of the precursor. Peaks were well matched with the hexagonal CdSe (ICDD: 00-008-0459) The intensity of peaks at the 2θ: 23.90° (100), 25.35° (002) and at 27.08° (101) indicated preferred orientation in these planes.

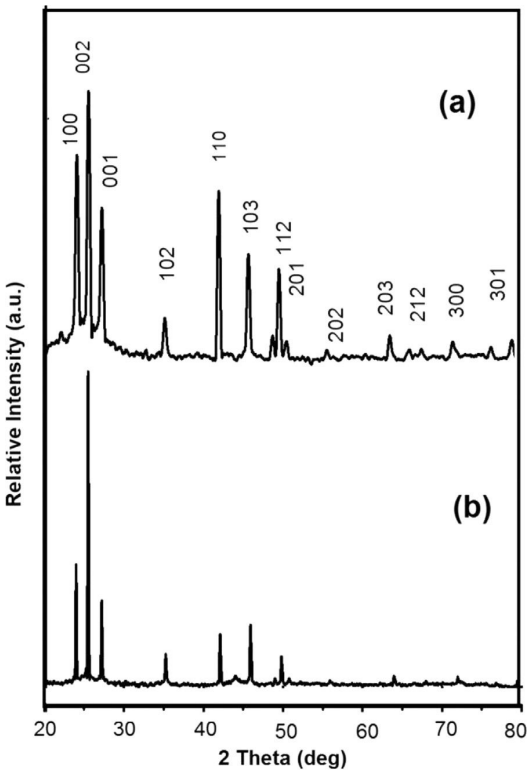

Fig. 2. p-XRD patterns of CdSe films deposited at 300 °C with input 7 mmol (a) and 14 mmol (b) precursors in 15 ml THF. The patterns are indexed with respect to hexagonal phase of CdSe (ICDD: 00-008-0459).

3.3. Scanning electron microscopy

Secondary electron SEM images of the films obtained at 300 °C using two different concentrations are shown in Fig. 3. The films deposited from lower concentration (7 mmol/15 ml THF) of the precursor showed the formation of crystallites with sizes of *ca.* 200 nm, which were found to be thinly dispersed all over the substrate (Fig. 3(a) and (b)). Films deposited from higher concentrations of the precursor (14 mmol/15 ml THF) showed the growth of perfect rhombohedral crystallites with size *ca.* 1 μm (Fig. 3(c)–(f)). Secondary electron SEM images at higher magnifications showed the crystallites forming floret like structures (Fig. 3 (f)). Quantitative EDX spectroscopy of the films showed the Cd:Se ratio to be 43.8:56.2 and 54.3:45.7 (Table 1) for the films deposited using 7 mM and 14 mM concentration of precursor solutions. We

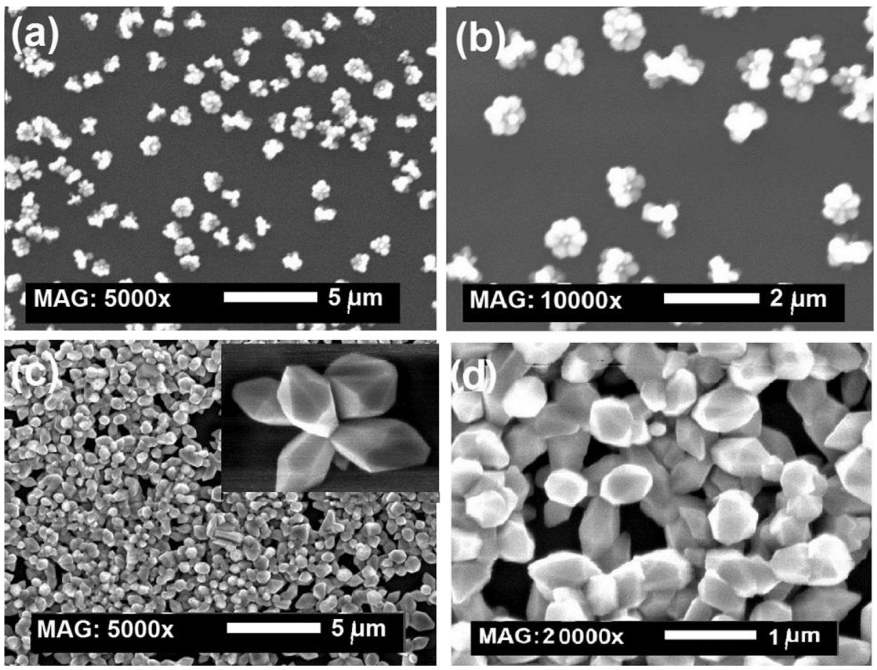

Fig. 3. SEM images of films deposited at 300 °C using different precursor ([$Cd(Se_2CNEt_2)_2$]) concentrations: (a), (b) 7 mmol; (c)–(d) 14 mmol (inset in image (c) is at 25,000 × magnification).

Table 1
EDX elemental analysis results of films obtained at 300 °C.

Precursor feed (mmol)	Line	Cd (at%)	Se (at%)
7	Kα	43.8	54.2
14	Lα-	56.2	45.7

have yet to understand as to why Se rich films are deposited at lower concentration of precursor and cadmium rich at higher concentration of precursor.

3.4. Raman spectroscopy

Raman spectra of CdSe thin films at 7 and 14 mmol precursor concentration with an excitation wavelength of 514.5 nm showed a strong peak at 210 cm^{-1} which is attributed to the optical phonon at 210 cm^{-1} (LO) and an overtone at 420 cm^{-1} (2LO) as reported previously [48,49] (Fig. 4(a)).

3.5. UV–vis absorbance and photoluminescence (PL) emission spectroscopies

UV–vis absorption spectra of films were measured and the band gap calculated by extrapolation the Tauc plots drawn using $(ahv)^2$ against hv (where a=absorbance coefficient, h=Plank's constant and $\nu=c/\lambda$, λ=wavelength in nm and c=velocity of light) displayed band gaps of 1.73 and 1.75 eV (Fig. 4(b) inset) which agree with the reported [1,2,49] values for the CdSe (Fig. 4 inset).

Photoluminescence (PL) emission spectra of CdSe thin films

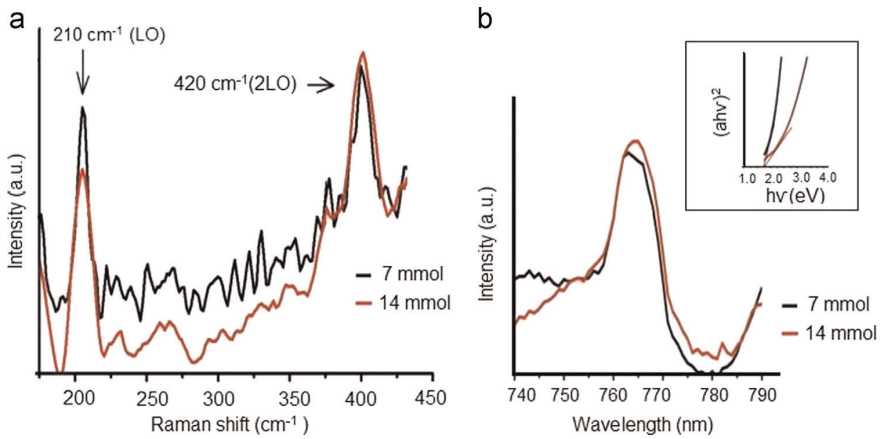

Fig. 4. (a) Raman spectra and (b) PL emission spectra of CdSe thin films obtained at 300 °C using 7 mmol (black) and 14 mmol (red) precursor concentrations. Spectra are corrected for instrument response. Inset: Tauc plots ($(ahv)^2$ *vs* hv) for CdSe thin films. (For interpretation of the references to color in this figure legend, the reader is referred to the web version of this article.)

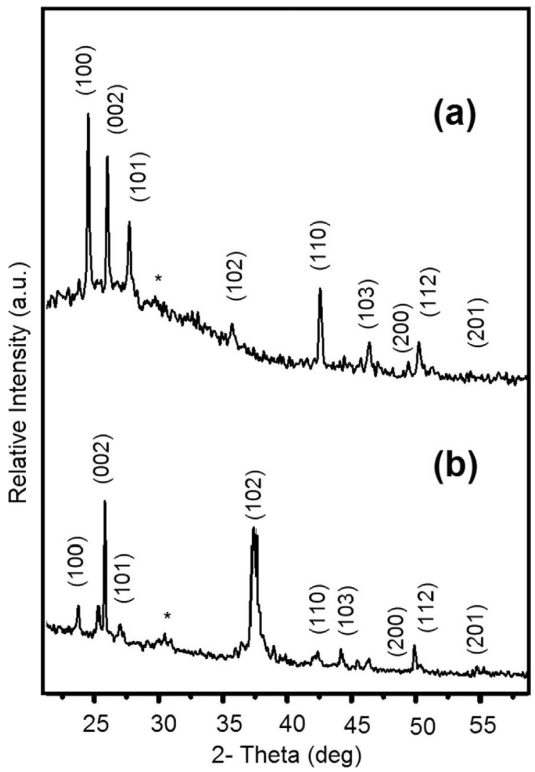

Fig. 5. p-XRD patterns for the CdSSe thin films deposited with (a) 1:1 and (**b**) 2:1 precursor mixtures at 300 °C. Peaks are indexed with respect to hexagonal CdSSe (ICDD: 00-050-0720) ratio of $[Cd(Se_2CNEt_2)_2]$ and $[Cd(S_2CNEt_2)_2]$ precursor mixtures sat 300 °C. Peaks marked with * sign are minor unidentified impurities.

deposited at 300 °C using 7 and 14 mmol concentration exhibited broad absorption and emission peaks at λ_{max} 765 nm (Fig. 4(b)), with little fine structure. The emission maxima was found be slightly higher for the CdSe thin films deposited from higher concentration of precursor than those from lower concentration of precursor.

3.6. AACVD of CdSSe

3.6.1. X-ray diffraction of CdSSe thin films

The p-XRD patterns obtained for CdSSe films deposited at 300 °C using 1:1 and 2:1 ratio of $[Cd(Se_2CNEt_2)_2]$ and $[Cd(S_2CNEt_2)_2]$ precursor mixtures are shown in Fig. 5(a) and (b) respectively.

For films obtained from the mixture of 1:1 ratio of precursor mixture gave reflections corresponding the (*hkl*) planes at 2θ: 24.29° (100), 25.89° (002), 27.69° (101), 35.00° (102), 42.88° (110), 46.89° (103), 49.93° (200), 50.79° (112), 51.78° (201) whereas the p-XRD pattern of the films deposited using 2:1 precursor mixture showed less intense peaks (Fig. 5(b)) indicating perhaps the reduced thickness of the deposited material. Both p-XRD patterns matched with the hexagonal CdSSe ($CdS_{0.42}Se_{0.58}$) with space group P63mc 186 (ICDD: 00-050-0720).

3.6.2. Scanning electron microscopy

SEM images of the films deposited from both mixtures (1:1 and 2:1) of the precursor are shown in Fig. 5(c) and (d) respectively. SEM images of the films deposited from 1:1 mixture of the precursors $[Cd(Se_2CNEt_2)_2]$ and $[Cd(S_2CNEt_2)_2]$ (Fig. 6(a)) showed the formation of small sharp edged randomly shaped crystallites with size range of *ca.* 500–1000 nm. EDX spectra of these films gave the elemental ratios as Cd (47.7%), Se (41.9%) and S (10.5%) which correspond to stoichiometric formula $Cd_{0.92}S_{0.2}Se_{0.8}$. EDX elemental mapping showed the uniform distribution of elements throughout the entire film (Fig. 6(b)–(d)), consistent with the formation of the alloy.

The films deposited from 1:2 mixture of $[Cd(Se_2CNEt_2)_2]$ and $[Cd(S_2CNEt_2)_2]$ showed random shaped crystallites (Fig. 6(e)) of varying sizes (100 nm to 2 μm). The texture appears to be less crystalline as compared to those deposited from 1:1 mixture. EDX analysis on these films of $Cd(S_xSe_{1-x})$ showed Cd (46.70%), Se (31.84%) and S (21.46%) which gave the stoichiometry as $Cd_{0.9}S_{0.4}Se_{0.6}$. Elemental mapping images of the films obtained from 1:1 mixture are given in Fig. 6(f)-(h) The mapping shows the uniform distribution of all elements (Cd, S, Se) over the entire area of the films.

3.6.3. Raman spectroscopy of CdSSe thin films

Raman spectra showed peaks at ~195 and ~400 cm^{-1} which

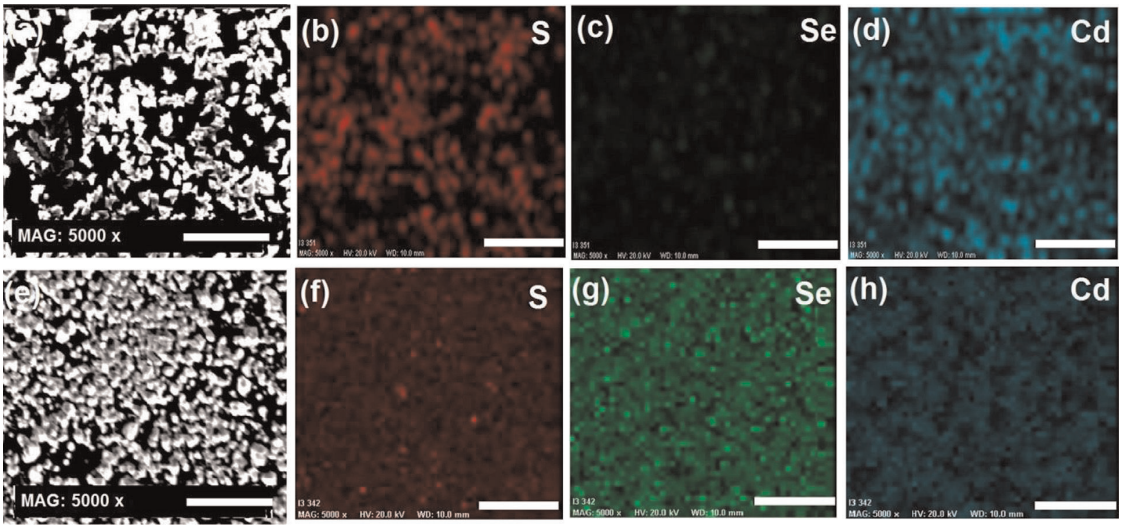

Fig. 6. (a) and (e) are the SEM images of CdSSe thin films deposited at 300 °C using 1:1 and 2:1 mmol of $[Cd(Se_2CNEt_2)_2]$ and $[Cd(S_2CNEt_2)_2]$ precursor mixtures respectively. (b)–(d) and (f)–(h) are the elemental maps of CdSSe the thin films. Scale bar shows *ca.* 5 μm.

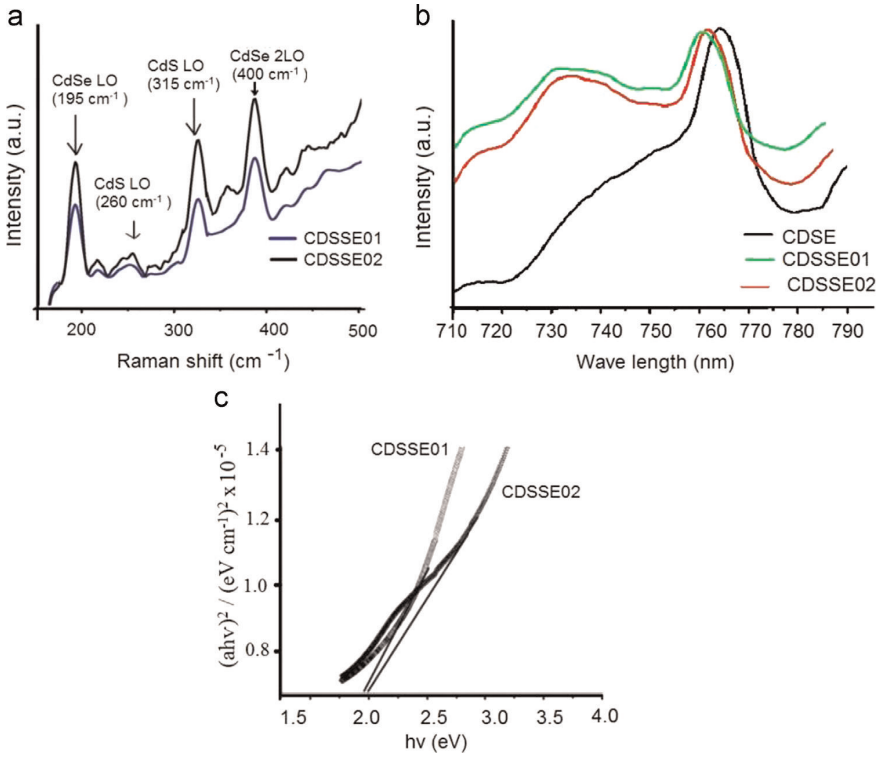

Fig. 7. (a) Raman spectra (b) PL spectra and (c) band gap of CdSSe films deposited at 300 °C using 1:1 and 2:1 ratios of $[Cd(Se_2CNEt_2)_2]$ and $[Cd(S_2CNEt_2)_2]$ precursors mixtures labelled as (CDSSE01) and (CDSSE02) respectively.

were shifted from the actual CdSe Raman LO and overtones at 212 and 410 cm^{-1} as reported previously [48,49] (Fig. 7(a)). There were some minor peaks at 260 and 310 cm^{-1} which were corresponding to CdS phases (for CdS first-order longitudinal optical phonon (LO) modes at 305 cm^{-1} and a low-frequency wing at 295 cm^{-1}[18,48–50].

3.6.4. UV/vis and photoluminescence

Fig. 7(b) shows the PL emission spectrum obtained for $CdS_{0.4}Se_{0.6}$ thin films. Broad peaks were observed at λ_{max} 758 and 726 nm. For $CdS_{0.2}Se_{0.8}$ the PL emission peaks were observed at λ_{max} 763 nm and 728 nm respectively. Owing to the similar excitonic nature of the edge emissions in both CdS and CdSe. The broadening of this excitonic peak can be attributed to the localised exci-tonic states with a broad distribution of energies [48] in alloys like CdSSe along with other effects like exciton-lattice coupling and scattering. The second peak observed ~720 nm shifts towards higher wavelength (~728) with increasing mol% of Se). This emission can be associated with the donor–acceptor transitions. In CdS type materials, the in-corporation of cations (Cd) produce shallow donor levels like S vacancies (with ionisation energies ~0.03 eV) where as that of anions (S or Se) introduce deep acceptor levels (Cd vacancies with ionisation energy typically ~1.1 eV for sulphides and ~0.6 eV for selenides) for the charge compensation of the system [48]. It can be seen that as the S content increased the emission maximum shifted towards lower wave length region which agreed with the previous literature reports [18,46–51]. The band gaps of both films were estimated by Tauc plotsof $(ah\nu)^2$ *vs* $h\nu$ (Fig. 7(c)), extrapolating the linear region of the curve. The measurements confirmed that the band gap increases as the sulphur content in the CdSSe material increases, *i.e.* a blue shift in the absorption edge consistent with PL emission spectra (*vide supra*). The band gap increased from 1.75 eV (CdSe) with no S content ($x=0$) to 1.90 and 2.00 eV as the S content in films increased from $x=0.2$ to $x=0.4$ ($CdS_{0.2}Se_{0.8}$ and $CdS_{0.4}Se_{0.6}$) [48–50].

4. Conclusions

CdSe and CdSSe thin films were deposited from diethyldiseleno-/dithiocarbamto-cadmium(II) complexes at 300 °C. The crystallite size of the CdSe deposited by using high concentration of precursor (14 mmol/15 ml THF) were found to be bigger than those obtained at lower concentrations (7 mmol/15 ml THF). The morphology of the grains changed from clusters of spherical particles to perfect rhombohedral crystallites. The band gap of CdSe decreased slightly from 1.75 to 1.73 eV as the crystallite size increased as expected. Thin films of CdS_xSe_{1-x} were deposited by using a combination of selenium and sulphur precursors in two different ratios. The band gaps of the films increased from 1.90 to 2.00 eV by increasing the sulphur content in the alloy. The morphology of the films changed from randomly shaped crystallites of different sizes to irregular lumps by increasing the amount of selenium precursor. PL showed a clear blue shift in the emission maximum by increasing the sulphur content in the CdSSe films.

Acknowledgements

PK is thankful to University of Manchester for funding. We also thank EPSRC for funding of instruments under Grant number EP/K039547/1) for characterisation of the compounds.

References

[1] S.J. Lade, M.D. Uplane, C.D. Lokhande, Mater. Chem. Phys. 68 (2001) 36–41.
[2] A.A. Yadav, M.A. Barote, E.U. Masumdar, Mater. Chem. Phys. 121 (2010) 53–57.
[3] Y. Choi, M. Seol, W. Kim, K. Yong, J. Phys. Chem. C 118 (2014) 5664–5670.
[4] J.M. Gary Hodes, David Cahen, J. Electrochem. Soc. 128 (11) (1981) 2325–2330.
[5] Herbert L. Wilson, William A. Gutierrez, J. Electrochem. Soc. 112 (1) (1965) 85–91.
[6] M. Bouroushian, Z. Loïzos, N. Spyrellis, G. Maurin, Thin Solid Films 229 (1993) 101–106.
[7] J.J. Kim, Y.L. Kim, K.H. Yoon, H.S. Song, M.S. Bae, S.H. Kim, Nanotechnology 20 (9) (2009) 095605.
[8] S. Surendran, J. Pokorný, K. Jurek, E. Bernstein, P. Malý, Mater. Sci. Eng. B 104 (2003) 54–57.
[9] Y.H.X. Duan, R. Agarwal, C.M. Lieber, Nature 421 (2003) 241–245.
[10] A. Pan, H. Yang, R. Liu, R. Yu, B. Zou, Z. Wang, J. Am. Chem. Soc. 127 (2005) 15692–15693.
[11] S.K. Apte, B.B. Kale, R.S. Sonawane, S.D. Naik, S.S. Bodhale, B.K. Das, Mater. Lett. 60 (2006) 499–503.
[12] (a) B. Ludolph, M.A. Malik, P. O'Brien, N. Revaprasadu, Chem. Commun. (1998) 1849;
(b) N. Revaprasadu, M.A. Malik, P. O'Brien, G. Wakefield, J. Mater. Res. 14 (1999) 3237;
(c) N. Revaprasadu, M.A. Malik, P. O'Brien, J. Mater. Res. 14 (1999) 3237;
(d) M.A. Malik, M. Motevalli, P. O'Brien, Inorg. Chem. 34 (1995) 6223;
(e) A.A. Memon, M. Afzaal, M.A. Malik, C. Nguyen, P. O'Brien, J. Raftery, Dalton Trans. (2006) 4499;
(f) D.J. Binks, S.P. Bants, D.P. West, M.A. Malik, P. O'Brien, J. Mod. Opt. 50 (2003) 299;
(g) M.A. Malik, M. Motevalli, T. Saeed, P. O'Brien, Adv. Mater. 5 (1993) 653;
(h) A. Panneerselvam, C.Q. Nguyen, M.A. Malik, P. O'Brien, J. Raftery, J. Mater. Chem. 19 (2009) 419–3242;
(i) A.N. Gleizes, Chem. Vap. Depos. 6 (2000) 155.
[13] B. Dabbousi, P.J. Bonasia, J. Arnold, J. Am. Chem. Soc. 113 (1991) 3186.
[14] P. Bonasi, J. Arnold, J. Inorg. Chem. 31 (1992) 2508.
[15] A. Adeogun, C.Q. Nguyen, M. Afzaal, M.A. Malik, P. O'Brien, Chem. Commun. (2006) 2179.
[16] C.Q. Nguyen, A. Adeogun, M. Afzaal, M.A. Malik, P. O'Brien, Chem. Commun. (2006) 2182.
[17] I. Abrahams, M.A. Malik, M. Motevalli, P. O'Brien, J. Organomet. Chem. 465 (1994) 73.
[18] M.B. Hursthouse, M.A. Malik, M. Motevalli, P. O'Brien, Organometallics 10 (1991) 730.
[19] M.A. Malik, P. O'Brien, Chem. Mater. 3 (1991) 999.
[20] M.A. Malik, M. Motevalli, P. O'Brien, J.R. Walsh, Organometallics 11 (1992) 3436.
[21] M.B. Hursthouse, M.A. Malik, M. Motevalli, P. O'Brien, J. Mater. Chem. 2 (1992) 949.
[22] M.A. Malik, M. Motevalli, P. O'Brien, Acta Crystallogr. C 52 (1996) 193.
[23] M.A. Malik, P. O'Brien, Adv. Mater. Opt. Electron. 3 (1994) 171.
[24] M. Afzaal, S.M. Aucott, D. Crouch, P. O'Brien, J.D. Woollins, J.H. Park, Chem. Vap. Deposit. 8 (2002) 187.
[25] M. Afzaal, D. Crouch, P. O'Brien, J.H. Park, Mater. Res. Soc. Symp. Proc. (2002) 692.
[26] K. Osakada, T. Yamamoto, J. Chem. Soc. Chem. Commun. (1987) 1117.
[27] J.G. Brennan, T. Siegrist, P.J. Carroll, S.M. Stuczynski, P. Reynders, L.E. Brus, M. L. Steigerwald, Chem. Mater. 2 (1990) 403.
[28] M. Afzaal, D. Crouch, M.A. Malik, M. Motevalli, P. O'Brien, Jin-Ho Park, J. D. Woollins, Eur. J. Inorg. Chem. (2004) 171.
[29] M. Afzaal, D. Crouch, M.A. Malik, M. Motevalli, P. O'Brien, Jin-Ho Park, J. Mater. Chem. 13 (2003) 639.
[30] J. Reicman, M.A. Russak, J. Appl. Phys. 708 (1982) 53.
[31] M. Hyugaji, T. Miura, Jpn. J. Appl. Phys. 24 (1985) 1575.
[32] G. Perna, V. Capozzi, M. Ambrico, J. Appl. Phys. 83 (1998) 3337.
[33] K.C. Mandal, O. Savadogo, J. Mater. Sci. 27 (1992) 4355.
[34] G. Gratzel, Nature 412 (2001) 338.
[35] Y.G. Gudage, N.G. Deshpande, A.A. Sagade, R.P. Sharma, S.M. Pawar, C. H. Bhosale, Bull. Mater. Sci. 30 (2007) 321.
[36] C.J. Liu, J.H. Wang, Appl. Phys. Lett. 36 (1980) 852.
[37] Y. Raviprakash, Kasturi V. Bangera, G.K. Shivakumar, Sol. Energy 83 (2009) 1645.
[38] T. Elango, V. Subramanian, K.R. Murali, Surf. Coat. Technol. 123 (2000) 8.
[39] K.R. Murali, V. Swaminathan, D.C. Triverdi, Sol. Energy Mater. Sol. Cells 81 (2004) 113.
[40] R.B. Kale, C.D. Lokande, Semicond. Sci. Technol. 1 (2005) 20.
[41] R.A. Boudreau, D.R. Rauh, J. Electrochem. Soc. 130 (1983) 513.
[42] H. Metin, S. Erat, M. Ari, M. Bozoklu, Optoelectron. Adv. Mater. 2 (2008) 92.
[43] (a) M. Froment, D. Lincot, Electrochim. Acta 40 (1995) 1293;
(b) X.W. Zhou, R.F. Lin, X.R. Xiao, Appl. Surf. Sci. 119 (1997) 203.
[44] (a) O. Niitsoo, S.K. Sarkar, C. Pejoux, S. Rühle, D. Cahen, G. Hodes, J. Photochem. Photobiol. A: Chem. 181 (2006) 306;
(b) A. Sobhani, M. Salavati-Niasari, Mater. Res. Bull. 53 (2014) 7–314.
[45] (a) A. Sobhani, M. Salavati-Niasari, J. Mater. Sci.: Mater. Electron. (2015), http://dx.doi.org/10.1007/s10854-015-3297-4;
(b) M. Elahi, N. Ghobadi, Iran. Phys. J. 2 (2008) 27.
[46] R.S. Mane, C.D. Lokhande, Thin Solid Films 304 (1997) 56–60.
[47] R.O. Loutfy, D.S. Ng, Sol. Energy Mater. 11 (1984) 319.
[48] S. Bhushan, A. Oudhia, Opto – Electron. Rev. 17 (1) (2009) 30–39.
[49] (a) S. Shevel, R. Fischer, G. Noll, E.O. Gobel, P. Thomas, C. Klingshirn, J. Lumin. 37 (1987) 45–50;
(b) J.E.B. Katari, V.L. Colvin, A.P. Alivisatos, J. Phys. Chem. 98 (1994) 4109–4117.
[50] Y.–T. Nien, B. Zaman, J. Ouyang, I.–G. Chen, C.-S. Hwang, K. Yu, Mater. Lett. 62 (2008) 4522–4524.
[51] K.K. Nanda, S.N. Sarangi, S.N. Sahu, S.K. Deb, S.N. Behera, Phys. B: Condens. Matter 262 (1999) 31–39.

CHAPTER - XI : PAPER - 8

"The deposition of $Cu_2ZnSnS_{(1-x)}Se_x$ thin films with tunable band gaps"

Punarja Kevin, Gary Harrison, Mohammad Azad Malik, Paul O'Brien

Re-submitted in *RSC Adv.* pages 1-9.

Journal Name

ARTICLE

The deposition of $Cu_2ZnSnS_{(1-x)}Se_x$ thin films with tunable band gaps

Received 00th January 20xx,
Accepted 00th January 20xx

DOI: 10.1039/x0xx00000x

www.rsc.org/

Punarja Kevin,[a] Gary Harrison,[b] Paul O'Brien*[a,b]

ABSTRACT: Thin films of CZTSSe with band gaps ranging from 1.0 to 1.6 eV have been deposited using a molecular-precursor approach in Aerosol Assisted Chemical Vapor Deposition (AACVD). The [S]:[Se] ratio has been varied and plays a key role in controlling the structure, morphology, electrical and optical properties of the deposited films. A Vegard-type analysis on the collected results showed a direct correlation between the concentration of selenium in the precursor mixture and key performance parameters of the deposited films.

Introduction

The family of materials described by the formula $Cu_2ZnSn(S_{1-x}Se_x)_4$ (CZTSSe) are potentially leading candidates as absorbers for PV-solar cells.[1] The materials are relatively cheap, environmentally benign, of low toxicity and based on earth abundant elements; they have band gaps ranging from 1.0 to 1.5 eV and absorption co-efficient between 10^4 and $10^5 cm^{-1}$.[2-3] A power conversion efficiency of ~12 % has been reported for CZTSSe based solar modules prepared by a hydrazine based solution processes followed by spin coating.[4,5] Such materials offer a promising alternative to those containing gallium, indium or cadmium.[4,5]

Several routes have been used to the deposition of $Cu_2ZnSn(S_{1-x}Se_x)_4$ thin films including vacuum based methods including: thermal co-evaporation of the constituent elements,[6] sputtering,[7] melt growth,[8] and other techniques sol-gel,[9] electro deposition,[10] pulsed laser deposition[11] and microwave irradiation.[12] There are many reports describing the synthesis of $Cu_2ZnSn(S_{1-x}Se_x)_4$ nanoparticles and their subsequent use as nano-inks for thin film solar cells. However, owing to complexity of the $Cu_2ZnSn(S_{1-x}Se_x)_4$, these methods often lead to the formation of binary phases and precise stoichiometric control of the composition of the material is still a challenge. Routes to CZTSSe and related materials have been reviewed.[12]

A wide range of materials have been prepared by AACVD over the last two decades. One main advantage of AACVD is that it does not require volatile precursors; the complex should be soluble in an appropriate solvent and is atomised. It is also potentially useful in depositing thin films with uniform composition that can be used in many applications. These materials include SnS,[13] CZTS,[14] $CuInSe_2$,[15] $CuGaSe_2$,[15] $CuIn_{0.7}Ga_{0.3}Se$,[15] MoS_2,[16] inorganic–organic perovskites $(CH_3NH_3)PbBr_3$,[17] SnSe and Cu_2SnSe_3,[18] FeSe,[19] and $BiVO_4$.[19] Very recently Carmalt *et al.* reviewed the importance of AACVD route which also highlighted it as an efficient technique in scaling up of hybrid perovskite film towards industrial deployment.[20]

The deposition of CZTSSe is quite challenging and the [S]:[Se] ratio plays a crucial role in determining the properties of the material. There are no reports in the literature on the deposition of this material by Aerosol Assisted (AA) CVD. We have previously used a series of molecular complexes to deposit the binary and ternary materials.[21] We now report the deposition of $Cu_2ZnSnS_{(1-x)}Se_x$ by AACVD using a mixture of dithio-/diselen-carbamato complexes of Zn, Sn and Cu and the acetylacetonato or acetates of Cu or Sn. Different precursor ratios are used to control the stoichiometry of the alloy.

Experimental Section

Synthesis of metal-organic precursors

The metal-diethyldithioithiocarbamato complexes: $[Cu(SCNEt)_2]$ (**1**), $[Zn(S_2CNEt)_2]$ (**2**) and $[Bu_2Sn(S_2CNEt)_2]$ (**3**), were prepared by the metathesis of $[Na(SCNEt_2)]$ with $Cu(NO_3)_2$, $Zn(NO)_3$ or Bu_2SnCl_2 respectively in methanol (Scheme **1**).[22-29] The metal-selenocarbamato complex $[Zn(Se_2CNEt)_2]$ (**4**), was prepared as described in literature (Scheme **1**).[30] The metal-acetylacetonato complexes $[Cu(acac)_2]$ (**5**) and metal acetate $[Sn(OAc)_4]$ (**6**) were purchased from Sigma Aldrich and used as purchased.

Deposition of thin film

The thin films were deposited using AACVD. Glass slides (1 cm x 2 cm) were used as substrates for the deposition of thin films.

[a] School of Chemistry, The University of Manchester, M13 9PL
[b] School of Materials, The University of Manchester, M13 9PL
[c] Corresponding author: Paul. O'Brien, email : paul.o'brien@manchester.ac.uk

Electronic Supplementary Information (ESI) available: [containing Rietveld refinements Tauc plots, Sheet resistance, Vegard calculation data and individual Vegard plots.]. See DOI: 10.1039/x0xx00000x

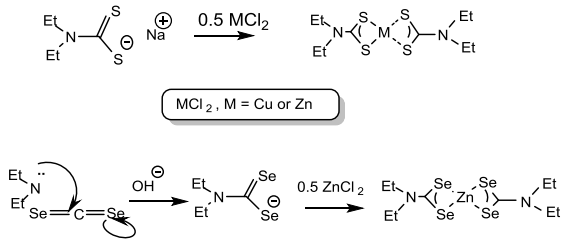

Scheme 1: Synthetic scheme for metal-organic complexes

Substrates were thoroughly cleaned and sonicated in acetone for 30 minutes before deposition. In a typical deposition experiment, the precursor complex (or a suitable combination of complexes) was dissolved in 20 mL THF and taken into a two-necked 100 mL round-bottom flask. The round-bottom flask was held in a water bath above the piezoelectric modulator of a PIFCO ultrasonic humidifier (model 1077). The aerosol droplets of the compounds thus generated were transferred into the hot-walled zone of the reactor by the carrier gas (Ar). The argon flow rate was controlled at 200 *sccm* by a Platon flow gauge. The solution was atomized and thin films were deposited at temperatures between 350 and 400 °C.

Depositions were carried out by using mixtures of $[Cu(S_2CNEt)_2]$, $[Bu_2Sn(S_2CNEt)_2]$, $[Zn(Se_2CNEt)_2]$ and $[Zn(S_2CNEt)_2]$ (Experiment 1-6) in different ratios (Table1) $[Cu(acac)_2]$ (3.7 mmol), $[Sn(OAc)_4]$ (1.8 mmol) and $[Zn(Se_2CNEt)_2]$ (1.8 mmol) (Experiment 7) all were from 20 mL of solution THF (Scheme. 2 and Table. 1).

Methods Used For the Characterization of Films

The p-XRD patterns were recorded on a Bruker D8 AXE diffractometer using Cu-Kα radiations. Rietveld analysis was carried out using the Topaz software package with the X'pert High Score Plus. The samples were mounted flat and scanned between 10 and 120° in a step size of 0.02 with a varying count rate depending upon the sample quality. The morphology and microstructure of thin films were investigated by using a Philips XL 30 FEGSEM and film composition was studied by EDX analysis using a DX4 instrument at 20 KV with WD 10 mm. Raman spectra measurements taken using a Renishaw 1000 Micro Raman system with an excitation wavelength of 520 nm, the measurement range set from 100 to 700 cm^{-1}. UV-VIS measurement carried with a Perkin Elmer Lambda 1050 spectrophotometer (PSI) and scanned across the range from 250–1000 nm. Electrical resistance measured were carried out using a Jandel four probe conductivity meters at room temperature using 1 μA current. XPS analysis was carried out by using a Kratos Axis Ultra in the School of Materials in the University of Manchester.

Results and Discussion

Thermogravimetric Analysis

Thermogravimetric analysis showed that all compounds undergo decomposition in the range 250-400 °C which makes them suitable for the deposition of CZTSSe thin films. Similar complexes were used in the deposition of CZTS thin films by AACVD.[22-29]

Optimization of Deposition Conditions

Initially the CZTS thin films were deposited using a 2:1:1 ratio of the [Cu], [Zn] and [Sn] precursors at 350 , 380 , 400 and 450 ℃ to find the optimum deposition temperature. The films deposited at all temperatures were thick black and adherent. Consolidated EDX measurements for the films are shown in the supplementary information Table S1. As the deposition temperature is increased the amount of Sn in the film decreases whereas the Zn composition increased and gave a [Cu]:[Zn]:[Sn]:[S] = 1.96:1.00:1.15:3.54 results at 400℃. The p-XRD patterns of the films deposited at these temperatures are shown in supplementary information Figure S1.

Based on these results the temperature for the rest of the experiments was set to 400℃ with a deposition time of 50 min and an Ar flow 200 *sccm.* Figure (1) shows p-XRD patterns of the thin films deposited at 400℃ using different ratios of precursor see Table 1 and Scheme 2.

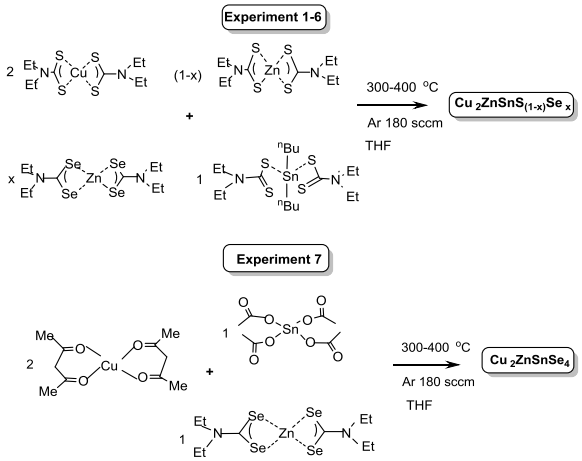

Scheme 2: Deposition of CZTSSe thin films by the AACVD method using mixture of precursors.

Effect of Precursor Composition on the Stoichiometry and Morphology of CZTSSe Thin Films

The p-XRD patterns of the films deposited at 40)℃ using precursor mixture in experiment 1 correspond to the kesterite CZTS (ICDD: 26-0575) (F-43m space group, a = 5.431 Å) (See Figure1). Rietveld analysis of the p-XRD patterns gave a good match with the F-43m space group of CZTS (Figure S2(a)), R_{wp} = 4.58, a = 5.431(1) Å with the d(112) peak at 2θ = 28.45°. Details of 2θ and d-spacing values are shown in supplementary information Table S2. The p-XRD patterns for the films deposited from experiments 2 and 3 were analysed using the standard p-XRD patterns of CZTS (ICDD: 26-0575) and CZTSe (ICDD: 52-0868). The 2θ position of d(112) planes of the films at 28.25 and 28.15° were very close to those of the

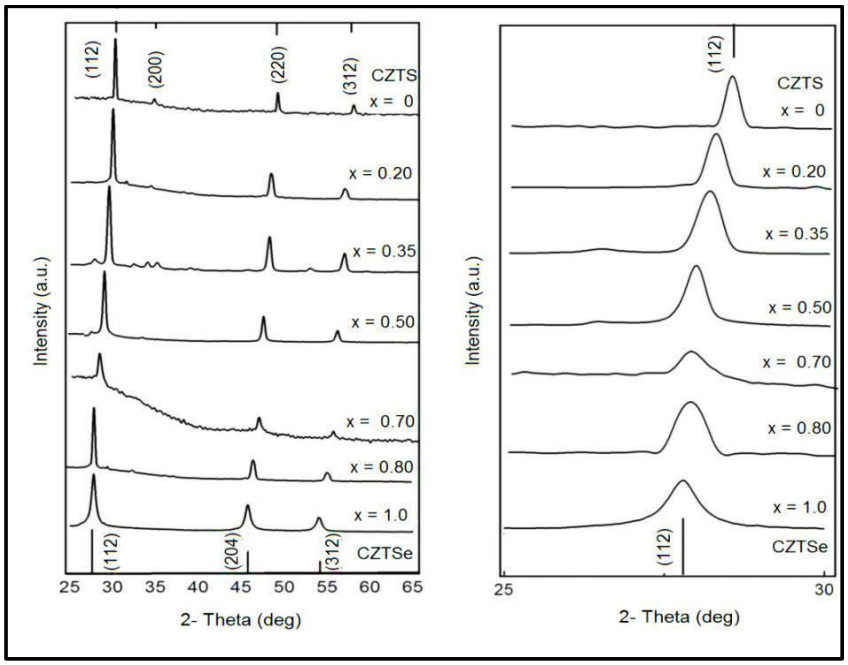

Figure 1: p-XRD patterns of $CZTS_{(1-x)}Se_x$ films with x = 0 to 1 at 400℃ (left). Stick patterns (black) shows standard patterns for CZTSe (ICDD: 52-0868) and stick patterns on top are the standard peaks of CZTS (ICDD: 26-0575). The region for the d(112) plane reflection (25- 30º) is expanded in the right hand diagram.

CZTS d(112) planes from the reference patterns (28.45°).The p-XRD patterns of the films deposited from experiment 2 on Rietveld refinement, did not give a good fit with any known phases of CZTS and CZTSe and the calculated lattice constant was a = 5.489 Å for these films. Films deposited from experiment 3 gave The refined lattice constant as a = 5.505(0) Å with an R_{wp} = 6.44 (Figure S2(b)). We can see evidences of some extra peaks which correspond to ZnS phases. Details of 2θ and d-spacing values are shown in supplementary information (Table S3).

The precursor mixture used in experiments 4 contained equal amounts of the zinc selenium and sulfur complexes with the concentration of the others the same as in other experiments (Table 1). Deposition from the mixture gave uniform dark brown films. The d(112) peak at 27.99° from the p-XRD patterns showed clear shift from the parent 2θ values.

The Rietveld analysis fitted well with the cubic F-43m space group R_{wp} = 7.2 (Figure S2(c)). The measured lattice parameters were a = 5.532(3) Å which found to be in between the F-43m space group with a = 5.431 (ICDD: 26-0575) of CZTS and I-42m space group with a = 5.690 Å (ICDD: 52-0868) of CZTSe. Detailed d-spacing and 2θ angles are given in supplementary document Table S4.

The 2θ values for the d(112) planes for the films from experiment 5 and 6 were at 2θ values of 27.77° and 27.72° respectively. The p-XRD patterns did not show a good fit for the CZTS or CZTSe structures. In experiment 7 no sulfur precursor was added, a mixture of $[Cu(acac)_2]$, $[Sn(OAc)_4]$ and $[Zn(Se_2CNEt)_2]$ was used for the deposition. The mixture was homogenous with good solubility in THF and the thermal decomposition temperatures range of these precursors was in line with that of the other used. The resultant films were thick and black in colour. The p-XRD patterns of these films correspond to standard ICDD: 52-0868 for tetragonal $Cu_2ZnSnSe_4$ (CZTSe) with I-42m space group, a = 5.690 Å. The d(112) peak was at 2θ = 27.59°. The p-XRD patterns on Rietveld analysis (Figure S2(d)) showed a near perfect match to the I-42m space group of CZTSe (ICDD: 52-0868), R_{wp} = 4.58 and a = 5.693(3) Å. Details of 2θ values are given in supplementary information (Table S5).

Figure 2 shows the SEM images for the films deposited from all seven precursor mixtures at 400ºC. The thin films deposited by Experiment 1 had an entirely different morphology from the others. The crystallites appear spherical at lower magnification but at higher magnification they appear to be hexagonal crystallites uniformly dispersed over the entire area of the substrate with crystallites size ranging from 400-500 nm. The SEM images of films deposited from mixtures 2 or 3 gave different shapes and sizes of crystallites

as compared to those deposited from the other mixtures. Mixture 4 gave a thick layer of flakes with rogue edges with sizes from 1 to 2 µm. This morphology significantly changed for mixture 5 which gave a network of plate like crystallites with sizes from 1 to 1.5µm whereas the films deposited from mixture 6 gave evenly distributed irregular crystallites with similar size range. The morphology of the films deposited from mixture 7 showed clusters of irregular crystallites with sizes in the range of 300-400 nm evenly spread on the entire area of the substrate.

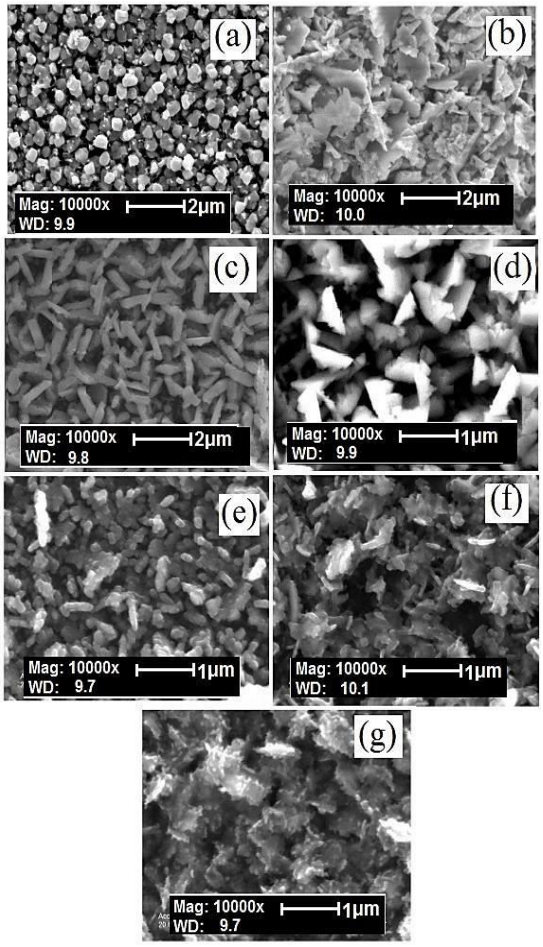

Figure 2: (a) - (f) SEM images of $CZTS_{(1-x)}Se_x$ thin films deposited at 400 °C for x values ranging from 0 to 1 from experiments 1 to 7.

All these results showed good control of Se stoichiometry as compared to electrochemically deposited CZTSSe films.[31] The absence of binary phases eg. ZnSe or $Cu_{2-x}Se$ seems to be promising as compared to the work of Fan et al.[31-33] which used a very high substrate temperature and insufficient Se-supply. The method works at lower temperature as compared to some methods reported previously.[31-39]

EDX elemental map gave uniform composition of elements throughout the films from experiment 4 (Figure 3). The results are in good agreement with those for CZTSSe powders with a Cu-poor and Zn-rich composition of $Cu_{1.9}Zn_{1.25}Sn(S_{0.4}Se_{0.6})_{4.5}$ deposited by printing and high pressure sintering processes at ~ 600 °C temperature.[32] The component elements are shown in different colours. EDX analysis of all films deposited at various combinations and composition of mixtures are shown in Table 1 It is clear from the analysis that the ratio of [S]:[Se] can be controlled by changing the ratio of $[Zn(Se_2CNEt)_2]$ and $[Zn(S_2CNEt)_2]$ in the precursor mixture.

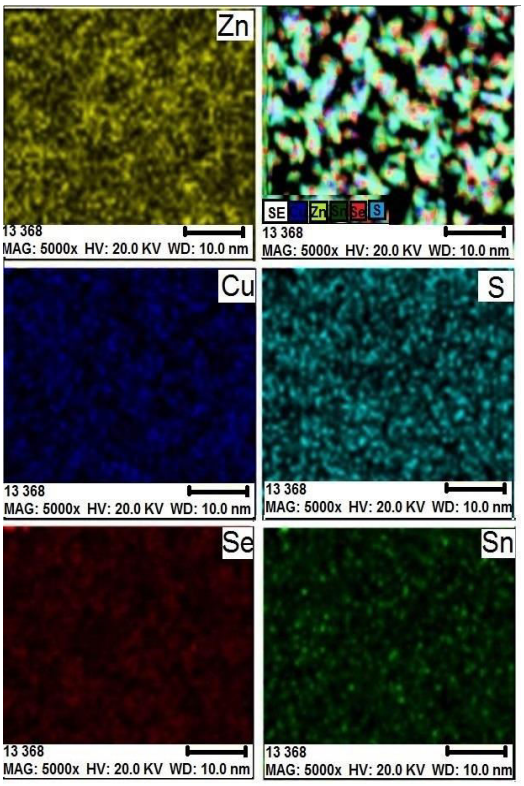

Figure 3: Elemental maps of $CZTS_{(1-x)}Se_x$ thin films deposited at 400 °C with Se precursor concentration (0.5) and Se EDX percentage x = 0.5, from experiment 4. Scale bar *ca* 2 µm.

X-ray Photoelectron Spectroscopy (XPS) measurement

Films deposited from experiment 4 were analysed by XPS to find the valence state of each metal (Figure 4). The valence state of Cu and Sn were Cu (I) and Sn (IV) respectively based on their peak splitting values. The value of Cu $2p_{1/2}$ and Cu $2p_{3/2}$ were at 945 and 928 eV respectively. The Binding Energies (BE) for $S3d_{3/2}$ and Sn $3d_{5/2}$ were found to be 493 and 483 eV respectively. The BE value 1016 eV showed Zn $2p_{3/2}$ in Zn^{2+} state. The BE of 2p peaks for S was lying in the range of 170 to 178 eV which corresponds to the sulphide states. Selenium peaks appeared at

Table 1: Molar concentrations of precursors used in each experiment, stoichiometric composition by EDX analysis, space group and calculated lattice parameters of the $CZTS_{(1-x)}Se_x$ films deposited 400 °C.

Exp No	Millimolar concentration of Precursors							Stoichiometric Composition of deposited thin films						Lattice parameters (p-XRD)	
	(1)	(2)	(3)	(4)	(5)	(6)	% Se	Cu	Zn	Sn	S_{1-x}	Se_x	Stoichiometric formula	Space group	a (Å)
1	3.70	1.80	1.80	-	-	-	0	26.0	13.2	15.20	45.6	0	$Cu_{2.0}Zn_{1.0}Sn_{1.1}S_{3.5}$	F-43m	5.431(1)
2	3.70	1.45	1.80	1.45	-	-	0.20	24.3	13.6	15.9	32.9	13	$Cu_{1.8}Zn_{1.0}Sn_{1.2}S_{2.4}Se_{0.95}$	F-43m	5.489(9)
3	3.70	0.55	1.80	1.25	-	-	0.35	22.4	13.1	17.9	33.0	13.7	$Cu_{1.7}Zn_{1.0}Sn_{1.4}S_{2.5}Se_{1.1}$	F-43m	5.505(0)
4	3.70	0.90	1.80	0.90	-	-	0.50	22.8	12.0	9.60	28.1	27.1	$Cu_{1.9}Zn_{1.0}Sn_{0.9}S_{2.3}Se_{2.2}$	F-43m	5.532(3)
5	3.70	1.17	1.80	0.63	-	-	0.70	27.5	12.7	14.3	18.3	27.5	$Cu_{2.2}Zn_{1.0}Sn_{1.1}S_{1.5}Se_{2.5}$	F-43m	5.590(9)
6	3.70	1.40	1.80	0.40	-	-	0.80	21.8	13.4	12.6	12.0	34.5	$Cu_{1.7}Zn_{1.0}Sn_{1.0}S_{0.9}Se_{2.7}$	I 42m	5.621(2)
7	-	-	-	1.80	3.70	1.80	1	22.4	14.4	10.7	0	52.4	$Cu_{1.9}Zn_{1.2}Sn_{0.9}Se_{4.3}$	I 42m	5.693(3)

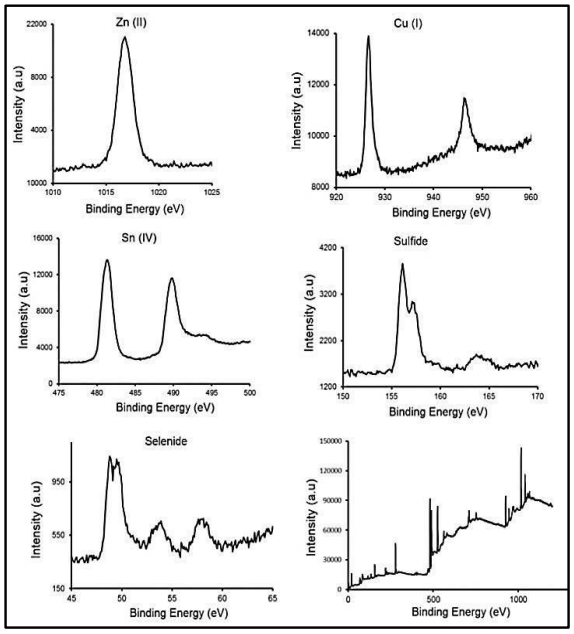

Figure 4: High resolution XPS analysis of $CZTS_{(1-x)}Se_x$ thin films deposited at 400 °C, x = 0.5 from experiment 4.

160 eV also between 50-56 eV for selenide states. The XPS depth profiling results presented by Wu et al. matched well with values of BE and valence state from this study.[32,33] The BE values also agree well with the reported values for Cu, Sn, Sn, S and Se in their respective valence states of Cu(I), Sn (IV), Zn (II),S (II) and Se (II) respectively.[32,33]

Raman spectroscopic studies

Raman spectra of all the films are given in Figure 5. The films deposited from mixture 1 showed a single peak at 196 cm^{-1} which correspond to the A_1 Raman mode for CZTSe confirming the p-XRD and EDX analysis. Raman spectra of the films deposited from mixture 2 to 4 gave two distinct Raman peaks around 196 and 338 cm^{-1} which corresponds to the Se and S stretches, the A_1 Raman modes for CZTSe (196 cm^{-1}) and CZTS (340 cm^{-1}) respectively.[20,21,38,39] These results are similar to the results presented by He *et al.* [38] The Raman spectra of CZTSSe thin films with intermediate values (i.e. x = 0.23, 0.48, and 0.69) exhibit a two mode behavior (CZTSe- like A_1 mode and CZTS-like A_1 mode). Furthermore, with increasing the S content in CZTSSe films, the CZTSe-like and CZTS-like A_1 modes shift approximately linearly towards the high frequency direction.

Raman spectrum of films deposited from mixtures 5 and 6 gave a major peak at 338 $cm^{-1}$and a low intensity peak at 295 cm^{-1} in the Raman spectra obtained for the CZTS films (x = 0). The Raman spectra results agree with the p-XRD and EDX analysis results. The positions of Raman shifts around 196 and 338 cm^{-1} give a good indication of the ratio of Se to S in the material (Figure 6). The relationship of the peak shifts with the mole fraction of S or Se is shown in Figure 6. It is clear from the figure that as the content of S increases in the material the A_1 peak move towards higher wave number ultimately corresponding to that of the CZTS Raman mode. Similarly the

decrease in the sulfur content in the material moves the Raman peak for selenium towards that of the pure CZTSe.

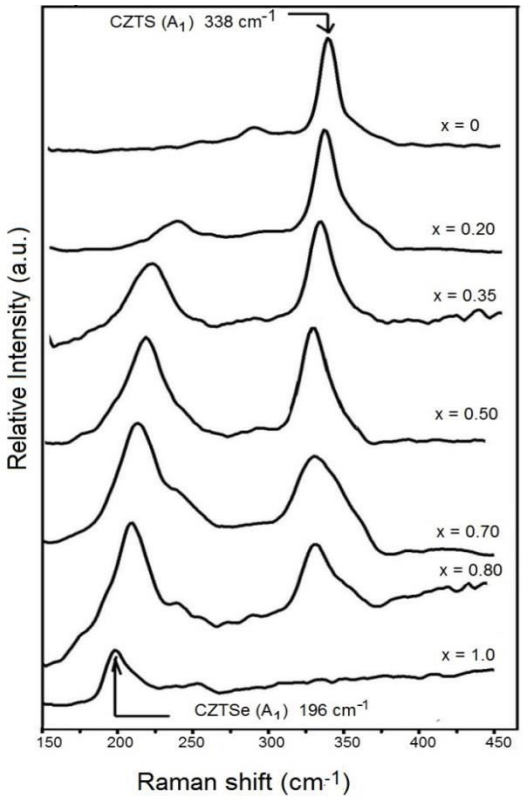

Figure 5: Raman spectra, of $CZTS_{(1-x)}Se_x$ thin films with x value ranging from 0 to 1 deposited at 400 °C from experiments 1 to 7.

Optical and electrical measurements

The band gaps of the films deposited from mixtures 1 to 5 at 400℃ are detailed in the supplementary information (Figure S3). The band gap can be tuned from 0.96 to 1.6 eV by changing the S to Se ratios in the material and increases with decreasing the selenium content. The band gap of the films deposited from mixture 4 was found to be exactly midway (~1.3 eV) between those reported for CZTS (~1.6 eV)[3,38] and CZTSe (~1.0 eV).[39] The results are promising in terms of the use of such films in PV-cells, as the band gap can be tuned to get absorption across the visible and near IR (Supplementary information Figure S3 table S6). The change in band gap is as expected for the replacement of sulfur by selenium as demonstrated previously for the CIGS and CIGSe.[2,3,34]

The room temperature sheet resistance of films (1 cm x 2 cm and thickness 1-2 µm) were measured using a four probe conductivity meter. The sheet resistance of the films decreases with increase in selenium content (supplementary information Figure S4)). The highest (11.3 kΩ/sq) and lowest (9.3 kΩ/sq) observed values of resistance of the deposited CZTSSe films are close to the reported values for CZTSSe films (6.93 kΩ/sq at 450 °C).[35] These values are in good agreement with those reported for thin films of the end materials CZTS and CZTSe.[32-38]

Vegard-type Analysis

All the measured parameters are plotted on a single Vegard-type plot (Figure 6) against the mole fraction of selenium in the precursor mixture for CZTSSe the thin films deposited at 400 °C. The measured parameters including: p-XRD (d(112)), lattice parameters a and c (from Rietveld), EDX (elemental analysis for Se), band gap, selenium-mode (A_1 mode from the Raman spectra) and electrical resistance.

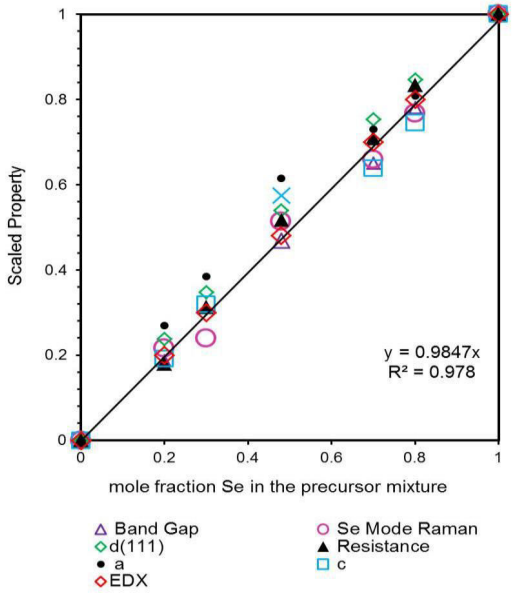

Figure 6: Overall Vegard-type analysis using all measured data for the $CZTS_{(1-x)}Se_x$ thin films deposited at 400 °C from experiments 1 to 7.

A linear correlation holds between all these values and mole fraction of selenium in the precursor mixture (Table S7 in supplementary information). These results further confirm that the composition of Se in the mixture can be controlled by changing the Se complex in the precursor mixture.

Conclusion

AACVD process relies on the solubility of the compounds, rather than their volatility and thus vastly extends the range of potentially useful precursors. CZTSSe thin films have been deposited by AACVD with different stoichiometric ratios using a mixture of a dithio-and diseleno-carbamato complexes.

The band gaps of these materials can be tuned from 0.96 to 1.6 eV by changing the sulfur to selenium ratios of the material and increases as the selenium content decreases, the sheet resistance of the films decreases with increasing selenium content. The highest (11.3 kΩ/sq) and lowest (9.3 kΩ/sq) resistance were observed for

CZTS and CZTSe respectively which correlate well with the reported values for these materials.[32-38]

The kesteritic phases show promise for photovoltaic systems.[39] One issue with such materials is their compositional complexity as compared to the more widely investigated and studied binary CdS/CdTe[40] or ternary CIGS based polycrystalline cells.[2] This issue has been addressed recently using a combinatorial approach with graded alloy films of metals prepared by Saucedo *et al.*[41] followed by selenizationation to form over 200 devices. In this way the impact of composition on performance was studied in a wide range of system, optimum metal ratios were found to be at Cu/Sn 1.6 -1.5 and Cu/Zn < 1.7. It was concluded that copper rich phases performed less well an observation that is consistent with work on CIGSe systems.[42] A related study of the composition of CZTS has also been reported.[14,43] Aydil *et at.*[44] investigated the Cu/Sn ratios in CZTS films and found out that this ratio is self- regulating and approaches 2, regardless of the initial composition of complexes materials used for depositing the films provided that there is an excess of tin compound used in the sulfidation process. The present paper demonstrates that CVD is able to provide good compositional control by changing the precursor ratios in the solution. The control of composition in CZTSSe system to optimise the performance should be possible.

ACKNOWLEDGMENTS

PK thanks the School of Chemistry, University of Manchester for funding. We also thank EPSRC for funding of instruments under grant number EP/K039547/1) used for characterization of the compounds. We thank John Walton for XPS analysis. The authors thanks Azad Malik for providing one precursor complex. We also thank the OMIC group in the School of Chemistry, The University of Manchester for electrical measurements.

ABBREVIATIONS

AACVD (Aerosol Assisted Chemical Vapor deposition), Band gap (Bg), Binding Energies (BE), Scanning Electron Microscopy, (SEM), powder X-ray Diffraction (p-XRD), X-ray Photoelectron Spectroscopy (XPS).

REFERENCES

1. T. K. Todorov, K. B. Reuter, D. B. Mitzi, *Adv Mater.* 2010, **22**, 156-159.
2. Q. Guo, G. M. Ford, W.C. Yang, B. C. Walker, E.A. Stach, H. W. Hillhouse, R. Agrawal, *J. Am. Chem. Soc.* 2010, **132**, 17384-17386.
3. R. Touati, M. B. Rabeh, M. Kanzari, *Energy Procedia*, 2014, **44**, 44-51.
4. M. T. Winkler, W. Wang, O. Gunawan, H. J. Hovel, T. K. Todorov, D. B. Mitzi, *Energy Environ. Sci.* 2014, **7**, 1029-1036.
5. D. A. R. Barkhouse, O. Gunawan, T. Gokmen, T. K. Todorov, D. B. Mitzi, *Prog. Photovoltaics*. 2012, **20**, 6-11.
6. H. Tampo, K. Makita, H. Komaki, A. Yamada, S. Furue, S. Ishizuka, H. Shibata, K. Matsubara, S. Niki, *Thin Solid Films.* 2014, **551**, 27-31.
7. A. Fairbrother, X. Fontane, V. Izquierdo-Roca, M. Placidi, D. Sylla, M. Espindola-Rodriguez, S. Lopez-Marino, F. A. Pulgarin, O. Vigil-Galan, A. Perez-Rodriguez, E. Saucedo, *Prog. Photovoltaics*. 2014, **22**, 479-487
8. A. Nagaoka, K. Yoshino, H. Taniguchi, T. Taniyama, K. Kakimoto, H. Miyake, *J. Cryst. Growth* 2014, **386**, 204-207.
9. Y. W. Li, Q. F. Han, T. W. Kim, W. Z. Shi, *J. Sol-Gel Sci. Technol.* 2014, **69**, 260-265.
10. W. Septina, S. Ikeda, A. Kyoraiseki, M. T. Harada, *Electrochim. Acta.* 2013*,* **88***,* 436-442.
11. P. Gecys, E. Markauskas, J. Dudutis, G. Raciukaitis, *Appl. Phy. A*. 2014, **114**, 231-241; K. V. Gurav , S. W. Shin , U. M. Patil , M. P. Suryawanshi , S. M. Pawar , M. G. Gang , S. A. Vanalakar , J. H. Yun , J. H. Kim *J. Alloys and Compds,* 2015, **631**, 178–182.
12. R. Kaigawa, S. Hirata, M. Sasaki, R. Klenk *Phys. Status Solidi C.* 2013, **10**, 1012-1014.
13. K. Ramasamy, V. L. Kuznetsov, K. Gopal, M. A. Malik, J. Raftery, P. P. Edwards, P. O'Brien, *Chem. Mater.* 2013, **25**, 266-276.
14. K. Ramasamy, M. A. Malik, P. O 'Brien, *Chem. Sci.* 2011, **2**, 1170-1172.
15. S. Mahboob, S. N. Malik, N. Haider, C. Q. Nguyen, M. A. Malik, P. O'Brien, *J. Crys. Growth,* 2014, **394**, 39-45.
16. A. Adeogun, M. Afzaal. P. O'Brien, *Chem. Vap. Deposition,* 2006, **12**, 597-599.
17. D. J. Lewis, P. O'Brien, *Chem. Commun.* 2014, **50**, 6319-6321.
18. P. Kevin, S. N. Malik, M. A. Malik, P. O'Brien, *Chem. Commun*. 2014, **50**, 14328-14330**.**
19. R. A. Hussain, A. Badshah, M. D. Khan, N. Haider, S. Bhajan lal, I. Khan, A. Shah, *Mater. Chem. and Phys.*, 2015, **30**, 1-7; P. Brack, J. S. Sagu, T. A. N. Peiris, A. McInnes, M. Senili, K. G. U. Wijayantha, F. Marken, E. Selli, *Chem. Vap. Deposition*. 2015, **21**, 41-45.
20. D. S. Bhachu, D. O. Scanlon, E. J. Saban, H. Bronstein, I. P. Parkin, C. J. Carmalt, R. G. Palgrave, *J. Mater. Chem. A***.** 2015, 3**,** 9071-9073.
21. N. Revaprasadu, M. A. Malik, P. O'Brien, *J. Mater. Res*.1999, **14**, 3237-3240.
22. K. Ramasamy, M. A. Malik, P. O'Brien, *Chem. Commun*. 2012, **48**, 5703-5714.
23. M. A. Malik, M. Motevalli, P. O'Brien, *Inorg. Chem*. 1995, **34**, 6223-6225.
24. M. A. Malik, M. Motevalli, P. O'Brien, J. R. Walsh, *Organometallics* 1992, **11***,* 3136-3139.
25. A. A. Memon, M. Afzaal, M. A. Malik, C. Nguyen, P. O'Brien, J. Raftery, *Dalton Trans*. 2006, 4499-4503.
26. D. J. Binks, S. P. Bants, D. P. West, M. A. Malik, P. O'Brien, *J. Mod. Optic*, 2003, **50**, 299-310.
27. C. Nguyen, A. Adeogun, M. Afzaal, M. A. Malik, P. O'Brien, *Chem. Commun*., 2006, 2182-2184.
28. M. A. Malik, M. Motevalli, T. Saeed, P. O'Brien, *Adv. Mater*. 1993, **5,** 653-654.
29. A. Panneerselvam, C. Q. Nguyen, M. A. Malik, P. O'Brien, J. Raftery, *J. Mater. Chem.* 2009, **19**, 419-427.

30. M. A. Malik, M. Motevalli, P. O'Brien, *J. Mater. Chem.* 1992, **2**, 949: M. A. Malik, P. O'Brien, *Chem.*, *Mater* 1991, **3**, 999-1001.
31. F. J. Fan, L. Wu, M. Gong, S. Y. Chen, G. Y. Liu, H. B. Yao, H. W. Liang, Y. X. Wang, S. H. Yu, *Sci. Rep.* 2012, **2**, 952-957; S. Zuo, J. Jiang, J. Ma, L. Yang, P.Yang, J. Chu, *Applied Surface Science* 2012, **258**, 7844-7848.
32. F. Gao, T. Maeda, T. Wada, Japanese *J. Appl. Phys*. 2014, **53**, 04ER11-5; K. L. Ou, J. C. Fan, J. K. Chen, C. C. Huang, L. Y. Chen, J. Ho, J. Y. Chang, *J. Mater. Chem.* 2012, **22**, 14667.
33. W. Wu, N.G. Tassi, Y. Cao, J. V. Caspar, K. Roy-Choudhury, L. Zhang, *Phys. Status Solidi RRL*, 2015, **9**, 236-240; Y. Cao, M. S. Denny, J. V. Caspar, W. E. Farneth, Q. Guo, A. S. Ionkin, L. K. Johnson, M. Lu, I. Malajovich, D. Radu, H. D. Rosenfeld, K. R. Choudhury, W. Wu, *J. Am. Chem. Soc.* 2012, **134**, 15644-15647.
34. S. Bag, O. Gunawan, T. Gokmen, Y. Zhu, T. K. Todorov, D. B. Mitzi, *Energy Environ. Sci.* 2012, **5**, 7060-7065.
35. C. Wang, C. Zhu, T. Zhang *Materials Letters* 2013**, 108**, 62–64.
36. M. Danilson, M. Altosaar, M. Kauk, A. Katerski J. Krustok, J. Raudoja, *Thin solid films,* 2011, **519**, 7404-7411.
37. X. Yu, A. Ren, F. Wang, C. Wang, J. Zhang, W. Wang, L. Wu, W. Li, G. Zeng, L. Feng, *Int. J. Photoener.* 2014, **6**, 1-8.
38. Q. Guo, G. M. Ford, W. C. Yang, B. C. Walker, E. A. Stach, H.W. Hillhouse, R. Agrawal, *J. Am. Chem. Soc.* 2010, **132**, 17384-17386; J. He, L. Sun, N. Ding, H. Kong, S. Zuo, S. Chen, Y. Chen, P. Yanga, J. Chu *J. Alloys. Compds*, 2012, **529**, 34-37.
39. D. Aaron, R. Barkhouse, O. Gunawan, T. Gokmen, T. K. Todorov, D. B. Mitzi, *Prog. Photovolt. Res. Appl.* 2012, **20**, 6-11.
40. D.W. Lane, G. J. Conibeer, D. A. Wood, K. D. Rogers, P. Capper, S. Romani, S. Hearne, *J. Crystal Growth*. 1999, **197**, 743-748
41. A. Fairbrother, M. Dimitrievska, Y. Sánchez,V. I. Roca, A. Pérez-Rodríguez, E. Saucedo*, J. Mater. Chem. A*. 2015, **3**, 9451-9455.
42. M. Kar, R. Agrawal, H. W. Hillhouse, *J. Am. Chem. Soc.* 2011, **133**,17239-17247.
43. U. Ghorpade, M. Suryawanshi, S. W. Shin, K. Gurav P. Patil, S. Pawar, C.W Hong, J. H. Kim, S. Kolekar, *Chem. Commun.* 2014**, 50**, 11258-73.
44. M. C. Johnson, C. Wrasman, X. Zhang, M. Manno, C.M. Leighton, E. S. Aydil, *Chem. Mater.* 2015**, 27***,* 2507-2514.

CHAPTER - XII : PAPER - 9

"Synthesis of Nanoparticulate Alloys of the Composition $Cu_2Zn_{1-x}Fe_xSnS_4$: Structural, Optical, and Magnetic Properties"

Punarja kevin, Simon Mcadams, Mohamad Azad Malik, Paul. O'Brien, *J. Am. Chem. Soc*. 2015, **137**, 15086-15089.

JACS
JOURNAL OF THE AMERICAN CHEMICAL SOCIETY

Communication

pubs.acs.org/JACS

Synthesis of Nanoparticulate Alloys of the Composition $Cu_2Zn_{1-x}Fe_xSnS_4$: Structural, Optical, and Magnetic Properties

Punarja Kevin,[†] Mohammad Azad Malik,[‡] Simon Mcadams,[†] and Paul O'Brien*[,†,‡]

[†]School of Chemistry and [‡]School of Materials, The University of Manchester, Oxford Road, Manchester M13 9PL, U.K.

Supporting Information

ABSTRACT: Nanoparticles of the semiconductor $Cu_2Zn_{1-x}Fe_xSnS_4$ with different mole fractions of iron (x_{Fe}) were synthesized by the decomposition of molecular precursors in oleylamine. The composition, structure, optical, and magnetic properties of the nanoparticles are reported. The parent (Cu_2ZnSnS_4) zinc material is usually reported as kesteritic and the corresponding iron phase as stannitic; with different site occupancies and tetragonalities. In the small ca. 8−10 nm particles prepared, the smooth variation in lattice parameters and other measured properties suggest that the phase change, with composition, may be absent. SQUID magnetometry suggests that the iron containing samples are ferromagnetic at 5 K and paramagnetic at 300 K.

Photovoltaic cells based on stannitic phases such as Cu_2FeSnS_4 (CFTS) have demonstrated power conversion efficiency (PCE) of 8.03%[1] and devices prepared from Cu_2ZnSnS_4 (CZTS) nanoparticles annealed in Se atmosphere gave a PCE 7.2%.[2] Hydrazine processed ($Cu_2ZnSn(S_{1-x}Se_x)_4$) CZTSSe solar cells have demonstrated PCEs of up to 12.6%.[2] It has hence been shown that the efficiency of CZTS solar cells can be improved by addition of iron.[3,4] The ionic radius of Zn^{2+} and Fe^{2+} are 0.64 and 0.66 Å,[5] and Fe shows good solubility in the CZTS lattice; hence, Zn/Fe alloying is effective and allows ready access to solid state materials of the type $Cu_2Zn_xFe_{1-x}SnS_4$ ($0 > x > 1$ CZFTS). As the Fe content in $Cu_2Zn_xFe_{1-x}SnS_4$ increases, a structural transition from kesterite to stannite is usually seen.[6,7] At higher zinc content the electronic band gap increases because of the exchange and redistribution of electrons due to lower electronegativity of Zn (1.65) than Fe (1.83).[6] The band gap energies of post-sulfurized CZFTS films can be tuned from ~1.51 to 1.36 eV depending on Zn content ($x = 0$, 1 to 0).[8] The lattice parameters calculated for the CZFTS alloys show only small changes with composition as the radius of Zn(II) ion is very similar to that of Fe(II).[9]

CZFTS thin films have been deposited by spray pyrolysis followed by sulfurization[8] and pulsed laser deposition.[10] The magnetic properties,[11,12] Mössbauer spectra,[13] structural,[14,15] and vibrational characteristics[16] of CZFTS kesterite-stannite systems have been reported. A number of reports have appeared using molecular precursors for the preparation of nanoparticles or thin films of semiconductor materials.[17] We have recently reported the deposition of thin films of CZFTS by aerosol assisted chemical vapor deposition (AACVD).[18] Herein, we report the colloidal synthesis of $Cu_2Zn_{1-x}Fe_xSnS_4$ nanoparticles using discrete molecular precursors. These materials are composed of comparatively cheap, abundant, and environmentally benign elements. The band gap can be tuned across the visible range, which makes them potentially useful in a variety of electronic, optoelectronic, and magneto electronic applications including solar energy harvesting. The magnetic properties are of interest as there are only a few studies[8,10,11,13,19] of such compounds especially in nanodispersed form.

The precursors used for the synthesis of CZFTS nanoparticles were $[Cu(S_2CNEt_2)_2]$, $[Zn(S_2CNEt_2)_2]$, $[Fe(S_2CNEt_2)_3]$, and $[^nBu_2Sn(S_2CNEt_2)_2]$. These metal−organic complexes were prepared by literature methods.[18,19] Initial screening experiments led to the selection of 220 °C and 1 h in oleylamine as good conditions for the reproducible preparation of nanocrystals (Supporting Information, Figure S1). The CZFTS samples were analyzed by energy dispersive X-ray (EDX) spectroscopy. An excellent correlation between the composition of the isolated materials and the mole fraction of the metal element (as a fraction of total metal in the solution) used for synthesis was observed. These results are summarized in Supporting Information (and Figure 1a, Table S1). The materials were analyzed by powder X-ray diffraction (p-XRD, Figure 1b). Figure S2 shows that selected *d*-spacings vary smoothly with the iron content of the material. The kesteritic to stannite transition has been discussed across the composition $x_{Fe} = 0-1$. The XRD analysis of CZFTS by Bonazzi[15] and the later neutron diffraction study by Schorr[6] are particularly useful in casting light on the complexity of the system.

Both of these reports give broadly similar lattice parameters for the two systems as a function of x_{Fe} and show a critical change in the ordering of the atoms and a phase change at $x_{Fe} = 0.3$. The neutron diffraction study suggests a slightly modified occupancy pattern for the zinc rich, kesteritic end of the series member involving disordering across all the metal sites except that of tin. The p-XRD patterns recorded in this study show only a limited number of peaks; such observations are common for small particles. However, phase identification is possible in such nanoparticles, and both CZTS and CFTS in a hexagonal form have been identified by crystallography.[20] Alivisatos et al. have demonstrated changes in the preferred form of CdTe nanocrystals with size.[21]

A least-squares method was used to index the peaks observed in the powder diffraction patterns by reference to standard patterns. The results of these calculations suggest that the tetragonality of the system is small and that the lattice parameter

Received: October 8, 2015
Published: November 20, 2015

DOI: 10.1021/jacs.5b10281
J. Am. Chem. Soc. 2015, 137, 15086−15089

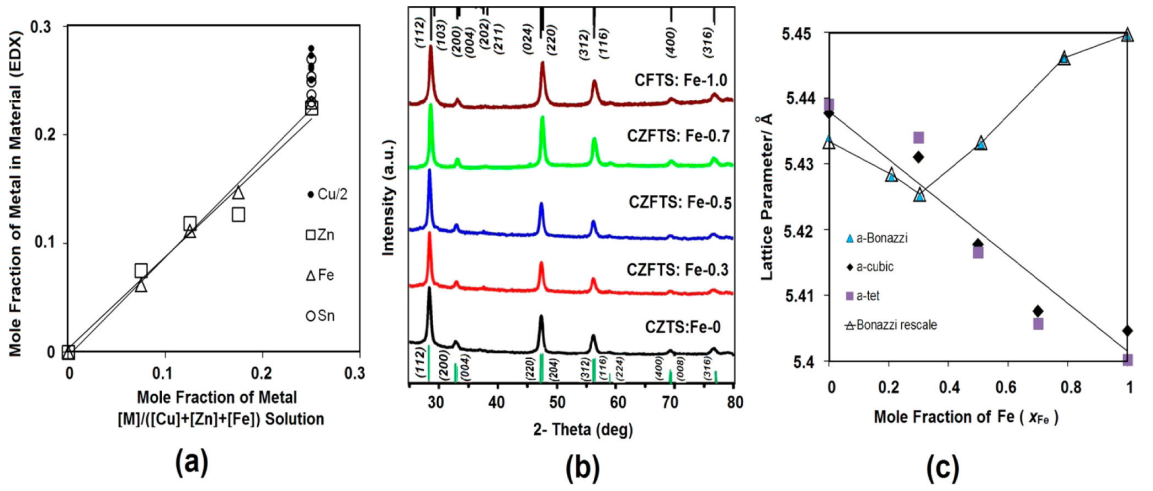

Figure 1. (a) Scatter plot showing the linear relationship between the mole fraction of metal in nanoparticles (by EDX) versus the mole fraction of metal (M) in the precursor mixture. (b) p-XRD patterns of CZFTS nanoparticles synthesized with increasing Fe/Zn ratios (220 °C, 1 h). Green and black stick patterns at the top and bottom of the panel are the standard patterns of CZTS (ICDD: 04−015−0223) and CFTS (ICDD: 04−015−0231). (c) Calculated and literature lattice parameters vs x_{Fe} for $Cu_2Zn_{1-x}Fe_xSnS_4$ nanoparticles.

a is similar to those of Bonazzi[15] and Schorr,[6] at low values of x_{Fe}. The monotonic decrease of *a* with increasing iron suggests that no phase change occurs in these small particles (Figure 1c). We have tested this model by indexing only the subset of data corresponding to the peaks we observed in the Bonazzi data sets.[15] Lattice constants *a* and *c* derived from this limited literature set are fully consistent with the results previously published and are overplotted in Figure 1c. In an interesting paper[7] Walsh et al. have shown that the *a*-values calculated by DFT for a kesteritic phase should decrease monotonically as the mole fraction of iron in the sample increases.[22] The *d*-spacings from the present samples change linearly with composition as is shown in Supporting Information Figure S2.

The morphologies and crystallinity of the CZFTS nanoparticles synthesized were investigated by high resolution transmission electron microscopy (HRTEM). The CZFTS nanoparticles were based on rhombohedra, whereas those of CFTS were oblate spheroids. A smooth transition was observed from one morphology to the other via hexagonal crystals at $x = 0.5$. All nanoparticles observed by TEM had a maximum length dimension in the range of ca. 9 ± 2 nm (Figure 2). The HRTEM images of the synthesized nanocrystals of $Cu_2Zn_{1-x}Fe_xSnS_4$ ($0 \geq x_{Fe} \geq 1$) (Figure 2) exhibit clear lattice fringes with measured *d*-spacing of 0.313(3), which can be assigned to the (112) lattice plane of the kesterite form.[20−23] These measured *d*-spacing also suggest that no phase change was occurring on changing the ratio of Zn to Fe; in agreement with the p-XRD results.

The analysis by EDX of atomic percentages in $Cu_2Zn_{1-x}Fe_xSnS_4$ nanoparticles showed the stoichiometric composition follows the amount of Fe in the precursor mixture as 26.4:11.4:0:12.9:49.3; 26.7:6.9:3.4:12.6:48.5; 29.8:6.3:6.0:13.3:44.6; 29.6:4.1:8.0:12.8:45.6; and 26.4:0:12.1:14.2:47.2, which give the stoichiometric formulas: $Cu_{2.3}Zn_{1.0}Fe_0Sn_{1.1}S_{4.3}$, $Cu_{2.7}Zn_{0.7}Fe_{0.3}Sn_{1.1}S_{4.7}$, $Cu_{2.4}Zn_{0.5}Fe_{0.5}Sn_{1.1}S_{3.6}$, $Cu_{2.4}Zn_{0.3}Fe_{0.7}Sn_{1.1}S_{3.8}$, and $Cu_{2.1}Zn_0Fe_{1.0}Sn_{1.2}S_{3.9}$, respectively (Supporting Information Table S1, Figure S3). An EDX elemental map showing the spatial distribution of the elements Cu, Zn, Fe, Sn, and S across a plane

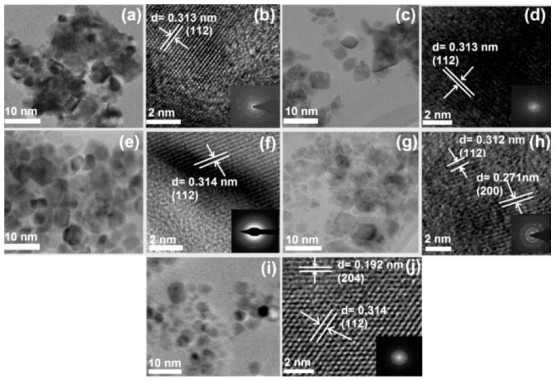

Figure 2. Bright-field TEM and HRTEM images for (a,b) CZTS (x_{Fe} − 0), (c,d) CZFTS (x_{Fe} − 0.3), (e,f) CZFTS (x_{Fe} − 0.5), (g,h) CZFTS (x_{Fe} − 0.7), and (i,j) CFTS (x_{Fe} − 1.0). Inset images show the selected area electron diffraction patterns of the same crystallites as in the associated bright field TEM and HRTEM images.

view of a sample of $Cu_2Zn_{1-x}Fe_xSnS_4$ ($x = 0.5$) was recorded (Supporting Information Figure S4) and demonstrates the homogeneity of the sample from the colocalization of the EDX signals for all elements analyzed. The composition of S was found to decrease with increasing Fe content, which agrees with other work.[8] Oxide phases can coexist with the sulfides that can compensate the sulfur deficiency in chalcogenide films.[8,24] The elemental analysis showed good control over the stoichiometry of the nanocrystals synthesized on varying the precursor composition for Zn and Fe. Figure 1a shows a linear correlation holds between the mole fractions of metal in feed and in the material formed.

X-ray photoelectron spectroscopy (XPS) was used to probe the chemical composition of the CZTS ($x = 0$), CFTS ($x = 1$), and $Cu_2Zn_{1-x}Fe_xSnS_4$ ($x = 0.5$) nanoparticles (Supporting Information Figures S5 and S6) and revealed the oxidation states of Cu, Sn, Zn, Fe, and Sn to be Cu^{1+}, Sn^{4+}, Zn^{2+}, Fe^{2+}, and S^{2-}.

DOI: 10.1021/jacs.5b10281
J. Am. Chem. Soc. 2015, 137, 15086−15089

The corresponding binding energies (BEs) for the Zn $2p_{3/2}$, Cu $2p_{3/2}$, Cu $2p_{1/2}$, Fe 2p, Fe $2p_{3/2}$, Fe $2p_{1/2}$, Sn $3d_{5/2}$, Sn $3d_{3/2}$, S $3p_{3/2}$, S $2p_{3/2}$, S $2p_{1/2}$, and S 2p are located at ~1019, 9232, 953, 711, 710, 725, 482, 492, 156, 160, 170, and 174 eV, respectively.

The as-prepared CZFTS nanocrystals were dispersed in hexane and filtered to give clear, dark brown suspensions. The band gaps have been estimated by plotting $(Ah\nu)^2$ versus $h\nu$ (A = absorbance, h = Planck's constant, and ν = frequency) and extrapolating the linear portion of the plots in the band edge region; the method of Tauc.[24] The photoluminescence spectra of nanoparticles in the range 500−800 nm were recorded in hexane solvent after excitation at 400 nm. The values were (bandgap/eV, PL max/eV ($[x_{Fe}]/[x_{Fe}] + [x_{Zn}]$)): 1.93, 1.90 (0), 1.89, 1.82 (0.3), 1.87, 1.77 (0.5), 1.85, 1.74 (0.7), and 1.79. 1.9 (1.0), respectively (Supporting Information Figure S7a and Table S2). All PL spectra maxima (Supporting Information Figure S7b) are Stokes shifted to the red by ca. 0.5 eV as expected; quantum yields for all samples were of the order of 1%. These band gap associated measurements are all at higher energy than those observed for other CZFTS systems, suggesting quantum confinement.[8] A linear correlation was found between the PL and UV−vis spectroscopic results for the CZFTS nanoparticles (Supporting Information Figure S8). The band gap of the materials can hence be tuned across the visible spectrum by varying the composition of iron content in CZTS.

Typical results for CZFTS band gaps with increasing iron content include: films deposited by spray pyrolysis 1.51−1.33 eV,[8] pulsed laser deposition 1.74−1.33 eV,[10] and AACVD with the same precursors set as in the present work gave 1.72 eV (Zn-rich) to 1.67 (Fe- rich).[18] Walsh et al.[7] used DFT calculations and predicted band gaps of kesteritic CZTS and CFTS as 1.74 and 1.54 eV, respectively; the band gap of stannitic CZTS and CFTS are calculated as 1.36 and 1.85 eV, respectively.[7]

Magnetic studies were performed at 5 and 300 K for the Fe-containing samples. There are no such studies on the nanodispersed phases of these materials.[8,10,11,13,19] At 5 K, all samples displayed hysteresis, indicating ferromagnetic behavior[10,11] with coercive fields increasing from 260.63 Oe (x = 0.3) to 736.9 Oe (x = 1.0) $Cu_2Zn_{1-x}Fe_xSnS_4$, respectively (Figure 3a). Field-dependent magnetization curves revealed all samples as paramagnetic at 300 K, with magnetization increasing with Fe content (Figure 3b) as expected.[25,26] The zero-field-cooled (ZFC) and field-cooled (FC) magnetic measurements confirmed that 5 K is below the blocking temperature for all samples as is shown in Figure 3c.[10,11,13] Stannitic CFTS has a Neel temperature as low as 6−8 K.[26,27] The magnetic moments/BM calculated for the $Cu_2Zn_{1-x}Fe_xSnS_4$ nanoparticles ($[x_{Fe}]/[x_{Fe}] + [x_{Zn}]$) were 0.020792(0.3), 0.02846347 (0.5), 0.0358049(0.7), and 0.02502683(1.0), respectively, as compared to $Zn_{1-x}Fe_xS$ (x = 0.4) (0.00659 μ_B per Fe atom) and for x = 0.6. (0.00452 μ_B per Fe atom).[28] Dense nanograined ZnO thin films doped with iron (0 to 40 atom %) showed ferromagnetic behavior with Js up to 0.10 emu/g (0.025 μB/f.u.ZnO)[29] (see also Supporting Information Figure S9).

Nanoparticles of $Cu_2Zn_{1-x}Fe_xSnS_4$ with mole fractions of Fe (x_{Fe}) from 0 to 1 had been prepared. Detailed compositional studies based on the p-XRD patterns and EDX analysis showed that the material, in contrast to bulk, maintained a stannite structure. TEM studies showed slight differences in the structures and crystallinities of the nanoparticles with changes in composition of Fe (x_{Fe}). The iron containing materials were ferromagnetic at low temperatures. Such materials may find applications in magnetoelectronic, optoelectronic, or photovoltaic applications. The fabrication of solar cells and devices using these relatively new nanoparticles are in hand and will be reported elsewhere.

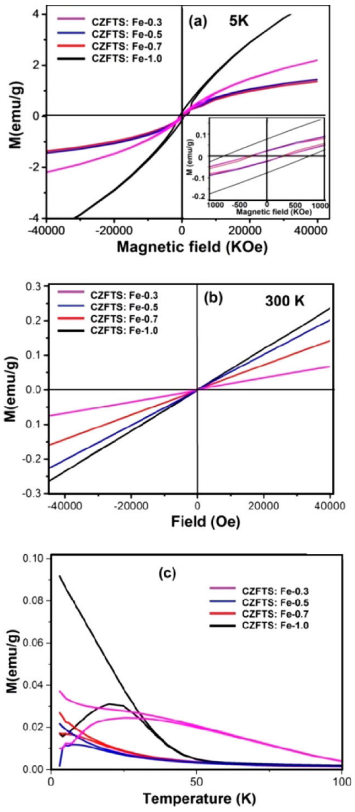

Figure 3. (a,b) Field-dependent magnetization curves of CZFTS nanocrystals at 5 K (inset: the magnification of typical hysteresis loops) and 300 K. (c) Temperature dependence of the magnetization for CZFTS (x_{Fe} = −0.3 to 1.0) nanocrystals.

■ ASSOCIATED CONTENT

Supporting Information

The Supporting Information is available free of charge on the ACS Publications website at DOI: 10.1021/jacs.5b10281.

Experimental details, characterization of nanoparticles, p-XRD detailed interpretation, elemental maps, EDX analysis, and additional optical characterization (PDF)

■ AUTHOR INFORMATION

Corresponding Author

*paul.obrien@manchester.ac.uk

Notes

The authors declare no competing financial interest.

■ ACKNOWLEDGMENTS

The authors thank EPSRC for providing the SQUID magnetometer. We thank Mathew Smith for the TEM elemental maps, Andrew Thomas (PSI) for XPS measurements, and David. J. Lewis for the PL measurements.

DOI: 10.1021/jacs.5b10281
J. Am. Chem. Soc. 2015, 137, 15086−15089

REFERENCES

(1) Prabhakar, R. R.; Loc, N. H.; Kumar, M. H.; Boix, P. P.; Juan, S.; John, R. A.; Batabyal, S. K.; Wong, L. H. *ACS Appl. Mater. Interfaces* **2014**, *6*, 17661−17667.

(2) Guo, Q.; Ford, G. M.; Yang, W.-C.; Walker, B. C.; Stach, E. A.; Hillhouse, H. W.; Agrawal, R. *J. Am. Chem. Soc.* **2010**, *132*, 17384−17386. Wang, W.; Winkler, M. T.; Gunawan, O.; Gokmen, T.; Todorov, T. K.; Zhu, Y.; Mitzi, D. B. *Adv. Energy Mater.* **2014**, *4*, 1301465−1301471.

(3) Haight, R.; Barkhouse, A.; Gunawan, O.; Shin, B.; Copel, M.; Hopstaken, M.; Mitzi, D. B. *Appl. Phys. Lett.* **2011**, *98*, 253502−253507.

(4) Chen, S.; Walsh, A.; Yang, J.-H.; Gong, X. G.; Sun, L.; Yang, P.-X.; Chu, J.-H.; Wei, S.-H. *Phys. Rev. B: Condens. Matter Mater. Phys.* **2011**, *83*, 125201.

(5) Shannon, R. D.; O'Keeffe, M.; Navrotsky, A. *Ind. Chem. Libr.* **1981**, *2*, 53−70.

(6) Schorr, S.; Hoebler, H.-J.; Tovar, M. *Eur. J. Mineral.* **2007**, *19*, 65−73.

(7) Shibuya, T.; Goto, Y.; Kamihara, Y.; Matoba, M.; Yasuoka, K.; Burton, L. A.; Walsh, A. *Appl. Phys. Lett.* **2014**, *104*, 0219121−0219124.

(8) Khadka, D. B.; Kim, J. H. *J. Phys. Chem. C* **2014**, *118*, 14227−14237.

(9) Zeier, W. G.; Pei, Y.; Pomrehn, G.; Day, T.; Heinz, N.; Heinrich, C. P.; Snyder, G. J.; Tremel, W. *J. Am. Chem. Soc.* **2013**, *135*, 726−732.

(10) Agawane, G. L.; Shin, S. W.; Vanalakar, S. A.; Moholkar, A. V.; Kim, J. H. *Mater. Lett.* **2014**, *137*, 147−149.

(11) Bernardini, G. P.; Borrini, D.; Caneschi, A.; Benedetto, F. D.; Gatteschi, D.; Ristori, S.; Romanelli, M. *Phys. Chem. Miner.* **2000**, *27*, 453−461.

(12) Cui, Y.; Deng, R.; Wangm, G.; Pan, D. *J. Mater. Chem.* **2012**, *22*, 23136−23140.

(13) Benedetto, F. D.; Bernardini, G. P.; Borrini, D.; Lottermose, W.; Tippelt, G.; Amthauer, G. *Phys. Chem. Miner.* **2005**, *31*, 683−690.

(14) Kissin, S. A.; Reinvestigation, A. *Can. Miner.* **1989**, *27*, 689−697.

(15) Bonazzi, P.; Bindi, L.; Bernardini, G. P.; Menhetti, S. *Can. Mineral.* **2003**, *41*, 639−647.

(16) Fontane, X.; Izquierdo-Roca, V.; Saucedo, E.; Schorr, S.; Yukhymchuk, V.; Valakh, O.; Ya, M.; Perez-Rodriguez, A.; Morante, J. R. *J. Alloys Compd.* **2012**, *539*, 190−194.

(17) Malik, M. A.; Afzaal, M.; O'Brien, P. *Chem. Rev.* **2010**, *110*, 4417−4446.

(18) Kevin, P.; Malik, M. A.; O'Brien, P. *J. Mater. Chem. C* **2015**, *3*, 5733−5741.

(19) Ramasamy, K.; Malik, M. A.; O'Brien, P. *Chem. Sci.* **2011**, *2*, 1170.

(20) Zhang, X.; Bao, N.; Ramasamy, K.; Wang, Y.-H. A.; Wang, Y.; Lin, B.; Gupta, A. *Chem. Commun.* **2012**, *48*, 4956−4958.

(21) Manna, L.; Milliron, D. J.; Meisel, A.; Scher, E. C.; Alivisiatos, P. *Nat. Mater.* **2003**, *2*, 382−385.

(22) Personal Communication between Paul O'Brien, The University of Manchester, UK and Aron Walsh, University of Bath, UK.. Concerning future work on ref 7.

(23) Zheng, H.; Li, X.; Zong, K.; Sun, Y.; Liu, J.; Wang, H.; Yan, H. *Mater. Lett.* **2013**, *110*, 1−3.

(24) Tauc, J.; Grigorovici, R.; Vancu, A. *Phys. Status Solidi B* **1966**, *15*, 627−637. O'Leary, S. K.; Lim, P. K. *Solid State Commun.* **1997**, *104*, 17−21. Tauc, J. Optical Properties of Noncrystalline Solids. In *Optical Properties of Solids*; Abelks, F., Ed.; Elsevier: New York, 1972; pp 277−313. Meinert, M.; Reiss, G.; Tumuluri, A.; Naidu, K. L.; Raju, K. C. J. *Int. J. ChemTech Res.* **2014**, *6*, 3353−3356.

(25) Dixit, N.; Vaghasia, J. V.; Soni, S. S.; Sarkar, M.; Chavda, M.; Agrawal, N.; Soni, H. P. *J. Environ. Chem. Eng.* **2015**, *3*, 1691−1701.

(26) Bernardini, G. P.; Borrini, D.; Caneschi, A.; Benedetto, F. D.; Gatteschi, D.; Ristori, S.; Romanelli, M. *Phys. Chem. Miner.* **2000**, *27*, 453−455.

(27) Caneschi, A.; Cipriani, C.; Benedetto, F. D.; Sessoli, R. *Phys. Chem. Miner.* **2004**, *31*, 190−92.

(28) Parra-Palomino, A.; Perales-Perez, O.; Singhal, R.; Tomar, M.; Hwang, J.; Voyles, P. M. *J. Appl. Phys.* **2008**, *103*, 121−123.

(29) Straumal, B. B.; Protasova, S. G.; Mazilkin, A. A.; Tietze, T.; Goering, E.; Schutz, G.; Straumal, P. B.; Baretzky, B. *Beilstein J. Nanotechnol.* **2013**, *4*, 361−369. Rumpf, K.; Granitzer, P.; Morales, P. M.; Poelt, P.; Reissner, M. *Nanoscale Res. Lett.* **2012**, *7*, 445.

DOI: 10.1021/jacs.5b10281
J. Am. Chem. Soc. 2015, 137, 15086−15089

Supporting Information

The Synthesis of Nanoparticulate Alloys of the Composition $Cu_2Zn_{1-x}Fe_xSnS_4$: Structural, Optical and Magnetic Properties

Punarja Kevin,[a] Mohammad Azad Malik,[b] Simon Mcadams,[a] Paul.O'Brien*[a,b]

Experimental

All synthesis was performed under an inert atmosphere of dry nitrogen using standard Schlenk techniques. All reagents were purchased from Sigma-Aldrich and used as received. Solvents were dried prior to use. Elemental analysis was performed by the University of Manchester micro-analytical laboratory. Mass spectra were recorded on a Kratos concept 1S instrument. Infrared spectra were recorded on a single reflectance ATR instrument (4000–400 cm^{-1}, resolution 4 cm^{-1}). Melting points were recorded on the Barloworld SMP10 Melting Point Apparatus. The p-XRD studies were performed on a Bruker AXSD8 diffractometer using CuKα radiation. The samples were mounted flat and scanned between 20 and 80° in a step size of 0.05 with a varying count rate depending upon the sample. For TEM measurements QDs in hexane were deposited on 400 mesh copper Formvar/carbon grids and analyzed by a Philips CM 200 STEM operating at 100 kV. TEM images were collected on Technai T20 microscope using accelerating voltage of 300 kV. TEM (nanoscale) elemental maps were measured using Aztec software transmission electron microscope using an accelerating voltage 300 kV. UV-VIS measurement carried with a Perkin Elmer Lambda 1050 spectrophotometer (PSI) and scanned across the range from 250–1000 nm. XPS analysis used a Kratos Axis Ultra in the School of Materials in the University of Manchester. Magnetic studies were performed at 5K and 300K using a using a Quantum Design MPMS-XL superconducting quantum interference device (SQUID) equipped with a 7 Tesla magnet. Photoluminescence measured using Horiba Flourilog Fluorimeter PSI using an excitation wavelength 500 nm.

Synthesis of Metal Organic complexes

The compounds $[Cu(S_2CNEt_2)_2]$, $[Fe(S_2CNEt_2)_3]$, $[^nBu_2Sn(S_2CNEt_2)_2]$, $[Zn(S_2CNEt_2)_2]$ were synthesised and recrystallized as reported in literature,[17-19] brief details follow.

$[Cu(S_2CNEt_2)_2]$: Sodium diethyldithiocarbamate (13 mmol) was dissolved in methanol in a 500 mL double necked round-bottom flask. Slow addition of a methanolic solution of $Cu(NO_3)_2$ (6.5 mmol) gave a black precipitate, which was isolated by filtration. Recrystallization was performed using chloroform resulted with dark green shiny crystals. Yield: 4.78g (73%), Mpt: 201 °C, IR (ν max/cm^{-1}): 2979(w), 2868(w), 1501(s), 1434(m), 1270(s), 1205(m) and 1144(m), Elemental analysis: Calc. for $C_{10}H_{20}N_2S_4Cu$: C, 33.4; H, 5.5; N, 7.7; S, 35.6; Cu, 17.6 %. Found: C, 33.2; H, 5.3; N, 7.3; S, 35.2; Cu, 17.2 %.

$[Fe(S_2CNEt_2)_3]$: Sodium diethyldithiocarbamate (13 mmol) with $Fe(NO_3)_3$ (4 mmol) gave a black powder which on recrystallization produced black shiny crystals. yield 4.81 g (79%), Mpt: 198-201 °C, IR (νmax/cm^{-1}): 2967(w), 2938(w), 1478(s), 1429(m), 1352(w), 1296(w), 1296(m), 1270(s), 1050(s) and 950(s), Elemental analysis: Calc. for $C_{15}H_{30}N_3S_6Fe$:C, 35.98; H, 6.04 N, 8.39; S, 38.43; Fe, 11.15 %. Found: C, 35.7; H, 6.3; N, 8.4; S, 37.82; Fe, 11.0 %.

$[Zn(S_2CNEt_2)_2]$: The complex was produced by the reaction between zinc acetate (6.5 mmol) and Sodium diethyldithiocarbamate (13 mmol) as described above. The crude product was obtained was a white powder which on recrystallization from chloroform gave colourless crystals. Yield 4.81 g (79%), Mpt: 181 °C, IR (νmax/cm^{-1}): 2967(w), 2938(w), 1499(s), 1427(m), 1352(w), 1296(w), 1296(m), 1270(s), 1200(s) and 1143(s), Elemental analysis: Calc. for $C_{10}H_{20}N_2S_4Zn$: C, 33.1; H, 5.5; N, 7.7; S, 35.4; Zn, 18.1 %. Found: C, 32.7; H, 5.3; N, 7.4; S, 35.0; Zn, 18.0 %.

$[Bu_2Sn(S_2CNEt_2)_2]$: The compound was synthesised by using mixture of di-n-butyltindichloride (6.5 mmol) and sodium diethyldithiocarbamate (13 mmol). A white powdered product was isolated by vacuum filtration and recrystallized from a mixture of ethanol-chloroform, white shiny crystals obtained. Yield 5.5 g, (67%), Mpt: 57 °C, IR (νmax/cm^{-1}): 2953(w), 2924(w), 1483(s), 1456(m), 1417(s), 1353(m), 1298(m) 1253(s), 1205(s) and 1138(s), Elemental analysis: Calc. for $C_{18}H_{38}N_2S_4Sn$: C, 40.8; H, 7.2; N, 5.3; S, 24.2; Sn, 22.4 %. Found: C, 39.9; H, 7.5; N, 5.1; S, 22.8; Sn, 21.4 %.

Synthesis of nanoparticles

The precursor mixture used for the synthesis of CZFTS nanoparticles are $[Cu(S_2CNEt_2)_2]$, $[Zn(S_2CNEt_2)_2]$, $[Fe(S_2CNEt_2)_3]$ and $[^nBu_2Sn(S_2CNEt_2)_2]$ complexes. The precursors have similar decomposition temperatures in the range 250-350 °C.[18] These compounds are soluble in oleylamine (OLA). For the synthesis of CZFTS nanoparticles the complexes $[Cu(S_2CNEt_2)_2]$, $[Zn(S_2CNEt_2)_2]$, $[Fe(S_2CNEt_2)_3]$ and $[^nBu_2Sn(S_2CNEt_2)_2]$ were added in the molar ratios: 2.0:1.0:0:1.0, 2.0:0.7:0.3:1.0, 2.0:0.5:0.5:1.0, 2.0:0.3:0.7:1.0 and 2.0:0:1.0:1 into 20 mL hot OLA and subsequently heated to 220 °C for an hour (supplementary material Table S1). The as synthesized nanoparticles were washed with methanol and dispersed in hexane.

CZTS nanoparticles

Synthesis of CZTS nanoparticles were carried out using 2:1:1 precursor mixtures at temperatures 220, 200 and 180 °C. Figure 5 shows the p-XRD patterns of nanoparticles synthesised at these temperatures. The p-XRD patterns were matched with the Kesterite phase of CZTS (ICDD: 04-015-0223) corresponding to the tetragonal I-42 m space group with lattice constants a = 5.4280 Å and c = 10.8640 Å. Nano particles synthesized at all three temperatures found to be matching with the reference patterns but there were some impurity peaks of unknown materials found in the p-XRD patterns of nanoparticles at 180 °C. The p-XRD patterns of the nanoparticles formed at 220 and 250 °C were well matched with standard phase and with no contamination. The TEM images (Figure 5) showed hexagonal shaped particles with an average size of 10 ± 5 nm. The average elemental composition of the synthesized CZTS nanocrystals at 220 °C for 1hr was determined by Energy-Dispersive X-ray Spectroscopy (EDX), which provided Cu/Zn/Sn/S composition (%) of 28.43:11.38:12.85:47.34. These values were closer to 2.5:1:1.1:4 which is slightly Cu rich (can be from the Cu-grid).

Table S1: Consolidated data Table for CZFTS nanoparticles (220 °C, 1h)

Material	Precursor in 20 ml Oleyl amine (mM)				EDX					a cubic	a tet	c tet	c/2a	a Bonazzi	c-Bonazzi	c/2a Bonazzi	BG/ (eV)	λmax/eV (PL)	Mag/ BM
	Cu	Zn	Fe	Sn	Cu	Zn	Fe	Sn	S										
CZTS (xFe-0)	2	1	0	1	26.4	11.4	0	12.85	49.3	5.4377	5.439	10.884	1.00055	5.434(1)	10.856(1)	0.9988(8)	1.93	1.905	0
CZFTS(xFe - 0.30)	2	0.7	0.3	1	28.7	6.9	3.4	12.56	48.5	5.431	5.434	10.88	1.00110	5.4254(6)	10.868(1)	1.001(6)	1.89	1.821	0.02072
CZFTS (xFe-0.50)	2	0.5	0.5	1	29.8	6.3	6.0	13.29	44.6	5.4177	5.4165	10.816	0.99843	5.4329(3)	10.8235(8)	0.9961(0)	1.87	1.769	0.028467
CZFTS (xFe-0.70)	2	0.3	0.7	1	29.6	4.1	8.0	12.82	45.6	5.4076	5.4057	10.824	1.00117	5.446(4)	10.757(8)	0.9876(1)	1.85	1.744	0.035809
CZFTS (xFe-1.0)	2	0	1	1	26.4	0	12.1	14.23	47.2	5.4046	5.40018	10.8165	1.00149	5.4495(6)	10.766(2)	0.9877(7)	1.79	1.696	0.02503

Values from Bonazzi[15] in lines 2 and 4 of table are for Fe_x values of 0.21 and 0.78 respectively

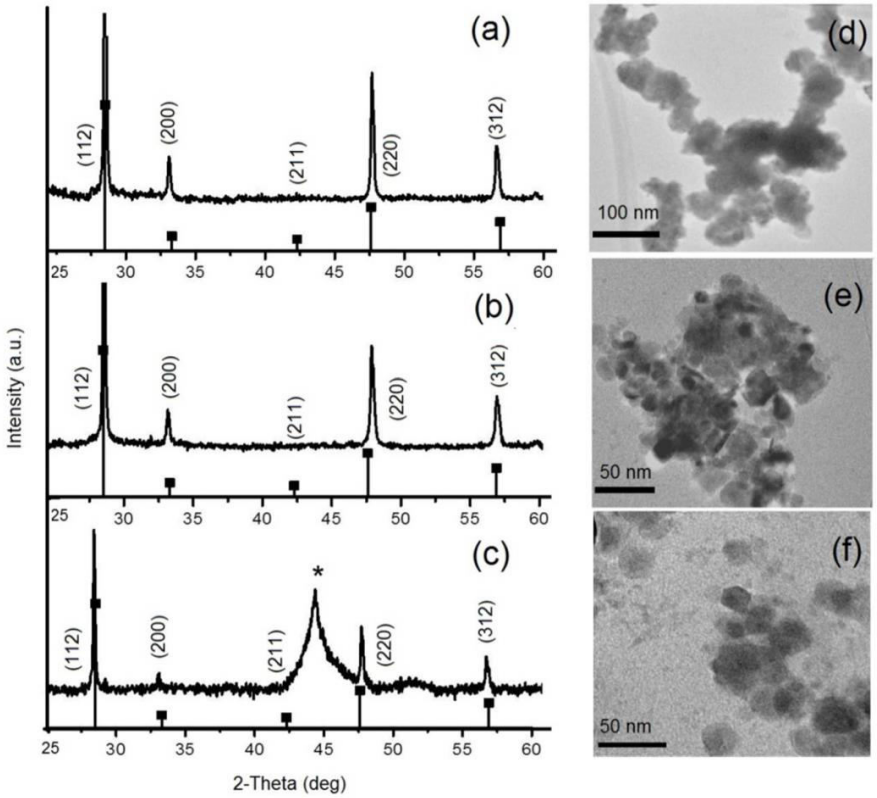

Figure S1: (a)-(c) are the p-XRD patterns of the CZTS nanoparticles synthesized at 220, 200 and 180 °C. Peaks are indexed according to Kesterite structure (ICDD: 04-015-0223) of CZTS (stick patterns). * mark showed unknown peak.

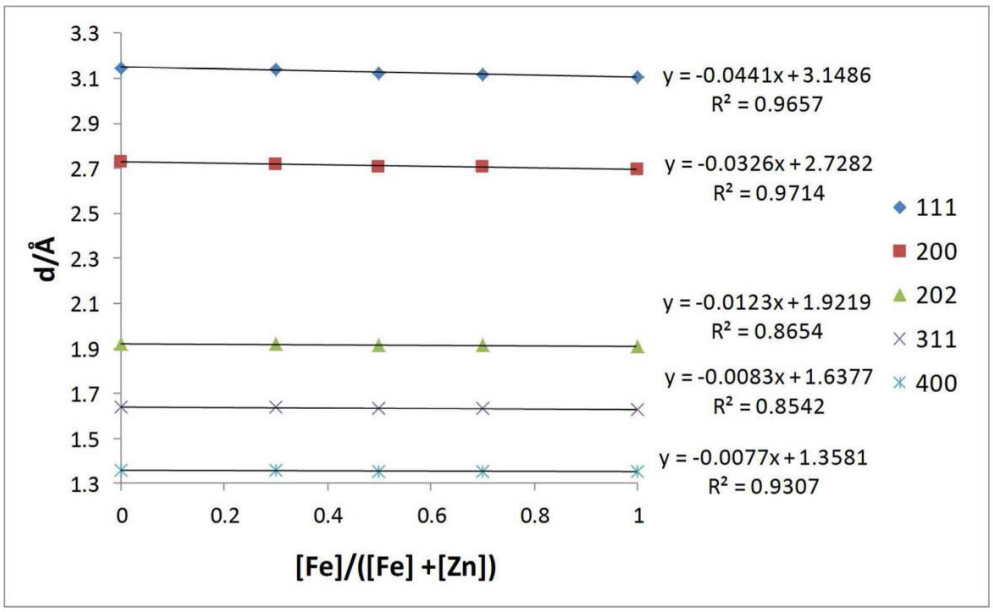

Figure S2: Variation of selected d-spacings with composition

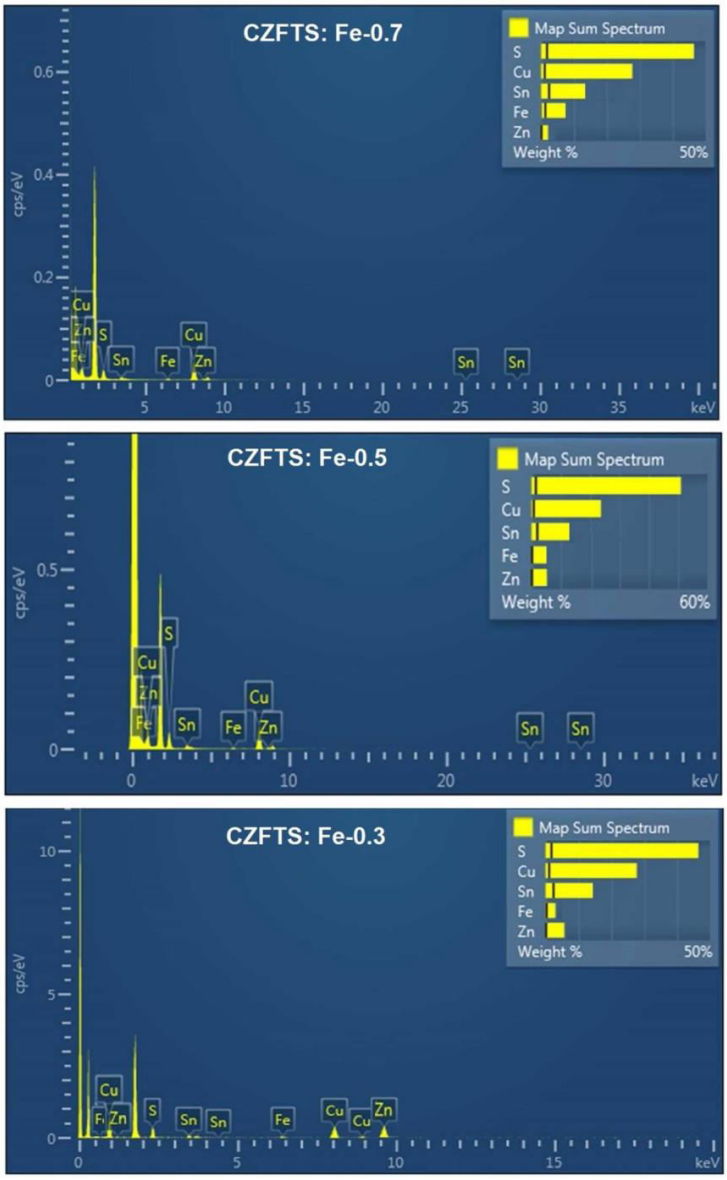

Figure S3: EDX analysis of the $Cu_2Zn_{1-x}Fe_xSnS_4$(where x = 0.3, 0.5 and 0.7) nanoparticles synthesised with Fe precursor ratio 0.3, 0.5 and 0.7 mM, 200 °C, 1hour.

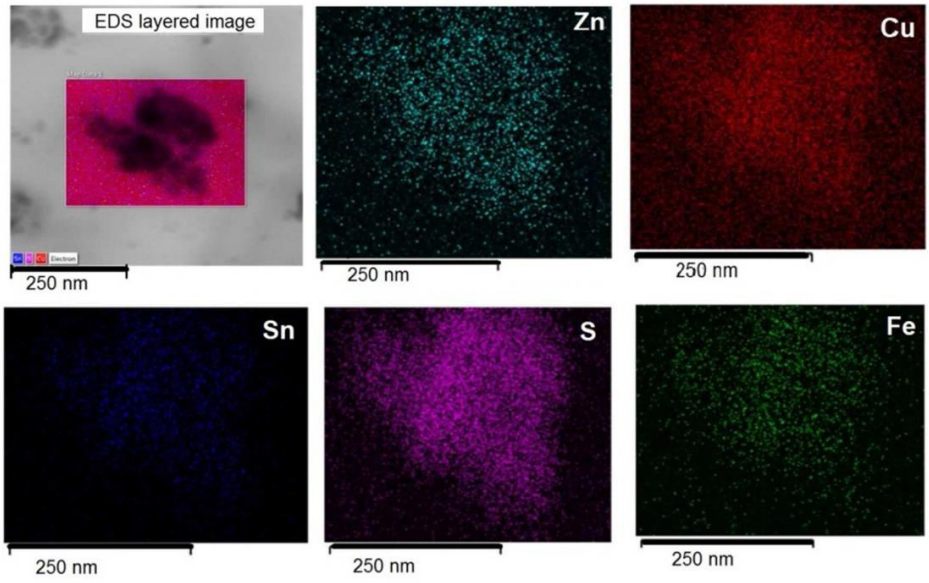

Figure S4: TEM Elemental map of $Cu_2Zn_{0.5}Fe_{0.5}SnS_4$ nanoparticles synthesised using 0.5 mM Fe precursor in the precursor mixture at 220 °C for 1 hour.

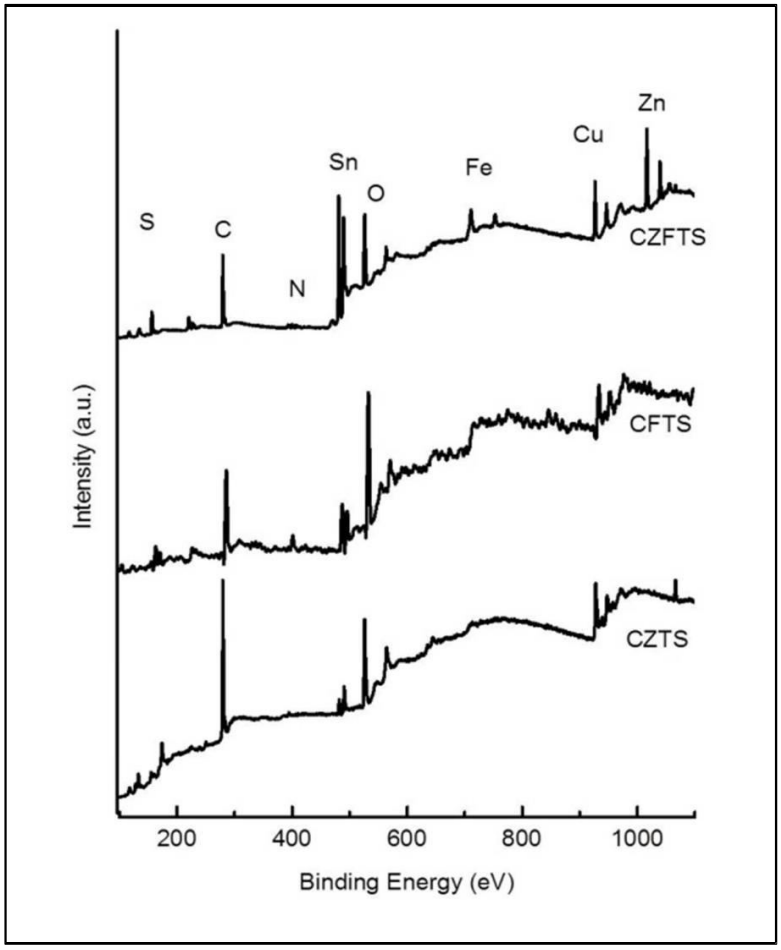

Figure S5: XPS spectra of Cu_2ZnSnS_4, Cu_2FeSnS_4 and $Cu_2Zn_{0.5}Fe_{0.5}SnS_4$ nanoparticles synthesised at 220 °C for 1 hour.

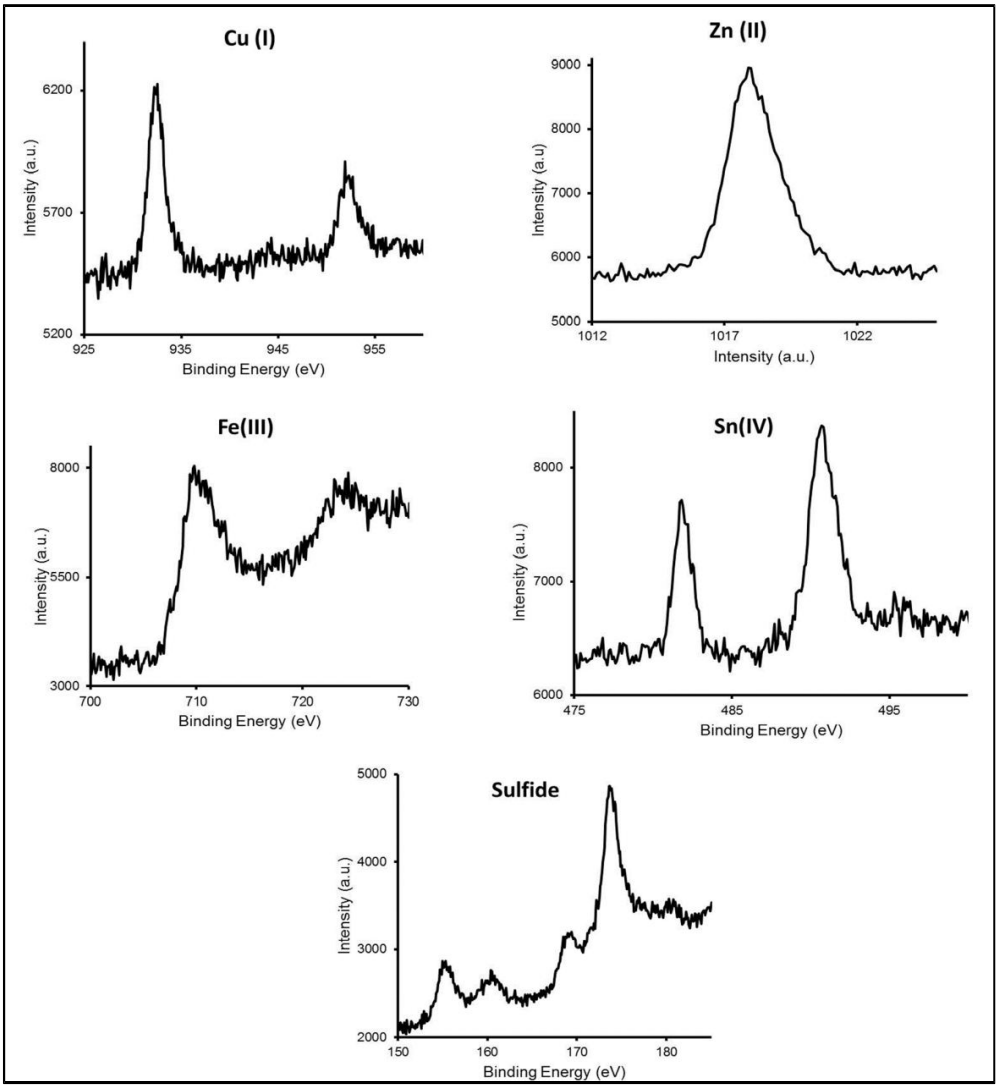

Figure S6: High resolution XPS spectra of $Cu_2Zn_{0.5}Fe_{0.5}SnS_4$ nanoparticles synthesised at 220 °C, 1 hour.

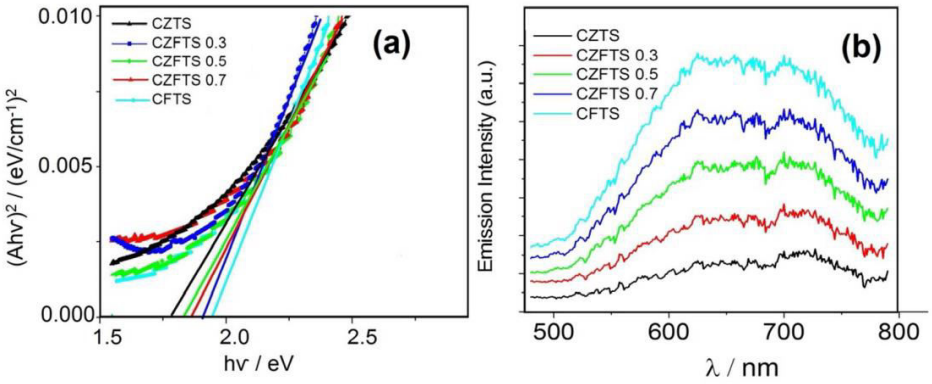

Figure S7: (a) and (b) are the UV-Vis Tauc plots and PL spectra for the $Cu_2Zn_{1-x}Fe_xSnS_4$ (x = 0 to 1) nanoparticles synthesised at 220 °C.

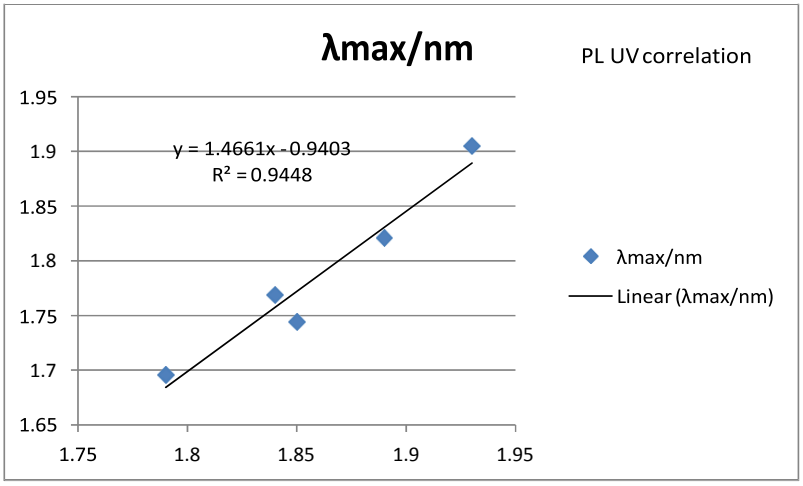

Figure S8: Correlation between the PL and UV- Vis spectra of $Cu_2Zn_{1-x}Fe_xSnS_4$ (x = 0 to 1) nanoparticles synthesised at 220 °C.

Table S2: Statistics for the band gap measurement from the UV-Vis Tauc plots.

Material	Intercept	Slope	Band gap (b/a)	R^2
CZTS	0.11004	0.05682	1.936	0.88465
CZFTS Fe 0.3	0.47173	0.25011	1.886	0.85266
CZFTS Fe0.5	0.11594	0.06206	1.868	0.87455
CZFTS Fe0.7	0.11143	0.06209	1.848	0.92818
CFTS	0.31154	0.13772	1.7933	0.88994

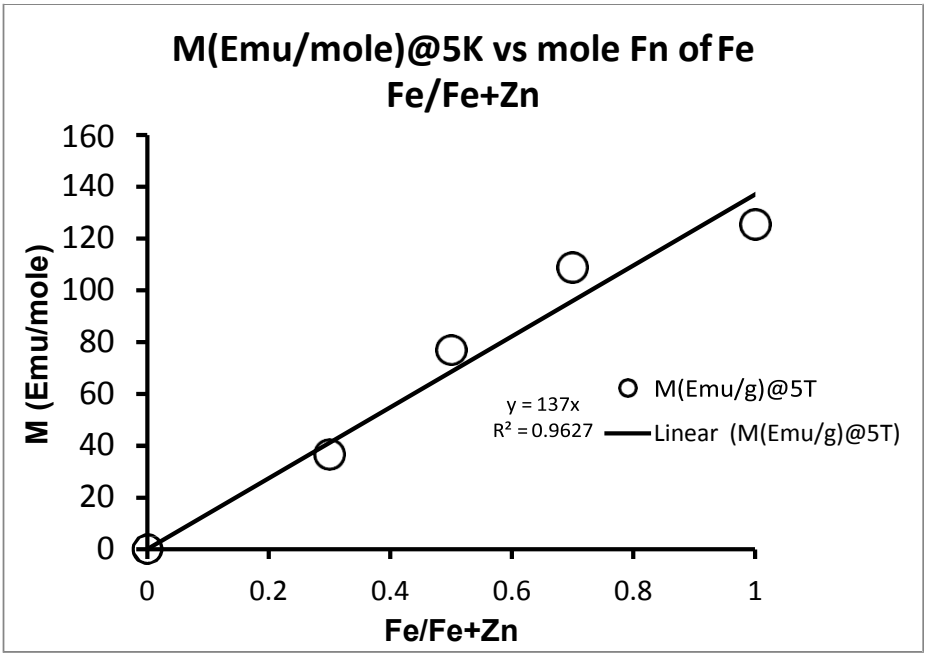

Figure S9: M (Emu/mole) at 5K vs mole Fn of [Fe]/[Fe+Zn]

CHAPTER – XIII : PAPER - 10

"Stannite Cu_2FeSnS_4 nanoparticles For Solar Energy Applications"

Punarja Kevin, M. Xiang Li Hong, Simon Mcadams, Paul O'Brien,

Draft ready: pages D1-D11

Stannite Cu_2FeSnS_4 Nanoparticles for Solar Energy Applications

Punarja Kevin,[a] M. Xiang Li Hong,[b] Simon Mcadams,[a] Paul O'Brien*[a,b]

[a]School of Chemistry, The University of Manchester, Oxford Road M13 9PL

[b]School of Materials, The University of Manchester, Oxford Road, M13 9PL

KEYWORDS: Thin films, powder XRD, photovoltaic, spectroscopy, nanoparticles, TEM, EDX.

ABSTRACT: Cu_2FeSnS_4 (CFTS), nanoparticles have been synthesized by a non-injection method using mixtures of $Fe(S_2CNEt_2)_3$, $Bu_2Sn(S_2CNEt_2)_2$ and $Cu(S_2CNEt_2)_2$. The structures, morphologies, compositions, optical and magnetic properties were studied by p-XRD, TEM, EDX and UV/Vis spectroscopy were studied. Valence state of constituents has been determined by XPS. The effect of time and temperature on the size and morphology of CFTS nanocrystals were studied. Magnetic properties of the nanoparticles were studied in detail.

Introduction

Copper-iron tin sulfides/selenides (CFTS and CFTSe) materials are formed from earth abundant, environmentally benign elements hence more cost-effective alternatives to the CIGS family.[1-4] Their band gaps lie between 0.9-1.5eV, making them suitable for collectors in PV-cells.[5,6] The magnetic properties and phase characteristics of CFTS semiconductors have been studied in detail.[7] The incorporation of iron into CZTS allows the selective tuning of the band gap and the lattice parameters which give a theoretical efficiency of 37%. The increase in band gap and decrease in lattice parameters with increase in Fe concentration makes the alloy suitable in Si-based tandem solar cells.[6-9] Dye-sensitized solar cells (DSSC) fabricated with CFTS thin films as a photocathode have been reported with promising PCE (8.03 %) which can be a potential and cheaper alternative to Pt counter electrodes in DSSCs.[10]

A solution based synthesis of CFTS was reported recently using metal salts and sulfur in hot oleylamine. The stannite phase of CFTS was obtained with particles of a diameter of 15–25 nm.[11] Jiang *et al* reported a non-aqueous strategy for the synthesis of hierarchical porous quaternary chalcogenide Cu_2FeSnS_4 as hollow chain microspheres by a microwave method using $CuCl_2$, $FeCl_3$, $SnCl_4$ and thiourea in benzyl alcohol and octadecyl amine.[12] Recently Guan *et al*. synthesized flowers like CFTS nanoparticles by a microwave method using $Fe(NO_3)_3$, $SnCl_2$, $Cu(NO_3)_2$ and thiourea in ethylene glycol.[13] Evastigneeva *et al* had studied the structure of $Cu_{2-x}Fe_{1-x}$ SnS_4 by the Rietveld method by.[14] Zhang *et al.* have reported the phase controlled synthesis of wurtzite CFTS nanoparticles with a band gap of 1.50 eV.[6] The performance of photovoltaic cells can be further improved by controlling the composition of the material and by the incorporation of extrinsic impurities such as Fe or Se in place of Zn and S respectively *e.g.* as in CZTS or CZTSe.[15,16] Studies showed that by varying the Fe: Zn in CFTS and CZTS both the band gap and lattice parameter can be tuned.[6-8,17,18] In this paper, we report the first synthesis of the CFTS by a non-injection method using mixtures of diethyldithiocarbamato complexes of Cu(I), Zn(II) and Sn(IV) in oleylamine.

Experimental

Precursor Synthesis and characterization

All reagents were purchased from Sigma-Aldrich chemical company and used as received. Solvents were distilled prior to use. Elemental analysis was performed by the University of Manchester microanalytical laboratory. TGA measurements were carried out by a Seiko SSC/S200 model from 10 to 600 °C with a heating rate of 10 $^{\circ}$C min^{-1} under nitrogen. Melting point was recorded on a Stuart melting point apparatus and uncorrected. The compounds $[Cu(S_2CNEt_2)_2]$ (**1**), $[Fe(S_2CNEt_2)_3]$ (**2**), $[^nBu_2Sn(S_2CNEt_2)_2]$ (**3**) were synthesized and recrystallized as reported in literature.[19-24]

Synthesis of Nanoparticles

CFTS nanocrystals were synthesized by the thermolysis of the metal dithiocarbamate complex in hot oleylamine. In a typical synthesis, 10 ml of oleylamine was heated at 90 °C for 10 min under vacuum in a three necked round bottom flask and then purged with nitrogen gas for 5 min. A solid mixture of $[Cu(S_2CNEt_2)_2]$ (2.78 mmol), $[Fe(S_2CNEt_2)_3]$ (1.40 mmol), and $[Bu_2Sn(S_2CNEt_2)_2]$ (1.40 mmol) in 2:1:1 molar ratio was added into the hot oleylamine and the reaction temperature was slowly increased to 220 °C. After maintaining temperature for 60 min the heating was stopped and the mixture was allowed to cool to room temperature. The addition of 20 ml methanol produced a black precipitate which was centrifuged, washed twice with methanol to remove any excess ligand. The black nanocrystals were redispersed in hexane for further investigation. The experiment was repeated at 180 and 250°C using the same molar ratio of precursor mixtures. Aliquots were collected at certain intervals of time to investigate the effect of reaction time on the characteristics of the nanoparticles

Characterisation of nanoparticles

The p-XRD studies were performed on a Bruker AXSD8 diffractometer using CuKα radiation. The samples were mounted flat and scanned between 20 and 70° in a step size of 0.05 with a varying count rate depending upon the sample. For TEM measurements, QDs in hexane were deposited on 400 mesh copper/carbon grids and analyzed by a Philips CM 200 STEM operating at 100 kV. TEM images were collected on a Technai T20 microscope using accelerating voltage of 300 kV. TEM (nanoscale) elemental maps were measured using Aztec software transmission electron microscope using an accelerating voltage 300 kV. UV-VIS measurement was carried with a Perkin Elmer Lambda 1050 spectrophotometer (PSI) and scanned across the range from 250–1000 nm. XPS analysis used a Kratos Axis Ultra in the School of Materials, University of Manchester.

Results and discussions

TGA analysis

Thermal decomposition studies were carried out between 10-600 °C; heating rate 10 °C min^{-1} under nitrogen. All compounds show rapid single step decomposition between 250-350 °C. The residual mass of $[Fe(S_2CNEt_2)_3]$ complex was found to be about 18% which was close to the calculated percentage of FeS (17.5%). The $[Bu_2Sn(S_2CNEt_2)_2]$ complex decomposed slightly faster than the other complexes and the residual mass found to be ~ 34 % which agrees with the calculated residual mass of SnS_2. $[Zn(S_2CNEt_2)_2]$ gave ~9-10 % residue which was found to be half or less than half of the mass of the expected metal chalcogenides; ZnS (27 %).

X-ray diffraction, TEM and EDX studies of CFTS nanoparticles synthesised in oleylaamine at 180, 220 and 250 °C for 1 hr

The p-XRD patterns of CFTS nanoparticles synthesized using 2:1:1 precursor mixtures at temperatures 180, 220 and 250 °C are shown in Figure 1. The p-XRD patterns were matched with the stannite phases of CFTS. At 180 °C the p-XRD patterns contain a mixture of two stannite phases of tetragonal I-42m (121) space groups CFTS; ICDD:

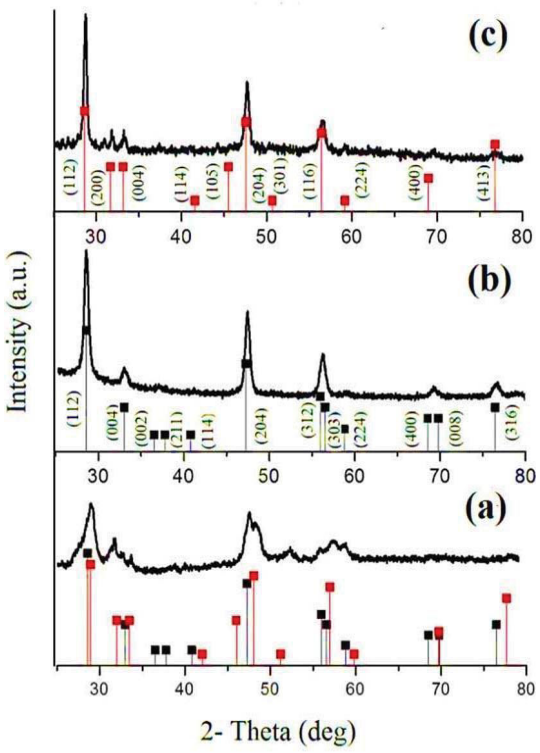

Figure 1: (a)-(c) are the p-XRD patterns of nanoparticles formed at 180, 220 and 250 °C for 1 hr in oleylamine. Red and black stick patterns represent stannite CFTS; ICDD: 00-002-0575 black ICDD: 00-011-0062 respectively

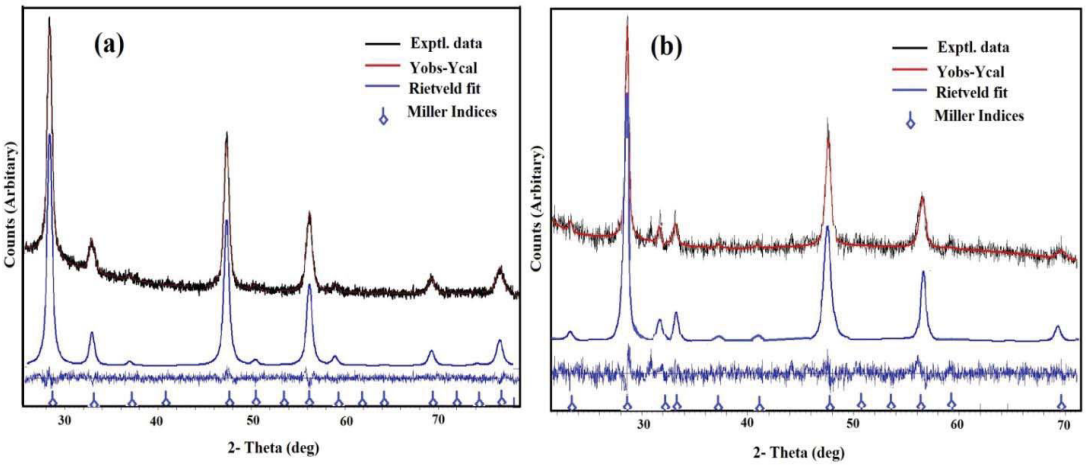

Figure 2: (**a**) and (**b**) are the Rietveld analysis of p-XRD patterns of nanoparticles synthesised at 220 and 250 for 1h and (a) fitted with standard patterns of CFTS ICDD: 00-011-0062 respectively and (b) is fitted with standard patterns of stannite CFTS; ICDD: 00-002-0575.

00-002-0575 with lattice parameters a = b = 5.4600 Å, c = 10.7520 Å and ICDD: 00-011-0062 with lattice parameters a = b = 5.4690 Å, c = 10.7690 Å, whereas the p-XRD patterns for the nanoparticles synthesized at 220 °C were well matched with the stannite CFTS ICDD: 00-011-0062.The p-XRD patterns were further analysed by Rietveld analysis showed good fit with a Rwp = 4.36, the resulting

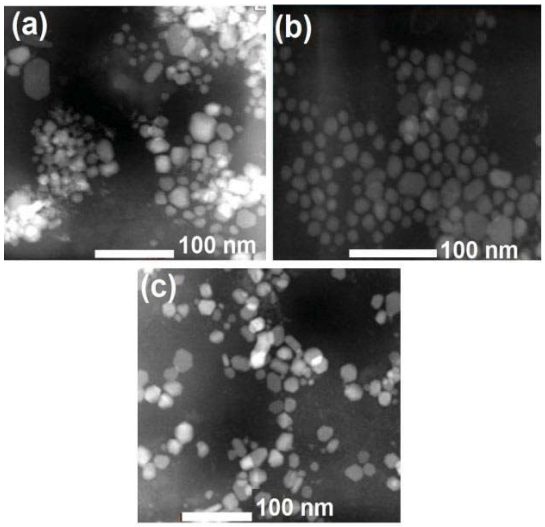

Figure 3: (a)-(c) are the STEM images of CFTS nanoparticles synthesised at 180, 220 and 250 °C.

lattice constants were a = 5.445 Å and c = 11.0921 Å (Figure 2, Supporting document Table S1). The p-XRD patterns of nanoparticles synthesised at 250 °C well matched with the stannite CFTS ICDD: 00-002-0575.The p-XRD patterns on Rietveld analysis gave lattice parameters a = 5.441 and c = 10.9962 Å with an Rwp = 5.23. (Figure 2(b) and supporting document Table S2).

The nanoparticles synthesised at 180 °C showed large and small hexagonal shaped morphologies with size between 5-10 nm along with very small irregular shaped morphologies (Figure 3). Nanoparticles synthesised at 220 °C were of the hexagonal type with size about 5-7 nm. Nanoparticles synthesised at 250°C were hexagonal in shape with almost same size (~10 nm). The HTEM images showed hexagonal shaped particles with an average size of 10 ± 2 nm for the nanoparticles synthesized at 220 °C. The high-resolution TEM (HRTEM) images of the nanocrystals synthesised at 220 °C (Figure 4) exhibit clear lattice fringes with measured d-spacing of 0.315 ± 0.002 nm, corresponding to the

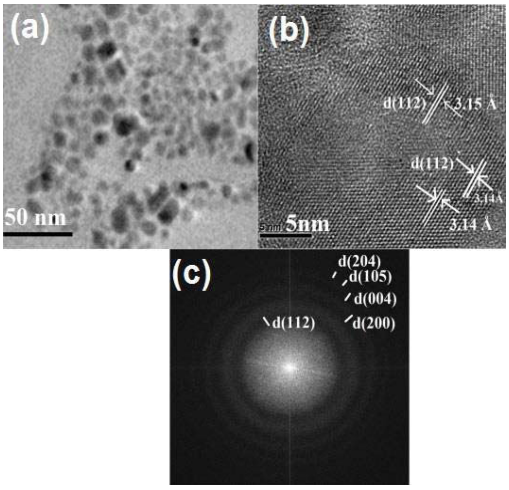

Figure 4: (a) - (c) are the HRTEM images of CFTS nanoparticles synthesised at 220 °C for 1 hr.

(204) lattice planes of the Stannite CFTS structure. The diffraction pattern showed concentric rings

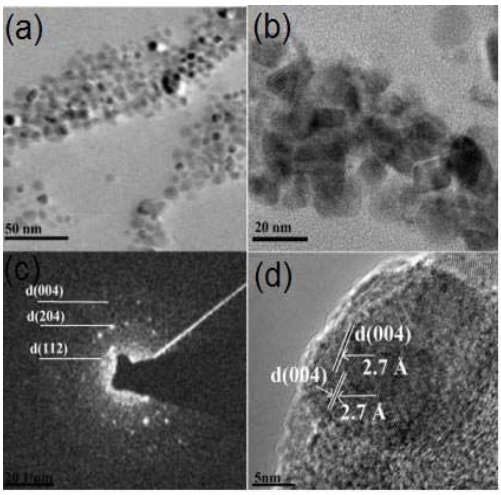

Figure 5: HRTEM images of CFTS nanoparticles synthesised at 250 °C for 1 hr.

shows different planes of the nanocrystallites. Figure 5 shows the clear diffraction patterns, with measured d-spacing corresponding to the lattice

planes of the stannite CFTS structure. The nanoparticles synthesized at 250 °C showed lattice fringe with a measured d-spacing of 0.27 ± 0.01 nm corresponding to the (004) lattice planes of CFTS structure.

The Energy-Dispersive X-ray Spectroscopy (EDX) for CFTS nanocrystals synthesized at 220 °C for 1 hr showed an average elemental composition as Cu/Fe/Sn/S (%) of 24.8:12.1:14.8:48.3. These values were closer to 2: 1:1.2:4 but slightly Sn-rich. The EDX analysis of nanoparticles synthesized at 250 °C gave Cu/Fe/Sn/S composition (%) of 26.6 :12:3 :13.6: 47.6 which gave a stoichiometry 2 :0.9: 1.0 : 3.5, slightly S deficient. The nanoparticles synthesized at 180 °C showed Sn-rich and S-deficient stoichiometry (Supporting document Figure S1). The selected area elemental map of CFTS nanoparticles synthesized at 220 °C for 1 hr is shown in Figure 6. It can be seen that there is a uniform distribution of constituent elements throughout the selected area.

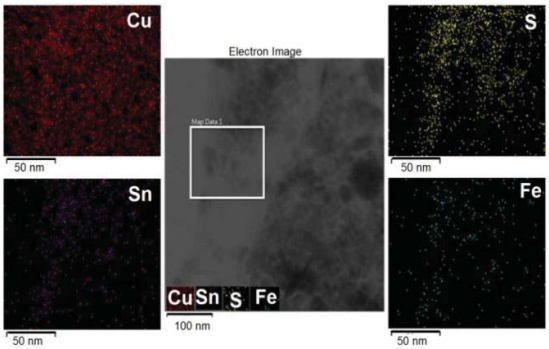

Figure 6.: Selected area elemental map of CFTS nanoparticles synthesised at 220 °C, 1h, using 2:1:1 ratio of precursor mixtures.

X-ray diffraction, TEM and EDX studies of CFTS nanoparticles synthesized at 30 min and 45 min at 220 °C

Aliquots were collected from the experimental mixture at 220 °C at 30 and 45 min during the synthesis of nanoparticles. The aliquots were then dispersed in methanol. The nanoparticles formed on p-XRD analysis showed a good match to the stannite phases of tetragonal I-42m (121) space groups CFTS; ICDD: 00-002-0575 with lattice parameters a = b = 5.4600Å, c = 10.7520 Å. The nanoparticles formed from 30 min aliquots showed less intense peaks compared to samples collected after 1 hr (Figure 7).

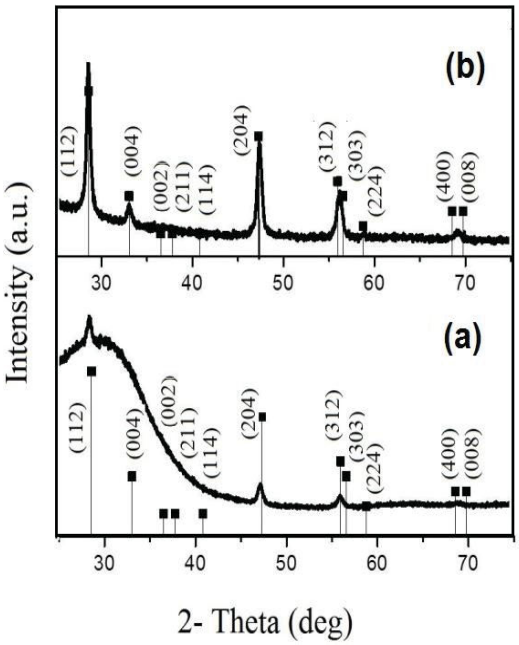

Figure 7: (a)-(c) p-XRD patterns for the nanoparticles deposited at 220 °C samples collected at 30 min, 45 min and 1 hr.

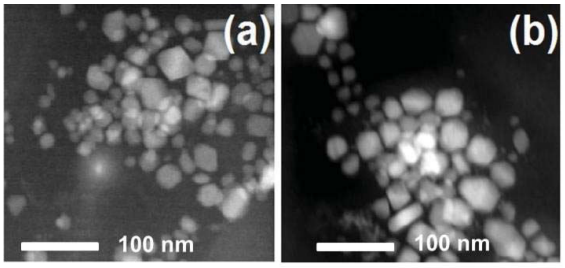

Figure 8: (a) and (b) are the STEM images of CFTS to those formed from the 30 min and 45 min at 220 °C.

The morphology of the nanoparticles synthesized from aliquots collected at 30 min showed large crystallites with more or less square as shown in Figure 8. The morphology of samples collected at 45 min contained large and small hexagonal shaped crystals between *ca*.5 - 10 nm size along with very small irregular shaped morphologies. The EDX

analysis (Supporting document Figure S1) showed Sn-rich and Fe-deficient composition in the aliquots collected at 30 min whereas, the Fe concentration increased in the case of samples collected at 45 min samples. The selected area elemental map of the CFTS nanoparticles synthesized from aliquots collected after 45 min and 30 min at 220 °C showed a lower percentage of Fe (*ca*. 9 % and 5 % respectively). The nanoparticles were comparatively rich in Cu (Supporting document Figure S1).

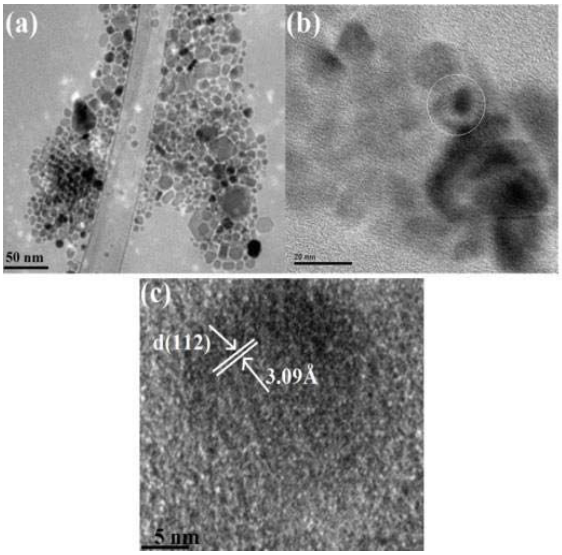

Figure 9: HRTEM images of CFTS nanoparticles formed from aliquots collected at 30 min from the 220 °C experiment.

The TEM images of the nanoparticles synthesized from the samples collected at 30 min at 220 °C showed square-shaped particles with an average size of 10 ± 5 nm (Figure 9). The diffraction patterns for the nanoparticles synthesized for 30 min showed concentric rings corresponding to the diffraction planes of the stannite type CFTS nanocrystallites. The high-resolution TEM (HRTEM) images of these nanocrystals exhibited clear lattice fringes with measured d-spacing of 0.309 ± 0.002 nm, corresponding to the (112) lattice planes of the stannite CFTS structure.

Nanoparticles formed from the aliquots collected at 45 min at 220 °C showed concentric rings corresponding to the different planes of the nanocrystallites. The TEM images showed hexagonal shaped particles with an average size of 10 ± 5 nm (Figure 10). The high-resolution TEM (HRTEM)

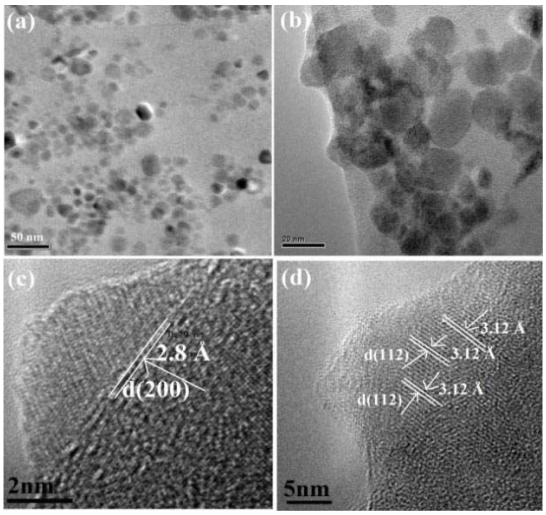

Figure 10: HRTEM images of CFTS nanoparticles formed from aliquots collected at 45 min from the 220 °C experiment.

images of the typical nanocrystals (Figure 10) exhibit clear lattice fringes with measured d-spacing of 0.312 ± 0.001 nm, corresponding to the (112) lattice planes of the Stannite CFTS structure

Magnetic Studies of CFTS nanoparticles

The Fe(II) oxidation state (d^6) in a tetrahedral environment results in a local magnetic moment of approximately 4 μB. The spins can order in- (ferromagnetic, FM) or out-of-phase (antiferromagnetic, AFM).[7,18,25,27-28] stannite structured CFTS has a Néel temperature as low as 6-8 K. The stannite structure contains Cu-Fe and Sn-Fe (001) layers, in addition to the FM configuration of Fe, two antiferromagnetic configurations of these layers also needs to be considered. By considering all these magnetic configurations, the calculated local magnetic moment of Fe is about 3.5 μB, which confirms the high-spin state of Fe in the structure.[7, 26-27]

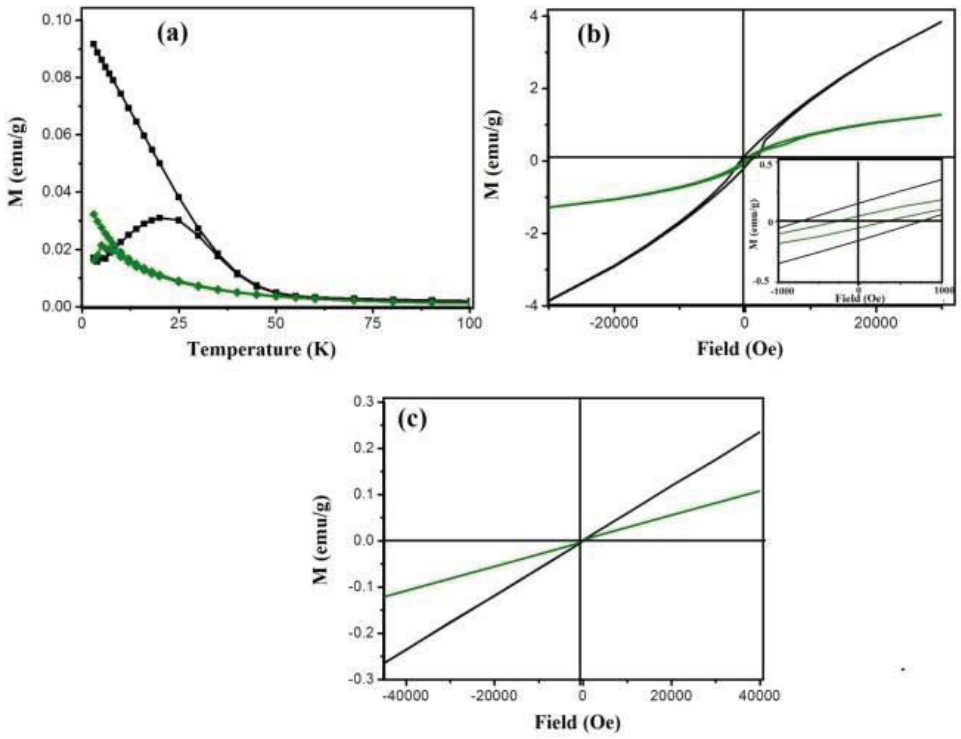

Figure 11: (**a**) Temperature dependence of the magnetization per gram for CZFTS (Fe-0.3 to 1.0) nanocrystals **(b)** Field-dependent magnetization curves a 5 K for CFTS nanoparticles synthesized at 220 and 250°C for 1 hr. (inset: the magnification of hysteresis loops)) **(c)** Field-dependent magnetization curves at 300K for CFTS nanoparticles synthesized at 220 and 250°C for 1 hr)

The antiferromagnetic ordering lowers the energy in st-CFTS. The average magnetisation per gram of spin-up and spin-down for the ferromagnetic (FM) configurations gives almost the same value as the anti-ferromagnetic (AFM) states, hence the alloy assume to have an FM structure. Magnetic studies were performed at 5 K and 300 K for the CFTS nanoparticles synthesised at 220 and 250 °C for 1 hr. The zero-field-cooled (ZFC) and field-cooled (FC) magnetic measurements confirmed that 5 K is below the blocking temperature for all samples Figure 11(a).[27,-30] At 5 K, both samples displayed hysteresis, indicating the ferromagnetic behaviour of these materials (Figure 11(b))[25-28] At 300 K the samples showed paramagnetic behavior with no hysteresis as shown in Figure 11(c).

Conclusion

Phase pure CFTS nanoparticles were synthesized. The structure, morphology, composition and optical properties were investigated by p-XRD, SEM, EDX and UV-Vis spectroscopy. The EDX for the nanoparticles synthesized at 220 °C for 1 hr gave a composition very close to stoichiometric for Cu_2FeSnS_4. The CFTS nanoparticles synthesized at different temperatures and at the different time showed variation in the stoichiometric composition, size, and shapes. It is clear from the results that the particle size decreases with increase in temperature. The shape of the crystals became more hexagonal when the synthesized at a longer reaction time, whereas the nanoparticles synthesized at shorter reaction time were more or less square/cubic shaped. The magnetic properties particles and optical band

gap studies showed similarity with stannite type CFTS material. The band gap of the material is ideal for solar energy applications.[31]

Author Information

Corresponding Author

Email: paul.obrien@manchester.ac.uk

Acknowledgement

PK is thankful to Gary Harrison for XRD and School of Chemistry and The University of Manchester for funding. We thank EPSRC for funding of instruments under grant number EP/K039547/1) for characterization of the compounds.

Abbreviations

Band gap (BG), Transmission Electron Microscope (TEM), Highresolution TEM (HRTEM), Energy-Dispersive X-ray Spectroscopy (EDX), Bohr Magneton (BM), Electron volt (eV).

References

1. P. Jackson, D. Hariskos, E. Lotter, S. Paetel, R. Wuerz, R. Menner, W. Wischmann, M. Powalla, *Prog. Photovolt. Res. Appl.* 2011, **19**, 894–897.
2. S. Niki, M. Contreras, I. Repins, M. Powalla, K. Kushiya, S. Ishizuka, K. Matsubara, *Prog. Photovolt. Res. Appl*. 2010, **18**, 453–466.
3. I. Repins, M. A. Contreras, B. Egaas, C. DeHart, J. Scharf, C. L. Perkins, B. To, R. Noufi, *Prog. Photovolt. Res. Appl*. 2008, **16**, 235–239.
4. J. Tang, Z. Huo, S. Brittman, H. Gao and P. Yang, *Nat. Nanotechnol*., 2011, **6**, 568–572.
5. F.-J. Fan, Y.-X. Wang, X.-J. Liu, L. Wu, S.-H. Yu, *Adv. Mater.* 2012, **24**, 6158.
6. X. Zhang, N. Bao, K. Ramasamy, Y.-H. A. Wang, Y.Wang, B. Lin, A. Gupta, *Chem. Commun*. 2012, **48**, 4956.
7. T. Shibuya, Y. Goto, Y. Kamihara, M. Matoba, K. Yasuoka, L.A. Burton, A. Walsh, *Appl. Phys. Lett.* 2014, **104**, 0219121–0219124.Rincón, M. Quintero, E. Moreno, C. Power, E. Quintero, A. Henao, M. A. JMacías, G. E. Delgado,
8. R. Tovar, M. Morocoima, *Solid State Commun*. 2011, **151**, 947.
9. S. R. Kurtz, P. Faine, and J. M. Olson, *J. Appl. Phys*. 1990, **68**, 1890.; C. H. Henry *J. Appl. Phys*., 1980, **51**, 4494.
10. R.R. Prabhakar, N.H. Loc, M.H. Kumar, P.P. Boix, S. Juan, R.A. John, S.K. Batabyal, L.H. Wong, *ACS Appl. Mater. Interfaces*, 2014, **6**, 17661–17667
11. L. Li, X. Liu, J. Huang, M. Cao, S. Chen, Y. Shen, L. Wang, *Mater. Chem. Phys.* 2012, **133**, 688
12. L. Ai, J. Jiang, *J. Mater. Chem.*, 2012, **22**, 20586.
13. H. Guan, Y. F. Shi, B. X. Jiao, X. Wang, F. L. Yu, *Chalcogenide Lett.* 2014, **11**, 9.
14. T. L. Evstigneeva, Y. K. Kabalov, *Crystallogr. Rep.* 2001, **46**, 368-377.
15. S. Chen, A. Walsh, J.-H. Yang, X. G. Gong, L. Sun, P.-X. Yang, J.-H. Chu, S.-H. Wei, *Phys. Rev. B*, 2011, **83**, 125201(5).
16. R. Haight, A. Barkhouse, O. Gunawan, B. Shin, M. Copel, M. Hopstaken, D. B. Mitzi, *Appl. Phys. Lett.* 2011, **98** ,253502 (7)
17. G. Marcano, C. Rincón, S. A. López, G. Sánchez Pérez, J. L. Herrera-Pérez, J. G. Mendoza-Alvarez, P. Rodríguez, *Solid State Commun.,* 2011**, 151**, 84-86.
18. D. B. Khadka, J. Kim, *J. Phys. Chem. C,* 2014, **118**, 14227-35.
19. M. Akhtar, J. Akhter, M. A. Malik, P. O'Brien, F. Tuna, J. Raftery, M. Helliwell, M. *Journal of Materials Chemistry,* 2011**, 21**, 9737-9745
20. K. Ramasamy, V. L. Kuznetsov, K. Gopal, M. A. Malik, J. Raftery, P. P. Edwards, P. O'Brien, *Chem. Mater.* 2013, 25, 266-276.
21. K. Ramasamy, M. A. Malik, P. O'Brien, *Chem. Sci.* 2011, **2**, 1170.
22. P. Kevin, D. J. Lewis, J. Raftery, M. A. Malik, P. O'Brien, *J. Cryst. Growth*, 2015, **415**, 93–99.
23. P. Kevin, S. N. Malik, M. A. Malik, P. O' Brien, *Chem. Commun*. 2014, 50, 14328 – 14330
24. Tauc, J.; Grigorovici, R.; Vancu, A., *Phys. Status Solidi*, 1**966**, *15*, 627-634.
25. D.B. Khadka, J. Kim, J. Alloys. Compd. 2015, **638**, 103–108.
26. P.kevin, M. A. Malik, P. O'Brien, *New. J. Chem.* 2015, **39**,7046-7053.
27. G. P. Bernardini, D. Borrini, A. Caneschi, F. D. Benedetto, D. Gatteschi, S. Ristori, and M. Romanelli, *Phys. Chem. Miner.* 2000, **27**, 453.

28. A. Caneschi, C. Cipriani, F. D. Benedetto, and R. Sessoli, *Phys. Chem. Miner.* 2004, **31**, 190.
29. G. L. Agawane, S. W. Shin, S. A. Vanalakar, A. V. Moholkar, J. H. Kim, *Mater. Lett.* **2014**, *137*, 147–149.
30. F. D. Benedetto, G. P. Bernardini, D. Borrini, W. Lottermose, G. Tippelt, G. Amthauer, *Phys. Chem. Miner.* 2005, **31**, 683−690
31. W. Schockley, H.J. Queisser, J. Appl. Phys. 1961, **32**, 510–519

Supporting document

Stannite Type Cu_2FeSnS_4 nanoparticles for Solar Energy Applications

Punarja Kevin,[a] M. Xiang Li Hong,[b] Simon Mcadams,[a] Paul O'Brien*[a,b]

Table S1: Rietveld analysis of p-XRD patterns synthesised at 220 °C for 1 hr. Reference patterns used are ICDD: 00-011-0062 with lattice parameters a = b = 5.4690 Å, c = 10.7690 Å Rwp = 4.36.

h	k	l	d	2θ	F^2
0	1	1	3.82828	23.21577	1.528
1	1	0	3.82828	23.21577	0.363
1	1	1	3.12577	28.53322	60.800
0	2	0	2.70700	33.06484	7.035
0	0	2	2.70700	33.06484	3.517
0	2	1	2.42121	37.10160	0.163
0	1	2	2.42121	37.10160	0.587
1	2	0	2.42121	37.10160	0.294
2	1	0	2.42121	37.10160	0.294
1	2	1	2.21026	40.79250	0.416
1	1	2	2.21026	40.79250	0.159
2	1	1	2.21026	40.79250	0.416
0	2	2	1.91414	47.45979	67.394
2	2	0	1.91414	47.45979	33.697
0	3	0	1.80467	50.53395	0.063
0	0	3	1.80467	50.53395	0.103
1	2	2	1.80467	50.53395	0.126
2	1	2	1.80467	50.53395	0.126
2	2	1	1.80467	50.53395	0.413
0	1	3	1.71206	53.47780	0.077
3	1	0	1.71206	53.47780	0.276
0	3	1	1.71206	53.47780	0.077
1	3	0	1.71206	53.47780	0.276
3	1	1	1.63238	56.31355	32.674
1	1	3	1.63238	56.31355	32.674
1	3	1	1.63238	56.31355	32.674
2	2	2	1.56289	59.05860	9.585
3	2	0	1.50157	61.72692	0.005
0	3	2	1.50157	61.72692	0.009
0	2	3	1.50157	61.72692	1.051
2	3	0	1.50157	61.72692	0.005
3	2	1	1.44695	64.32996	0.004
3	1	2	1.44695	64.32996	1.234
2	1	3	1.44695	64.32996	0.004
1	3	2	1.44695	64.32996	1.234
2	3	1	1.44695	64.32996	0.004
1	2	3	1.44695	64.32996	0.004
0	4	0	1.35350	69.37716	21.489
0	0	4	1.35350	69.37716	10.744
0	1	4	1.31309	71.83659	0.014
1	4	0	1.31309	71.83659	0.007
4	1	0	1.31309	71.83659	0.007
0	4	1	1.31309	71.83659	1.803

3	2	2	1.31309	71.83659	0.014
2	3	2	1.31309	71.83659	0.014
2	2	3	1.31309	71.83659	1.803
4	1	1	1.27609	74.26183	0.022

Table S2: Rietveld analysis of p-XRD patterns synthesised at 220 °C for 1 hr. Reference patterns used are CFTS; ICDD: 00-002-0575 (a = b = 5.4600Å, c = 10.7520 Å)Rwp = 5.23

h	k	l	d	2θ	F^2
0	1	1	3.82828	23.21577	2.850
1	1	0	3.82828	23.21577	0.875
1	1	1	3.12577	28.53322	86.370
0	2	0	2.70700	33.06484	10.223
0	0	2	2.70700	33.06484	7.170
0	2	1	2.42121	37.10160	3.691
0	1	2	2.42121	37.10160	1.448
1	2	0	2.42121	37.10160	1.126
2	1	0	2.42121	37.10160	0.667
1	2	1	2.21026	40.79250	0.959
1	1	2	2.21026	40.79250	5.773
2	1	1	2.21026	40.79250	1.389
0	2	2	1.91414	47.45979	85.109
2	2	0	1.91414	47.45979	48.960
0	3	0	1.80467	50.53395	1.297
0	0	3	1.80467	50.53395	2.322
1	2	2	1.80467	50.53395	0.444
2	1	2	1.80467	50.53395	0.515
2	2	1	1.80467	50.53395	1.071
0	1	3	1.71206	53.47780	0.150
3	1	0	1.71206	53.47780	0.114
0	3	1	1.71206	53.47780	0.248
1	3	0	1.71206	53.47780	0.136
3	1	1	1.63238	56.31355	46.797
1	1	3	1.63238	56.31355	42.688
1	3	1	1.63238	56.31355	47.656
2	2	2	1.56289	59.05860	17.999
3	2	0	1.50157	61.72692	1.373
0	3	2	1.50157	61.72692	1.506
0	2	3	1.50157	61.72692	6.753
2	3	0	1.50157	61.72692	0.923
3	2	1	1.44695	64.32996	0.339
3	1	2	1.44695	64.32996	3.073
2	1	3	1.44695	64.32996	0.187
1	3	2	1.44695	64.32996	3.085
2	3	1	1.44695	64.32996	0.849
1	2	3	1.44695	64.32996	0.158
0	4	0	1.35350	69.37716	30.412
0	0	4	1.35350	69.37716	8.383
0	1	4	1.31309	71.83659	0.406
1	4	0	1.31309	71.83659	0.670
4	1	0	1.31309	71.83659	0.265
0	4	1	1.31309	71.83659	1.312
3	2	2	1.31309	71.83659	0.317

2	3	2	1.31309	71.83659	0.465
2	2	3	1.31309	71.83659	4.068
4	1	1	1.27609	74.26183	2.687
1	4	1	1.27609	74.26183	2.111
3	3	0	1.27609	74.26183	0.146
1	1	4	1.27609	74.26183	7.026
0	3	3	1.27609	74.26183	0.236

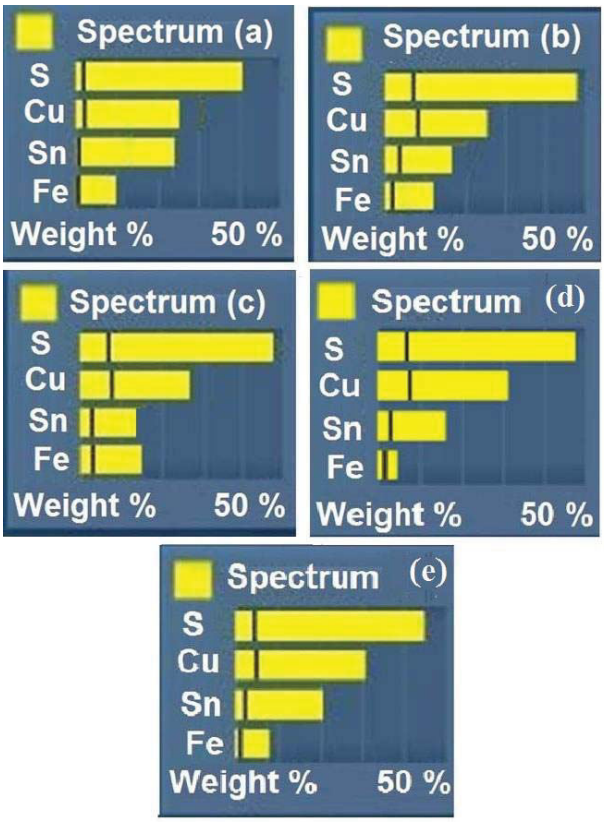

Figure S1: Spectrum (a) to (c) are the EDX analysis of the CFTS nanoparticles synthesized at 180, 220 and 250 °C for 1 hr. Spectrum (d) to (e) is the EDX of CFTS nanoparticles synthesised at 220 °C for 30 min and 45 min respectively.

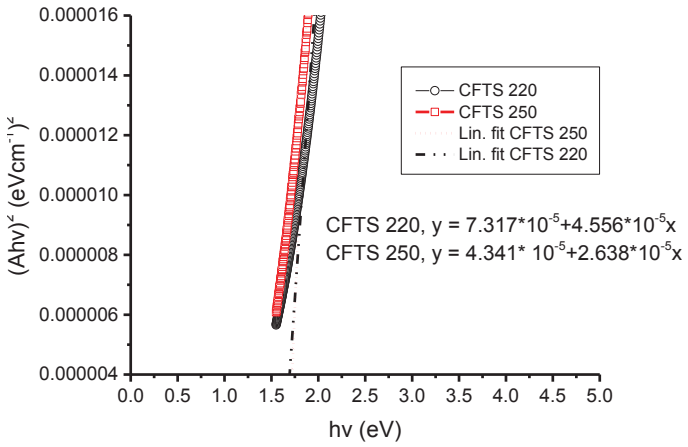

Figure S2: Tauc plots of CFTS nanoparticles synthesised at 220 and 250 °C for 1hr. The equation for the line of best fit is shown in the plot.

CHAPTER - XIV : PAPER - 11

"Nanoparticles of Cu_2ZnSnS_4 Performance Enhancing Additives in Organic Field-Effect Transistors"

Punarja Kevin, Azad. M. Malik, Paul O'Brien, Joseph Cameron, Rupert G. D. Taylor, Neil J. Findlay, Anto R. Inigo, Peter J. Skabara, *J. Mater. Chem. C,* 2016, **4**, 5106-5115

Journal of Materials Chemistry C

PAPER

Cite this: J. Mater. Chem. C, 2016, 4, 5109

Nanoparticles of Cu_2ZnSnS_4 as performance enhancing additives for organic field-effect transistors†

Punarja Kevin,[a] Mohammad Azad Malik,[b] Paul O'Brien,[ab] Joseph Cameron,[c] Rupert G. D. Taylor,[c] Neil J. Findlay,[c] Anto R. Inigo[c] and Peter J. Skabara*[c]

Received 22nd April 2016,
Accepted 4th May 2016

DOI: 10.1039/c6tc01650b

www.rsc.org/MaterialsC

The addition of oleylamine coated Cu_2ZnSnS_4 (CZTS) nanoparticles to solutions of an organic semiconductor used to fabricate organic field-effect transistors (OFETs) has been investigated. The oligothiophene-based small molecule 5T-TTF and the polymer poly(3-hexylthiophene) (P3HT) were each applied in the transistors with various concentrations of CZTS (5–20%). Atomic force microscopy (AFM) was applied to characterise the surface morphology of the OFETs. The use of 5 and 10 wt% of the CZTS nanoparticles in 5T-TTF and P3HT solutions, respectively, appears to be a simple and effective way of improving OFET performance.

Introduction

Organic semiconductors are low cost materials for organic electronic devices, such as organic field-effect transistors (OFETs), which utilise small molecules[1–3] or polymers[4–6] to achieve high charge carrier mobilities in excess of 40 $cm^2\ V^{-1}\ s^{-1}$.[7] However, attempts have been made to improve the charge carrier mobility of OFETs by providing more effective pathways for charge transport by using materials such as graphene,[8,9] which acts as an electrically conducting bridge between domains in composites comprising of mainly P3HT. This led to an increased mobility with increase in the composition of graphene, showing highly stable transfer characteristics, a highest hole mobility of 1.82 $cm^2\ V^{-1}\ s^{-1}$ and a moderately high I_{ON}/I_{OFF} ratio of 10^4.[9] Similarly, carbon nanotubes (CNTs)[10–12] have been used in OFETs and have produced a 60-fold increase in the effective mobility of the starting semiconducting material with a minor decrease of the I_{ON}/I_{OFF} current ratio.[12] In a separate study, the addition of CNTs at a concentration of up to 10 wt%, led to a 10-fold improvement in field-effect mobility in P3HT OFETs.[11] The use of inorganic nanomaterials in OFET devices is under-explored and yet there is a vast array of such materials with broadly varying properties to choose from. Kesterites such as Cu_2ZnSnS_4 (CZTS) have attracted considerable recent interest[13–17] because they are composed of elements that are earth abundant, of low toxicity and hence relatively environmentally benign. In addition to their good absorption characteristics, such as broad absorption spectra and tunable band gaps, kesterite nanoparticles exhibit good charge transport and have been used in devices such as FETs with good performance.[15,18] These materials are therefore exciting potential additives for improving the transistor characteristics of organic semiconductors in OFETs, as well as in organic solar cells and organic layers (hole and electron transport layers) of perovskite solar cells.

In this work we demonstrate that oleylamine coated CZTS nanoparticles, used in low concentration, can be used as an additive in organic semiconductor solutions for the enhancement of charge carrier mobility in OFET devices. Often nanoparticles are processed in a ligand-exchange solution, with the long ligands of the nanoparticles exchanged for shorter ligands such as butylamine,[19] ethanedithiol[20] or benzenedithiol[21] in order to reduce the distance between particles. However, in this study we show that the kesterite nanoparticles capped with long ligands can be used to improve the performance of transistor devices. The simple addition of these nanoparticles to organic semiconductor solutions reduces the need for complex processing techniques or toxic ligands normally required.

Synthesis of CZTS nanoparticles

The compounds $[Cu(S_2CNEt_2)_2]$ (**1**), $[Zn(S_2CNEt_2)_2]$ (**2**) and $[^nBu_2Sn(S_2CNEt_2)_2]$ (**3**) were synthesised as reported in the literature.[22–25] The CZTS nanocrystals were synthesised, under dry nitrogen atmosphere, using a Schlenk line by a modification of a published procedure.[27] In a typical synthesis, 20 ml oleylamine was heated to 90 °C and purged under N_2. The complexes were used as follows: 1.0 g (2.8 mmol) of $[Cu(S_2CNEt_2)_2]$, 0.50 g (1.4 mmol) of

[a] School of Chemistry, The University of Manchester, M13 9PL, UK
[b] School of Materials, The University of Manchester, M13 9PL, UK
[c] WestCHEM, Department of Pure and Applied Chemistry, University of Strathclyde, G1 1XL, UK. E-mail: peter.skabara@strath.ac.uk

† Electronic supplementary information (ESI) available: p-XRD data for CZTS grown under different temperatures (180 °C, 220 °C and 250 °C); OFET data for transistors fabricated with oleylamine only as the additive; TGA analyses of samples **1–3**. See DOI: 10.1039/c6tc01650b

$[Zn(S_2CNEt_2)_2]$ and 0.73 g (1.4 mmol) of $[^nBu_2Sn(S_2CNEt_2)_2]$ were mixed and ground in a mortar and pestle, and then added to the hot degassed oleylamine. The temperature of the solution was then raised to the processing temperature: 180, 220 or 250 °C. This temperature was maintained for 1 hour. The nanocrystals were precipitated by dispersing in methanol and were centrifuged for 5–10 min at 4000 rpm. The supernatant was discarded and the nanocrystals were redispersed in hexane. The precipitation and dispersion steps were repeated several times to remove excess oleylamine. Finally, the nanocrystals were stored for later use by dispersing in hexane or dried and kept under N_2. The nanoparticles appear to be stable for more than six months.

Nanoparticle characterisation

The nanoparticles were characterised using p-XRD, TEM, HRTEM, UV-vis absorption spectroscopy and photoluminescence spectroscopy. The X-ray diffraction (XRD) studies were performed on a Bruker AXSD8 diffractometer using CuKα radiation. The samples were mounted flat and scanned between 20° and 80° in a step size of 0.05°. Nanoparticles in hexane were deposited on 400 mesh copper Formvar/carbon grids for TEM work. TEM images were collected on a Technai T20 microscope using an accelerating voltage of 300 kV. STEM imaging and energy dispersive X-ray (EDX) spectrum imaging were performed using a probe side aberration corrected Titan ChemiSTEM instrument operated at 200 kV with a probe current of ~440 pA. The nanoscale elemental map images were analysed using Aztec software. TEM images were analysed by Gatan Digital Micrograph software. The XPS spectra were collected using a Kratos Axis Ultra in the School of Materials in the University of Manchester.

OFET fabrication

Organic field-effect transistors were fabricated on SiO_2 substrates with prefabricated interdigitated Au source-drain channels with lengths of 2.5, 5, 10 and 20 μm and width of 1 cm. N-doped Si and SiO_2 were the gate electrode and gate dielectric materials, respectively. The substrates were cleaned using water, acetone and ethanol before being treated in UV-ozone for 30 seconds. A pentafluorobenzenethiol (PFBT) self-assembled monolayer (SAM) was prepared by drop-casting a solution of PFBT (10 mM in ethanol) onto the substrate. After 1 min, the residual PFBT was then washed away with ethanol and the substrate was dried over a stream of compressed air. Similarly, an octadecyltrichlorosilane (OTS) SAM was prepared by drop-casting an OTS solution (13 mM in toluene) onto the substrate which was washed with toluene and dried after 1 minute.

The conditions for the fabrication of OFETs using 4,4′,6,6′-tetrakis(3′-hexyl-5′-methyl-[2,2′-bithiophen]-5-yl)-2,2′-bithieno[3,4-d]-[1,3]dithiolylidene (5T-TTF) were the same as those previously reported[26] with the addition of differing amounts of CZTS as the only variable. All OFETs fabricated using P3HT were made using PFBT and OTS SAMs by spin-coating a 5 mg ml^{-1} solution of the polymer at 2000 rpm with varying amounts of CZTS onto the substrate and annealing at 150 °C. Every OFET fabricated was spin-coated from a solution which had been subjected to ultra-sonication for 20 minutes.

Current–voltage characteristics were recorded using a Keithley 4200 semiconductor characterisation system at room temperature in a nitrogen filled glove box where oxygen and water levels were maintained below 0.1 ppm. The field-effect mobilities were determined from the saturation regime and calculated using the following equation:

$$\mu_{sat} = \frac{2L}{WC_i} \times \left(\frac{\partial\sqrt{I_{DS}}}{\partial V_{GS}}\right)^2$$

where I_{DS} is the drain current, μ_{sat} is the saturation carrier mobility, V_{GS} is the gate voltage, L is the channel length, W is the channel width and C_i is the capacitance per unit area of the insulator material. The mobility values reported were calculated from the average mobility of six devices and the standard deviation (σ) is shown for the OFETs fabricated. The surface morphologies of the OFETs were characterised using a Dimension 3100 atomic force microscope (AFM) in tapping mode.

Results and discussion

CZTS nanoparticles

The synthesis of CZTS nanoparticles was previously carried out using a mixture of $[Cu(S_2CNEt_2)_2]$ (**1**), $[Zn(S_2CNEt_2)_2]$ (**2**) and $[Sn(S_2CNEt_2)_4]$ (**4**) in octadecene and oleic acid, followed by injection into oleylamine.[27] Herein we report a method using $[^nBu_2Sn(S_2CNEt_2)_2]$ (**3**) in place of $[Sn(S_2CNEt_2)_4]$ (**4**) in oleylamine. The reported decomposition temperatures of copper, zinc and tin diethyldithiocarbamates (**1**), (**2**) and (**4**)[27] are 220 °C (**1**), 240 °C (**2**), and 174 °C (**4**),[18,24,27] which may have led to premature decomposition/over-incorporation of tin due to the lower decomposition temperature of the $[Sn(S_2CNEt_2)_4]$. In our studies, thermogravimetric analysis (TGA) of the complexes (**1**), (**2**) and (**3**) (Fig. S3, ESI†), showed more compatible and sharp

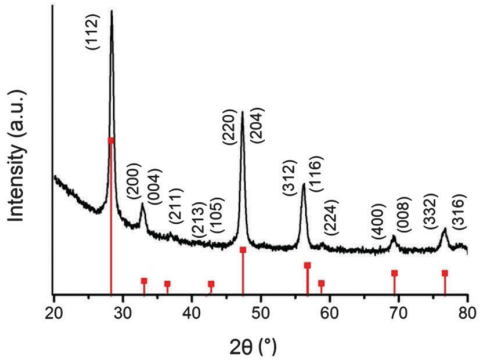

Fig. 1 The p-XRD patterns of CZTS nanoparticles synthesised at 220 °C for 1 hour. The reference patterns are of kesterite CZTS (ICDD: 04-015-0223). The TEM images showed hexagonal particles with an average size of 10 ± 2 nm. The high resolution TEM (HRTEM) images shown in Fig. 2a and b, exhibit clear lattice fringes with measured *d*-spacing of *ca.* 0.313(1) nm corresponding to the (112) lattice plane of the kesteritic CZTS structure (Fig. 2c). The elemental composition of the CZTS nanocrystals was determined by energy dispersive X-ray spectroscopy (EDX), which gave a Cu/Zn/Sn/S composition (atomic%) of Cu (28.43%), Zn (11.38%), Sn (12.85%) and S (47.34%).

decomposition starting at 284 °C (**1**), 303 °C (**2**) and 300 °C (**3**), all leading to their corresponding metal sulphides. The mid-point of each decomposition is within 5 °C of 330 °C. These TGA results for complexes (**1**), (**2**) and (**3**) match well with our previous reports.[28] The difference in the decomposition temperatures between this work and earlier reports may be due to the method of reporting or experimental differences.

The p-XRD pattern (Fig. 1) of the sample prepared at 220 °C for 1 hour shows main peaks at *d*-spacings of: 3.14, 2.73, 1.92, 1.64, 1.35, 69.34 and 1.24 for the (112), (200), (204), (312), (400) and (316) spacings of kesterite CZTS (ICDD: 04-015-0223).[24] The p-XRD patterns of samples formed at other temperatures are shown in the ESI† (Fig. S1).

The stoichiometry of the material is $Cu_{2.5}Zn_1Sn_{1.1}S_4$, which is slightly Cu rich (however Cu grids were used for the TEM). Fig. 2d shows the selected area elemental map for the nanoparticles synthesised at 220 °C; it shows a uniform distribution of the elements in the entire area of analysis.

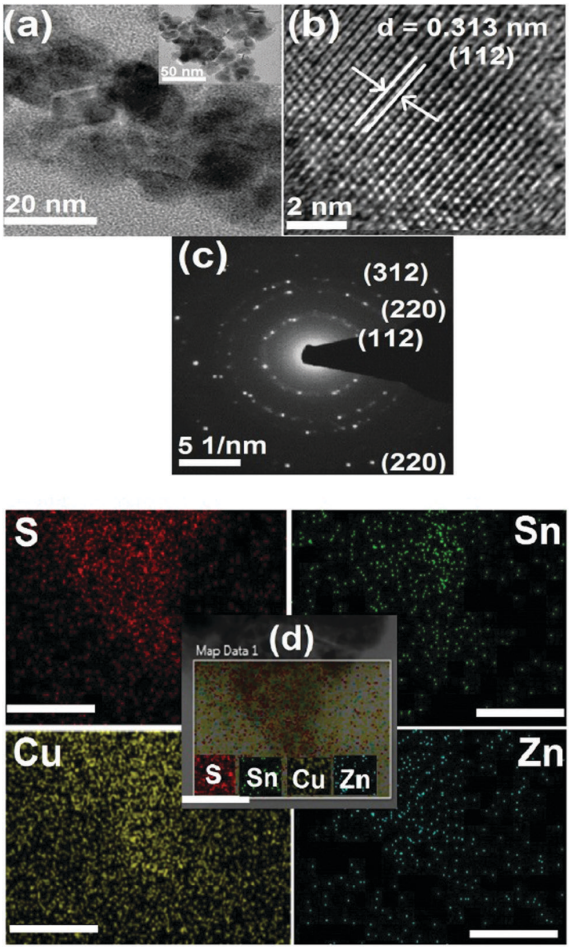

Fig. 2 (a) and (b) are the HRTEM images, (c) the diffraction patterns and (d) the elemental map of CZTS nanoparticles synthesised at 220 °C. The scale bar shown for the elemental map is *ca.* 50 nm.

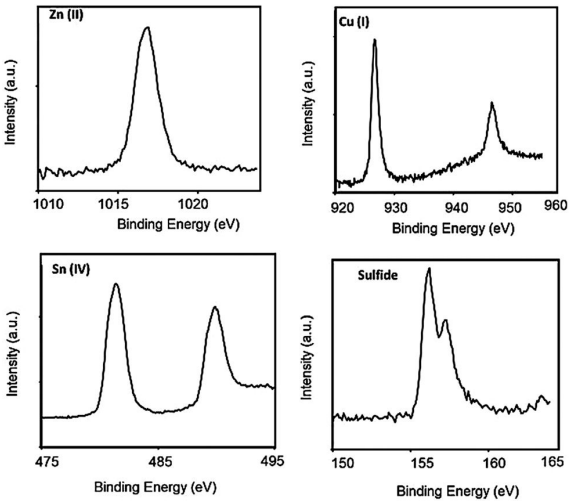

Fig. 3 High resolution XPS spectra of CZTS nanoparticles synthesised at 220 °C.

The valence state of the elements in the nanoparticles synthesised at 220 °C were determined by XPS (Fig. 3); binding energies were as follows: Zn $2p_{3/2}$, 1017 eV; Cu $2p_{3/2}$, 926 eV; Cu $2p_{1/2}$, 947 eV; Sn $3d_{5/2}$, 480 eV; Sn $3d_{3/2}$, 491 eV; S $2p_{3/2}$, 156 eV; S $2p_{1/2}$ 158 eV. The values are commensurate with the valence states Cu(I), Sn(IV), Zn(I) and S^{2-}.[25]

Organic field-effect transistors

The details of OFET fabrication using both 5T-TTF and P3HT organic semiconductors are given in the experimental section. The results for OFETs fabricated using 5T-TTF are summarised below in Table 1. OFETs fabricated using only 5T-TTF show an average hole mobility of 9.5×10^{-3} cm^2 V^{-1} s^{-1}, which is similar to that determined previously.[26] The output and transfer characteristics for the devices tested are shown below in Fig. 4a and b. The current response is increased (Fig. 4c) for the OFET fabricated using 5 wt% CZTS and the hole mobility calculated is 0.016 cm^2 V^{-1} s^{-1}, a 68% increase with respect to the device fabricated using pristine 5T-TTF. The I_{ON}/I_{OFF} ratio remains the same for both devices. When the nanoparticle concentration is increased, there is no saturation observed in the output graph. In order to investigate the OFET performance further, AFM was used in tapping mode to characterise the surface morphology of the different devices; these images are

Table 1 Data for OFETs fabricated from 5T-TTF with various concentrations of CZTS nanoparticles

Compound	V_{Th} (V)	ON/OFF ratio	Average μ_{hole} (cm^2 V^{-1} s^{-1})	$\sigma\mu_{hole}$
5T-TTF	−13	10^3	9.5×10^{-3}	5.8×10^{-3}
5T-TTF + 1% CZTS	−17	10^3	8.5×10^{-3}	3.8×10^{-3}
5T-TTF + 2.5% CZTS	−17	10^3	8.3×10^{-3}	4.6×10^{-3}
5T-TTF + 5% CZTS	−15	10^3	0.016	4.6×10^{-3}
5T-TTF + 10% CZTS	—	—	—	

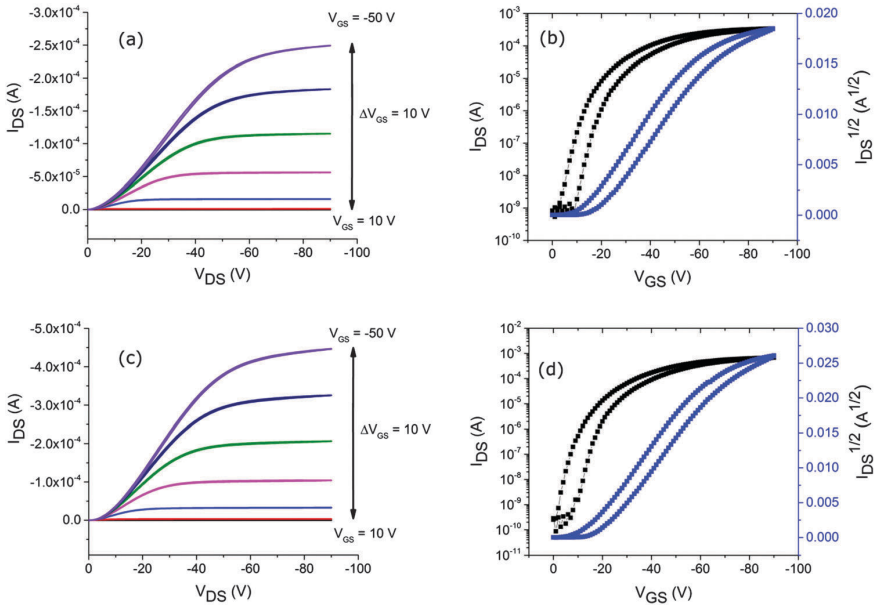

Fig. 4 (a) and (b) show the output and transfer characteristics for an OFET fabricated using 5T-TTF; (c) and (d) are the output and transfer characteristics for an OFET fabricated with 5T-TTF + 5% CZTS.

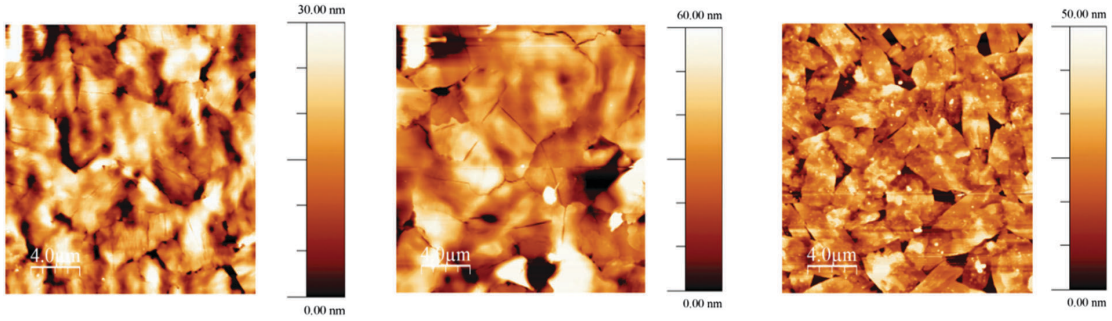

Fig. 5 AFM images of OFETs fabricated from 5T-TTF (left), 5T-TTF + 5% CZTS (centre) and 5T-TTF + 10% CZTS (right)

shown in Fig. 5. The surface of the OFET fabricated using 5T-TTF is comparable to the image of the surface from the previously fabricated device.[26] Surprisingly, despite the increased roughness of the surface of the device fabricated with 5 wt% CZTS, compared to the pristine organic film, the hole mobility is higher. As the concentration of CZTS is increased to 10%, there is a significant change in morphology with the 5T-TTF domains being broken up. The emergence of a number of gaps in the film explains the poor performance for this device.

The behaviour of the OFETs fabricated using P3HT and CZTS is slightly different to those from 5T-TTF and the device data for each OFET are summarised in Table 2. The output and transfer characteristics for the OFET fabricated using P3HT without any additives are shown in Fig. 6a and b. The average hole mobility calculated for P3HT is 0.041 $cm^2\ V^{-1}\ s^{-1}$ and in a similar trend to the 5T-TTF OFET, when 5 wt% CZTS is added to the solution used for OFET fabrication there is an increase in the mobility. The output and transfer graphs for this device are shown in Fig. 6c and d. The calculated hole mobility (0.053 $cm^2\ V^{-1}\ s^{-1}$) is 29% higher than the OFET fabricated without any nanoparticles. However, unlike the oligomer based OFETs where 10% CZTS led to a deterioration in performance, OFETs fabricated with P3HT and 10% CZTS (Fig. 6e and f) showed a further increase in charge carrier mobility, with the

Table 2 Results for fabricated OFETs from P3HT with various concentrations of CZTS

Compound	V_{Th} (V)	ON/OFF ratio	Average μ_{hole} ($cm^2\ V^{-1}\ s^{-1}$)	$\sigma\mu_{hole}$
P3HT	−8	10^2	0.041	0.015
P3HT + 5% CZTS	−9	10^2	0.053	0.012
P3HT + 10% CZTS	−10	10^2	0.088	0.013
P3HT + 15% CZTS	−10	10^2	0.037	9.6×10^{-3}
P3HT + 20% CZTS	−10	10^2	0.033	0.016

average mobility calculated as 0.088 $cm^2\ V^{-1}\ s^{-1}$, a 115% increase compared to the value for the device fabricated using only the polymer. In contrast, a further increase in nanoparticle concentration to 15% or 20% shows charge carrier mobilities only slightly lower than the OFET fabricated with a neat P3HT film, showing that performance is not enhanced by the addition of higher concentrations of nanoparticles.

The AFM images for P3HT devices are shown in Fig. 7 and give a clear trend. The device fabricated using neat P3HT shows a number of polymer aggregates on the surface. As 5 wt% CZTS is added to the solution, the resulting device still shows P3HT aggregates, but overall there are fewer of these domains. There is a further reduction in the surface roughness as the CZTS concentration is increased to 10% and there appears to be a significant decrease in the size of the P3HT aggregates. The domain sizes are slightly larger when the concentration is increased to 15% CZTS and the surface roughness also increases, but the aggregates are smaller than those present in the neat polymer film. This suggests that, although the P3HT aggregates are being broken up in films formed from 15% and 20% CZTS solutions, charge transport is inhibited by the increased nanoparticle concentration and therefore leads to a charge carrier mobility that is slightly reduced with respect to OFETs fabricated using P3HT. It is worth noting that the OFET performance does not tail off as significantly as when the CZTS concentration is increased for 5T-TTF containing OFETs.

Finally, in an attempt to determine if the nanoparticles or the oleylamine ligands are responsible for the improved performance, P3HT OFETs were fabricated using 5% v/v and 10% v/v oleylamine. The output and transfer characteristics for each of these OFETs are shown in the ESI† (Fig. S2). The addition of 5% oleylamine leads to a severely reduced mobility (μ_h = 2.83 × 10^{-3} $cm^2\ V^{-1}\ s^{-1}$) and

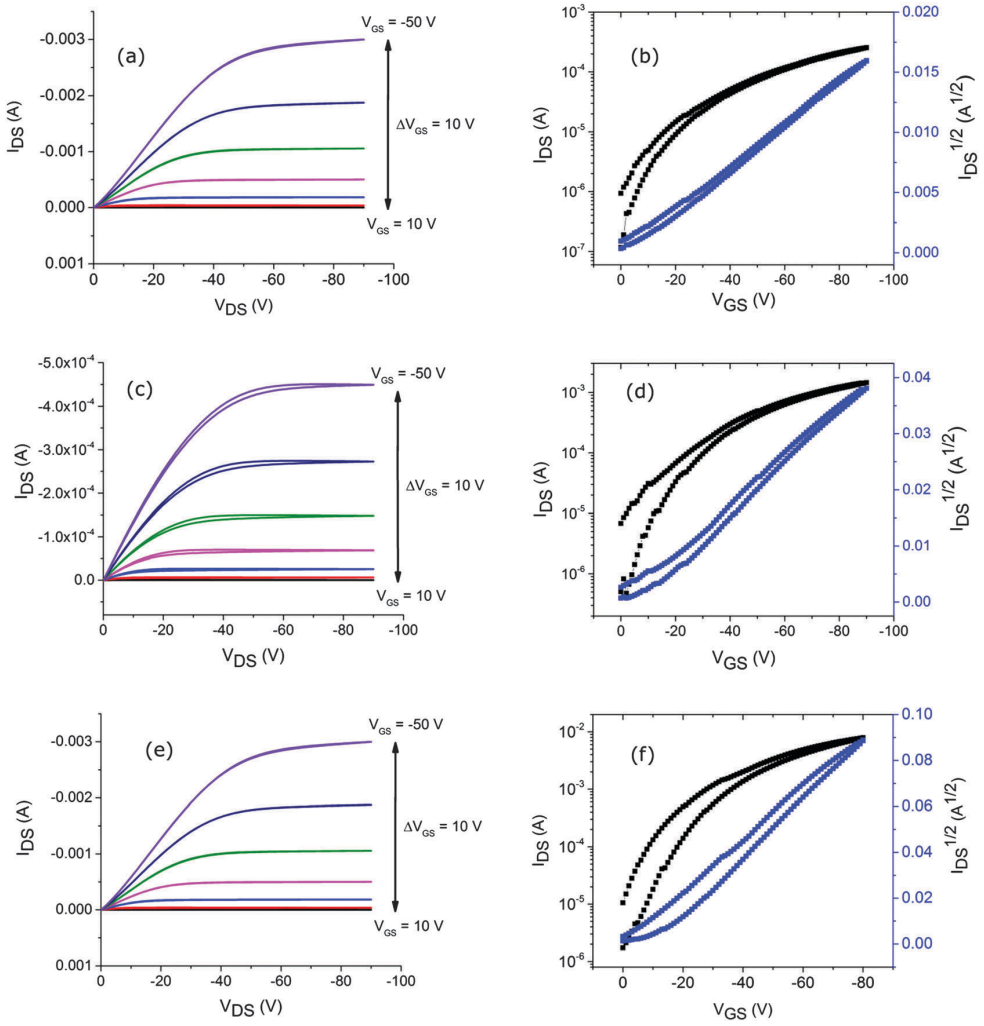

Fig. 6 Output and transfer characteristics (left and right columns, respectively), for OFETs fabricated using neat P3HT [(a) and (b)], P3HT + 5% CZTS [(c) and (d)], and P3HT + 10% CZTS [(e) and (f)].

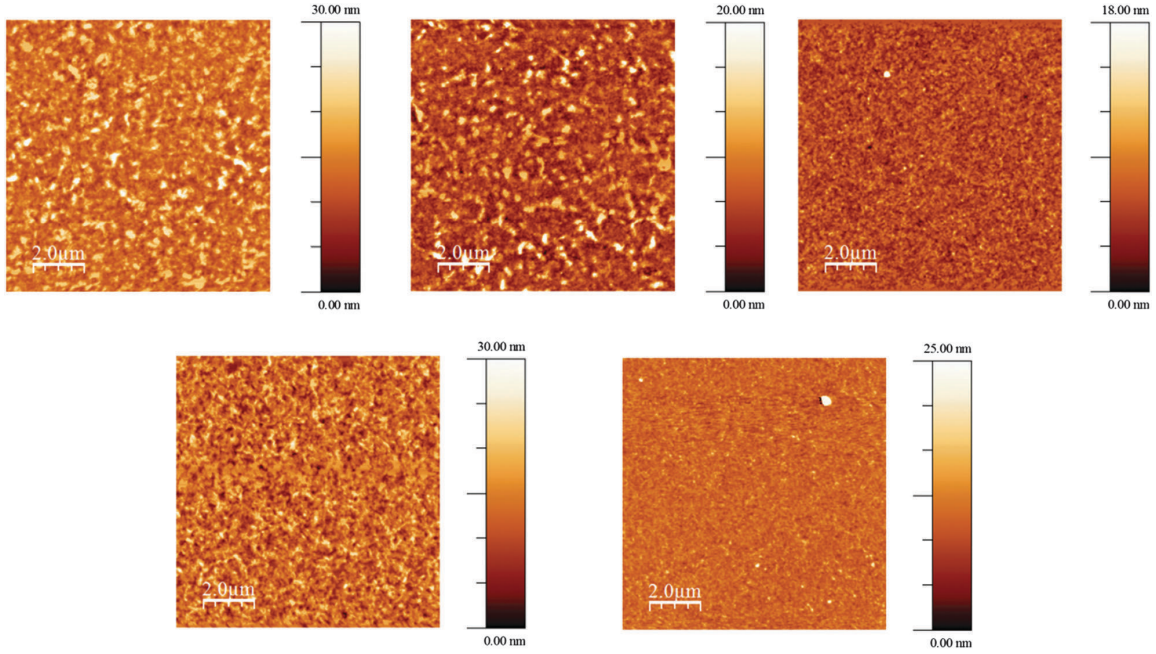

Fig. 7 AFM images for OFETs fabricated using P3HT (top, left), P3HT + 5% CZTS (top, centre), P3HT + 10% CZTS (top, right), P3HT + 15% CZTS (bottom, left) and P3HT + 20% CZTS (bottom, right).

although this is improved with 10% oleylamine (μ_h = 6.07 × 10^{-3} cm^2 V^{-1} s^{-1}), the performance of both devices is considerably poorer than any of the devices fabricated using P3HT and CZTS. This would suggest that the nanoparticles are responsible for improving the OFET performance rather than the long oleylamine ligands.

Conclusion

CZTS nanoparticles have been used as additives for the fabrication of solution-processed OFETs. The nanoparticle composites (5% CZTS) with 5T-TTF had a hole mobility 68% higher than devices using only the oligomer, whilst 10% addition to P3HT devices led to a hole mobility more than double (115% increase) that of the OFET with neat P3HT. The additives are inexpensive and environmentally benign, which suggests that they have potential for the improvement of OFETs. Reports on applications of inorganic nanoparticles in OFETs are sparse in the literature and have been limited mainly to their use as nanocomposites in gate dielectric layers.[29–31] Zinc oxide nanoparticles have been used in polyfluorene composites for light-emitting field effect transistors,[32] whilst Q-ZnO has been applied as a component in a hybrid OFET bilayer device fabricated with P3HT as the organic film.[33] Blends of P3HT and CdSe have been studied in OFETs[34] and also in organic photovoltaics devices.[35] However, the mechanism of charge transport in these composites is not well understood. It has been shown by low temperature light-induced electron spin resonance studies that the morphology of P3HT changes in the presence of CdSe nanoparticles[34] and that charge transfer between the two components only takes place efficiently if the CdSe capping ligand is removed. In OFETs, however, the structure of the capping ligand in P3HT/CdSe composites influences the value of the mobility.[35] This begs the question whether or not the inorganic nanoparticles in hybrid OFETs change the characteristics of the device as a function of morphology or if the role of the inorganic material is more complex. It is perhaps more intuitive to assume the former and our work clearly shows that morphology changes with different loadings of CZTS nanoparticles. However, an in-depth study needs to be conducted to elucidate the full role of CZTS in composites. One would expect that the inclusion of nanoparticles into pristine molecular (5T-TTF) and polymeric (P3HT) materials would disrupt long-range order and affect charge transport detrimentally, and remarkably we see an enhancement of hole mobility upon the application of CZTS nanoparticles. One possible explanation is that the inorganic material reduces the density of traps in the organic layer and this has been seen in the case of MEH-PPV/ZnO blends.[36]

Acknowledgements

P. K. thanks the School of Chemistry, The University of Manchester for funding. We thank EPSRC for funding the instruments under grant number (EP/K039547/1) for characterisation of the CZTS compounds. P. J. S. thanks the Royal Society for a Wolfson Research Merit Award. R. G. D. T. thanks the EPSRC for funding (EP/L012200/1). All data supporting this research are openly available from http://dx.doi.org/10.15129/2527c5db-bde6-48cd-b145-55f15f837fb2.

Notes and references

1 Y. Qiao, Y. Guo, C. Yu, F. Zhang, W. Xu, Y. Liu and D. Zhu, *J. Am. Chem. Soc.*, 2012, **134**, 4084–4087.

2 R. Pfattner, M. Mas-Torrent, I. Bilotti, A. Brillante, S. Milita, F. Liscio, F. Biscarini, T. Marszalek, J. Ulanski, A. Nosal, M. Gazicki-Lipman, M. Leufgen, G. Schmidt, L. W. Molenkamp, V. Laukhin, J. Veciana and C. Rovira, *Adv. Mater.*, 2010, **22**, 4198–4203.

3 E. D. Głowacki, M. Irimia-Vladu, M. Kaltenbrunner, J. Gsiorowski, M. S. White, U. Monkowius, G. Romanazzi, G. P. Suranna, P. Mastrorilli, T. Sekitani, S. Bauer, T. Someya, L. Torsi and N. S. Sariciftci, *Adv. Mater.*, 2013, **25**, 1563–1569.

4 H.-R. Tseng, H. Phan, C. Luo, M. Wang, L. A. Perez, S. N. Patel, L. Ying, E. J. Kramer, T.-Q. Nguyen, G. C. Bazan and A. J. Heeger, *Adv. Mater.*, 2014, **26**, 2993–2998.

5 I. Meager, M. Nikolka, B. C. Schroeder, C. B. Nielsen, M. Planells, H. Bronstein, J. W. Rumer, D. I. James, R. S. Ashraf, A. Sadhanala, P. Hayoz, J.-C. Flores, H. Sirringhaus and I. McCulloch, *Adv. Funct. Mater.*, 2014, **24**, 7109–7115.

6 S. Park, B. T. Lim, B. Kim, H. J. Son and D. S. Chung, *Sci. Rep.*, 2014, **4**, 5482.

7 Y. Yuan, G. Giri, A. L. Ayzner, A. P. Zoombelt, S. C. B. Mannsfeld, J. Chen, D. Nordlund, M. F. Toney, J. Huang and Z. Bao, *Nat. Commun.*, 2014, **5**, 3005.

8 J. Huang, D. R. Hines, B. J. Jung, M. S. Bronsgeest, A. Tunnell, V. Ballarotto, H. E. Katz, M. S. Fuhrer, E. D. Williams and J. Cumings, *Org. Electron.*, 2011, **12**, 1471–1476.

9 M. El Gemayel, A. Narita, L. F. Dossel, R. S. Sundaram, A. Kiersnowski, W. Pisula, M. R. Hansen, A. C. Ferrari, E. Orgiu, X. Feng, K. Mullen and P. Samori, *Nanoscale*, 2014, **6**, 6301–6314.

10 S. Park, S. Jin, G. Jun, S. Jeon and S. Hong, *Nano Res.*, 2011, **4**, 1129–1135.

11 Y. D. Park, J. A. Lim, Y. Jang, M. Hwang, H. S. Lee, D. H. Lee, H.-J. Lee, J.-B. Baek and K. Cho, *Org. Electron.*, 2008, **9**, 317–322.

12 X.-Z. Bo, C. Y. Lee, M. S. Strano, M. Goldfinger, C. Nuckolls and G. B. Blanchet, *Appl. Phys. Lett.*, 2005, **86**, 182102.

13 P. Jackson, D. Hariskos, E. Lotter, S. Paetel, R. Wuerz, R. Menner, W. Wischmann and M. Powalla, *Prog. Photovoltaics*, 2011, **19**, 894–897.

14 W. Wang, M. T. Winkler, O. Gunawan, T. Gokmen, T. K. Todorov, Y. Zhu and D. B. Mitzi, *Adv. Energy Mater.*, 2014, **4**, 1301465.

15 W. Yang, H.-S. Duan, K. C. Cha, C.-J. Hsu, W.-C. Hsu, H. Zhou, B. Bob and Y. Yang, *J. Am. Chem. Soc.*, 2013, **135**, 6915–6920.

16 B. Shin, O. Gunawan, Y. Zhu, N. A. Bojarczuk, S. J. Chey and S. Guha, *Prog. Photovoltaics*, 2013, **21**, 72–76.

17 H. Zhou, H.-S. Duan, W. Yang, Q. Chen, C.-J. Hsu, W.-C. Hsu, C.-C. Chen and Y. Yang, *Energy Environ. Sci.*, 2014, **7**, 998–1005.

18 L. Arora, V. Singh, G. Partheepan, T. D. Senguttuvan and K. Jain, *Appl. Nanosci.*, 2015, 1–10.

19 G. Konstantatos, I. Howard, A. Fischer, S. Hoogland, J. Clifford, E. Klem, L. Levina and E. H. Sargent, *Nature*, 2006, **442**, 180–183.

20 J. M. Luther, M. Law, Q. Song, C. L. Perkins, M. C. Beard and A. J. Nozik, *ACS Nano*, 2008, **2**, 271–280.

21 G. I. Koleilat, L. Levina, H. Shukla, S. H. Myrskog, S. Hinds, A. G. Pattantyus-Abraham and E. H. Sargent, *ACS Nano*, 2008, **2**, 833–840.

22 N. Revaprasadu, M. A. Malik and P. O'Brien, *S. Afr. J. Chem.*, 2004, **57**, 40–43.

23 M. B. Hursthouse, M. A. Malik, M. Motevalli and P. O'Brien, *J. Mater. Chem.*, 1992, **2**, 949–955.

24 K. Ramasamy, V. L. Kuznetsov, K. Gopal, M. A. Malik, J. Raftery, P. P. Edwards and P. O'Brien, *Chem. Mater.*, 2013, **25**, 266–276.

25 A. V. Moholkar, S. S. Shinde, G. L. Agawane, S. H. Jo, K. Y. Rajpure, P. S. Patil, C. H. Bhosale and J. H. Kim, *J. Alloys Compd.*, 2012, **544**, 145–151.

26 I. A. Wright, N. J. Findlay, S. Arumugam, A. R. Inigo, A. L. Kanibolotsky, P. Zassowski, W. Domagala and P. J. Skabara, *J. Mater. Chem. C*, 2014, **2**, 2674–2683.

27 S. Ji, T. Shi, X. Qiu, J. Zhang, G. Xu, C. Chen, Z. Jiang and C. Ye, *Sci. Rep.*, 2013, **3**, 2733.

28 K. Ramasamy, M. A. Malik and P. O'Brien, *Chem. Sci.*, 2011, **2**, 1170–1172.

29 M. R. Beaulieu, J. K. Baral, N. R. Hendricks, Y. Tang, A. L. Briseño and J. J. Watkins, *ACS Appl. Mater. Interfaces*, 2013, **5**, 13096–13103.

30 L. Huang, Z. Jia, I. Kymissis and S. O'Brien, *Adv. Funct. Mater.*, 2010, **20**, 554–560.

31 R. P. Ortiz, A. Facchetti and T. J. Marks, *Chem. Rev.*, 2010, **110**, 205–239.

32 N. A. Andrey and P. S. Igor, *J. Phys. D: Appl. Phys.*, 2010, **43**, 315104.

33 R. A. Picca, M. C. Sportelli, D. Hötger, K. Manoli, C. Kranz, B. Mizaikoff, L. Torsi and N. Cioffi, *Electrochim. Acta*, 2015, **178**, 45–54.

34 U. Bielecka, P. Lutsyk, M. Nyk, K. Janus, M. Samoc, W. Bartkowiak and S. Nespurek, *Mater. Sci.-Pol.*, 2013, **31**, 288–297.

35 M. D. Heinemann, K. von Maydell, F. Zutz, J. Kolny-Olesiak, H. Borchert, I. Riedel and J. Parisi, *Adv. Funct. Mater.*, 2009, **19**, 3788–3795.

36 Z.-X. Xu, V. A. L. Roy, P. Stallinga, M. Muccini, S. Toffanin, H.-F. Xiang and C.-M. Che, *Appl. Phys. Lett.*, 2007, **90**, 223509.

Supplementary Information section

Nanoparticles of Cu_2ZnSnS_4 as Performance Enhancing Additives for Organic Field-Effect Transistors

Punarja Kevin,[a] Azad. M. Malik,[b] Paul O'Brien,[ab] Joseph Cameron,[c] Rupert G. D. Taylor,[c] Neil J. Findlay,[c] Anto R. Inigo[c] and Peter J. Skabara*[c]

[a]School of Chemistry, The University of Manchester, M13 9PL, UK
[b]School of Materials, The University of Manchester, M13 9PL, UK
[c]WestCHEM, Department of Pure and Applied Chemistry, University of Strathclyde, G1 1XL, UK

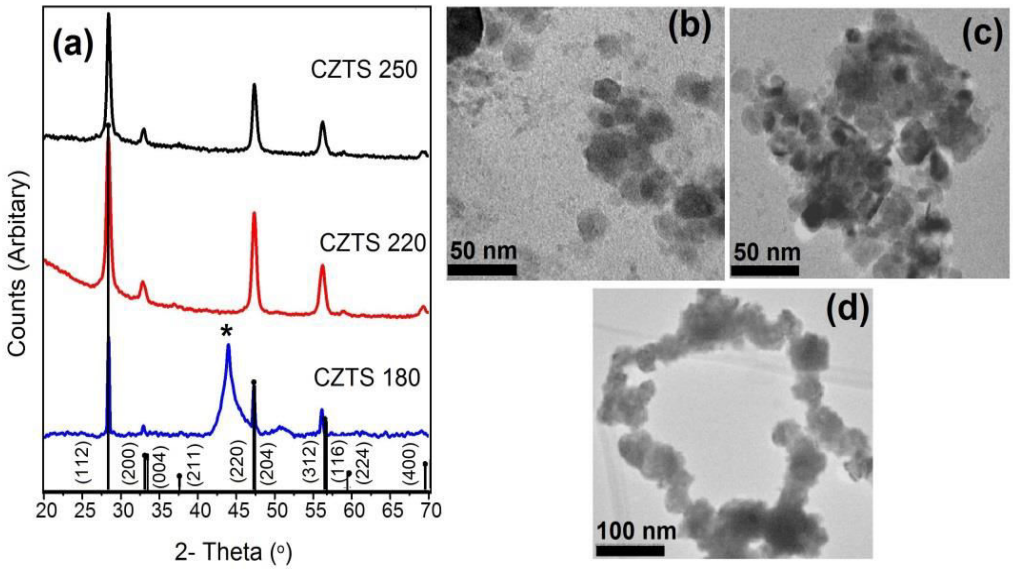

Figure S1: (**a**) are the p-XRD patterns of the CZTS nanoparticles synthesised at 180, 220 and 250°C. Peaks are indexed according to the kesterite structure (ICDD: 04-015-0223) of CZTS (stick patterns). The * mark shows unknown peaks. (**b**)-(**d**) are the TEM images of CZTS nanoparticles synthesised at 180, 220 and 250°C respectively.

Supplementary Information section

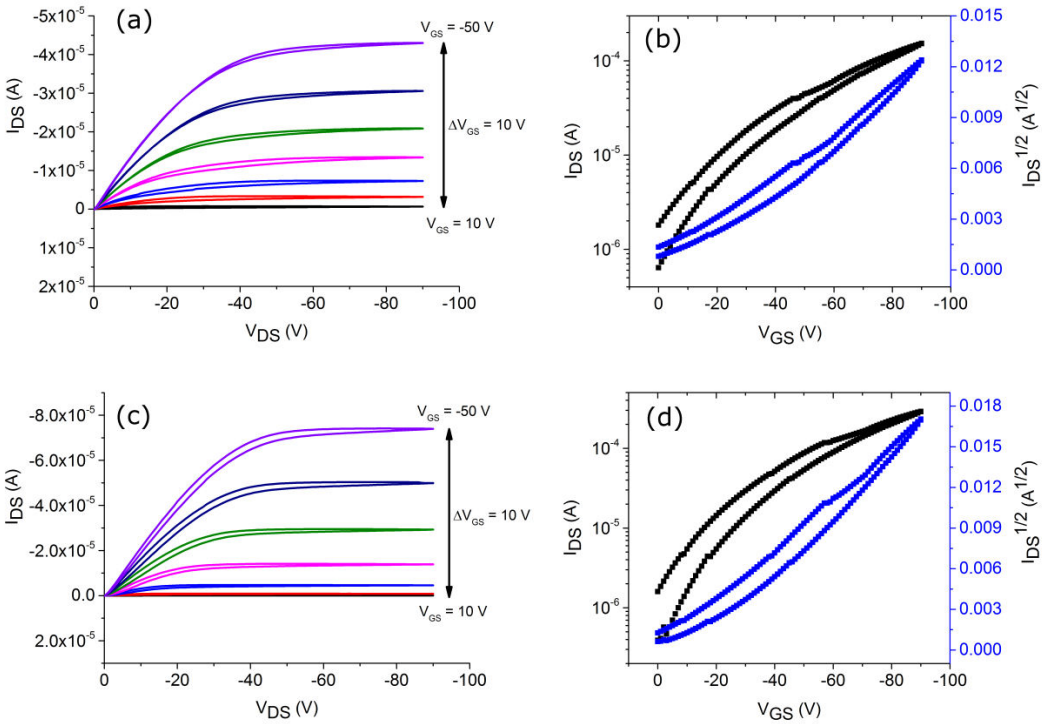

Figure S2: Output and transfer characteristics (left and right columns, respectively) for OFETs fabricated using P3HT + 5% oleylamine [(a) and (b)] and P3HT + 10% oleylamine [(c) and (d)]

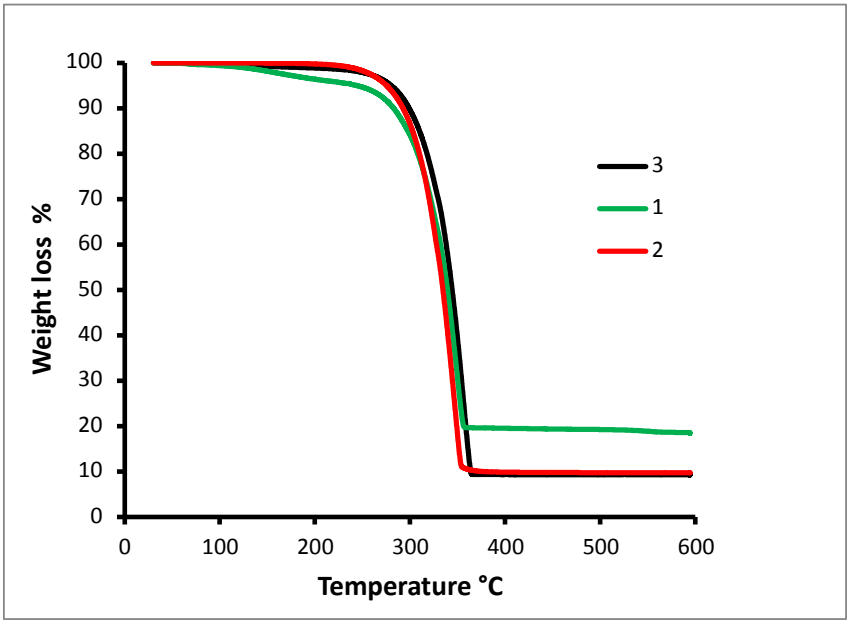

Figure S3: TGA analysis of the samples $[Cu(S_2CNEt_2)_2]$ (**1**), $[Zn(S_2CNEt_2)_2]$ (**2**) and $[^nBu_2Sn(S_2CNEt_2)_2]$ (**3**). Analyses of the samples were carried out by a Seiko SSC/S200 model from 10 to 600°C with a heating rate of 10°C min^{-1} under nitrogen.

CHAPTER - XV

Conclusion and Future work

Copper and tin based chalcogenides are widely used because of their potential use in solar energy applications. The band gap of these materials can be tuned between 1.0 to 2.0 eV by addition of elements such as Zn, Fe, In, Ga etc. Chapter II to III contain a detailed introduction and literature review on the copper and tin based materials and their solar energy applications. Chapter IV of this thesis summarises the synthesis of a series of dithiocarbamates of tin(II) with the formula $[Sn(S_2CNRR')_2]$ (R = Et, R' = n-Bu; R = Me, R' = n-Bu; R = R' = Et) and the deposition of SnS thin films using these complexes by aerosol-assisted chemical vapour deposition (AACVD). The effects of both temperature and the concentration of the precursors on deposition were investigated. The experimental results can be concluded as the stoichiometry of SnS films was best at higher concentrations of precursors and deposition at 450 °C deposition temperature. The direct band gap of the SnS produced was estimated as 1.2 eV. SnS devices with about 4.4 % efficiencies were reported in 2014 by Sinsermsuksakul *et al*. [326] hence in future there is an imperative need to fabricate solar cells with SnS thin films deposited by AACVD using these precursors.

SnSe thin films and nanoparticles are used in optoelectronic devices and as thermoelectric material in lithium ion batteries, the focus of Chapter V was the detailed report on the AACVD of SnSe using a novel complex $[Sn(Ph_2PSe_2)_2]$. The report also includes the deposition of Cu_2SnSe_3 thin films as these materials possess a simple crystal structure and phase diagram as compared to other quaternary chalcogenides. Cu_2SnSe_3 is one of the best candidates for a variety of optoelectronic and solar energy applications. The uses of Cu_2SnSe_3 are being explored in: acousto-optic applications, thermo-

electronics, and biomedical applications and had been deposited by using the combination of $[Sn(Ph_2PSe_2)_2]$ with $[Cu(acac)_2]$ by AACVD. The best films of SnSe and Cu_2SnSe_3 were obtained at 400 and 450 °C.

Many researchers suggests that the properties of Cu_2ZnSnS_4 can be strongly affected by the changes in its stoichiometry mainly the Cu/(Zn+Sn) or Zn/Sn ratio on the morphology, phase purity and optical properties. Chapter VI of this thesis reports a comprehensive study on the deposition parameters of Cu_2ZnSnS_4 thin films by AACVD using dithiocarbamato complexes of Cu, Zn and Sn in different molar composition as precursors. The results were promising and we showed that the mole ratio of [Cu]:[Zn] precursors and deposition temperature play a crucial role in determining the stoichiometry, band gap and morphology of the deposited films. A device was fabricated with a thin layer of mesoporous TiO_2 and a layer of thin layer of CZTS deposited at optimum composition showed an efficiency of 2.39 % under one sun radiation. Further studies to improve the efficiency of the device and the publication of achieved results are in progress.

Chapter VII and VIII of the thesis mainly targeted the development of thin films of Cu_2FeSnS_4, $Cu_2FeSnSe_4$, $Cu_2FeSnSe_4$ and $Cu_2FeSn(S_xSe_{1-x})_4$ by AACVD using a mixted precursor approach. The best films of each type, in terms of the stoichiometry, structure and properties were successfully deposited at 350 °C. These results are exciting but still need more compositional studies especially in the deposition of $Cu_2FeSn(S_xSe_{1-x})_4$ thin films. The use of mixed precursors by AACVD opens a potential route towards synthesising these quaternary materials. The sheet resistance of Cu_2FeSnS_4, $Cu_2FeSnSe_4$ and $Cu_2FeSn(S_xSe_{1-x})_4$ were 2.13 $k\Omega\ cm^{-2}$, 1.48 $k\Omega\ cm^{-2}$ and 1.89 $k\Omega\ cm^{-2}$ respectively and band gap values were between 1.1-1.6 eV which is ideal for solar cells. Further studies on thermal resistance, photovoltaic and magnetic properties of thin films will be

carried out in future. The results of the study of the deposition of $Cu_2ZnSnSe_4$ and $Cu_2FeSnSe_4$ showed that the materials adopt kesterite and stannite structures respectively. The measured band gaps of iron-containing materials were comparatively lower than those of zinc in the quaternary materials. These results also showed that selenium-rich films were found to have lower band gap and resistance values as compared to those with selenium-deficient or sulfide films. Moreover, films deposited at higher temperatures were found to be selenium-deficient and hence gave higher optical band gaps than those deposited at the lower temperatures.

Kesterite materials containing iron and zinc are considered to be amongst the better absorbers for polycrystalline PV-solar cells, but experimental studies on the phase transition between kesterite and stannite phases are underexplored. In Chapter IX, the relationship between the [Zn]:[Fe] ratio on these materials was studied using Ritveld analysis of the p-XRD results from films deposited b AACVD. These kesterite and stannite polymorphs had very small difference in their thermodynamic stability, and addition of iron into Cu_2ZnSnS_4 thin films decreases the optical band gap. The composites: $Cu_2(Zn_yFe_{1-y})SnS_4$ (CZFTS), $Cu_2(Zn_yFe_{1-y})SnSe_4$ (CZFTSe) and $Cu_2(Zn_yFe_{1-y})Sn(SSe)_4$ (CZFTSSe) showed; band gaps, absorption coefficients and transport properties similar to those of Cu_2ZnSnS_4 (CZTS). The solubility of iron in the CZTS derivatives plays a key role in controlling many parameters. Thin films of CZFTS, CZFTSe and CZFTSSe deposited by AACVD showed that the ratios of the constituents: Zn, Fe, S and Se can be controlled by varying the concentrations of corresponding precursors and the deposition temperature. The band gaps of these materials lie between 1.0 eV and 1.7 eV, on changing the [Zn]:[Fe] and [S]:[Se] ratios in the material. The sheet resistance of the materials are good for polycrystalline CZTS PV-cells. The structural parameters for the films do not show any consistent variation with composition; given the wide range of differing radii of the ions involved, this observation

is perhaps not surprising. The band gap and resistance of each film is overwhelmingly controlled by the selenium content as Khadka and Kim demonstrated previously. [56] The potential for the use of these materials in devices will be investigated in the future.

Chapter X summarises the deposition of CdSe and CdS_xSe_{1-x} layers by AACVD using diseleno-carbamato-metal precursors. The results showed the deposited CdSe and CdS_xSe_{1-x} thin films had high crystallinity and comparatively good composition, but further studies are needed for different composition sets. Moreover, films were slightly contaminated by excess Cd and Se which can possibly alter the properties of these films hence detailed studies need to be carried to deposit extra CdSe and CdS_xSe_{1-x} thin films by AACVD.

Chapter XI describes the deposition of CZTSSe thin films with tunable band gaps by AACVD using dithio-and diseleno-carbamato complex as precursor sources. It can be concluded that the band gaps of these materials can be tuned from 0.96 to 1.6eV by changing the S:Se ratios of the material. The sheet resistance of the films decreases with increasing selenium content and the highest (11.3 $k\Omega\ cm^{-2}$) and lowest (9.3 $k\Omega\ cm^{-2}$) resistance observed for CZTS and CZTSe respectively which correlates well with reported values. Detailed optical and photovoltaic applications of these materials will be explored in future.

Chapters XII and XIII demonstrate the novel synthesis and characterisation of $Cu_2Zn_{1-x}Fe_xSnS_4$ nanoparticles with mole fractions of Fe from 0 to 1. Detailed compositional studies (p-XRD patterns and EDX) analysis showed that these materials, in contrast to bulk, maintained a stannite structure. The iron-containing materials are ferromagnetic at low temperatures. Such materials may find applications in magnetoelectronic, optoelectronic, or photo the fabrication of solar cells and devices.

Organic semiconductors are low cost materials for electronic devices such as field-effect transistors (OFETs). Attempts to improve the charge carrier mobility of OEFT devices are poorly explored. Chapter XIV reports the use of CZTS nanoparticles as additives in the fabrication of solution-processed OFETs. The nanoparticle composites (5% CZTS) with 5T-TTF had a hole mobility 68% higher than devices using only the oligomer, whilst the 10% addition to P3HT devices led to a hole mobility more than double (114 % increase) that of the OFET with neat P3HT. The nanoparticles used as additives are inexpensive and environmentally benign. The inclusion of nanoparticles into molecular (5T-TTF) and polymeric (P3HT) materials may disrupt long-range order and affect charge transport detrimentally, yet remarkably we see an enhancement. However, a more in-depth study needs to be conducted to elucidate the full role of CZTS in composites. Also in future the effect of Fe containing composites can be studied as a continuation of this project.

CHAPTER - XVI

References

1. M. G. Bawendi, M. L. Steigerwald, L. E. Brus, *Annu. Rev. Phys. Chem*., 1990, **41**, 477-496.
2. L. Brus, *J. Chem. Phys.* 1986, **90**, 2555-2560.
3. M. L. Steigerwald, L. E. Brus, *Acc. Chem. Res*., 1990, **23**, 183-188.
4. L. E. Brus, *J. Chem. Phys*. 1983, **79**, 5566-5571
5. D. J. Norris, M. G. Bawendi, *Phys. Rev. B: Condens. Matter Mater. Phys*., 1996, **53**, 16338-16346.
6. J. Y. Kim, O. Voznyy, D. Zhitomirsky, E. H. Sargent, *Adv. Mater.*, 2013, **25**, 4986-5010.
7. Y. Xia, P. Yang, Y. Sun, Y. Wu, B. Mayers, B. Gates, Y. Yin, F. Kim, H. Yan, *Adv. Mater.* 2003, **15**, 353-389.
8. D. Koziej, A. Lauria, M. Niederberger, *Adv. Mater*. 2014, **26**, 235-257.
9. M. R. Gao, Y. F. Xu, J. Jiang and S. H. Yu, *Chem. Soc. Rev.* 2013, **42**, 2986-3017.
10. A. Urbieta, P. Fernandez, J. Piqueras, *J. Appl. Phys.* 2004, **96**, 2210-2213.
11. S. Chen, X. G. Gong, A. Walsh, S. H. Wei, *Phys. Rev. B* 2009, **79**, 165211-5.
12. S. Chen, X. G. Gong, A. Walsh, S. H. Wei, *Appl. Phys. Lett.* 2000, **94**, 041903-5.
13. S. Chen, W. J. Yin, J. H. Yang, X. Gong, A. Walsh, S. H. Wei, *Appl. Phys. Lett.* 2009, ***95***, 052102-6.
14. C. Sevik, T. Cagin, *Appl. Phys. Lett.* 2009, **95**, 112105-9.
15. S. Chen, X. Gong, C. G. Duan, Z. Q. Zhu, J. H. Chu, A. Walsh, Y. G. Yao, J. Ma, S. H. Wei, *Phys. Rev. B* 2011, **83**, 245202-245208 .
16. C. Eric, E. Jeremy, E. Barton, T. W. Odom, *small* 2006, **2**, 368-371

17. L. A. Burton, A. Walsh, *J. Solid State Chem*. 2012, **196**, 157-160.

18. A. Walsh, D. J. Payne, R. G. Egdell, G. W. Watson, *Chem. Soc. Rev*. 2011, **40**, 4455-63 ,

19. J. Bordast, J. Robertson, A. Jakobsson, *J. Phys. C: Solid State Phys*. 1978, **11**, 2607-2621

20. J. Vidal, S. Lany, M. d'Avezac, A. Zunger, A. Zakutayev, J. Francis, J. Tate, *Appl. Phys. Lett*. 2012, **100**, 032104-11.

21. W. Albers, C. Haas, H. J. Vink, J. D. Wasscher, *J. Appl. Phys.* 1961, **32**, 2220-8).

22. T. Löher, W. Jaegermann, C. Pettenkofer, *J. Appl. Phys*. 1995,**77** ,731-738

23. G. Teeter, *J. Appl. Phys*. 2007, **102**, 034504 -6.

24. Y. Hinuma, F. Oba, Y. Kumagai, and I. Tanaka, *Phys. Rev*. B, 2012, **86**, 245433-9.

25. Y. Li, A. Walsh, S. Chen, W. Yin, J. Yang, J. Li, J. Da Silva, X. Gong, and S. Wei, *Appl. Phys. Lett*. 2009, **94**, 212109 -7.

26. S. G. Hickey, C. Waurisch, B. Rellinghaus, A. Eychmuller, J. Am. Chem. Soc. 2008, **130**, 14978-14980

27. L. A. Burton, A. Walsh, *J. Solid State Chem*. 2012, **196**, 157-163.

28. R. Laihia, J. A. Leiro, K. Kokko, K. Mansikka, J. *Phys. Condens. Matter* 1996, **8**, 6791–6801.

29. F. Kurnia, J. N. Hart, *Chem. Phys. Chem*, 2015, **16**, 2397- 2402.

30. S. M. Sze, K. K. Ng, *Phys. Semiconductor Devices, Wiley, Hoboken, New Jersey*, 2007.

31. I. Tsuji, H. Kato, H. Kobayashi, A. Kudo *J. Phys. Chem. B*, 2005, 1**09**, 7323-7329.

32. P. Kar, S. Farsinezhad, X. Zhang, K. Shank, *Nanoscale*, 2014, **6**, 14305–14318.

33. S. H. Choi, K. An, E. G. Kim, J. H. Yu, J. H. Kim, T. Hyeon, *Adv. Funct. Mater*. 2009, **19**, 1645-1649.

34. P. C. Dai, X. N. Shen, Z. J. Lin, Z. Y. Feng, H. Xu, J. H. Zhan, *Chem. Commun*., 2010, **46**, 5749-5751.

35. G. M. Ford, Q. J. Guo, R. Agrawal, H. W. Hillhouse, *Chem. Mater*., 2011, **23**, 2626-2629.

36. J. Paier, R. Asahi, A. Nagoya, G. Kresse, *Phys. Rev. B* 2009, **79**, 115126-8.

37. S. Y. Chen, A. Walsh, Y. Luo, J. H. Yang, X. G. Gong, S. H. Wei, *Phys. Rev. B: Condens. Matter Mater. Phys.*, 2010, **82**, 195203-7.

38. S. Chen, X. G. Gong, S.-H. Wei, *Phys. Rev. B*, 2007, **75**, 205209.

39. M. Kumar, C. Persson, *Int. J. Theore. Appl. Sci.* 2013, **5**, 1-8

40. S. Chen, A. Walsh, J-H. Yang, X. G. Gong, L. Sun, P-X. Yang, J-H. Chu, S-H. Wei, *Phys. Rev. B*.2011, **83**, 125201-5.

41. Y. H. Li, A. Walsh, S. Chen, W. J. Yin, J. H. Yang, J. Li, J. L. F. Da Silva, X. G. Gong, S.-H. Wei, *Appl. Phys. Lett.* 2009, **94**, 212109-3.

42. C. Perrson, *J. Appl. Phys*. 2010, **107**, 053710-9.

43. D. J. Vaughan, J. A. Tossell, *Can Miner*, 1980, **18**, 157-163.

44. J. A. Tossell, *Phys. Chem. Miner*. 1978, **2**, 225-236

45. Y. Zhang, X. Yuan, X. Sun, B. Shih, P. Zhang, W. Zhang, *Phys. Rev. B*. 2011, **84**, 0751271− 0751279.

46. S. C. Ameta, R. Ameta, 2015, 10, *Solar Energy Conversion and Storage*: *Photochemical Modes*, CRC Press (UK).

47. Y. Zhang, X. Sun, P. Zhang, X. Yuan, F. Huang, W. Zhang, *J. Appl. Phys*. 2012, **111**, 063709.

48. D. Li, G. M. Bancroft, M. Kasrai, M. E. Fleet, X. H. Feng, B.X. Yang, K.H. Tan, *Phys. Chem. Miner.*1994, **21**, 317-324.

49. S. R. Hall, J. T. Szymanski, J. M. Stewart, *Can. Miner*. 1978, **16**, 131-137.

50. S. Chen, X. G. Gong, A. Walsh, S. H. Wei, *Appl. Phys. Lett*. 2009, **94**, 041903-4.

51. T. Washio, H. Nozaki, T. Fukano, T. Motohiro, K. Jimbo, H. Katagiri. *J. Alloys. Compd*. 2012, **524**, 22-31.

52. R. D. Shannon, M. O'Keeffe, A. Navrotsky, *Structure and Bonding in Crystals*, 1981, **2**, 53-70.

53. P. Bonazzi, L. Bindi, G. P. Bernandini, S. Menchetti, *Can. Miner.* 2003, **41**, 639-647.

54. S. Schorr, H.-J. Hoebler, M. Tovar, *Eur. J. Miner.* 2007, **19**, 65-73.

55. S. Botti, D. Kammerlander, M. A. L. Marques, *Appl. Phys. Lett*. 2011, **98**, 241915-3.

56. D. B. Khadka and J.H. Kim, *J. Phys. Chem. C* 2014, **118**, 14227−14237.

57. T. Shibuya, Y. Goto, Y. Kamihara, M. Matoba, K. Yasuoka, L.A. Burton, A. Walsh, *Appl. Phys. Lett.* 2014, **104**, 0219121−0219124.

58. T. L. Evstigneeva, Y. K. Kabalov. *Crystallography Reports*, 2001, **46**, 368–372.

59. X. Huang, G. Yin, H. Qi, Gong, *Phys. Status Solidi RRL*, 2014, **8,** 735–762–372.

60. M. Himmrich, H. Haeuseler, *Spectrochim. Acta* 1991, **47**, 933−942.

61. T. K. Todorov, K. B. Reuter, D. B. Mitzi, *Adv. Mater.* 2010, **22**, E156−E159

62. H. Katagiri, N. Sasaguchi, S. Hoshino, J. Ohashi, T. Yokota, *Sol. Energy Mater. Sol. Cells* 1997, **49**, 407−414.

63. X. Jiang, W. Xu, R. Tan, W. Song, Chen, *Mater. Lett.* 2013, **102−103**, 39−42.

64. X. Zhang, N. Bao, K. Ramasamy, Y.H.A. Wang, Y. Wang, B. Lin, A. Gupta, *Chem. Commun*. 2012, **48**, 4956-4958

65. W. Wang, H. Shen, H. Yao, J. Li, *Mater. Lett*. 2014, **125**, 183–186

66. J. Zhou, Z. Ye, Y. Wang, Q. Yi, J. Wen, *Mater. Lett*. 2015, **140**, 119–122.

67. W. Schfifer, R. Nitsche, *Mater. Res. Bull*. 1974, **9**, 645–654.

68. M. Cao, C. Li, B. Zhang, J. Huang, L. Wang, Y. Shen, *J. Alloys Comp*. 2015, **622,** 695–702.

69. Z. Shadrokh, A. Yazdani, H. Eshgh, *Semicond. Sci. Technol*. 2016, **31**, 045004-12.

70. D.B. Khadka, J.H. Kim, *J. Alloys Compds*. 2015, **638**, 103-108.

71. E.R. Infante, J.M. Delgado, S.A.L. Rivera, *Mater. Lett.* 1997, **33**, 67–70.

72. M. Cao, B.L. Zhang, J. Huang, Y. Sun, L.J. Wang, Y. Shen, *Chem. Phys. Lett*. 2014, **604**, 15-21.

73. X. Meng, H. Deng, J. He, L. Zhu, L. Sun, P. Yang, J. Chu, *Mater. Lett*. 2014, **177**, 1–3

74. S. Siebentritt and S. Schor, *Prog. Photovolt: Res. Appl*. 2012, **20**, 512–519.

75. Q. J. Guo, H. W. Hillhouse, R. Agrawal, *J. Am. Chem. Soc.* 2009, **131**, 11672-769.

76. X. Jiang, L. X. Shao, J. Zhang, D. Li, W. Xie, C. W. Zou, J. M. Chen, *Surf. Coat. Technol*. 2013, **228**, S408−S411.

77. K. Yu, E. A. Carter, *Chem. Mater.* 2015, **27**, 2920−2927

78. R. F. Service, *Science,* 2005, **309**, 548-551.

79. J. C. Scott, J. H. Kaufman, P. J. Brock, R. D. Pietro, J. Salem, J. A. Goitia, *J. Appl. Phys.* 1996, **79**, 2745-2751.

80. N. Asim, K. Sopian, S. Ahmadi, K. Saeedfar, M. A. Alghoul, O. Saadatian, S. H. Zaidia, *Renew. Sust. Energy. Rev*. 2012, **16**, 5834-5847.

81. A. Shah, P. Torres, R. Tscharner, N. Wyrsch, H. Keppner, *Science*, 1999, **285**, 692-698

82. W. Hermes, D.l Waldmann, M. Agari, K. Schierle-Arndt, P. Erk, *Chem. Ing. Tech*. 2015, **87**, 376–389

83. P. Peumans, S. Uchida, S. Forrest, *Nature* 2003, **425**, 158 – 162.

84. J. Xue, B. Rand, S. Uchida, S. Forrest, *J. Appl. Phys*. 2005, **98**, 124903-9.

85. B. O'Regan, M. Gratzel, *Nature*, 1991, **353**, 737-742.

86. M. Gratzel, *Nature*, 2001, **414**, 338-345.

87. A. Hagfeldt, G. Boschloo, L. Sun, L. Kloo, H. Pettersson, *Chem. Rev*., 2010, **110**, 6595-6663.

88. M. Gratzel, *Acc. Chem. Res*. 2009, **42**, 1788-1798.

89. C. D. Bailie, E. L. Unger, S. M. Zakeeruddin, M. Gra¨tzel, M. D. McGehee, *Phys. Chem. Chem. Phys.* 2014, **16**, 4864-4870.

90. S. S. Mali, P. S. Patil, C. K. Hong, *ACS Appl. Mater. Interfaces*, 2014, **6**, 1688-1696.

91. S. Chen, J. Tao, H. Tao, Y. Shen, L. Zhu, J. Jiang, X. Zeng, T. Wang, *Materials Technology: Advanced Performance Materials*, 2015, **30**, 306-312

92. P. Dai, G. Zhang, Y. Chen, H. Jiang, Z. Feng, Z. Lin, J. Zhan, *Chem. Commun.*, 2012, **48**, 3006-3008

93. J.-Y. Lin, Y.-T. Tsai, S.-Y. Tai, Y.-T. Lin, C.-C. Wan, Y.-L. Tung, Y.-S. Wu, *J. Electrochem. Soc.* 2013, **160**, D46-D52.

94. M. Wu, X. Lin, Y. Wang, L. Wang, W. Guo, D. Qi, X. Peng, A. Hagfeldt, M. Grätzel, T. Ma, *J. Am. Chem. Soc*. 2012, **134**, 3419-3428.

95. Y. C. Wang, D. Y. Wang, Y. T. Jiang, H. A. Chen, C.- C. Chen, K.-C. Ho, H.-L. Chou, C.-W. Chen, *Angew. Chem., Int. Ed*. 2013, **52**, 6694-6698.

96. J.-Y. Park, J. H. Noh, T. N. Mandal, S. H. Im, Y. Jun, S. I. Seok, *RSC Adv*. 2013, **3**, 24918-24921.

97. H. K. Mulmudi, S. K. Batabyal, M. Rao, R. R. Prabhakar, N. Mathews, Y. M. Lam, S. G. Mhaisalkar, *Phys. Chem. Chem. Phys*. 2011, **13**, 19307-19309.

98. G. Wang, J. Zhang, S.Kuang, S. Liu and S. Zhuo, *J. Power Sources*, 2014, **269**, 473-478.

99. S. Ahmed, K. B. Reuter, O. Gunawan, L. Guo, L. T. Romankiw, H. Deligianni, *Adv. Energy Mater.* 2012, **2**, 253-259.

100. R. R. Prabhakar, N. H. Loc, M. H. Kumar, P. P. Boix, S. Juan, R. A. John, S. K. Batabyal, L. H. Wong, *ACS Appl. Mater. Interfaces* 2014, **6**, 17661−17667

101. B. M. Kayes, N. Hui, R. Twist, S. G. Spruytte, F. Reinhardt, I. C. Kizilyalli, G. S. Higashi, *37th IEEE Photovoltaic Specialists Conference, Seattle, USA*, 2011 (IEEE), 000004–000008.

102. M. A. Green, K. Emery, Y. Hishikawa, W. Warta, E. D. Dunlop, *Prog. Photovolt*. 2014, **22**, 1-5.

103. V. M. Fthenakis, S. C. Morris, P. D. Moskowitz, and D. L. Morgan, *Prog. Photovolt*. 1999, **7**, 489-95.

104. V. Fthenakis and K. Zweibel, *National Center for Photovoltaics and Solar Program Review Meeting, Denver, USA*, 2003, 1-3.

105. A. Tanaka, *Toxicol. Appl. Pharmaco*l. 2004, **198**, 405-409.

106. G. Phipps, C. Mikolajczak, T. Guckes, *Renew. Energy Focus*, 2008, **9**, 56-61.

107. R. B. Hall, R. W. Birkmire, J. E. Phillips, J. D. Meakin, *Apl. Phys. Lett*. 1981, **38**, 925-926.

108. W. Wang, M. T. Winkler, O. Gunawan, T. Gokmen, T. K. Todorov, Y. Zhu, D. B. Mitzi, *Adv. Energy Mater*. 2014, **4**, 13014651−13014655.

109. H. Kim, J. Lee, N. Yantara, P. P. Boix, S. A. Kulkarni, S. Mhaisalkar, M. Gratzel, N. Park, *Nano Lett*. 2013, **13**, 2412−2417.

110. H. Kim, C. Lee, J. Im, K. Lee, T. Moehl, A. Marchioro, S. Moon, R. Humphry-Baker, J. Yum, J. E. Moser, M. Gratzel, N. Park, *Nat. Sci. Rep*. 2012, **2**, 1-7.

111. A. Kojima, K. Teshima, Y. Shirai, T. Miyasaka, *J. Am. Chem. Soc*. 2009, **131**, 6050 – 6051.

112. M. Liu, M. B. Johnston, H. J. Snaith, *Nature 2013*, **501**, 395-398.

113. A. Urbieta, P. Fernandez, J. Piqueras, *J. Appl. Phys.*, 2004, **96**, 2210-2213.

114. J. J. Wu, S. C. Liu, *Adv. Mater*. 2002, **14**, 215-218.

115. X. Xing, K. Zheng, H. Xu, F. Fang, H. Shen, J. Zhang, J. Zhu, C. Ye, G. Cao, D. Sun, G. Chen, *Micron*, 2006, **37**, 370-373.

116. G. A. Ozin, M. R. Steele, A. J. Holmes, *Chem. Mater.*, 1994, **6**, 999-1010.

117. S. H. Xin, P. D. Wang, A. Yin, C. Kim, M. Dobrowolska, J. L. Merz, J. K. Furdyna, *Appl. Phys. Lett.*, 1996, **69**, 3884-3886.

118. S. V. Ivanov, A. A. Toropov, S. V. Sorokin, T. V. Shubina, I. V. Sedova, A. A. Sitnikova, P. S. Kop'ev, Z. I. Alferov, H. J. Lugauer, G. Reuscher, M. Keim, F. Fischer, A. Waag, G. Landwehr, *Appl. Phys. Lett*., 1999, **74**, 498-500.

119. J. J. Berry, S. H. Chun, K. C. Ku, N. Samarth, I. Malajovich, D. D. Awschalom, *Appl. Phys. Lett.*, 2000, **77**, 3812–3814.

120. Y. Jouane, S. Colis, G. Schmerber, P. Kern, A. Dinia, T. Heiser and Y. A. Chapuis, *J. Mater. Chem*., 2011, **21**, 1953–1958.

121. H. Usui, Y. Shimizu, T. Sasaki and N. Koshizaki, *J. Phys. Chem. B*, 2004, **109**, 120–124.

122. J. Y. Kim, O. Voznyy, D. Zhitomirsky and E. H. Sargent, *Adv. Mater*., 2013, **25**, 4986–5010

123. D. B. Mitzi, *Adv. Mater*. 2009, **21**, 3141–3158.

124. D. B. Mitzi, O. Gunawan, T. K. Todorov, K. Wang, S. Guha, *Sol. Energy Mater. Sol. Cells*, 2011, **95**, 1421-1436.

125. L. E. Brus, *J. Chem. Phys*. 1984, **80**, 4403-4409.

126. L. Spanhel, M. Haase, H. Weller, A. Henglein, *J. Am. Chem. Soc*. 1987, **109**, 5649–5655.

127. M.-M. Titirici, M. Antonietti, A. Thomas, *Chem. Mater*. 2006, **18**, 3808–3812.

128. D. L. Morgan, H.-Y. Zhu, R. L. Frost, E. R. Waclawik, *Chem. Mater*. 2008, **20**, 3800–3802.

129. A. Mamakhel, C. Tyrsted, E. D. Bøjesen, P. Hald, B. B. Iversen, *Cryst. Growth Des*. 2013, **13**, 4730–4734.

130. Z. Zhuang, Q. Peng, Y. Li, *Chem. Soc. Rev*., 2011, **40**, 5492-5513.

131. Y. Yin and A. P. Alivisatos, *Nature*, 2005, **437**, 664-670.

132. Z. Zhang, M. Lu, H. Xu, W. S. Chin, *Chem.Eur. J*. 2007, **13**, 632-638.

133. S. Mourdikoudis, L. M. Liz-Marz´an, *Chem. Mater*. 2013, **25**, 1465-1476.

134. E. A. Weiss, *Acc. Chem. Res*. 2013, **46**, 2607-2615.

135. C. B. Murray, D. J. Norris, M. G. Bawendi, *J. Am. Chem. Soc*. 1993, **115**, 8706-8715.

136. W. Zhang, H. Zhang, Y. Feng, X. Zhong, *ACS Nano*, 2012, **6**, 11066-11073.

137. H. Zhong, S. S. Lo, T. Mirkovic, Y. Li, Y. Ding, Y. Li, G. D. Scholes, *ACS Nano*, 2010, **4**, 5253-5262.

138. M. D. Regulacio, C. Ye, S. H. Lim, M. Bosman, E. Ye, S. Chen, Q.-H. Xu, M.-Y. Han, *Chem. Eur. J*., 2012, **18**, 3127-3131.

139. Y. Li, H. Liao, Y. Ding, Y. Fan, Y. Zhang, Y. Qian, *Inorg. Chem*., 1999, **38**, 1382-1387.

140. J. Xu, J.-P. Ge, Y. D. Li, *J. Phys. Chem. B*, 2006, **110**, 2497-2501.

141. H. G. Yang, G. Liu, S. Z. Qiao, C. H. Sun, Y. G. Jin, S. C. Smith, J. Zou, H. M. Cheng, G. Q. Lu, *J. Am. Chem. Soc*. 2009, **131**, 4078-4083.

142. X. Wang, J. Zhuang, Q. Peng, Y. D. Li, *Nature*, 2005, **437**, 121-124.

143. X. Wang, Q. Peng, Y. Li, Acc. *Chem. Res*. 2007, **40**, 635- 643.

144. D. Pan, Q. Wang, L. An, *J. Mater. Chem*. 2009, **19**, 1063-1073.

145. Q. Wang, D. Pan, S. Jiang, X. Ji, L. An, B. Jiang, *Chem. Eur. J*., 2005, **11**, 3843–3848.

146. V. K. LaMer, R. H. Dinegar, *J. Am. Chem. Soc*. 1950, **72**, 4847-4854.

147. J. Chang, R. Waclawick, *RSC Adv*., 2014, **4**, 23505-23527.

148. P. Marchand, I. A. Hassan, I. P. Parkin, C. J. Carmalt, *Dalton Trans*., 2013, **42**, 9406-9422

149. M. Nyman, M. J. H. Smith E. A. Duesler, *Chem. Vap. Deposition*. 1996, **2**, 171-173

150. M. N. McCain, S. Schneider, M. R. Salata, T. J. Marks, *Inorg. Chem.* 2008, **47**, 2534-2542.

151. C. R. Crick, I. P. Parkin, *J. Mater. Chem*. 2009, **19**, 1074-1076.

152. M. R. Waugh, G. Hyett, I. P. Parkin, *Chem. Vap. Deposition* 2008, **14**, 366-372.

153. K. G. U. Wijayantha, S. Saremi-Yarahmadia , L. M. Peter, *Phys. Chem. Chem. Phys*. 2011**, 13**, 5264-5270.

154. A. A. Tahir, M. Mazhar, M. Hamid, K.G. U. Wijayantha, K. C. Molloy, *Dalton Trans.*, 2009, **19**, 3674-3680.

155. A. A.Tahir, K. G. U. Wijayantha, S.Saremi-Yarahmadi, M. Mazhar, V. McKee, *Chem. Mater*. 2009, **21**, 3763-3772.

156. K. Ramasamy, V. L. Kuznetsov, K. Gopal, M. A. Malik, J. Raftery, P. Edwards, P. O'Brien, *Chem. Mater*. 2013, **25**, 266-276.

157. K. Ramasamy, M. A. Malik, P. O'Brien, *Chem. Sci*. 2011, **2**, 1170-1176.

158. S. Mahboob, S. N. Malik, N. Haider, C. Q. Nguyen, M. A. Malik, P. O'Brien, *J. Crys.Growth*, 2014, **394**, 39-48.

159. A. Adeogun, M. Afzaal and P. O'Brien, *Chem. Vap. Deposition*, 2006, 12, 597-599.

160. D. J. Lewis, P. O'Brien, *Chem.Commun.* 2014, **50**, 6319-6321.

161. R. A. Hussain, A. Badshah, M. Dilshad Khan, N. Haider, Bhajan lal, S. Ishtiaq Khan a, A. Shah, *Mater. Chem. and Phys.*, 2015, **30**, 1-7.

162. P. Brack, J. S. Sagu, T. A. N. Peiris, A. McInnes, M. Senili, K. G. U. Wijayantha, F. Marken, E. Selli, *Chem. Vap. Deposition* 2015, **21**, 41-45.

163. R. Klenk, J. Klaer, R. Scheer, M. C. Lux-Steiner, I. Luck, N. Meyer and U. Ruhle, *Thin Solid Films*, 2005, **480**, 509-514.

164. J. E. Jaffe, A. Zunger, *Phys. Rev. B*, 1983, **28**, 5822-5847.

165. M. G. Brik, J. Phys. *Condens. Matter*, 2009, **21**, 48502-8.

166. S. B. Zhang, S. H. Wei, A. Zunger, H. Katayama-Yoshida, Phys. Rev. B: *Condens. Matter*, 1998, **57**, 9642-9656.

167. L. M. Liborio, C. L. Bailey, G. Mallia, S. Tomic, N. M. Harrison, *J. Appl. Phys.* 2011, **109**, 023519-9.

168. X. G. Peng, R. G. Xie, M. Rutherford, *J. Am. Chem. Soc*. 2009, **131**, 5691-5697.

169. A. Nagoya, R. Asahi, R. Wahl, G. Kresse, *Phys. Rev. B: Condens. Matter Mater. Phys*., 2010, **81**, 113202

170. K. Ito, T. Nakazawa, *Jpn. J. Appl. Phys*. 1988, **27**, 2094-2097.

171. N. Nakayama, K. Ito, *Appl. Surf. Sci*. 1996, **92**, 171-175.

172. H. Katagiri, J. Jimbo, Y. Yamada, T. Kamimura, W. S. Maw,T. Fukano, T. Ito, T. Motohiro, *Appl. Phys. Exp.* 2008, **1**, 041201-3.

173. C. Wadia, A. P. Alivisatos, D. M. Kammen, *Environ.Sci. Technol*. 2009, **43**, 2072-2077.

174. J. Tauc, R. Grigorovici, A. Vancu, *Phys. Status Solidi*, 1966, **15**, 627-637.

175. E. A. Davis, N. F. Mott, *Philos. Mag.* 1970, **22**, 903-908.

176. I. V. Pankove, *Optical Processes in Semiconductors, Dover Inc. New York*, 1975, 34-95.

177. S. Siebentritt, *Thin Solid Films* 2013, **535**, 1-6.

178. W. Shockley and H. J. Queisser, *J. Appl. Phys*. 1961, **32**, 510-515.

179. A. G. Aberle, *Thin Solid Films*, 2009, **517**, 4706-11.

180. S. Niki, M. Contreras, I. Repins, M. Powalla, K. Kushiya, S. Ishizuka, and K. Matsubara, *Prog. Photovolt*. 2010, **18**, 453-459.

181. R. Caballero, E. Garcia-Llamas, J.M. Merino, M. Leon, I. Babichuk, V. Dzhagan, V. Strelchuk, M. Valakh, *Acta Mater*. 2014, **65,** 412-417.

182. J. Han, S. W. Shin, M. G. Gang, J. H. Kim, Y. Lee, *Nanotechnology,* 2013**24**, 095706-8.

183. A. Fairbrother, X. Fontané, V. Izquierdo-Roca, M. Espíndola-Rodríguez, S. López-Marino, M. Placidi, L. Calvo- Barrio, A. Pérez-Rodríguez, E. Saucedo, *Sol. Energy Mater. Sol. Cells* 2013, **112**, 97-103.

184. X. Yin, C. Tang, L. Sun, Z. Shen, H. Gong, *Chem. Mater*. 2014, **26**, 2005-12.

185. S. Chen, A. Walsh, X. G. Gong, S. H. Wei, *Adv. Mater*. 2013, **25**, 1522-29.

186. C. Zhang, J. Zhong, J. Tang, *Front. Optoelectron*. 2015, **8**, 252-268.

187. K. Hönes, E. Zscherpel, J. Scragg, S. Siebentritt, *Physica B,* 2009, **404**, 4949-56.

188. V. Chawla, B. Clemens, *38th IEEE Photovoltaic Specialists Conference, Austin, USA*, 2012 (IEEE), pp. 002990–002992.

189. T. Gershon, B. Shin, T. Gokmen, S. Lu, N. Bojarczuk, and S. Guha, *Appl. Phys. Lett*. 2013, **103**, 193903-8.

190. T. Schwarz, O. Cojocaru-Mirédin, P. Choi, M. Mousel, A. Redinger, S. Siebentritt, and D. Raabe, *Appl. Phys. Lett*. 2013, **102**, 042101-7.

191. M. A. Contreras, K. Ramanathan J. AbuShama, F. Hasoon, D. L. Young B. Egaas, R. Noufi *Progress in Photovoltaics: Research and Applications*, 2005, **13**, 209-216.

192. R. Haight, A. Barkhouse, O. Gunawan, B. Shin, M. Copel, M. Hopstaken, and D. B. Mitzi, *Appl. Phys. Lett.* 2011, **98**, 253502-3.

193. Q. Guo, G. M. Ford, W. C. Wang, B. C. Walker, E. A. Stach, H. W. Hillhouse, R. Agrawal, *J. Am. Chem. Soc*. 2010, **132**, 17384-86.

194. J. R. Herring, *Proc. of the 1990 Billings Land Reclamation Symposium on Selenium in Arid and Semiarid Environments, Billings, USA*, 1990 (U.S. Geological Survey), pp. 5-24.

195. J. J. Scragg, P. J. Dale, L. M. Peter, G. Zoppi, I. Forbes, *Phys. Status Solidi B*, 2008, **245**, 1772-1778.

196. D. M. Schleich, A. Wold, *Mater. Res. Bull*. 1977, **12**, 111-116.

197. I. Repins, M. A. Contreras, B. Egaas, C. DeHart, J. Scharf, C. L. Perkins, B. To, R. Noufi, *Prog. Photovoltaics* 2008, **16**, 235-239.

198. S. A.Vanalakar, G. L. Agawane, S.W. Shin, M.P. Suryawanshi, K.V. Gurav, K. S. Jeon, P. S. Patil, C.W. Jeong, J. Y. Kim, J. H. Kim, *J. Alloys Compd*. 2015, **619**, 109-121.

199. S. R. Kurtz, P. Faine, J. M. Olson, *J. Appl. Phys*. 1990, **68**, 1890-4.

200. C. H. Henry, *J. Appl. Phys*. 1980, **51**, 4494-6.

201. S. C. Riha, B. A. Parkinson, A. L. Prieto, *J. Am. Chem. Soc.* 2011, **133**, 15272-15275.

202. M. Bar, W. Bohne, J. Rohrich, E. Strub, S. Lindner, M. C. L. Stenier, C. H. Fischer, T. P. Niesen, F. Karg, *J. Appl. Phys*. 2004, **96**, 3857-3860.

203. J. E. Bernard, A. Zunger, *Phys. Rev*. 1987, **36**, 3199-3228.

204. Y. Arba, M. Rafi, H. Tchognia, B. Hartiti, A. Ridah, P. Thevenin, *J. Optoelectron. Adv. Mater.* 2013, **15**, 1200-1203.

205. M. R. Byeon, E. H. Chung, J. P. Kim, T. E. Hong, J. S. Jin, E. D. Jeong, J. S. Bae, Y. D. Kim,. S. Park, W. T. Oh, Y. S. Huh, S. J. Chang, S. B. Lee, I. H. Jung, J. Hwang, *Thin Solid Films* 2013, **546**, 387-392.

206. U. Chalapathi, S. Uthanna, V. S. Raja, *J. Renew. Sustain. Energy* 2013, **5**, 031610-7.

207. S. Chen, Walsh, A.; Luo, Y.; Yang, J. H.; Gong, X. G.; Wei, S. H. *Phys. Rev. B* 2010, **82**, 1952031- 1952038.

208. S. Park, S. Sung, J. Sim, K. Yang, D. Hwang, J. Kim, G. Y. Kim, W. Jo, D. Kim, J. Kaung, *Nanoscale*, 2015, **7**, 11182-11189.

209. H. Katagiri K. Jimbo, S. Yamada, T. Kamimura, W. S. Maw, T. Fukano, T. Ito T. Motohiro, *Appl. Phys. Exp*. 2008, **1**, 041201-2.

210. K. Wang, O. Gunawan, T. Todorov, B. Shin, S. J. Chey, N. A. Bojarczuk, D. Mitzi, S. Guha *App. Phys. Lett.* 2010, **97**, 143508-3.

211. D. A. R. Barkhouse, O. Gunawan, T. Gokmen, T. K. Todorov and D. B. Mitzi, *Prog. Photovolt.* 2012, **20**, 6-11.

212. I. Repins, C. Beall, N. Vora, C. DeHart, D. Kuciauskas, P. Dippo, B. To, J. Mann, W.C. Hsu, A. Goodrich, R. Noufi, *Sol. Energy Mater. Sol. Cells.* 2012, **101**, 154-159

213. T. K. Todorov, J. Tang, S. Bag, O. Gunawan, T. Gokmen, Y. Zhu, D. B. Mitzi, Adv. *Energy Mater.* 2013, **3**, 34-48.

214. W. Wang, M. T. Winkler, O. Gunawan, T. Gokmen, T. K. Todorov, Y. Zhu and D. B. Mitzi, *Adv. Energy Mater.*, 2014, **4**, 1301465-5.

215. W. Ki, H. W. Hillhouse, *Adv. Energy Mater*. 2011, **1**, 732-375.

216. J. V. Embden, A. S. Chesman, E. D. Gaspera, N.W. Duffy, S. E. Watkins, J. Jasieniak, *J. Am. Chem. Soc*. 2014, **136**, 5237-5240.

217. J. Kim, H. Hiroi, T. K. Todorov, O. Gunawan, M. Kuwahara, T. Gokmen, D. Nair, M. Hopstaken, B. Shin, Y. S. Lee, *Adv. Mater*. 2014, **26**, 7427-7431

218. C. K. Miskin, W. C. Yang, C. J. Hages, N. J. Carter, C. S. Joglekar, E. A. Stach, R. Agrawal, *Prog. Photovoltaics.* 2015, **23**, 654-659.

219. G. Larramona, S. Bourdais, A. Jacob, C. Chone, T. Muto, Y. Cuccaro, B. Delatouche, C. Moisan, D. Pere, G. Dennler, *J. Phys. Chem. Lett*. 2014, **5**, 3763-3767.

220. H. Xin, J. K. Katahara, I. L. Braly, H. W. Hillhouse, *Adv. Energy Mater*. 2014, **4**, 13018231-13018235.

221. J. O. Jeon, K. D. Lee, L. S. Oh, S. W. Seo, D. K. Lee, H. Kim, J. H. Jeong, M. J. Ko, B. S. Kim, H. J. Son, *Chem. Sus. Chem*. 2014, **7**, 1073-1077

222. D. A. R. Barkhouse, R. Haight, N. Sakai, H. Hiroi, H. Sugimoto, D. B. Mitzi, *Appl. Phys. Lett.* 2012, **100**, 1939041-1939045.

223. S. Y. Kim, J. H. Kim, *Thin Solid Films* 2013, **547**, 178-180.

224. W. Ki, H.W. Hillhouse, *Adv. Energy Mater*. 2011, **1**, 732-735

225. V. Chawla, B. Clemens, Photovoltaic Specialists Conference (PVSC), 38th IEEE, 2012, p. 2990.

226. B. Zhang, M. Cao, L. Li, Y. Sun, Y. Shen, L. Wang, *Mater. Lett*. 2013, **93**,111–114.

227. G. Brammertz, M. Buffie`re, S. Oueslati, H. ElAnzeery, K. Ben Messaoud, S. Sahayaraj, C. Koble, M. Meuris, and J. Poortmans, *Appl. Phys. Lett*. 2013, **103**, 163904-11.

228. B. Shin, Y. Zhu, N. A. Bojarezuk, S. J.Chey, S. Guha, *Appl. Phys. Lett.* 2012, **101**, 053903-9.

229. A. Ahmed, K. B. Reuter, O. Gunawan, L. Guo, L. T. Ramankiw, H. Deligianni, *Adv. Energy Mater*. 2012, **2**, 253-259

230. M. G. Gang, K. V. Gurav, S. W. Shin, C.W. Hong, J. H. Min, M. P. Suryawanshi, S. A. Vanalakar, D. S. Lee, J. H. Kim, *Phys. Status Solidi C*, 2015, **12**, 713-716.

231. A. V. Moholkar, S. S. Shinde, G. L. Agawane, S. H. Jo, K. Y. Rajpure, P. S. Patil, *J. Alloys Compds*. 2012, **544**, 145-151.

232. Y. Cao, M. S. Denny, J. V. Caspar, W. E. Farneth, Q. Guo, A. S. Ionkin, L. K. Johnson, M. Lu, I. Malajovich, D. Radu, H. D. Rosenfeld, K. R. Choudhury, W. Wu, *J. Am. Chem. Soc*. 2012, **134**, 15644-15647

233. M. A. Contreras, M. J. Romero, B. To, F. Hasoon, R. Noufi, S. Ward, K. Ramanathan, *Thin Solid Films*, 2002, **403**, 204-211.

234. T. Eguchi, T. Maki, S. Tajima. T. Ito, T. Fukano, *Technical Digest, 21st International Photovoltaic Science and Engineering Conference, Fukuoka, November 2011*: 4D-3P-24.

235. S. Chen, J. Tao, H. Tao, Y. Shen, L. Zhu, J. Jiang, X. Zeng and T. Wang, *Mater.s Techn.* 2015, **30**, 306-312.

236. K. Ito and T. Nakazawa: Proc. 4th Int. Conf. on '*Photovoltaics science and engineering*' Sydney, Australia, February 1989, Institution of Radio and Electronics Engineers Australia, 341.

237. H. Katagiri, K. Saitoh, T. Washio, H. Shinohara, T. Kurumadani, S. Miyajima: *Sol. Energy Mater. Sol. Cells*, 2001, **65**, 141-148.

238. J. S. Seol, S. Y. Lee, J. C. Lee, H. D. Nam, K. H. Kim, *Sol. Energy Mater. Sol. Cells*, 2003, **75**, 155-162.

239. T. Tanaka, T. Nagatomo, D. Kawasakil, M. Nishio, Q. Guo, A. Wakahara, A. Yoshida, H. Ogawa, *J. Phys. Chem. Solids*, 2005, **66**, 1978-1981.

240. T. Kobayashi, K. Jimbo, K. Tsuchida, S. Shinoda, T. Oyanagi, H. Katagiri: *Jpn J. Appl. Phys*. 2005, **44**, 783-787.

241. J. Zhang, L. X. Shao, Y. J. Fu, E. Q. Xie, *Rare Met.* 2006, **25**, 315-319.

242. K. Sekiguchi, K. Tanaka, K. Moriya, H. Uchiki, *Phys. Stat. Sol. C*. 2006, **3**, 2618-2621.

243. N. Kamoun, H. Bouzouitaand, B. Rezig, *Thin Solid Films*, 2007, **515**, 5949-5952.

244. H. Araki, Y. Kubo, A. Mikaduki, K. Jimbo, W. S. Maw, H. Katagiri, M. Yamazaki, K. Oishi, A. Takeuchi, *Sol. Energy Mater. Sol. Cells*, 2009, **93**, 996-999,

245. J. J. Scragg, D. M. Berg, P. J. Dale, *J. Electroanal. Chem*. 2010, **646**, 52-59

246. A. Ennaoui, M. Lux-Steiner, A. Weber, D. Abou-Ras, I. Kotschau, H.-W. Schock, R. Schurr, A. H. Olzing, S. Jost, R. Hock, T. Vob, J. Schulze, A. Kirbs, *Thin Solid Films*, 2009, **517**, 2511-2514.

247. H. Araki, Y. Kubo, K. Jimbo, W. S. Maw, H. Katagiri, M. Yamazaki, K. Oishi, A. Takeuchi, *Phys. Status Solidi C*, 2009, **6C**, 1266–1268.

248. K. Tanaka, N. Moritakeand, H. Uchiki, *Sol. Energy Mater. Sol. Cells*, 2007, **91**, 1199-1201

249. K. Tanaka, M. Oonuki, N. Moritake, H. Uchiki, *Sol. Energy Mater. Sol. Cells*, 2009, **93**, 583-587.

250. N. Moritake, Y. Fukui, M. Oonuki, K. Tanaka, H. Uchiki, *Phys. Status Solidi C*, 2009, **6C**, 1233-1236.

251. K. Tanaka, Y. Fukui, N. Moritake, H. Uchiki, *Sol. Energy Mater. Sol. Cells*, 2011, **95**, 838-842.

252. M. Y. Yeh, C. C. Lee, D. S. Wuu, *J. Sol-Gel Technol*. 2009, **52**, 65-68.

253. K. Moriya, K. Tanaka, H. Uchiki, *Jpn J. Appl. Phys*., 2007, **46**, 5780-5781.

254. K. Jimbo, R. Kimura, T. Kamimura, S. Yamada, W. S. Maw, H. Araki, K. Oishi, H. Katagiri: *Thin Solid Films*, 2007, **515**, 5997-5999.

255. H. Araki, A. Mikaduki, Y. Kubo, T. Sato, K. Jimbo, W. S. Maw, H. Katagiri, M. Yamazaki, K. Oishi, A. Takeuchi, *Thin Solid Films*, 2008, **517**, 1457-1460.

256. H. Katagiri, K. Jimbo, M. Tahara, H. Araki, K. Oishi, *Mater. Res. Soc. Symp. Proc.* 2009, **1165**, 1166- M04-01.

257. P. A. Fernandes, P. M. P. Salome, A. F. da Cunha, *Semicond. Sci. Technol*. 2009, **24**, 2519-2523.

258. P. A. Fernandes, P. M. P. Salome, *A. F.* da Cunha, *Semicond. Sci. Technol*., 2009, **24**, 105013-19.

259. Y. B. K. Kumar, G. S. Babu, P. U. Bhaskar, V. S. Raja, *Sol. Energy Mater. Sol. Cells*, 2009, **93**, 1230- 1237.

260. S. M. Pawar, A. V. Moholkar, I. K. Kim, S. W. Shin, J. H. Moon, J. I. Rhee, J. H. Kim, *Curr. Appl. Phys*., 2010, **10**, 565-569

261. F. Liu, Y. Li, K. Zhang, B. Wang, C. Yan, Y. Lai, Z. Zhang, J. Li, Y. Liu, *Sol. Energy Mater. Sol. Cells*, 2010, **94**, 2431–2434.

262. N. Momose, M. T. Htay, T. Yudasaka, S. Igarashi, T. Seki, S. Iwano, Y. Hashimoto, K. Ito, *Jpn J. Appl. Phys.*, 2011, **50**, 01BG091-4.

263. R. B. V. Chalapathy, S. J. Gwang, T. A. Byung, *Sol. Energy Sol. Mater. Cells*, 2011, **95**, 3216-3221.

264. B. A. Schubert, B. Marsen, S. Cinque, T. Unold, R. Klenk, S. Schorr, H.-W. Schock, *Prog. Photovolt. Res. Appl*., 2011, **19**, 93-96.

265. B. Shin, O. Gunawan, Y. Z. Nestor, A. Bojarczuk, S. Jay Chey, S. Guha, *Prog. Photovolt. Res. Appl.*, 2011, 1174-1179.

266. L. Sun, J. He, H. Kong, F. Yue, P. Yang, J. Chu: *Sol. Energy Mater. Sol. Cells*, 2011, **95**, 2907–2913.

267. A. V. Moholkar, S. S. Shinde, A. R. Babar, K.-U. Sim, H. K. Lee, K. Y. Rajpure, P. S. Patil, C. H. Bhosale, J. H. Kim, *J. Alloy. Compd*, 2011, **509**, 7439-7446.

268. A. V. Moholkar, S. S. Shinde, A. R. Babar, Kyu-Ung Sim, Ye-bin Kwon, K. Y. Rajpure, P. S. Patil, C. H. Bhosale, J. H. Kim: *Sol. Energy*, 2011, 85, 1354-1363.

269. V. G. Rajeshmon, C. Sudha, K. Artha, K. P. Vijayakuma, C. Sanjeeviraja, T. Abe, Y. Kashiwaba, *Sol. Energy Mater. Sol. Cells*, 2011, **85**, 249–255.

270. T. Prabhakar, N. Jampana, *Sol. Energy Mater. Sol. Cells*, 2011, **95**, 1001-1004.

271. Z. Zhou, Y. Wang, D. Xu, Y. Zhang, *Sol. Energy Mater. Sol. Cells*, 2010, **94**, 2042-2045.

272. A. Wangperawong, J. S. King, S. M. Herron, B. P. Tran, K. Pangan-Okimoto, S. F. Bent, *Thin Solid Films*, 2011, **519**, 2488-2492.

273. X. Xin, M. He, W. Han, J. Jung, Z. Lin, *Angew. Chem. Int. Ed*, 2011, **50**, 11739-11742.

274. N. M. Shinde, D. P. Dubal, D. S. Dhawale, C. D. Lokhande, J. H. Kim, J. H. Moon, *Mater. Res. Bull.*, 2012, **47**, 302-307.

275. S. S. Mali, P. S. Shinde, C. A. Betty, P. N. Bhosale, Y. W. Oh, P. S. Patil, *J. Phys. Chem. Solids*, 2012, **73**, 735-740.

276. M. Guc, R. Caballero, K.G. Lisunov, N. López, E. Arushanov, J. M. Merino , M. León, *J. Alloys Compds*. 2014, **596**, 140-144.

277. Z. Su, K. Sun, Z. Han, H. Cui, F. Liu, Y. Lai, J. Li, X. Hao, Y. Liu, M. A. Green, *J. Mater. Chem. A*, 2014, **2**, 500-509.

278. M. P. Suryawanshi, S.W. Shin, U. V. Ghorpade, K.V. Gurav, G. L. Agawane , C. W. Hong, J. H. Yun, P. S. Patil, J. H. Kim, A. V. Moholkar, *Solar Energy*, 2014, **110**, 221–230.

279. U. Chalapathi, S. Uthanna, V. S. Rajan, *Sol. Energy Mater. Sol. Cells*, 2015, **132**, 476–484.

280. J. He, L. Sun, Y. Chen, J. Jiang, P. Yang, J. Chu, *J. Power Sources*. 2015, **273**, 600- 607.

281. M. Fan, J. Chen, C. Li, K. Cheng, K. Ho, *J. Mater. Chem. A*, 2015, **3**, 562–569.

282. T. Washio, T. Shinji, S. Tajima, T. Fukano, T. Motohiro, K. Jimbo, H. Katagiri, *J. Mater. Chem.*, 2012, **22**, 4021-4025.

283. Y. Kim, K. Woo, I. Kim, Y. S. Cho, S. Jeong, J. Moon, *Nanoscale*, 2013, **5**, 10183-10188.

284. S. C. Riha, B. A. Parkinson, A. L. Prieto, *J. Am. Chem. Soc*., 2009, **131**, 12054-12055.

285. C. Steinhagen, M. G. Panthani, V. Akhavan, B. Goodfellow, B. Koo, B. A. Korgel, *J. Am. Chem. Soc.*, 2009, **131**, 12554-12555.

286. M. Cao, Y. Shen, *J. Cryst. Growth*, 2011, **318**, 1117-1120.

287. X. Lu, Z. Zhuang, Q. Peng, Y. Li, *Chem. Commun*. 2011, **47**, 3141-3143.

288. H. Liao, M. Jao, J. Shyue, Y. Chen and W. Su, *J. Mater. Chem. A*, 2013, **1**, 337-341.

289. A. S. R. Chesman, N. W. Duffy, S. Peacock, L. Waddington, N. A. S. Webster, J. J. Jasieniak, *RSC Advances*, 2013, **3**, 1017-1020.

290. C. A. Cattley, C. Cheng, S. M.Fairclough, L. M. Droessler, N. P. Young, J. H. Warner, J. M. Smith, H. E. Assender, A. A. R. Watt, *Chem. Commun.*, 2013, **49**, 3745-3747.

291. W. Zhang, L. Zhai, N. He, C. Zou, X. Geng, L. Cheng, Y. Donga, S. Huang, *Nanoscale*, 2013, **5**, 8114-8121.

292. K. Mokurala, P. Bhargava, S. Mallick, *Mater. Chem. Phys*., 2014, **147**, 371-374

293. R. Ahmad, M. Brandl, M. Distaso, P. Herre, E. Spiecker, R. Hock, W. Peukert, *Cryst. Eng. Comm*. 2015, **17**, 6972-6984

294. S. A. Vanalakar, G. L. Agwane, M. G. Gang, P. S. Patil, J. H. Kim, J. Y. Kim, *Phys. Status Solidi C*, 2015, **12**, 500-503.

295. A. Pateter, W. Haas, B. Chernev, B. Kunert, R. Resel, F. Hofer, G. Trimmel, T. Rath, *Mater. Chem. Phys*. 2015, **149/150**, 94-98

296. C. M. Fella, A. R. Uhl, Y.E. Romanyuk, A. N. Tiwari, *Phys. Status Solidi A*, 2012, **209/6**, 1043–1048.

297. L. Guo, Y. Zhu, O. Gunawan, T. Gokmen, V. R. Deline, S. Ahmed, L. T. Romankiw, H. Deligianni, *Prog. Photovolt: Res. Appl*. 2014, **22**, 58-68.

298. G. Brammertz, Y. Ren, M. Buffière, S. Mertens, J. Hendrickx, H. Marko, A. E. Zaghi, N. Lenaers, C. Köble, J. Vleugels, M. Meuris, J. Poortmans, *Thin Solid Films,* 2013, **535**, 348-352.

299. K. M. Kim, K. H. Liao, H. Tampo, H. Shibata, S. Niki, *Appl. Phys. Exp.* 2015, **8**, 0423011-4.

300. S. Oueslati, G. Brammertz, M. Buffière, H. ElAnzeery, O. Touayar, C. Köble, J. Bekaert, M. Meuris, J. Poortmans, *Thin Solid Films*, 2015, **582**, 224-228.

301. H. Wei, W. Guo, Y. Sun, Z. Yang and Y. Zhang, *Mater. Lett*. 2010, **64**, 1424-1426.

302. S. Zuo, J. Jiang, J. Ma, L. Yang, P.Yang, J. Chu, *Applied Surface Science* 2012, **258**, 7844-7848.

303. S. W. Shin, I. Y. Kim, K.V. Gurav, C. H. Jeong, J. H. Yun, P.S. Patil, J. Y. Lee, J. H. Kim, *Current Appli. Phys.*, 2013, **13**, 1837-1843.

304. F. Gao, T. Maeda, T. Wada, Japanese *J. Appl. Phys*. 2014, **53**, 04ER11-5.

305. W. Wu, N.G. Tassi, Y. Cao, J. V. Caspar, K. R. Choudhury, L. Zhang, *Phys. Status Solidi RRL*, 2015, **9**, 236-240.

306. K. V. Gurav, S. W. Shin, U. M. Patil, M. P. Suryawanshi, S. M. Pawar, M. G. Gang, S. A. Vanalakar, J. H. Yun, J. H. Kim, *J. Alloys and Compds*, 2015, **631**, 178-182.

307. F. Fan, L. Wu, M. Gong, S.Y. Chen, G. Y. Liu, H. Yao, H. Liang, Y. Wang, S. Yu, *Sci. Reports*, 2012, **2**, 1-6.

308. J. He, L. Sun, S. Chen, Y. Chen, P.X. Yang, J.H. Chu, *J. Alloy. Compd*. 2012, **511**, 129-132.

309. J. He, L. Sun, N. Ding, H. Kong, S. Zuo, S. Chen, Y. Chen, P. Yanga, J. Chu *J. Alloy. Compd.* 2012, **529**, 34-37.

310. S. W. Shin, J. H. Han, Y. C. Park, G. L. Agawane, C. H. Jeong, J. H. Yun, A. V. Moholkar, J. Y. Lee and J. H. Kim, *J. Mater. Chem*. 2012, **22**, 21727-21732.

311. Y. Zhang, N. Suyama, M. Goto, M. Yin and A. Yamada, *Appl. Phys. Express*, 2013, **6**, 072302 1-3.

312. G. Larramona, S. Bourdais, A. Jacob, C. Choné, T. Muto, Y. Cuccaro, B. Delatouche, C. Moisan, D. Péré, G. Dennler, *RSC Adv*. 2014, **4**, 14655−14622.

313. H. Katagiri, K. Jimbo, W. S. Maw, K. Oishi, M. Yamazaki,H. Araki, A. Takeuchi *Thin Solid Films,* 2009, **517**, 2455-2460.

314. An, K. Tang, G. Shen, C. Wang, L. Huang, Y. Qian, *Materials Research Bulletin* 2003, **38**, 823-830.

315. L. Li, X. Liu, J. Huang, M. Caoa, S. Chen, Y. Shen, L. Wang, *Mater. Chem. Phys.2012*, **133**, 688-691.

316. C. Yan, C. Huang, J. Yang, F. Liu, J. Liu, Y. Lai, J. Li, Y. Liu, *Chem. Commun*., 2012, **48**, 2603-2605.

317. K. Mokurala, P. Bhargava, S. Mallick, *Mater. Chem. Phys*. 2014, **147**, 371-374.

318. H. Guan, Y. Shi, B. Jiao, X. Wang, F. Yu, *Chalcogenide Lett*., 2014, **11**, 9-12.

319. F. Ozel, M. Kus, A. Yar, E. Arkan, M. Can, A. Aljabour, N. M. Varal, M. Ersoz, *J Mater. Sci*. 2015, **50**, 777-783.

320. B. Zhang, M. Cao, L. Li, Y. Sun, Y. Shen, L. Wang, *Mater. Lett.* 2013, **93**, 11-4.

321. X. Meng, H. Cao, H. Deng, W. Zhou, J. Zhang, L. Huang, L. Sun, P. Yang, J. Chu, *Mater. Sci. Semiconduct. Process.* 2015, **39**, 243–250.

322. Y. Liu, M. Hao, J. Yang, L. Jiang , C. Yan, C. Huang, D. Tang, F. Li Y. Liu, *Mater. Lett*. 2014, **136**, 306-309.

323. X. Fontane, V. Izquierdo-Roca, E. Saucedo, S. Schorr, V. O. Yukhymchuk, M. Valakh, A. Ya, P. Rodriguez, J. R. Morante, *J. Alloys Compd*. 2012, **539**, 190-194.

324. G. L. Agawane, S.W. Shin, S. A. Vanalakar, A.V. Moholkar, J. H. Kim, *Mater. Lett.* 2014, **137**, 147-149.

325. C. Huang, Y. Chan, F. Liu, D. Tang, J. Yang, Y.Lai, J. Li, Y. Liu, *J. Mater. Chem. A*, 2013, **1**, 5402-5407.

326. P. Sinsermsuksakul, L. Sun, S.W. Lee, H.H. Park, S.B. Kim, C. Yang, R. G. Gordon, *Adv. Energy Mater*. 2014, **4**, 1400496-1400503.

APPENDIX - I

Measurement Methodologies

Thermogravimetric analysis (TGA)

TGA is a thermal analysis method in which physical and chemical properties of materials are measured as a function of temperature at constant time or as a function of time at constant temperature. TGA can give information about physical phenomena, such as phase transitions such as sublimation, vaporization, absorption and desorption, chemical phenomena such as dehydration, decomposition and solid-gas reactions oxidation or reduction. TGA is used to determine some selected characteristics of materials which relate to either the mass loss or gain due to decomposition, oxidation, or loss of volatiles (such as water). TGA can be used to find the material characteristics by analysing the decomposition patterns, degradation mechanisms and reaction kinetics, organic and inorganic contents in a sample. The measurements were carried out on a Seiko SSC/S200 model under a heating rate of 10 °C min^{-1} under nitrogen. Indium metal is used as a reference to calibrate the instrument.

Elemental analysis

Carbon (C), Hydrogen (H) and Nitrogen (N) analysis carried out on a calibrated Carlo Erba EA 1108 elemental analyser with standard reference material. The samples were placed in a tin container which then dropped into a furnace at 1000 °C and burnt in oxygen inside the furnace. Carbon in the sample burns and forms carbon dioxide, hydrogen as water vapours nitrogen and sulfur as dioxides. The gases were analysed in a gas chromatography (GC) column to determine the percentage of each element in the given sample. Metals such as Cu, Fe, Co, Ni, Zn and Cd analysis were carried out by

digesting a weighed amount of given compound in an acid which was then heated to the temperature at which the sample is digested and decomposed by the acid. The residue was then transferred to a volumetric flask and made up with water. This solution was then analysed by Fisons Horizon ICP-OES and measures the concentration of the individual element in the solution. All elemental analysis for the whole project was performed by School of Chemistry microanalysis team.

Mass spectrometry

Mass spectrometry analyses molecular species by measuring their mass. To conduct electrospray the samples were dissolved in a carrier solvent and dispersed into a fine aerosol. The aerosol then passed through a highly charged nozzle to evaporate and generate charged ions, which are then accelerated towards a detector by counter electrodes. The time taken by the ions to reach the detector as a function of its charge, *Z*, and mass M and the mass spectra consists of counts against (M/Z). The positive ions are generally associated with small cations such as H^+, Na^+ or K^+ and the negative ions formed by association with ions like I^-or by removal of H^+. In electrospray, the technique is based on the soft ionisation and the structure is mostly maintained. Matrix assisted laser desorption ionisation (MALDI) is another soft ionisation technique available.

UV/Vis spectroscopy

The UV/Vis spectroscopy refers to the absorption spectroscopy in the ultraviolet-visible region (UV to near IR range) of light. The rate of absorption varies because of the electronic transitions in the compound. UV/Vis spectroscopic technique measures the transitions from the ground state to the excited state which is complementary to the fluorescence spectroscopy which involve the transition from the excited to ground state. UV/Vis spectroscopy can be effectively used for studying the effect of change in wavelength of maximum absorption (λ_{max}) in transition metals in presence of anions or

ligands, as the colour of metal ion solutions is strongly affected by anions or ligands. This technique is also used to determine the degree of conjugation in the systems as the molecules with high degree of conjugation absorb light in the UV or visible region. The solvents such as water, ethanol, hexane or toluene can be used.

According to the Beer-Lambert law, the absorbance of a solution varies directly with the concentration of the absorbing species and the path length. Hence the concentration of a fixed path length can be measured using UV/Vis spectroscopy according to the equation;

$$A = \log_{10} (I_o/I) = \mathcal{E}cL \quad \ldots\ldots\ldots\ldots \quad \text{Eq.7}$$

where A = measured absorbance I_o = intensity of the incident light at a given wavelength, I = transmitted intensity, L = path length through the sample, c = concentration of the absorbing species and $\mathcal{E}$ = constant known as the molar absorptivity or extinction coefficient, which is a constant and shows fundamental molecular property in a given solvent, at a particular temperature and pressure.

X-ray diffraction (XRD) [1, 2]

X-ray crystallography is considered as one of the most powerful tools in solid state structure determination. It provides information regarding bond lengths/angles, symmetry and molecular packing. The diffraction patterns were then compared to the documented patterns in the ICDD index. The technique relies on the diffraction of X-rays through the lattice planes in crystals. Crystals are made of regular arrays of atoms; hence primarily the electron of atoms diffract these X-ray waves and secondary spherical waves are emitted. This phenomenon is called elastic scattering. A regular array of scatterers (electrons) produces a regular array of spherical waves, some of these waves cancel one another by destructive interference, and some may add in some specific directions called constructive interference, which can be determined by Bragg's law;

$$n\lambda = 2dSin\theta \quad \ldots\ldots\ldots \quad \text{Eq. 8}$$

$$d = n\lambda/2Sin\theta \quad \ldots\ldots\ldots\ldots \quad \text{Eq. 9}$$

Where *d* is the spacing between diffracting planes, θ is the incident angle, *n* is any integer, and λ is the wavelength of the reflected beam. The diffraction patterns from specific directions appear as spots in single crystals and as concentric circles in powder samples; which shows a regular array or the repeating arrangement of atoms within the crystal. The path length depends on the distances between the source and the detector.

When a monochromatic X-ray beam with wavelength λ (Cu_{Ka} λ = 154.18 pm) is projected onto a crystalline material at an angle θ, diffraction occurs only when the distance travelled by the rays reflected from successive planes differs by a complete number of wavelengths (Figure 20). By varying the angle θ, Bragg's Law is satisfied by different *d*-spacing in

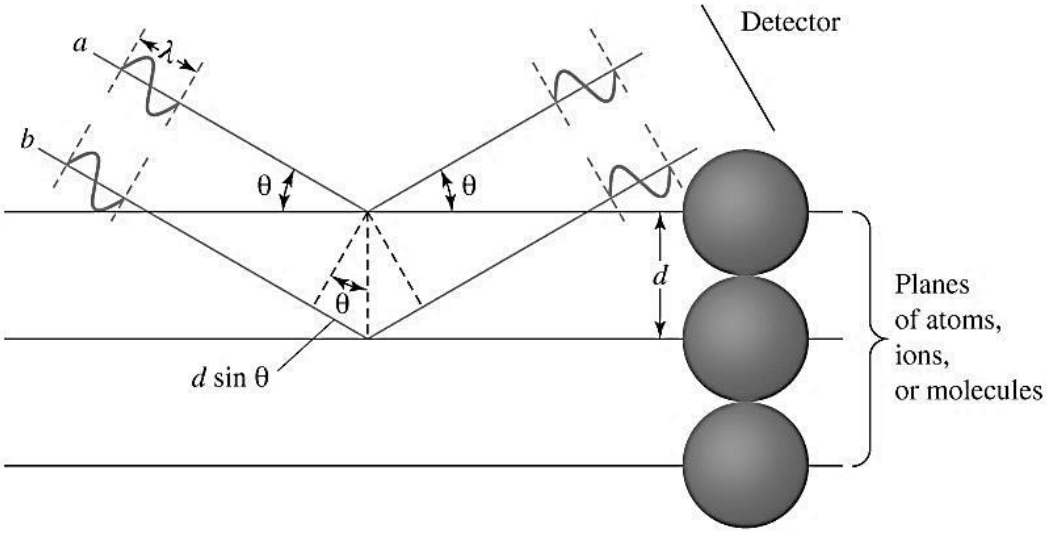

Figure 20: Schematic representation of Bragg's Diffraction.

polycrystalline materials. Plotting the angular positions and intensities of the resultant diffracted peaks produces a pattern, which is characteristic of the sample. A mixture of different phases seen in the resultant diffractogram is formed by addition of the

individual patterns. The diffraction characteristics of any set of planes are governed by their inter-plane spacing or d-spacing. The relationship between the Miller indices and d-spacing for a given set of planes is determined using 3D geometry. This relationship is termed an indexing equation as it is used to assign Miller indices to each reflection in a powder XRD pattern in a process known as indexing. Using Pythagoras' theorem it can be shown that the indexing equation for the cubic crystal system is;

$$\frac{1}{d^2} = \frac{h^2 + k^2 + l^2}{a^2} \quad \text{..... Eq. 9}$$

In the cubic crystal system only one unknown, *a*, links the *d*-spacing to the Miller indices. For the other crystal systems the indexing equations get successively more complex. For example in the orthorhombic crystal system the d-spacing and the Miller indices are related via three unknowns *a*, *b* and *c*.

$$\frac{1}{d^2} = \frac{h^2}{a^2} + \frac{k^2}{b^2} + \frac{l^2}{c^2} \quad \text{..... Eq. 10}$$

Single-crystal X-ray diffraction data for the dithiocarbamato complexes of tin(II) were collected using graphite monochromated Mo-Kα radiation (λ = 0.71073 Å) on a Bruker APEX diffractometer. The structure was solved by direct methods and refined by full-matrix least squares on F2.

Nuclear Magnetic Resonance (NMR) [3-6]

NMR technique is considered as a physical phenomenona in which atomic nuclei resonate in a magnetic field, absorb and re-emit electromagnetic radiation. This energy depends on a specific resonance frequency which in turn depends on the strength of the magnetic field and the magnetic properties of the isotope of the atoms. Each nucleus possesses nuclear angular momenta, *I* which is specific for each type of nucleus and takes integer or half integer values. Each nucleus possesses the corresponding magnetic

quantum numbers m, ranging from $+I$ to $-I$. In the absence of a magnetic field, the energy of an isolated nucleus is independent of the quantum number m_I. However, when a magnetic field of strength B is applied in a direction z, a magnetic moment m would have energy U given by;

$$U = -\mu_z B = -\gamma \hbar m_I B \quad \cdots\cdots\cdots\cdots\cdots \quad \text{Eq. 11}$$

There are thus $2I+1$ non-degenerate energy levels shown in Figure 21 corresponding to the $2I + 1$ values of m_I and are separated by 1 unit of angular momentum. The chemical shift (δ) is quoted in parts per million or ppm.

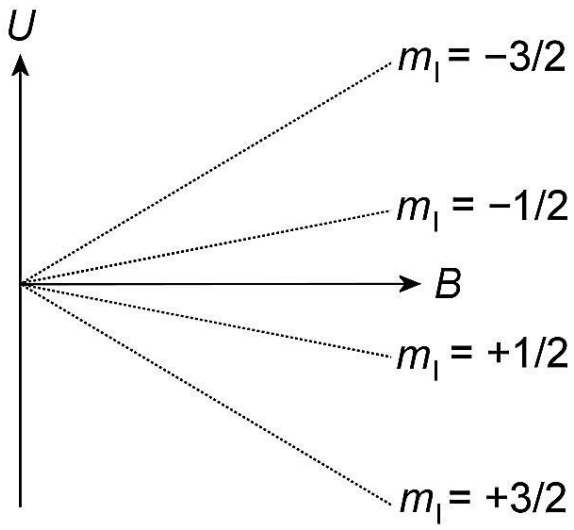

Figure 21: Schematic representation of degenerate energy level in an applied magnetic field.

The reference nucleus for ^{1}H and ^{13}C NMR is usually referred to that of tetramethylsilane (TMS) which possesses 12 identical protons in the same chemical environments and only four carbon toms in the same environment. In this molecule the nuclei de-shielded more strongly than those in TMS take positive value whereas more shielded ones take negative values.

Scanning electron microscopy (SEM) and energy dispersive X-ray spectroscopy (EDX) [7, 8]

Films were carbon coated using Edward's E306A coating system before carrying out SEM and EDX analyses. SEM analysis was performed using a Philips XL 30FEG and EDX was carried out using a DX4 instrument. SEM electron microscope makes use of a focused beam of electrons to scan the images of a sample. Specimens can be observed in high and medium vacuum, in low vacuum, in wet conditions (in environmental SEM), and at a wide range of cryogenic or elevated temperatures. The surface morphology and composition of the samples were analysed by the secondary electrons emitted by the atoms excited by the beam of electrons. SEM can produce resolution better than 1 nanometre. The number of secondary electrons produced depends on the angle at which beam meets the surface of specimen (topography). By scanning the sample and collecting the secondary electrons with a special detector, an image displaying the topography of the surface is created. SEM signals include secondary electrons (SE), back-scattered electrons (BSE), characteristic X-rays, light cathodoluminescence (CL), specimen current and transmitted electrons. Secondary electron detectors are standard equipment in all SEMs, but it is rare that a single machine would have detectors for all possible signals. The signals result from interactions of the electron beam with atoms at or near the surface of the sample. SEM micrographs have a large depth of field due to the very narrow electron beam. BSE are the beam electrons reflected from the sample by elastic scattering. BSE are often used in analytical SEM along with the spectra made from the characteristic X-rays, because the intensity of the BSE signal is strongly related to the atomic number (Z) of the specimen. BSE images can provide information about the distribution of different elements in the sample. Characteristic X-rays are emitted when

the electron beam removes an inner shell electron from the sample, causing a higher-energy electron to fill the shell and release energy. These characteristic X-rays are used to identify the composition and measure the abundance of elements in the sample.

Transmission Electron Microscopy (TEM) [9]

In this technique images of ultrathin specimens are produced by the interaction with a transmitted beam of electrons passing through it. The image is then magnified and focused onto a fluorescent screen, or on a photographic film, or to a sensor such as a CCD camera. TEMs are capable of imaging at a significantly higher resolution than other light microscopes, owing to small de Broglie wavelength of electrons which enable the TEM instrument to examine fine details thousands of times smaller than the ones that can be seen in a light microscope. TEM is one of the major forms of analysis method used in both physical and biological sciences. TEMs find applications mainly in materials science research, cancer research, semiconductor research, pollution and nanotechnology.

According to de Broglie hypothesis all matter such as electrons shows wave particle like behaviour. The waves produced by matter are called matter waves or de Broglie waves. The wavelength, λ, associated with a massive particle and is related to its momentum, p, through the Planck constant, h is called de Broglie wavelength which can be calculated.

$$\lambda = h/p \qquad \ldots\ldots\ldots\ldots \quad \text{Eq.12}$$

The TEM images produce contrast by the absorption of electrons in the material which depends on the thickness and composition of the material. The projector lenses allow the correct positioning of this electron wave distribution. It mainly depends on the mode of operation. In some complex imaging techniques by changing the ability to change lens strength or to deactivate a lens, allows many different operating modes based on the

particular interest to the investigator. TEM is used to observe chemical identity, orientations in crystal, electronic structure etc.

The bright field imaging mode is the most common operation mode for a TEM. The thicker regions or regions with a higher atomic number of the sample appear as dark and no sample regions will appear bright. This dark and bright field give two dimensional projection of the sample along the optic axis. When the electron beam undergoes Bragg scattering, the samples can exhibit diffraction contrast in crystalline sample. By placing the apertures in the back focal plane with desired Bragg reflections, the regions with no samples appear dark. This is known as a dark-field image. Crystal structure of a sample can be investigated by a high-resolution transmission electron microscopy (HRTEM). Based on the differences in phase of electron waves with the specimen images are formed. The images depend on the number of electrons hitting the screen, which give a phase contrast. By adjusting the magnetic lenses in the back focal plane of the lens in place of the imaging plane produce a diffraction pattern. For crystalline samples the diffraction patterns consists of a pattern of dots or a series of rings in the case single crystal. The single crystal diffraction patterns depend upon the orientation of the specimen and the structure of the sample illumination. The diffraction image provides information about the space group and the crystal's orientation

Electron energy loss (EELS) is an advanced technique for TEMs using magnetic sector based devices known as EELS spectrometers. These devices allow the selection of particular energy values based on the electron-electron interaction with the sample. This technique is used for the identification of different elements in a sample and also can be used to generate an image which provides different elemental composition, based upon the atomic transition during electron-electron interaction. EELS spectrometers can be operated in spectroscopic and imaging modes by allowing for isolation or rejection of beams of elastically scattered electrons. TEM was performed using a Philips CM200

(200 kV) microscope. Samples were briefly ultrasonicated in toluene, which produces a suspension and then a drop of the suspension was placed on a carbon-coated copper grid.

Raman spectroscopy [10]

This technique is a vibrational spectroscopic technique used to analyse the fingerprint region of molecules. It is similar to IR spectroscopy. However, the IR bands arise from a change in the dipole moment of a molecule due to an interaction of light with the molecule, Raman bands arise from a change in the polarizability of the molecule due to the same interaction. When the energies of these transitions are plotted as a spectrum, they can be used to identify the molecule as they provide a "molecular fingerprint" of the molecule being observed. Certain vibrations that are allowed in Raman are forbidden in IR, whereas other vibrations may be observed by both techniques although at significantly different intensities thus these techniques can be thought of as complementary. When a beam of light fall upon a molecule, photons are absorbed by the material and scattered. Majority of these scattered photons have exactly the same wavelength as the incident photons and are called as *Rayleigh scatter*. In the scattering process, the incident photon excites an electron into a higher energy level called *virtual states* and then the electron decays back to a lower level, emitting a scattered photon. In Rayleigh scattering the electron decays back to the same level from which it started and thus it is often referred as elastic scattering. In the Raman effect the electron excited in the scattering process decays to a different level than that where it started and is termed inelastic scattering.

The energy difference between the incident and scattered photons is represented by the arrows of different lengths in Figure 22. Numerically, the energy difference between the initial and final vibrational levels, $\overline{\nu}$, or Raman shift in wave numbers (cm^{-1}), is

calculated through Eqn. 13 in which $\lambda_{incident}$ and $\lambda_{scattered}$ are the wavelengths (in cm) of the incident and Raman scattered photons, respectively.

$$\bar{\nu} = 1/\lambda_{incident} - 1/\lambda_{scattered} \quad \text{.....Eqn. 13}$$

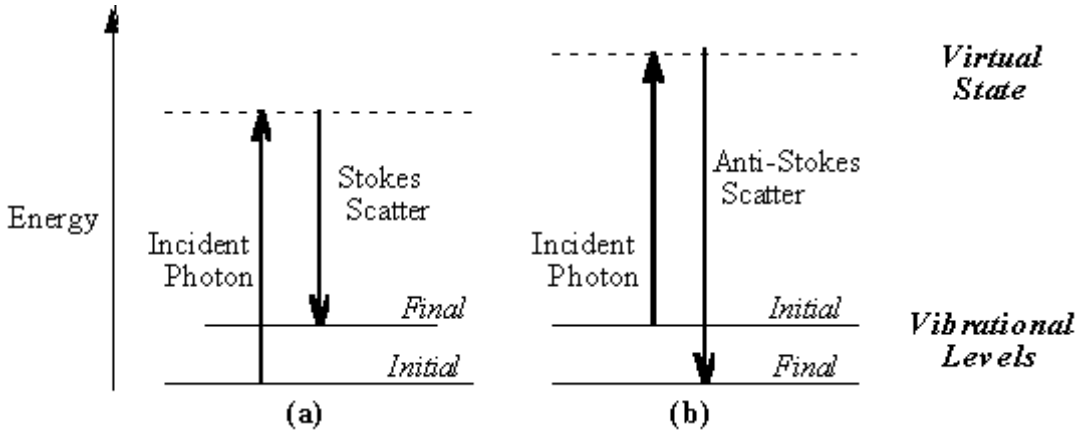

Figure 22: energy level diagram for Raman scattering (a) Stokes and (b) anti-Stokes Raman scattering.

The vibrational energy is ultimately dissipated as heat. Because of the low intensity of Raman scattering, the heat dissipation does not cause a measurable temperature rise in a material. At room temperature the thermal population of vibrational excited states is low, although not zero. Therefore, the initial state is the ground state, and the scattered photon will have lower energy (longer wavelength) than the exciting photon. This Stokes shifted scatter is what is usually observed in Raman spectroscopy. Figure 22 (a) depicts Raman Stokes scattering. A small fraction of the molecules are in vibrationally excited states. Raman scattering from vibrationally excited molecules leaves the molecule in the ground state. The scattered photon appears at higher energy, as shown in Figure 22 (b). At room temperature the anti-Stokes-shifted Raman spectrum is always weaker than the Stokes-shifted spectrum and since the Stokes and anti-Stokes spectra contain the same frequency information most Raman experiments look at Stokes-shifted scatter only.

The energy of a vibrational mode depends on molecular structure and environment. Atomic mass, bond order, molecular substituents, molecular geometry and hydrogen bonding affect the vibrational force constant which, in turn dictates the vibrational energy. Vibrational Raman spectroscopy is not limited to intramolecular vibrations. Crystal lattice vibrations and other motions of extended solids are Raman-active. Their spectra are important in such fields as polymers and semiconductors. In the gas phase, rotational structure is resolvable on vibrational transitions. Raman spectra of the nanomaterials and thin films were analysed in Renishaw system 1000 with a 632 nm HeNe laser available in School of Materials University of Manchester.

X-ray photoelectron spectroscopy (XPS) [11, 12]

XPS is a surface chemical analysis technique that can be used to analyze the surface chemistry of a material in its as-received state. It also used as a quantitative spectroscopic technique to measure the elemental composition in the parts per thousand ranges of the material. XPS techniques used to find empirical formula, electronic state and chemical state of the elements that present in a material. The spectra are collected by irradiating the material with a beam of X-rays, meanwhile measuring the kinetic energy and number of electrons simultaneously escaping from the top 0 to 10 nm surface of the material. XPS technique works at high vacuum ($P \sim 10^{-8}$ mBar) or ultra-high vacuum (UHV; $P < 10^{-9}$ mBar) conditions. Photo emitting surface with uniform charge neutralization was achieved by exposing the surface to low energy electrons using a magnetic immersion lens system (Kratos Ltd) at pressure was 1 x 10^{-9} mBar. Spectra collected were analysed by subtracting a Shirley background and then fitting peaks using a mixed Gaussian/Lorenzian line shape. During the peak fitting, spin orbit split components were constrained to have identical line width, elemental spin orbit energy separations and theoretical spin orbital area ratios. The XPS spectra were recorded using a Kratos Axis

Ultra spectrometer employing a monochromatic Al-Kα X-ray source and analyser pass energy of 80 eV for survey scans and 20 eV for elemental scans. The binding energy electron of each of the emitted electrons can be determined by the equation 14 based on Ernest Rutherford's work;

$$E_{binding} = E_{photon} - (E_{kinetic} + \phi) \qquad \text{…….. Eq. 14}$$

Where, $E_{binding}$ is the binding energy of the electron, E_{photon} is the energy of the X-ray photons used; $E_{kinetic}$ is the kinetic energy of the electron as measured by the instrument and ϕ is the work function which depends on both the spectrometer and the material. The work function term ϕ is an adjustable instrumental correction factor.

Magnetic measurements Magnetic susceptibility [13]

The application of a magnetic field creates a slight alignment of individaul moments and hence a low magnetization in the same direction as the applied field. As temperature increases, the thermal agitation also increases and it becomes harder to align the atomic magnetic moments and hence the susceptibility (χ) also decreases. This behaviour is known as the Curie law and is given by equation 15

$$\chi = \frac{C}{T} \qquad \text{……Eq. 15}$$

Where C is material constant called the Curie constant, T- Absolute temperature (K). If we consider two interacting spins of equal amplitude. A plot of χT versus T, the curve representing the ferromagnetically-coupled material curves up, the curve for the paramagnet is a horizontal line, and the curve for the antiferromagnetically-coupled material curves down.

In case of ferrite materials Curie law is a special case of the more general Curie- Weiss law, which incorporates a temperature constant (θ) and derives from Weiss theory,

proposed for ferromagnetic material, that incorporates the interaction between magnetic moments.

$$\chi = \frac{C}{T-\theta} \qquad \text{…….. Eq. 16}$$

In this equation, θ can either be positive, negative or zero.

If we plot χ^{-1} versus T there are three possible outcomes: for paramagnetic materials, θ = 0 K and its x-intercept = 0 K, an example the ferromagnetically-coupled material has θ = 1 K and its x-intercept = 1 K, and the same relationship applies for the antiferromagnetically-coupled material but with a negative value. The Curie constant, can be determined from the slope of χ^{-1} vs. T which is C^{-1}.

SQUID magnetometers contain a large superconducting magnet which provides a uniform field in which the sample is magnetised. The sample is then oscillated perpendicular to the field within a superconducting detection coil through which a current is induced. By determination of the voltage of the induced current it is then possible to calculate the susceptibility of the sample. A micro SQUID operates under the same principles as SQUID magnetometry, but at much lower temperatures (often sub-Kelvin) and on smaller samples (usually very small single crystals). Magnetic measurements of the thin films and nanoparticles were performed in the temperature range 1.8-300 K, by using a Quantum Design MPMS-XL SQUID magnetometer. The diamagnetic corrections for the compounds were estimated using Pascal's constants, and magnetic data were corrected for diamagnetic contributions of the sample holder.

References

1. W. Clegg, *Crystal Structure Determination*, Oxford University Press, Oxford, 1998.
2. M. M. Woolfson, *An Introduction to X-ray Crystallography*, 2nd Edition, Cambridge University Press, Cambridge, 1997.

3. P. J. Hore, *Nuclear Magnetic Resonance*, Oxford University Press, Oxford, 1995.
4. J. A. Iggo, *NMR Spectroscopy in Inorganic Chemistry*, Oxford University Press, Oxford, 1999.
5. H. Gunther, *NMR Spectroscopy*, 2nd Edition, John Wiley & Sons, Chichester, 1995.
6. J. K. M. Saunders. B. K. Hunter, *Modern NMR Spectroscopy*, 2nd Edition, Oxford University Press, Oxford, 1993.
7. C.W. Oatley, W. C. Nixon, R. F. W. Pease. *Adv. Electronics Electron Phys*.1965, 21, 181–247.
8. B. R. Leili, D. I. Y. Jun, A. David, P. R. W. Fabian, *J. Vacuum Sci. Techn.* 2007, **25**, 2425-2431.
9. M. A. Haque, M. T. A. Saif, *Experimental Mechanics*, 2001, **42**.
10. R. Singh, *Physics in Perspective*, 2002, **4**/4, 399–420
11. D. W. Turner, M. Jobory, I. Al, *J. of Chem. Physi. 1962, **37**, 3007-3011*.
12. S. Ray, A.G. Shard, *Analytical Chemistry*, 2011. **83**, 8659-8666
13. A. F. Orchard, *Magnetochemistry*, Oxford University Press, Oxford, 2003.

APPENDIX - II

Review Chapter

"**Routes to tin chalcogenide materials as thin films or nanoparticles: a potentially important class of semiconductor for sustainable solar energy conversion**."

David J. Lewis, Osman Bakr, Christopher A. Muryn, Mohammad A. Malik, *Inorg. Chem. Front.*, 2014, **1**, 577-598

INORGANIC CHEMISTRY
FRONTIERS

REVIEW

View Article Online
View Journal | View Issue

Cite this: *Inorg. Chem. Front.*, 2014, **1**, 577

Routes to tin chalcogenide materials as thin films or nanoparticles: a potentially important class of semiconductor for sustainable solar energy conversion

David J. Lewis,*[a,b] Punarja Kevin,[a] Osman Bakr,[c] Christopher A. Muryn,[a] Mohammad Azad Malik[a] and Paul O'Brien*[a,b]

Received 26th April 2014,
Accepted 1st August 2014

DOI: 10.1039/c4qi00059e

rsc.li/frontiers-inorganic

Thin films of tin chalcogenides may find use in photovoltaic devices, and nanocrystals of such materials are attractive due to their tuneable band gaps and potential in photovoltaic, photonic and optoelectronic applications. Tin(II) sulfide (SnS) is of particular interest due to its band gap of 1.4 eV, which is similar to that of silicon (1.1 eV). This review seeks to provide an overview of the chemical routes currently known for the synthesis of tin chalcogenides as thin films or in nanocrystalline form, as well as exploring routes to copper zinc tin sulfide (CZTS) and mesoporous tin chalcogenides.

[a]*School of Chemistry, The University of Manchester, Oxford Road, Manchester, M13 9PL Northern Ireland, UK. E-mail: Paul.O'Brien@manchester.ac.uk, david.lewis-4@manchester.ac.uk; Tel: +44 (0)161 275 4653*
[b]*School of Materials, The University of Manchester, Oxford Road, Manchester, M13 9PL Northern Ireland, UK*
[c]*King Abdullah University of Science and Technology (KAUST), Thuwal, Saudi Arabia*

1. Introduction

Tin is a group IV element typically classified as a hard acid in Pearson's hard-soft acid–base (HSAB) paradigm. There is interesting redox chemistry and both tin(II) and tin(IV) species, and

David J. Lewis

David J. Lewis obtained his Ph.D. in 2006 from the University of Birmingham, U.K. This was followed by a short sojourn in industry as a process chemist (2006–2009). DJL returned to the University of Birmingham to work under Professor Zoe Pikramenou, developing luminescent nanoparticles for flow velocimetry measurements in collaboration with Professor Panagiota Angeli, University College London. In 2013, DJL took up his current position as a research associate under Professor Paul O'Brien FRS at The University of Manchester, U.K., as part of the newly established BP International Centre for Advanced Materials (BP-ICAM), working towards the understanding and development of inorganic lubricant additives for automotive engines. In league with Professor O'Brien, DJL has also recently developed a novel ambient-pressure route toward the deposition of inorganic–organic perovskites, potentially important for next-generation photovoltaic device manufacture. DJL is a Member of the Royal Society of Chemistry.

Punarja Kevin

Punarja Kevin is a final year PhD student in the School of Chemistry at the University of Manchester. She holds a Graduate Diploma in IT (1998) from ER&DCI, India, a B.Sc. in Chemistry, Physics and Mathematics (1999) from the University of Kerala, India, MSC chemistry (2001) from Govt. Of Kerala, India, Bachelors in Education (2002) MG Uty, India, SET (2002) and PG in Business Management (2011) from London School of Business Management, U.K. She was appointed as a junior lecturer in Chemistry by the Government of Kerala in July 2002. From 2009 she took on an additional role as a state resource group member in chemistry under the Directorate of Higher Education, Government of Kerala, India. Since 2012 she has been studying for a Ph.D. under the supervision of Professor Paul O'Brien FRS, in the development of precursors for the preparation of semiconductor nanoparticles and thin films for photovoltaic and optoelectronic applications.

its organometallic and metal–organic complexes are stable, it also has a wide-range of alloy compositions with various properties. Tin chalcogenides of the type SnE where E = S, Se or Te have recently attracted considerable interest due to their semiconducting properties. Typically, these materials are observed to have intense absorption across the electromagnetic (EM) spectrum, and narrow band gaps and they therefore have potential as materials for optoelectronic and photovoltaic applications. A summary of band gaps in relation to the atmospheric solar spectrum is presented in Scheme 1. Tin is a far less toxic and, indeed, a relatively earth-abundant metal compared with many of other elements used in semiconductor materials. There has been great interest in the controlled deposition of thin films of tin chalcogenides and the synthesis of tin chalcogenide nanocrystals of controlled size and shape with tuneable band gaps.

Photovoltaic cells are devices that convert photons into direct-current electricity by the photovoltaic effect. Solar cells rely on an absorber layer that can absorb photons and produce an exciton (electron–hole pair) that can be separated in space to produce an electrical current in a circuit. In this sense, photovoltaic cells act as diodes in parallel with a current source.[1] Measurement of the current *vs.* voltage behaviour under illumination allows the characteristics of the photovoltaic cell to be determined. The maximum current possible is known as the short circuit current (I_{SC}) whilst the maximum voltage occurs at open circuit (V_{OC}). The overall power conversion efficiency (PCE, η) is defined as the ratio of the optical power in and the electrical power out:

$$\eta = \frac{P_{max,electrical}}{P_{max,optical}}$$

The so-called fill factor (FF) of a photovoltaic cell is defined as the ratio of the maximum electrical power to the product of the short circuit current and open circuit voltage so that:

$$FF = \frac{P_{max,electrical}}{V_{OC} I_{SC}}$$

And thus the PCE of a photovoltaic cell can be defined as:

$$\eta = \frac{V_{OC} I_{SC} FF}{P_{max,optical}}$$

where $P_{max,optical}$ is the product of the solar irradiance and the surface area of the active layer of the cell. The sun itself is a black-body emitter with peak emission around 500 nm, the full emission spectrum of which is attenuated by the absorbing species in the atmosphere (Scheme 1). The angle at which the sun hits the absorbing layer as well as the climate can affect device PCE; thus to standardise the measurement conditions a solar irradiance of 1000 W m^{-2} with an air mass of 1.5 is used (ASTM G173-03) and a cell temperature of 298 K when reporting PCEs. These conditions correspond to a cloudless day with sunlight incident on a 37°-tilted surface and the sun itself at 41.81° above the horizon.

Osman Bakr

Osman M. Bakr is an Assistant Professor of Materials Science and Engineering, SABIC Presidential Career Development Chair, at King Abdullah University of Science and Technology (KAUST), Saudi Arabia. He holds a B.Sc. in Materials Science and Engineering from MIT (2003) as well as a M.S. and Ph.D. in Applied Physics from Harvard University (2009). He was a postdoctoral fellow in the Laboratory for Nanoscale Optics at Harvard University. In 2010 he moved to KAUST and founded the Functional Nanomaterials Lab, a research group dedicated towards the study of nanoparticles and quantum dots; particularly advancing their synthesis and self-assembly for applications in photovoltaics, optoelectronics, and photocatalysis.

Christopher A. Muryn

Christopher A. Muryn is Head of Research and Analytical Services in the School of Chemistry, The University of Manchester. He holds a B.Sc. in Chemical Physics (1986) as well as a M.Sc. in Instrumentation and Analytical Science (1987) from UMIST. He obtained a PhD in Surface Science from Manchester University (1991). He was then a postdoctoral research associate in the Interdisciplinary Research Centre for Surface Science, University of Liverpool followed by Senior Experimental Officer (1991–1997). Then an SEO at Manchester University until 2010 where initially he continued his involvement in surface science until 2003, when he moved into X-ray crystallography. He became Head of Research and Analytical services in 2009 and has continued his research interests in surface science through synchrotron studies of rutile TiO_2 primarily concerned with fundamental catalytic investigations. Whilst also supporting numerous research projects within the University, with X-ray diffraction and surface imaging techniques employing atomic force microscopy and scanning tunneling microscopy.

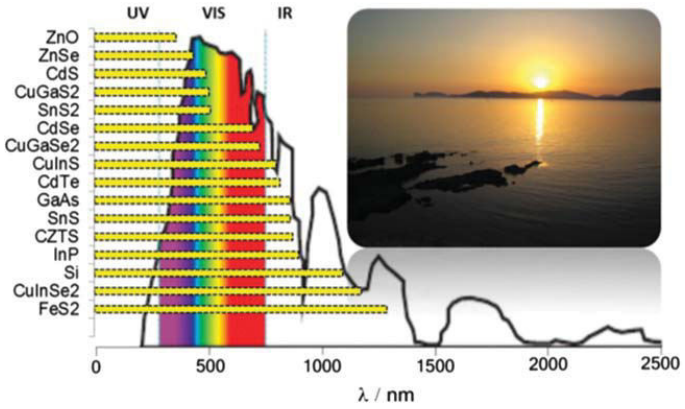

Scheme 1 The optical band gaps of selected semiconductors with respect to the atmospheric solar emission spectrum.

Tin sulfide is a promising material for the absorber layer in solar cells, primarily due to the earth-abundant elements comprising the material but secondly it has an optical band gap commensurate with that of silicon (1.1 eV). It absorbs light across the visible spectrum, typically with absorption coefficients of the order of 10^4–10^5 (Fig. 1). The highest efficiency for a solar cell using SnS as an absorber layer was recently reported by Gordon and co-workers to be 4.4% under standard test conditions,[2] though this PCE is far from optimal; theoretical PCEs for SnS are *ca.* 24%.[3]

Mohammad Azad Malik

Mohammad Azad Malik completed his Ph.D. degree at the University of London in 1990 and then worked with Professor Paul O'Brien FRS initially at Queen Mary, University of London (1990–1995), then Imperial College (1995–2000), and currently The University of Manchester (2000 to 2014). He has been involved in various fields of research and has over 100 peer-reviewed articles on topics including single-source molecular precursors for II/VI, III/V, III/VI, and IV/VI semiconductors, MOCVD, AACVD, CBD, and the colloidal synthesis of nanoparticles. He was recently appointed as an independent research fellow at the University of Manchester (2014-present).

Paul O'Brien

Paul O'Brien FRS is Chair of Inorganic Materials Chemistry in the Schools of Chemistry and of Materials at the University of Manchester; he was Research Dean (2000–2003), Head of the School of Chemistry (2002–2009) and is now Head of the School of Materials. He held academic positions at Chelsea, Queen Mary and Imperial Colleges in the University of London. External appointments have included: Vice-President of the RSC (2009–2011), visiting Professor at Georgia Tech (1996–1999), visiting Fellow Magdalen College, University of Oxford (2009) and Distinguished Fellow at the Institute for Advanced Studies, Durham (2011). He has received distinguished alumni awards: the Potts Medal (Liverpool) and the A. G. Evans Memorial Medal Lecture (Cardiff). He was also awarded the Kroll, Sir Colin Humphreys and the Platinum medals of the IOMMM and the first Peter Day Award from the RSC. His research centres on developing new chemical processes for semiconducting thin films and nanoparticles, especially those comprised of metal chalcogenides. He has authored ca. *600 peer-reviewed publications (*h *> 55) as well as being the editor of a number of books and specialist periodical reports. He holds honorary D.Sc. degrees from both the Universities of Zululand and Liverpool. In 2002 he founded Nanoco, now listed on AIM/LSE. In 2013 he was elected a Fellow of the Royal Society, London.*

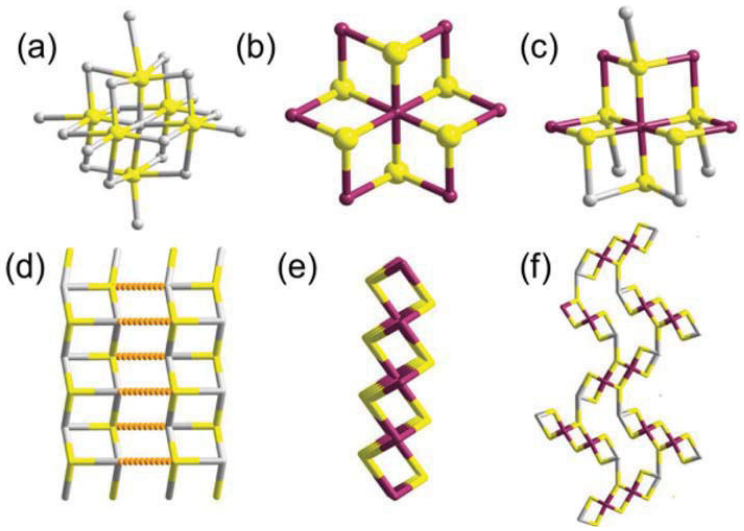

Fig. 1 Local Sn environments in (a) SnS, (b) SnS_2 and (c) Sn_2S_3; and Sn···S connectivity in (d) SnS, (e) SnS_2 and (f) Sn_2S_3. (Sn(II)-grey, Sn(IV)-violet, S-yellow). Reprinted with permission from Ramasamy *et al.*, *Chem. Mater.*, 2013, **25**, 266–276. Published 2013 American Chemical Society.

This review outlines methods for the deposition of thin films of binary tin chalcogenides, specifically the sulfides (SnS), selenides (SnSe) and tellurides (SnTe), as well as covering methods to make their nanocrystalline analogues. We outline some of the latest research into the quaternary tin chalcogenide material copper zinc tin sulfide, Cu_2ZnSnS_4 (CZTS), which is a potentially low-cost and sustainable material for solar energy conversion. We also detail research into mesostructured tin chalcogenide materials. The applications for these materials are discussed on a case-by-case basis. The reader should gain a sense of the *avant garde* as well as new and future directions in this field.

2. Tin sulfides

Tin sulfides are a class of IV–VI semiconductors which exists in three main forms: SnS, SnS_2 and Sn_2S_3. Tin can take co-ordination numbers from 2 to 9 and often displays varying bonding preferences, commonly tetrahedral, trigonal bipyramidal and octahedral for tetravalent tin.

The structures of orthorhombic SnS, SnS_2 and Sn_2S_3 give unambiguous information regarding the arrangement of atoms around the Sn^{2+} and Sn^{4+} ions in the different types of tin sulfide (Fig. 1). SnS crystallizes in a deformed NaCl structure (herzenbergite) containing double layers of Sn and S atoms which are tightly bonded. The layers are weakly held together by van der Waals forces. Each Sn^{2+} ion is bonded to six sulfur atoms in a distorted octahedral geometry, with three short (*ca.* 2.7 Å) and three long (*ca.* 3.4 Å) bonds in an octahedral configuration. Interestingly, SnS is known to undergo a transformation from a GeS to a TlI-type structure above 605 °C with movement of Sn and S along the [100] direction, caused apparently by thermal expansion.

Tin disulfide (SnS_2) most often exists in the PbI_2 layered structure in which the Sn^{4+} centres are coordinated to six sulfur atoms at *ca* 2.6 Å. The layers are comprised of edge-sharing octahedral SnS_6 units, which stack along the crystallographic *c*-axis with weak van der Waals interactions. A rich coordination chemistry of tin sulfides has been developed and has been discussed by Ozin *et al.*[4] The polytypism observed in SnS_2 leads to over seventy different forms with *hcp* layers, but with varying *c* parameters in the unit cell.[4] Sn_2S_3 is a mixed valence compound with ribbon like structure. The Sn^{2+} ion is coordinated with sulfur in a trigonal bipyramidal geometry through two Sn–S distances of *ca.* 2.6 Å and *ca.* 2.7 Å. The Sn^{4+} sites in the ribbon are octahedrally coordinated with Sn–S distances of *ca.* 2.5–2.6 Å.

Tin sulfides have attracted attention as sustainable low-cost materials for photovoltaic solar energy absorbers. The bulk band gaps of the tin sulfides SnS, SnS_2 and Sn_2S_3 are 1.4 eV, 2.3 eV and 1.1 eV respectively.[5] All the forms of tin sulfides exhibit semiconducting properties, though as alluded to above SnS has attracted most attention due to its direct electronic band gap of 1.4 eV which is commensurate with the current industry-standard semiconductors silicon and gallium arsenide (Scheme 1).

2.1. Synthetic routes to tin sulfide thin films

A myriad of methods have been reported for the controlled deposition of tin sulfide thin films. Ray *et al.* reported the synthesis of tin(II) and tin(IV) sulfide thin films by dip deposition.[6]

Glass substrates were immersed in an methanolic solution of tin(II) chloride and thiourea followed by annealing at either 300 °C or 360 °C to produce the films. Optical measurements of the films established band gaps of 1.4 eV and 2.4 eV for SnS and SnS_2 films respectively by photoconductivity measurements. Transmission spectra of SnS films demonstrated their absorbance over the majority of the visible spectrum (Fig. 2).

The films were observed to be granular in appearance by SEM. Abou Shama *et al.* used thermal evaporation to deposit thin films of SnS on glass substrates at two temperatures.[7] In this technique, a beam of electrons is targeted at the precursor materials immobilised on a substrate. The kinetic energy of the electrons is partially converted to thermal energy on impact, and the precursor components mutually decompose to the product. Analysis of films by powder XRD showed that films deposited at 27 °C were amorphous whilst those deposited at 145 °C were crystalline. Band gaps of 1.4 eV (indirect) and 2.2 eV (direct) for the amorphous films and 1.4 eV (indirect) and 2.3 eV (direct) for annealed crystalline films were determined.

Chemical bath deposition (CBD) is a cheap and versatile method for the large-area deposition of thin films relying on the spontaneous decomposition of precursors in solution to coat an immersed substrate. Variables such as bath temperature and solution pH can be adjusted to tune deposition. Ultrasonication can also be used to modulate the process. Ristov *et al.* used CBD to deposit SnS thin films onto glass substrates using a two-bath process with separate aqueous solutions of tin(II) chloride and either Na_2S or $(NH_4)_2S$. The substrate was first immersed at room temperature in a solution of the sulfur source, followed by immersion in a bath of the metal salt at 80–90 °C.[8] Nair *et al.* deposited SnS thin films at 60 °C from a 5% acetone solution in water containing tin(II) chloride and thioacetamide as the precursors with a mixture of amines.[9] Engelken *et al.* used elemental sulfur and tin(II) chloride to deposit SnS thin films at 90 °C from propionic acid solution.[10] Tanusevski prepared SnS thin films from tin(II) chloride and sodium thiosulfate in water at pH 7 with a post-deposition annealing at 250–300 °C.[11] Gao and co-workers used CBD and the same tin and sulfur sources to investigate the influence of deposition temperature in the range 60–80 °C and precursor concentration ratios on the morphologies, compositions and optoelectronic properties of the deposited SnS thin films.[12] It was found that high temperatures were detrimental to film compactness, whereas increasing the S to Sn ratio in the precursor mixture increased the compactness. The dark conductivities and photoconductivities of the films were found to increase with deposition temperature and S to Sn ratio. Band gaps in the range 1.0–1.3 eV were measured, with optical absorption edges located in the range 950–1200 nm with intense absorbance across the visible and near-infrared regions of the electromagnetic spectrum (Fig. 3), of importance for photovoltaic applications.

Direct chemical vapour transport (CVT) was used by Arora *et al.* to grow crystalline thin films of SnS_2 using stoichiometric amounts of elemental tin and sulfur as the precursors and traces of iodine to assist transport.[13] The elements were heated to over 600 °C in a sealed vessel which was cooled extremely slowly to deposit the crystals. Crystal growth was found to be greatly dependent on temperature, with variations of 1 °C found to significantly alter quality of the deposited crystallites. The optoelectronic properties of crystallites grown in this way have been measured with direct and indirect band gaps 2.1 eV observed.[14] Other approaches toward the growth of tin sulfide films have included atomic layer deposition,[15] spray pyrolysis[16] and melt growth.[17]

Arguably the most popular approach for the deposition of thin tin sulfide films has been metal–organic chemical vapour deposition (MOCVD).[18–21] A molecular precursor (or precursor mixture) is delivered as a vapour to a solid substrate, typically glass, and the precursors decomposed at moderate to high

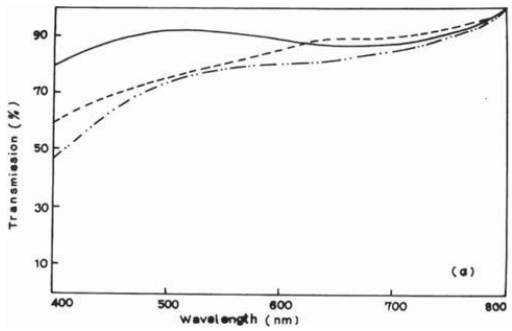

Fig. 2 Visible transmission spectrum of SnS films produced by Ray *et al.* using dip deposition.[6] Reprinted from Ray *et al.*, *Thin Solid Films*, 1999, **350**, 72–78. Copyright 1999 with permission from Elsevier.

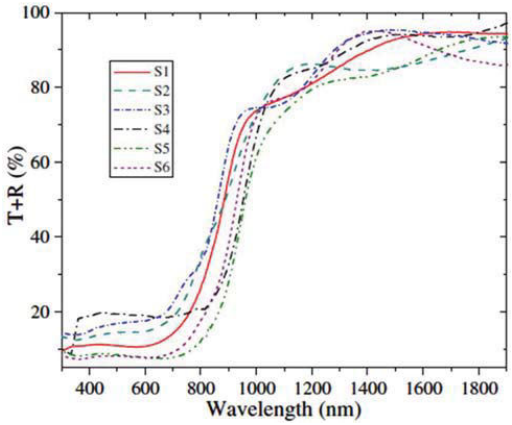

Fig. 3 Combined transmittance-reflectance curves for SnS films produced by Gao and co-workers by chemical bath deposition with band gaps in the range 1.0–1.3 eV.[12] Reprinted from Gao *et al.*, *Thin Solid Films*, 2012, **520**, 3523–3527. Copyright 2012 with permission from Elsevier.

temperatures to leave a residue of the products on the substrate, with volatile elements carried away as vapour.[22] These methods have the attraction of being able to deposit relatively large area films over relatively short periods of time compared with other techniques.

CVD using single-source precursors possesses some potentially intrinsic advantages over other techniques.[23] The presence of a single molecular entity in the supply stream can avoid pre-reactions, important for semiconductor applications as the presence of impurities is detrimental, often scaling non-linearly with device performance. Various single source precursors for the deposition of tin sulfide thin films have been investigated in recent years, examples of which include: tin thiolates, $Sn(SCH_2CF_3)_4$, $Sn(SPh)_4$ and $Sn(S\text{-cyclohexane})_4$,[19,24] tin dithiolates $Sn(SCH_2CH_2S)_2$,[25] tin dithiocarbamates $Sn(S_2CNEt_2)_4$[24] and unsymmetrical organotin dithiocarbamates.[26] Some of these precursors require the employment of hydrogen sulfide gas as a sulfur source to deposit tin sulfide, this approach being undesirable due to the high toxicity of hydrogen sulfide. Recently, O'Brien and co-workers have studied the deposition behaviour of tribenzyltinchloride–thiosemicarbazone compounds by aerosol assisted chemical vapour deposition (AACVD).[18] O'Brien and co-workers have also reported the synthesis and characterization of symmetric and unsymmetric diorganotin dithiocarbamates as single source precursors for tin(II) sulfide.[27] Single source precursors $[Sn(C_4H_9)_2(S_2CN(RR')_2)_2]$ (R,R′ = ethyl; R = methyl, R′ = butyl; R,R′ = butyl; R = methyl, R′ = hexyl; and $[Sn(C_6H_5)_2(S_2CN(RR')_2)_2]$ (R,R′ = ethyl; R = methyl, R′ = butyl; R,R′ = butyl; R = methyl, R′ = hexyl were synthesized, with crystal structures obtained for three derivatives (Fig. 4). Aerosol-assisted chemical vapour deposition (AACVD) at temperatures from 400 °C to 530 °C deposited thin films of orthorhombic tin(II) sulfide, confirmed by powder X-ray diffraction.

The morphology of films deposited using toluene solutions of precursors was characterized by SEM (Fig. 5 and 6). In all cases, sheet-like crystallites were deposited from precursors with variation in size the only difference between films, suggesting that variation in alkyl group on external coordination zone does not have profound effect decomposition pathway, and therefore the products produced. The morphology of crystallites deposited by this method is markedly different from the films deposited using tin(IV) dithiol, dithiolates and thiosemicarbazone complexes by AACVD.[18,20] Spherical crystallites with sheet-like morphology have been observed in LPCVD growth of SnS films. This tends to indicate that the aerosol of precursor solution does not play a major role in morphology of SnS films.

2.2. Synthetic routes to tin sulfide nanocrystals

A variety of methods have been employed to prepare tin sulfide nanostructures including: hydrothermal[28] and solvothermal[29] routes, hot injection methods,[30] aqueous solution methods[31] and polyol methods,[32] the latter which exploits the reducing properties of high boiling glycols towards a suitable metal salt precursor.

Triangular and spherical SnS nanocrystals have been produced by Eychmüller and co-workers by the hot injection of an oleylamine solution of thioacetamide into a mixture of bis[bis(trimethylsilyl)amino]tin(II), oleic acid, trioctylphosphine (TOP) and octadecene at 170 °C.[30] The temperature of the reaction mixture falls to 125 °C and is then held there for

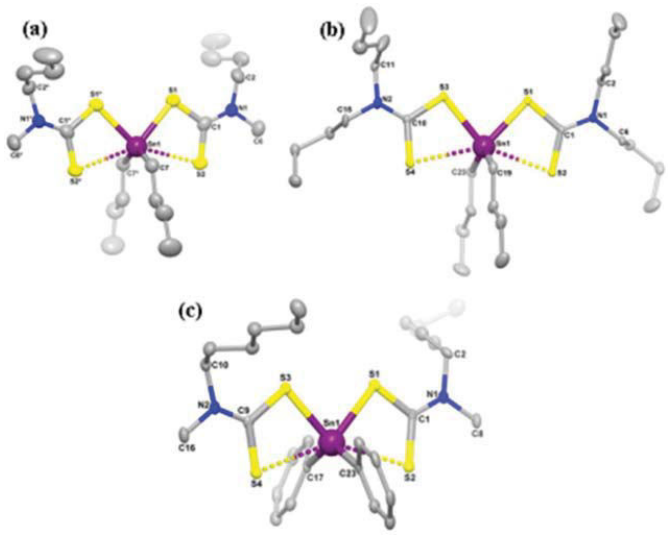

Fig. 4 Diorganotin dithiocarbamate single source pre-cursors developed by O'Brien and co-workers for the deposition of SnS thin films.[27] Reprinted with permission from Ramasamy *et al.*, *Chem. Mater.*, 2013, **25**, 266–276. Published 2013 American Chemical Society.

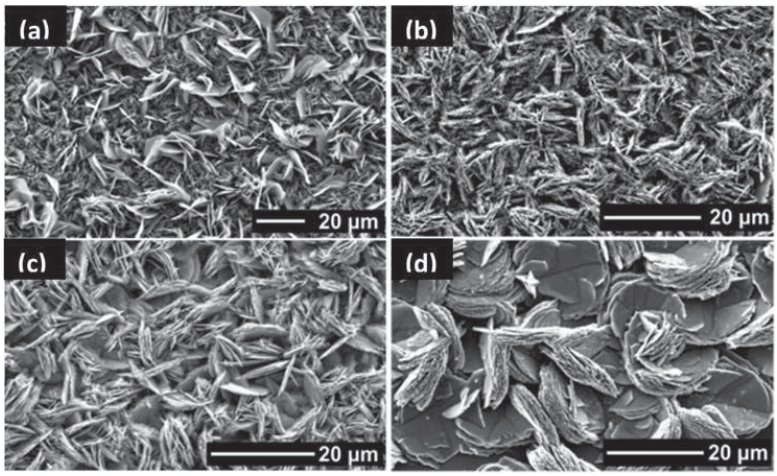

Fig. 5 SEM images of SnS films deposited f on glass substrates from $[Sn(C_4H_9)_2(S_2CN(C_2H_5)_2)_2]$ at (a) 450 °C, (b) 500 °C, and from $[Sn(C_4H_9)_2(S_2CN(CH_3)(C_4H_9))_2]$ (c) 450 °C and (d) 500 °C.[27] Reprinted with permission from Ramasamy *et al.*, *Chem. Mater.*, 2013, **25**, 266–276. Published 2013 American Chemical Society.

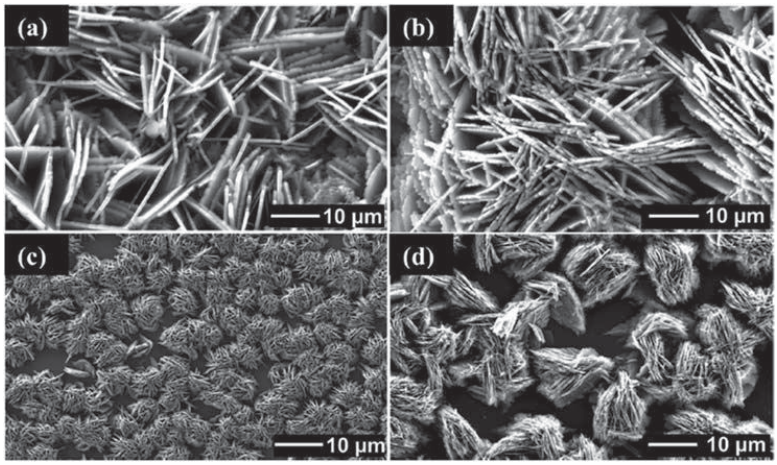

Fig. 6 SEM images of SnS films deposited on glass substrates from $[Sn(C_4H_9)_2(S_2CN(C_4H_9)_2)_2]$. (a) 450 °C, (b) 500 °C and from $[Sn(C_4H_9)_2(S_2CN(CH_3)(C_6H_{13}))_2]$ at (c) 450 °C and (d) 500 °C.[27] Reprinted with permission from Ramasamy *et al.*, *Chem. Mater.*, 2013, **25**, 266–276. Published 2013 American Chemical Society.

3–5 minutes, followed by cooling to ambient temperature. The oleic acid–oleylamine ratio can be varied to establish control of nanocrystal shape (Fig. 7). The absorption profile of the 7 nm diameter nanocrystals produced by this method is dominated by scattering, with an indirect band gap of 1.6 eV reported. A similar synthetic procedure has been used by Schaak and co-workers to produce SnS cubes and polyhedra which display a pseudo-tetragonal distortion of their unit cells.[33]

Similarly, Liu *et al.* have used the reaction of bis(trimethylsilyl)sulfide with tin(II) chloride to enable the fast nucleation of purely orthorhombic nanocrystals of SnS in a mixture of octadecene and oleylamine.[34] The nanocrystals produced by this method were characterised by TEM, HRTEM and EDX, which revealed that the particle size could be controlled by varying the reaction temperature; 6 nm, 12 nm and 20 nm diameter particles are produced at 120 °C, 150 °C and 210 °C respectively. A direct band gap of 1.3 eV for the nanocrystals was revealed from optical absorbance measurements, with no quantum confinement effects observed regardless of the diameter of the nanocrystals. Spin coating of the nanocrystals

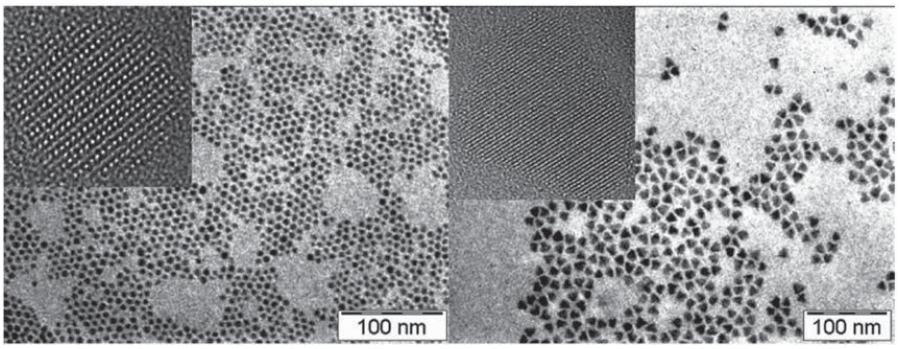

Fig. 7 TEM and HRTEM (insets) of spherical and triangular SnS nanocrystals produced by Eychmüller and co-workers *via* hot injection-thermolysis of precursors.[30] Reprinted with permission from Hickey *et al.*, *J. Am. Chem. Soc.*, 2008, **130**, 14978–14980. Copyright 2008 American Chemical Society.

onto indium tin oxide (ITO) substrates followed by treatment with methanol afforded an enhanced photoresponse compared with non-treated films thus rendering them better-suited for solar energy conversion.

Tilley and co-workers have reported a room-temperature synthesis of SnS nanocrystals using the reaction of tin(II) bromide and sodium sulfide in the presence of various ethanolamine ligands: triethanolamine (TEA), *N*-methyldiethanolamine (MDEA) *N*,*N*-dimethylethanolamine (DMEA).[35] SnS particles with average diameters of 3.2 ± 0.5 nm, 4.0 ± 2.0 nm and 5.0 ± 4.0 nm were produced with TEA, MDEA and DMEA respectively; the monodispersity and diameter of the particles is thus controlled by the number of hydroxyl groups on the stabilising ethanolamine ligand. EDX spectra of the particles revealed a Sn : S stoichiometry of 1 : 1 as expected for SnS. An indirect band gap of 1.1 eV for the DMEA-stabilised nanocrystals was revealed by optical absorbance measurements. Rajalakshmi and co-workers produced orthorhombic SnS nanosheets by a direct route involving the reaction of tin(II) chloride with sodium sulfide in ethylene glycol at 80 °C.[36] Optical absorbance measurements revealed a direct transition at 1.9 eV due quantum confinement. Sohila *et al.* carried out optical and Raman spectroscopic studies on SnS nanoparticles produced using the same chemical method.[37] Raman spectroscopy revealed that the predicted modes appeared at lower energy in comparison to bulk SnS. Atomic force microscopy (AFM) images of single nanoparticles were presented.

Zhang *et al.* have produced large single crystal SnS rectangular nanosheets of dimensions 7000 nm × 3000 nm × 20 nm by pyrolysis of the 1,10-phenanthroline adduct of tin(II) bis-(diethyl dithiocarbamate).[38] The material was incorporated as an anode in a Li-ion battery, and showed improved cycling reversibility though capacity decrease was observed after 5 cycles, attributed to structure collapse due to the ultrathin nature of the nanosheets. Various SnS nanostructures have been prepared by Han *et al.* using the reaction of tin(II) chloride and potassium ethyl xanthate in dimethyl formamide at 180 °C.[39] Nanosheets, nanoribbons, nanobelts and nanorods

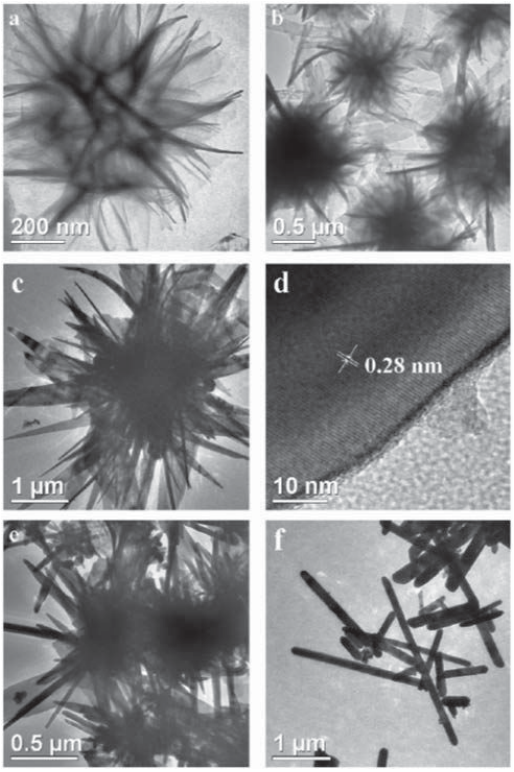

Fig. 8 TEM images of the nanocrystalline products obtained at various reaction stages for the ratio of $C_2H_5OCS_2K$–$SnCl_2$ = 2.4: (a) 12 h, (b, c) 24 h, (d) HRTEM image of an individual SnS nanobelt, (e) 36 h, (f) 48 h.[39] Reprinted from Han *et al.*, *J. Alloy Compd.*, 2011, **509**, 2180–2185. Copyright 2011, with permission from Elsevier.

could be produced by variation of temperature, reaction time and ratios of reagents; for example, an excess potassium ethyl xanthate gave SnS flower-like superstructures (Fig. 8). Optical absorbance measurements revealed direct band gaps for rod-based SnS flowers and belt-based SnS flowers of 1.3 eV and 1.4 eV respectively, similar to bulk SnS. Both rod-based SnS flowers and belt-based SnS flowers displayed photoluminescence after excitation at 210 nm with emission maxima at 409 nm.

A facile synthesis of SnS nanocrystals using $Sn_6O_4(OH)_4$, as the tin precursor with thioacetamide as the sulfur source in oleic acid and oleylamine was reported by Ning *et al.*[40] Modification of the reaction conditions (reaction temperature and Sn/S molar ratio) produced SnS nanocrystals with different shapes and sizes (Fig. 9). SnS nanoparticles and nanoflowers with the orthorhombic crystal structure were observed to possess uniform size distributions. The SnS nanoflowers transformed to polycrystalline nanoflowers, and then become amorphous nanosheets. The authors claim that the reduction in crystallinity reduces the high free energy of the nanocrystals, with the layered crystal structure of SnS claimed to be the main reason for the shape evolution observed. Optical measurements revealed direct and indirect band gaps of 3.6 eV and 1.6 eV, respectively, which are both blue-shifted; indicative of quantum confinement effects. Nanoflowers of tin sulfide have also been synthesised by Yousefi *et al.* using a simple hydrothermal reaction between tin(II) chloride and thioglycolic acid at relatively low temperature.[41] The SnS nanoflowers were added to acrylonitrile–butadiene–styrene (ABS) copolymers. Through thermogravimetric analysis, the thermal properties of polymer analysis were studied: thermal decomposition of ABS copolymers shifted towards higher temperature in the presence of the SnS nanoflowers. SnS nanoflowers and nanocomposites (ABS/SnS) were characterized by XRPD, SEM, TEM, Fourier transform infrared (FT-IR) spectra and AFM. Cone calorimeter measurements showed that the heat release rate significantly decreased in the presence of SnS. Vaughn II *et al.* recently reported the synthesis of SnS nanoflowers suitable for use as an anode material in lithium-ion batteries by the thermolysis of tin(II) iodide with oleylamine sulfide and hexamethyldisilazane in oleylamine at 200 °C.[42] Patra *et al.* have unveiled an approach toward monodisperse orthorhombic SnS nanocrystals of diameter *ca.* 20 nm 'in just 5 seconds' by the reaction of tin(II) chloride with elemental sulfur in a matrix of alkylamine and alkylphosphine.[43]

There has been research into control of the phase of SnS nanocrystals, with the zinc blende phase attracting particular attention. The driving force for this research is the search for novel optical properties compared to the usual orthorhombic phase; particularly the optical properties in the near-infrared region of the EM spectrum can potentially be perturbed. Greyson *et al.* described a simple seedless route towards zinc blende SnS nano- and micro-crystals using the thermolysis of tin(II) chloride and sulfur in oleylamine.[44] SEM revealed the tetrahedral morphology of the nanocrystals, with p-XRD used to confirm the zinc blende phase. The mild reaction temperature (170 °C) used in this synthesis could be responsible for the formation of the zinc blende phase; reaction at higher temperatures (230–300 °C) gave orthorhombic SnS plates. The plates have optical absorption characteristics commensurate with bulk SnS, whereas the zinc blende nanocrystals absorption edge extended into the visible region of the EM spectrum. Deng *et al.* have synthesised metastable SnS nanocrystals of the zinc blende (sphaleritic) phase.[45] A mixture of sulfur and oleylamine was injected into a mixture of tin(IV) iodide and oleylamine in the presence of hexamethyldisilazane. The diameters of SnS nanocrystals produced by this method are 8 nm, 60 nm and 700 nm. Smaller nanocrystals were spherical in shape whereas the larger particles (*ca.* 700 nm) displayed unique truncated tetrahedron sixteen-facet polyhedral crystal morphology. Optical absorption spectroscopy revealed direct band gaps in the range 1.6–1.7 eV for the different sized SnS nanocrystals. Cubic SnS nanocrystals have also been synthesised by Ren *et al.* using thermolysis of tin(II) chloride and

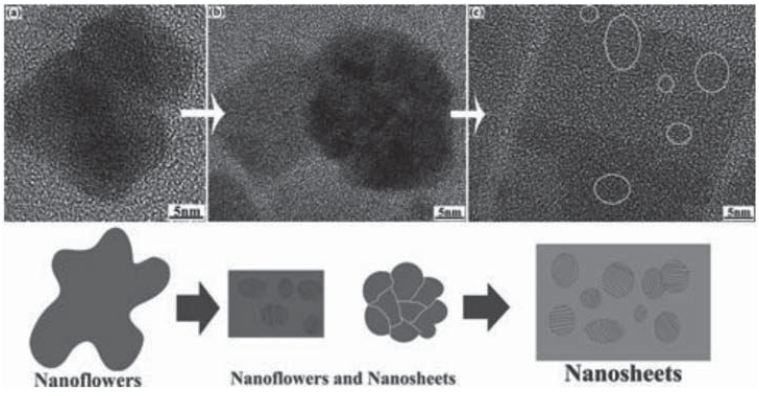

Fig. 9 TEM images of the transition from SnS nanoflowers to nanosheets described by Ning *et al.* and a scheme depicting the transition process.[40] Reproduced from ref. 40 with permission from The Royal Society of Chemistry.

thioacetamide in diethylene glycol at 180–220 °C, with triethanolamine added to control nanocrystal phase. The nanocrystals produced either display orthorhombic or zinc blende phase with nanorod and nanosheet morphology respectively, depending on the triethanolamine concentration used in the reaction.[46] Orthorhombic nanocrystals produced by this method have a direct band gap of 1.3 eV, similar to bulk SnS. In contrast, the zinc blende phase nanocrystals display a direct forbidden band gap of 1.7 eV.

3. Tin selenide

Tin selenide (SnSe) is a semiconducting metal chalcogenide which currently attracts major interest for photovoltaic applications. SnSe has both indirect and direct band gaps of around 0.9 and 1.3 eV respectively.[2,47] It shares the orthorhombic GeS structure with SnS (Fig. 10). Continuous solid-solutions of the formula SnS_xSe_{1-x} where x = 0–1 are known. SnSe is a useful material for energy conversion devices, in particular displaying a variety of properties potentially expedient to materials in photo-electrochemical (PEC) solar cells including suppression of photocorrosion and enhancement of fill factor. Hence, the deposition of thin films and nanoparticles in a controlled manner is of great interest. We outline synthetic strategies toward both phases in the following sections.

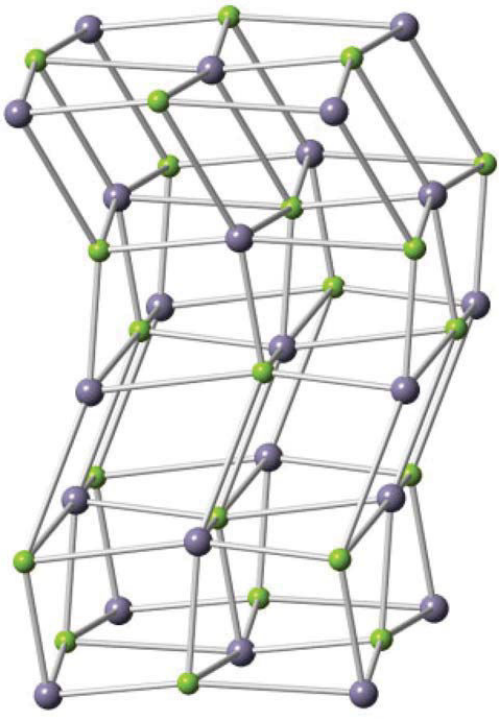

Fig. 10 Orthorhombic SnSe.

3.1. Synthetic routes to tin selenide thin films

The deposition of tin selenide films in a controlled manner is of importance for its application in photovoltaic devices. Singh *et al.* prepared SnSe microparticles by using elemental selenium and tin as precursors in an evacuated bomb heated the 1150 K for 50 h.[48] Tin selenide films were prepared by flash evaporation at 1200 K of the microparticles onto either glass slides, mica or (100) potassium chloride crystals. The films were all found to be p-type conductors. Mathai and co-workers used a 'reactive evaporation' approach to deposit SnSe thin films with elemental tin and selenium evaporated onto a common target kept at elevated temperatures (473–600 K).[49] p-XRD was used to characterise the films, revealing the (400) plane as the preferred orientation. Optical measurements revealed an allowed direct band gap of 1.2 eV. SnS and SnSe thin films were produced from single source precursors of the type $[Sn\{(SiMe_3)_2CH\}_2(\mu\text{-}E)]_2$ (where E = Se or Te) using MOCVD and quality of deposits assessed by p-XRD, XPS and SEM.[50] The decomposition and volatility of the precursors was assessed from TGA data. A range of temperatures and substrates (metallic and non-metallic) were investigated for film growth by CVD using a cold wall reactor. No deposition was found on quartz or silicon with a natural oxide surface in the temperature range of 300–600 °C. Thick films were deposited on a (100) oriented copper surface for both compounds. SnSe films were not efficiently deposited on quartz surfaces covered with either sputtered gold or silver, in contrast to SnTe films, which were deposited efficiently at temperatures as low as 300 or 400 °C for silver and gold substrates respectively. Zainal and co-workers used alkaline media to form SnSe films on indium tin oxide (ITO) using a chemical bath deposition approach, where sodium selenosulfate was decomposed in aqueous sodium hydroxide solution at pH 11.4 in the presence of tin(II) chloride. SnSe films were found to be polycrystalline with preferred orientation in the (201) plane by p-XRD. Optical absorbance measurements revealed a band gap of around 1.3 eV with a p-type direct transition.

Atmospheric pressure chemical vapour deposition (APCVD) was used by Parkin and co-workers to deposit SnSe and $SnSe_2$ thin films on glass substrates.[51] Tin(IV) chloride and diethyl selenide were used as precursors with deposition temperatures in the range 300–650 °C. Deposits were observed on both the top and the bottom of the substrates with varying film composition; EDX analysis of the films grown on top side of the substrate revealed mostly $SnSe_2$ whilst the same analysis performed on the bottom side showed the growth of mostly SnSe. All films were crystalline from as shown by p-XRD data, corresponding with the deposition of SnSe and/or $SnSe_2$. SEM images demonstrated a range of morphologies including plates for top films and flowers for bottom substrates (Fig. 11).

A thermal evaporation approach was employed by Indirajith *et al.* to deposit tin selenide thin films from SnSe precursors.[52] Nanoparticles were first produced by the reaction of tin(II)

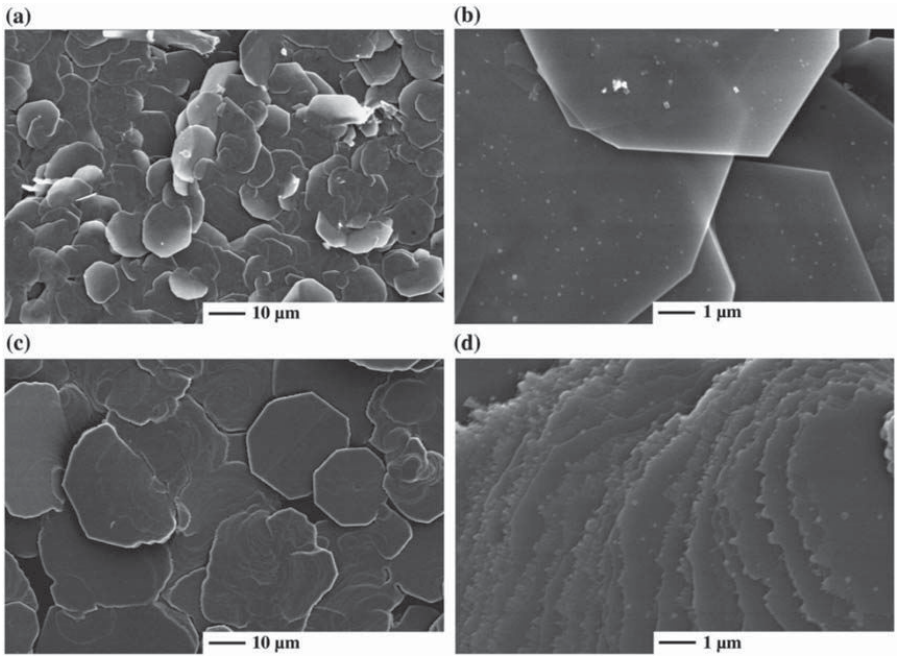

Fig. 11 SEM images of SnSe thin films produced by Parkin and co-workers by APCVD from two different ratios of tin(IV) chloride to diethyl selenide. (a) & (b) $SnCl_4$–Et_2Se = 1 : 1. (c) & (d) $SnCl_4$–Et_2Se = 10 : 1.[51] Reprinted from Boscher *et al.*, *Thin Solid Films*, 2008, **516**, 4750–4757. Copyright 2008, with permission from Elsevier.

chloride with elemental selenium in alkaline medium and were characterised as SnSe by p-XRD. Nanoparticles were thermally evaporated onto glass substrates at various temperatures in the range 150–450 °C. p-XRD and EDX were used to confirm the material type and stoichiometry as SnSe.

The single source precursor approach has also been popular for the deposition of SnSe, Bahr *et al.* used phenylated group IV–VI six-membered ring systems of the formula $(Ph_2SnX)_3$ (where X = S, Se) to produce both SnSe and SnS thin films.[53] The thermolysis of precursors at temperatures greater than 300 °C led to the production of either SnS or SnSe depending on the precursor used. SEM demonstrated that SnS films had plate-like morphologies, whilst SnSe films had a prismatic habitat (Fig. 12).

Boudjouk and co-workers used bis(triphenyltin) chalcogenide single source precursors of the formula $(Ph_3Sn)_2X$ (where X = S, Se and Te) to deposit polycrystalline agglomerates of SnS and SnSe with plate-like morphology and SnTe with cubo-octahedral habit as imaged by SEM.[54] Precursors were synthesised from reaction of Ph_3SnCl with anhydrous Na_2X in THF in the presence of a catalytic amount of naphthalene. The mechanism of the decomposition of precursor to metal chalcogenide is discussed in detail and held to proceed through a series of phenyl migrations; the compounds pyrolyse to eliminate tetraphenyltin and Ph_2X to leave the SnX films. Boudjouk and co-workers have also reported linear and cyclic benzyl substituted organotin single-source precursors of the type $(Bn_3Sn)_2X$ and $(Bn_2SnX)_3$ respectively (where X = S, Se) for the production of SnS, SnSe films and solid solutions.[55] Pyrolysis of linear precursors led to the formation of SnX contaminated by elemental tin. In contrast, pyrolysis of cyclic precursors led to the formation of pure SnX. Mixtures of the two cyclic Se and S-containing precursors led to the formation of solid solutions of the formula $SnS_{1-x}S_x$. Brennan and co-workers used a homoleptic tin(II) pyridylselenoate complex of the formula $[Sn(2\text{-}SeC_5H_4N)_2]$ to deliver SnSe using pyrolysis.[56] The reported complexes are quite suitable for CVD. Using similar complexes, Sharma *et al.* attempted the deposition of tin selenide thin films onto silicon or glass substrates by AACVD using diorganotin(IV) 2-pyridyl selenolate single source precursors of the formula $[R_2Sn(2\text{-}SeC_5H_4N)_2]$ where R = Me, Et or ^{t}Bu.[57] Although the three organometallic complexes were tested for deposition, it was found that only the di-*tert*-butyl derivative was effective in the formation of orthorhombic SnSe films (the latter elucidated by p-XRD), and even the then the temperature range was severely limited; no deposition was observed below 490 °C and coverage deemed poor for deposition temperatures above 530 °C. SEM demonstrated rectangular sheet-like morphologies for films grown on glass substrates while those grown on silicon substrates possessed wool-like morphology (Fig. 13). The photovoltaic properties of the films grown in this manner were reported.

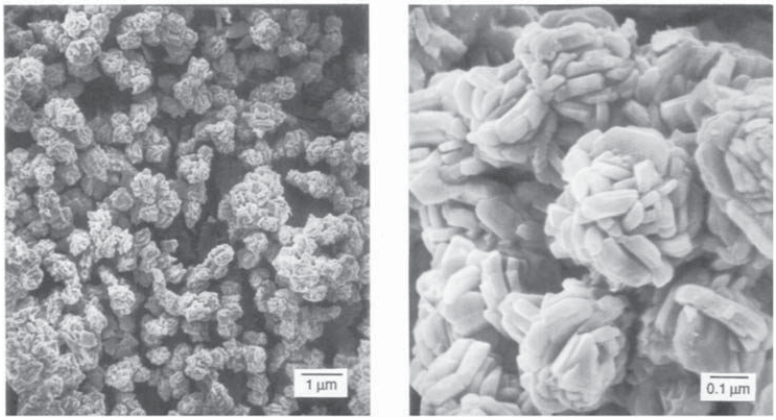

Fig. 12 SnSe produced by Bahr *et al.* from a cyclic single source precursor of the type $(Ph_2SeSn)_3$.[53] Reprinted with permission from Bahr *et al.*, *Chem. Mater.*, 1992, **4**, 383–388. Copyright 1992 American Chemical Society.

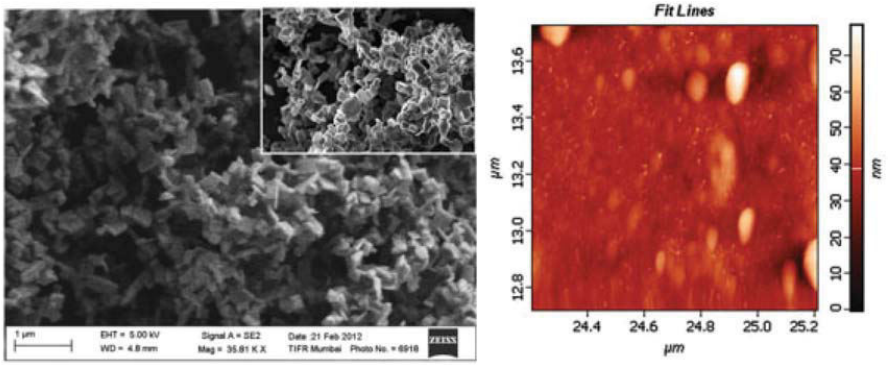

Fig. 13 SEM and AFM images of SnSe films deposited by AACVD from diorganotin(IV) 2-pyridyl selenolate single source precursors.[57] Reproduced from ref. 57 with permission from The Royal Society of Chemistry.

Kumar *et al.* reported the synthesis of SnSe thin films from SnSe pulverised powder using thermal evaporation onto a glass substrate at 350 K.[58] The films were found to be polycrystalline and orthorhombic with preferred orientation in the (111) plane. Crystalline size, strain and dislocation density were calculated from the p-XRD pattern. SEM results of the studies shows that the SnSe films exhibited uniformly distributed grains over the entire surface of the substrate. The average sizes of the grains were reported to be 16 nm. Optical measurements revealed a direct band gap of 1.9 eV. A shallow donor level near conduction band, around 0.3 eV, was confirmed through calculation of activation energies from temperature dependent resistivity measurements.

3.2. Synthetic routes to tin selenide nanoparticles

Wang and co-workers studied the production of nanocrystalline SnSe from a range of alkaline solutions using tin(II) chloride and elemental selenium as precursors.[59] Products from solutions of sodium hydroxide, ammonium hydroxide, ethylenediamine and hydrazine hydrate at a range of different temperatures were investigated. Various morphologies and preferred orientations were revealed by SEM and p-XRD, the latter demonstrating growth predominantly in either the (400) or (111) orientations depending on the conditions employed. In the case of deposition from sodium and ammonium hydroxides, high temperatures (>170 °C) were found to be unsuitable for deposition due to decomposition of the SnSe product.

Pejova *et al.* have reported a chemical bath deposition technique of SnSe nanocrystals as thin films onto glass substrates using a solution of tin(II) chloride in the presence of sodium selenosulfate at pH 9.[60] Ethylene diamine tetraacetic acid (EDTA) was used to modulate the rate of the deposition as if the metal is sequestered. A pre-deposition treatment involving

immersion of the glass substrates into a solution of tin(II) chloride followed by thermal annealing was used to assist growth, the latter held to be by the formation of seed crystals of tin(II) oxide which improve both film growth and adhesion. Nanocrystals were found to be 15 nm as-deposited and 23 nm upon annealing using the Scherrer equation. Optical measurements revealed blue shifts in the indirect band gap and an additional higher energy direct band gap transition in as-deposited (1.2 eV indirect; 1.7 eV direct) and annealed films (1.1 eV indirect; 1.6 eV direct) compared to macrocrystalline SnSe (0.95 eV indirect) and thus strongly infer quantum confinement effects are present in the nanocrystalline thin films. The photophysical, electrical and photoelectrical properties of films produced in this manner have been reported.[61]

Ning *et al.* extended their approach to SnS nanocrystals (*vide supra*)[40] to the production of colloidal SnSe using the same tin precursor, $Sn_6O_4(OH)_4$. Injection of selenourea into a solution of $Sn_6O_4(OH)_4$ in oleylamine–oleic acid at 140 °C followed by precipitation afforded nanocrystals of orthorhombic SnSe confirmed by p-XRD and SAED. Interestingly, the nanocrystal size and shape could be tuned by varying the Sn/Se reagent ratio and temperature. Nanoparticles, nanocubes, and nanopeanuts (!) could all be obtained by this method from TEM images. The SnSe nanocrystals obtained were tested as anode materials in lithium ion batteries.

Vaughn II *et al.* recently reported a simple method for producing SnSe with uniform lateral dimensions and tuneable thickness using the reaction of tin(II) chloride with trioctylphosphine selenide (TOP-Se) in the presence of hexamethyl disilazane at 240 °C in oleylamine.[62] Sheets produced by this method are square with lateral dimensions of around 500 nm × 500 nm, with the thickness of the film readily adjustable in the range 10–40 nm by changing the ratio of TOP-Se to $SnCl_2$. An aliquot analysis approach by TEM revealed the growth as shown in Fig. 14. The as-synthesised nanosheets were shown to have a direct band gap of around 1.0 eV with an indirect band gap of around 0.9 eV by optical diffuse reflectance measurements.

Liu *et al.* reported the synthesis of single-crystalline SnSe nanowires using the reaction of TOP-Se with $Sn[N(SiMe_3)_2]_2$ in oleylamine.[63] Nanowire length exceeded 10 μm by SEM, with TEM confirming a mean diameter of around 20 nm. Direct and indirect optical band gaps of 1.1 eV and 1.6 eV, both blue-shifted compared to the bulk material, were reported, as the manifestation of quantum confinement effects.

Achimovicova *et al.* reported a direct mechanochemical synthesis of tin selenide and tin selenide/tin diselenide composites from elemental tin and selenium by high-energy milling at room temperature. The SnSe produced by this method is orthorhombic whereas in the $SnSe/SnSe_2$ composite orthorhombic SnSe and hexagonal $SnSe_2$ co-exist. The smallest crystals in this sample averaged in sizes between 2–8 nm with pseudo spherical or square-like morphology.[64] A similar process using the elemental precursors has been reported for the production of hexagonal $SnSe_2$.[65] $SnSe_2$ quantum dot sensitized solar cells have been prepared by Dai and co-workers using the cluster compound $(N_2H_4)_3(N_2H_5)_4Sn_2Se_6$, the latter formed from reaction of hydrazine with a mixture elemental tin and selenium.[66] Immersion of TiO_2 anodes in the precursor solution followed by annealing under an argon atmosphere immobilised $SnSe_2$ nanoparticles at the metal oxide surface. A TiO_2 solar cell constructed with the deposited $SnSe_2$ as anode material displayed a power conversion efficiency of 0.12% compared to 0.004% when left uncoated.

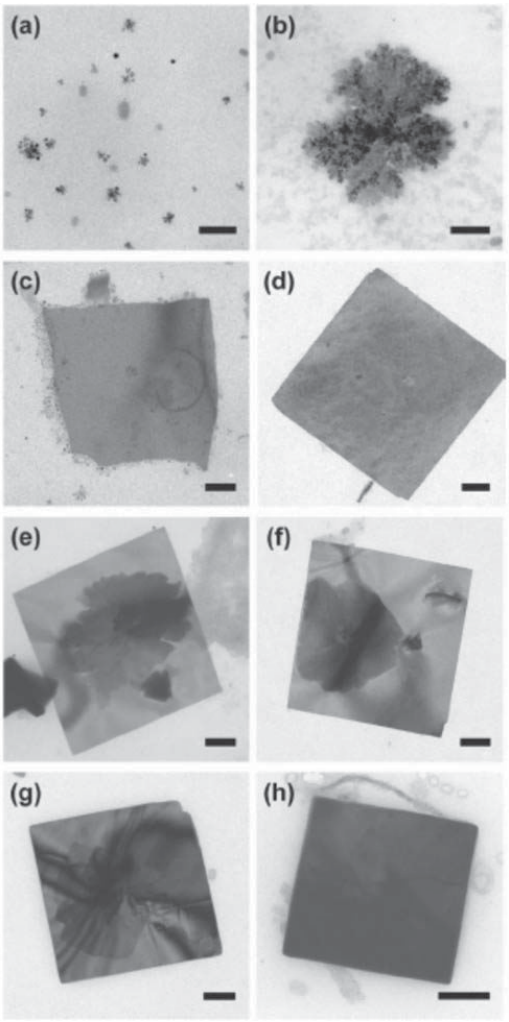

Fig. 14 TEM study of growth mechanism of SnSe nanosheets by Vaughn II *et al.*[62] Images (a) and (b) represent nucleation, (c) and (d) lateral growth from nanoparticle attachment whilst images (e) to (h) represent layer by layer vertical growth. All scale bars 100 nm. Reprinted with permission from Vaughn II *et al.*, *ACS Nano*, 2011, **5**, 8852–8860. Copyright 2011 American Chemical Society.

Baumgardner and co-workers synthesised oleic acid capped SnSe nanocrystals by thermolysis of $Sn[N(SiMe_3)_2]_2$ in the presence of trioctylphosphine selenide (TOP-Se) and oleylamine.[67] Particles produced by this synthetic method possess irregular pseudo-spherical shape with tenability in diameters in the range 4–10 nm from both TEM images and Scherrer analysis of peak broadening in the p-XRD patterns. EDX confirmed the SnSe stoichiometry. HRTEM was used to identify stacking faults in the (200) plane of the crystals. Tuneable band gaps in the range 0.9–1.3 eV were elucidated for diameters in the range 4–10 nm by optical absorption measurements, commensurate with band gaps ideal for single junction solar energy conversion devices (Fig. 15).

Another solution-phase synthesis of SnSe or $SnSe_2$ nanocrystals suitable for use in solar cells was reported by Franzman *et al.*[68] Nanocrystals were synthesised by the reaction of di-*tert*-butyl diselenide with tin(II) chloride in a mixture of dodecylamine and dodecanethiol at 95 °C with brief heating at 180 °C followed by cooling and precipitation by addition of ethanol. The ratio of di-*tert*-butyl diselenide to tin(II) chloride allowed the control of the product composition with stoichiometric ratios leading to phase pure SnSe and excess (2.0 eq. di-*tert*-butyl diselenide) leading to phase pure berndtite $SnSe_2$ by p-XRD pattern analysis. SnSe nanocrystals were observed to be anisotropic by TEM, with a diameter of 19 nm but having an elongated and polydisperse length (Fig. 16). A near-stoichiometric tin-selenium ratio was confirmed by EDX. Optical measurements confirmed a blue-shifted direct band gap of around 1.7 eV compared with bulk SnSe suggesting quantum confinement with absorption across the EM spectrum up to the NIR region. Functional solar cells incorporating the SnSe nanocrystals exhibited superior power conversion efficiencies (η_p) compared to the devices fabricated without SnSe (η_p = 0.06% *vs.* η_p = 0.03%).

Recently, Sharma *et al.* prepared tin selenide nanocrystals using diorganotin(IV) 2-pyridylselenolate single source precursors of the formula $[R_2Sn(2\text{-}SeC_5H_4N)_2]$ where R = Me, Et or ^{t}Bu.[57] Thermolysis of the precursors in oleylamine furnished SnSe nanoparticles with a range of product morphologies observed by SEM – from rectangular bars to rectangular and hexagonal sheets depending on the precursor used.

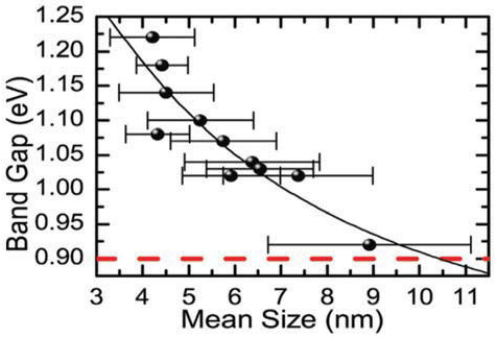

Fig. 15 Relationship between the energy of the band gap and the mean size (diameter) for SnSe nanocrystals produced by Baumgardner *et al.* using thermolysis.[67] Reprinted with permission from Baumgardner *et al.*, *J. Am. Chem. Soc.*, 2010, **132**, 9519–9521. Copyright 2010 American Chemical Society.

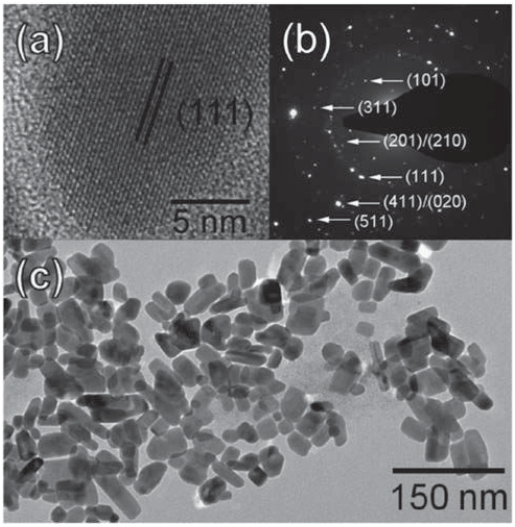

Fig. 16 Imaging of SnSe nanocrystals produced by the method of Franzman *et al.* for use in solar cells. (a) HRTEM of a single nanocrystal, (b) SAED pattern with indexing of SnS crystal planes and (c) TEM of SnSe nanocrystal ensemble.[68] Reprinted with permission from Franzman *et al.*, *J. Am. Chem. Soc.*, 2010, **132**, 4060–4061. Copyright 2010 American Chemical Society.

4. Tin telluride

Tin telluride (SnTe) is garnering much interest due to its semiconducting properties. Bulk SnTe exhibits a direct band gap of 0.19 eV at 300 K, which lies in the mid-IR region of the electromagnetic spectrum.[5] The material hence has potential application in IR detection, radiation receivers and thermoelectric devices.

SnTe crystallises with the cubic rock salt structure (Fig. 17) but can undergo a structural transformation to an orthorhombic form under pressure.[69] Sharma *et al.* have performed detailed analysis of the electronic structure and ground state properties of the SnTe using a linear combination of atomic orbitals (LCAO) approach based on density functional theory (DFT) calculations.[70] The calculated Compton profiles were used to discuss the electronic properties of SnTe. Comparative studies of SnTe with GeTe have been performed to contrast the nature of bonding found within the two compounds; it was found that SnTe is less covalent and more ionic than GeTe.

As with other metal chalcogenides, several approaches to SnTe are known, but the frequency of such reports is far lower than for either the sulfide or selenide thin films.

in the range 7 nm–17 nm diameter (Scherrer equation), with size distributions below 10%. The size of the crystals produced in this range could be easily controlled by adjustment of injection and growth temperatures, and the amount of oleylamine in the oleylamine–octadecene mixture. Absorption spectra of the nanoparticles produced by this method allowed estimation of the band gap energies of the as-synthesised SnTe: 0.4 eV and 0.5 eV for 14 nm and 7 nm nanocrystals respectively.

Using a tin oxide hydroxide precursor for the synthesis of tin chalcogenide nanoparticles, $[Sn_6O_4(OH)_4]$, Ning *et al.* have also outlined the synthesis of nanocrystalline SnTe nanoparticles and nanowires, the latter *via* oriented attachment.[76] Formation of nanocrystals was initiated by injection of TOP-Te into $Sn_6O_4(OH)_4$ dissolved in mixtures of either oleic acid–oleylamine or oleic acid–octylamine held at 180 °C. Nanocrystals were characterised as cubic SnTe by p-XRD, TEM and HRTEM. The diameters of highly crystalline nanocrystals produced from oleylamine-containing solutions were around 4 nm. In contrast, nanocrystals produced from octylamine-containing solutions were around 8 nm with low crystallinity. It was found that prolonged reaction times for the latter case afforded an *in situ* conversion of SnTe nanocrystals to rather polydisperse nanowires of around 50 nm in length and around 5 nm in diameter. The authors suggest from HRTEM images of the wires that an *oriented attachment* growth mechanism is responsible for the growth of the wires by the growth of (200) planes in the <100> direction. A time-course study by TEM tends to reinforce these mechanistic suggestions (Fig. 19).

Salavati-Niasari *et al.* reduced tellurium(IV) chloride with potassium borohydride in the presence of tin(II) chloride under alkaline conditions,[77] the precipitates obtained were analysed by p-XRD, SEM and TEM, which confirmed the product to be SnTe nanocrystals with diameters in the range of 40–50 nm, and quasi-spherical morphologies. The same tin and tellurium containing precursors were also shown to produce SnTe nanocrystals by this approach. SnTe nanocrystals produced by this method were 30–40 nm in diameter and almost monodisperse.

Tilley and co-workers have reported a solution synthesis of SnTe nanocrystals using triethanolamine (TEA) as a stabilising agent.[78] The nanoparticles are characterised by p-XRD, SAED and EDX. The reaction is said to be as a greener phosphine-free alternative to the Talapin synthesis,[75] though the nanocrystals produced by this method seem to be somewhat more polydisperse. The diameter of the nanoparticles could be controlled by the amount of TEA added to the $SnBr_2$–telluride reagent mixture, allowing access to sizes from 3 to 32 nm. Nanocrystals exhibited quantum confinement effects, with band gaps measured as 0.5 eV and 0.4 eV for nanoparticles with diameters of 6.5 nm and 14 nm respectively. The method

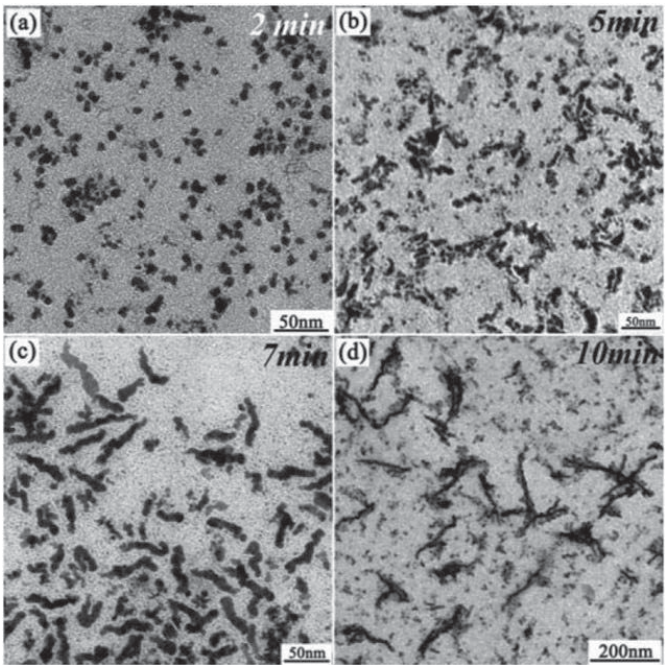

Fig. 19 Temporal study of the *oriented attachment* mechanism of SnSe nanowire growth by Ning *et al.*[76] TEM images show the nanocrystalline products from aliquots taken from a reaction at various time points over a period of 10 min. Reproduced from ref. 73 with permission from the Royal Society of Chemistry.

is expected to be applicable to the production of other metal chalcogenide nanocrystals.

Schaak and co-workers recently described a rather interesting general method for the conversion of libraries of tin(II) sulfide and selenide nanosheets into telluride nanosheets by reaction with TOP-Te.[79] The mechanism is believed to proceed *via* direct anion exchange of the chalcogenide ions, and could represent a general reaction for accessing previously inaccessible tin telluride nanostructures.

5. Synthetic routes to copper zinc tin sulfide

Copper zinc tin sulfide (Cu_2ZnSnS_4; CZTS) is an emergent material for solar energy conversion.[80] It has a band gap of *ca.* 1.5 eV with a high absorption coefficient of 10^4 cm^{-1}. Like tin sulfide, it is composed of non-toxic and relatively earth-abundant elements and hence is attractive for sustainable solar energy. It is an alternative material to $CuInGaS_2$ (CIGS) in thin film solar cells as it is cheaper to produce in theory and there has recently been considerable research focused on the synthesis and growth of CZTS nanocrystals and thin films. CZTS based absorber layers processed from solution have been shown to have higher solar energy conversion efficiencies than vacuum deposited films, thus leading to the prospect of mass production from scale-up.[81] Current record solar cell power conversion efficiencies from CZTS-based materials stand at *ca.* 11%, making the prospect of commercialisation likely.[82] CZTS displays polymorphism, existing in the wurtzite kesterite, wurtzite stannite, zinc blende stannite and zinc blende kesterite forms with varying theoretical stabilities.[83]

Ryan and co-workers used a colloidal synthesis to produce CZTS nanorods in the wurtzitic phase[84] (Fig. 20). A mixture of copper(II) acetyl acetonate, zinc acetate, tin(IV) acetate and TOP oxide was mixed in octadecene and heated to 240–260 °C. At 150–160 °C a mixture of 1-dodecane thiol and *tert*-dodecyl mercaptan was injected into the reaction. Nanorod growth was allowed for up to 30 min, after which cooling and addition of toluene quenched the reaction. The nanoparticles were purified by centrifugation. Dark-field scanning transmission electron microscopy (DF-STEM) of the product showed nanorods of 11 nm × 35 nm dimensions. Selected area electron diffraction (SAED) revealed that the nanorods were of wurtzite phase. Optical absorbance measurements revealed a band gap of *ca.* 1.4 eV.

CZTS nanocrystals have been synthesized by Khare *et al.* using the thermal decomposition of diethyl dithiocarbamate complexes of copper(II), zinc and tin(IV) in mixtures of oleic acid and octadecene.[85] The spherical nanocrystals produced by this method had diameters of 2, 2.5, 5 or 7 nm by HRTEM depending on the decomposition conditions employed. Injection of oleylamine at 150 °C produced nanocrystals of 2 nm diameter. Injection of oleylamine and octadecene at 150 °C gave 2.5 nm nanocrystals. A higher decomposition temperature of 175 °C afforded nanocrystals with diameters of 5 and 7 nm were formed. To avoid the thermal decomposition of the tin precursor under the latter synthetic conditions, it had to be co-injected with oleylamine and octadecene. An increase in the band gap from 1.5 eV to 1.8 eV with decreasing particle radius was determined from optical absorbance measurements thus demonstrating quantum confinement. Similarly, Han and co-workers have reported the synthesis of CZTS nanocrystals in the wurtzite phase from the decomposition of copper(II) and zinc(II) diethyldithiocarbamate complexes along with tin(IV) diethyl dithiocarbamate.[86] Heating of the complexes at 250 °C for 30 min in a hexadecanethiol–trioctylamine mixture afforded monodisperse bullet-shaped nanorods of dimensions 15.1 ± 1 nm × 7.6 ± 0.6 nm characterised by TEM, EDX, XPS and p-XRD. Trimmel and co-workers have developed routes towards CZTS films from the decomposition of copper(I), tin(IV) and zinc xanthate precursors. Solar cells incorporating close-to stoichiometric CZTS from this method have an efficiency of 0.1% with a band gap of 1.3 eV.[87]

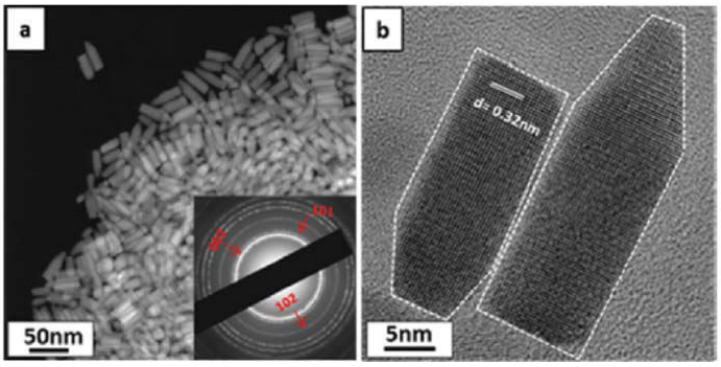

Fig. 20 DF-STEM and HR-TEM images of bullet-shaped CZTS nanorods produced by Ryan and co-workers.[84] (a) DF-STEM image of nanorods inset: SAED pattern revealing wurtzite phase. (b) HR-TEM image of two nanorods revealing elongation in the [002] direction. Reprinted with permission from Singh *et al., J. Am. Chem. Soc.*, 2012, **134**, 2910–2913. Copyright 2012 American Chemical Society.

Jiang *et al.* isolated metastable Cu_2ZnSnS_4 nanocrystals with an orthorhombic phase.[88] using the reaction of $CuCl_2$, $ZnCl_2$, $SnCl_2$ and thiocarbamide at 200 °C for 24 h. The as-synthesised nanocrystals had plate-like morphology with size varying from 20 to 50 nm. It was reported that the metastable orthorhombic phase can be transformed to stable kesterite phase by annealing at 500 °C.

Cabot and co-workers have demonstrated that continuous-flow processing may be a viable method for the production of CZTS nanocrystals.[89] Precursor solutions containing copper(II) chloride, tin(IV) chloride and zinc oxide in mixtures of oleylamine and octadecene were flowed through a 1 m × 3 mm tube in diameter at a rate of 1–5 mL min^{-1}. Heating *in situ* to 300–320 °C caused decomposition of the precursor solution, affording nanocrystals of CZTS of various sizes, shapes and compositions depending on the specific reaction conditions.

Prieto and co-workers used thermal decomposition of a mixture copper(II) acetylacetonate, zinc acetate, and tin(II) acetate, and a mixture of sulfur–selenium with sodium borohydride in oleylamine and trioctylphosphine oxide (TOPO) to afford $Cu_2ZnSn(S_{1-x}Se_x)_4$ nanocrystals with tunable selenium–sulfur composition.[90] Band gap of the nanocrystals decreased from 1.54 eV to 1.47 eV as selenium replaced sulfur in the CZTS nanocrystals. Similarly, Ou *et al.* used a hot injection of copper, zinc and tin stearate complexes in oleylamine into thiourea and selenium in octadecene at 270 °C to produce $Cu_2ZnSn(S_xSe_{1-x})_4$ nanocrystals. Optical band gaps ranging from 1.5 eV to 1.0 eV were observed, the energy decreasing as the amount of selenium increased.

Sol–gel processing of CZTS nanowires and nanotubes using an anodized alumina (AAO) template with 200 nm pore size has been reported by Su *et al.*[91] The CZTS sol–gel was prepared by dissolving copper(II) acetate, zinc(II) acetate and tin(II) chloride in 2-methoxyethanol. Immersion of the AAO templates into the precursor solution followed by annealing at 550 °C under a sulfurous atmosphere and etching with sodium hydroxide afforded the immobilised nanowire/nanotube array. CZTS nanowires and nanotubes of dimensions 200 nm × 60 μm were produced, the width dictated by the AAO template. Optical band gaps of 1.57 eV and 1.61 eV were measured for nanowires and nanotubes respectively.

There has been further research into solar cell device fabrication using solution-processed CZTS. CZTS solar cells with 1.9% solar energy conversion efficiency, 0.484 V open-circuit voltage, 8.91 mA cm^{-2} short-circuit current density and a 45% fill factor have been reported by Hu and co-workers.[92] CZTS nanocrystals use to fabricate the cell were synthesized by the reaction of copper(II) and tin(II) chloride and zinc sulfate with Na_2S in ethylene glycol solution heated at 180 °C for 12 hours. Pal and co-workers prepared a CZTS-fullerene pn-junction hybrid solar cell with power conversion efficiency of 0.9% and a fill factor of 43%.[93] CZTS nanocrystals were synthesised by the reaction of tin(IV) chloride, copper(II) chloride and zinc chloride with sulfur in oleylamine at 180 °C. Nanoparticles were spin-coated on an ITO substrate and then coated with a layer of the fullerene [6,6]-phenyl-C_{61}-butyric acid methyl ester (PCBM) to form the pn-junction.

O'Brien and co-workers presented the first report of CZTS thin films deposited by a chemical vapour deposition

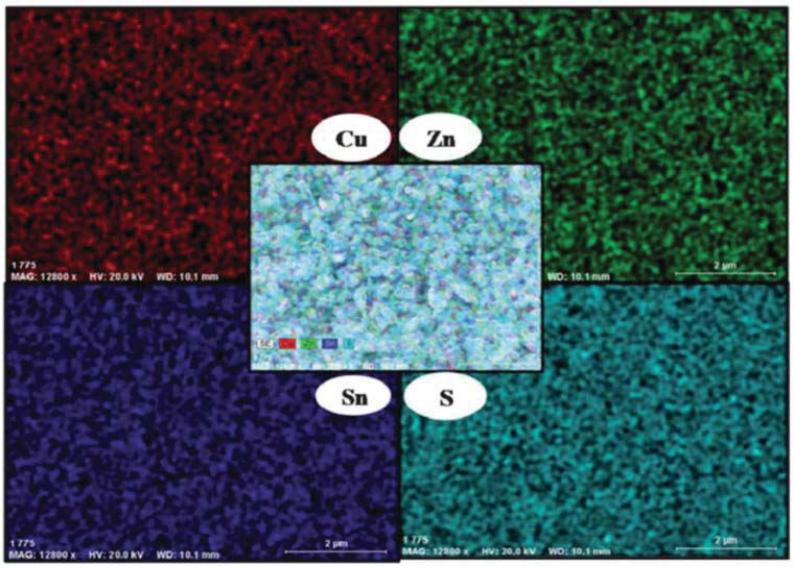

Fig. 21 EDX elemental mapping of CZTS thin films produced by O'Brien and co-workers by using AACVD with a mix of three discrete molecular precursors.[94] Reproduced from ref. 94 with permission from The Royal Society of Chemistry.

approach from discrete molecular precursors. Compatible precursors based on simple metal diethyldithiocarbamate complexes of formula $[M(S_2CNEt_2)]$ (where M = Cu^{2+}, Zn^{2+}) and diorganotin complexes of the type $[Sn(Bu)_2(S_2CNEt_2)_2]$ were mixed in the correct 2Cu : 1Zn : 1Sn stoichiometry and AACVD performed from toluene solutions at various furnace temperatures. p-XRD was used to confirm the phase of deposited Cu_2ZnSnS as either kesterite or stannite. SEM showed granular crystallites with sizes dependent on temperature. EDX was used to confirm the correct stoichiometry of the thin films deposited at 360 °C. EDX elemental mapping demonstrated the even distribution of Cu, Zn, Sn and S across the entire substrate (Fig. 21).

6. Synthetic routes to mesostructured tin chalcogenide materials

Mesostructured compounds are a hugely important class of condensed phase materials which contain regular repeating motifs to produce three-dimensional ordering of the material which leads to higher ordering in the crystalline material *e.g.* formation of pores of defined size and shape. Pore sizes in mesoporous materials lie between those of microporous materials (<2 nm) and macroporous solids (>50 nm).[95] Traditionally these materials have been based on alumina, silica or aluminosilicate superstructures with popular examples such as zeolites, molecular sieves and mesoporous silica finding use in catalysis, ion exchange, drying of solvents and optoelectronic applications. Recently, however, there has been a paradigm shift with non-oxide inorganic materials used to produce novel mesostructured compounds.[96] The synthesis, structural, spectroscopic and sorption properties of microporous tin chalcogenides have been reported,[97–100] but more recently, reports of novel syntheses of mesostructured materials have appeared.

Ozin and co-workers described the synthesis of a novel class of tin(IV) sulfide thermotropic liquid crystals.[101] Reaction of tin(IV) chloride with ammonium sulfide and hexadecylamine (HDA) in the aqueous alkaline media formed a light yellow gel which was crystallised at 150 °C over 19 hours to form an intriguing yellow monolith of formula $SnS_{2.07}(HDA)_{2.34}(H_2O)_{2.23}$ by elemental analysis with a large *d*-spacing of 5.1 nm by p-XRD. Further washing with excess acetone afforded material with reduced *d*-spacing. p-XRD, SEM and TEM revealed a mesoporous structure consisting of stacked two-dimensional layers of hexagonal SnS_2 with a fully-extended hexadecylamine bilayer in the inter-lamellar space. Solid-state magic angle spinning NMR of the ^{119}Sn metallocentres revealed two tin coordination environments: 5- and 6-coordinate. Raman spectroscopy revealed a new band implying a changed bond distance consistent with a lower coordination than 6. The UV-Vis absorption spectrum revealed an absorption edge lying between that of five-coordinate and six-coordinate tin species. Thermal behaviour was studied by TGA and DSC and variable-temperature p-XRD, with crystalline (RT – 45 °C), semi-liquid (45 °C–85 °C) and liquid crystalline (>85 °C) phases identified. The material is electrically conducting, especially so in the liquid crystalline phase compared to the other phases, and can reversibly adsorb water and carbon dioxide, thus heralding the material as having use in optoelectronic and sensing applications. The lamellae were later imaged by tapping-mode AFM, with parallel stacked layers in the *z*-direction observed with an inter-lamellar distance of 5 nm. Imaging in the *x*, *y* plane by two-dimensional fast Fourier transform-AFM revealed a periodic arrangement of mesopores with sizes in the range of 3–10 nm.[102] Similarly, Rao and Neeraj reported mesostructured SnS_2 composites produced by the reaction of tin(IV) chloride with sodium sulfide in the presence of dodecylamine surfactant.[103] The composites displayed a lamellar structure with a periodic interlamellar spacing of 3.12 nm as measured by p-XRD. Kessler and co-workers produced mesostructured tin(IV) sulfide by the reaction of sodium sulfide and tin(IV) chloride in the presence of cetyl trimethyl ammonium bromide surfactant under alkaline conditions.[104] The reaction produced lamellar mesostructured tin(IV) sulfide with spacing between layers of around 2.6 nm. The reaction can be translated to produce a number of materials with differences in long and short range order throughout the material.[105] Indeed, tin coordination geometry can be varied between octahedral and tetrahedral by variation of surfactant amount. Transformation between various lamellar phases has been described.[106]

Solution phase co-assembly of zintl clusters of the type SnE_4^{4-} (where E = Se, Te) have been exploited by the groups of Tolbert and Kanatzidis to prepare a range of mesostructured tin chalcogenides. This novel approach relies on the templating of the zintl clusters by surfactant molecules, either with or without the presence of transition metal cations. Initially, assembly of the zintl clusters using square-planar platinum(II) ions was presented,[107] giving rise to platinum tin telluride mesostructured composites, with periodic mesostructure as-imaged by TEM. EXAFS was used to demonstrate the structure consisting of a square planar d^8 platinum(II) centres bonded to four Sn_2Te_6 clusters (Fig. 22), with reduction of the platinum(IV) starting material presumably occurring during reaction. This approach, draws parallels with supramolecular chemistry; the development of metal templated structures by Lehn,[108] for instance, being especially salient to the principles used here, where the ligand field preferences of a metal cation dictates the structure of the final assembly. Riley and Tolbert cite the work of Ozin which states that square planar geometry of the linking metal cation in Ge_4S_{10} systems is crucial to the formation of mesophases.[109] The narrow band gap of 0.8 eV is potentially useful in optoelectronic applications.

Korlann *et al.* later reported the use of cross-linking with either Pt(II) or Pt(IV) salts in varying ratios to perturb the electronic structure of the composites and modulate properties.[110] A range of different transition metals ions (Ni^{2+}, Pt^{2+}, Zn^{2+}) have been investigated for the templating of the zintl ions

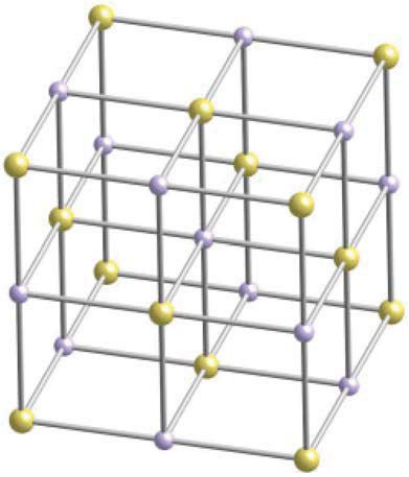

Fig. 17 Cubic SnTe.

4.1. Synthetic routes to tin telluride thin films and nanocrystals

Bulk SnTe has a band gap of *ca.* 0.19 eV (mid-IR)[2] and quantum confinement leads to blue-shift of the band gap toward the near-infrared region of the electromagnetic spectrum, thus SnTe potentially has uses in biomedical imaging applications *in vivo* or telecommunications. However, there are currently relatively few reports of syntheses of monodisperse nanocrystals of SnTe despite its great potential.

Boudjouk *et al.* produced cubo-octahedral SnTe from single-source precursors of the type $(Ph_3Sn)_2Te$.[54] This approach was expanded later with the introduction of cyclic precursors of the type $(Bn_2SnTe)_3$ also to produce cubic SnTe.[71] The homoleptic tin(II) chalcogenolate complexes $Sn[TeSi(SiMe_3)]_2$ were reported by Arnold and co-workers and are suitable as single-source precursors for the synthesis of SnTe materials.[72] The pyrolysis of $Sn[TeSi(SiMe_3)]_2$ at modest temperatures (250 °C) under a nitrogen atmosphere leads to the production of SnTe with the single by-product: $Te[Si(SiMe_3)]_2$. SnTe produced in this manner was characterised by p-XRD and elemental analysis. Decomposition of the precursor in hydrocarbon solvents to the metal chalcogenide could also be elicited by thermolysis, UV irradiation or the presence of Lewis bases, in this instance one equivalent of pyridine, at even lower temperatures than the pyrolysis method. Similar silylated compounds have also been reported by Chuprakov *et al.* of the type $[Sn\{(SiMe_3)_2CH\}_2(\mu\text{-}E)]_2$ (where E = Se or Te) (*vide supra*).[50]

Schlecht *et al.* reported the use of nanocrystalline tin as a template for SnTe nanocrystal growth.[73] The finely divided metal, produced from the reaction of $SnCl_2$ with $Li[Et_3BH]$, was reacted with Ph_2Te_2 in boiling diglyme. Cubic SnTe nanoparticles with diameters of 15–60 nm, characterised by p-XRD, were produced. Nanoparticles with *ca.* 15 nm diameter had star-shaped morphology whilst those of 60 nm diameter were organised in random spherical agglomerates. The diameter and morphology of the particles, was controlled by concentration, with high dilutions favouring the smaller SnTe nanostars.

Tang and co-workers describe a reductive method to SnTe nanoparticles.[74] Reaction of hydrated tin(IV) chloride with potassium borohydride in ethylenediamine led to a grey powder characterised by p-XRD as cubic SnTe. TEM images revealed polydisperse crystals with diameters in the range of 30–40 nm, in agreement estimated diameters calculated from p-XRD using the Scherrer equation. XPS was used to confirm the SnTe stoichiometry. The method was not compatible with tin(II) chloride or solid anhydrous tin(IV) chloride, which led to the formation of elemental tellurium in both cases.

The first examples of *monodisperse* SnTe nanocrystals was reported Talapin and co-workers.[75] The reaction of $Sn[N(SiMe_3)_2]$, with TOP-Te in an oleylamine–octadecene mixture at 150 °C. This precursor has been used for the synthesis of both SnS[30] and SnSe[67] nanoparticles (*vide supra*), and thus the methodology represents a crucial addition to the canon of semiconductor nanocrystal synthesis. SnTe nanocrystals were characterised by p-XRD, imaged with TEM and EDX was used to confirm stoichiometry (Fig. 18). Various sizes were produced

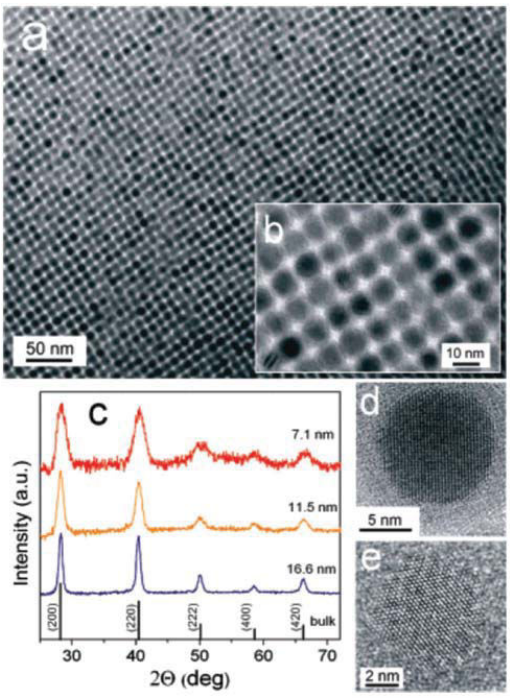

Fig. 18 (a), (b) TEM images of SnTe NCs capped with oleic acid. (c) Powder XRD patterns of SnTe NCs with various sizes. (d), (e) HRTEM of SnTe NCs viewed along [001] and [111] zone axes.[75] Reprinted with permission from Kovalenko *et al.*, *J. Am. Chem. Soc.*, 2007, **129**, 11354–11355. Copyright 2007 American Chemical Society.

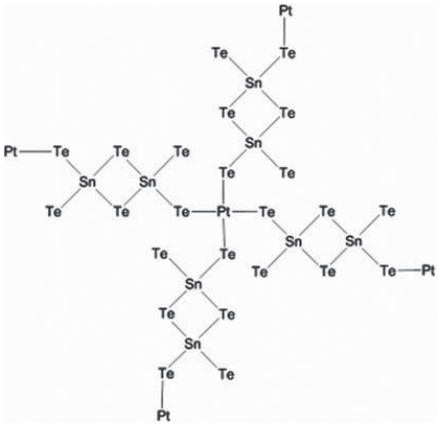

Fig. 22 Platinum tin telluride structure deduced by Riley and Tolbert from EXAFS data.[107]

$SnSe_4^{4-}$ and $SnTe_4^{4-}$.[111] Composites produced had wormlike morphology. Rhodium gave tin telluride materials with hexagonal honeycombed (*P6mm*) habit. Platinum combined with $SnSe_4^{4-}$ gave materials with cubic (*la3d*) architecture. The $SnTe_4^{4-}$ alone, with no metal ions, gave lamellar structures. Thus, the morphology of the materials is easily controllable by judicious choice of metal ion. Recent work has focused on tuning the band gap of these materials with even greater precision.[112]

Hexagonally ordered mesostructured ternary metal tin sulfide materials have been reported by Kanatzidis and coworkers.[113] New mesophases designated as $(CP)_xM_ySn_2S_6$ (where M = Zn^{2+}, Cd^{2+}, Ga^{3+}) were synthesized by linking $Sn_2S_6^{4-}$ clusters with metal ions in the presence of cetylpyridinium (CP) surfactant molecules in formamide solution under basic conditions. The materials are semiconductors in the with band gaps in the energy range 2.5–3.1 eV. Additionally, $(CP)_xM_ySn_2S_6$ exhibits photoluminescence when irradiated with light of energies larger than the band gap.

7. Conclusions

Research into synthetic routes for tin chalcogenides is *currently* flourishing due to a need for efficient and tuneable materials in various applications. The inherent band gap of many of the tin chalcogenides is commensurate with many current ubiquitous and useful semiconductor materials. Quantum confinement effects allow tuning of band gap energies by changing the size of the nanocrystal allowing the formation of tailor-made materials for any given application *e.g.* photovoltaics. Relatively newer alloyed materials such as the copper zinc tin sulfides (CZTS) are providing new opportunities for materials research especially for solar energy applications. The move to nanoscale materials from thin films is essential for tuning the semiconductor properties. A mastery of thin film deposition in this area, which arguably does not exist at the moment, will be the key to the further development of novel nanoscale CZT-chalcogenide materials. Exciting new mesostructured composite materials are being made with novel syntheses, often based on templating by cluster compounds. This area of research will grow ever more important as the search for more efficient, environmentally benign and cheaper semiconducting materials continues.

References

1 H. Xuebo and Z. Jing, in *Nanofabrication and its Application in Renewable Energy*, Royal Society of Chemistry, Cambridge, 2014, pp. 199–215.
2 P. Sinsermsuksakul, L. Sun, S. W. Lee, H. H. Park, S. B. Kim, C. Yang and R. G. Gordon, *Adv. Energy Mater.*, 2014, DOI: 10.1002/aenm.201400496.
3 J. J. Loferski, *J. Appl. Phys.*, 1956, **27**, 777–784.
4 T. Jiang and G. A. Ozin, *J. Mater. Chem.*, 1998, **8**, 1099–1108.
5 O. Madelung, *Semiconductors – Basic Data*, Springer-Verlag, Berlin, 2nd edn, 1996.
6 S. C. Ray, M. K. Karanjai and D. DasGupta, *Thin Solid Films*, 1999, **350**, 72–78.
7 A. Abou Shama and H. M. Zeyada, *Opt. Mater.*, 2003, **24**, 555–561.
8 M. Ristov, G. Sinadinovski, I. Grozdanov and M. Mitreski, *Thin Solid Films*, 1989, **173**, 53–58.
9 P. K. Nair, M. T. S. Nair and J. Campos, *J. Electrochem. Soc.*, 1993, **140**, 539–541.
10 R. D. Engelken, H. E. McCloud, C. Lee, M. Slayton and H. Ghoreishi, *J. Electrochem. Soc.*, 1987, **134**, 2696–2707.
11 A. Tanusevski, *Semicond. Sci. Technol.*, 2003, **18**, 501–505.
12 C. Gao and H. Shen, *Thin Solid Films*, 2012, **520**, 3523–3527.
13 S. K. Arora, D. H. Patel and M. K. Agarwal, *J. Cryst. Growth*, 1993, **131**, 268–270.
14 S. K. Arora, D. H. Patel and M. K. Agarwal, *J. Mater. Sci.*, 1994, **29**, 3979–3983.
15 P. Sinsermsuksakul, J. Heo, W. Noh, A. S. Hock and R. G. Gordon, *Adv. Energy Mater.*, 2011, **1**, 1116–1125.
16 M. Calixto-Rodriguez, H. Martinez, A. Sanchez-Juarez, J. Campos-Alvarez, A. Tiburcio-Silver and M. E. Calixto, *Thin Solid Films*, 2009, **517**, 2497–2499.
17 E. Schonherr and W. Stetter, *J. Cryst. Growth*, 1975, **30**, 96–98.
18 B. P. Bade, S. S. Garje, Y. S. Niwate, M. Afzaal and P. O'Brien, *Chem. Vap. Deposition*, 2008, **14**, 292–295.
19 T. G. Hibbert, M. F. Mahon, K. C. Molloy, L. S. Price and I. P. Parkin, *J. Mater. Chem.*, 2001, **11**, 469–473.
20 L. S. Price, I. P. Parkin, T. G. Hibbert and K. C. Molloy, *Chem. Vap. Deposition*, 1998, **4**, 222–225.
21 A. Sanchez-Juarez, A. Tiburcio-Silver and A. Ortiz, *Thin Solid Films*, 2005, **480–481**, 452–456.

22 M. Lazell, P. O'Brien, D. J. Otway and J. H. Park, *J. Chem. Soc., Dalton Trans.*, 2000, 4479–4486.
23 M. A. Malik, M. Afzaal and P. O'Brien, *Chem. Rev.*, 2010, **110**, 4417–4446.
24 G. Barone, T. G. Hibbert, M. F. Mahon, K. C. Molloy, L. S. Price, I. P. Parkin, A. M. E. Hardy and M. N. Field, *J. Mater. Chem.*, 2001, **11**, 464–468.
25 I. P. Parkin, L. S. Price, T. G. Hibbert and K. C. Molloy, *J. Mater. Chem.*, 2001, **11**, 1486–1490.
26 A. T. Kana, T. G. Hibbert, M. F. Mahon, K. C. Molloy, I. P. Parkin and L. S. Price, *Polyhedron*, 2001, **20**, 2989–2995.
27 K. Ramasamy, V. L. Kuznetsov, K. Gopal, M. A. Malik, J. Raftery, P. P. Edwards and P. O'Brien, *Chem. Mater.*, 2013, **25**, 266–276.
28 H. L. Zhu, D. R. Yang, Y. J. Ji, H. Zhang and X. F. Shen, *J. Mater. Sci.*, 2005, **40**, 591–595.
29 C. An, K. Tang, G. Shen, C. Wang, Q. Yang, B. Hai and Y. Qian, *J. Cryst. Growth*, 2002, **244**, 333–338.
30 S. G. Hickey, C. Waurisch, B. Rellinghaus and A. Eychmüller, *J. Am. Chem. Soc.*, 2008, **130**, 14978–14980.
31 Y. K. Liu, D. D. Hou and G. H. Wang, *Chem. Phys. Lett.*, 2003, **379**, 67–73.
32 G. Z. Shen, D. Chen, K. B. Tang, L. Y. Huang, Y. T. Qian and G. Zhou, *Inorg. Chem. Commun.*, 2003, **6**, 178–180.
33 A. J. Biacchi, D. D. Vaughn and R. E. Schaak, *J. Am. Chem. Soc.*, 2013, **135**, 11634–11644.
34 H. Liu, Y. Liu, Z. Wang and P. He, *Nanotechnology*, 2010, **21**, 105707.
35 Y. Xu, N. Al-Salim, C. W. Bumby and R. D. Tilley, *J. Am. Chem. Soc.*, 2009, **131**, 15990.
36 S. Sohila, M. Rajalakshmi, C. Muthamizhchelvan, S. Kalavathi, C. Ghosh, R. Divakar, C. N. Venkiteswaran, N. G. Muralidharan, A. K. Arora and E. Mohandas, *Mater. Lett.*, 2011, **65**, 1148–1150.
37 S. Sohila, M. Rajalakshmi, C. Ghosh, A. K. Arora and C. Muthamizhchelvan, *J. Alloys Compd.*, 2011, **509**, 5843–5847.
38 Y. Zhang, J. Lu, S. Shen, H. Xu and Q. Wang, *Chem. Commun.*, 2011, **47**, 5226–5228.
39 Q. Han, M. Wang, J. Zhu, X. Wu, L. Lu and X. Wang, *J. Alloys Compd.*, 2011, **509**, 2180–2185.
40 J. Ning, K. Men, G. Xiao, L. Wang, Q. Dai, B. Zou, B. Liu and G. Zou, *Nanoscale*, 2010, **2**, 1699–1703.
41 M. Yousefi, M. Salavati-Niasari, F. Gholamian, D. Ghanbari and A. Aminifazl, *Inorg. Chim. Acta*, 2011, **371**, 1–5.
42 D. D. Vaughn II, O. D. Hentz, S. Chen, D. Wang and R. E. Schaak, *Chem. Commun.*, 2012, **48**, 5608–5610.
43 B. K. Patra, S. Sarkar, A. K. Guria and N. Pradhan, *J. Phys. Chem. Lett.*, 2013, **4**, 3929–3934.
44 E. C. Greyson, J. E. Barton and T. W. Odom, *Small*, 2006, **2**, 368–371.
45 Z. T. Deng, D. R. Han and Y. Liu, *Nanoscale*, 2011, **3**, 4346–4351.
46 L. Ren, Z. Jin, W. Wang, H. Liu, J. Lai, J. Yang and Z. Hong, *Appl. Surf. Sci.*, 2011, **258**, 1353–1358.
47 I. Lefebvre, M. A. Szymanski, J. Olivier-Fourcade and J. C. Jumas, *Phys. Rev. B: Condens. Matter*, 1998, **58**, 1896–1906.
48 J. P. Singh and R. K. Bedi, *Thin Solid Films*, 1991, **199**, 9–12.
49 K. J. John, B. Pradeep and E. Mathai, *J. Mater. Sci.*, 1994, **29**, 1581–1583.
50 I. S. Chuprakov, K. H. Dahmen, J. J. Schneider and J. Hagen, *Chem. Mater.*, 1998, **10**, 3467–3470.
51 N. D. Boscher, C. J. Carmalt, R. G. Palgrave and I. P. Parkin, *Thin Solid Films*, 2008, **516**, 4750–4757.
52 R. Indirajith, T. P. Srinivasan, K. Ramamurthi and R. Gopalakrishnan, *Curr. Appl. Phys.*, 2010, **10**, 1402–1406.
53 S. R. Bahr, P. Boudjouk and G. J. McCarthy, *Chem. Mater.*, 1992, **4**, 383–388.
54 P. Boudjouk, D. J. Seidler, S. R. Bahr and G. J. McCarthy, *Chem. Mater.*, 1994, **6**, 2108–2112.
55 P. Boudjouk, D. J. Seidler, D. Grier and G. J. McCarthy, *Chem. Mater.*, 1996, **8**, 1189–1196.
56 Y. Cheng, T. J. Emge and J. G. Brennan, *Inorg. Chem.*, 1996, **35**, 342–346.
57 R. K. Sharma, G. Kedarnath, A. Wadawale, C. A. Betty, B. Vishwanadh and V. K. Jain, *Dalton Trans.*, 2012, **41**, 12129–12138.
58 N. Kumar, V. Sharma, U. Parihar, R. Sachdeva, N. Padha and C. J. Panchal, *J. Nano- Electron. Phys.*, 2011, **3**, 117–126.
59 C. Wang, Y. D. Li, G. H. Zhang, J. Zhuang and G. Q. Shen, *Inorg. Chem.*, 2000, **39**, 4237–4239.
60 B. Pejova and I. Grozdanov, *Thin Solid Films*, 2007, **515**, 5203–5211.
61 B. Pejova and A. Tanusevski, *J. Phys. Chem. C*, 2008, **112**, 3525–3537.
62 D. D. Vaughn II, S.-I. In and R. E. Schaak, *ACS Nano*, 2011, **5**, 8852–8860.
63 S. Liu, X. Guo, M. Li, W.-H. Zhang, X. Liu and C. Li, *Angew. Chem., Int. Ed.*, 2011, **50**, 12050–12053.
64 M. Achimovicova, A. Recnik, M. Fabian and P. Balaz, *Acta Montan. Slovaca*, 2011, **16**, 123–127.
65 M. Achimovicova, K. L. da Silva, N. Daneu, A. Recnik, S. Indris, H. Hain, M. Scheuermann, H. Hahn and V. Sepelak, *J. Mater. Chem.*, 2011, **21**, 5873–5876.
66 X. Yu, J. Zhu, Y. Zhang, J. Weng, L. Hu and S. Dai, *Chem. Commun.*, 2012, **48**, 3324–3326.
67 W. J. Baumgardner, J. J. Choi, Y.-F. Lim and T. Hanrath, *J. Am. Chem. Soc.*, 2010, **132**, 9519–9521.
68 M. A. Franzman, C. W. Schlenker, M. E. Thompson and R. L. Brutchey, *J. Am. Chem. Soc.*, 2010, **132**, 4060–4061.
69 T. Chattopadhyay, H. G. Vonschnering, W. A. Grosshans and W. B. Holzapfel, *Physica B+C*, 1986, **139**, 356–360.
70 G. Sharma, P. Bhambhani, N. Munjal, V. Sharma and B. K. Sharma, *J. Nano- Electron. Phys.*, 2011, **3**, 341–347.
71 P. Boudjouk, M. P. Remington, D. G. Grier, W. Triebold and B. R. Jarabek, *Organometallics*, 1999, **18**, 4534–4537.

72 A. L. Seligson and J. Arnold, *J. Am. Chem. Soc.*, 1993, **115**, 8214–8220.
73 S. Schlecht, M. Budde and L. Kienle, *Inorg. Chem.*, 2002, **41**, 6001–6005.
74 C. An, K. Tang, B. Hai, G. Shen, C. Wang and Y. Qian, *Inorg. Chem. Commun.*, 2003, **6**, 181–184.
75 M. V. Kovalenko, W. Heiss, E. V. Shevchenko, J.-S. Lee, H. Schwinghammer, A. P. Alivisatos and D. V. Talapin, *J. Am. Chem. Soc.*, 2007, **129**, 11354–11355.
76 J. Ning, K. Men, G. Xiao, B. Zou, L. Wang, Q. Dai, B. Liu and G. Zou, *CrystEngComm*, 2010, **12**, 4275–4279.
77 M. Salavati-Niasari, M. Bazarganipour, F. Davar and A. A. Fazl, *Appl. Surf. Sci.*, 2010, **257**, 781–785.
78 Y. Xu, N. Al-Salim, J. M. Hodgkiss and R. D. Tilley, *Cryst. Growth Des.*, 2011, **11**, 2721–2723.
79 I. T. Sines, D. D. Vaughn II, A. J. Biacchi, C. E. Kingsley, E. J. Popczun and R. E. Schaak, *Chem. Mater.*, 2012, **24**, 3088–3093.
80 K. Ramasamy, M. A. Malik and P. O'Brien, *Chem. Commun.*, 2012, **48**, 5703–5714.
81 D. A. R. Barkhouse, O. Gunawan, T. Gokmen, T. K. Todorov and D. B. Mitzi, *Prog. Photovoltaics*, 2012, **20**, 6–11.
82 T. K. Todorov, J. Tang, S. Bag, O. Gunawan, T. Gokmen, Y. Zhu and D. B. Mitzi, *Adv. Energy Mater.*, 2013, **3**, 34–38.
83 S. Chen, A. Walsh, Y. Luo, J. H. Yang, X. G. Gong and S. H. Wei, *Phys. Rev. B: Condens. Matter*, 2010, **82**, 195203.
84 A. Singh, H. Geaney, F. Laffir and K. M. Ryan, *J. Am. Chem. Soc.*, 2012, **134**, 2910–2913.
85 A. Khare, A. W. Wills, L. M. Ammerman, D. J. Norris and E. S. Aydil, *Chem. Commun.*, 2011, **47**, 11721–11723.
86 M. D. Regulacio, C. Ye, S. H. Lim, M. Bosman, E. Ye, S. Chen, Q.-H. Xu and M.-Y. Han, *Chem. – Eur. J.*, 2012, **18**, 3127–3131.
87 A. Fischereder, A. Schenk, T. Rath, W. Haas, S. Delbos, C. Gougaud, N. Naghavi, A. Pateter, R. Saf, D. Schenk, M. Edler, K. Bohnemann, A. Reichmann, B. Chernev, F. Hofer and G. Trimmel, *Monatsh. Chem.*, 2013, **144**, 273–283.
88 H. Jiang, P. Dai, Z. Feng, W. Fan and J. Zhan, *J. Mater. Chem.*, 2012, **22**, 7502–7506.
89 A. Shavel, D. Cadavid, M. Ibanez, A. Carrete and A. Cabot, *J. Am. Chem. Soc.*, 2012, **134**, 1438–1441.
90 S. C. Riha, B. A. Parkinson and A. L. Prieto, *J. Am. Chem. Soc.*, 2011, **133**, 15272–15275.
91 Z. Su, C. Yan, D. Tang, K. Sun, Z. Han, F. Liu, Y. Lai, J. Li and Y. Liu, *CrystEngComm*, 2012, **14**, 782–785.
92 Q. Tian, X. Xu, L. Han, M. Tang, R. Zou, Z. Chen, M. Yu, J. Yang and J. Hu, *CrystEngComm*, 2012, **14**, 3847–3850.
93 S. K. Saha, A. Guchhait and A. J. Pal, *Phys. Chem. Chem. Phys.*, 2012, **14**, 8090–8096.
94 K. Ramasamy, M. A. Malik and P. O'Brien, *Chem. Sci.*, 2011, **2**, 1170–1172.
95 J. Rouquerol, D. Avnir, C. W. Fairbridge, D. H. Everett, J. H. Haynes, N. Pernicone, J. D. F. Ramsay, K. S. W. Sing and K. K. Unger, *Pure Appl. Chem.*, 1994, **66**, 1739–1758.
96 M. G. Kanatzidis, *Adv. Mater.*, 2007, **19**, 1165–1181.
97 T. Jiang, A. Lough, G. A. Ozin and R. L. Bedard, *J. Mater. Chem.*, 1998, **8**, 733–741.
98 T. Jiang, A. Lough, G. A. Ozin, R. L. Bedard and R. Broach, *J. Mater. Chem.*, 1998, **8**, 721–732.
99 T. Jiang, G. A. Ozin and R. L. Bedard, *J. Mater. Chem.*, 1998, **8**, 1641–1648.
100 T. Jiang, G. A. Ozin, A. Verma and R. L. Bedard, *J. Mater. Chem.*, 1998, **8**, 1649–1656.
101 T. Jiang and G. A. Ozin, *J. Mater. Chem.*, 1997, **7**, 2213–2222.
102 I. Sokolov, T. Jiang and G. A. Ozin, *Adv. Mater.*, 1998, **10**, 942–946.
103 Neeraj and C. N. R. Rao, *J. Mater. Chem.*, 1998, **8**, 279–280.
104 J. Li, L. Delmotte and H. Kessler, *Chem. Commun.*, 1996, 1023–1024.
105 J. Q. Li, H. Kessler and L. Delmotte, *J. Chem. Soc., Faraday Trans.*, 1997, **93**, 665–668.
106 J. Q. Li and H. Kessler, *Microporous Mater.*, 1997, **9**, 141–147.
107 A. E. Riley and S. H. Tolbert, *J. Am. Chem. Soc.*, 2003, **125**, 4551–4559.
108 B. Hasenknopf, J.-M. Lehn, B. O. Kneisel, G. Baum and D. Fenske, *Angew. Chem., Int. Ed. Engl.*, 1996, **35**, 1838–1840.
109 M. J. MacLachan, N. Coombs and G. A. Ozin, *Nature*, 1999, **397**, 681.
110 S. D. Korlann, A. E. Riley, B. L. Kirsch, B. S. Mun and S. H. Tolbert, *J. Am. Chem. Soc.*, 2005, **127**, 12516–12527.
111 A. E. Riley, S. D. Korlann, E. K. Richman and S. H. Tolbert, *Angew. Chem., Int. Ed.*, 2006, **45**, 235–241.
112 S. D. Korlann, A. E. Riley, B. S. Mun and S. H. Tolbert, *J. Phys. Chem. C*, 2009, **113**, 7697–7705.
113 K. K. Rangan, P. N. Trikalitis, C. Canlas, T. Bakas, D. P. Weliky and M. G. Kanatzidis, *Nano Lett.*, 2002, **2**, 513–517.